NUREG/CR—4805 (2 of 2)
SAND86—2752 (2 of 2)
R3, R5, R7
Printed November 1987

Reactor Safety Research Semiannual Report July – December 1986 Volume 36

Reactor Safety Research Department 6420

Prepared by
Sandia National Laboratories
Albuquerque, New Mexico 87185 and Livermore, California 94550
for the United States Department of Energy
under Contract DE-AC04-76DP00789

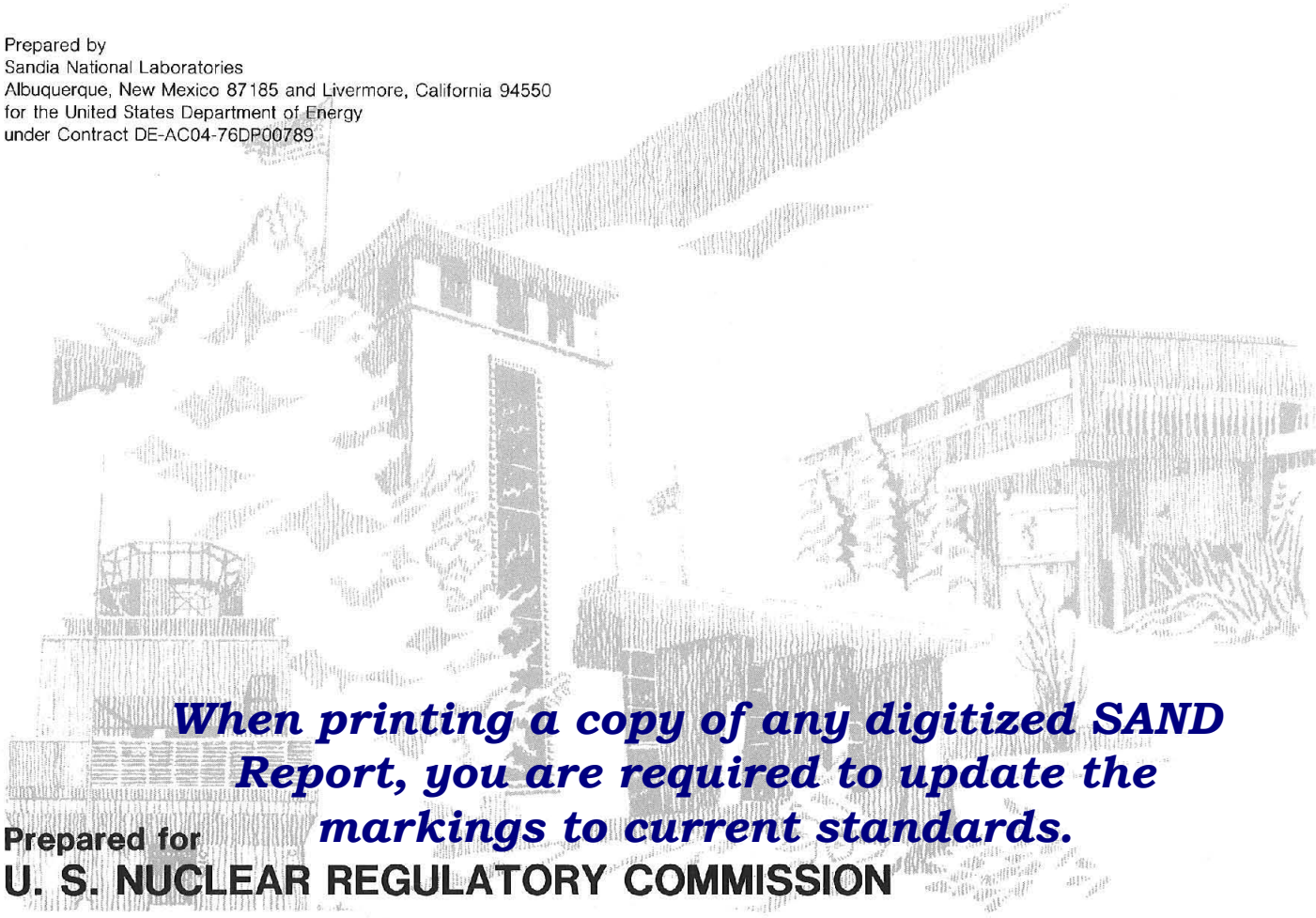

Prepared for
U. S. NUCLEAR REGULATORY COMMISSION

Available from

Superintendent of Documents
U.S. Government Printing Office
Post Office Box 37082
Washington, D.C. 20013-7082

and

National Technical Information Service
Springfield, VA 22161

NUREG/CR-4805 (2 of 2)
SAND86-2752 (2 of 2)
Vol. 36
R3, R5, R7

REACTOR SAFETY RESEARCH SEMIANNUAL REPORT
July-December 1986

Reactor Safety Research Program

Printed November 1987

APPROVED:

Manager, Reactor Safety Research

Director, Nuclear Regulatory Research

Sandia National Laboratories
Albuquerque, NM 87185
Operated by
Sandia Corporation
for the
U.S. Department of Energy

Prepared for
Division of Accident Evaluation
Office of Nuclear Regulatory Research
U.S. Nuclear Regulatory Commission
Washington, DC 20555
Under Memorandum of Understanding DOE 40-550-75
NRC FINs (A1016, A1019, A1030, D1124, A1181, A1218,
A1227, A1246, A1263, A1264, A1335, A1336, A1340,
A1342, A1383, A1385, A1389, A1390)

FOREWORD

Sandia National Laboratories is conducting, under U.S. Nuclear Regulatory Commission sponsorship, phenomenological research related to the safety of commercial nuclear power reactors. The research includes experiments to simulate the phenomenology of accident conditions and the development of analytical models, verified by experiment, which can be used to predict reactor and safety systems performance behavior under abnormal conditions. The objective of this work is to provide NRC requisite data bases and analytical methods to (1) identify and define safety issues, (2) understand the progression of risk-significant accident sequences, and (3) conduct safety assessments. The collective NRC-sponsored effort at Sandia National Laboratories is directed at enhancing the technology base supporting licensing decisions.

CONTENTS

CONTENTS (Continued)

CONTENTS (Continued)

CONTENTS (Concluded)

LIST OF FIGURES

LIST OF FIGURES (Continued)

LIST OF FIGURES (Continued)

LIST OF FIGURES (Continued)

LIST OF FIGURES (Continued)

LIST OF FIGURES (Continued)

LIST OF FIGURES (Continued)

LIST OF FIGURES (Concluded)

LIST OF TABLES

NOMENCLATURE

ACRR	-Annular Core Research Reactor
AICC	-Adiabatic Isochoric Complete Combustion
APS	-Aerodynamic Particle Sizer
BCL	-Battelle Columbus Laboratories
BNL	-Brookhaven National Laboratories
BWR	-Boiling Water Reactor
CDA	-Core Disruptive Accident
CMCI	-Core Melt-Coolant Interaction
CORCON	-Core/Concrete Interaction Code
DCC	-Degraded Core Coolability
DCH	-Direct Containment Heating
DF	-Damaged Fuel
DFR	-Debris Formation and Relocation
ECCS	-Emergency Core Cooling System
EDX	-Energy Dispersive X-Ray
EURATOM	-European Atomic Energy Community
EXO-FITS	-Outside of Fully Instrumented Test Sites
FCI	-Fuel-Coolant Interaction
FITS	-Fully Instrumented Test Sites
FLAME	-Flame Acceleration Measurements and Experiments
FRG	-Federal Republic of Germany
FPRF	-Fission Product Reaction Facility
HCDA	-Hypothetical Core Disruptive Accident
HDT	-Heated Detonation Tube
HECTR	-Hydrogen Event: Containment Transient Response
HEDL	-Hanford Engineering Development Laboratory
HIPS	-High-Pressure Melt Ejection and Direct Containment Heating
HPIS	-High-Pressure Injection System
HPME	-High-Pressure Melt Ejection
IC	-Ion Chromatography
IDCOR	-Industry Degraded Core Rulemaking
IFCI	-Integrated Fuel Coolant Interaction
IRIS	-Inductive Ring Susceptor Technique
ISE	-Ion Specific Electrode
KfK	-Kernforschungszentrum Karlsruhe
LANL	-Los Alamos National Laboratory
LCS	-Limestone/Common Sand
LMF	-Large Melt Facility
LMFBR	-Liquid Metal Fast Breeder Reactor
LOAC	-Loss of Coolant Accident
LOF	-Loss of Flow
LWR	-Light Water Reactor
MAAP	-Modular Accident Analysis Program
MELPROG	-Melt Progression Code
NRC	-Nuclear Regulatory Commission
NTS	-Nevada Test Site
ORNL	-Oak Ridge National Laboratory
PIE	-Postirradiation Examination
PIXE	-Photon Induced X-Ray Emission

NOMENCLATURE (Concluded)

PRA	-Probabilistic Risk Assessment
PWR	-Pressurized Water Reactor
QUEST	-Quantitative Uncertainty Evaluation for the Source Term
RCS	-Reactor Coolant System
RSR	-Reactor Safety Research
RPV	-Reactor Pressure Vessel
S/A	-Subassembly
SARRP	-Severe Accident Risk Rebaselining Program
SASA	-Severe Accident Sequence Analysis
SEALS	-Steam Explosions at Large Scale
SEM	-Scanning Electron Microscope
SFD	-Severe Fuel Damage
SHE	-Straight High Explosive
SPIT	-System Pressure Injection Test
ST	-Source Term
SURC	-Sustained Urania-Concrete Interactions
SWISS	-Sustained Water Interactions With Stainless Steel
TEXAS	-Thermal Explosion Analysis System
TGT	-Thermal Gradient Tube
TMBDB	-Thermal Margin Beyond Design Basis
TRAN	-Transition Phase
TURC	-Transient Urania Concrete
UT	-Ultrasonic Thermometer
VGES	-Variable Geometry Experimental System
WDX	-Wavelength Dispersive Analysis
XRD	-X-Ray Diffraction
XRF	-X-Ray Fluorescence

EXECUTIVE SUMMARY

1. CONTAINMENT LOADING AND RESPONSE

The containment of a reactor is the last barrier that prevents radionuclide release to the environment during a severe reactor accident. Considerable priority is given to understanding the accident phenomena that may threaten the integrity of reactor containments. Direct containment heating caused by pressure-driven expulsion of melt from the reactor vessel and the interactions of core debris with structural concrete have been identified as two important, ex-vessel phenomena that may place significant loads on reactor containments. These phenomena would also be important contributors to possible radionuclide release to the environment. Fuel-coolant interactions (FCIs) have also been identified as a mechanism that, within our current uncertainties, may result in direct containment damage either by driving a missile through the containment dome (alpha-mode failure) or by failing the pedestal supporting wall by an ex-vessel steam explosion in BWR Mark II or III containments. FCIs can also affect containment loads and accident consequences by their influences on the rapid generation of hydrogen and steam, the fragmentation and dispersal of molten fuel, the release of fission products, the mode of vessel failure, and the particle sizes of resulting debris beds. Combustion of hydrogen can lead to direct containment failure due to quasi-static (deflagrations) or dynamic (accelerated flames and detonations) loads. High temperatures generated during combustion may also pose a threat to the survivability of key safety equipment. Research continues to quantify these potential containment threats so that individual plant vulnerabilities may be identified.

Highlights of recent experimental research on these phenomena are described in this report. The recent developments in models of core debris interactions with concrete--CORCON and VANESA--are also described. The experimental results are not only being used to support model development for CORCON and VANESA, but also for the integrated systems containment code, CONTAIN, and the melt progression code, MELPROG. FCI experiments are under way to investigate the behavior of single and multiple molten fuel jets pouring through water and to determine the rates of generation of hydrogen and steam. Based on these experiments, phenomenological models are being developed and incorporated into the MELPROG module, IFCI; development, applications, and assessment of this module is an active area of FCI research. Hydrogen detonation experiments are being completed in the Heated Detonation Tube. The ZND model is being assessed against these data and extrapolated to estimate detonability in untested regions of high temperature and high steam concentration. Work is also continuing on the development and validation of the HECTR code. HECTR combustion models are being incorporated into CONTAIN as soon as feasible.

1.1 Sustained Core Debris-Concrete Interactions

The SURC3 experiment was executed on August 21, 1986. This 50-kg Fe-Zr test was designed to examine the additional effects of Zr metal oxidation on the heat transfer mechanisms, gas release chemistry, and aerosol release caused by sustained steel-limestone concrete interactions to which fission products had been added. Four substantive observations were made:

1. Zr addition greatly increased limestone concrete ablation, flammable gas production, and aerosol release.

2. Steady melt pool temperatures of greater than 1900 K were measured throughout the test.

3. Copious aerosol production accompanied the entire melt-concrete reaction. These aerosols were mostly comprised of Te with only small amounts of Ca.

4. No evidence of intense carburization (coking) during the Zr reaction was observed.

In addition to the SURC3 test results, a summary of the current understanding of combustible gas generation during core debris interactions with concrete is presented. Generation of hydrogen and carbon monoxide during a core debris-concrete interaction is the result of chemical reactions of the steam and carbon dioxide produced during concrete pyrolysis with the metallic phases of core debris. The extent of reaction varies with the composition of the core debris. When either Zr or C is present, reactions are nearly complete. Once these reactive constituents are depleted and the metal phase is primarily steel, the reaction may be limited to 50 to 90 percent completion. Water poured over core debris interacting with concrete has been found to neither quench the melt and arrest hydrogen production nor to contribute significantly to hydrogen production.

1.2 High-Pressure Melt Ejection and Direct Containment Heating

Descriptions of high-pressure melt ejection accident phenomena have assumed that the sequence of events in the cavity is initiated by failure of one or more of the instrument tubes penetrating the lower head of the reactor pressure vessel (RPV). This critical aspect of the accident and the events following have not been studied extensively by analyses or experiments. The location, timing, and failure mode of the primary system affects the disposition of core debris in the reactor cavity, containment loads, and the aerosol source term.

Analyses indicate that global creep-rupture of the lower head competes with ablation of the weldment retaining the instrument tubes. The current results are unclear as to which event will occur first. Failure of the primary coolant system may also occur in other locations such as the upper head bolts, hot leg nozzles, steam generator tubes, pump seals, etc. Relieving the pressure in the primary system prior to failure of an instrument tube will then reduce the motive power for debris ejection into the cavity. Debris in the lower RPV head may also cause thermal stresses that exceed the strength of the vessel resulting in a catastrophic failure of the RPV. Creep of the material, however, may limit the induced stress and eliminate thermal stress fracture as a failure mechanism.

Heating of the lower head will cause thermal expansion of the vessel components. Because the instrument tubes are a different material than the head, differential expansion may cause the tubes to be retained in the head even after the weld is failed. If this is the situation, high-pressure

ejection of the debris will be averted until such time that distortion of the lower head may release the tube. The MELPROG Validation Experiment program is performing tests to investigate the failure mechanism for these circumstances.

More sophisticated analyses have been initiated of the stresses in the lower RPV head at accident conditions. The data from these calculations will be coupled with the thermal predictions to determine the condition of the critical components. The results will be used to determine the adequacy of the present direct containment heating (DCH) test strategy and to guide the development of codes to model vessel behavior for accident predictions.

Modern reactor accident analyses recognize that core degradation may occur within a pressurized reactor coolant system and that core debris may be expelled from the system followed by the violent depressurization of the system. Experiments have shown that during the depressurization process, the expelled core debris can be entrained as small droplets. These droplets can react with the atmosphere. Early considerations focused on the debris transport into the containment compartments and the heating loads placed on the containment by these reactions. More recently our attentions were directed toward the immediate reactions of the entrained droplets with steam in the blowdown gases to form hydrogen as predicted by recent CONTAIN code calculations. The threat to containment integrity posed by the pressure-driven expulsion of the core debris appears to be, by current understanding, the hydrogen source term rather than debris dispersal.

1.3 CORCON and VANESA Code Development

Past comparisons of CORCON-Mod2 calculations to the results of experiments at Sandia and Kerforschungzentrum Karlsruhe (KfK) have demonstrated that the heat transfer models in the code need to be modified. Substantial effort has been devoted to the development of improved models for this very important aspect of core-concrete interactions.

Recently, an improved heat transfer model has been developed that accurately represents both the Sandia and KfK experiments. The model assumes that intermittent contact between the molten core material and the concrete takes place throughout the interaction. (Previously, CORCON has assumed that a stable gas film forms and then remains throughout the interaction.) This assumption is based on classical film stability analyses, which show that the gas fluxes most likely to be encountered during a core-concrete interaction are far below what is required to produce a stable film. Upon contact, simultaneous melting of the concrete surface and solidification of the molten core material are possible. Coincident with this is the growth of bubbles at the interface due to the release of concrete decomposition gases. When the bubbles depart from the surface they remove concrete slag and may fragment any crust that has been formed. Subsequently, new molten material contacts the concrete surface and the cycle is repeated.

This complex process has been analyzed for the limiting cases of molten steel on hot and cold concrete and molten oxide on hot and cold concrete.

The results of these analyses have been incorporated into a set of equations for the effective heat transfer coefficient due to the slag/crust growth and removal processes, and these equations have been added to a working version of CORCON. Comparisons between calculations made using the revised version of CORCON and the results of the Sandia and KfK experiments have been excellent. Although validation of the new heat transfer models is still required for oxidic melts, and work remains in other areas of the code, the new heat transfer model represents a major step toward the goal of a validated, mechanistic version of CORCON that can be used with confidence in the analysis of severe reactor accidents.

The first two correction sets for CORCON-Mod2 (Version 2.00) were released to code users during the last six months. The first correction set corrected coding errors that had been identified since the original release of the code. Only a few minor model changes were included in this package and as a result, the corrections had very little effect on the results from several sample calculations. Version 2.01 was created by implementation of this correction set. The second correction set was a substantial modification of the decay heat package in the code. This change was required since the old decay heat calculation significantly overestimated decay power during the first two hours after reactor shutdown. However, even in sample calculations in which core-concrete interactions began during the first two hours following shutdown calculated results using the old and new decay heat packages were not dramatically different. Implementation of this correction set created Version 2.02 of the code.

1.4 Molten Fuel-Coolant Interactions

Previous analysis and also observations inside the Three Mile Island-Unit 2 reactor core indicate that a likely mode of molten fuel-coolant contact is through jets rather than one coherent pour. We have thus begun an extensive investigation of the coarse-mixing characteristics of jets of molten fuel falling through water. We have conducted four series of experiments that address the important phenomena associated with liquid-jet mixing. The fours series are (1) jets of molten iron-alumina falling through air, (2) jets of water falling through air, (3) jets of molten iron-alumina falling through water, and (4) isothermal Freon jets falling through water. As a result of these studies, we have concluded that small-scale liquid-liquid jets, which make up a considerable portion of the existing data base, are not representative of reactor-scale jet behavior. Furthermore, data for liquid jets injected into a gaseous atmosphere should not be used blindly to predict the coarse mixing of a corium-water system. From the isothermal liquid-liquid jet experiments, we also found that the center line velocity profile follows self-similar buoyant gas-gas flows in the buoyancy-dominated regime, provided a new empirical constant is calculated. Further, these large-scale liquid-liquid jets spread linearly with depth in the buoyancy-dominated regime.

As a result of these experimental series, we believe that if the temperature of the jet material is well above the saturation temperature of the coolant, the jet breakup is affected (and possibly dominated) by the generation and flow of steam. The water subcooling also appears to be important, affecting the timing and rate of jet fragmentation. Comparison of

the isothermal and boiling-jet data shows that very different breakup mechanisms occur, and therefore, neither liquid-gas or isothermal liquid-liquid jet data should be directly extrapolated to predict the fragmentation behavior of molten jets falling through water.

We have made significant progress with the Integrated Fuel-Coolant Interactions (IFCI) code. Many numerical and analytical approaches have been taken in this modeling effort. We have begun to develop and incorporate dynamic fragmentation and surface-area transport models into IFCI. This fragmentation model is a time-dependent model which calculates the characteristic melt diameter as a function of instantaneous hydrodynamic conditions. Currently, the code is operational, and we have begun the first "integrated" calculation by modeling a generic FITS-D experiment.

We also have begun to model the propagation of a steam explosion using our one-dimensional code (TEXAS). In this work we are beginning to investigate the physics governing the explosive fragmentation of centimeter-sized particles down to micron-sized particles and the subsequent propagation and escalation to neighboring particles. Although this work was recently begun and no firm conclusions can be drawn, the code is operational and we have begun to evaluate three different drop-fragmentation models. The knowledge gained from this work will lead to the incorporation of a fragmentation model into the IFCI code.

1.5 Hydrogen Behavior

The objectives of this research program are (1) to quantify the threat, if any, to nuclear power plants (containment structure, safety equipment, and the primary system) posed by hydrogen combustion; (2) to disseminate information on hydrogen behavior, detection, control, and disposal; and (3) to provide program management and technical assistance to the NRC on hydrogen-related matters.

A comparison was made between the HECTR code and the MAAP (Modular Accident Analysis Program) code to determine the impact of differences in results and to assist the NRC in determining the acceptability of the codes for performing risk assessment. For an S2HF accident sequence in a PWR ice condenser, the HECTR analysis predicted incomplete in-cavity oxidation with a subsequent accumulation and combustion of hydrogen and carbon monoxide in the upper and lower compartments, which posed an early threat to containment. The MAAP analysis, on the other hand, predicted complete in-cavity combustion, which did not pose an early threat to containment. The discrepancy is a result of too few control volumes used in the MAAP analysis. The small number of control volumes overpredicts the supply of oxygen to the cavity and results in complete oxidation. Another difference between the two codes is that the MAAP ignition criterion does not consider any steam-inerting effect, while the HECTR criterion considers the mixture inert for steam concentrations greater than 55 percent. While the effect of ignition criteria differences was minor in this problem because of insufficient oxygen supply in the cavity, the steam-inerting effect could be quite important if there were a sufficient supply of oxygen.

A new computational model was formulated for large-scale flames and was used to simulate the FLAME F-23 flame acceleration experiment. While the computed pressures agreed well with experimentally measured pressures at the locations where the computed flame speed approximately coincided with the experimental flame speed, there were some significant discrepancies in the flame trajectory. The simulation also provides insight into the processes accompanying flame acceleration in the FLAME facility experiments.

Six tests have been completed in the Heated Detonation Tube in the current hydrogen-air-steam series. The purpose of this test series is to quantify the effect of steam concentration on hydrogen-air mixtures at 1 atm initial pressure and 100°C initial temperature. These initial conditions are at the lower range of initial conditions calculated in a local detonation study.

1.6 Hydrogen Mitigative and Preventive Schemes

We have performed seven "add-on" experiments in two large combustion facilities to investigate the capability of hydrogen burns to remove simulated structural and fission-product aerosols previously deposited on small metal discs that have surfaces prototypical of those found in nuclear reactor containments. Our results suggest that hydrogen combustion provides an especially effective mechanism for removal (and, presumably, resuspension) of sedimented aerosols produced in a hypothetical nuclear reactor core-degradation or core-melting accident. The presence of condensing steam does not seem to assure adhesion of sedimented aerosols during hydrogen burns. Differences are exhibited between different surfaces as well as between types of aerosols. In-depth studies will be required to assess the impact that an exposure of sedimented aerosols to hydrogen burns might have on the radiological source term.

2. FISSION-PRODUCT SOURCE TERM

The High-Temperature Fission-Product Chemistry program provides experimental data on the thermodynamics and kinetics of chemical processes affecting the chemical form of released radionuclides, the interactions of these radionuclides with structural and aerosol surfaces, and the revaporization of deposited radionuclides. The ACRR Source Term Experiments are in-pile tests of radionuclide release under high-pressure, high-radiation intensity, and high hydrogen concentration conditions. They supplement out-of-pile experiments of radionuclide release being conducted elsewhere in the NRC-sponsored research. Both experimental programs provide crucial data needed for accident models. The primary thrusts of the experimental programs are to provide data for the development and validation of the NRC's best-estimate model of fission-product behavior, VICTORIA.

2.1 High-Temperature Fission-Product Chemistry and Transport

The reaction of CsOH vapor with 304SS in steam and hydrogen has been studied over a range of conditions that includes those that are thought to have existed during the TMI-2 accident. In all cases, the cesium reaction product existed in the inner oxide formed on the steel. Where a correlation could be established, it was between cesium and silicon (as silica). In a few of these cases, where the reaction had gone to completion, the product was identified as $Cs_2Si_4O_9$. A model was developed for the kinetics of this reaction as controlled by the temperature, oxide growth, and availability of CsOH. A similar reaction between cesium and silicon was observed to have occurred in the TMI-2 accident.

Results of early work showed CsI to be quite stable in a steam environment in the presence of structural materials. CsI instability was first observed in a radiation field and was attributed to the ionizing radiation. Subsequent experiments have shown that this instability can be produced by purely thermal effects. The magnitude of the instability varies from test to test. Some pattern to the instability may be obtained by examining the kinetics of the reaction of the cesium-bearing compound resulting from decomposition.

Surface reaction rate constants for CsOH and CsI in these accident environments are presented for use in severe accident codes such as TRAPMELT.

2.2 ACRR Source Term Experiments

Understanding the release of radionuclides during fuel degradation in a core uncovery accident is the first stage in determining the amount and nature of the overall radioactive release from the damaged nuclear plant. Current estimates of the release of the principal fission products over the range of relevant accident conditions are subject to significant uncertainty (e.g., the QUEST study). A key element in reducing the uncertainty in predicted overall releases is an improved understanding of release of fission products from the fuel under severe fuel damage conditions. Major progress is being made in the development of mechanistic release models (e.g., MELPROG's VICTORIA model) to significantly decrease these uncertainties. The ACRR Source Term (ST) program is being conducted to provide

a data base for fission-product release over a range of fuel temperatures, system pressures, and fuel damage states. Significantly, these experiments will be performed in well-controlled, well-known, in-pile conditions and in the presence of ionizing radiation, where little or no data currently exist, to allow the validation of these improved fission-product release models.

Major activities during this period involved completion of development testing and qualification of the fission-product filter samplers, continued development of posttest analytical methods, completion of the hot cell plant modifications, fabrication and procurement of components for the ST-1 experiment, and the beginning of assembly of the ST-1 experiment package.

Development of the ST fission-product filter samplers has been completed. The final filter design meets the design goals of operation within the ST environment, of high collection efficiency, and of ease of disassembly and analysis. Qualification tests of the final sampler design have been completed. These tests demonstrated the performance of the samplers under conditions similar to those anticipated for the ST-1 experiment. The samplers were found to have overall collection efficiencies greater than 98 percent for the mixture of fission-product species anticipated (including Cs, CsI, Ba, Te, and SnTe). The pressure drop across the filter assembly is acceptable with the anticipated material loadings. Deposition wires from the development test have been examined using SEM and X-ray diffraction methods. Aerosol species and morphologies which might be anticipated in the ST-1 experiment have been identified from examination of the wires.

The posttest analysis methods have been defined, have been implemented in the hot cell, and are being rehearsed. The posttest examination of the filter components includes gamma spectroscopy (primarily for Cs), ion chromatography for Ba and Sr, ion specific electrode for iodine, voltametry for Te, gas analyses by mass spectroscopy for Kr and Xe, and precipitations to separate Sr, Te, and rare earth elements from Cs followed by gamma or beta counting.

The plant modifications to the TA-5 Hot Cell Facility are now complete. The cask assembly is nearing completion. Nearly all of the components for the ST-1 experiment package have been delivered except for some of the dense zirconia parts. A rehearsal mock-up of the experiment package has been assembled for use in the development of hot cell methods. Routing and assembly of the interconnecting plumbing in the ST-1 package is in progress as are the qualification tests on components and subassemblies.

3. LWR DAMAGED FUEL PHENOMENOLOGY

Sandia's LWR Damaged Fuel Phenomenology program includes analyses and experiments that are part of the integrated NRC Severe Fuel Damage (SFD) Research programs. Sandia is investigating, both analytically and in separate-effects experiments, the important "in-vessel" phenomenology associated with severe LWR accidents. This investigative effort provides for two related research programs: (1) the Debris Formation and Relocation (DFR) program and (2) the Degraded Core Coolability (DCC) program. The focus of these activities is to provide a data base and improved phenomenological models that can be used to predict the progression and consequences of LWR severe core-damage accidents. Radionuclide source term uncertainty studies (e.g., the QUEST study) indicate large sensitivity of source terms to core-temperature distributions, geometric configurations, and coolant flows. The DFR experiment program provides unique data on in-vessel fuel-damage processes that are of central importance in determining the release and transport of fission products in the primary system. The DCC experiment program, completed in CY86, provided data on the ultimate coolability of damaged fuel configuration. Models coming from both programs are used directly in the MELPROG code.

3.1 ACRR Debris Formation and Relocation (DFR)

The focus of the DFR experiment program is directed toward providing separate-effects phenomenological data on important severe in-vessel fuel-damage processes to aid in the development of second generation severe accident analysis codes. Core-damage configuration, hydrogen generation, and fission-product release are the primary areas of interest. The DFR test series uses cinematography to record the fuel-damage progression during the course of in-pile experiments in which accident conditions are simulated in a small LWR fuel bundle. Decay heating in these experiments is simulated by fission heating of the fuel in the ACRR. Steam conditions and clad preoxidation, similar to expected accidents in a local region of a degrading core, are provided. Three DFR tests have been completed to date. Preparations for the final test, DF-4, are discussed in this report.

Assembly of the DF-4 BWR Control Blade/Channel Box Experiment has been completed and final preparations for conduct of the test, including pretest calculations are underway. A description of the notable package features is given, which includes a review of the generic DFR features as well as features unique to the DF-4 design. One of the central issues to be addressed in the experiment is the performance of the steel control blade and the zircaloy channel box. This issue relates to IDCOR assertions that hydrogen production in BWRs is significantly diminished owing to the formation of tight blockages in the lower canister region, which prevents steam from reaching the upper core fuel cladding. Pretest calculations using the MARCON-DF4 experiment analysis code are presented along with the proposed operating sequence for the experiment.

4. MELT PROGRESSION PHENOMENOLOGY CODE DEVELOPMENT (MELPROG)

The objective of this program is the development of a mechanistic computer model for the analysis of the in-vessel phases of severe accidents in LWRs. This model, MELPROG, is implicitly linked with the TRAC-PF1 thermal hydraulics code to provide a complete, integrated treatment of the reactor primary system from accident inception up to and through release of core materials and fission products from the reactor vessel. The model also provides materials and thermohydrodynamic input to the CONTAIN reactor containment analysis model.

The approach used in MELPROG has been to develop stand-alone modules to analyze specific phenomena that may be encountered during a severe accident sequence. These modules are then explicitly linked within the MELPROG code in order to treat the entire accident sequence in an integrated manner. In this way, we may obtain accurate predictions of both the various phenomena and the coupling between the phenomena. This approach allows key quantities, such as fission-product release and transport, to be calculated in a consistent manner. In addition, the modular structure has the advantage that it is relatively easy to improve or substitute new models into the code.

4.1 MELPROG Code Development

Development of MELPROG continued and was centered in the CORE model. The material relocation modeling received the most attention. In particular, a new model for conduction-limited crust formation was added to the code. This model provides a more realistic treatment of the crusting/candling phenomena than does a bulk-freezing model.

4.2 MELPROG Code Applications

The results of the calculation of a TMLB' sequence in the Surry reactor are being used to gain insights into severe accident phenomena. The most notable insight is that natural circulation is a dominant phenomena and has a major effect on the core meltdown sequence. Calculations indicate that early failure of the primary system boundary may occur with natural circulation for this sequence in the absence of intervention.

4.3 MELPROG Validation Experiments

Degradation of a reactor core under accident conditions may result in frozen debris on the lower head of the RPV. This "crust" may inhibit the heat flux to the steel underneath, affecting the mode and location of vessel failure.

Experiments have shown that the discharge of molten core material will ablate the steel of the lower head and create a larger aperture for the subsequent blowdown of the primary coolant system. If the resulting hole size is small, then the gas velocities in the reactor cavity may not be sufficient to cause entraining and levitating of the debris into the containment. A large-diameter aperture (on the order of 0.5 m or greater) is required to develop the necessary gas mass flux. The refractory nature of

the crust layer may make it resistant to ablation by the high velocity core debris. Little or no ablation of the crust layer may be effective in limiting the growth of the exit aperture in the steel head.

Results from a preliminary model indicate that the initial temperature of the crust material is the determining factor in the ablation of the steel head. At higher temperatures, the energy of the core debris passing through the aperture will be sufficient to ablate the crust at the same rate as the steel. For this situation, the crust will have no mitigative influence on debris dispersal. At a lower temperature, the crust will not ablate and the subsequent gas discharge will be limited by the size of the opening in the crust.

Experiments are under way to assess the influence of a crust layer on the growth of the exit aperture. The initial temperature of the crust and the steel underneath will be established over a range of conditions to provide the data needed to refine the phenomenological model. The results will be incorporated in the MELPROG code.

REACTOR SAFETY RESEARCH
SEMIANNUAL REPORT
July-December 1986

1. CONTAINMENT LOADING AND RESPONSE

1.1 Sustained Core Debris-Concrete Interactions

The containment of a reactor is the last barrier that prevents radionuclide release to the environment during a severe reactor accident. Considerable attention then needs to be devoted to accident phenomena that may threaten the integrity of reactor containments. Two important ex-vessel phenomena that may place significant loads on reactor containments are direct containment heating caused by pressure-driven expulsion of melt from the reactor vessel and the interactions of core debris with structural concrete. Highlights of recent experimental research on these phenomena are described in this report. The recent developments in models of core debris interactions with concrete--CORCON and VANESA--are also described. The results will not only be used to support model development for CORCON and VANESA, but also for the integrated systems development containment code, CONTAIN, and the melt progression code, MELPROG.

1.1.1 Sustained Urania-Concrete Interactions (SURC): Experiments and Analysis

(E. R. Copus, D. A. Powers, J. E. Brockmann, and R. E. Blose, 6422; D. R. Bradley, 6425)

1.1.1.1 Introduction

In the event of a severe reactor accident in which molten core debris penetrates the reactor vessel, the interaction of the molten debris with structural concrete in the reactor cavity is an important factor in the reactor containment loading and aerosol source terms associated with the accident. Since the time of the Reactor Safety Study,[1] this aspect of reactor safety analysis has been poorly understood, with little substantive experimental data available. Out of necessity then, computer models were initially developed based on data from simulant experiments and on observations from the few existing melt-concrete experiments. The CORCON[2] and VANESA[3] computer models were developed using this limited data base.

In the last two years, experimental programs at Sandia and at Kernforschungszentrum Karlsruhe (KfK) have investigated metallic steel melts interacting with concrete. Experiments at both facilities have been well-instrumented and have yielded an abundance of useful data. The availability of these data has allowed validation of CORCON and VANESA and further model development. However, there are still important gaps in the experimental data base for molten core-concrete interactions. Specifically, little or no data is available for sustained prototypic oxide melts interacting with concrete or for the effects of Zr oxidation on melt-concrete interactions. Zirconium has been found in previous CORCON/VANESA calculations[4] to have a major influence on almost every aspect of the interaction from melt-concrete heat transfer to aerosol and fission-product

release. The SURC experiments at Sandia are designed to extend the data base in these areas and consequently, to provide validation of the models in CORCON and VANESA.[5,6]

This report summarizes recent results obtained from the first experiment in the SURC test series, SURC3.

1.1.1.2 SURC3 Experiment Description and Results

The SURC3 experiment was designed to examine the interaction of a sustained stainless steel melt with concrete both before and after the addition of zirconium. The interaction crucible used in the experiment had a limestone concrete test bed approximately 20 cm in diameter and 40 cm deep. The test bed was surrounded by an MgO annulus that was 10 cm thick and 90 cm high. This crucible design limited concrete erosion to the axial direction. A 0.3-m^3 top hat was sealed to the MgO annulus to direct aerosol and gas effluents through the instrumentation stream. The charge in SURC3 was composed of 50 kg of stainless steel and 2 kg of fission product simulants. An additional 5 kg of Zr metal were added to the charge during the test. The charge was inductively melted and sustained using a 55-cm induction coil and a 250 kW-1000 Hz power supply.

Instrumentation for the test consisted of 50 thermocouples embedded in the concrete to measure pool temperatures and axial erosion; 40 thermocouples in the MgO and top hat to measure sideward and upward heat losses; five independent flow measurement devices; gas composition measurement by means of an infrared CO/CO_2 monitor, a mass spectrometer, and an integral grab sampling device; and aerosol source term measurements using cyclone impactors, filters, and a photometer.

The experimental procedure for SURC3 was to first melt the steel and allow it to erode 6 to 8 cm of concrete. Zirconium metal was then added to the melt to determine the impact of Zr oxidation on concrete erosion, gas flow, gas composition, and aerosol and fission-product release. Posttest inspection of the crucible and its contents revealed that only 1.5 kg of Zr had actually entered the melt during this phase. After Zr oxidation had apparently been completed and the interaction had returned to pre-Zr steady-state behavior, the experiment was terminated by turning off the induction power supply.

Preliminary results of the test indicate that during the 30 min prior to Zr addition the concrete erosion rate was 0.14 cm/min, the flow rate of effluent gases was 50 L/min, aerosols created an opacity of 25 percent, the gas composition was 85 percent CO and 15 percent CO_2, and pressure in the containment top hat was 0.75 lb/in^2 gauge. Two minutes after Zr was added to the melt, the flow rate jumped to 135 L/min, the aerosol opacity increased to 50 percent, pressure increased to 2 lb/in^2 gauge, and the gas composition shifted to 96 percent CO and 4 percent CO_2. This excursion continued for approximately 10 min, during which time the erosion rate averaged 0.4 cm/min. After 10 min of interaction, the pressure, flow rate, erosion rate, and gas composition all returned to their original values for the remainder of the test. Forty-five minutes after the first Zr addition, an attempt was made to add an additional 5 kg of Zr. This attempt failed

because of a thick buildup of overlying crust material in the MgO annulus. The test was terminated 1 h later.

1.1.1.3 SURC3 Posttest Analysis

Four substantive observations pertaining to the interaction of sustained stainless steel melts with concrete both before and after the addition of Zr were made based on the initial SURC3 data, which is shown in Figures 1.1-1 through 1.1-5 and Table 1.1-1. The observations are:

1. Zr addition had a major effect on limestone concrete ablation, effluent gas production, gas composition, and aerosol production.

2. Steady melt pool temperatures of greater than 1900 K were measured throughout the test.

3. Copious aerosol production accompanied the entire melt-concrete reaction. These aerosols were mostly comprised of Te with only small amounts of Ca.

4. No evidence of intense carburization (coking) during the Zr reaction was observed.

Figures 1.1-1, 1.1-3, 1.1-4, and 1.1-5 demonstrate the major effects of Zr addition to steel-concrete attack. They show that the erosion rate, gas production, and carbon monoxide concentration in the effluent gas all increase in the presence of Zr reactions.

Figure 1.1-1 shows the ablation distance in the limestone concrete as a function of time for SURC3. Prior to the addition of Zr, the erosion rate averaged 0.14 cm/min. The ablation rate increased to 0.34 cm/min following Zr addition and then decreased to a rate of 0.24 cm/min for the remainder of the test. Figure 1.1-3 shows the effluent gas flow in standard liters per minute versus time for the SURC3 test. The gas flow ranged from 20 to 30 sL/min before Zr addition, from 80 to 160 sL/min during the Zr reaction, and from 20 to 40 sL/min after the completion of the Zr reaction. Figure 1.1-4 shows that the composition of the gaseous effluent varied from 80 percent CO and 20 percent CO_2 in the absence of Zr reactions to 96 percent CO and 4 percent CO_2 in their presence. Also, Figure 1.1-5 shows the aerosol source term ranges from 5 to 15 mg/s throughout the test.

A second major observation of the SURC test was that the melt temperature remained significantly higher than the melting point of stainless steel throughout the test. Twelve data points ranging from 1925 to 2040 K are shown in Figure 1.1-2. The addition of Zr to the melt appeared to have minimal effect on the pool temperature.

A third major observation of the SURC experiment pertains to steel-concrete interactions in general as well as interactions with Zr-steel melts. The aerosol source term is seen to remain at significant levels (5 to 10 mg/s as seen in Figure 1.1-5) throughout the test with a large portion of that aerosol being metals or fission products such as Te, Fe, and Cr rather than

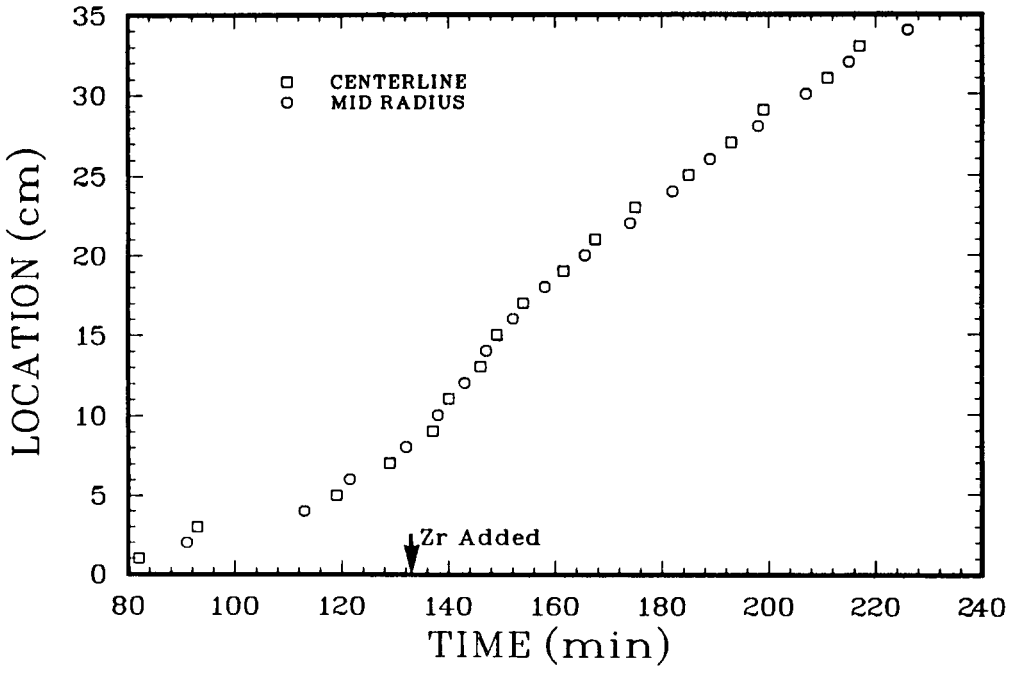

Figure 1.1-1. SURC3 Ablation Front

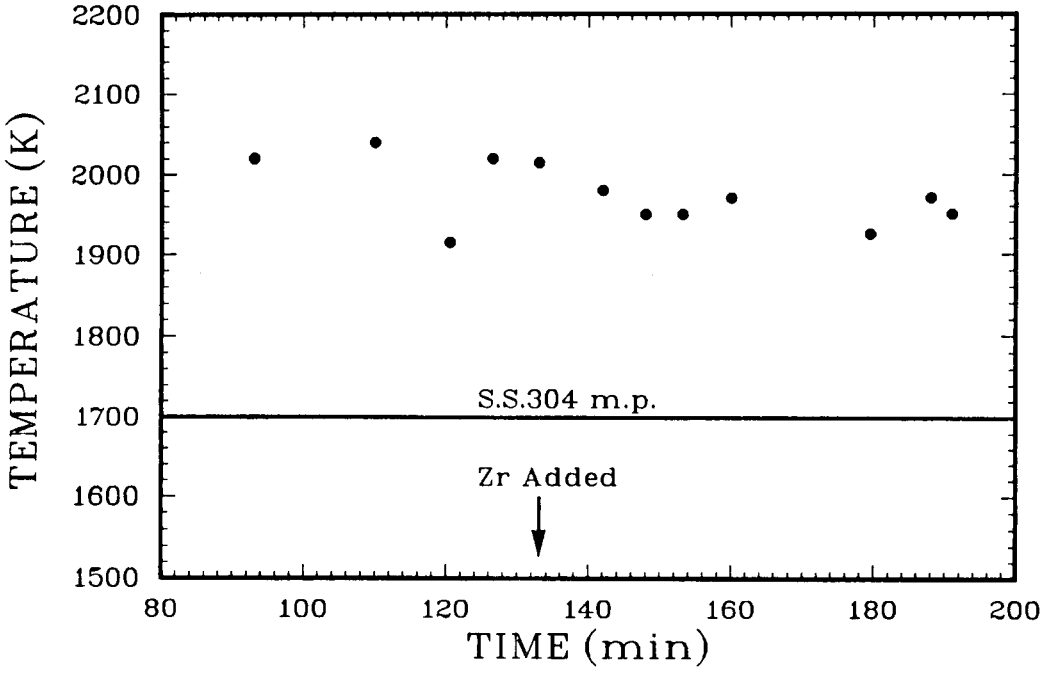

Figure 1.1-2. SURC3 Melt Temperature

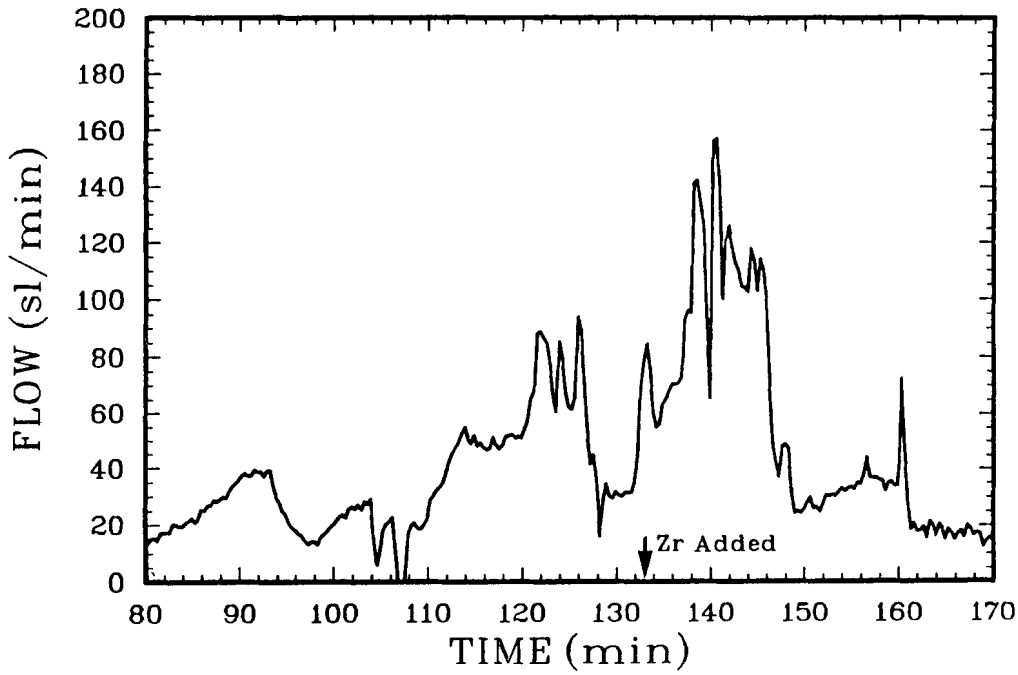

Figure 1.1-3. SURC3 Gas Flow

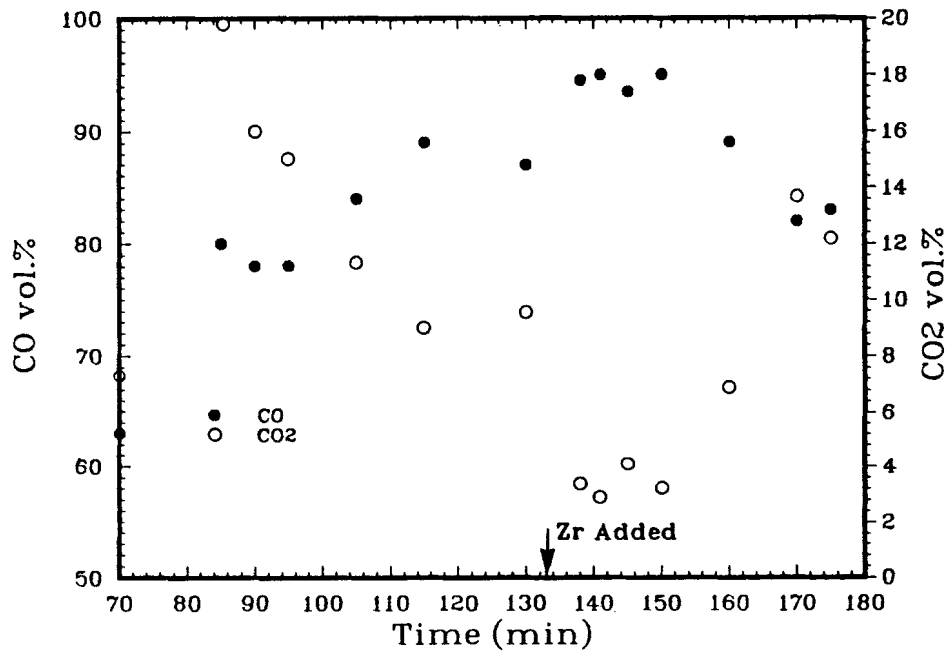

Figure 1.1-4. SURC3 CO and CO_2

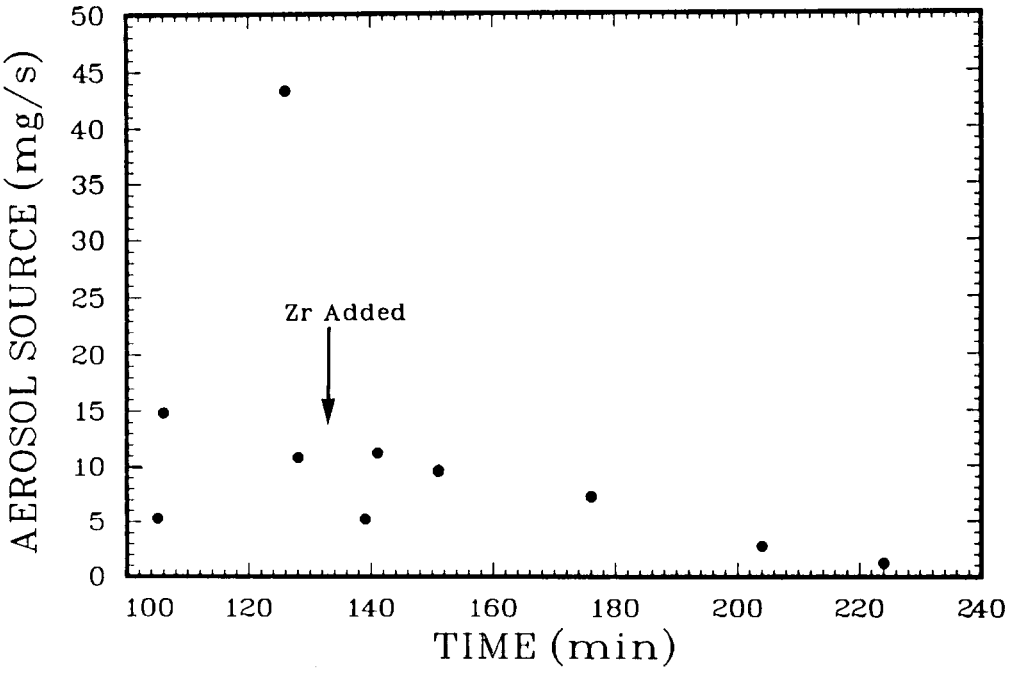

Figure 1.1-5. SURC3 Aerosol Source

Table 1.1-1

SURC3 Composite Aerosol

Te	48.5%
Mo, Nb, Zr	< 0.02%
Ba, Ce, La	< 0.02%
Fe	1.9%
Cr	3.4%
Mn	4.3%
Ni	0.1%
Ca	0.2%
Si	0.2%
Mg	1.2%
Na	2.3%

concrete products such as Na or Ca. Table 1.1-1 shows an abbreviated elemental analysis of the aerosol composition.

Finally results of the SURC3 test show no evidence of an intense carburization reaction such as coking during the Zr reaction phase. This is best illustrated by Figures 1.1-3 and 1.1-4, which show no severe decrease in either gas flow rate or the overall carbon content of effluent gas.

1.1.2 Combustible Gas Generation During the Interactions of Core Debris With Concrete

(D. A. Powers, 6422)

The uninterrupted progression of a severe reactor accident leads, eventually, to the escape of reactor core debris from the reactor coolant system into the reactor cavity. This escape of the reactor core debris marks the start of the ex-vessel phase of a severe accident. In the conventional analysis of severe reactor accidents, the predominant physical and chemical phenomena taking place in the ex-vessel phase of a severe accident are those associated with the interaction of core debris with structural concrete in the reactor cavity. Of particular interest, is the production of noncondensable and flammable gases during these interactions of core debris with concrete.

Gases are produced during core debris interactions with concrete in three ways:

1. Core debris directly attacks, decomposes, and ablates concrete.

2. Convection and radiation of heat from the core debris decomposes concrete not in direct contact with the core debris.

3. Liquid water overlying or inundating the core debris boils to form steam or reacts to form hydrogen.

The production of gases during the interactions of core debris ex-vessel threatens the integrity of containment by overpressurization. The production of flammable gases ex-vessel can enhance the combustibility of the containment atmosphere. For the purposes of this report, the most immediate interest is in the production of flammable gases as a result of core debris-concrete interactions or core debris-coolant interactions. The production of nonflammable gases by heating of concrete not exposed to core debris is also of interest because these "inert" gases, too, affect the combustibility of the containment atmosphere.

An understanding of gas generation during core debris-concrete interactions begins with an understanding of how concrete decomposes. A discussion of concrete decomposition is presented in Section 1.1.2.1 and is followed by a discussion of the chemical behavior of the gaseous products of decomposition. An abbreviated account of gas production during ex-vessel core debris-coolant interactions concludes this section.

1.1.2.1 Thermal Decomposition of Concrete

Concretes used in the construction of nuclear power plants are quite diverse. Some typical compositions of concretes from existing reactors are shown in Table 1.1-2. All the concretes consist of a cementituous material binding together large and small aggregates. Worldwide the cementituous material is very nearly the same in all reactors. Dry, it consists of:

60-67 weight % CaO

17-25 " " SiO_2

3-8 weight % Al_2O_3

0.5-6 " " Fe_2O_3

0.1-4 " " MgO

0.2-1.3 " " Na_2O and K_2O

Upon hydration, complex species are formed in the course of slow chemical processes that can take years to reach completion. The more important hydrated species are:[7,8,9]

$$Ca(OH)_2$$

$$3CaO \cdot [Al(OH)_6]_2$$

$$3CaO \cdot 2SiO_2 \cdot 3H_2O$$

$$3CaO \cdot Al_2O_3 \cdot 3CaSO_4 \cdot 31H_2O$$

The aggregates in the concrete are chemically diverse. It is both convenient and traditional to group these aggregates as either (1) siliceous (i.e., shist, granite, granodierite, basalt) or (2) calcareous (i.e., calcite, dolomite).

For some special shielding purposes, other high density aggregates such as a barite and magnetite have been employed in nuclear power plants. These aggregates do not fall conveniently in the two categories listed above, but such specialty concretes seldom constitute a significant fraction of the concrete found in modern nuclear power plants.

Upon heating concretes begin to decompose and the decomposition involves the loss of gaseous materials. A plot of the weight-loss of a concrete

Table 1.1-2

Compositions of Some Reactor Concretes

CONSTITUENT	Weight % in the Reactor at INDIAN POINT	MILLSTONE	ZION	WPPSS #1	RANCHO SECO	HARTSVILLE	WOLF CREEK	PALO VERDE
K_2O	0.4 - 0.7	1.2	0.18	1.45	1.33	0.37	1.12	3.01
Na_2O	0.8 - 1.3	0.8	0.05 - 0.13	2.01	1.82	0.07	0.05	2.45
CaO	14.5 - 23.7	8.7	24.1	19.6	17.21	48.6	37.50	12.87
MgO	a	0.95	8.2	a	a	a	a	a
Fe_2O_3	2.6 - 3.6	1.8	0.77	7.2	5.15	1.57	1.50	2.72
Al_2O_3	6.3 - 9.7	5.3	1.72	10.4	10.8	2.46	2.46	11.5
SiO_2	43.4 - 60	71.9	38.3	46.0	51.1	8.99	8.99	57.1
H_2O	2.4 - 3.2	8.0	6.2	10.9	10.7	a	a	a
CO_2	0 - 14.2	0.43	20.3	a	a	a	a	a

	ENRICO FERMI	TURKEY POINT	PATHFINDER	HUMBOLDT BAY	WATERFORD	BELLEFONTE
K_2O	0.72	0.06	0.73	1.01	0.1	0.35
Na_2O	0.71	0.02	0.85	2.55	a	0.09
CaO	24.5	41.14	11.61	11.9	16.8	45.33
MgO	a	a	a	a	a	a
Fe_2O_3	1.57	0.71	1.72	6.3	1	1.29
Al_2O_3	3.58	1	4.16	9.6	3	2.83
SiO_2	19.7	18.18	54.34	43.4	69.3	8.34
H_2O	a	a	a	a	a	a
CO_2	a	a	a	a	a	a

[a]substance not reported.

sample heated at 10°C/min is shown as a function of temperature in Figure 1.1-6. A qualitatively similar pattern of weight loss would be obtained for any concrete.[10] There is continuous loss of material at all temperatures up to about 1000°C. The continuous weight-loss is punctuated by three significant, rapid weight-loss events traditionally labeled as:[11]

1. Loss of free water (80° to 140°C)

2. Loss of chemically bound water (350° to 520°C)

3. Loss of carbon dioxide (550° to 1000°C)

Though all three of these "weight-loss events" occur in all concretes when heated, the magnitudes of the events vary among the different concretes.

The so-called "free water" in concrete, also known as "gel water," is molecular H_2O coordinated to cations or condensed in the pore structure of the cementituous phases of the concrete. Over time, free water in the concrete is converted to "chemically bound water" as the hydration reactions in the cementituous phases of concrete progress. There is, however, always some free water present. There is seldom less than 1.5 to 2 percent by weight free water in concrete. There may be more free water depending on the ambient relative humidity.[12] A plot of the free water content of concrete as a function of relative humidity is shown in Figure 1.1-7. The variability of the free water content of concrete arises because of the Kelvin effect on vapor pressure of water within the pore structure of concrete. The cementituous phases of concrete are, typically, 45 to 55 percent porous.[13]

Since the relative humidity in the vicinity of the cavity in a reactor power plant will be high, free water contents of the structural concretes may exceed 5 weight percent.

Chemically bound water is, in fact, water present in the cementituous phases of concrete as hydroxide groups. The most important constituent of the hydrated cementituous phase containing bound water is $Ca(OH)_2$. The amount of $Ca(OH)_2$ in the cementituous phases of concrete increases with the time of concrete curing. Typically, the chemically bound water content of concrete is 1.8 to 3 weight percent.

The highest temperature weight loss event in the pyrolysis of concrete is caused by the decomposition of carbonates. All concretes contain some carbonate. If nothing else, the carbonates are produced by the reaction of atmospheric CO_2 with $Ca(OH)_2$ in the cementituous phases:[14]

$$Ca(OH)_2 + CO_2 \longrightarrow CaCO_3 + H_2O\uparrow \quad .$$

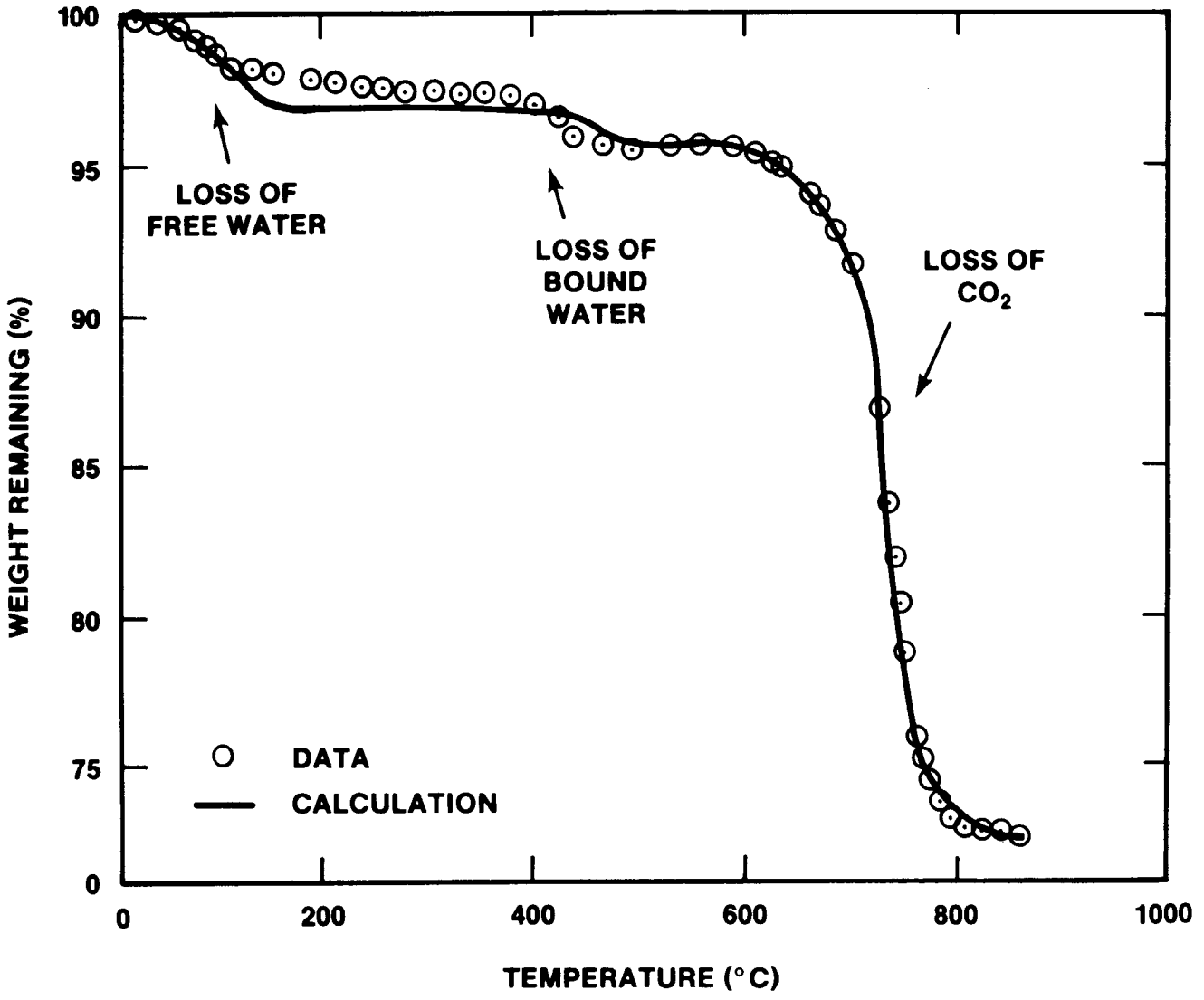

Figure 1.1-6. Weight Changes Observed When Concrete Specimens Are Heated at 10°C/min in Air. Calculated weight changes are described in the text.

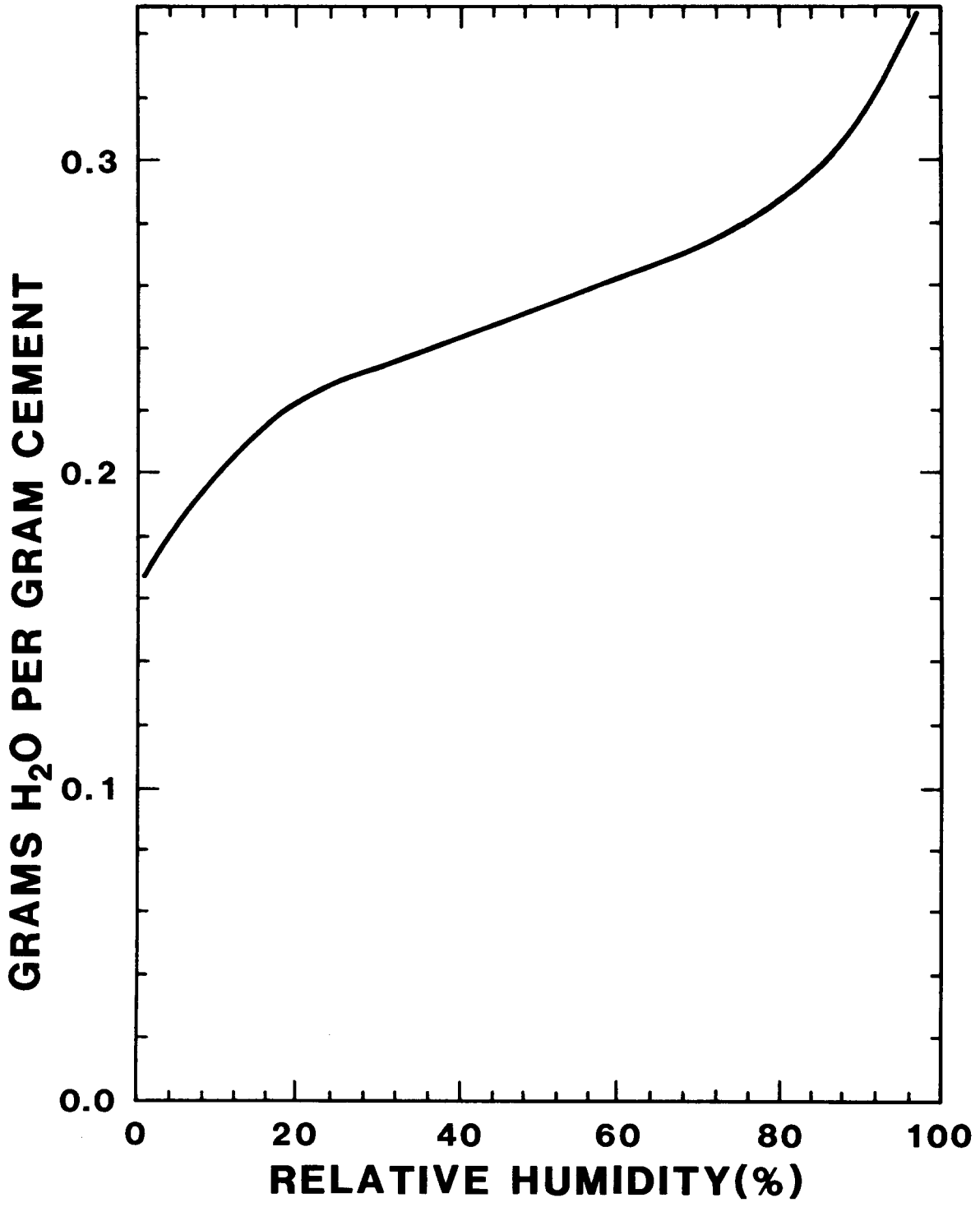

Figure 1.1-7. Free Water Content of Cement as a Function of Relative Humidity (Reference 12)

But the most important carbonates are those used as aggregates. The most common calcareous aggregates are calcite ($CaCO_3$) and dolomite ($MgCa(CO_3)_2$). Seldom are the calcareous aggregates purely one or the other of these materials. When calcareous aggregates are used, the CO_2 content of concrete can be between 20 and 38 weight percent depending on whether or not calcareous material is used as both the large and fine aggregate.

Heating of the concrete initiates first the loss of free water. This loss of free water, like all decomposition processes of concrete, is a kinetic process--that is, the rate and extent of decomposition depend both on time, temperature, and ambient partial pressure of the product gas. Powers has characterized the forward reaction as a first order rate process:[15]

$$\frac{d\alpha(1)}{dt} = K_o^{(1)} \exp\left(-E_1/RT\right)\left(1-\alpha_1\right) \quad ,$$

where

$\alpha(1)$ = fraction of free-water loss,

$K_o^{(1)}$, E_1 = rate parameters,

R = gas constant,

T = absolute temperature.

This rate expression applies only to the forward reaction in the absence of any significant partial pressure of water vapor in the gas. To accommodate finite ambient partial pressures of steam, the rate expression is

$$\frac{d\alpha(1)}{dt} = K_o^{(1)} \exp\left(-E_1/RT\right)\left(1-\alpha_1\right)\left[1 - \frac{P\left(H_2O\right)}{P_{eq}\left(H_2O\right)}\right] \quad ,$$

where

$P(H_2O)$ = actual partial pressure of steam,

$P_{eq}(H_2O)$ = equilibrium partial pressure of steam.

The rate expression does not address the evaporation of water condensed in the pore structure of concrete. For very precise work, an additional rate expression treating surface curvature effects on the vapor pressure of water should be developed.

The rate of chemically bound water from concrete is also a kinetic process, which again can be characterized by first order kinetics:[15,16]

$$\frac{d\alpha_2}{dt} = K_o^{(2)} \exp\left(-E_2/RT\right)\left(1-\alpha_2\right)\left[1 - \frac{P\left(H_2O\right)}{P_{eq}^{(2)}\left(H_2O\right)}\right] \quad ,$$

where

α_2 = fraction of bound water loss,

$K_o^{(2)}$, E_2 = rate parameters,

$P_{eq.}^{(2)}(H_2O) = 3.83 \times 10^7 \exp[-13133/T]$ atmospheres .

The value of $P_{eq}^{(2)}(H_2O)$ has been estimated by assuming the decomposition reaction to be

$$Ca(OH)_2 \rightleftharpoons CaO + H_2O\uparrow \quad .$$

The decomposition of carbonates in the concrete can be more complex than the loss of free or chemically bound water. Powers[16] has examined the decomposition of calcite in concrete. In the absence of significant ambient partial pressures of CO_2, the rate of decomposition is

$$\frac{d\alpha_3}{dt} = K_o^{(3)} \exp\left(-E_3/RT\right)\left(1-\alpha_3\right)^{2/3} \quad ,$$

where α_3 = fraction of CO_2 lost. When there is a nonnegligible partial pressure of ambient CO_2, the above rate must be multiplied by

$$1 - \frac{P_{CO_2}}{P_{CO_2}(eq.)} \quad ,$$

where $P_{CO_2}(eq.) = 2.45 \times 10^8 \exp\left[\frac{-21450}{T}\right]$.

Rate constants for the various decomposition reactions are shown in Table 1.1-3. Comparisons of observed and calculated weight losses are shown in Figure 1.1-6.

Decomposition of pure dolomite has been studied frequently.[17-20] The reaction is best considered to progress in two steps:

$$MgCa(CO_3)_2 \rightleftharpoons MgO + CaCO_3 + CO_2\uparrow$$

$$CaCO_3 \rightleftharpoons CaO + CO_2\uparrow \quad .$$

The rate of the first step of the reaction reaches a maximum at about 735°C under the conditions of differential thermal analysis.[20] The rate of the second reaction is not the same as that for pure calcite. This rate is a maximum at about 900°C. The rate of decomposition of pure dolomite seems to follow the 2/3 order kinetics found for calcite.[21] The decomposition is, however, sensitive to impurities in the dolomite. For instance, $CaCl_2$ can reduce the temperature of the first reaction step to 515°C.[20]

All the decomposition processes of concrete that yield gas are endoergic. The enthalpies of decomposition are:

1. Loss of free water*: 12.5 kcal/mole

2. Loss of chemically bound water: 26.1 kcal/mole

3. Loss of carbon dioxide: 42.6 kcal/mole

The chemical kinetics of concrete decomposition cannot be applied to bulk concrete without making some effort to describe the transport of gaseous products away from the site of reaction. This is particularly important for the loss of water from the concrete. Water vapor formed by decomposition must migrate through a thickness of porous, decomposed concrete. To drive the water vapor through this bed of material, a fairly high pressure head must develop. Water vapor may then be driven from the reaction zone either toward the source of heat or away from the source of heat. That driven toward the source of heat will, of course, escape. That driven away from the source of heat will condense. In dynamic heating tests of concrete, the condensation of water becomes a major mechanism of heat transfer within the concrete. The condensation of water creates a temperature arrest in the concrete. This temperature arrest can be seen in the data for concrete subjected to a heat flux on one surface as shown in Figure 1.1-8.[22]

*This enthalpy applies to water coordinated to cations. The enthalpy of vaporization of water condensed in the pore structure of the cementituous phase is about 10 kcal/mole.

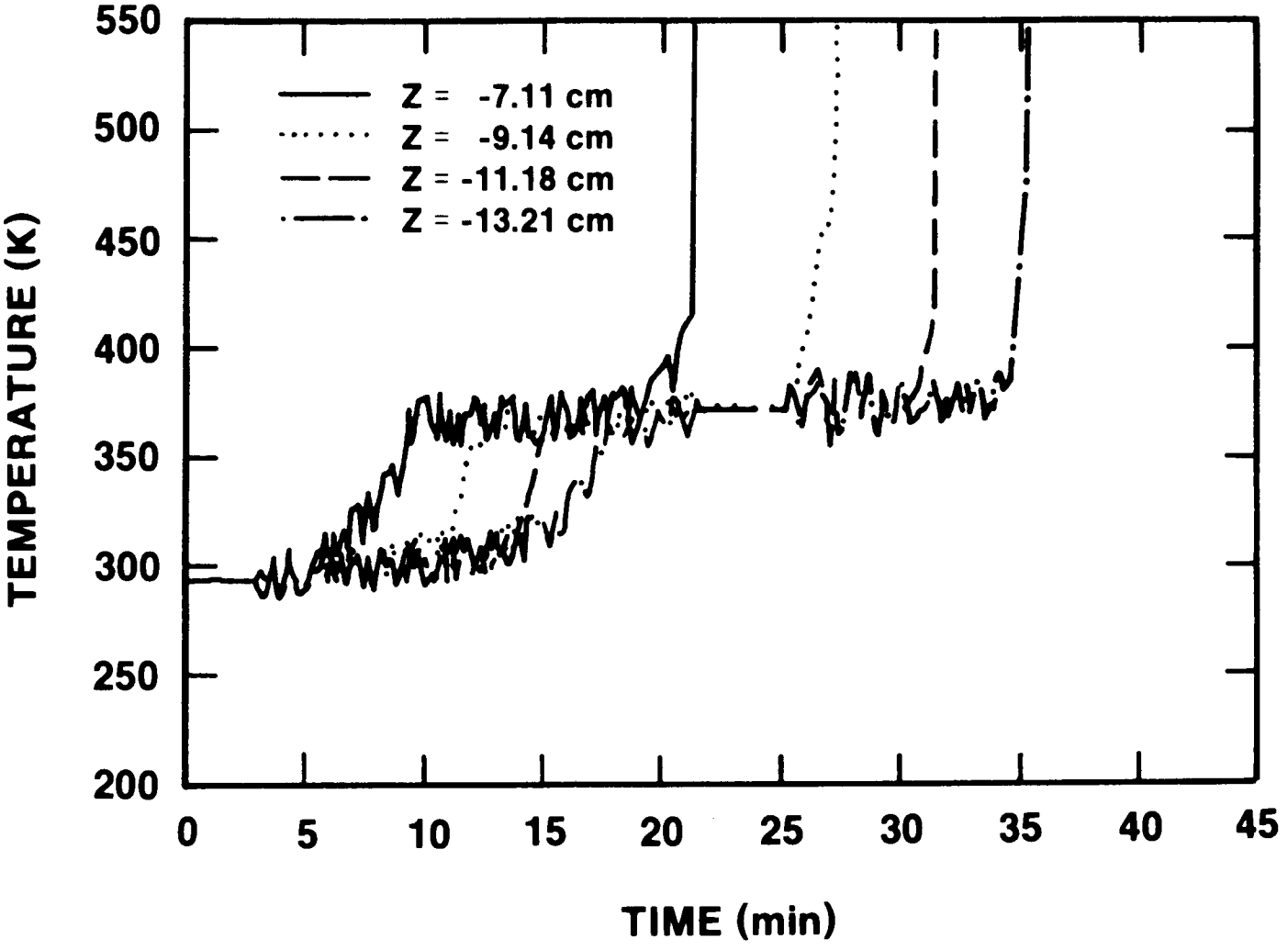

Figure 1.1-8. Temperatures Recorded by Thermocouples Embedded in a Block of Concrete Being Ablated on One Surface by Molten Steel (Reference 22). Labels indicate depth of thermocouple below the original melt-concrete interface.

Table 1.1-3

Kinetic Parameters for the Weight Loss
Events During Concrete Heating

Reaction	Parameters for Siliceous Concrete	Parameters for Limestone Concrete
Free water loss	E = 11600 cal	E_1 = 11000 cal
	$K_o(1) = 4.4 \times 10^6$ min^{-1}	$K_o(1) = 1.29 \times 10^6$ min^{-1}
Bound water loss	E_2 = 41900 cal	E_2 = 40800 cal
	$k_o(2) = 2.8 \times 10^{12}$ min^{-1}	$K_o(2) = 1.96 \times 10^{12}$ min^{-1}
Loss of CO_2	E_3 = 42600 cal	E_3 = 44900 cal
	$K_o(3) = 3.6 \times 10^6$ min^{-1}	$K_o(3) = 1.94 \times 10^6$ min^{-1}

The drying of concrete has been much studied.[23-28] A notable development of equations of combined heat and mass transport in terms of irreversible thermodynamics has been presented by Bazant.[25] Several computer codes have been written to describe gas production during the pyrolysis of concrete.[29,30,31] The USINT code[29] deserves special mention because of its endorsement by an independent assessment group.[32] Comparison of the predictions of this code with data obtained by investigators of the Hanford Engineering and Development Laboratory[33] are shown in Figure 1.1-9. It has generally been found that temperatures within concrete can be rather easily calculated with simple models. Pressures within the concrete pore structures and water loss rates are more sensitive indicators in determining whether a model is an adequate description of the gas release process.

Water release models such as USINT have been incorporated into accident analysis models for breeder reactors.[34] Relatively less attention has been given to accurate modeling of the gas release processes in the analysis of accidents in light water reactors. This inattention is not especially consequential in considering concrete directly exposed to core debris. Significant errors in the gas production rates from concrete exposed to hot gases or radiant energy may arise when simplistic models are employed. Gas production from concrete not directly attacked by core debris can be important in the analysis of pressurization in small containments.[35]

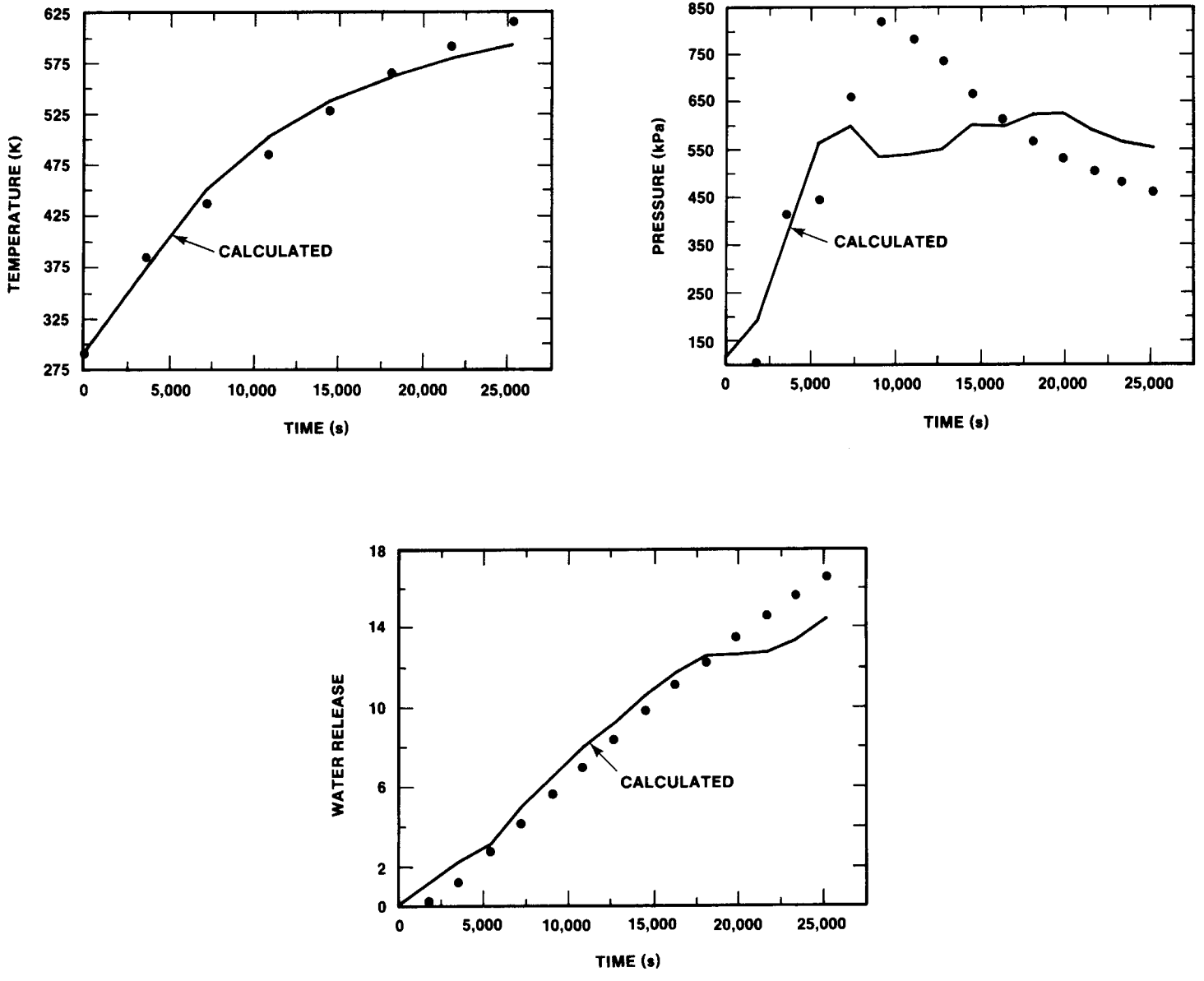

Figure 1.1-9. Comparison of Predictions by the USINT Model (Reference 29) to Experimental Data (Reference 33)

There is a complexity in the treatment of gas generation from concrete structures that goes beyond heat and mass transport within the concrete. That complexity is the ablation of the concrete structures not in contact with the core debris. Often, it is assumed that these structures will ablate by melting. There are, however, other possible mechanisms of concrete ablation. Heated concrete loses strength and, in fact, powderizes. Ablation of concrete could be by decrepitation. The enthalpic cost of concrete ablation by this mechanism is much less than ablation by melting. Thus, at a given heat flux, faster ablation could occur and would lead to more rapid gas generation.

An even more rapid means of concrete ablation is spallation. Concrete exposed to direct attack by molten core debris is known not to spall significantly.[36] But concrete exposed to convective and radiant heat from core debris can spall. Spallation and especially explosive spallation of concrete has been studied primarily in connection with fire safety.[37,38,39] As yet, predictive models of spallation under reactor accident conditions have not been developed.

1.1.2.2 Reactions of Gases With Core Debris

The gaseous products of concrete decomposition are H_2O and CO_2. The production of these gases contribute to containment pressurization in a reactor accident, and these gases could affect the combustibility of the containment atmosphere primarily by acting as inerting agents. Much greater interest arises in gas generation during core debris-concrete interactions when the gaseous products of concrete decomposition can react with the core debris to form flammable hydrogen and carbon monoxide.

Among the most important results of experimental investigations of high temperature melt interactions with concrete was that gases evolved from the concrete sparged through the melt.[11,16,36] This sparging behavior of the gases afforded an opportunity for steam and carbon dioxide to react to form flammable gases. Indeed, flammable gas production is an important feature of all high-temperature melt-concrete interactions. Recent results have shown that gases evolved from the concrete will react with core debris to form hydrogen and carbon monoxide even when the core debris is not molten.[40,41,42]

Core debris produced in a severe reactor accident will consist of two largely immiscible phases--a metallic phase composed primarily of steel, stainless steel, and unoxidized zirconium and an oxide phase composed primarily of zirconium dioxide and urania fuel. Some recent work has indicated that metallic uranium might also be present the metallic phase.[43,44]

The metal phase of core debris readily reacts with the gases produced by decomposition of concrete. Formally, some of the reactions are:

$$Zr + H_2O \longrightarrow ZrO_2 + 2H_2$$

$$Fe + H_2O \longrightarrow FeO + H_2$$

$$2Cr + 3H_2O \longrightarrow Cr_2O_3 + 3H_2$$

$$2Fe + 3CO_2 \longrightarrow Fe_2O_3 + 3CO$$

$$2Cr + 3CO_2 \longrightarrow Cr_2O_3 + 3CO \quad .$$

Zirconium metal is sufficiently electropositive that it can reduce CO_2 completely to carbon:

$$Zr + CO_2 \longrightarrow ZrO_2 + C \quad .$$

Once all the zirconium in the melt has been depleted, any carbon formed in the melt will react with gases evolved from the concrete:

$$C + CO_2 \longrightarrow 2CO$$

$$C + H_2O \longrightarrow CO + H_2 \quad .$$

The formation of carbon and its subsequent reactions have an important bearing on the calculation of containment atmosphere combustibility. While zirconium metal is present in the core debris, the carbon formation reactions prevent significant generation of carbonaceous gases by core debris-concrete interactions. Once the zirconium inventory is depleted, the reactions of carbon result in two moles of combustible gases escaping into the reactor containment for every mole of gas evolved from concrete being attacked by core debris. This effect of zirconium on gas generation is shown in Figure 1.1-10 by the results of a calculation for a hypothetical reactor accident.

Some models of core debris-concrete interactions have attempted to describe the reactions of gases with core debris in terms of the reactions listed above.[44,45] A more realistic portrayal, however, recognizes the solution nature of the metallic phase.[3] For thermodynamic equilibrium conditions, the extent of gas reaction with the core debris is characterized by the hydrogen-to-steam partial pressure ratio of the gas evolving from the core debris. A plot of this ratio as a function of time for a particular accident analysis is shown in Figure 1.1-11. For this calculation, the composition dependent activity coefficients of melt constituents shown in Table 1.1-4 were used. When zirconium is present, carbon is formed from carbonaceous gases evolved from the concrete and the hydrogen-to-steam partial pressure ratio varies between 10^5 and 10^4. The condensed product of reaction, aside from carbon, is nearly entirely CO_2. Once the zirconium is almost entirely reacted, carbon in the melt begins to react. When this happens, there is very little condensed phase product of reaction. The hydrogen-to-steam partial pressure ratio varies during this stage between

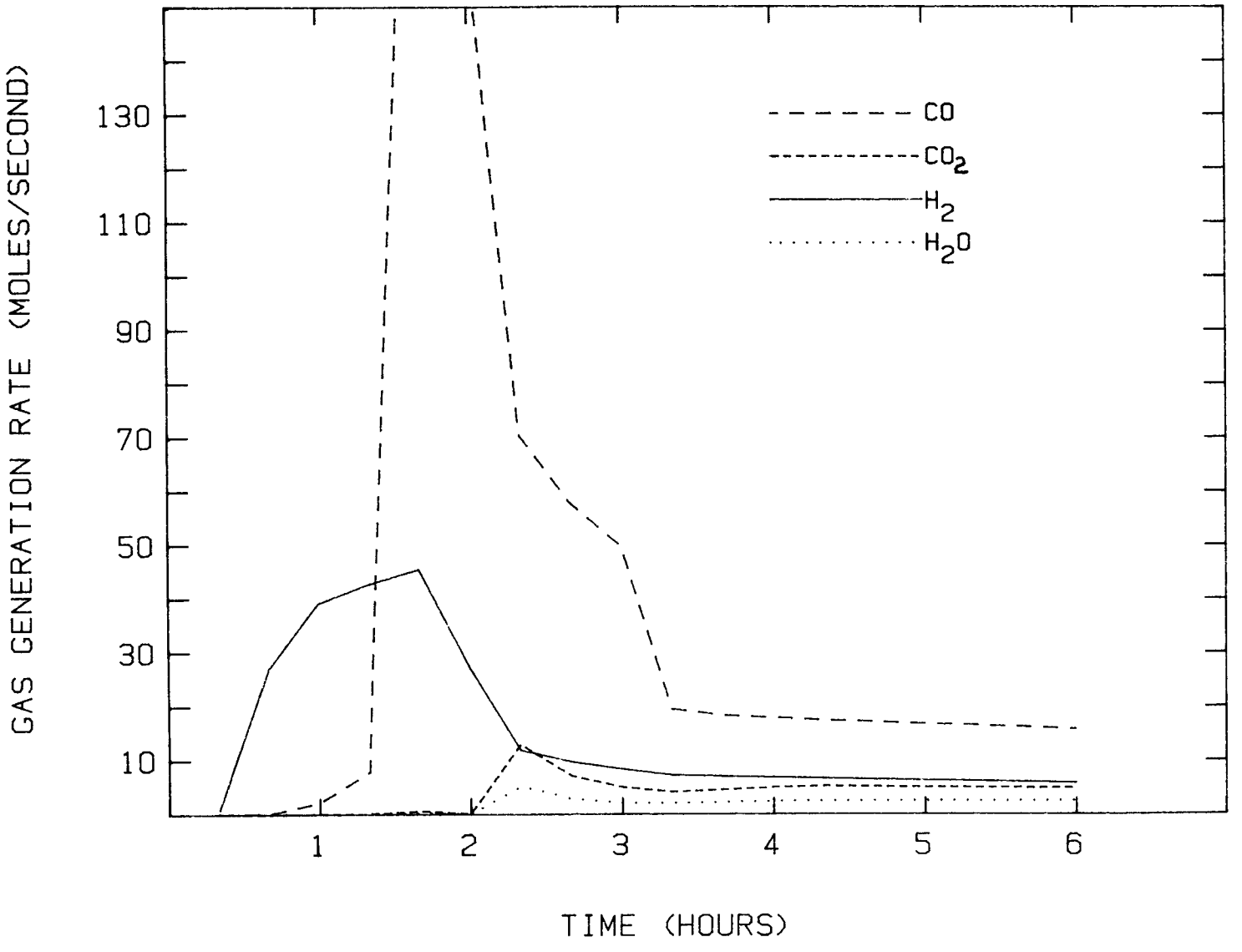

Figure 1.1-10. Gas Generation During Zirconium-Bearing Core Debris-Concrete Interactions

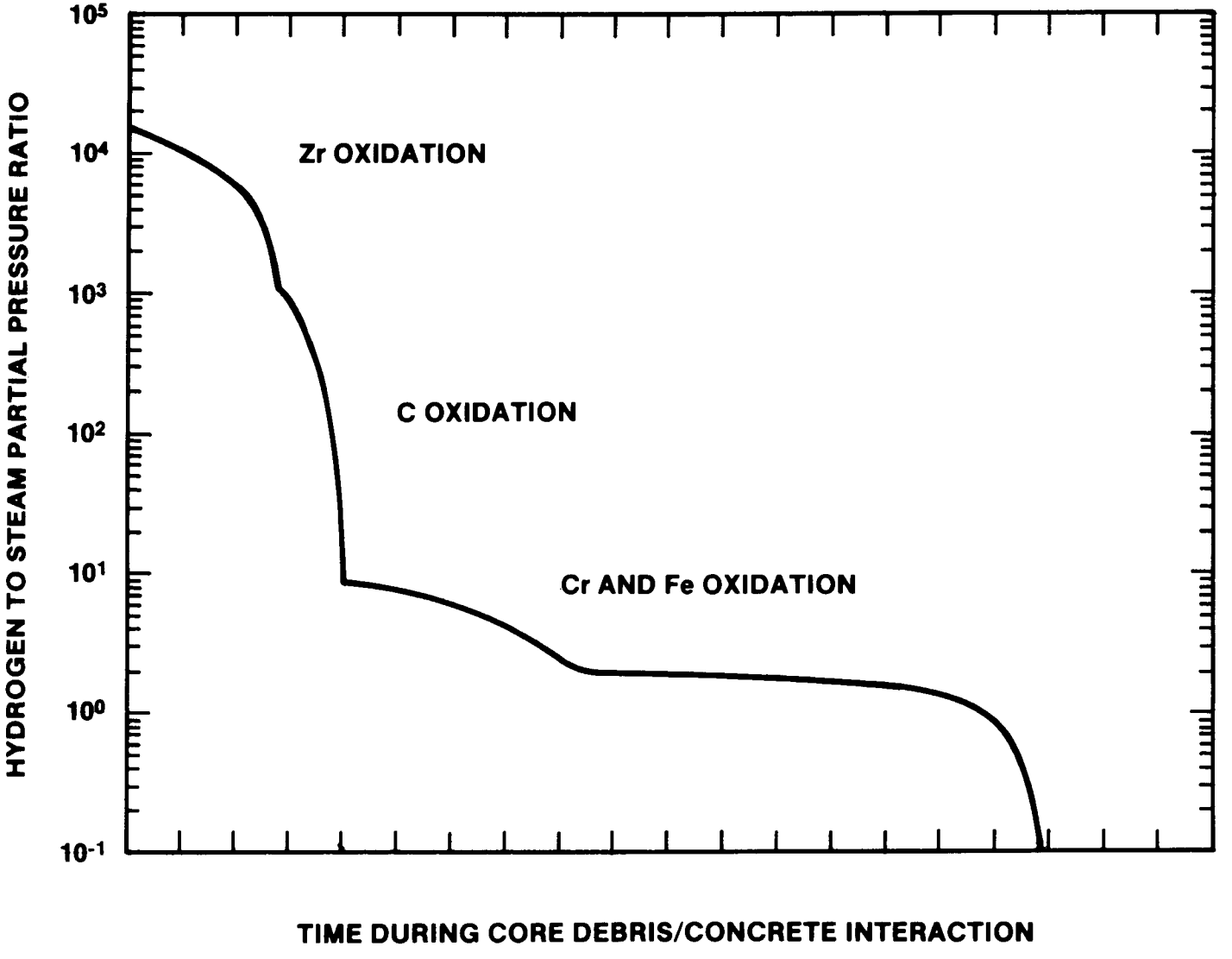

Figure 1.1-11. Equilibrium Hydrogen-to-Steam Partial Pressure Ratio for the Metallic Phase of Reactor Core Debris as a Function of Time During Interactions With Concrete

Table 1.1-4

Activity Coefficients for the Metallic Phases of Core Debris (Reference 3)

Carbon

$$\ln[\gamma(c)] = -0.3567 - 5.1\ X(Cr) + 2.9\ X(Ni) + (7808/T + 2.871)\ X(C) + (15{,}624/T + 5.323)[X(C)]^2 - 0.4[X(Cr)]^2$$

Chromium

$$\ln[\gamma(Cr)] = -5.1\ X(Cr)$$

Iron

$$\ln[\gamma(Fe)] = -0.1(X(Ni))^2 + (3904/T + 1.436)[X(C)]^2 + 5.1\ X(Cr)X(C) - 2.9\ X(Ni)X(C)$$

Nickel

$$\ln[\gamma(Ni)] = -0.4155 + 0.2\ X(Ni) + 2.9\ X(C)$$

Zirconium

$$\ln[\gamma(Zr)] = -(6175/T)[1-X(Zr)]^2$$

where

$\gamma(i)$ = activity coefficient of species i,

$X(i)$ = mole fraction of species i.

10^3 and 10^2. Once the carbon content of the core debris has been reduced to a few tenths of percent, then Cr and Fe in varying proportions are oxidized. When Cr is the predominant reactant, the hydrogen-to-steam partial pressure ratio is about 100. As more iron becomes involved in the reactions, the hydrogen-to-steam partial pressure ratio falls to about 3. Thus, as an interaction of core debris with concrete begins, there is nearly complete reduction of gases evolved from the concrete to flammable species. As the interaction progresses, the amount of reduction decreases. When iron is the most reducing constituent of the gas, only about 0.75 of the gas evolved from the concrete is converted to flammable species. Were all the iron oxidized from the core debris so that nickel was the predominant constituent of the metal phase, very little reduction of the evolved gas would occur. For typical accident analyses, this complete oxidation of iron seldom happens because the iron inventory of the core debris is replenished by iron from reinforcing steel in the concrete.

Several computer codes have been written to describe gas generation during core debris-concrete interactions.[2,3,45-50] Typical predictions for combustible gas generation in accidents with siliceous and limestone concrete are shown in Figure 1.1-12. Note that the limestone concrete can produce much more gas than siliceous concrete.

The actively used models of core debris concrete interactions[2,3,45-50] have several characteristics in common:

1. They neglect conduction into the concrete--gas generation from the concrete is proportional to concrete ablation.

2. The gas generation is dependent on the heat flux to the concrete.

3. They assume gases equilibrate with the melt.

4. They neglect the effects of boron carbide control rod material on gas composition.

The complexities of heat conduction into concrete have been discussed above. As long as the rate of concrete ablation is sufficiently rapid, the rate of heat conduction into the concrete will be the same (following aninitial transient) as the rate of ablation. This can be seen in the location of the ablation front and the location of the interface where "free water" is being lost as observed in a test of steel/concrete interactions shown in Figure 1.1-13. Once ablation slows, heat conduction can no longer be neglected. The existing models would be expected to underpredict particularly the rate of water release from concrete when the core debris has solidified.[40]

Models of the melt-to-concrete heat transfer used in the existing computer codes are, then, very important in the determination of how much gas is produced during core debris-concrete interactions. Recent results of experiments conducted in West Germany[51] have questioned some of the older models of this heat transfer process.[52,53] Active development of improved models of the heat transfer is now underway.[54,55]

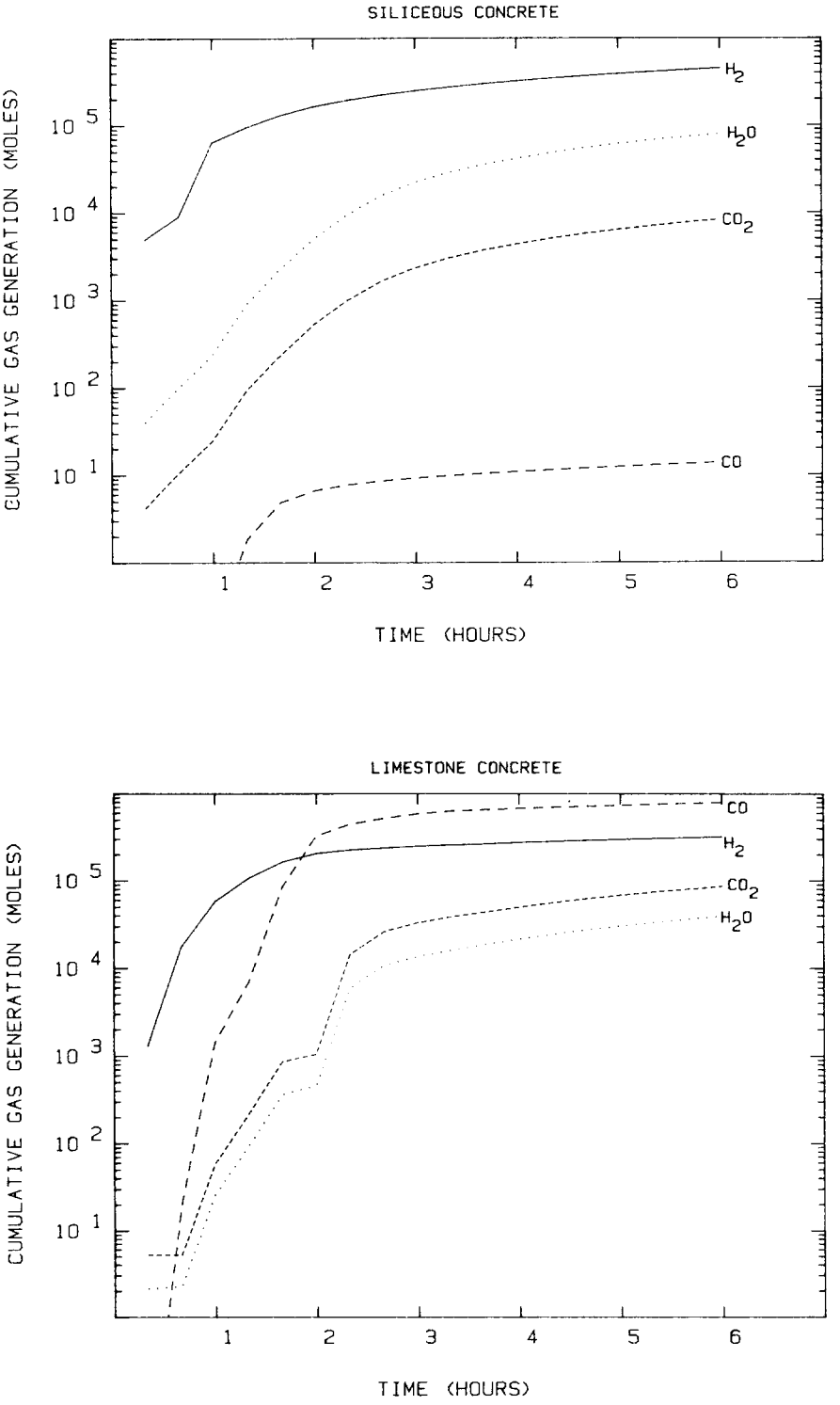

Figure 1.1-12. Gas Generation During Core Debris Interactions With Siliceous and Limestone Concretes

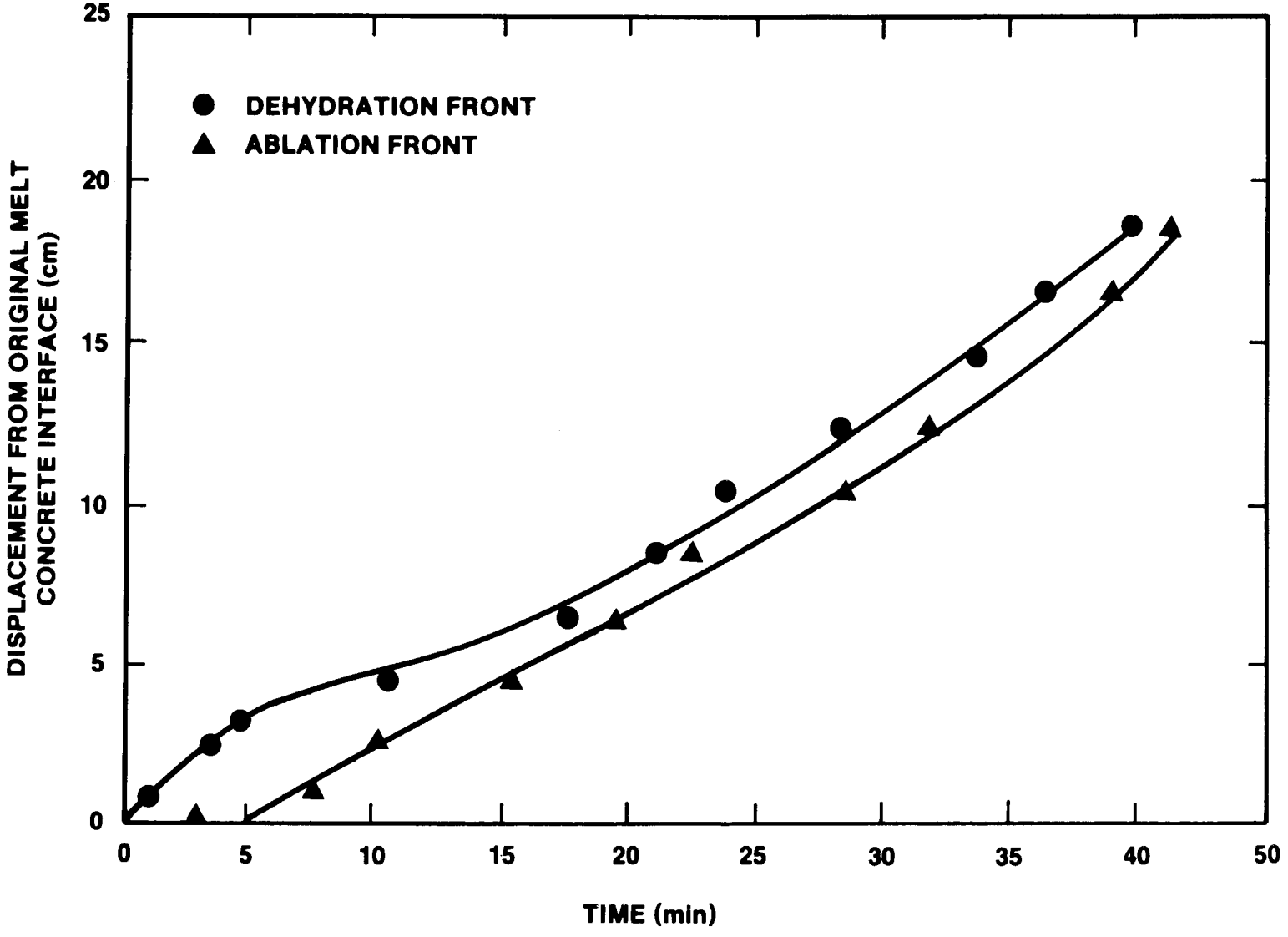

Figure 1.1-13. Location of the Erosion Front and the Isotherm Corresponding to Free Water Loss in Concrete Being Attacked by Molten Steel (Reference 22)

The assumption that gases entering the melt quickly equilibrate with the melt seems adequate. Attempts to describe the kinetics of gas reactions with the melt (as described in Reference 3) usually indicate equilibrium is achieved after gases have passed through only a few centimeters of melt. Unfortunately, the existing models assume the gases only react with the metallic phase. Consequently, gas from the concrete that interact with the oxide phase are not converted to flammable species. This assumption neglects the variable stoichiometry of urania and the reactions:[56]

$$UO_{2+x} + yH_2O \longrightarrow UO_{2+x+y} + yH_2 \quad .$$

Recent experiments with urania melts have shown, indeed, that gases will react with these melts.[52]

A reactive constituent of core debris expected to form during accidents, especially in boiling water reactors, is boron carbide. There have been neither experimental studies nor extensive analyses of the effects of boron carbide on gas generation. It is well-established that boron carbide will react with steam:[57,58]

$$B_4C + 6H_2O \longrightarrow 2B_2O_3 + C + 6H_2$$

$$B_4C + 7H_2O \longrightarrow 2B_2O_3 + CO + 7H_2 \quad .$$

These reactions of B_4C have been observed at temperatures as low as 380°C. Above about 460°C the B_2O_3 product is a liquid and the presence of this liquid product layer slows the rate of reaction. The product layer is itself reactive with steam:

$$B_2O_3 + H_2O \longrightarrow 2HBO_2 \text{ (gas)}$$

$$B_2O_3 + 3H_2O \longrightarrow 2H_3BO_3 \text{ (gas)} \quad .$$

As a consequence, the liquid layer reaches a constant thickness as the reaction progresses.

Boron carbide will also react with hydrogen to form boranes:

$$B_4C + 6H_2 \longrightarrow 2B_2H_6(\text{gas}) + C \quad .$$

Parker,[59] has simulated core meltdown in steam and involving fuel and B_4C control blades. In these experiments, the steam reacted with zirconium clad on the fuel and the product hydrogen reacted with B_4C to form boranes. The boranes are of interest because they are (1) quite volatile, (2) quite toxic, and (3) readily combustible.

1.1.2.3 Reactions of Gases Above the Core Debris

Gases emerging from the core debris will be hot enough to continue to react. If a water pool overlies the core debris, it may be that the gases will be quenched rapidly so that their compositions upon emerging from the core debris will be preserved. Otherwise, the gas composition can evolve as the gas passes along the thermal gradient between the reactor cavity and the reactor containment. Little attention has been given in reactor accident analyses to the reactions of gases once they emerge from the core debris.

In experimental studies of core debris-concrete interactions, the gases have been conducted along pathways from the site of interactions to sampling positions that are much cooler than the core debris. It has been possible to examine the gas compositions to infer the last temperature at which the gas composition was at equilibrium. These analyses have indicated that gases continue to react sufficiently rapidly to maintain chemical equilibrium at temperatures as low as about 1000 K.[41,60] This result is consistent with the expectations based on the known kinetics of gas phase reactions.

An example of the temperature dependence on the equilibrium composition of a gas produced during core debris-concrete interaction is shown in Figure 1.1-14. The predominant reactions affecting the gas composition are:

$$H_2O + CO \longrightarrow H_2 + CO_2$$

$$CO + 3H_2 \longrightarrow CH_4 + H_2O \quad .$$

With decreasing temperatures, both these reactions are displaced increasingly to the right. That is, residual water vapor is converted to hydrogen and carbon monoxide is converted to methane. Below about 1000 K, according to the available data, these reactions slow enough that equilibrium compositions cannot be maintained.

Gases very rich in carbonaceous species emerging from core debris may give rise to another reaction:

$$2\ CO \longrightarrow CO_2 + C$$

This reaction can occur whenever

$$\left[\frac{P_{CO_2}}{P_{CO}^2}\right] < \exp[-\Delta G/RT]$$

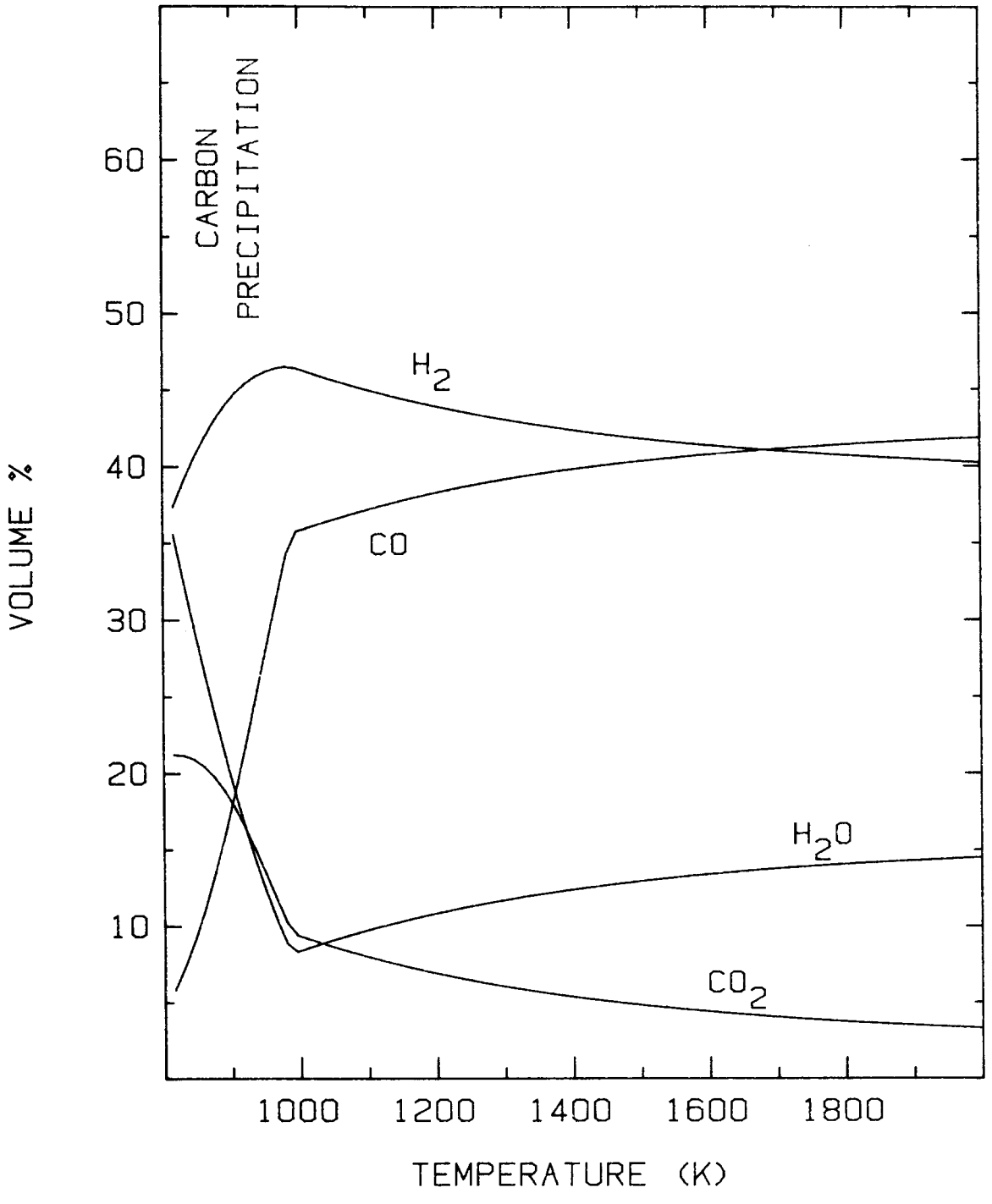

Figure 1.1-14. Variation in the Gas Phase Speciation as a Function of Temperature. Original gas had an H_2/H_2O ratio of 10 and an H_2/CO ratio of 1.

where

$$\Delta G/R = -20744 + 21.15\ T,$$

P_{CO_2} = partial pressure of CO_2,

P_{CO} = partial pressure of CO.

Because the reaction is heterogeneous--a condensed product is produced--some surface catalysis is often found necessary to facilitate the reaction. Both iron and steel can act as such catalysts.

Reactions of the gases emerging from core debris may involve the containment atmosphere drawn by natural circulation into the cavity region.[61] Gas temperatures in excess of about 800 K are sufficient to assure that oxygen from the containment atmosphere will react with hydrogen and carbon monoxide. The gases produced by these reactions could, of course, react with metal structures along the flow path to regenerate both hydrogen and carbon monoxide. These reactions with structures are, of course, kinetic processes discussed elsewhere.

1.1.2.4 Effects of an Overlying Water Pool

For many reactor accidents, it is hypothesized that core debris expelled from the reactor vessel will fall into a pool of water in the reactor cavity. This, of course, presents the possibility of fuel-coolant interactions which are discussed elsewhere in this report. Whether or not violent fuel coolant interactions occur, it is possible that reactor accidents may progress to involve core debris attacking concrete with a water pool overlying the core debris. This simultaneous interaction of core debris with concrete and coolant, too, involves the possibility of violent fuel-coolant interactions--the so-called "alternate contact mode" of interactions. But this simultaneous interaction has historically been studied and analyzed within the context of core debris-concrete interactions.

Because there is such a dirth of data, the physical phenomena involved in combined core debris-concrete-coolant interactions have been the subject of much speculation. Three possible scenarios have emerged from this speculation:

1. The coolant quenches and fragments the debris into a coolable mass of particulate.

2. Quenching of the core debris occurs; but because of the enhanced surface area of the reactive debris, there is vigorous reaction to form hydrogen associated with the quenching.

3. A coolant pool benignly boils on a crust over the core debris acting only as a way of removing heat from the core debris.

To date, there have been about five tests of combined core debris-coolant-concrete interactions.[22,41,62,63] In every case, the experimental studies have supported the third of these possibilities. The coolant layer boils benignly over the core debris. A plot of concrete erosion against time for tests with and without a water pool present is shown in Figure 1.1-15. Within the experimental error, there is no difference in the rate of concrete attack caused by an overlying water pool. At the same time, no sharp increase in the production of combustible gases seems to be associated with the addition of water to core debris attacking concrete (Figure 1.1-16). In all the tests, the core debris is quickly separated from the water pool by a quenched crust of frozen material, which is permeable to gas but, apparently, impermeable to liquid water. In some cases, these crusts have been found to have an extremely strong monogogue structure.[41]

Tests of combined core debris-concrete-coolant interactions have involved only about 50 kg of core debris and melt diameters of only about 20 cm. There is then a question of whether the observations to date would be replicated at a larger-scale. To date, the only analyses of this that have been published suggest that indeed the same behavior would be expected for masses of debris encountered in reactor accidents spread over diameters in excess of 6 m.[22] Experiences in the field of volcanology too support the contention that even at very large-scales self-supporting crusts can form which may prevent overlying water pools from either quenching the core debris or prompting vigorous production of combustible gases.[64]

1.2 High-Pressure Melt Ejection and Direct Containment Heating

(W. Tarbell, J. Brockmann, R. Nichols, and N. Yamano, 6422; M. Pilch, 6425)

High pressure ejection of core debris into the reactor cavity is predicted if the reactor pressure vessel (RPV) fails while the primary system is at elevated pressure. Accident analysis assume that RPV failure in a pressurized water reactor (PWR) will occur at an instrument guide tube penetration in the lower head.[65] Although critical to initiate the high-pressure melt ejection (HPME), the failure of the instrument tube has not been experimentally verified. Tube failure experiments are being planned under the MELPROG validation experiment program. Because head failure directly affects HPME and Direct Containment Heating (DCH), program personnel have analyzed the phenomena associated with this type of accident sequence. The results of the analysis follow.

1.2.1 Introduction

Failure of the primary system can occur in a variety of ways:

1. Thermal shock resulting from injection of cold water into the primary system.

2. Natural circulation induced creep-rupture failure of the head bolts, hot leg nozzle, surge line, steam generator tubes, or pump seals.

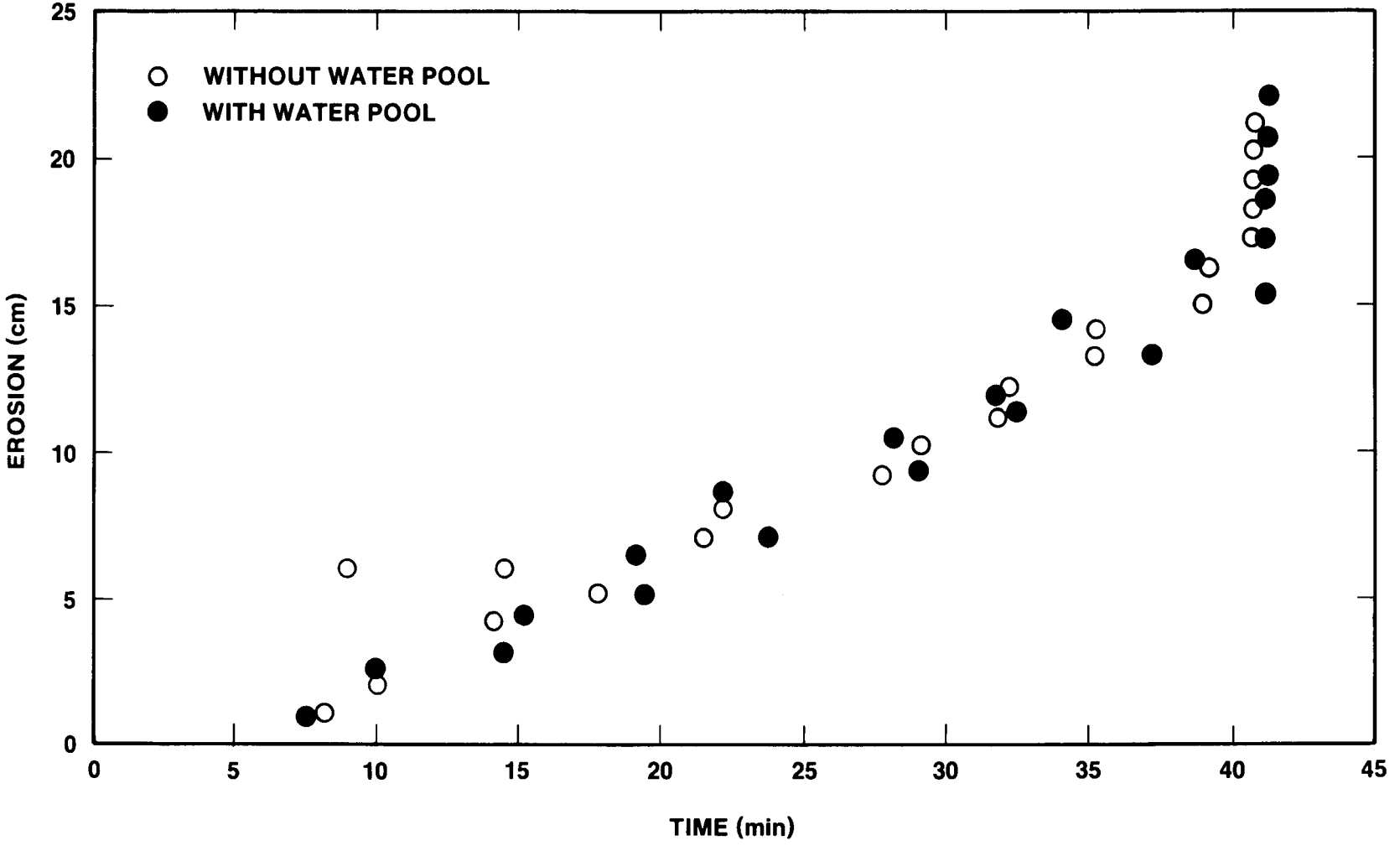

Figure 1.1-15. Effect of an Overlying Water Pool on Concrete Erosion by a Steel Melt (Reference 22)

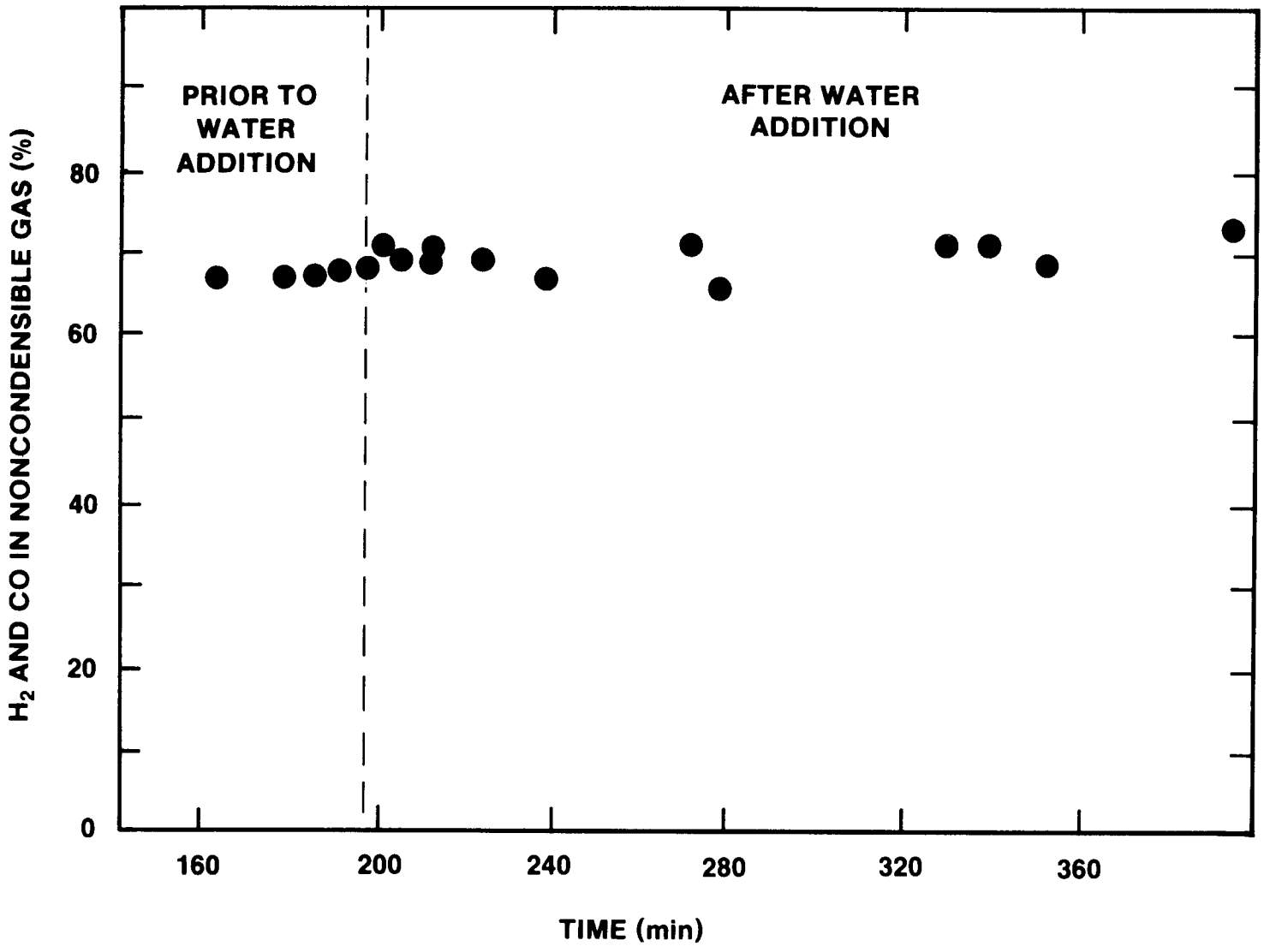

Figure 1.1-16. Effect of Water Addition on the Generation of Combustible Gas During Steel-Concrete Interactions (Reference 41)

3. Steam explosion induced failure of the upper head, head bolts (stretch), or the lower head.

4. Global creep-rupture/ablation of the lower head by relocated core debris in the lower plenum.

5. Ablation of lower head at the stagnation point of impinging jet of molten core material.

6. Ejection of an in-core instrument guide tube.

The location, timing, and failure mode of the primary system affects the disposition of core debris in the containment, the resulting containment loads, and the aerosol source term. The first two failure modes could occur prior to debris relocation into the lower plenum, while the remaining modes can only occur after debris relocation. The 3rd and 5th failure modes might occur during the relocation phase itself. The emphasis of this discussion is on the last three failure modes.

The failure mechanisms considered here all result from the thermal attack of core debris on the lower head. While considering the response of the lower head to thermal loads, it is equally important to realize that the thermal loads themselves are strongly dependent upon physics of fuel relocation into the lower plenum. This history dependence of fuel relocation cannot be resolved here; consequently, the two limiting cases as depicted in Figure 1.2-1 are considered.

In both cases, a layer (~0.05 m thick) of low melting point (~1000 K) control rod material resides on the lower head (~0.13 m thick). The control rod material is assumed to relocate into the lower plenum when its steel clad melts, but well before any significant melting of fuel or its clad material begins.

The relocated core material may be in the form of a debris bed, caused by quenching of molten material in the water residing on the lower head. If the material reheats, it could form a molten pool. A molten pool could also be created from a sudden relocation of molten material, such as failure of a blockage within the core region. In all cases, it is expected that a crust layer of solidified debris will be in contact with the lower head.

The debris bed could be achieved if the relocation rate is slow (dripping) or if significant fragmentation and quenching of a coherent melt occurs as it falls through the water pool. Because the fuel is largely quenched, it might be 20 min before remelting of the fuel occurs; then the molten material will sink into the interstitial void in the lower region of the debris bed. The final state of the degraded core material will resemble a crusted molten pool.

Quenching of fragmented melt as it settles into the lower plenum is an important criteria determining whether a debris bed or a dense crust-

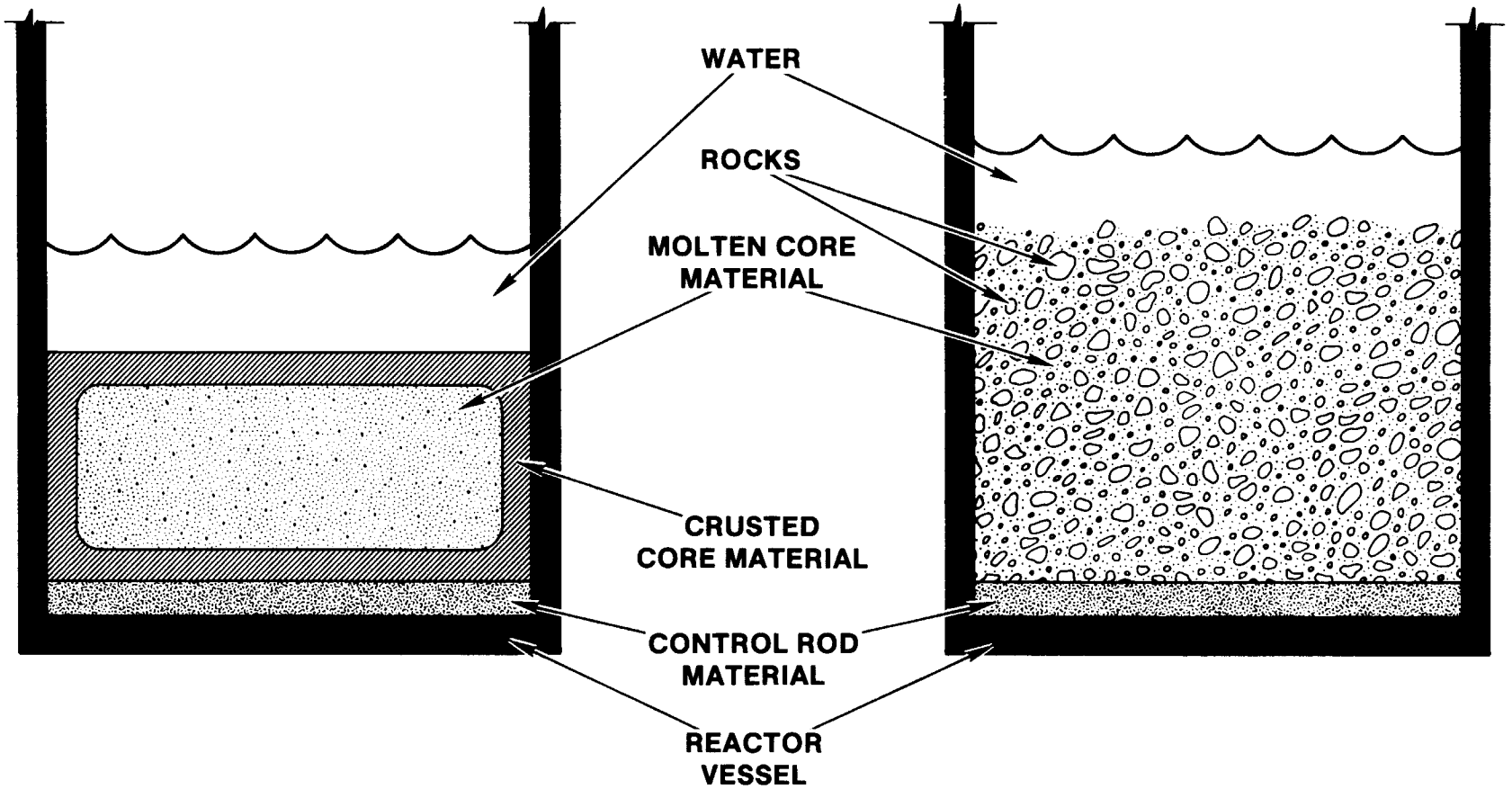

Figure 1.2-1. Possible Debris States Following Core Slumping

molten-pool forms. Particles of 1-cm diameter will be about 15 percent solidified by the time they settle through 1 m of water. Thus particles (or jets) significantly larger than 1 cm might be expected to reagglomerate, flow, and spread radially across the lower head, whereas particles significantly smaller than 1 cm might lead to a debris bed that may or may not spread radially. Particles of in-between-size might form a partially reagglomerated structure of significantly reduced coolability.

There is experimental evidence that a partially reagglomerated state might be the expected, provided, of course, that a steam explosion does not occur. The EJET tests at Sandia[66] delivered a molten mixture of iron and alumina into a 1.6-m deep tank of water. The melt was delivered as a gravity driven jet. Jet diameters of 4, 8, and 16 cm were used in single and multiple-jet tests. These jet diameters are characteristic of the flow paths melt must flow through as it enters the lower plenum in a reactor. Although significant fragmentation was observed as the melt settled through the water, a debris bed was not observed in any of the tests. In all cases, the melt agglomerated into a nearly solid slug (dense) on the tank bottom.

1.2.2 Global Creep-Rupture and Ablation of Lower Head

Creep-rupture and ablation of the lower head are competing failure mechanisms with one dominating over the other depending on the temperature and load history. Creep-rupture occurs when heating of the lower head significantly degrades its strength.

The creep-rupture model in the MELPROG code is applied at each radial node. The principal stresses are calculated using analytic formulations derived for simplified geometries assuming uniform load across the entire member. Stress concentrations for holes are accounted for. Thermal stresses are not modeled, but ablation is included for reducing the member thickness.

The load on the lower head is the sum of internal pressure, the weight of debris and water on the lower head, and the weight of the lower head itself. Nonuniform loads are modeled by calculating the stress in each radial node as if the load on that node were applied uniformly (not averaged) over the entire member.

Given the principal stress, a Larson-Miller correlation is used to calculate the time to creep-rupture based on the average axial temperature across the lower head. This correlation applies to members loaded to a given stress and at a specified, constant temperature. In an accident, the loading and heating of the head are transient. A "lifetime rule" is used to account for time variations in applied load and temperature.

It is useful to estimate the dominate contributions to stress in the lower head. Results are summarized in Table 1.2-1. The stress (σ) induced in the hemispherical lower head due to uniform internal pressure (P) is given by[67]

Table 1.2-1

Dominant Stresses on Lower Head

Source	Principal Stress MPa
Uniform Internal Pressure 17.2 MPa	124
Weight of Lower Head ΔT = 1000 K	0.07
Lower Head Filled With Corium	1.1
Potential Thermal Stress ΔT = 1000 K	1882

$$\sigma = P \frac{D}{4\delta} \quad , \tag{1.2-1}$$

where D = diameter of hemisphere, and δ = thickness of the lower head.

For a maximum system pressure of 17.2 MPa (2500 psi) and typical reactor dimensions (D = 4 m, δ = 0.14 m), the stress is about 124 MPa (18,000 psi), which is approximately a factor of 5 below the failure stress for the vessel. Thus, even in the extremes of normal operation, the reactor vessel provides a wide margin of safety.

The maximum stress induced in the lower head by its own weight is given by[67]

$$\sigma = \rho_s g \frac{D}{4} \quad , \tag{1.2-2}$$

where ρ_s = density of steel, and g = acceleration due to gravity.

This maximum stress is located at the extreme lower point of the vessel. The weight of the lower head contributes only about 0.07 MPa (10 psi) to the total stress in the lower head and consequently plays no real role in failure of the lower head.

The maximum stress induced by the weight of molten core material filling the lower head is given by[67]

$$\sigma = \rho g \frac{D^2}{8\delta} \quad , \tag{1.2-3}$$

where ρ = density of the core material.

This maximum stress is also located at the extreme lower point of the vessel. Assuming dense core material, the maximum stress induced in the lower head is about 1.13 MPa (165 psi). The weight of core debris on the lower head plays no real role in vessel failure.

In the absence of thermal gradients, the preceding analysis clearly shows that the system pressure is the dominant load on the lower head. Under normal conditions, the reactor vessel is designed to provide a wide margin of safety, but under accident conditions, the ultimate strength of the vessel could be significantly reduced as core material heats the lower head.

The methodology described above does not account for the thermal stresses created by temperature gradients associated with vessel heating. Temperature gradients induce a stress distribution in the lower head that is compressive on the inside (hot on the inside) and tensile on the outside, consequently, thermal stresses reduce the total stress on the inside of the vessel while adding to the tensile stresses already present on the outside of the vessel.

For a linear temperature gradient, the thermal stress induced on the outside of the vessel is given by[68]

$$\sigma = \frac{\alpha E \Delta T}{2(1-\nu)} \left(1 - \frac{2}{3}\delta\right) \quad , \tag{1.2-4}$$

where

α = coefficient of thermal expansion,

E = modulus of elasticity,

ΔT = temperature difference between the inside and outside of the vessel,

ν = Poisson ratio.

The estimated thermal stress for a 1000 K temperature gradient in the lower head is 1882 MPa (273,000 psi), which exceeds the ultimate strength of the lower head by at least a factor of 3.

Thermal stresses, however, differ fundamentally from mechanical stresses in that the former are "self limiting." The differential expansion associated

with thermal stresses requires that the stress pattern satisfy the requirements for equilibrium of internal forces; hence, plastic deformation or yielding produces relaxation of the thermal stress. Thermal stresses are self limiting in the sense that stresses above the yield point cannot be sustained without plastic deformation reducing the internal force and thus, the stress. In the case of mechanical loads (i.e., pressure), the internal stress must be in equilibrium with the external load which remains constant; consequently, the internal stress cannot relax if the member begins to flow plastically. In this case, yielding will continue until the member breaks or until the deformation is limited by strain hardening or stress redistribution.

The transient heating of the lower head also tends to reduce the importance of thermal stresses because thermal stresses are only important in regions where the temperature gradient is large. Thus, for thermal stress to be significant on the outside surface of the head, the temperature gradient must be large near the outside surface; but by that time, the mean temperature is likely to be high enough that the global strength of the vessel is weakened. In this case, the role of thermal stress in hastening head failure may be significantly decreased.

It is clear that thermal stresses potentially play an important role in global failure of the lower head. However, the unique features of thermal stress (i.e., temperature gradients must first be established and thermal stresses are self limiting) tend to reduce their importance. Demonstration problems using a stress analysis code can provide valuable insight into the coupling between mechanical stresses and thermal stresses in a member undergoing transient heating.

1.2.3 Description of In-Core Instrument Guide Tubes

During the normal operation of a PWR, it is necessary to map the neutron flux distribution within the core. This is accomplished by inserting in-core instruments (neutron detectors) into the core through thimbles, which in turn are housed in guide tubes.[69] There are 58 thimble/guide-tube assemblies in the Zion reactor (52 at Three Mile Island). Typically, the number of detectors is small, on the order of five or less, and each detector can be inserted into any of approximately 10 thimbles. Because there may be only five in-core instruments, most of the thimble/guide-tube assemblies are always open, and generally all positions are open (i.e., no in-core instruments are inserted into the core). In some plants (Zion for instance), a small number ($\neq 8$) of the guide tubes are dedicated to thermocouples. The following sections provide added detail on guide tubes, thimbles, and in-core instruments.

1.2.3.1 Guide Tubes

Figure 1.2-2 shows some details of the guide tubes in the vicinity of the lower head. Not shown are the thimbles or in-core instruments. Guide tubes are composed of two components: The section that passes through the lower head (termed the "penetration nozzle") and the long portion that extends through and beyond the cavity to the seal table. The penetration

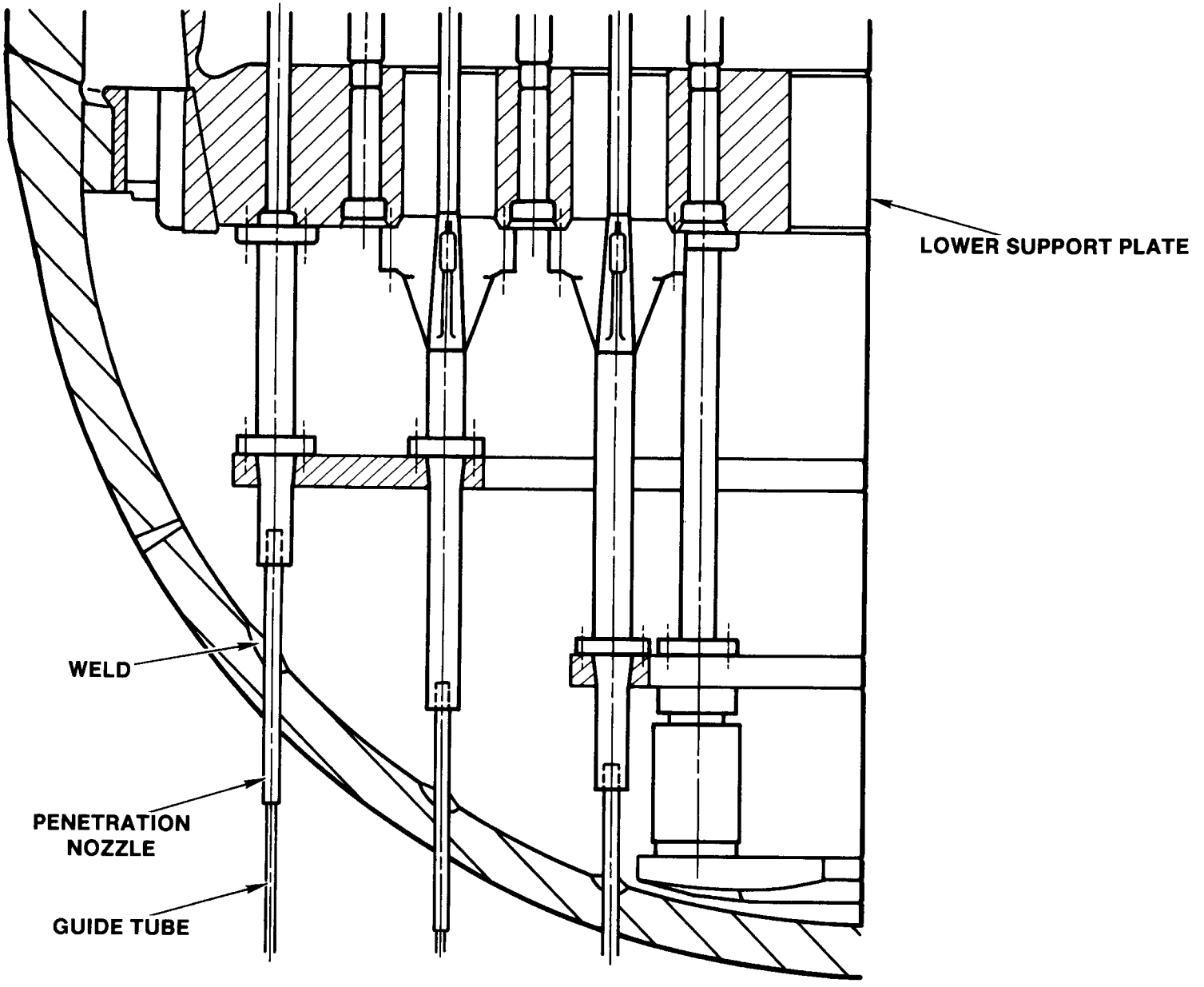

Figure 1.2-2. Schematic of Guide Tube Penetrations

nozzle is generally made from stainless steel (type 304), but Inconel is used in some plants. The guide tubes are continuous stainless steel tubing (with unions) passing from the seal table, located in the containment building above the top of the reactor, down through the instrument tunnel and reactor cavity, up to the RPV. They join the penetration nozzles approximately 30 cm from the lower head.

Except for the penetration nozzles, the guide tubes typically have a 2.5-cm OD and either a 1- or 1.5-cm ID. The nozzles themselves, which actually pass through the vessel and protrude about 30 cm on either side, have 3.8-cm diameters with the ID matching that of the guide tube.

The guide tubes inside the vessel are open to the primary system environment; consequently, the tubes form part of the pressure boundary and contain primary system water all the way to the seal table where the tubes are sealed to the thimbles. The guide tubes can be viewed as pressurized straws hanging from the bottom of the reactor vessel.

The guide tube penetrations are installed by the vessel manufacturer after the cladding on the inside surface of the lower head is in place. The lower head is machined to form a "J-groove" as shown in Figure 1.2-3. The exposed base metal is covered with a thick "buttered" layer of stainless steel or Inconel. After stress relieving of the entire head, a fillet weld is made from the tube to the vessel with stainless steel or Inconel filler material to match the composition of the penetration nozzle.

The pressure vessel code requires that all material compensation be made internally (i.e., the weld is on the inside of the vessel), and that the weld is of sufficient size to develop the full strength of the attachment. The penetrations normally have an interference fit (head at elevated temperature) or a minimum clearance fit. The welds are J-groove plus-fillet with minimum depth of 1.25 times the nominal thickness of the penetration.

1.2.3.2 Thimbles

Figure 1.2-4 shows details of a typical thimble. The thimble is a continuous tube passing through the entire length of the guide tube and up into the core. The thimbles are always fully inserted into the core during normal operation, but are withdrawn approximately 4.5 m during refueling operations.

Thimbles are flexible, thin walled tubes (9.78-mm OD and 8.51-mm ID) made from Type-304 stainless steel. The terminus of the thimble inside the core is sealed with a bullet nose. The space inside the thimble is gas filled at containment pressure while the annulus between the thimble and the guide tube is water filled at primary system pressure. The thimble is also part of the pressure boundary. The seal between the thimble and the guide tube is shown in Figure 1.2-5.

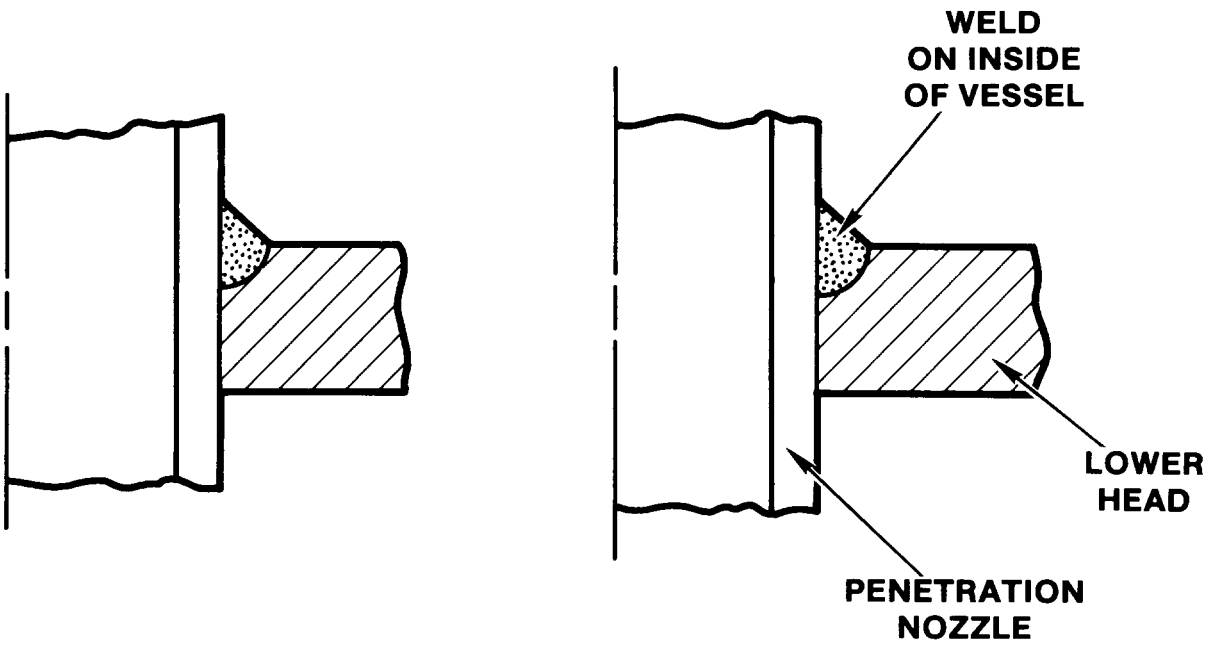

Figure 1.2-3. Details of Guide Tube Weldment

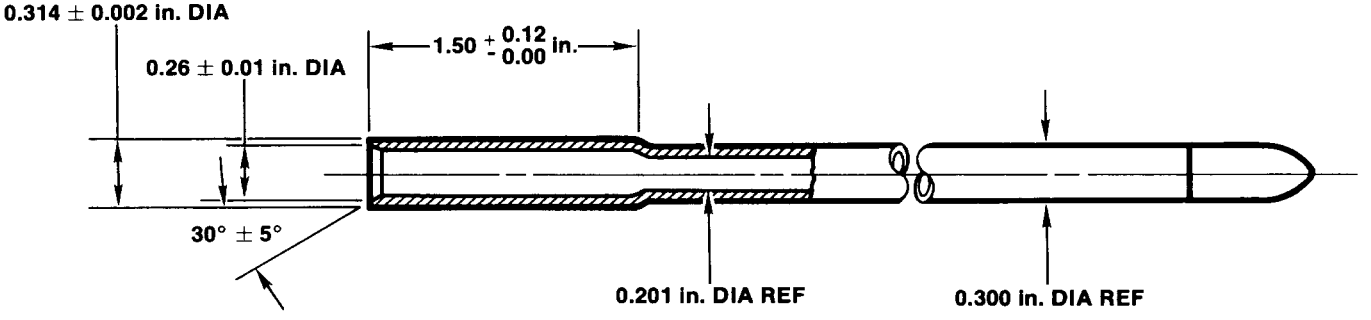

Figure 1.2-4. Thimble Details

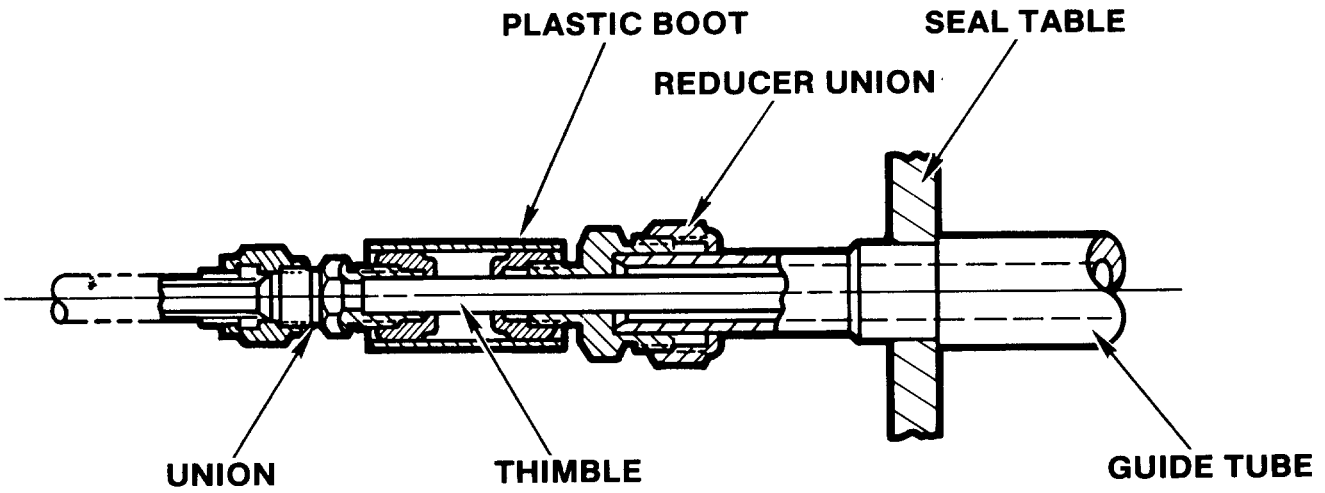

Figure 1.2-5. Thimble to Guide Tube Seal

1.2.3.3 In-Core Instruments

The in-core instruments penetrating the bottom head consist of flux detectors and, in some plants, thermocouples. The flux detectors run the length of the selected fuel assemblies to measure the neutron flux distribution in the core. Typically, only a small number (~5) of flux detectors are available. Typical detector dimensions are 0.6 cm in diameter by 5.33 cm long. Other detectors can also be used in the system.

The neutron detectors are inserted into the core using a helical wrap drive cable that pushes the instrument through the thimbles. A stainless steel sheathed, mineral insulated, coaxial cable passes from the detector through the helical wrap drive cable past the seal table and into the containment. Each drive assembly consists of a gear motor, a path group selector, and a rotary selector, which allows use of one of ten guide tubes. Figure 1.2-6 shows a schematic of the system for inserting instruments into the core.

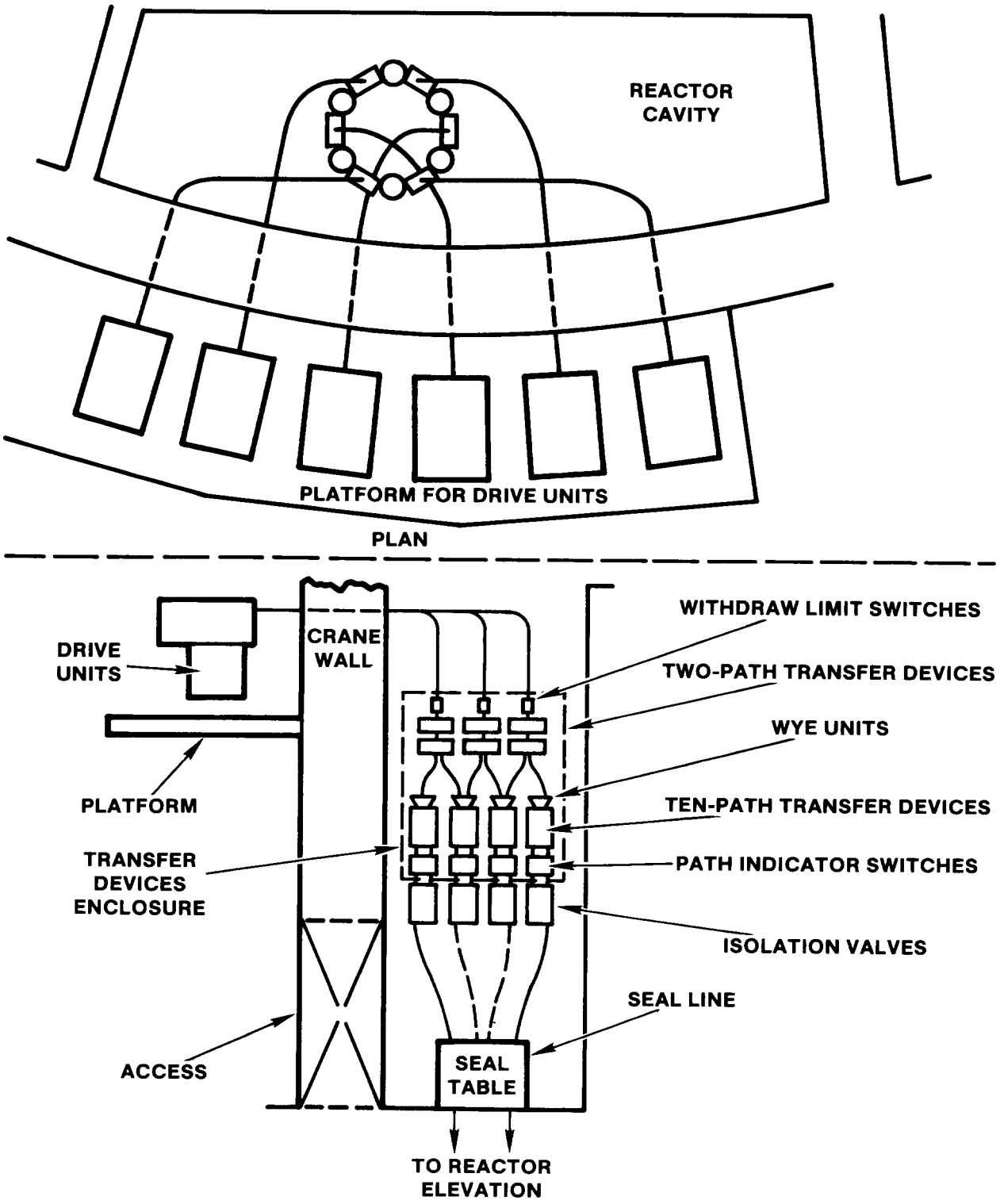

Figure 1.2-6. Arrangement of In-Core Flux Detector Drive System

Isolation valves are placed between the seal table and drive units to provide leakage protection in the event of thimble failure. This protection is provided for empty tubes only; the cable from the in-core instruments prevents isolating those thimbles containing instruments.

In some plants (Zion for instance), a small number (8) of guide tubes are dedicated to thermocouples; while in other plants, the thermocouples are inserted into the core through the top head. The thermocouples are positioned to measure fuel assembly coolant outlet temperatures at selected locations. Two seals are used: one at the seal table, and the other at the vessel head. The thermocouples are enclosed in stainless steel sheaths within the guide tube to allow replacement if necessary.

1.2.4 Ablation of the Lower Head at the Stagnation Point of an Impinging Jet

If there is a sudden massive release of molten core material into the lower plenum, it is conceivable that a coherent jet of molten core material will pass through the water pool and impinge upon the lower head. The jet might possibly penetrate the lower head due to ablation at the stagnation point. Alternatively, the jet might impinge on the fillet weld between the penetration nozzle and the lower head. Ablation of this weld could lead to a pressurized ejection of nozzle and guide tube.[65]

The picture of a coherent jet passing through water and impinging on the lower head should be questioned based on the observations of the EJET tests. In addition, the instrument guide tubes passing through the lower plenum should promote the mixing of any melt entering this region. Nonetheless, it is useful to investigate the effect of jet impingement on the lower head.

High temperature melt flowing into the lower plenum impinges upon the relatively cold steel of the lower head. The contact temperature (T_c) between the jet and the cold steel is given by

$$T_c = \frac{k_j \rho_j c_{pj} T_j + k_s \rho_s c_{ps} T_s}{k_j \rho_j c_{pj} + k_s \rho_s c_{ps}} \quad , \tag{1.2-5}$$

where

k_j, k_s = thermal conductivities of the molten jet and cold steel, respectively,

ρ_j, ρ_s = densities of molten jet and cold steel, respectively,

c_{pj}, c_{ps} = specific heats of molten jet and cold steel, respectively,

T_j, T_s = initial temperatures of molten jet and cold steel, respectively.

The molten jet can be either steel or oxidic material. Table 1.2-2 summarizes relevant thermophysical properties for this analysis and those that follow. Table 1.2-3 summarizes additional conditions and calculated quantities for the sample calculations that follow.

Consider the case where molten steel or oxidic materials are released from the core at 2550 K. This is 850 K above the freezing point of a steel jet and only 50 K above the melting point of an oxidic jet. The temperature of the cold steel of the lower head is assumed to be 500 K. Under these conditions, the contact temperature between the jet and the lower head is 1470 K in the case of a steel jet and 846 K in the case of an oxidic jet. In both cases, the temperatures are below the freezing point of the jet material and an insulating crust of frozen jet material will begin to form.

The cold steel of the lower head loses its ability with time to conduct heat away from the crust interface because of the ever growing thickness of the thermal boundary layer on the lower head. As a consequence, the crust begins to remelt and the lower-head/crust interface begins to heat up. For steel jets, the lower head will begin to melt at approximately the same time that the crust disappears. Melting of the lower head begins before complete remelting of the crust for oxidic jets. In either case, the approximate delay time (t_d) required to initiate ablation of the lower head is given by[70]

$$t_d = \frac{\pi \rho_s c_{ps}}{4k_s} \left[\frac{k_s (T_{ms} - T_s)}{h(T_j - T_{mj})} \right]^2 , \qquad (1.2\text{-}6)$$

where h = convective heat transfer coefficient from the jet to the lower head.

This represents the time required to heat the surface of a semi-infinite body to its melting point by application of a constant heat flux to the surface.

The heat transfer coefficient for the stagnation region of an impinging jet is calculated from

$$\frac{hD_j}{k_j} = 0.553 \, Re_j^{0.50} Pr_j^{0.33} , \qquad (1.2\text{-}7)$$

$$Re_j = \frac{\rho_j V_j D_j}{\mu_j} , \qquad (1.2\text{-}8)$$

and

Table 1.2-2

Thermophysical Properties of Reactor Materials

	Solid Steel	Molten Steel	Solid Corium	Molten Corium
k (W/m)	25	18	2.2	5.5
ρ (kg/m^3)	7000	7000	8000	8000
c_p (J/kg•K)	600	776	365	485
μ (Pa•s)	----	6×10^{-3}	----	4×10^{-3}
T_m (K)	----	1700	----	2500
h_f (J/kg)	----	2.7×10^5	----	2.08×10^5

Table 1.2-3

Conditions and Results for Sample Calculations

	Steel Jet	Oxiditic Jet
T_j (K)	2550	2550
T_s (K)	500	500
T_c (K)	1470	1470
V_j (m/s)	1	1
D_j (m)	0.01	0.01
h (W/m^2•K)	2.2×10^4	9.6×10^3
t_d (s)	0.34	511
t_p (s) at 3 cm	11	25
t_p (s) at 15 cm	55	127

$$Pr_j = \frac{c_{pj}\mu_j}{k_j} \quad , \tag{1.2-9}$$

where d_j = diameter of jet, V_j = velocity of jet, and μ_j = viscosity of jet.

Calculated heat transfer coefficients for 0.01-m diameter jets falling at 1 m/s are presented in Table 1.2-3.

The time required to initiate ablation of the lower head is very short for steel jets; however, ablation is delayed for a long time in the case of oxidic jets. The oxide crust is a significant barrier to ablation of the lower head. The mechanical stability of the crust becomes important once ablation of the substrate begins; a stable crust will continue to be a barrier to heat transfer until it remelts. However, for this analysis it is assumed that any remaining crust is swept away once ablation of the lower head is initiated.

Ablation of the lower heads proceeds very rapidly following this initial delay. The time (t_p) required for ablation to penetrate a thickness (L) is given by

$$t_p = \frac{L\,\rho_s\left[c_{ps}\left(T_{ms} - T_s\right) + h_{fs}\right]}{h\left(T_j - T_{ms}\right)} \quad . \tag{1.2-10}$$

Here, it is assumed that heat transfer from the jet proceeds directly to the ablating steel.

The time required to ablate through the lower head (L = 0.15 m) is 55 s for the steel jet and 127 s for the oxidic jet. Because it is smaller in size, the weld on an instrument guide tube will ablate in only 20 percent of these times. The ablation times (t_p) should be added to the times required to initiate ablations (t_d) in order to assess the overall timing of any threat to the lower head. Clearly, the massive relocation of large quantities of hot steel is a much greater threat to the lower head than corium melt.

The analysis and conclusions drawn here are in substantiated agreement with experiment observations.[71] The erosion rate of steel plates subject to the impingement of low velocity jets (D_j ~0.02 m) has been correlated by Powers[71]; he concludes that quenching of hot steel jets to form a frozen crust on the steel structure constituted a negligible barrier to the erosion process. It was also observed that relatively thin (2 mm) coatings of urania on the steel substrate substantially inhibited erosion by steel melts, thus demonstrating that oxidic crusts represent a significant barrier to erosion.

1.2.5 Tube Ejection

The Zion Safety Study[65] postulated that jet impingement and sustained heating from the layer of overlying core material will heat the reactor vessel to the point where the penetration tube weld has no strength. Under high system pressures, the weld will fail, which will release the penetration nozzle, allowing it to be forcibly ejected from the lower head, which in turn will initiate discharge of molten material from the reactor vessel.

The shear stress on the fillet weld between the penetration nozzle and the reactor vessel is[72]

$$\sigma = P \frac{\pi d^2/4}{\pi dL} = \frac{Pd}{4L} \quad , \tag{1.2-11}$$

where P = system pressure, d = outside diameter of penetration nozzle, and L = depth of the weld.

For a system pressure of 17.2 MPa and a 2.5-cm weld, the shear stress on the weld is 6.5 MPa (937 psi). Thus, under normal operation, there is a wide margin of safety afforded by the weld.

Under the severe conditions of a degraded core accident, however, the weld will be heated to temperatures approaching its melting point and begin to ablate. It appears that the weld will have to be very near its melting point before failure and possible tube ejection might be expected.

The weld is not the only mechanism preventing the ejection of the penetration nozzles and guide tubes. At the time of vessel manufacture, the penetrations are inserted into the lower head with a minimum clearance or interference fit. Owing to the difference in materials (the vessel is mild steel while the penetrations are either stainless steel or Inconel), there is a differential expansion under accident conditions that works to hold the penetration in the vessel. The unconfined interference (δ) created by differential expansion is given by

$$\frac{2\delta}{D} = \Delta\alpha \, \Delta T \quad , \tag{1.2-12}$$

where

D = outside diameter of penetration nozzle,

$\Delta\alpha$ = difference in the coefficients of linear expansion between the nozzle and the vessel wall,

ΔT = temperature difference between operating or accident conditions and ambient conditions at the time of vessel manufacture.

The interference, if any, between the nozzle and the vessel at the time of manufacture should be added to that created by thermal expansion, but only the latter is considered here.

Given this interference, the interface pressure (P_i) between the nozzle and the vessel is given by[73]

$$P_i = \frac{1}{2} E \frac{2\delta}{D} \left[1 - \left(\frac{d}{D}\right)^2\right] \quad , \tag{1.2-13}$$

where E = modulus of elasticity for both the nozzle and the vessel (assumed the same for both), and d = inside diameter of the nozzle. Under normal operation, the interface pressure is 74.7 MPa (11,000 psi).

The system pressure (P) required to push the nozzle from the vessel (assuming no weld) is given as[72]

$$P = f \frac{\pi DL}{\pi D^2/4} P_i = 4f \frac{L}{D} P_i \quad , \tag{1.2-14}$$

where L = thickness of the lower head, and f = friction coefficient.

Reference (72) notes that values of f varying from 0.03 to 0.33 have been reported with averages around 0.10 to 0.15. Taking the lower bound of f = 0.03, the system pressure required to eject the penetration is 30.3 MPa (4,400 psi), which is significantly greater than the maximum anticipated system pressure of 17.2 MPa (2500 psi). Even higher system pressures would be required if the nozzle were installed with an interference fit.

This analysis suggests that differential thermal expansion may be a dominant mechanism preventing ejection of the penetration nozzles. However, as the conditions for creep rupture are approached, the lower head will begin to yield and balloon outwards. This process will enlarge the holes into which the penetration nozzles are wedged, thus relieving the interference between the nozzle and the vessel due to manufacture and differential thermal expansion. The circumferential strain (ε) required to release the nozzles is

$$\varepsilon = \frac{2\delta}{D} \quad , \tag{1.2-15}$$

where the right hand side is the total interference between the nozzle and the vessel. Under accident conditions, a strain of about 0.4 percent is sufficient to release the nozzles. This corresponds to a sag (δ) in the lower head of about 8 mm.

1.2.6 Hydrogen Generation During the Pressure-Driven Expulsion of Core Debris From the Reactor Vessel

(D. A. Powers, 6422)

Probabilistic risk assessments since the time of the Reactor Safety Study[1] have established that the risk-dominant accidents in modern nuclear power reactors will involve core degradation while the reactor coolant system is at or near operating pressure.[1,65,74,75] That is, the most important accidents will be initiated by transient events-such as the loss of on-site power--or small breaks in the cooling system. Such pressurized core degradation accidents are significant even for boiling water reactors since the automatic depressurization features of these reactors may fail to function.[76] Under such accident conditions, depressurization of the reactor coolant system is slow. Certainly, the core degradation process will be affected if high pressures exist in the coolant system. The expulsion of core debris from the reactor vessel into the reactor containment will also be affected.

In the past, severe accident analyses have been based on the assumption that core debris slumping into the lower plenum will initiate a global failure of the lower vessel head. The debris will then fall into the cavity and may initiate attack on the structural concrete of the reactor containment.

Since the publication of the Zion Probabilistic Safety Study[65], an alternate view of severe accident phenomena has developed. Core debris slumping into the lower plenum may initiate local failures in the lower vessel head. Penetrations through the vessel head for instrumentation or reactor control devices are particularly vulnerable to rapid attack by the slumping melt. The molten core debris within a pressurized vessel may, then, be forcibly expelled. The expulsion will be followed by blowdown of the reactor coolant system. Core debris behavior during this sequence of events will be quite different than the mere initiation of core debris attack on concrete envisaged in the past.

Experimental studies have shown that blowdown of the reactor coolant system will disperse debris from the reactor cavity.[77,78,79] The debris is not dispersed as a coherent mass. Rather, it is entrained in the flow, the liquid droplets disintegrate to a stable size,[80] and the droplets are lofted out of the cavity. An X-ray photograph of debris emerging from a model of a reactor cavity during expulsion of melt from a pressurized vessel is shown in Figure 1.2-7. Commination of the debris may be caused by processes other than flow entrainment. For instance, the effervescence of dissolved hydrogen as the debris escapes the reactor vessel may disperse and fragment the debris.[81,82] Similarly, simultaneous expulsion of debris and gas from the vessel can lead to "pneumatic atomization" of the expelled debris.[83] By whatever mechanism, the expelled core debris is converted from a coherent mass within the reactor cavity to a particulate mass lofted from the reactor cavity. The size distributions of core debris seen in

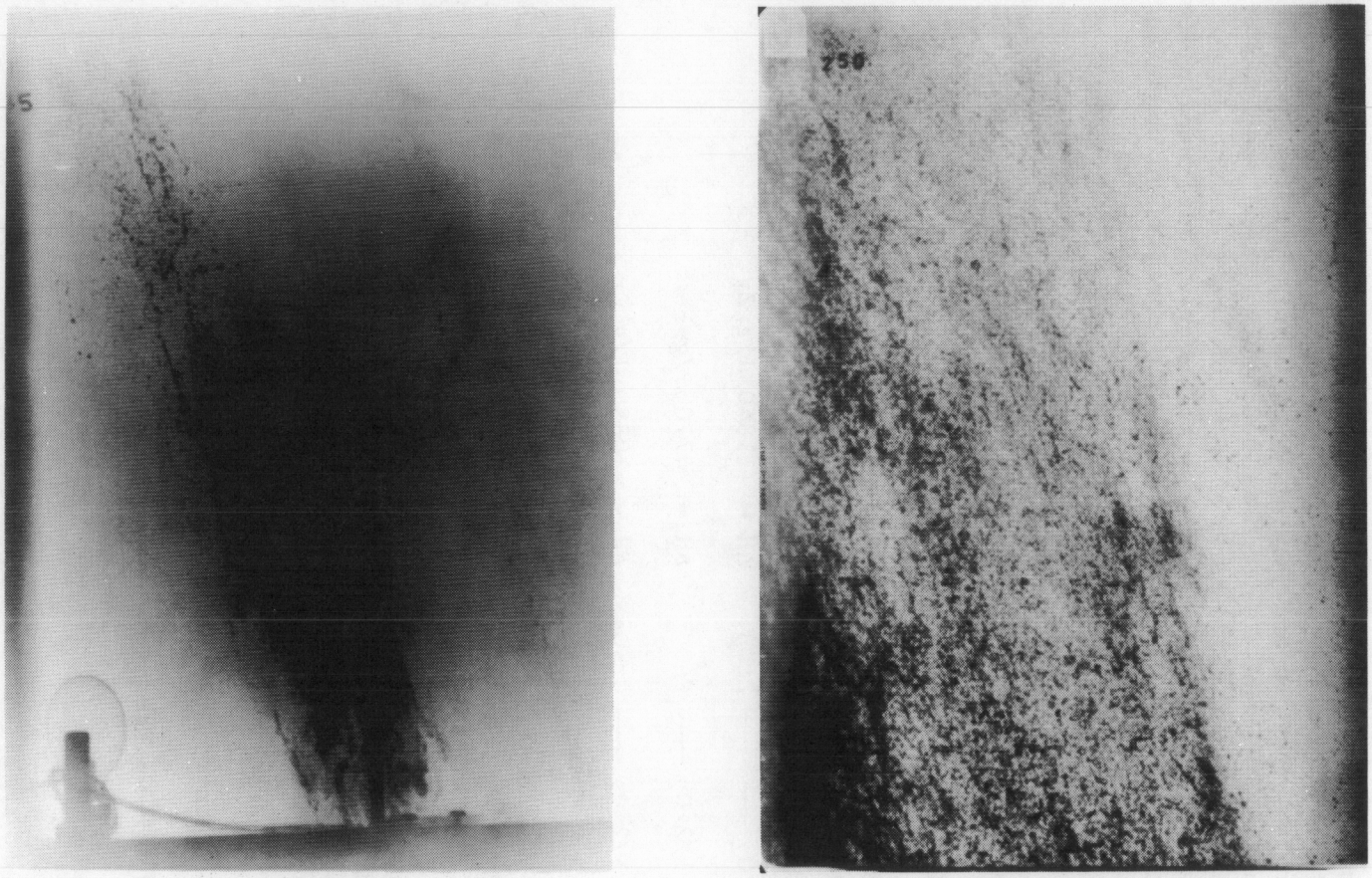

SPIT-19
M = 10.3 kg
P = 12.6 MPa

HIPS-2C
M = 80.0 kg
P = 11.6 MPa

Figure 1.2-7. X-Ray Photograph of Fragmented Debris Being Expelled From a 1:10 Scale Model of a Reactor Cavity (Reference 77) (M = Mass of Melt Tested; P = Driving Pressure)

tests[77,84] of pressure-driven melt expulsion are shown in Figure 1.2-8. The mean size of the expelled droplets is seen from these data to be something less than 1 mm.

The current state-of-the-art of modeling core degradation under severe accident conditions makes impossible definitive conclusions concerning either the amount or the composition of core debris available for pressurized melt expulsion. The evidence obtained during the dissection of the damaged core at Three Mile Island is that a significant amount of the core may be present in the lower plenum of a reactor when a localized failure of the vessel occurs.[85] Clearly, the debris will consist of much reactor fuel. It will also contain amounts of steel and unoxidized zirconium clad. This material, when expelled from the vessel, will be both hot and chemically reactive. Because the debris is commutated during expulsion from the vessel or the cavity, it will have a very high surface area so chemical reactions with the ambient atmospheric gases can be rapid.

Initial examinations of the behavior of debris fragmented and lofted from the reactor cavity have focused on two classes of chemical reactions. The first concern was over reactions of the metallic components with oxygen in the reactor containment:*[86]

$$Zr + O_2 \longrightarrow ZrO_2 \qquad \Delta H = -11840 \text{ J/g Zr}$$

$$Fe + 1/2\ O_2 \longrightarrow FeO \qquad \Delta H = -4770 \text{ J/g Fe}$$

$$2Cr + 3/2\ O_2 \longrightarrow Cr_2O_3 \qquad \Delta H = -10850 \text{ J/g Cr} \quad .$$

These reactions are quite exothermic and consequently they can impart additional heat to the containment atmosphere, which may lead to an overpressurization of the containment. It was recognized, however, that prior to encountering the oxygen of the containment atmosphere, the fragmented debris would be exposed to steam. Steam might be in the lower compartments of the containment and would certainly be in the gases blowing down from the reactor coolant system. The second class of chemical reactions of interest then are:

$$Zr + 2H_2O \longrightarrow ZrO_2 + 2H_2 \qquad \Delta H = -6380 \text{ J/g Zr}$$

$$Fe + H_2O \longrightarrow FeO + H_2 \qquad \Delta H = -310 \text{ J/g Fe}$$

$$2Cr + 3H_2O \longrightarrow Cr_2O_3 + 3H_2 \qquad \Delta H = -3660 \text{ J/g Cr} \quad .$$

Though far less exothermic, these reactions yield hydrogen.

The production of hydrogen is a most significant aspect of pressure-driven melt expulsion and subsequent debris dispersal. Chemical reactions of the

*Enthalpies of reaction, ΔH, are calculated for isothermal processes at 298 K.

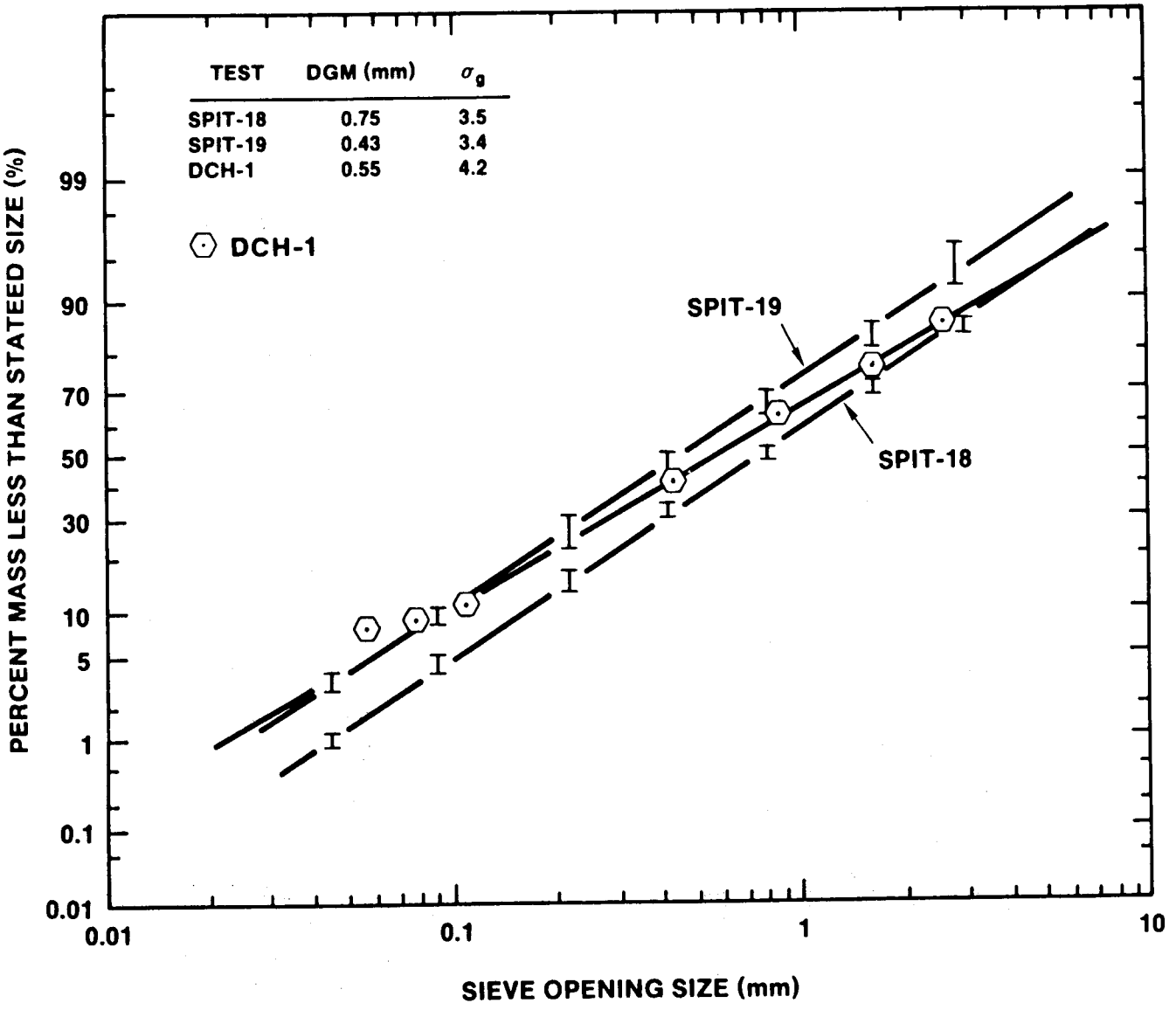

Figure 1.2-8. Size Distribution of Debris Produced During Pressure-Driven Melt Expulsion Tests (References 77 and 84)

debris with oxygen in the containment atmosphere depends on the ability of debris to reach the oxygenated atmosphere. The many structures and convoluted passages between the cavity region and the bulk containment atmosphere make the question of debris exposure to oxygen problematic, however, also see Reference 87. Exposure to steam is, on the other hand, far more assured. This exposure to steam will occur even in Mark I and Mark II boiling water reactor containments that are inerted and have no oxygen.

The extent of hydrogen production during debris dispersal depends on the kinetics of reaction. There have been several studies of the rates of metal droplet reactions when exposed to oxidative environments.[88-91] It is generally found that such reactions are limited in rate by the ability of oxidant to reach the particle surface. Thus

$$\frac{dN(H_2)}{dt} = \frac{N_p A_p K_m^{H_2O}}{RT} \left[P_{H_2O}(\text{bulk}) - P_{H_2O}(\text{eq.}) \right] \quad ,$$

where

$N(H_2)$ = moles of hydrogen produced,

t = time,

N_p = number of particles,

A_p = surface area of a particle,

$K_m^{H_2O}$ = gas phase mass transport coefficient,

R = Universal Gas Constant,

T = absolute temperature,

$P_{H_2O}(\text{bulk})$ = steam partial pressure in the bulk gas phase,

$P_{H_2O}(\text{eq.})$ = steam partial pressure that would be in equilibrium with the particle.

The gas phase mass transport coefficient in these studies of single droplet reactions is given by

$$N_{Sh} = \frac{K_m^{H_2O} d_p}{D_{(H_2O)}} = 2 + 0.69 \, Re^{1/2} \, Sc^{1/3}$$

where

d_p = diameter of the droplet,

$D_{(H_2O)}$ = diffusion coefficient for steam in the gas phase,

N_{Sh} = Sherwood number,

$N_{Re} = \frac{d_p U \rho_g}{\mu_g}$ = Reynolds number,

$N_{Sc} = \mu_g / \rho D(H_2O)$ = Schmidt number,

μ_{gas} = viscosity of the gas phase,

U = velocity of the droplet relative to the gas phase.

When applied to reactor accident analysis, these single droplet kinetics lead to predictions of very rapid reaction and hydrogen production. The extent of particle reaction as a function of distance of travel is shown in Figure 1.2-9 for several particle sizes.

Were such single particle kinetics applicable to reactor accidents analyses of debris dispersal, the results would be quite consequential. Integrated accident analyses have shown that for ice condenser containments, a safety problem could arise.[92,93] Though debris transport from the cavity is sharply limited by the ice beds, sufficient hydrogen is produced that upon ignition of the hydrogen, there is a threat of containment overpressurization. Overpressurization by combustion of hydrogen produced during pressure-driven melt expulsion and debris dispersal is a concern in other types of containments as well.[93]

The applicability of single particle reaction kinetics is open to doubt. It is well known that in clouds of particles the mass transport of oxidant to the particle surface can be substantially slower than that predicted for single particles.[94,95] One of the critical determining factors in the analyses of reactions of particle clouds is the spacing of the particles. The spacing in the reactor accident analysis will depend on the rate at which core debris is entrained in the flow of gas from the reactor cavity. Currently, there is no satisfactory model of the rate of debris entrainment. The criterion for entrainment seems accepted to be[79]

$$Ku^c = \frac{\rho_g U^2}{\left[\left(\rho_l - \rho_g\right) g \sigma_l\right]^{1/2}} = 20 \quad ,$$

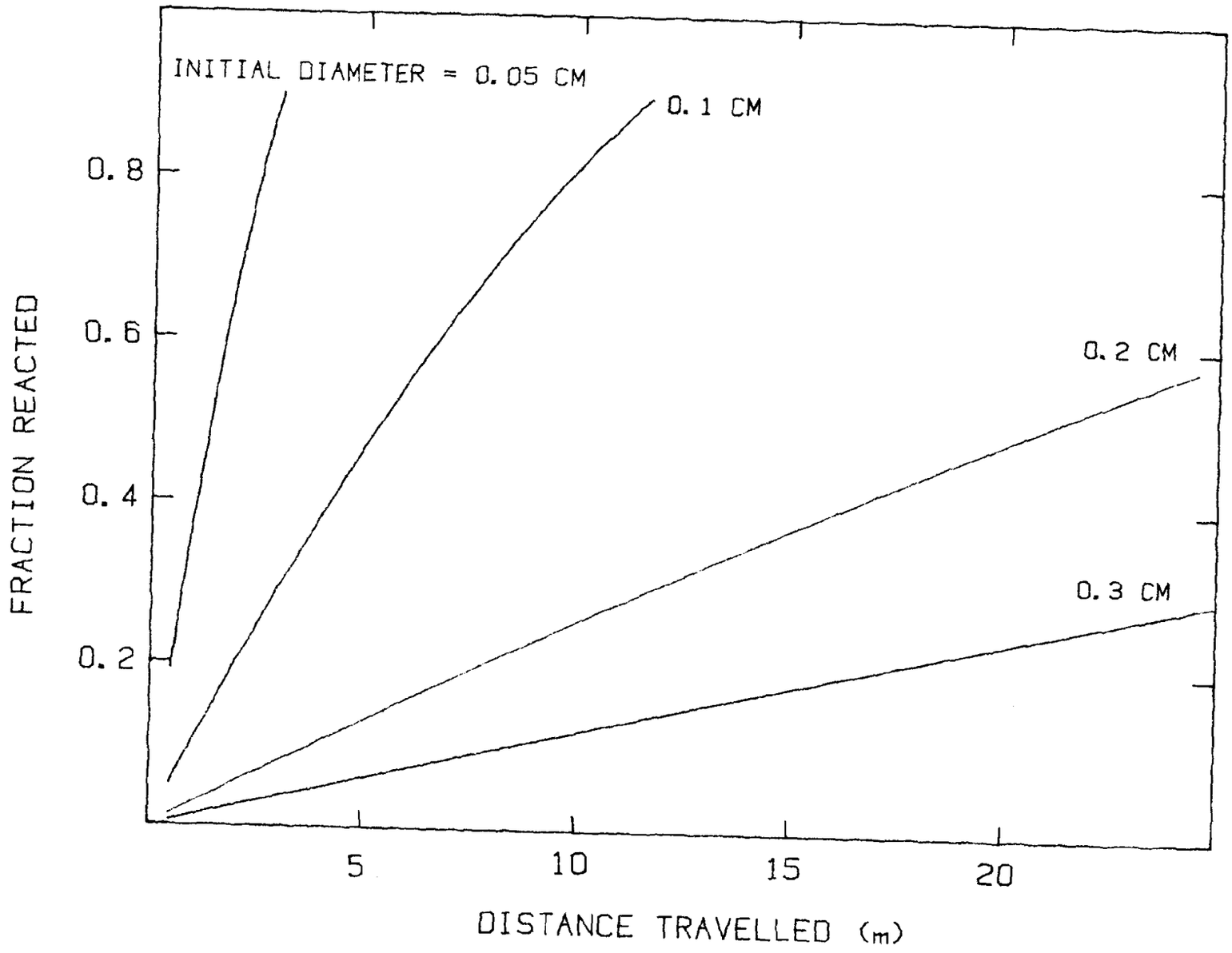

Figure 1.2-9. Extent of Reaction of Particles of Various Sizes as a Function of the Distance of Travel

where

ρ_g = gas density,

ρ_l = melt density,

g = gravitational acceleration,

σ_l = surface tension of the melt,

Ku^c = critical Kutateladze number.

Modeling of the rate of entrainment is now based on the assumption that the rate is proportional to the difference between the actual and the above critical Kutateladze number. A verification of this assumption is not available.

The obvious potential of pressure-driven melt expulsion and subsequent reactions of dispersed debris have led to experimental studies of the phenomena. The U.S. Nuclear Regulatory Commission is sponsoring, at Brookhaven National Laboratory, investigations of the dispersal of simulant fluids in models of reactor cavities and containments.[96] Studies of high temperature melt behavior are being conducted at Sandia.[77,79,97] The high temperature experiments involve melts, weighing about 80 kg, that are expelled from vessels pressurized up to 150 atmospheres. Melts are expelled into model cavities (1:10 linear scaling) and from the cavities into the Surtsey model containment building. A typical cavity model is shown in Figure 1.2-10. The Surtsey containment is shown in Figure 1.2-11. The Surtsey containment is 3.66 m in diameter, 11.6 m high and has an internal volume of about 103 m^3. The atmosphere composition, temperature and pressure in the Surtsey containment can be both controlled and monitored sufficiently to permit studies of reaction kinetics. A photographic sequence taken within the Surtsey facility during a test of pressure-driven melt expulsion is shown in Figure 1.2-12. Pressurization of the facility during this test and the pressure calculated with the CONTAIN code[98] is shown in Figure 1.2-13.

It is expected that forthcoming results from the simulant and the high temperature melt studies being sponsored by the NRC will clarify the nature of chemical reactions with dispersed debris. Of particular interest will be the results of tests done with steam to assess hydrogen production.

The effects of core debris dispersal as a result of pressure-driven debris expulsion may not be restricted to just the generation of hydrogen. Dispersed debris may also prompt hydrogen ignition. Quite clearly, very hot particles dispersed in the containment atmosphere could each act as an ignition source if the atmosphere were combustible. Dispersal of the debris could then be the connecting event that renders simultaneous containment pressurizing events of vessel blowdown, hydrogen combustion, and steam production by quenching debris with water. When these three events are coincident or nearly coincident, even very robust reactor containments have been found to be threatened by overpressurization.[65]

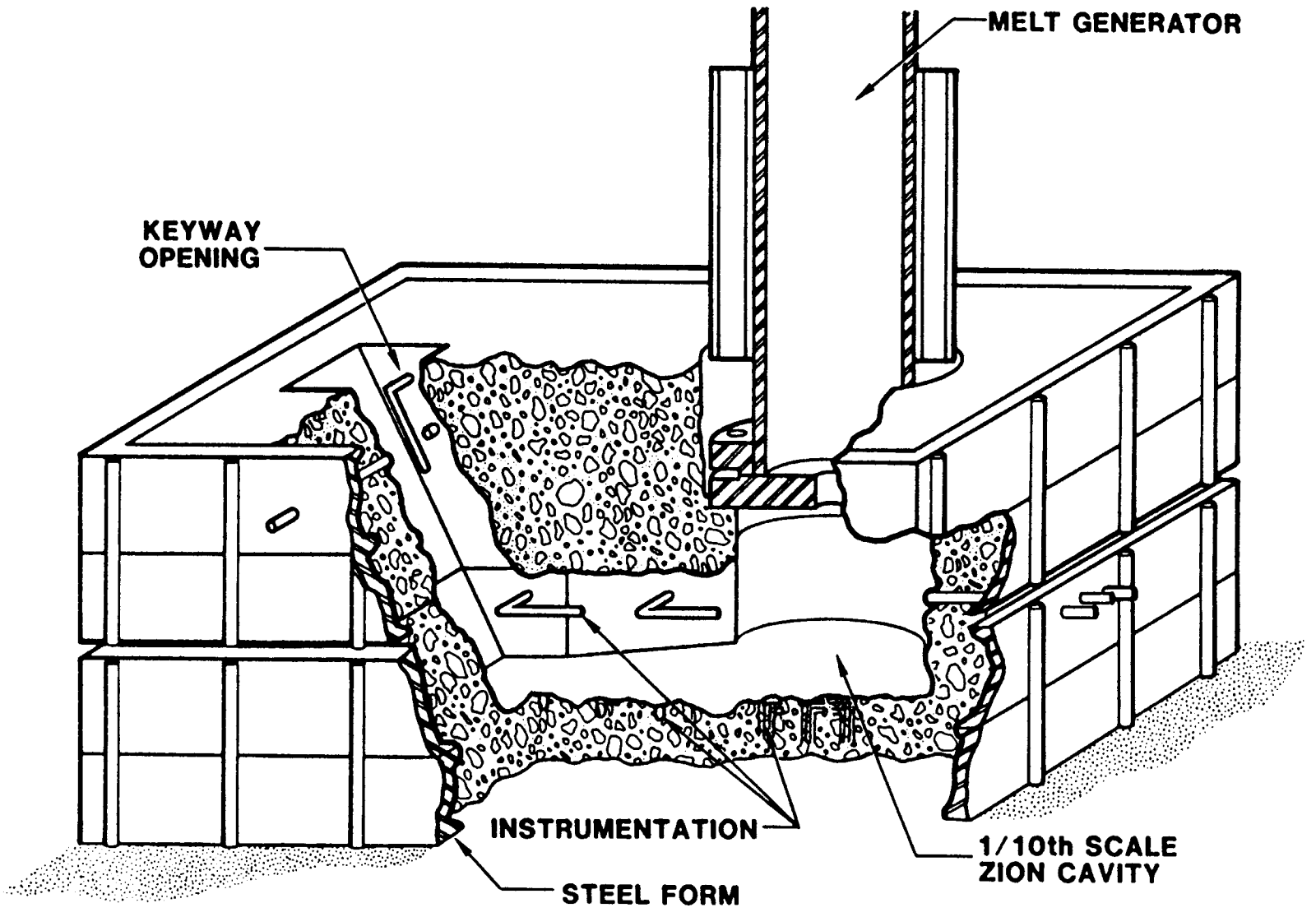

Figure 1.2-10. Model Cavity Used in Tests of Debris Dispersal

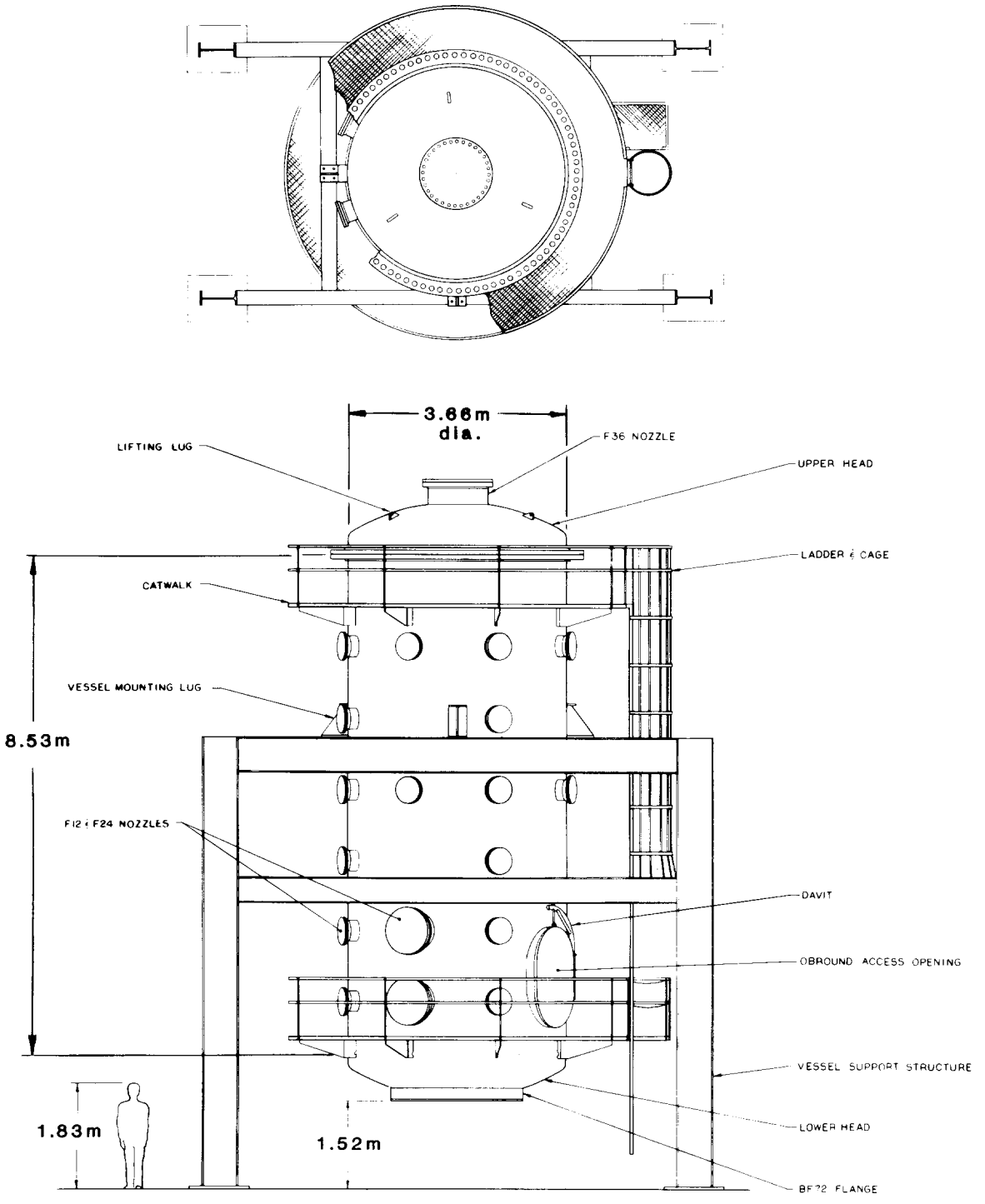

Figure 1.2-11. Surtsey Experimental Facility

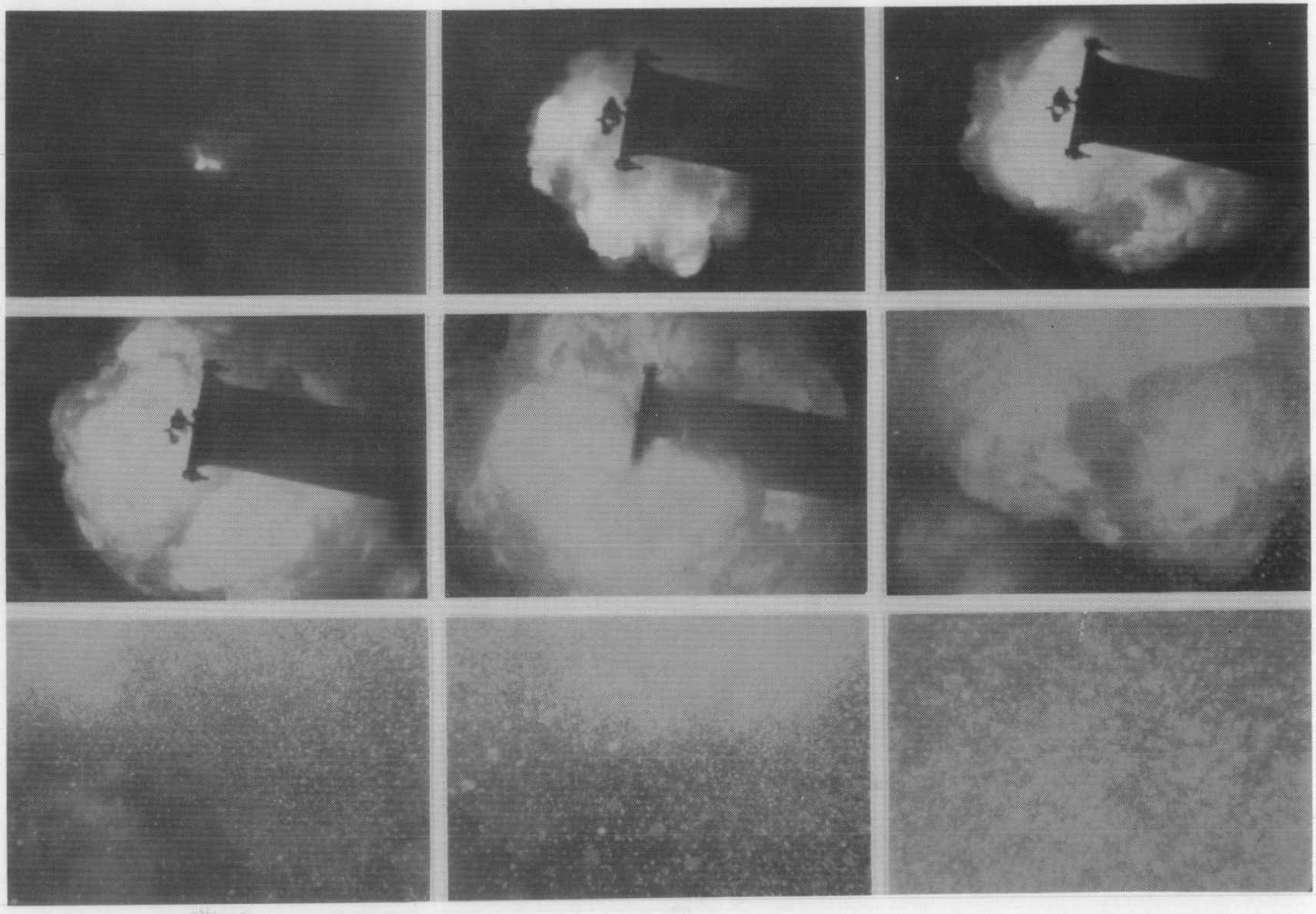

Figure 1.2-12. Photographic Sequence Taken Within the Surtsey Facility During a Test of Pressure Driven Melt Expulsion

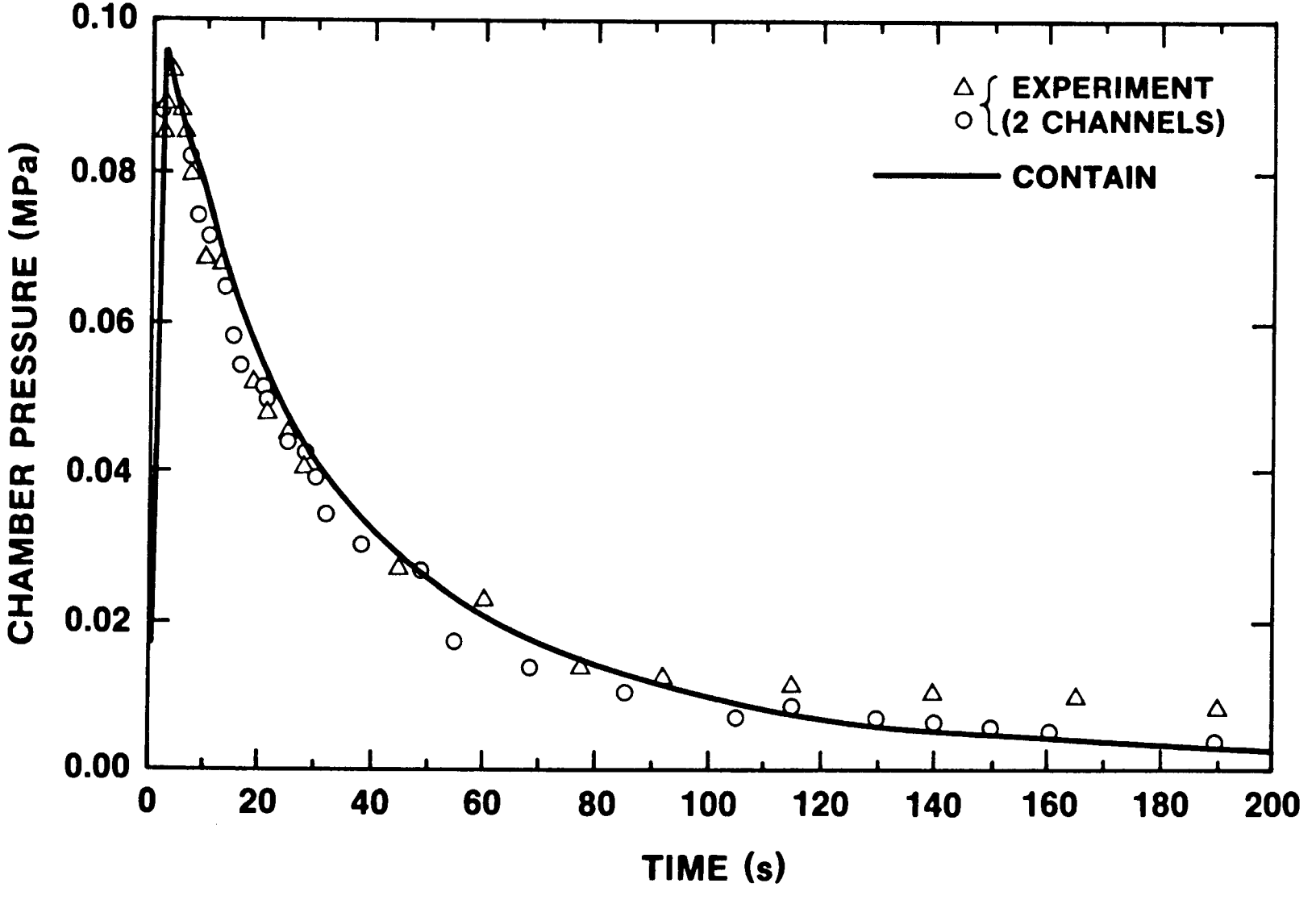

Figure 1.2-13. Pressurization of the Surtsey Facility During the Test DCH-1 (Reference 84) and the Pressure Calculated With the CONTAIN Code (Reference 98)

At the time of vessel blowdown, the containment atmosphere may not be combustible. The atmosphere may contain a sufficiently high partial pressure of steam that it is inert with respect to self-propagating hydrogen burns--the so-called "steam inerting." Debris dispersal could remove the inerting effect simply by raising sufficiently the containment atmospheric temperature. Dispersed debris might also prompt hydrogen combustion in steam not by a self-propagating gas phase reaction but by a surface catalyzed reaction. Many of the materials found in core debris are known to catalyze* the recombination reaction of hydrogen and oxygen. A possible sequence of elementary steps to explain the reaction might be

$$H_2 + \text{surface} \rightleftharpoons 2[H]_{\text{surface}}$$

$$[H]_{\text{surface}} + O_2 \longrightarrow [HO]_{\text{surface}} + 1/2\ O_2$$

$$[HO]_{\text{surface}} + [H]_{\text{surface}} \longrightarrow [H_2O]_{\text{surface}}$$

$$[H_2O]_{\text{surface}} \rightleftharpoons H_2O\ (\text{gas}) \quad .$$

Though this reaction sequence still involves reaction inhibition by steam, the inhibition is the result of blocking surface sites for hydrogen absorption. As such, this inhibition will have a decidedly different character than conventional "steam inerting," which affects the heat capacity of the gas phase. Because so much surface area is created by debris dispersal, the net effect of surface recombination would be similar to a gas phase hydrogen combustion even though the atmosphere was inert by conventional considerations.

To date, no investigations of the possible effects of dispersed debris on hydrogen recombination have yet appeared. The issue is significant and tests of this effect are planned in the Surtsey facility.[97]

1.3 CORCON and VANESA Code Development

(D. A. Powers, 6422; D. R. Bradley, 6425)

The later stages of a severe nuclear reactor accident are marked by the deposition of molten core debris into the reactor cavity. This leads to vigorous interactions between the molten core material and the reactor cavity concrete. Included in these interactions are ablation of the concrete followed by intense aerosol generation and gas and fission-product release. These phenomena are an important concern in severe accident source term evaluation and risk/consequence assessment. The CORCON and VANESA computer codes were developed at Sandia to model this aspect of severe reactor accidents. Both models are integral components of the suite of computer codes used by the NRC for severe accident analyses.

*The word "catalysis" was coined by Berzelius in the course of studies of hydrogen-oxygen recombination reactions on surfaces.[99]

Virtually every aspect of the core-concrete interaction is controlled to some extent by the heat transfer between the core debris and the concrete. It is therefore of utmost importance to accurately model this part of the interaction. Past comparisons of CORCON calculations to the results of experiments have shown that the heat transfer models in the code need to be improved.[100] A substantial effort has recently been devoted to the improvement and validation of the heat transfer models in CORCON. Some of the early work in this area was reported previously.[101] The work discussed here is a continuation of that effort.

In the following discussion, a brief overview of the phenomena involved in debris-concrete heat transfer is presented first. Next, proposed improvements to the heat transfer models are discussed. Finally, the significance of these proposed modifications are detailed.

Also discussed in the sections that follow are two updates to CORCON which were released to users during the last six months. These updates create versions 2.01 and 2.02 of the code.

1.3.1 Debris-Concrete Heat Transfer Phenomena

Heat transfer between the molten core debris and the reactor cavity concrete is controlled by the bubbling through the melt of gases produced during concrete decomposition. This process is fundamentally similar to nucleate boiling or gas barbotage heat transfer, and an abundance of heat transfer correlations are available to describe it. The problem left to the analyst is one of determining which among the available correlations is most applicable for the materials of interest in reactor accidents. As indicated in Reference 101, a correlation attributed to Kutateladze[102] appears to be applicable for the wide range of Prandtl numbers characteristic of molten core debris. The Kutateladze correlation is, therefore, implemented in a working version of CORCON to describe heat transfer within the bulk core melt pool.

At the interface between the core debris and the concrete, gas is being released from the concrete coincident with melting of the concrete surface. Past model development has neglected, for the most part, the melting of the concrete. The exception to this is a model proposed by Benjamin[103] that treats the formation of a concrete slag layer and removal of slag due to buoyancy, but neglects the influence of the gas bubbles on interfacial heat transfer or slag removal. In every other model, gas bubbling at the surface is assumed to control heat transfer, and the concrete slag is assumed to have a negligible influence on the interaction.

In most models (including the original CORCON model), gas release has been assumed to be sufficient to form a stable gas film when the core debris contacts the concrete. This assumption has been shown to be incorrect under most conditions.[54] Gas release is usually far less than that required to form a stable gas film, and instead, intermittent debris-concrete contact occurs.

At contact, the interface temperature between a bubbling fluid and a solid surface almost immediately reaches what is commonly referred to as the

"instantaneous contact temperature" or "instantaneous interface temperature." This temperature is between the temperature of the bulk fluid and the initial temperature of the surface. This sudden temperature change has been experimentally observed in numerous studies[104-109] of boiling or gas bubbling heat transfer. When the thermal conductivity of the surface is much greater than that of the bubbling fluid, such as in boiling of water on a metallic surface, the interface temperature remains almost constant at near the initial surface temperature.[104] However, when the boiling fluid is a high conductivity liquid such as a liquid metal or when the surface is a low conductivity material such as glass or teflon, the interface temperature is quite different from the initial heater surface temperature.[105-109] Instead, the surface temperature is observed to fluctuate as the liquid contacts the surface and is then evaporated. (Figure 1.3-1 shows an example of the surface temperature fluctuations that are observed in these experiments.) When a numerical value for the convective heat transfer coefficient is determined based on these experiments, the appropriate surface temperature used in this evaluation is the time-averaged value.

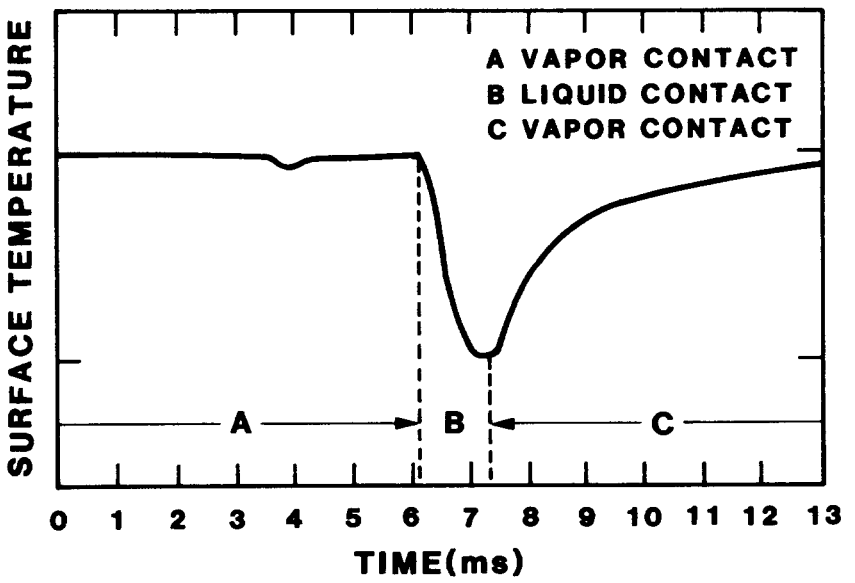

Figure 1.3-1. Typical Local Surface Temperature History for a Liquid-Solid Contact During Film Boiling (Reference 9)

Heat transfer between molten core debris and concrete is another case in which the interface temperature will be quite different from the initial surface temperature of the solid substrate. In fact, since core debris has a greater thermal conductivity than the concrete, the interface temperature will be closer to the debris temperature than to the concrete surface temperature. (In existing debris-concrete interaction computer models this temperature is usually assumed to be the concrete ablation temperature.) Substantial errors will therefore result if the concrete surface temperature is used in the calculation of heat transfer to the concrete rather than the actual interface temperature.

In previous analyses, only Lee and Kazimi[110] have incorporated the instantaneous contact temperature concept in their model for debris-concrete heat transfer. However, in their analysis they neglected phase change at the interface. This greatly simplified their analysis, but it also greatly limits the applicability of their model since substantial melting of the concrete surface occurs during the interaction. In addition, solidification of the molten core debris will occur unless the debris temperature is sufficiently above the solidus temperature. A more accurate approach would therefore be to treat both melting of the concrete and solidification of the core melt in the calculation of the interface temperature.

Coincident with melting of the concrete and solidification of the debris is the growth of gas bubbles due to the release of concrete decomposition gases at the interface. As the bubbles grow, both the slag layer and the crust become thicker. Then at bubble departure, concrete slag is removed from the interface by the buoyancy of the slag in the denser core melt and by the suction caused by the low pressure region in the wake of the rising bubble. If a crust has formed, it may fragment at this time and also may be carried away by the rising bubble. Subsequently, new molten material contacts the concrete surface, and the bubbling cycle outlined above is repeated. During a bubble cycle, temperature profiles grow in each of the regions. Figure 1.3-2 illustrates a bubble cycle and shows the growth of the temperature profiles in the four possible regions.

The next section presents an analysis of the instantaneous contact temperature which includes phase changes at the interface. Results of sample calculations are then provided to illustrate application of the model to prototypic materials. Finally, implementation of the contact temperature analysis in the CORCON model for debris-concrete heat transfer is discussed.

1.3.2 Calculation of the Instantaneous Contact Temperature

An analytical method proposed by Epstein[111] can be used to determine the interface temperature during a bubble cycle. His solution, which is outlined in the following discussion, considers four regions: the initially molten phase; the solid substrate; the solidifying molten phase, which forms a solid crust; and the layer of melting substrate.

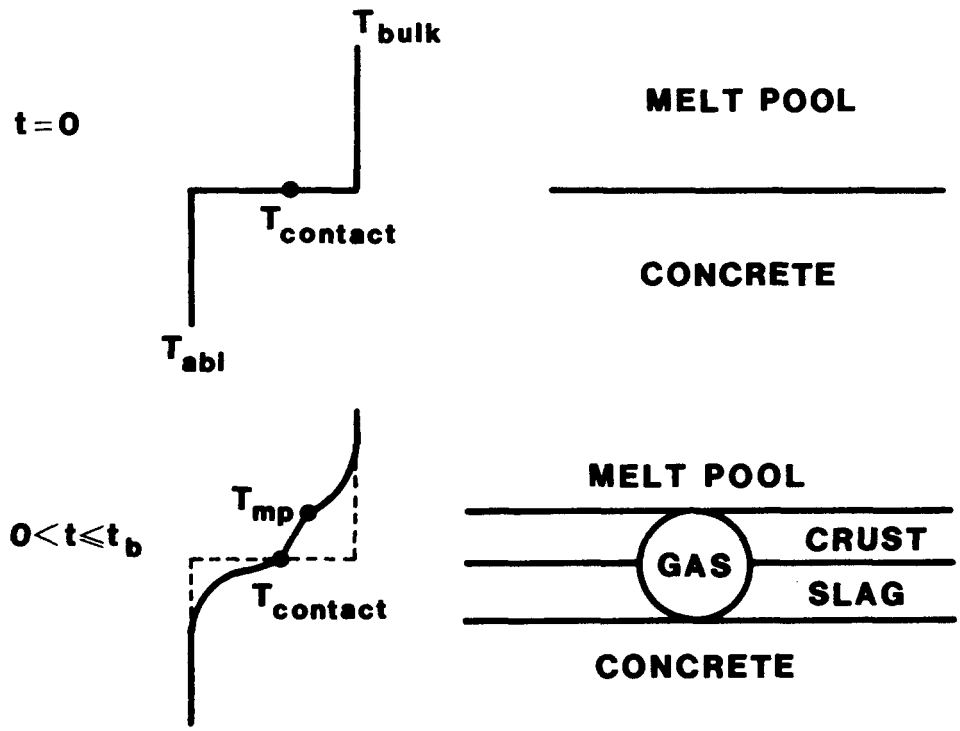

Figure 1.3-2. Growth of Temperature Profiles During a Bubble Cycle (t_b = Cycle Period)

The energy equation in each of these four regions has the form

$$\frac{\partial^2 T}{\partial x^2} = \frac{1}{\alpha} \frac{\partial T}{\partial t} \quad , \tag{1.3-1}$$

where T is the temperature of the region, α is the thermal diffusivity of the region, x is the spatial location, and t is the time.

Designating the initially molten material as material 1, the initially solid material as material 2, and the positions of the solidification and melting fronts (relative to the coordinate system origin at the interface between the two materials) as X_1 and X_2, the following boundary conditions apply:

$$T_{1s}(X_1,t) = T_{1m}(X_1,t) = T_{1mp} \quad , \tag{1.3-2a}$$

$$T_{2s}(-X_2,t) = T_{2m}(-X_2,t) = T_{2mp} \quad , \tag{1.3-2b}$$

$$k_{1s} \frac{\partial T_{1s}}{\partial x} - k_{1m} \frac{\partial T_{1m}}{\partial x} = L_1 \rho_1 \frac{\partial X_1}{\partial t} \quad \text{at } x = X_1(t) \quad , \tag{1.3-2c}$$

$$k_{2s}\frac{\partial T_{2s}}{\partial x} - k_{2m}\frac{\partial T_{2m}}{\partial x} = -L_2\rho_2\frac{\partial X_2}{\partial t} \quad \text{at } x = -X_2(t) \quad , \tag{1.3-2d}$$

$$T_{1s}(0,t) = T_{2m}(0,t) \quad , \tag{1.3-2e}$$

$$k_{1s}\frac{\partial T_{1s}}{\partial x} = k_{2m}\frac{\partial T_{2m}}{\partial x} \quad \text{at } x = 0 \quad , \tag{1.3-2f}$$

$$T_{1m}(\infty,t) = V_1 \quad , \tag{1.3-2g}$$

and

$$T_{2s}(-\infty,t) = V_2 \quad , \tag{1.3-2h}$$

where the subscripts s and m refer to the solid and molten phases, respectively, of materials 1 and 2, and k, ρ, and L are the thermal conductivity, density, and enthalpy of fusion for the material or region of interest.

As shown in Reference 112, solutions for the two semi-infinite regions composed of materials 1 and 2 have the general form

$$T_{1s} = A_1 + B_1\text{erf}\left(\frac{x}{2\left(\alpha_{1s}t\right)^{0.5}}\right) \quad 0 < x < X_1(t) \quad , \tag{1.3-3}$$

$$T_{1m} = V_1 - C_1\text{erfc}\left(\frac{x}{2\left(\alpha_{1m}t\right)^{0.5}}\right) \quad X_1(t) < x < \infty \quad , \tag{1.3-4}$$

$$T_{2m} = A_2 + B_2\text{erf}\left(\frac{x}{2\left(\alpha_{2m}t\right)^{0.5}}\right) \quad -X_2(t) < x < 0 \quad , \tag{1.3-5}$$

and

$$T_{2s} = V_2 + C_2\text{erfc}\left(\frac{x}{2\left(\alpha_{2s}t\right)^{0.5}}\right) \quad -\infty < x < -X_2(t) \quad , \tag{1.3-6}$$

with the positions of the solidification and melting fronts given by

$$X_1(t) = 2\lambda_1\left(\alpha_{1s}t\right)^{0.5} \tag{1.3-7}$$

and

$$X\ (t) = 2\lambda_2\left(\alpha_{2m}t\right)^{0.5} \quad . \tag{1.3-8}$$

The eight constants, A_1, B_1, C_1, A_2, B_2, C_2, λ_1, and λ_2, are determined by applying the eight boundary conditions listed above.

Application of these boundary conditions results in a set of eight algebraic equations for the eight constants. By algebraic manipulation, this set of equations can be reduced to two simultaneous transcendental equations for λ_1 and λ_2, which can be solved numerically. The two equations for λ_1 and λ_2 follow:

$$\frac{\sigma}{\exp\left(\lambda_1^2\right)\mathrm{erf}\left(\lambda_2\right) + \sigma\exp\left(\lambda_1^2\right)\mathrm{erf}\left(\lambda_1\right)} - \frac{\theta_1}{\exp\left(\beta_1^2\lambda_1^2\right)\mathrm{erfc}\left(\beta_1\lambda_1\right)}$$

$$= \lambda_1\Lambda_1 \quad , \tag{1.3-9}$$

and

$$\frac{1}{\sigma\exp\left(\lambda_2^2\right)\mathrm{erf}\left(\lambda_1\right) + \exp\left(\lambda_2^2\right)\mathrm{erf}\left(\lambda_2\right)} - \frac{\theta_2}{\exp\left(\beta_2^2\lambda_2^2\right)\mathrm{erfc}\left(\beta_2\lambda_2\right)}$$

$$= \lambda_2\Lambda_2 \quad , \tag{1.3-10}$$

where

$$\sigma = \left(\frac{\alpha_{1s}}{\alpha_{2m}}\right)0.5\ \frac{k_{2m}}{k_{1s}} \quad ,$$

$$\beta_1 = \left(\frac{\alpha_{1s}}{\alpha_{1m}}\right)0.5 \quad ,$$

$$\beta_2 = \left(\frac{\alpha_{2m}}{\alpha_{2s}}\right)0.5 \quad ,$$

$$\theta_1 = \frac{\beta_1 k_{1m}}{k_{1s}}\left(\frac{V_1 - T_{1mp}}{T_{1mp} - T_{2mp}}\right) \quad ,$$

$$\theta_2 = \frac{\beta_2 k_{2s}}{k_{2m}} \left(\frac{T_{2mp} - V_2}{T_{1mp} - T_{2mp}} \right) \quad ,$$

$$\Lambda_1 = \frac{\pi^{0.5} L_1}{c_{1s}\left(T_{1mp} - T_{2mp}\right)} \quad ,$$

$$\Lambda_2 = \frac{\pi^{0.5} L_2}{c_{2m}\left(T_{1mp} - T_{2mp}\right)} \quad .$$

After λ_1 and λ_2 have been determined, the interface temperature can be calculated from

$$\frac{T_i - T_{2mp}}{T - T_{2mp}} = \frac{\text{erf}\left(\lambda_2\right)}{\text{erf}\left(\lambda_2\right) + \sigma \text{erf}\left(\lambda_1\right)} \quad . \tag{1.3-11}$$

This compares to the simple equation for T_i in the absence of phase changes,

$$\frac{T_i - V_2}{V - V_2} = \frac{1}{1 + \sigma} \quad . \tag{1.3-12}$$

Under some conditions, solidification of the molten phase does not occur. The interface temperature then is determined by a different equation that is derived following a solution procedure similar to that outlined above. However, in this solution, only three possible regions are considered. The equation for the melting front growth constant, λ_2, is

$$\frac{1}{\exp\left(\lambda_2^2\right)\text{erf}\left(\lambda_2\right) + \sigma \exp\left(\lambda_2^2\right)} - \frac{\theta_2}{\exp\left(\beta_2^2 \lambda_2^2\right)\text{erfc}\left(\beta_2 \lambda_2\right)}$$

$$= \lambda \Lambda_2 \quad , \tag{1.3-13}$$

while the interface temperature, T_i, is given by

$$\frac{V_1 - T_i}{V - T_{2mp}} = \frac{\sigma}{\sigma + \left(\text{erf } \lambda_2\right)} \quad . \tag{1.3-14}$$

The method discussed above has been incorporated into a computer program which solves for the interface temperature given the thermophysical properties of the four possible regions and the initial temperatures of the molten phase and solid substrate. The program first determines the critical temperature for the onset of solidification of the molten phase. If the molten phase temperature is above that critical temperature, no solidification occurs, while if it is below the critical temperature, a crust will begin to grow at the interface. In the former case, the three-region solution is used. In the latter case, the four-region solution is used.

A series of sample calculations have been performed for four sets of prototypic material combinations: metallic debris on cold concrete, metallic debris on hot concrete, oxidic debris on cold concrete, and oxidic debris on hot concrete. For each combination, the bulk molten phase temperature was increased in 20 K increments from a reasonable lower limit to a reasonable upper limit. Table 1.3-1 shows the material properties used in these calculations.

Figures 1.3-3 through 1.3-6 present the results of the sample calculations. Plotted in these figures are the calculated instantaneous interface temperatures as a function of debris temperature. Also included are the calculated growth constants for solidification of the molten debris. Superimposed on the figures are the assumed values for the solidus temperature of the metallic or oxidic core debris. The intersection of each interface temperature curve with the solidus temperature line indicates the critical debris temperature for the onset of solidification. This is also the temperature at which the value of the crust growth constant goes to zero.

For molten steel on cold concrete (350 K in the example), solidification of the steel is predicted to occur if the initial steel temperature is below 2100 K. This result is at least qualitatively verified by results of the SWISS[22] and TURC[100] experiments at Sandia. In the SWISS1 and SWISS2 experiments, the initial temperature of the molten steel was between approximately 1900 and 1950 K. In both experiments, rapid ablation of the concrete, characteristic of molten debris-concrete interactions, was not observed until several minutes after initial contact. This is believed to be due to initial formation of a steel crust at the interface with the concrete. Heat transfer to the concrete was therefore limited by conduction until the crust remelted. These results were quite different from the ablation behavior observed in the earlier TURC1SS experiment. Here the initial temperature of the molten steel was greater than 2300 K, and extremely rapid ablation was observed at the onset of the interaction.

It is important to realize that a contact temperature below the solidus of the molten debris does not guarantee that concrete ablation will be conduction-limited. The crust may be unstable and quickly break up under the influence of the bubbling gases. If a crust is present for only a fraction of a bubble cycle, the effective heat transfer coefficient will approach the convection-limited value. The transition between stable and unstable crust behavior is, therefore, an important additional consideration in the analysis of debris-concrete heat transfer.

Table 1.3-1

Material Properties Used in Contact Temperature Analyses

	k(W/m-K)	ρ(kg/m^3)	C_p(J/kg•K)	h_f(J/kg)	T_{mp}(K)
Stainless Steel					
Solid	35.0	7300	680	2.7×10^5	1730
Liquid	19.5	6700	780		
Mixed Oxide (UO_2/ZrO_2)					
Solid	4.0	8200	800	2.6×10^5	2600
Liquid	3.5	7700	1000		
Cold Concrete (T = 350 K)					
Solid	1.2	2300	2000	6.0×10^5	1550
Liquid	2.0	2500	1200		
Hot Concrete (T = 1350 K)					
Solid	2.5	2600	1000	6.0×10^5	1550
Liquid	2.0	2500	1200		

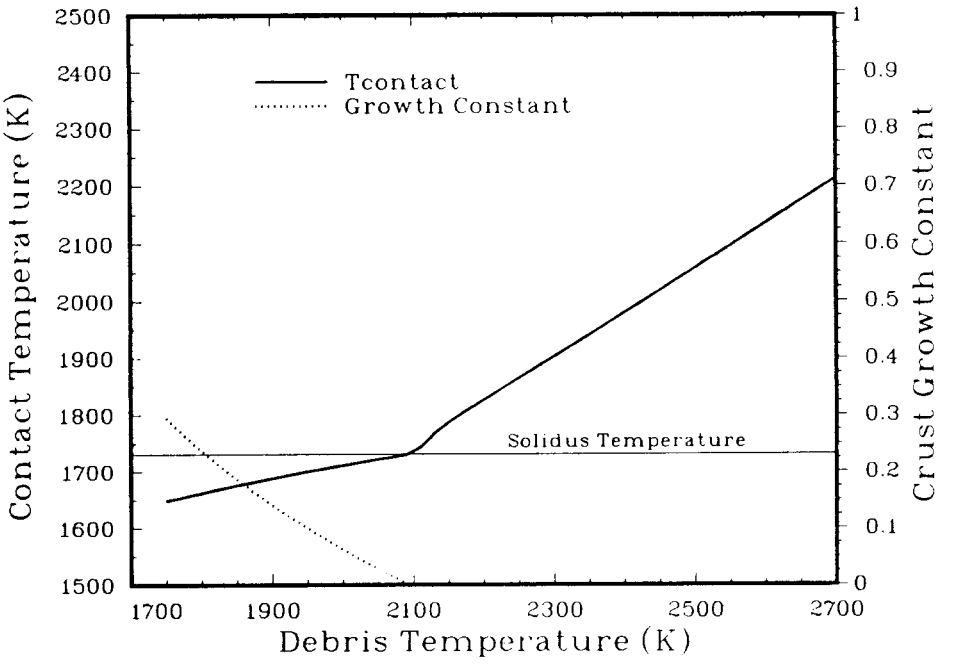

Figure 1.3-3. Contact Temperature and Crust Growth Constant for Molten Steel on Cold Concrete

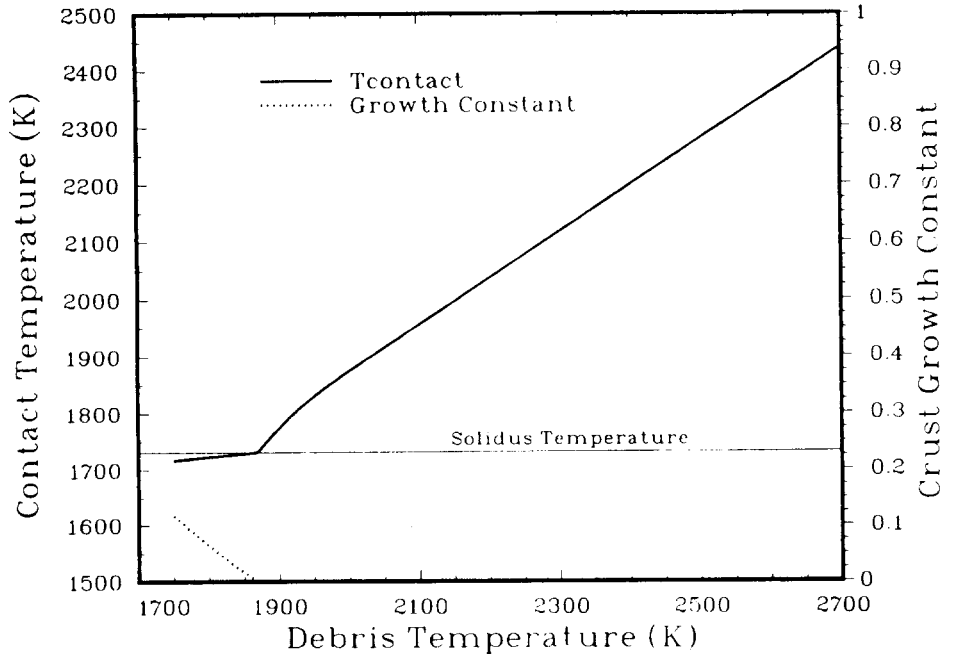

Figure 1.3-4. Contact Temperature and Crust Growth Constant for Molten Steel on Hot Concrete

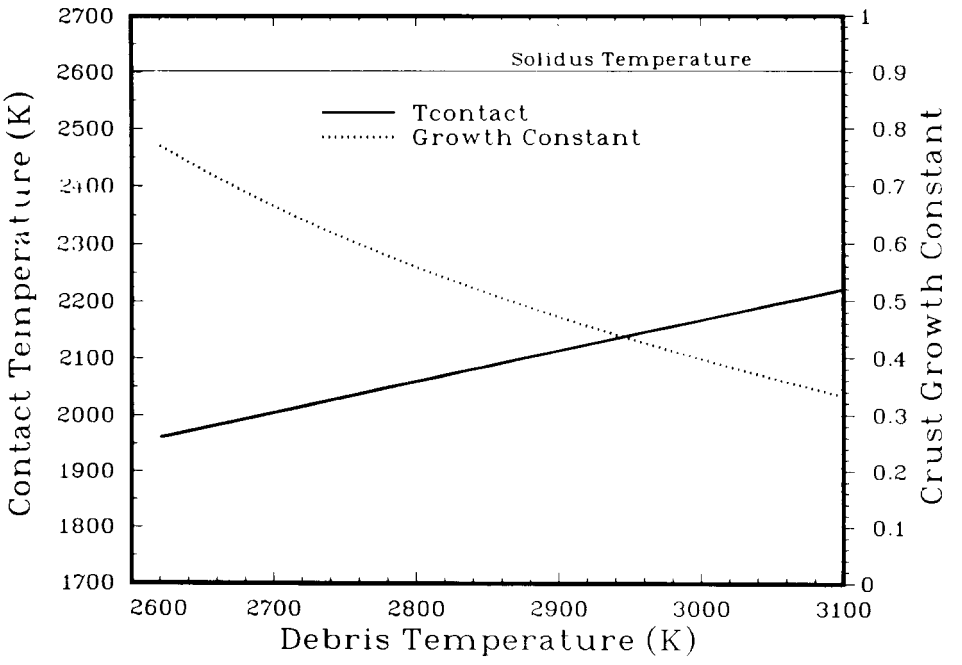

Figure 1.3-5. Contact Temperature and Crust Growth Constant for Molten Oxide on Cold Concrete

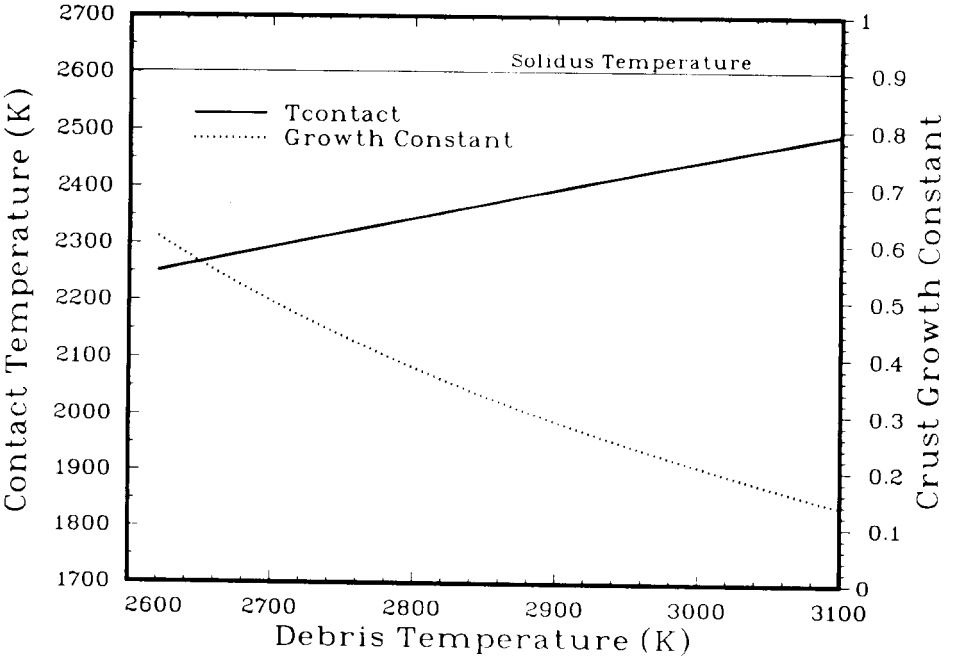

Figure 1.3-6. Contact Temperature and Crust Growth Constant for Molten Oxide on Hot Concrete

Although the analysis of crust stability is beyond the scope of the current work, a qualitative stability criterion can be obtained from the results of the SWISS experiments. At 1900 to 1950 K, which was the initial temperature of the steel in the SWISS tests, the crust growth constant is calculated to be on the order of 0.15. For this growth constant, the steel crust grows to 2 mm in less than 10 s. Apparently, this growth rate is sufficient for the crust to be stable. It might be concluded from this that a growth constant of 0.15 or greater will result in stable crust formation with metallic melts. At below this value, stable crust formation may also occur. However, there is currently no analytical or experimental evidence to support crust stability at these lower growth rates.

This criterion can be extended to the case of molten steel contacting hot concrete (1350 K in the example). The results of this calculation are presented in Figure 1.3-4. When steel contacts hot concrete, solidification at the interface is predicted to occur only when the steel temperature falls below approximately 1870 K. The growth constants for molten steel temperatures down to 1750 K (the minimum temperature chosen in the sample calculation) are all less than the stability limit, 0.15, determined from the SWISS results. However, as stated above, stable crust formation cannot be ruled out at these low growth rates.

Shown in Figures 1.3-5 and 1.3-6 are the results for oxidic core debris on concrete. When the molten oxide contacts cold concrete, it is predicted to begin to solidify immediately at the interface under all conceivable initial conditions. The same is true for molten oxide contacting hot concrete. The primary reason for this is that the molten oxide has a relatively low thermal conductivity so the contact temperature is always well below the bulk temperature of the oxide.

The former result is qualitatively verified by the results of two of the TURC experiments, TURC2 and TURC3.[56] In both of these experiments, an oxidic melt composed primarily of UO_2 and ZrO_2 was added onto a cold concrete substrate. The initial temperature of the melt was, in both experiments, only 50 to 100 K above the solidus temperature. In neither experiment was any significant early erosion detected. As in the two SWISS experiments discussed previously, this was apparently due to freezing of the melt upon contact.

The crust growth constants predicted for the molten oxide are also shown in Figures 1.3-5 and 1.3-6. At most temperatures, the growth constants are predicted to be much larger than those predicted for the molten steel contacting concrete. Unfortunately, no conclusions with regard to the stability of oxide crusts can be drawn based on these results since the strength properties of steel and mixed oxide are very different. More importantly, core debris oxides are known to be at least partially soluble in molten concrete. As concrete is incorporated into the core debris oxides, the solidus temperature of the resulting oxide mixture decreases. In the TURC2 and TURC3 experiments, posttest examination of the debris in the crucible showed that the solidus temperature of the debris adjacent to the concrete surface had been reduced by 300 K relative to that of the original debris material. This large reduction occurred despite the very limited concrete erosion that took place during the test. Depression of

the solidus temperature would certainly make crust formation less likely. It would also reduce the stability of any crusts that did begin to form. At present, no model for incorporating the effects of reduction in the solidus temperature has been developed.

1.3.3. Implications of These Results to Debris-Concrete Heat Transfer Modeling in CORCON

The contact temperature model presented in the previous section is implemented into CORCON by considering that the transient slag growth and removal process supplies an additional heat transfer resistance in series with convective heat transfer in the bulk molten pool. (Note that in this description, the slag growth and removal process supplies a thermal resistance, which takes the place of heat transfer across the gas film that was assumed in the original CORCON heat transfer model.) At the interface between the transient slag layer and the molten debris pool,

$$h_p\left(T_p - T_i\right) = h_s\left(T_i - T_c\right) \quad , \tag{1.3-15}$$

where the subscripts p, i, and c refer to the debris pool, the interface, and the concrete surface, respectively, and h_s is the effective heat transfer coefficient attributed to the slag growth and removal process. Solving this equation for h_s results in the following simple relationship:

$$h_s = h_p \frac{\left(T_p - T_i\right)}{\left(T_i - T_c\right)} \quad . \tag{1.3-16}$$

The slag heat transfer coefficient is therefore determined by evaluating the bulk pool heat transfer coefficient and the interface temperature. The latter is calculated using the contact temperature solution discussed in the previous section.

It is instructive to examine the effect that the slag growth and removal process has on the overall heat transfer between the debris and the concrete. Since the two convective heat transfer processes act in series, the overall heat transfer coefficient between the bulk molten pool and the concrete surface is given by

$$h_o = \frac{h_s h_p}{h_s + h_p} \quad , \tag{1.3-17}$$

where h_o, the overall heat transfer coefficient, is defined such that

$$q = h_o\left(T_p - T_c\right) = h_s\left(T_i - T_c\right) = h_p\left(T_p - T_i\right) \quad . \tag{1.3-18}$$

Substituting for h_s into the above equation results in the following:

$$h_o = h_p \left(\frac{\gamma}{\gamma + 1}\right) \quad , \tag{1.3-19}$$

where γ is the temperature difference ratio shown in the equation for h_s. As this equation demonstrates, the overall heat transfer between the debris and the concrete is reduced when the slag growth and removal process is included.

Table 1.3-2 presents calculated results for γ and $\gamma/(\gamma + 1)$ based on the contact temperature results shown in Figures 1.3-3 through 1.3-6. In the evaluation of γ, the concrete surface temperature, T_c, was assumed to be the concrete ablation temperature in order to be consistent with the assumptions in CORCON. A value of 1500 K was assumed in the calculations.

For molten material on hot concrete, the quantity $\gamma/(\gamma + 1)$ falls within a fairly narrow range of from 0.22 to 0.36 or 0.29 ± 0.07 regardless of whether the material is steel or mixed oxide. This 24 percent variation corresponds to a 24 percent variation in heat transfer to the concrete. Since it would be unreasonable to expect much less than a 25 percent uncertainty in the calculated debris-concrete heat flux, choosing a constant value of 0.29 for $\gamma/(\gamma + 1)$ regardless of debris temperature or molten phase properties is probably a reasonable first approximation to the effect of the transient slag film on the overall heat transfer. The corresponding value for γ is 0.41. Hence

$$h_s = 0.41 h_p \quad \text{(for debris on hot concrete)} \quad , \tag{1.3-20}$$

where h_p is given by the convective heat transfer correlation used for the debris pool. This correlation can be used to represent slag film heat transfer when the concrete has been heated to its melting temperature. In most cases, this phase of the interaction is estimated to begin within minutes or even seconds of the onset of the interaction.

For molten material poured onto cold concrete, $\gamma/(\gamma + 1)$ falls within an even narrower range of from 0.44 to 0.62 or 0.53 ± 0.09 regardless of debris temperature or molten phase properties. This corresponds to only a 17 percent variation in debris-concrete heat transfer. Again, choosing a constant value of 0.53 to represent all possible conditions is probably a reasonable approximation to make. The corresponding value for γ is 1.13. For interactions with cold concrete, the slag heat transfer coefficient is therefore approximated by

$$h_s = 1.13 h_p \quad \text{(for debris on cold concrete)} \quad . \tag{1.3-21}$$

This equation applies only to the initial transient prior to the onset of concrete melting.

Table 1.3-2

Values for $\gamma/(\gamma+1)$ From Contact Temperature Analyses

T_{pool}(K)	γ	$\gamma/(\gamma + 1)$	γ	$\gamma/(\gamma + 1)$
	Steel/Cold Concrete		Steel/Hot Concrete	
1800	0.88	0.47	0.36	0.27
1900	1.16	0.54	0.45	0.31
2000	1.33	0.57	0.33	0.25
2100	1.60	0.62	0.32	0.24
2200	1.12	0.53	0.31	0.23
2300	0.98	0.49	0.29	0.22
2400	0.88	0.47	0.29	0.22
2500	0.79	0.44	0.29	0.22
	Oxide/Cold Concrete		Oxide/Hot Concrete	
2650	1.4	0.58	0.51	0.34
2700	1.4	0.58	0.51	0.34
2800	1.32	0.57	0.54	0.35
2900	1.28	0.56	0.56	0.36

As indicated in Section 1.3.2, the Kutateladze correlation[102] has been selected to represent heat transfer within the bulk debris pool. This correlation follows:

$$Nu_A = 1.5 \times 10^{-3}\ Ku^{2/3} \text{ (bubbly flow)} \quad , \tag{1.3-22}$$

and

$$Nu_A = 3.0 \times 10^{-5}\ Ku^{2/3}\ \left(V_s \mu/\sigma\right)^{-0.5} \text{ (churn-turbulent flow)} \quad , \tag{1.3-23}$$

where Nu_A is the Nusselt number based on a characteristic length equal to the Laplace constant, A, which is defined by

$$A = \left(\frac{\sigma}{g\left(\rho_l - \rho_g\right)}\right)^{0.5} \quad ,$$

and Ku is given by

$$Ku = \frac{Pr\ p\ V_s}{g\mu} \quad .$$

In these equations, σ is the liquid surface tension, μ is the liquid viscosity, Pr is the Prandtl number for the liquid, ρ_l and ρ_g are the densities of the liquid and gas, and p is the pressure at the interface. In the above correlations, the transition between bubbly and churn-turbulent flow occurs at a superficial gas velocity given by $V_s = 4.3 \times 10^{-4} \sigma/\mu$. (Alternate models for this transition velocity could easily be incorporated into the correlation.) The slag heat transfer coefficient is calculated by substituting for h_p into the appropriate equation for h_s.

Reference 54 presents a slag heat transfer correlation based on a best comparison to the concrete ablation data in the Sandia SWISS experiments. That correlation was implemented into a working version of CORCON which was then used to calculate the results from several of the TURC and SWISS experiments at Sandia and the BETA experiments at Kernforschungszentrum Karlsruhe.[51,113] In almost every case, the comparisons were excellent. It would be interesting, therefore, to determine how the correlations represented by the above equations for h_s compare to the correlation developed in Reference 54.

Since each of the experiments mentioned above used steel melts, the following steel properties were used in the calculation of h_p: k = 20 W/m^2•K, ρ = 7000 kgm^3, c_p = 750 J/kg•K, μ = 0.004 kg•m/s, and σ = 1.5 N/m. Also, the pressure at the interface was chosen to be 10^5 Pa. Applying these properties to the Kutateladze correlation and substituting into the appropriate equation for h_s gives, for molten steel on hot concrete,

$$h_s = 12400 V_s^{2/3} \quad \text{for bubbly flow} \quad , \tag{1.3-24}$$

and

$$h_s = 4800 V_s^{1/6} \quad \text{for churn-turbulent flow} \tag{1.3-25}$$

The equations for molten steel on cold concrete are, of course, very similar; the only differences being that the leading coefficients in the two equations are 34200 and 13200.

The churn-turbulent equation shown above is very close to the Reference 54 slag correlation,

$$h_s = 4720 V_s^{1/6} \tag{1.3-26}$$

Hence the results presented in Reference 54 also apply to the new slag film heat transfer model if the initial transient period in the experiments is short and gas flow is churn-turbulent.

Except for the SWISS experiments, the initial temperature of the molten steel was sufficiently high that freezing of the steel did not occur upon contact with the concrete, and melting of the concrete surface began almost immediately. Only for the first few seconds of the interaction was the cold concrete correlation required. As the figures in Reference 54 demonstrate, these experiments are represented quite well by the hot concrete correlation. In the SWISS experiments, the molten steel solidified upon contact with the concrete so heating of the concrete surface was much slower. Application of the hot concrete correlation from the beginning of the interaction resulted in as overestimation of the initial interface temperature. No initial freezing of the steel was predicted. Although overall ablation of the concrete was predicted quite well, early time ablation was overpredicted.

This error could be corrected by employing the cold concrete correlation to determine the initial debris-concrete heat transfer. Initial freezing of the steel would then be predicted in calculations of the SWISS experiments. The initial heat transfer rate would apply to the first CORCON time step. The hot concrete correlation would be used for subsequent time steps. Until a more exact treatment of heatup of the concrete is available, this approximate method for treating the cold-to-hot concrete transition will be used in CORCON.

For the steel melts in the experiments, the gas velocity for transition between the bubbly and churn-turbulent flow regimes is 0.15 m/s. All of the experiments except for BETA V2.1 had gas velocities greater than this critical value. Therefore, flow was churn-turbulent and, except for the BETA V2.1 result, all of the comparisons presented in Reference 54 also apply to the new slag film heat transfer model. BETA V2.1 was the only analyzed experiment that had radial heat transfer to the concrete sidewalls

that was comparable to the axial heat transfer to the concrete bottom. Unfortunately, heat transfer to the sidewalls was not modeled well in the calculation. This is significant because the BETA crucible has a sidewall surface area exposed to the molten steel that is eight times greater than the bottom surface area. Therefore, until better models for heat transfer to the vertical sidewalls are developed, the BETA V2.1 result will have limited use in validating the axial heat transfer model in CORCON.

It appears from the above discussion that the mechanistic analysis just presented offers an approach that is valid for metallic melts and one which, in theory, can be applied to other core debris materials. Unfortunately, no experimental data is currently available for the interaction of prototypic oxide core debris with concrete. It is important to realize that validation of the model for oxidic core debris must be accomplished before CORCON can be applied with confidence to reactor accidents. Until that time, results from CORCON, and for that matter any other unvalidated computer model, must be considered as uncertain. Fortunately, the ongoing SURC experimental program at Sandia is being designed to provide the data required to complete the validation of CORCON.

1.3.4 Release of the First Update to CORCON

A memo transmitting the first correction set for CORCON-MOD2 was distributed to users of the code. This correction set eliminated many of the coding and modeling bugs that had been identified since the release of CORCON-MOD2. Version 2.01 was created by implementation of the correction set.

The correction set was presented in UPDATE format, that is, in a format acceptable to UPDATE processors on CDC and CRAY computers. This was done to help simplify communications between code users and the maintenance staff and to reduce problems with differing versions of the code at various installations.

Sample calculations were included in the package sent to the users. These calculations were for the CORCON Standard Problem and for a sample accident sequence, Peach Bottom AE. An output listing for the Standard Problem was included along with plots of selected CORCON output variables. Plots were also included for the Peach Bottom calculation. These plots compared results from the released and updated versions.

The plots, which are reproduced as Figures 1.3-7 through 1.3-10, showed that the modifications to the code had very little effect on calculated results. In fact, for the Peach Bottom calculations, the results were virtually identical. This similarity was not too surprising since few of the modifications dealt with model changes.

The only model changes included in the first correction set concerned the treatment of partially solidified layers. Hence, the only significant differences between version 2.00 and version 2.01 results occurred either early in the calculation, when the debris was partially solidified, or late in the calculation, when the molten core material was beginning to solidify. However, even then the differences were not great. Although it

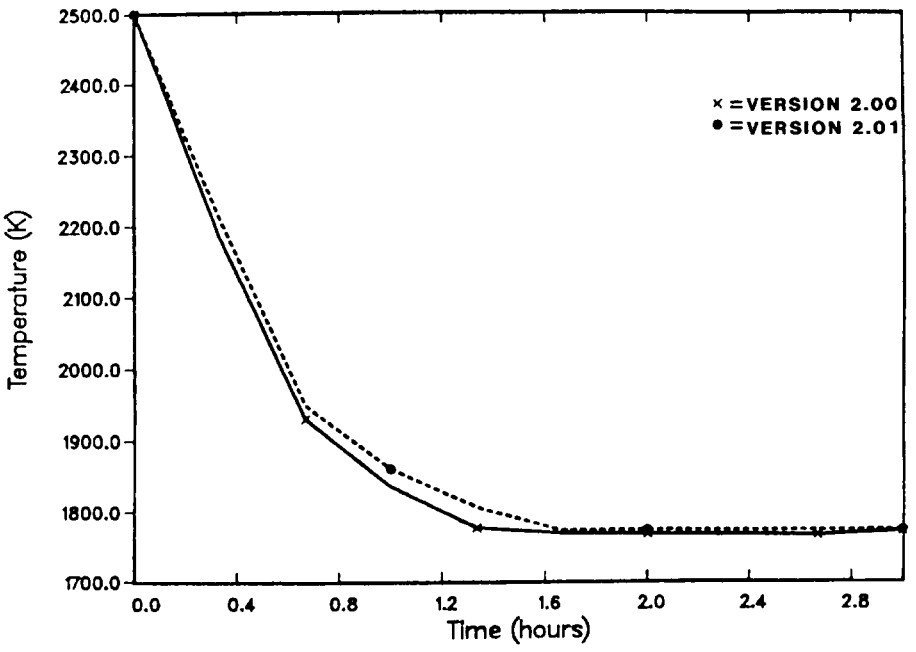

Figure 1.3-7. Comparison of CORCON Versions 2.00 and 2.01 Calculated Melt Temperature for the CORCON Standard Problem

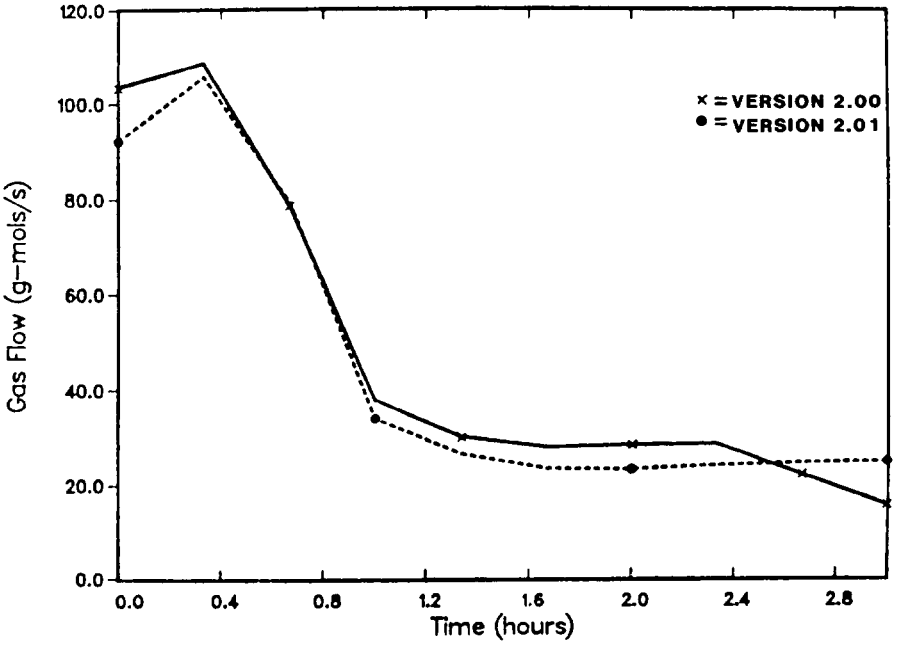

Figure 1.3-8. Comparison of CORCON Versions 2.00 and 2.01 Calculated Gas Flow for the CORCON Standard Problem

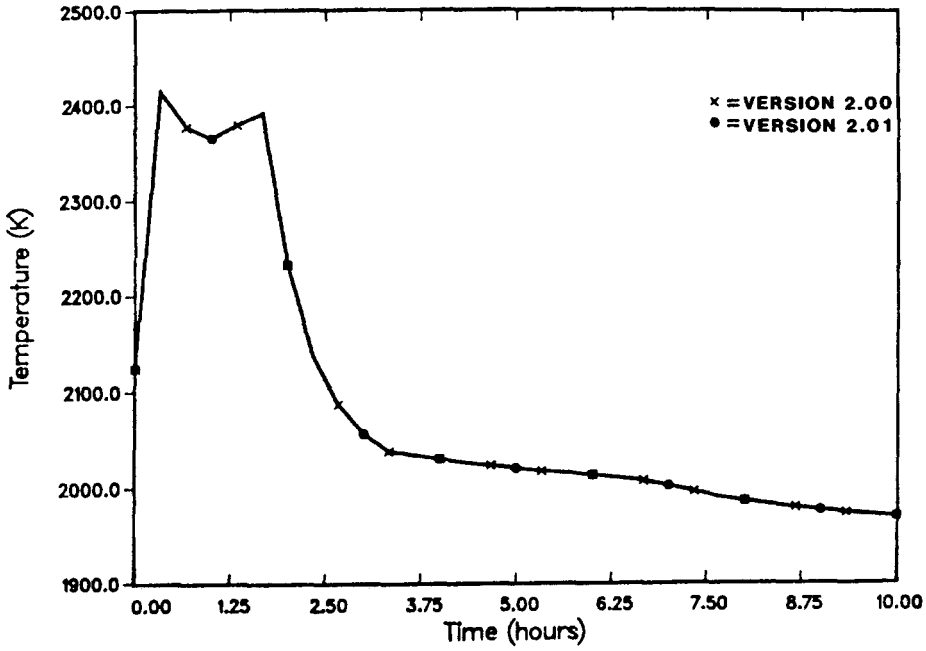

Figure 1.3-9. Comparison of CORCON Versions 2.00 and 2.01 Calculated Melt Temperature for a Peach Bottom AE Accident

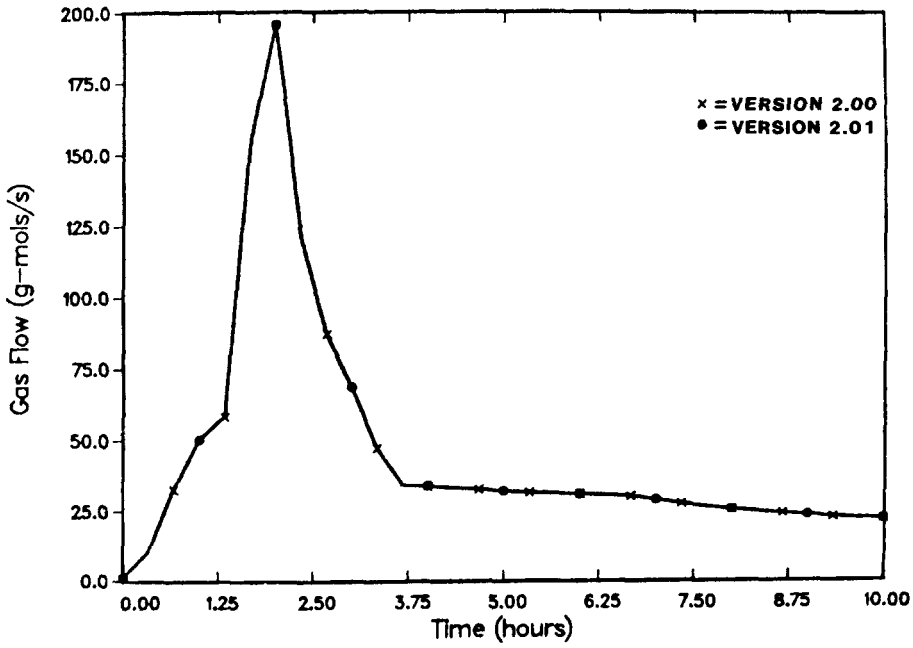

Figure 1.3-10. Comparison of CORCON Versions 2.00 and 2.01 Calculated Gas Flow for a Peach Bottom AE Accident

is not inconceivable that a particular set of input might trigger differences between the two versions, in general we would expect the two versions to yield very similar results.

1.3.5 Release of the Second CORCON Correction Set

A memo transmitting the second correction set for CORCON-MOD2 was distributed to users of the code. This correction set eliminated the sometimes significant overestimation of the decay power caused by the interpolation scheme employed in the released version of the code. Version 2.02 was created by the implementation of this update.

The decay heat package in CORCON calculates the decay heat attributable to 25 fission-product elements, to core uranium, and to structural zirconium. It is based on an ORIGEN calculation for a standard Westinghouse PWR.[114] In essence, it interpolates for each element separately based on decay powers at selected times.

In the released version of the code, five times were selected, corresponding to 0.0, 0.1, 0.6, 2.2, and 20 days after reactor shutdown. The interpolation assumed an exponential time variation between the tabulated points. This scheme can significantly overpredict the decay power at early times, particularly within two hours of reactor shutdown. At one hour, the error is almost a factor of 2.

The primary change in the new decay heat package is the method used to interpolate between tabulated points. Data are now tabulated at 0.5, 1, 2, 4, 10, 24, 72, and 240 hours after reactor shutdown, and a power-law interpolation is used. In other words, log-power is assumed to be linear in log-time. The tabulated points are based on ORIGEN calculations for the same standard Westinghouse PWR core and operating history described in Reference 114. Differences from the previous ORIGEN calculation are minor. The new ORIGEN calculation better accounts for the contribution of decay heat to the total thermal output of the core during reactor operation and, therefore, predicts slightly less fission-product burnup and slightly lower fission-product inventories at the time of reactor shutdown. However, there are no major differences in the total decay powers of the elements in the two calculations.

The elemental powers, summed over the four groups considered in CORCON (metals, oxides, halogens, and alkali metals), have been calculated as a function of time using the new and old decay heat packages. The results are compared in Figures 1.3-11 through 1.3-14. In these plots, 100 percent fission-product retention has been assumed. Also included in the figures are the normalized group powers calculated from the tables in Reference 114.

The new CORCON representation of total power in the oxide is seen to agree very well with that from Reference 114. However, the power in the metal as calculated in CORCON is significantly lower and that in the halogens is significantly higher than those in Reference 114. This difference has been traced to differences between the two in the treatment of the tellurium-to-iodine transition. In Reference 114, the decay power from the daughter

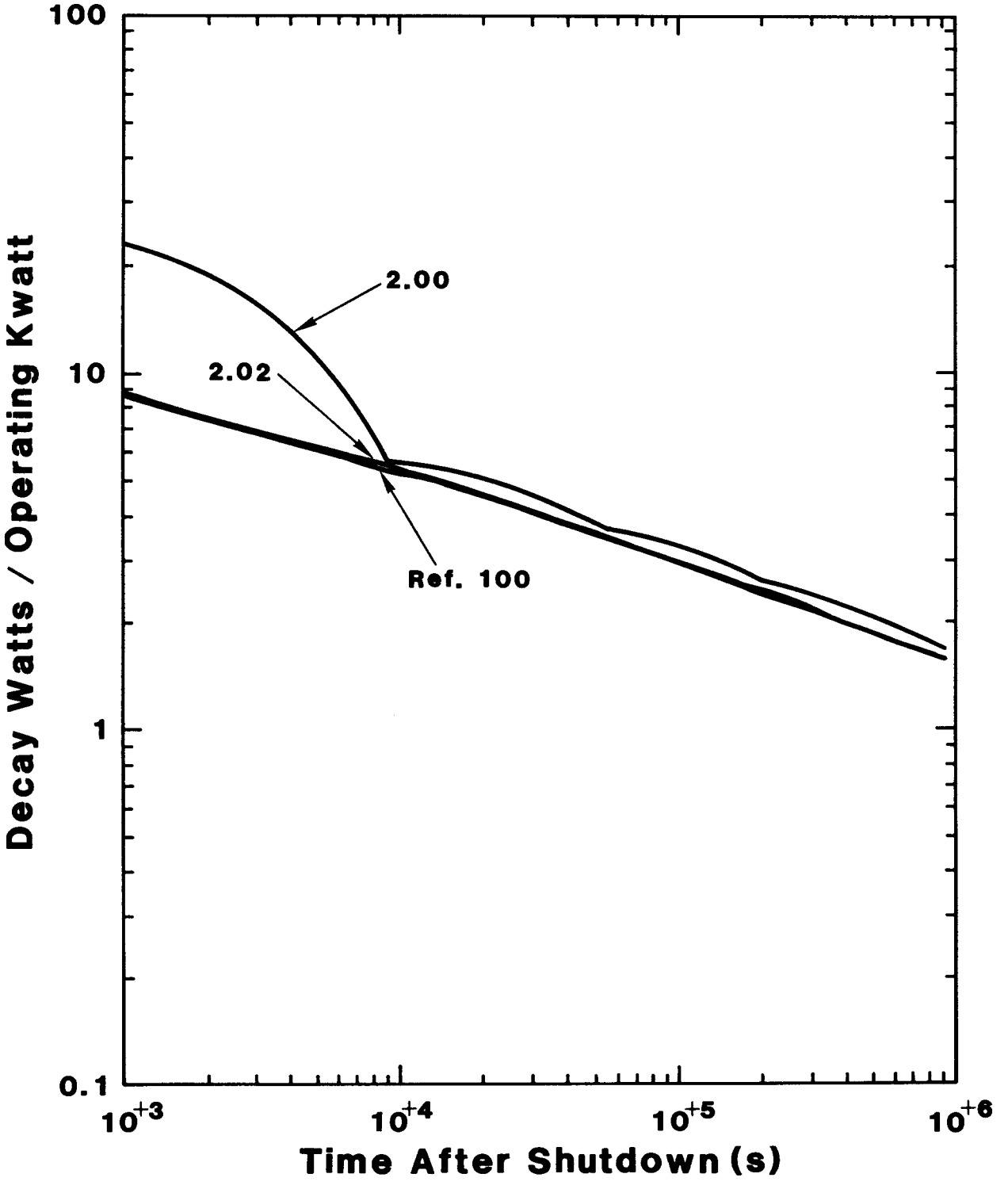

Figure 1.3-11. Decay Power Generated by Oxide Fission Products

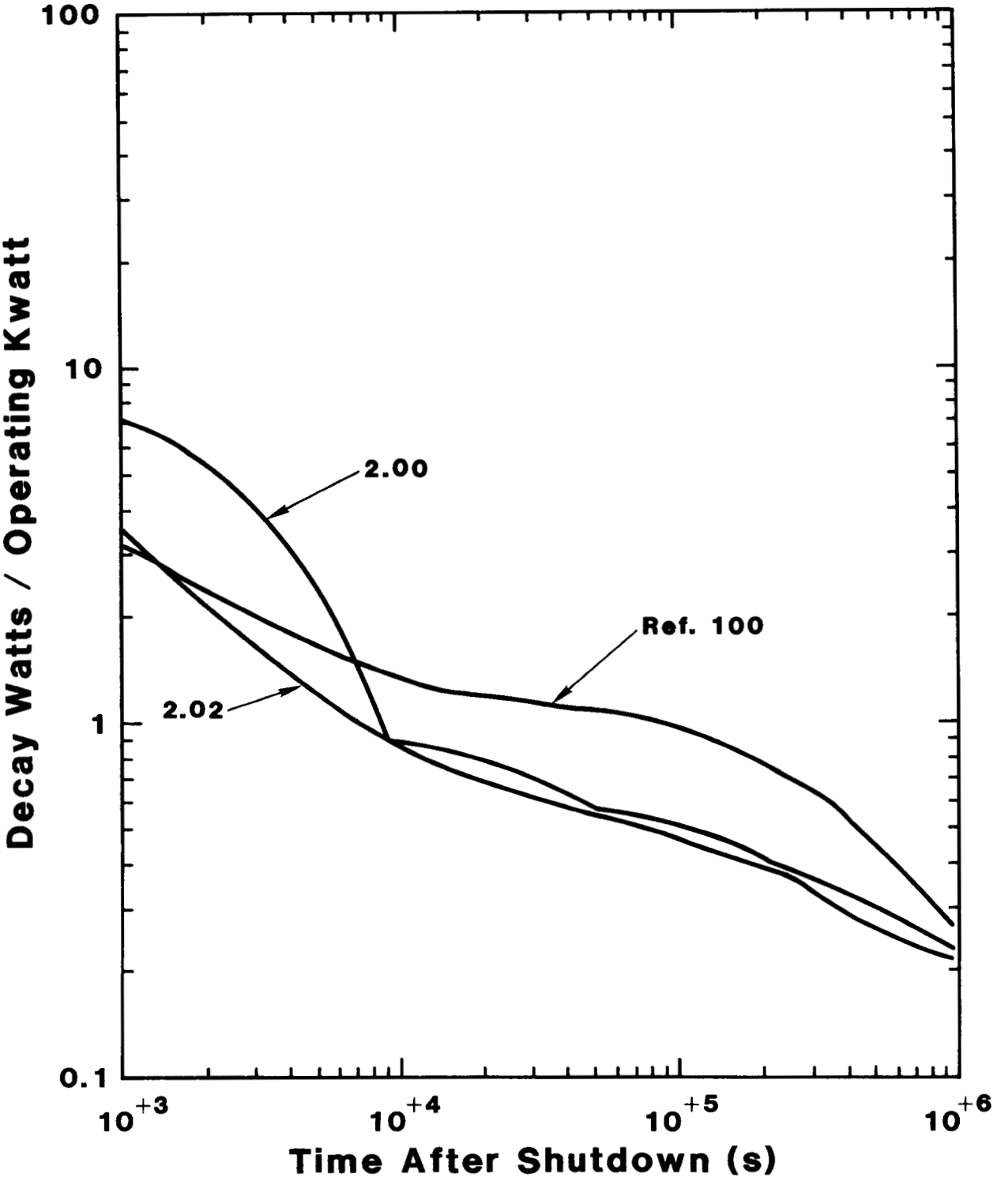

Figure 1.3-12. Decay Power Generated by Metal Fission Products

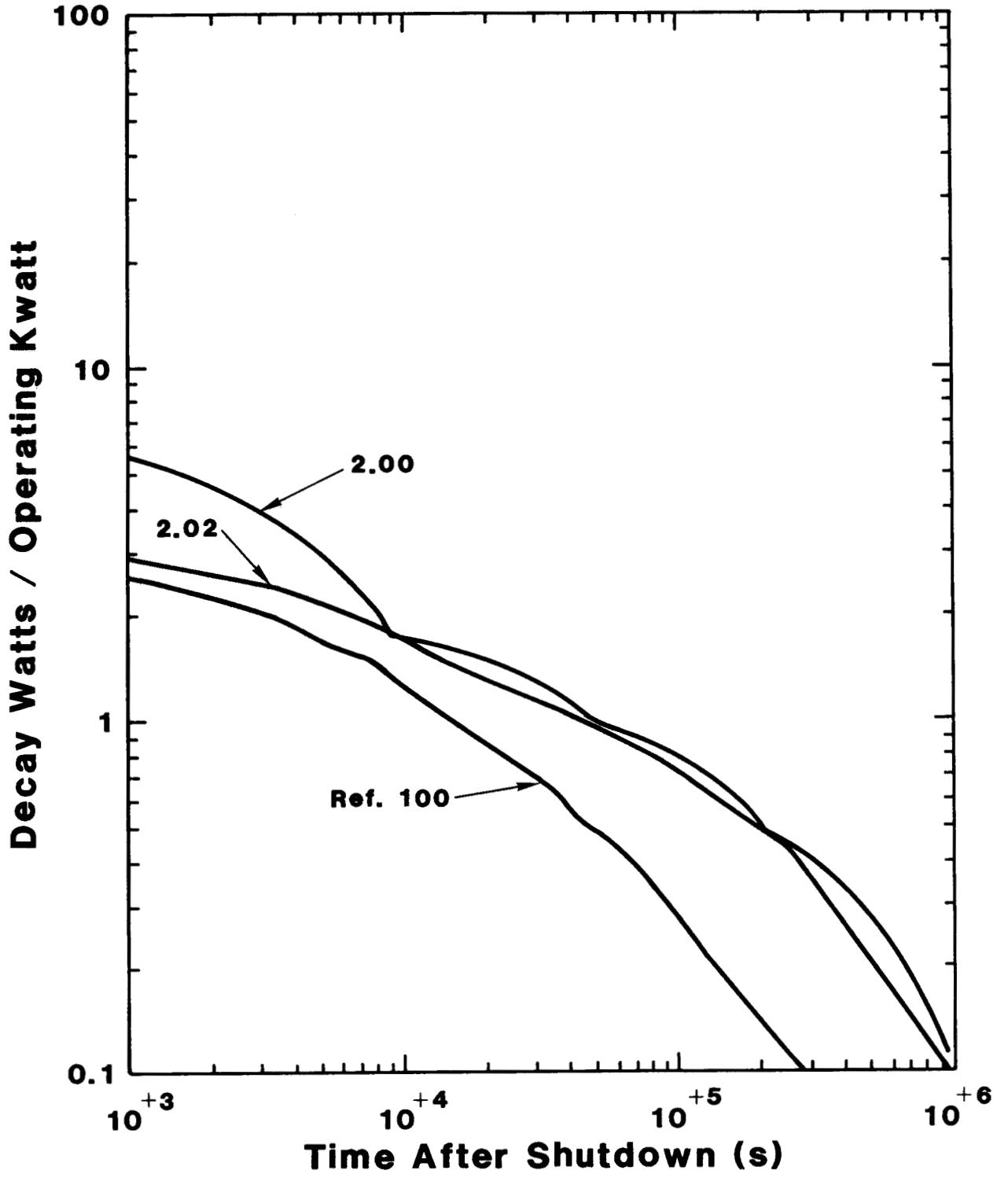

Figure 1.3-13. Decay Power Generated by Halogen Fission Products

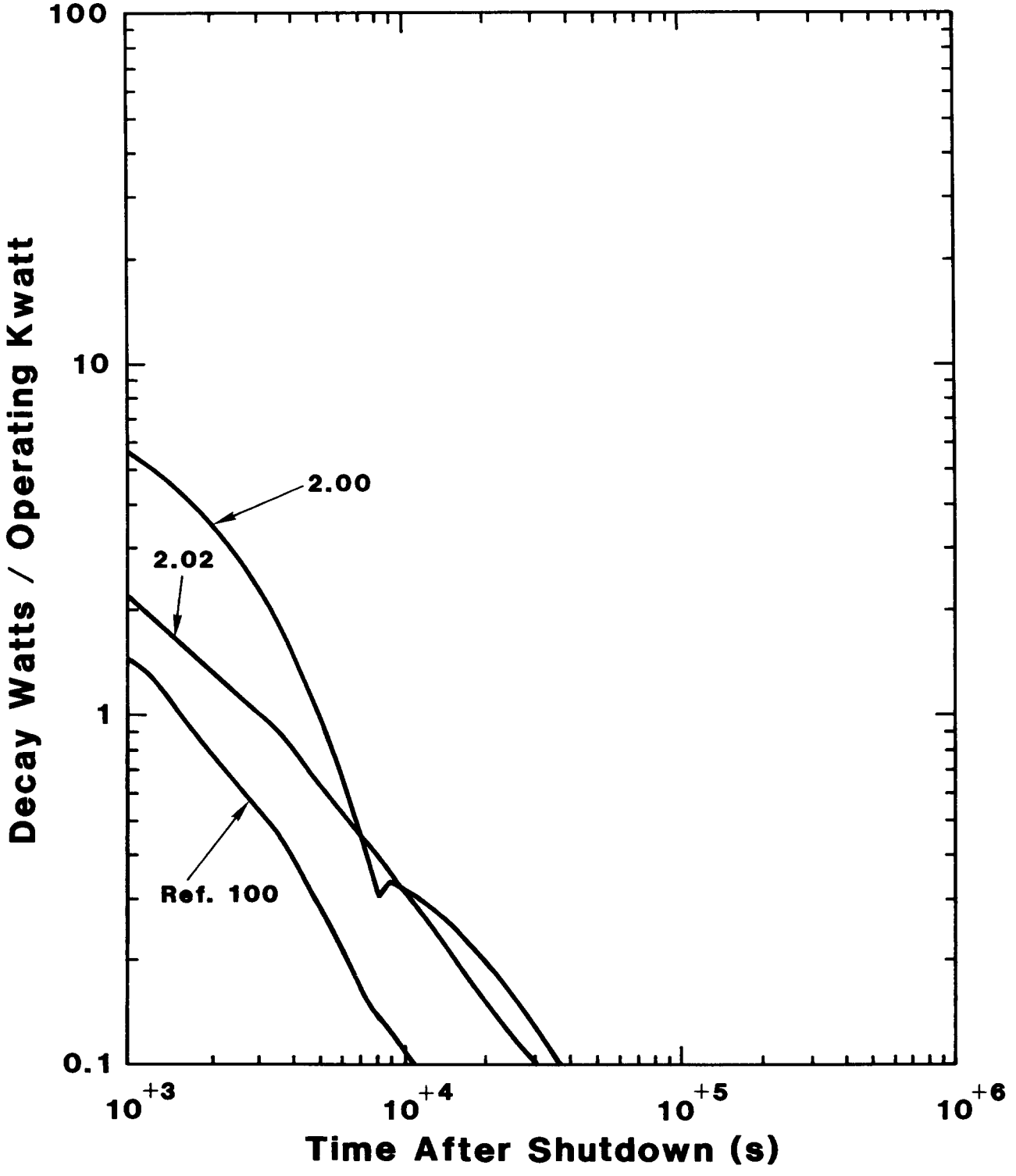

Figure 1.3-14. Decay Power Generated by Alkali Metal Fission Products

iodine produced after the reactor shutdown is attributed to tellurium, while in the CORCON routines, it is attributed to iodine. In this case, the CORCON procedure seems more appropriate since iodine born of tellurium decay is unlikely to remain in the melt pool for any extended period of time.

Sample calculations were performed for the CORCON Standard Problem and the Peach Bottom AE accident, and plots comparing results from versions 2.01 and 2.02 were included in the package sent to the users. In addition, variations on the two sample calculations were run with earlier times for the onset of the core-concrete interaction. (One hour was used in both cases.) These calculations were included to emphasize the differences between the two decay heat interpolation schemes.

Only for the early time calculations were there significant differences between the version 2.01 and version 2.02 results. For the modified CORCON Standard Problem, there was a general reduction in the calculated debris temperature and gas generation during the interaction due to the lower decay energy available to drive the interaction. For the modified Peach Bottom accident calculation, heatup of the initially solidified core debris was slower in the Version 2.02 calculation, and consequently the peaks in the debris temperature and gas generation were shifted in time by 20 minutes. These results are reproduced in Figures 1.3-15 through 1.3-18.

We conclude from these results that the differences between results obtained with Versions 2.01 and 2.02 will only be significant when core-concrete interactions begin within two hours after reactor shutdown. Even then, however, the differences are probably not significant when one considers the great uncertainty in the modeling of core-concrete interactions and other severe accident phenomena.

1.4 Molten Fuel-Coolant Interactions

(B. W. Marshall, Jr. and M. Berman, 6427)

The objective of this program is to develop an understanding of the nature of fuel-coolant interactions (FCIs) during hypothetical accidents in light water reactors (LWRs). The understanding of FCIs achieved in this program is expected to resolve key reactor safety issues for both terminated and unterminated accidents. Models are being developed to quantitatively determine:

1. The rates and magnitudes of steam and hydrogen generation.

2. The degree of mixing and coarse fragmentation of the fuel.

3. The degree of the fine fragmentation of the individual droplets composing the coarse mixture.

4. The fraction of the available thermal energy that is converted into mechanical energy.

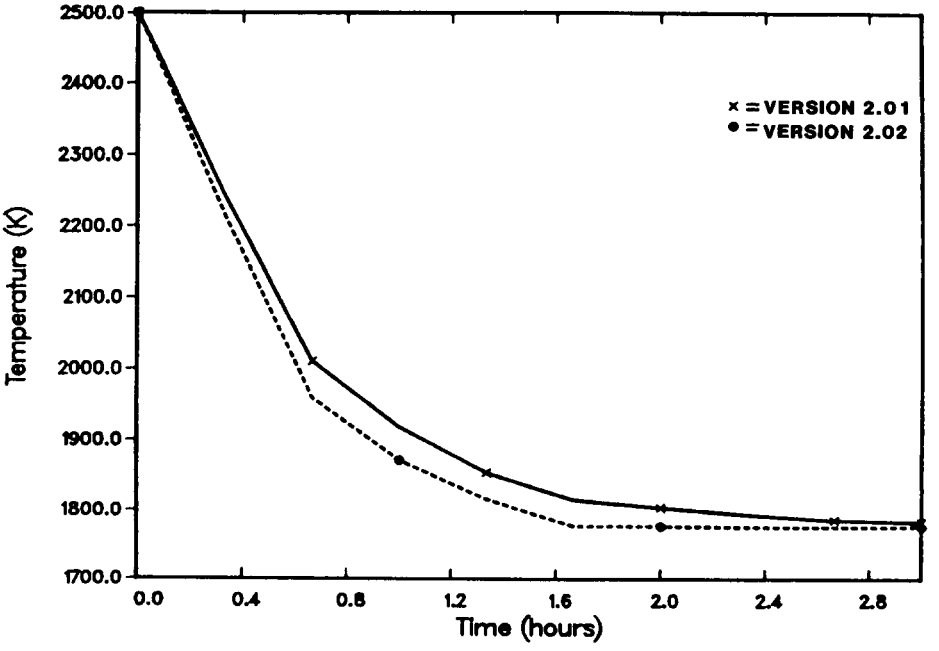

Figure 1.3-15. Comparison of CORCON Versions 2.01 and 2.02 Calculated Melt Temperature for the CORCON Standard Problem - Early Time

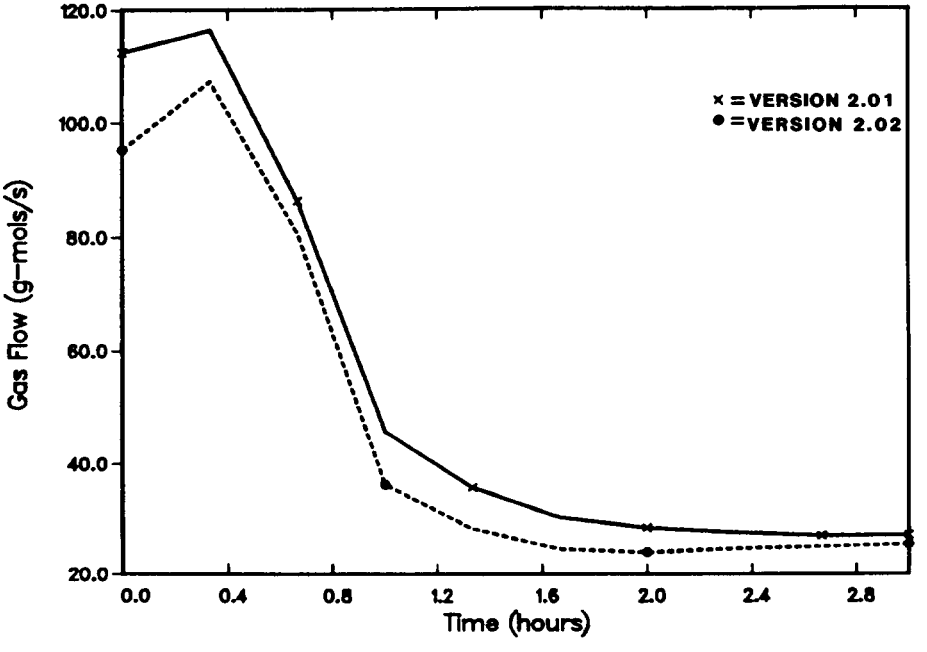

Figure 1.3-16. Comparison of CORCON Versions 2.01 and 2.02 Calculated Gas Flows for the CORCON Standard Problem - Early Time

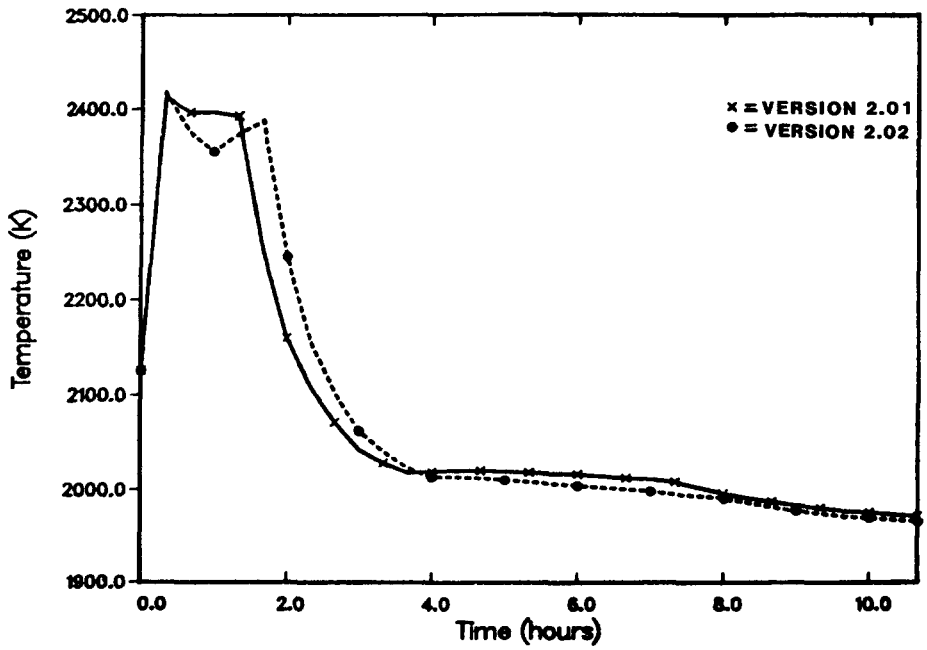

Figure 1.3-17. Comparison of CORCON Versions 2.01 and 2.02 Calculated Melt Temperature for a Peach Bottom Accident - Early Time

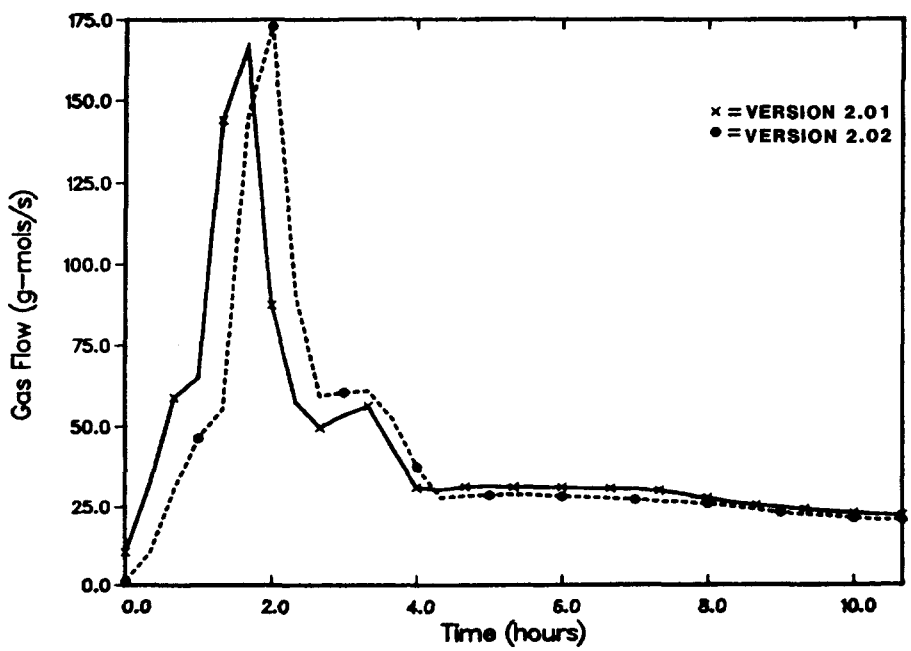

Figure 1.3-18. Comparison of CORCON Version 2.01 and 2.02 Calculated Gas Flows for a Peach Bottom Accident - Early Time

Experiments are being conducted to determine the influence of three classes of important independent variables; thermodynamic conditions (temperature of the fuel and the coolant and the ambient pressure); scale variables (amount of fuel and coolant initially involved); and boundary conditions (pour diameter and rate, shape and degree of confinement of the interactions region, presence of structures, water depth, and fuel-coolant contact mode). Measurements being made during the experiments include photographic observation of the FCIs, pressures generated in the coolant and the cover gas, steam and hydrogen generation, and the resulting debris characteristics.

1.4.1 FITS Experiments

There were no FCI experiments conducted in the FITS (Fully Instrumented Test Site) Vessel during this period. We currently expect the final FITSD test to be conducted in May.

1.4.2 Jet Mixing Program

(B. W. Marshall, Jr., 6427)

Recent observations inside the Three Mile Island-Unit 2 (TMI-2) reactor core have shown that about 20 tons of core material melted and poured into the lower plenum about 3.8 h into the accident.[115,116] Contrary to some previous assumptions, the lower core support and flow distribution plates appear to be undamaged. These observations change the earlier idea that large coherent pours would occur. It appears that the molten core poured through and around the structural plates creating jets which were surrounded by saturated water. The purpose of the jet-mixing program, therefore, is to begin to develop an understanding of the mixing processes and explosibility of jets of molten material falling through water. The assumed conditions inside the reactor core are a corium temperature of ~2800 K, saturated water, and an ambient pressure, which can range from 1 to 170 bars. The ratios of the densities and viscosities of the molten corium to water are approximately 7.8 and 4, respectively. For TMI-2, the range of possible orifice sizes are from 8.3 to 16.5 cm. Furthermore, the possible aspect ratios (i.e., the plate thickness to hole diameter) range from 0.3 to 2.0 and since there are numerous holes in each structural plate, multiple jets of corium will be created.

To date, four series of experiments addressing the importance of liquid-jet mixing have been either completed or are currently in progress. The four series are (1) jets of molten iron/alumina falling through air (MDJET series), (2) jets of water falling through air (WAT series), (3) jets of molten iron/alumina falling through water (EJET series); and (4) isothermal jets falling through water (IJET series). Each of these series is described and preliminary results are discussed. However, before presenting our experimental data, a brief literature review covering liquid-gas jet data, isothermal liquid-liquid jet data, and boiling liquid-liquid jet data is appropriate.

1.4.2.1 Literature Review

- Liquid-Gas Jet Data

The majority of the currently published data are for liquid jets injected into gaseous atmospheres. This system has been investigated experimentally for over a hundred and fifty years; the earliest known work was performed by Bidone and Savart in the early 1800s.[117,118] One of the earliest known theoretical investigations into jet stability was reported by Rayleigh.[119,120,121] Lord Rayleigh evaluated the instabilities of an inviscid jet falling through a vacuum. Some of the most useful and comprehensive reviews of the currently existing data have been prepared by Kryzwoblocki,[122] McCarthy and Molloy,[123] Chen and Rodi,[124] and Windquist and Corradini.[125]

The stability curve represents the experimentally-measured jet breakup length as a function of the jet velocity. In Figure 1.4-1, a schematic representation of the stability curve for a liquid-gas system is shown. The stability domain is generally broken into four regimes; the Rayleigh regime (points A to B), the transition regime (points B to C), the turbulent regime (points C to D) and the atomization regime (above point D). The Rayleigh regime, or capillary-instability regime, was first treated by Rayleigh for an inviscid jet.[119] Weber also analyzed this regime for the viscous jet falling through a vacuum.[126] Under ideal conditions and at these low velocities, the fragmentation of a jet is caused by axisymmetric instabilities induced by surface tension and inertial forces.

The breakup mechanisms in the transition region are not as clearly understood as the Rayleigh regime. This regime is characterized by much uncertainty because of differences in nozzle design,[123] ambient system pressure,[127] and turbulence within the jet. Jet disintegration is thought to be due to surface tension and inertial forces as well as turbulence-induced fragmentation, usually producing drops on the order of the jet diameter.

The turbulent regime is also characterized by a relatively large scatter in the experimental data. Jet disintegration appears not only to be a function of the velocity, but also of the nozzle design and turbulence level in the jet. In this regime, jet breakup can be induced by a number of phenomena including the growth of unstable transverse waves, the growth of axisymmetric waves, and boundary-layer stripping of smaller particles.

The stability curve in the atomization regime is not clearly defined. Here, the velocities of the jet are so high that a coherent core of material appears to be surrounded by a spray of particles, which are usually much smaller than the jet diameter. Jet breakup is thought to be due to aerodynamic forces, jet-flow conditions, and nozzle design. However, as others have observed,[128] the exact shape of the stability curve in the atomization regime is currently uncertain.

Given the uncertainties that exist, the fragmentation of a liquid-gas jet system is relatively well understood compared to other systems. Some important parameters for the liquid-gas system include the initial jet

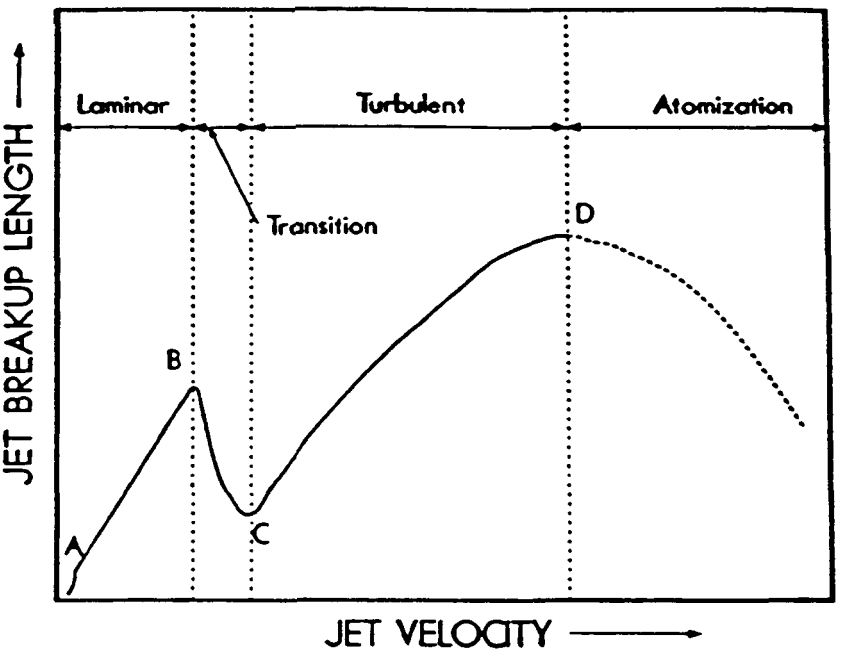

Figure 1.4-1. Schematic of the Liquid-Gas Stability Curve

diameter (current data are on the order of millimeters), the jet velocity, the liquid-gas surface tension and jet viscosity, the turbulence in the reservoir, the nozzle and reservoir geometry, and the smoothness and streamlining of the nozzle surfaces.

- Isothermal Liquid-Liquid Jet Data

The most comprehensive review of isothermal liquid-liquid jet data has been compiled by Kitamura and Takahashi.[129] Jet orifice diameters used in their referenced works ranged from 0.05 to 0.26 cm with jet entrance velocities of up to about 150 cm/s. Furthermore, the properties of the system fluids (i.e., viscosity, density, and interfacial tension) affect the jet-mixing behavior significantly more than in the liquid-air system.

When a liquid is injected into another stagnant immiscible liquid, the fragmentation of a jet depends upon numerous parameters. Comparison of the liquid-gas and liquid-liquid data reveals that the jet-breakup behavior depends strongly on the viscosity and density ratios (i.e., ratio of the jet-to-pool properties). If the viscosity ratio is less than about unity, the breakup length increases linearly with the jet velocity to a maximum and then decreases linearly with further increases in velocity. If the viscosity ratio is greater than about 2, then the jet breakup length curve becomes nonlinear.[129,130] The density ratio also affects the breakup length; it appears that as the density ratio increases, the maximum breakup length also increases. Note, however, that experimental difficulties exist in changing the density ratio without changing the viscosity ratio of the system, and observations from the current data are not conclusive. We also believe that the interfacial tension is an important

parameter for liquid-liquid systems. However, data in this area are also sparse and further work is needed. Thus, in addition to the jet velocity, the interfacial tension and the ratios of the system viscosities and densities govern the nature of the jet breakup.

The first analytical work in this area was performed by Tomotika.[131] He analyzed the stability of a liquid column injected into a second continuous liquid, for general cases where both inertial and viscous forces are significant and for two limiting cases where either inertial or viscous force is negligible. Note that the analytical solution developed by Rayleigh,[119,120,121] is a subset of this generalized solution. Additionally, analytical work in this area was performed by Meister and Scheele[132] in which a number of limiting solutions were derived from Tomotika's generalized solutions.

The currently published data[129,130,132-140] pertain to jet diameters less than 3 mm, jet velocities less than about 1.5 m/s, density ratios between 0.6 and 1.6, viscosity ratios between 0.1 and 1.6, and interfacial tensions which range from 1 to 50 dynes/cm.

- Boiling Liquid-Liquid Jet Data

Although there are numerous FCI experiments in which globs of molten fuel are dropped into a second condensable fluid, there is a very limited data base related to the dynamic mixing processes of jets of molten fuel falling through the condensable fluid. Numerous authors have attempted to model this configuration by assuming that the steam film is thick and that the important jet-mixing behavior can be assumed to be that of a liquid-air system.[128,141,142]

The earliest experimental work in this area was performed by Bradley and Witte.[143] They conducted experiments using 1.6-mm-diameter jets at temperatures that ranged from about 300 to 650 K and which were injected into water at ambient conditions (~295 K). The molten materials (tin, Asarcolo-158, mercury, and a lead-tin alloy) were injected horizontally into the water and steam explosions occurred in numerous cases. However, the violence appeared to be a strong function of the initial melt temperature; at low melt temperatures, no significant breakup of the material was observed whereas at temperatures near 600 K, violent explosive interactions were observed and the posttest debris was finely fragmented.

More recent experimental work has been reported by Spencer et al.,[144,145] in which jets of molten material having an initial diameter of 2.2 cm were injected into water and liquid sodium. In the first system, jet materials (molten corium, tin, or Wood's Metal) were injected into water at either saturated (~5°C subcooled) or highly subcooled conditions (~75°C subcooled). In the second system, molten corium was injected into sodium at a temperature of 1200 to 1450 K, depending upon the test. In all but one of these experiments, no explosive interactions were observed. Instead, very limited mixing of the jet with the coolant occurred.

The fragmentation of molten jets falling through water is an important reactor-safety concern. However, very limited data are currently available

in the literature. The important parameters are those listed for the isothermal liquid-liquid systems and liquid-gas systems in addition to the temperature and composition of the molten-jet material. If the molten material is significantly above the boiling point of the water, vapor generation may play an important role in the dynamic mixing process. Also, the composition of the molten jet material will be important in the evolution of noncondensable gases such as hydrogen, possibly affecting the triggerbility and explosibility of these jets as well as the breakup behavior.

1.4.2.2 Liquid-Air Jet Experiments

(B. W. Marshall, Jr., 6427)

a. Molten Jets Falling Through Air (MDJET Series)

In this series we conducted six experiments investigating the behavior of molten jets of iron/alumina falling through ~1.8 m of air. Another important purpose was to develop the techniques needed to deliver jets of molten iron/alumina into deep water chambers. Table 1.4-1 shows the initial and boundary conditions for each of the experiments. As shown, experiments were conducted using single- and three-jet configurations.

- Single-Jet Tests

In the single jet experiments (MDJET-1, -2, and -6), we observed some interesting and unexpected trends in the jet behavior. The integral jet breakup was unusual and could not be described by a single characteristic.

Table 1.4-1

Initial and Boundary Conditions of the Molten-Jet/Air Experiments

Test	Fuel Mass[a] (kg)	Jet Diameter (cm)	Number of Jets	Jet Fall Distance (m)
MDJET-1	41.5	3.8	1	1.8
MDJET-2	40.0	3.8	1	1.8
MDJET-4	40.0	3.8	3[b]	1.8
MDJET-5[c]	40.0	3.8	3[b]	1.8
MDJET-6[c]	40.0	7.6	1	1.8
MDJET-7[c]	40.0	3.8	3[b]	1.8

[a]Mass of thermite initially loaded into the crucible.
[b]The jet holes were 120° apart and at a pitch of ≠5.7 cm.
[c]Continuous X-ray imaging of the molten jet as it fell through the air.

Rather, the jet breakup was a combination of characteristics depending upon the time into the melt-pour. Early in the pour, the breakup resembled that of a jet in the turbulent regime; e.g., transverse wave disturbances (also referred to as sinuous breakup) dominated the jet fragmentation. This sinuous breakup phase generally lasted for the duration of the melt-pour from the reaction crucible into the reservoir. Subsequent to this phase, the breakup characteristics changed from sinuous to varicose-type behavior. Varicose jet breakup is caused by surface tension and inertial forces and, in the absence of turbulence, is the expected jet breakup behavior at these relatively low velocities.

Jet breakup can be affected by numerous factors. In particular, turbulence in the reservoir above the nozzle can affect the breakup behavior. The sharpness of the edge of the nozzle, the smoothness of the nozzle walls, and other factors will also affect the jet fragmentation. Each of these parameters could result in turbulent jet-breakup behavior when velocities are low enough that laminar behavior (i.e., varicose jet breakup) would otherwise be predicted. In these experiments, however, turbulence in the reservoir is believed to dominate the breakup of the jet. Early in the pour, the turbulence generated by the relocation of the melt from the reaction crucible to the reservoir resulted in sinuous-type jet breakup. Furthermore, when the relocation was complete, the jet changed character and began to fragment because of surface tension and inertial forces (e.g., varicose jet breakup). To further evaluate these observations, we conducted a similar series of experiments using water as the jet material. These experiments are discussed in Section 1.4.2.2.b.

- Three-Jet Tests

Three experiments (MDJET-4, -5 and -7) were conducted using a three-jet geometry. The jet configuration consisted of three 3.8-cm-diameter jets, 120° apart and at a pitch of 5.7 cm. One purpose of these experiments was to analyze the differences and similarities between the single-jet and three-jet configurations. We believe that the influences of neighboring jets may be important in reactor safety analysis. Furthermore, the delivery techniques developed in these experiments would be used in future experiments.

During these experiments, we observed the same general jet-breakup behavior, two distinct breakup characteristics depending upon the time into the pour. As with the single-jet experiments, the early-time jet behavior was characterized by turbulent sinuous wave breakup while the late times were characterized by surface tension and inertial effects. Furthermore, we observed that during the early part of the pour, the three jets spread away from one another and rotated slightly about the center line. This may be an indication that vortices were being established in the reservoir above the nozzle, causing the jet to spin. Late into the pour the jets converged and fell vertically with very little spin about the centerline. As observed in the single-jet experiments, this change in behavior appeared to coincide with the completion of the relocation of the melt from the reaction crucible to the reservoir. After the relocation, the turbulence level decreased and varicose-type jet breakup was observed.

b. Water-Jets Falling Through Air (WAT Series)

To assist in our understanding and interpretation of the MDJET experiments, we conducted a series of experiments in which jets of colored water fell through ~1.8 m of air. In this series, as shown in Table 1.4-2, all experimental parameters were identical to those in the MDJET series. However, to study the importance of reservoir turbulence, we conducted experiments with and without a 30-cm prefall distance above the reservoir. Two single-jet experiments and two three-jet experiments were conducted. The turbulent reservoir conditions (i.e., 30-cm prefall) were compared to the MDJET results and to the quiescent reservoir conditions allowing us to evaluate the jet-breakup behavior as a function of the reservoir turbulence. Finally, two additional experiments were conducted evaluating the importance of nozzle geometry (e.g., the ratio of the nozzle length to diameter) for the turbulent reservoir conditions.

As shown in Figure 1.4-2, the jet breakup length is shown as a function of the time into the melt-pour and is strongly influenced by reservoir turbulence. For the quiescent reservoir conditions (i.e., the no prefall conditions), the breakup of the single- and three-jet configurations is representative of varicose behavior. The jets exit from the nozzle and fall vertically through the air without significant breakup. However, there is evidence of varicose-type breakup as the jet falls and begins to "pinch off" at regular intervals. This implies that surface tension and inertial forces are acting, but that longer fall distances would be required before the jet actually fragments into drops. Also note that in the case of the quiescent three-jet configuration, the jets converge together within a few jet diameters and appear to fall as one single large jet.

Table 1.4-2

Initial and Boundary Conditions of the WAT Series

TEST	Jet Dia. (cm)	Prefall (cm)	Number of Jets	T/D^a	Jet Fall Dist. (m)
WAT-1	3.8	0	1	0.67	1.8
WAT-2	3.8	0	3	0.67	1.8
WAT-3	3.8	30	1	0.67	1.8
WAT-4	3.8	30	3	0.67	1.8
WAT-5	3.8	30	1	10.0	1.8
WAT-6	3.8	30	1	10.0	1.8

[a] T/D is the ratio of the nozzle length to diameter or aspect ratio.

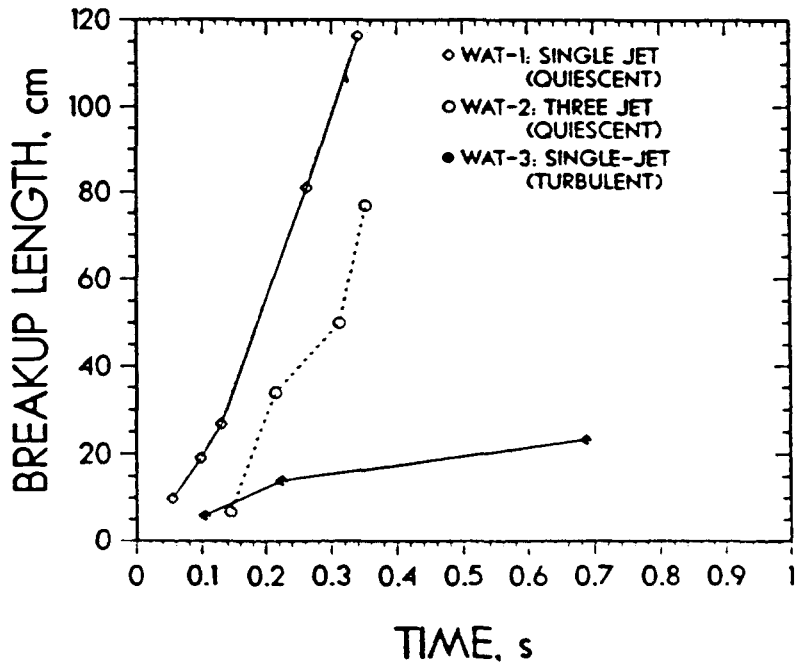

Figure 1.4-2. Jet Breakup Length for Single- and Three-Jet Tests

As in the MDJET series, the turbulence reservoir conditions resulted in jet-breakup for the single- and three-jet configurations, which could not be described by a single jet-breakup characteristic. As shown in Figure 1.4-2, the breakup length is a strong function (for an aspect ratio of 0.67) of the reservoir turbulence, reducing the breakup length by nearly an order of magnitude. For the three-jet experiments with reservoir turbulence, the turbulence level was so high that we could not identify a jet-breakup length; the jet began to fragment immediately as it left the nozzle. Therefore, the jet-breakup length is assumed to be zero.

If the spread of the three-jet configuration is considered, as shown in Figure 1.4-3, the effect of reservoir turbulence is clearly evident compared to the quiescent-reservoir conditions. For turbulent conditions, the spread of the three-jet configuration ranges from 24° to 6° and is a function of time while the single jet deviates from the centerline by about 6° for the duration of the relocation. Another interesting observation is the fact that the spread angle goes to zero for both single- and three-jet cases as the relocation of the fluid from the crucible to the reservoir is completed (about 1.7 s).

In the final two experiments (WAT-5 and -6), the importance of the nozzle geometry was considered for the turbulent reservoir conditions. The ratio

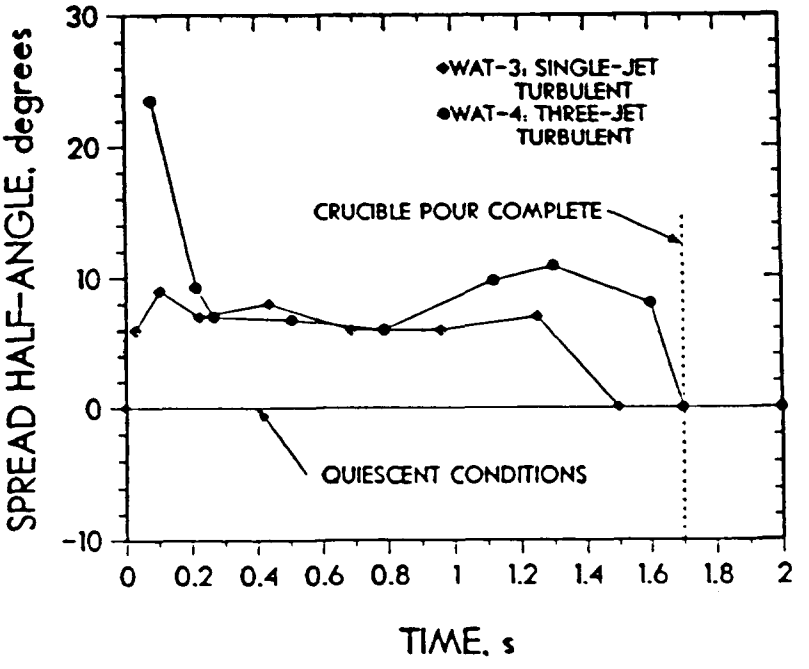

Figure 1.4-3. Jet Spread for the Single- and Three-jet Tests With and Without Reservoir Turbulence

of the nozzle length to diameter, or aspect ratio, is an important parameter when evaluating the influence of reservoir turbulence. As the aspect ratio increases, the influence of turbulence should decrease since the longer nozzles would streamline the flow. As expected for both the single- and three-jet configurations, the longer nozzle reduced the influences of reservoir turbulence. The jet-breakup behavior was similar to the quiescent reservoir conditions in that the jets fell vertically with no significant spread.

We have clearly demonstrated that reservoir turbulence can strongly affect the jet-breakup characteristics. For nozzles with small aspect ratios and turbulent reservoir conditions, the jet-breakup behavior is dominated by the turbulence in the reservoir. However, for longer nozzles, the influence of reservoir turbulence is reduced, or even eliminated, by the streamlining effect of the nozzle.

Inside a typical reactor core, the aspect ratios of the flow distribution and core support plates range from about 0.3 to 2.0. Thus the turbulence created by the relocation of melt from the core region onto the structural plates in the lower plenum may affect the jet-breakup characteristics, especially in the absence of water. However, as described in a later section, reservoir turbulence is less important for a liquid-liquid system.

1.4.2.3 Boiling Liquid-Liquid Jet Experiments (EJET Series)
(B. W. Marshall, Jr., 6427)

Using the experimental techniques developed in the MDJET series, a series of experiments was conducted which investigated the mixing characteristics and explosive nature of boiling jets. The experimental setup, shown in Figure 1.4-4, incorporated a 56-cm square lucite water chamber in which a single jet of molten iron/alumina was gravity-poured into both saturated and highly subcooled water. The initial and boundary conditions of the five experiments are shown in Table 1.4-3. The purpose of this series was to begin to understand the breakup process of molten jets falling through water ($T_{melt} >> T_{sat}$).

The experiments generally progressed as follows: The thermite powder was ignited and reacted to completion inside the reaction crucible. The molten products then melted through a 0.64-cm-thick steel plate in the bottom of the reaction crucible (the hole-diameter was 12.7 cm). The melt then fell about 30 cm into the reservoir, flowed through a hole in the bottom of the reservoir and into the water. The bottom of the reservoir nozzle was placed at the water surface minimizing the entrance velocity of the jet. The water chamber was manufactured of 2.54-cm-thick lucite to allow high-speed photographic coverage. Discussion of the EJET-4 experiment is omitted due to experimental difficulties with the high-speed cameras.

- EJET-0

This was the first boiling-jet experiment conducted to check our experimental techniques, timing, and setups. This ambient water-temperature test could be compared to the EJET-1 experiment to evaluate the importance of water subcooling.

The melt flowed into the reservoir and through the 3.8-cm-diameter nozzle. From the high-speed film records, a coherent jet of molten iron/alumina could not be identified. Rather, as the melt entered the water, it fragmented into particles having drop diameters which were less than the initial jet diameter. The jet breakup curves are shown in Figure 1.4-5 and indicate that the mixture region almost immediately grows to twice the initial jet diameter. The region then continues to grow at a much reduced rate until about 2.5 s into the pour. At 2.5 s, a rapid expansion of the mixture region occurs, filling the entire water-chamber. This jet mixing behavior was unexpected since most of the literature indicated that no significant breakup would occur for these conditions.[141,144,145]

- EJET-1

This experiment was a repeat of the EJET-0 experiment except that the water temperature was 362 K (89°C) and the melt mass delivered was 47 kg. As before, significant fragmentation of the melt occurred as it fell through the water. As shown in Figure 1.4-6, the mixture region immediately grew to twice the initial jet diameter and then propagated, at that diameter, into the water chamber for about 600 ms. After the first 600 ms, the mixture region appeared to be in a quasi-equilibrium state for the next 700 to 800 ms; i.e., no further growth in the mixture region occurred. At

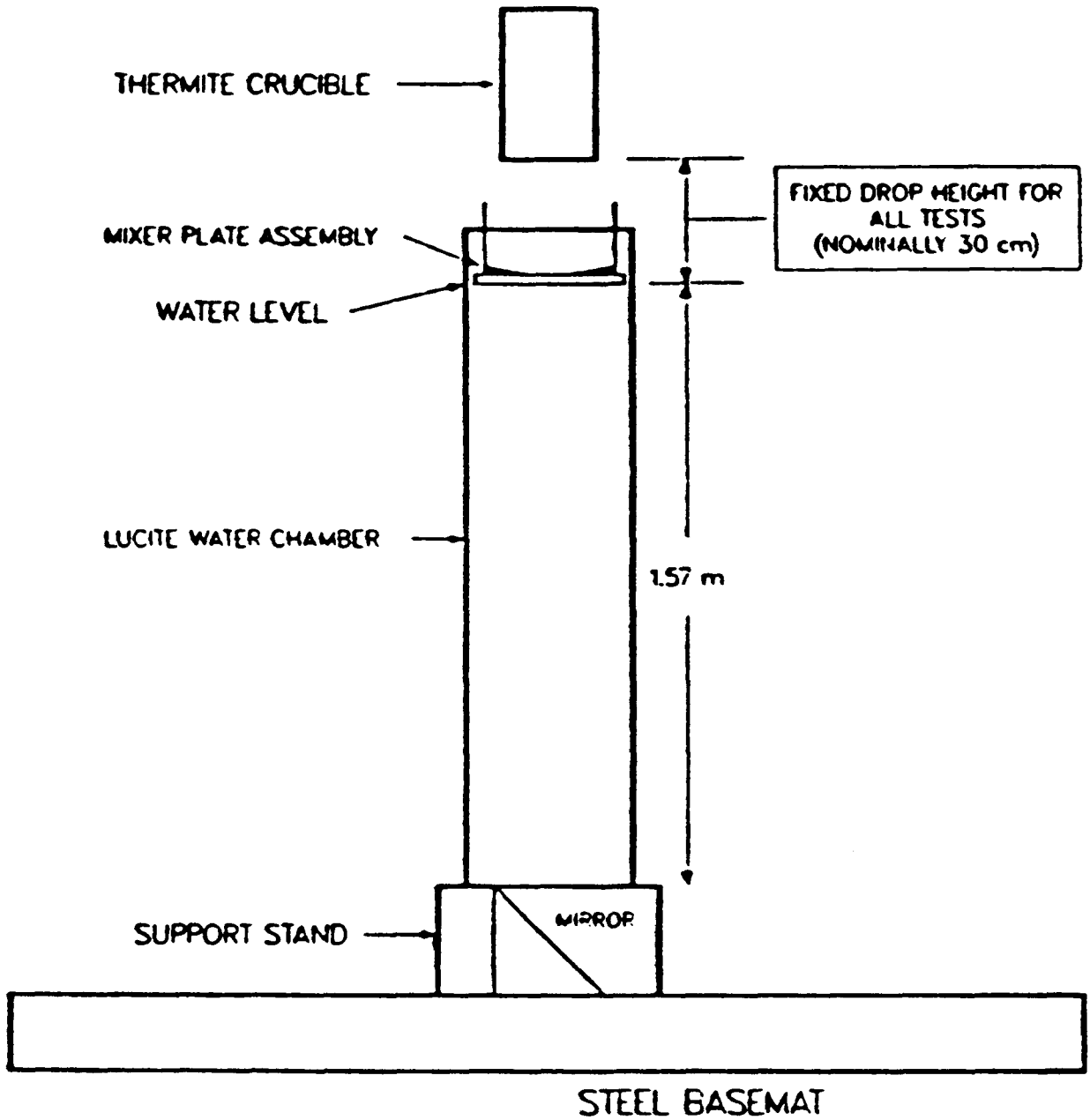

Figure 1.4-4. Experimental Setup for the EJET Series

Table 1.4-3

Initial and Boundary Conditions for the Molten-Jet/Water Experiments

Test	Fuel mass (kg)	Jet diameter (cm)	Coolant mass (kg)	Coolant Depth (m)	Coolant Temp. (K)
EJET-0[a]	37.0	3.8	489.3	1.57	303
EJET-1	47.0	3.8	472.1	1.57	362
EJET-2	47.0	7.6	472.1	1.57	361
EJET-3[b]	47.0	16.3	472.1	1.57	359
EJET-4[b]	47.0	16.3	489.3	1.57	303

[a]EJET-0 was previously named MDJET-8.
[b]No prefall. The 16.3-cm-diameter hole was in the reaction crucible itself.

~1.3 s into the melt-pour, a second rapid expansion of the mixture region occurred, filling the entire water chamber. This type of nonlinear mixing behavior suggests a threshold of some kind was achieved. Furthermore, comparison of Figures 1.4-5 (EJET-0) and -6 (EJET-1), indicates that the second rapid expansion of the mixture zone occurs at different times into the pour (~2.6 s for EJET-0 and ~1.3 s for EJET-1). Since the water subcooling was the only parameter changed in these two experiments, this time dependence may be related to the water subcooling. For initially saturated water conditions, each unit of energy leaving the melt would result in steam generation. Since the melt has a temperature of about 2700 K, rapid and extensive steaming rates would be expected for initially saturated water. However, for highly subcooled water, energy from the melt must first heat the surrounding water to saturated conditions before rapid steaming rates can be achieved. Therefore, differences in timing between highly subcooled (EJET-0) and saturated (EJET-1) water conditions would be expected and were observed.

Based on these two experiments, we can state that the generation of vapor significantly affects the jet breakup. Furthermore, the initial temperature of the water appears to determine the timing of the second rapid expansion of the jet-mixture region. We did not observe any indication of a steam explosion in either the EJET-0 or EJET-1 experiments.

- EJET-2

In this experiment, 47 kg of iron-alumina thermite were used to generate a molten jet 7.6 cm in diameter. The water chamber dimensions were identical to those used in the EJET-1 test. The water temperature was 361 K (88°C), which is approximately 5° subcooled.

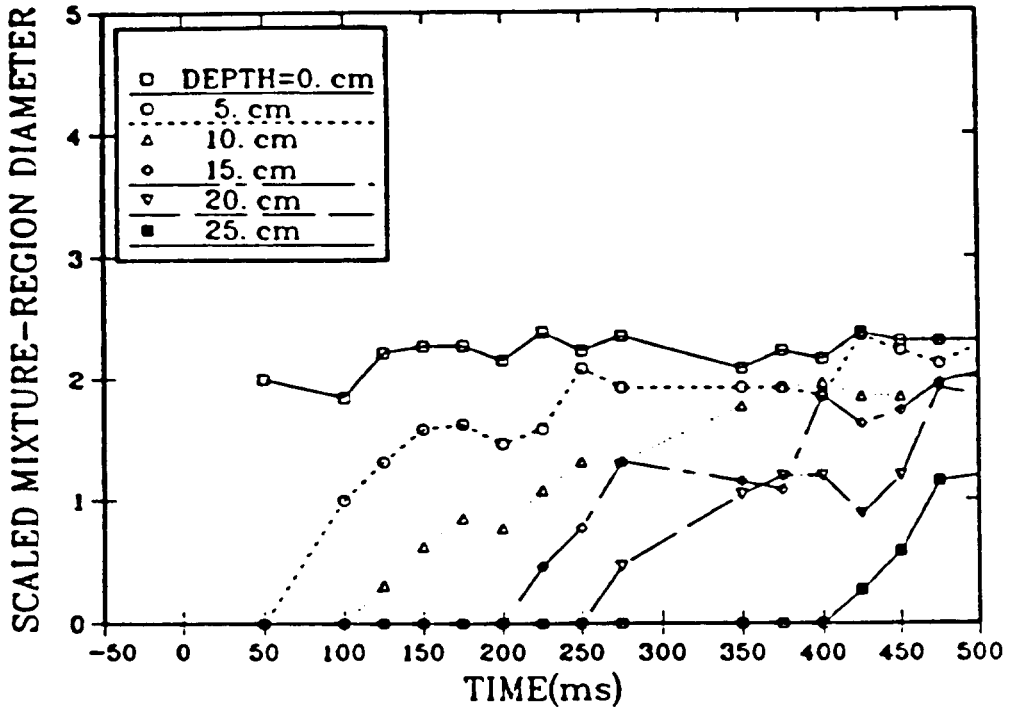

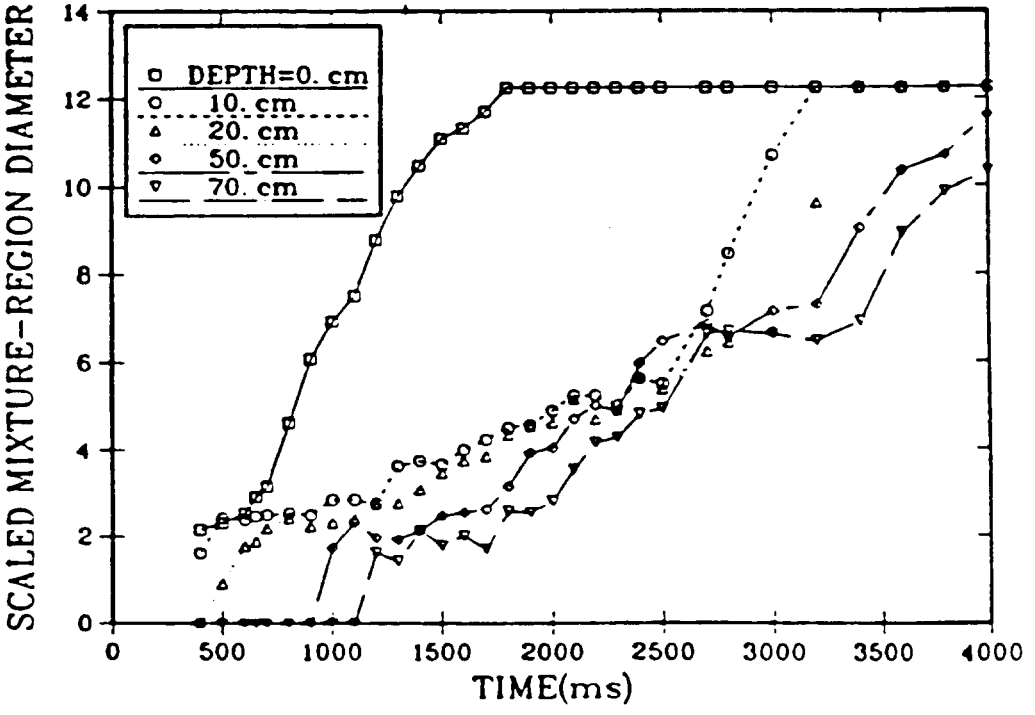

Figure 1.4-5. Scaled Diameter of the Mixture Region for the EJET-0 Test

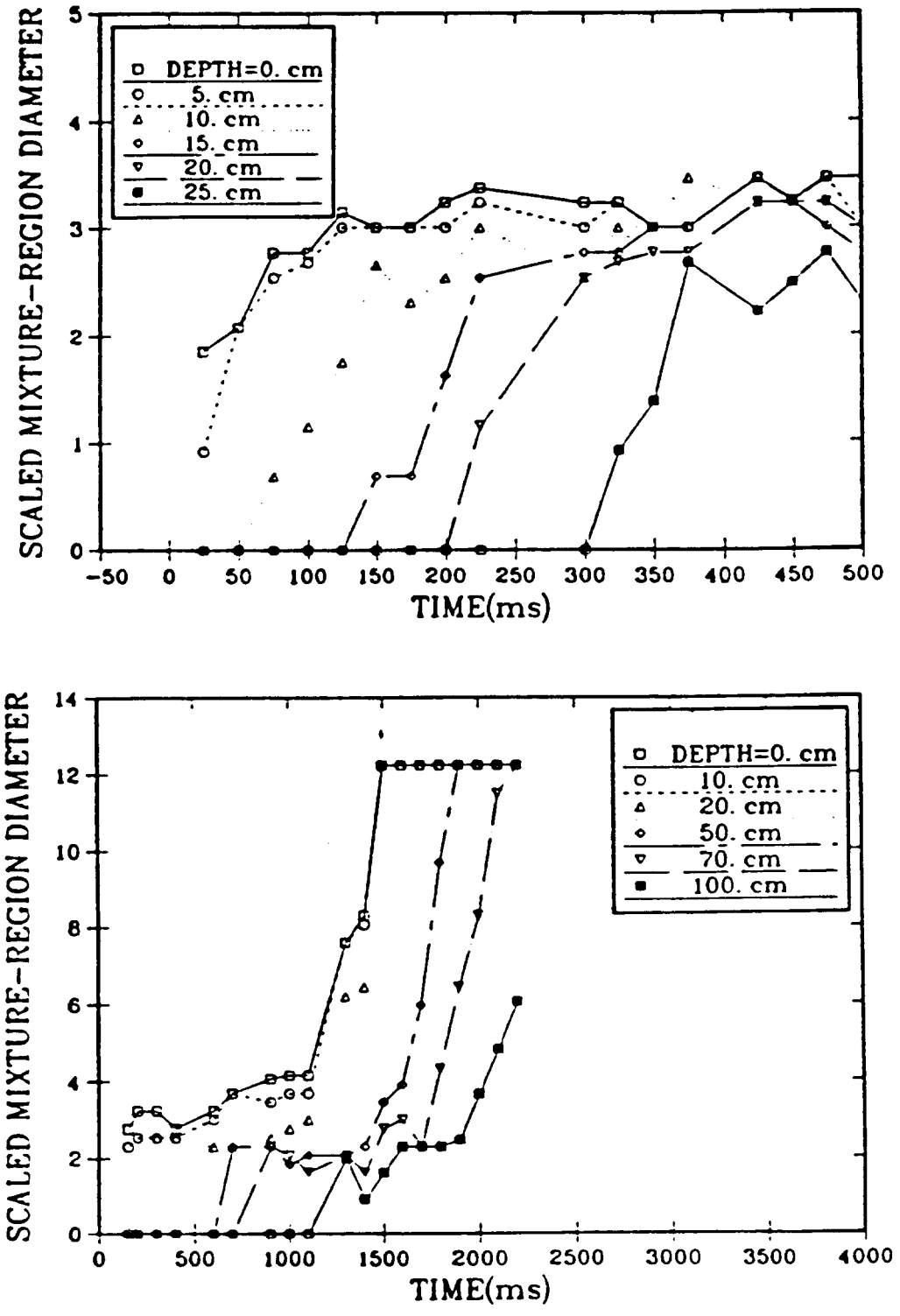

Figure 1.4-6. Scaled Diameter of the Mixture Region for the EJET-1 Test

From the high-speed films, we again observed significant fragmentation of the molten-jet as it entered the water. As shown in Figure 1.4-7, the same general jet breakup behavior occurred in this experiment as in the previous two; the mixing plateau occurs almost immediately. Subsequent to the mixing plateau, the mixture-region expansion occurs somewhat sooner than observed in the EJET-1 test. Furthermore, the duration of the mixing plateau appeared to decrease with increases in jet diameter. As in the previous experiments, the rate and magnitude of the vapor generation appear to play an important role in the fragmentation and growth of the mixture region of these boiling jets.

- EJET-3

There are important questions that must be addressed before we can understand the complex mixing of molten jets of core material with residual water inside a reactor core. We feel that one of the most important questions for reactor safety analyses is that of scaling. We conducted an experiment which modeled the largest jet diameters that could have occurred inside the TMI-2 reactor; i.e., the 16.3-cm holes in the core forging. This experiment was a repeat of EJET-1 and 2 except for the initial jet diameter. As shown in Figure 1.4-8, the early mixing phase was similar to the previous experiments in that a plateau occurs almost immediately. However, the delivery of a uniform jet having an initial diameter of 16 cm is difficult. We encountered problems with the melt-through plug (a 0.64-cm-thick plate in the bottom of the crucible) failing uniformly, resulting in a leading edge smaller than the actual desired jet diameter. Also, since only 50 kg of melt were used, the unperturbed length of the jet was less than 4 diameters.

Given the uncertainties associated with these data, a comparison of the results from these three saturated-water tests reveals that as the jet diameter increases, the scaled mixture-region diameter decreases at all times. The duration of the mixing plateau appears to be a function of the jet diameter. We observed an early mixing-region plateau whose scaled diameter ranged from 3 for the 3.8-cm-diameter jet to about 1 for both the 8- and 16-cm-diameter jets. The duration of these plateaus also appears to decrease with increasing jet-diameter.

In the EJET series, we have begun to address the possibility of whether a jet of molten core material can significantly mix with water in the lower plenum. Furthermore, we have begun to assess the differences between isothermal (described in the next section) and boiling liquid-liquid jet systems at this scale. Contrary to experiment work reported by Spencer et al.,[144,145] all boiling-jet experiments conducted in this series resulted in significant mixing and growth of the jet mixture region. We believe that some of these differences may be due to the relatively low-melt temperatures used in Spencer's experiments, e.g., the temperatures of the tin and Wood's metal were below 580 and 400 K, respectively. The temperature of the jet will govern the steam generation rate and magnitude. The lower the jet temperature, the lower the heat flux to the surrounding water and, therefore, the lower the steam generation rate. As we have observed in the EJET series, vapor generation plays an extremely important role in the fragmentation of jets of iron/alumina melt falling through water.

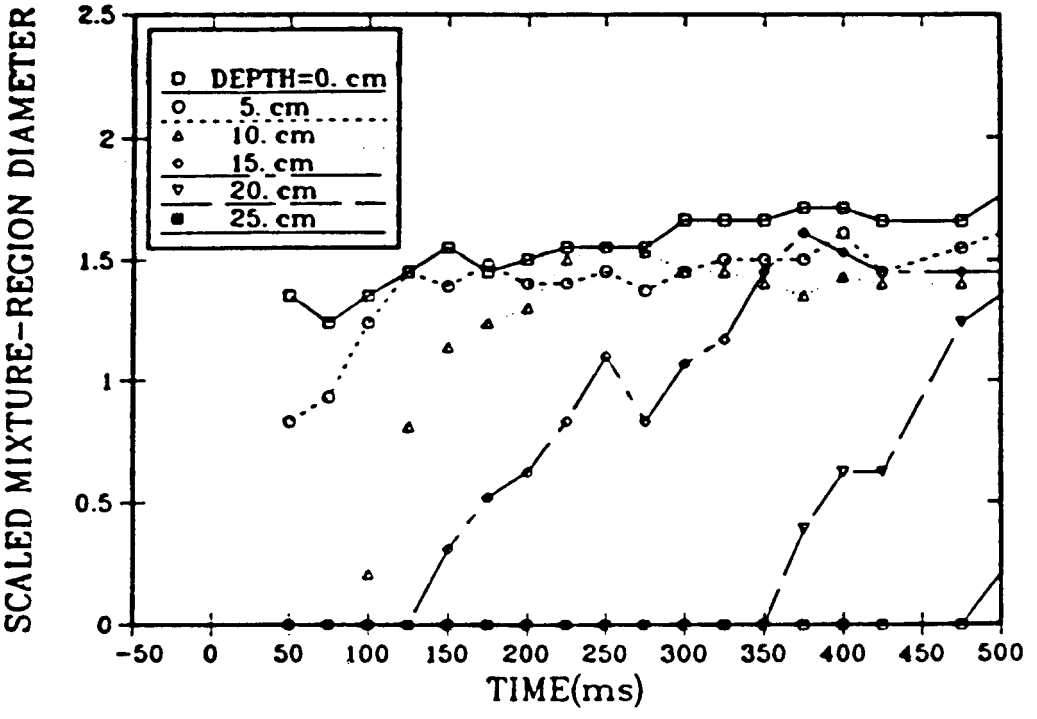

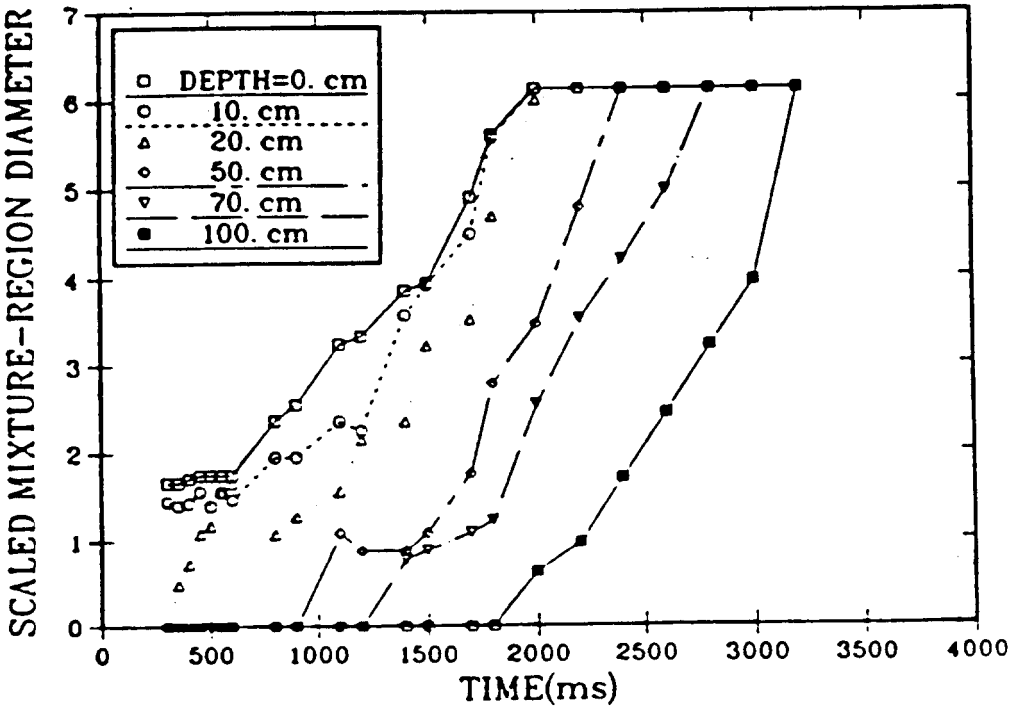

Figure 1.4-7. Scaled Diameter of the Mixture Region for the EJET-2 Test

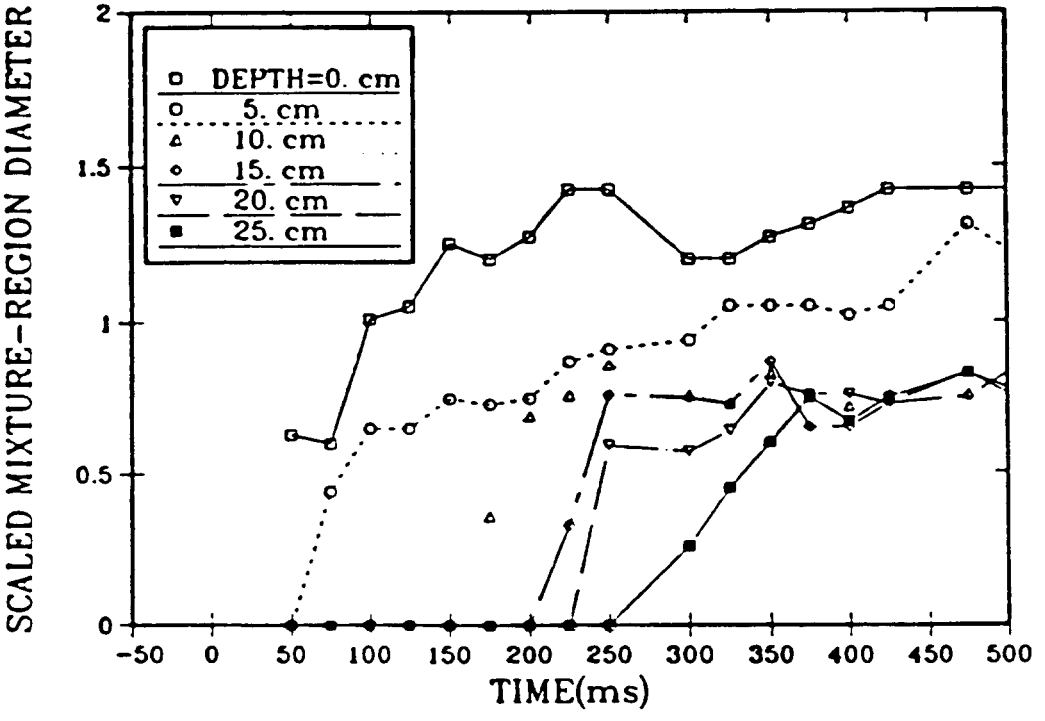

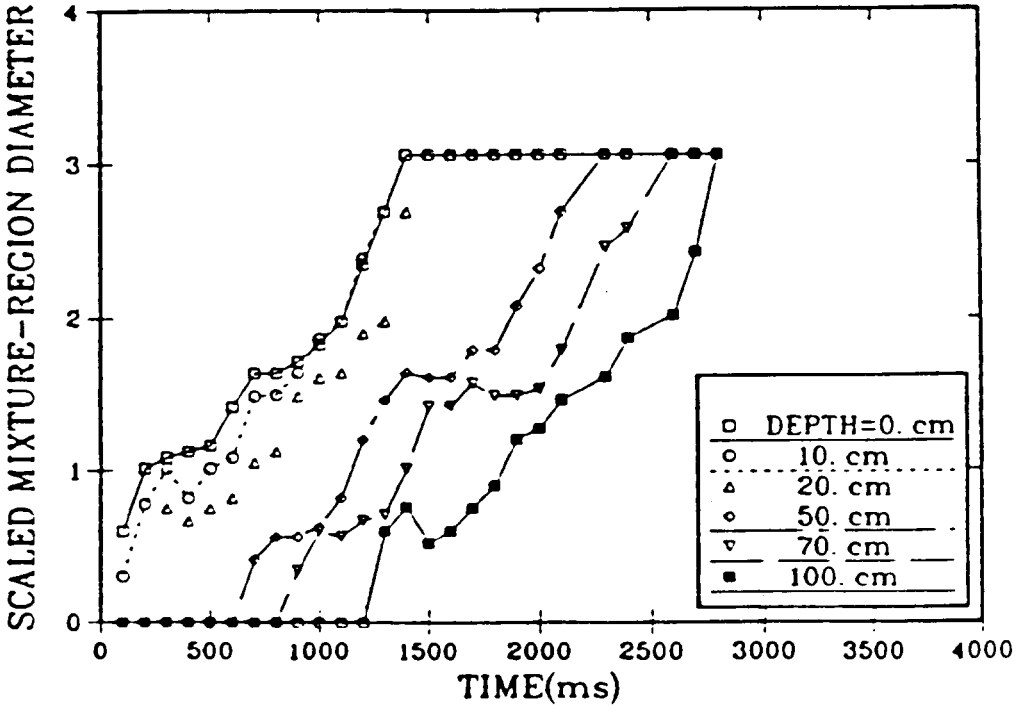

Figure 1.4-8. Scaled Diameter of the Mixture Region for the EJET-3 Test

We did not observe any spontaneously triggered steam explosions in this series of experiments, suggesting that these configurations may be relatively benign. However, if an external trigger were available, these coarse mixtures may be explosive; triggers will be considered in future experiments.

1.4.2.4 Isothermal Liquid Into Liquid Jet Studies (IJET)
(D. F. Beck and B. W. Marshall, Jr., 6427)

As we discussed previously in Section 1.4.2.1, no large-scale isothermal liquid-liquid jet experiments exist in the literature. We believe that experiments of this type are necessary to assist in our interpretation of the boiling liquid-liquid jet experiments described in Section 1.4.2.3. Furthermore, we believe that large-scale isothermal experiments would assist in our efforts to model the jet-mixing processes. Therefore, we have begun a series of experiments that investigates the hydrodynamic mixing of two separable isothermal fluids.

a. Apparatus and Procedure

Plans for conducting an isothermal liquid-into-liquid jet test series were established using TMI-2 core support and flow plates as a guide for scaling. Two initial orifice diameters were chosen, 4 and 8 cm, resulting in data that ranges from one-quarter to full reactor scale, depending upon which plate in the lower plenum is considered. Additionally, tests with initial orifice diameters of 0.1 and 1.0 cm were conducted in order to correlate the data in the literature with these experiments. Orifice length-to-diameter ratios (T/D) ranged from 0.2 to 20 in order to evaluate the sensitivity of jet behavior to this variable. Obviously, such a large span covers the various T/D ratios found inside current LWRs. Square-edged entrances were also used throughout. Large scale tests are planned using both single- and triple-orifice configurations allowing us to assess the effects of multiple coflowing jets upon transient mixing behavior.

The jet orifice exits were located at the surface of a quiescent tank of water and were oriented such that the jets were injected vertically downward into the pool. Jet flow was driven only by gravity. An initial fluid depth of 13 cm was selected, resulting in entrance velocities of about 1 to 2 m/s. An additional experiment (IJET-3) was performed to assess the importance of reservoir turbulence. The fluid relocated from a crucible down onto a 4-cm orifice plate from a height of ~30 cm. This experiment was intended to simulate any effects due to core relocation.

The water chamber used in these tests was 1.2 m deep, approximately the separation distance between the flow distribution plate and the vessel bottom in TMI-2. The tank had a cross section of 0.6 m square and the orifice plate was located at the geometric center of the cross section.

Ideally, the density and viscosity ratios of the two isothermal fluids should be equal to that of the corium-water system. However, due to safety and economic considerations, the fluid selected was Freon-TF (Trichlorotrifluoroethane or R-113). This resulted in a fully separable system having a density and viscosity ratio of 1.6 and 0.8, respectively. These ratios are

within a factor of five of that estimated for the corium-water system, and should allow for close approximation of resulting hydrodynamic characteristics. Furthermore, estimated Reynolds and Ohnesorge numbers place the expected jet behavior for the freon-water system well within the breakup regime expected for the corium-water system. Any differences caused by material properties will be addressed in some Wood's metal experiments currently being planned.

High speed cameras were used to gather most of the experimental data. Several 16 mm cameras and one 70 mm camera were located around the water tank. The tank was constructed of a transparent plexiglass on all sides to facilitate photography. Various scaling aids were used to correct for refraction through both the water and the lucite walls. Film speeds varied from 30 to 1000 frames per second, depending upon the camera, subject, and test conditions. Timing signals were also recorded on the films to allow correlation of events between cameras and other data recorded such as level-swell.

b. Test Descriptions and Observations

This section provides an overview of the tests conducted to date. Specific test parameters are given in Table 1.4-4. All tests conducted during this period used a single orifice. Initial jet diameters ranged from 0.1 to 8 cm. Orifice aspect ratios (T/D) varied between 0.2 and 2. IJET-1 was a water-into-water experiment and was used only for evaluation of the experimental apparatus and, therefore, will not be discussed further. However, the integral mixing behavior and spread rates of the jet appears to be similar to that observed for the Freon-water system.

Table 1.4-4

Descriptions of Completed Jet Tests

Test	Orifice Dia (cm)	Orifice T/D	Prefall (30 cm)
1[a]	3.81	0.67	N
2[b]	3.81	0.17	N
3[b]	3.81	0.67	Y
4[b]	3.94	1.94	N
5[b]	0.12	2.09	N
6[b]	0.95	2.00	N
7[b]	7.62	2.08	N

[a]Test No. 1 was a water-water system
[b]Test 2 to 7 were Freon-water systems with density ratios of 1.6 and viscosity ratios of 0.8

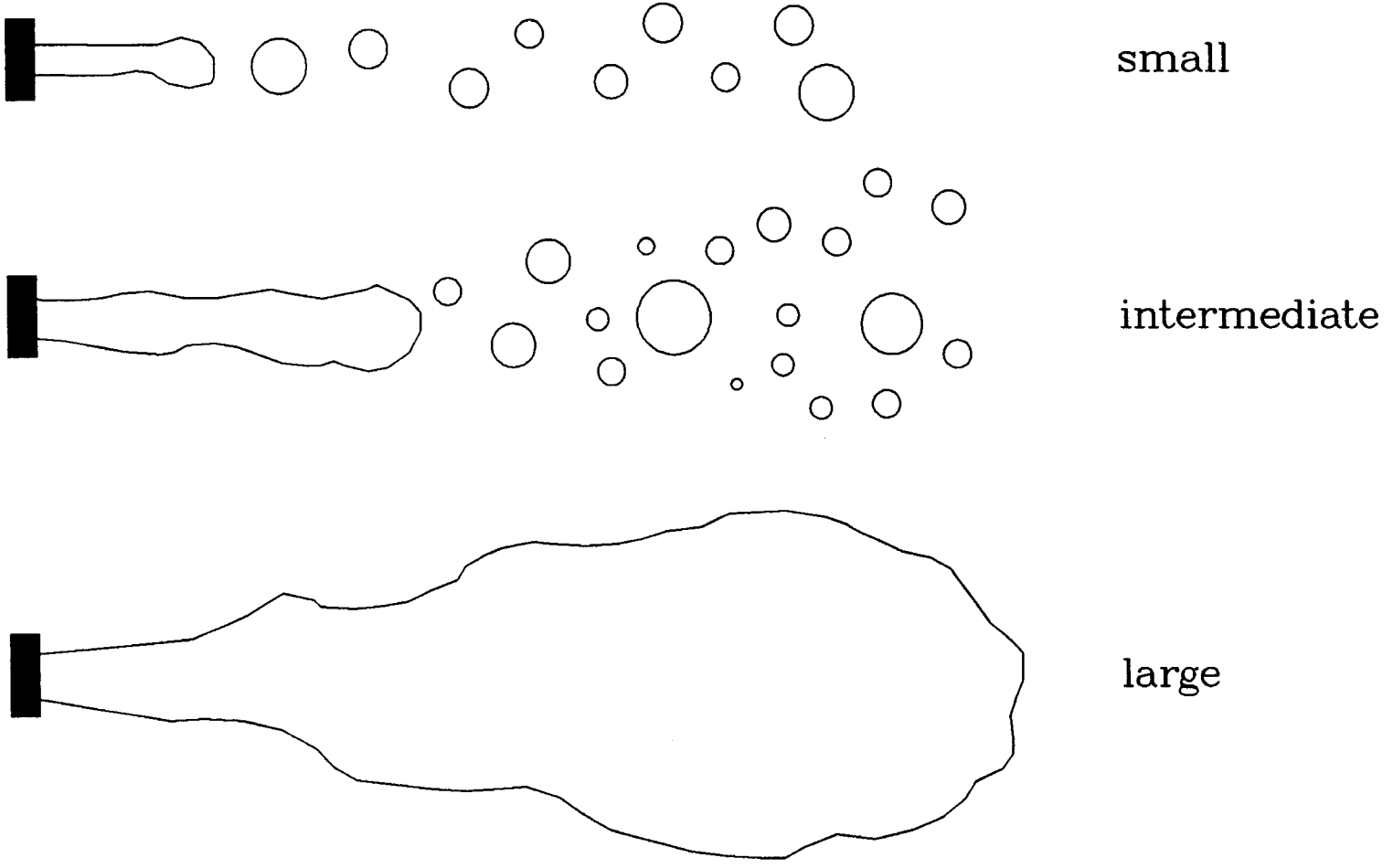

Figure 1.4-9. Sketch of Macroscopic Behavior Exhibited by Isothermal Liquid-Liquid Jets for Different Scales

The jet-mixing behavior varied widely between small- (0.1 cm) and large-scale (4 and 8 cm) experiments. A sketch of different jet outlines, shown in Figure 1.4-9, provides a qualitative view of the different behavior. Further discussion follows below under the appropriate section.

- Small- and Intermediate-Scale Tests

Small-scale jet penetration occurred in a fairly coherent fashion, followed by breakup from axisymmetric disturbances. The breakup point was well defined, although the actual length oscillated about some mean value. Jet behavior at the intermediate diameter (1 cm) appeared similar to those observed at small scale. However, expected differences include a noticeably longer breakup length and a more pronounced droplet spread after breakup occurred.

- Large-Scale Tests

Large-scale jet behavior was distinctly different from the 0.1- and 1-cm tests, and could best be described as a plume. As the Freon jet entered into the water, a vortex ring (similar to that reported by Turner[146] for "starting plumes") was formed. This has also been modeled using computer simulation of liquid-into-liquid jet penetration behavior.[147] In our experiments, however, the vortex does not appear to precede the main body of the jet during the initial penetration as described by Turner. Rather, the jet rapidly leaves this disturbance behind and is preceded only by a limiting "cap" or vortex sphere having a diameter that is within the range of the observed disturbances once the jet has formed. Any jet-material left behind in the entering vortex quickly dissipates into an array of scattered droplets, which appear to fall at their respective terminal velocity.

As expected, linear spread rates of the jet were observed. Not expected was the variation found in this parameter from test to test due to changes in the entrance velocity of the jet. Also, disturbances generated by Kelvin-Helmholtz instabilities appeared to be superimposed upon the jet edge.

Close inspection of the films seemed to indicate that the main body of the jet was composed of a myriad of small droplets that spread with depth, decreasing the volume fraction of Freon. Since the jet liquid is immiscible, this would be expected rather than the decreasing concentration ratio found with a gas-gas system.

The third test in the series was used to study the effects of reservoir turbulence created by the relocation of fluid from a crucible onto the orifice plate. For this experiment a "crucible" with a 13-cm-diameter opening was suspended 30 cm above the orifice plate. A 3.8-cm-diameter hole in a 2.5-cm-thick plexiglass sheet formed the orifice plate. The test was initiated by releasing fluid through the crucible from a point directly above the center of the orifice plate. Twelve liters of Freon were delivered. The jet-mixing behavior appeared very similar to that observed in the other large-scale tests. The only obvious effect caused by the fluid relocation was the generation of waves in the orifice-plate reservoir due

to its limited cross-sectional area (34-cm diameter). This, in turn, impressed small "steering" or "pointing" actions on the jet during and after the pour was complete; i.e., the jet center line tended to oscillate about the orifice center line with a period equal to that of the wave action in the reservoir. Variations in the effective gravitational head also occurred as a wave passed over the orifice causing "starvation" or "flooding" of the jet. However, the duration of these effects appeared to be only slightly longer than the relocation time since the waves were rapidly dampened.

c. Preliminary Data Reduction

The following data should be considered as preliminary in nature. Refraction corrections used were carried out in one dimension only. We expect to correct the data for two-dimensional refraction before the final results are presented. For all calculations, the density, viscosity, and surface tension of each fluid were assumed to be that at 25°C. Actual temperature data were recorded for each experiment and will be used to provide a more accurate description of the fluid-dynamic properties. Additionally, there was some uncertainty in determining the time at which jet penetration began (e.g., "time zero"), which will be addressed as a part of our final results. Finally, incorporation of these refinements will serve to decrease the size of the error terms discussed in this section.

- Exit Conditions

In order to study and classify jet behavior, it is first necessary to determine the entrance velocity of the jet, U_o. No direct velocity measurements were made in any of the IJET experiments. However, very detailed penetration measurements were possible using the high speed photographs. Figure 1.4-10 provides a typical example of the time-valued penetration data from experiment 3. From this graph the initial penetration appears to be very uniform. Therefore, the slope in this region should provide a reasonably accurate measure of the initial jet-entrance velocity. Since velocity-dependent data were only taken during the first few seconds of the pour, this value is assumed to be representative of average center line entrance velocity, throughout the duration of the pour, for the purposes of data correlation.

Table 1.4-5 provides a listing of exit velocities as determined by a least squares linear fit of the initial penetration data for tests completed to date. Additional parameters found in this table are discussed below.

Reynolds numbers were calculated in order to provide a measure of jet turbulence at the orifice exit. The Reynolds number is given by the ratio of the inertia and viscous forces as follows:

$$Re = \frac{\rho_o D_e U_o}{\mu_o} \quad ,$$

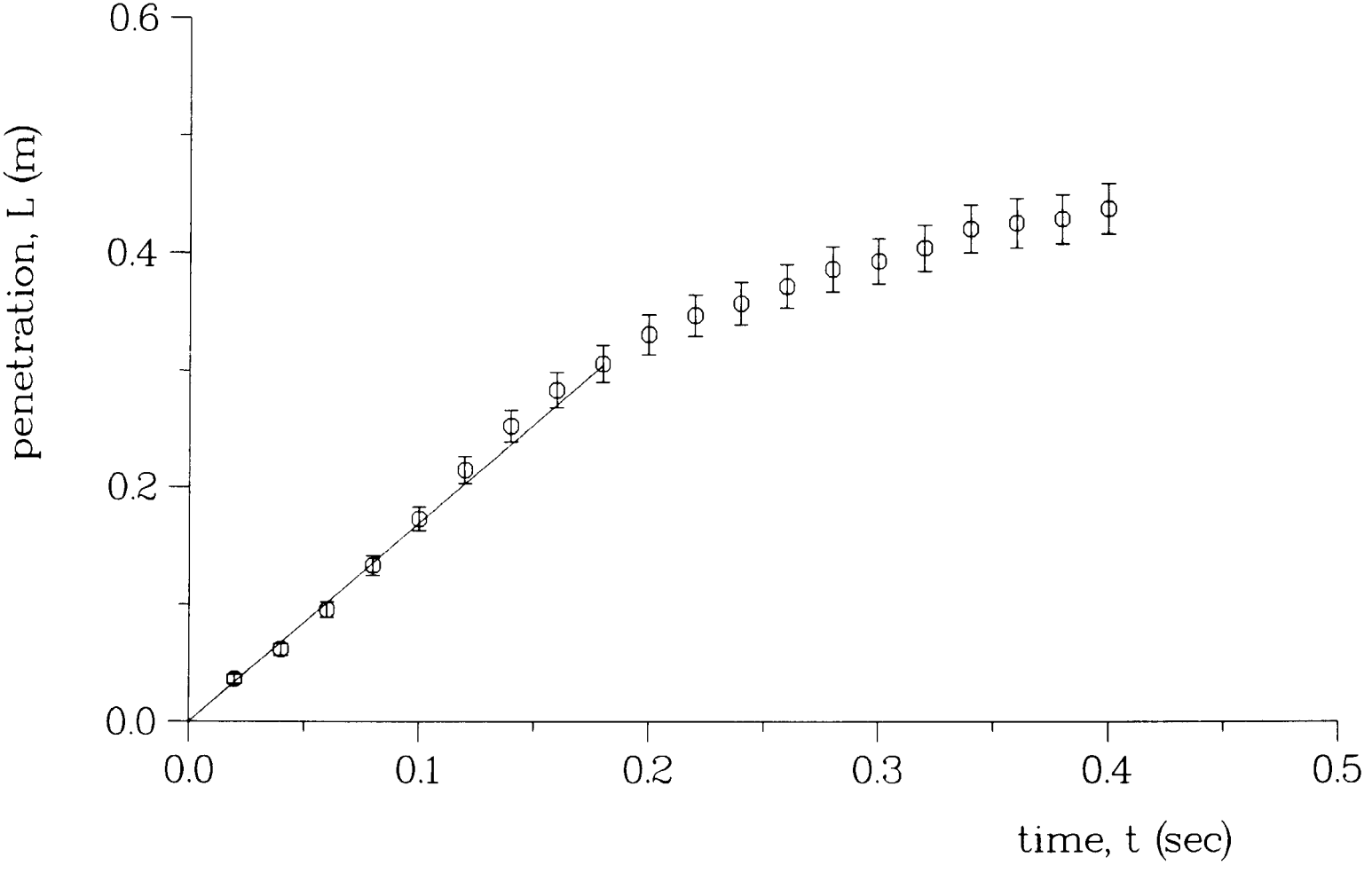

Figure 1.4-10. Initial Penetration Data for IJET3

where

ρ_o = the jet density at the orifice exit (kg/m^3),

D_e = the orifice diameter (m),

U_o = the average jet exit velocity (m/s),

μ_o = the jet viscosity at the orifice exit (Poise).

As shown in Table 1.4-5, the orifice-exit Reynolds numbers range from 1 x 10^3 to 2 x 10^5. Therefore, based upon these calculations and the velocity and buoyancy vector directions, each of these experiments is classified as a vertical turbulent buoyant jet.

Table 1.4-5

Summary of Critical Parameters

Test	U_o (m/s)	X_t (m)	1(m)	$\dot{Y}_{.5}$	Re	F	We	Z
2	1.0	0.2	-	0.12	$8(10^4)$	7	$3(10^3)$	$7(10^{-4})$
3	1.7	0.3	-	0.20	$1(10^5)$	20	$9(10^3)$	$7(10^{-4})$
4	0.9	0.2	-	0.08	$8(10^4)$	6	$3(10^3)$	$7(10^{-4})$
5	0.5	0.01	0.025	-	$1(10^3)$	68	20	$4(10^{-3})$
6	0.8	0.1	0.140	-	$2(10^4)$	16	500	$1(10^{-3})$
7	1.2	0.4	-	-	$2(10^5)$	5	$1(10^4)$	$5(10^{-4})$

Froude numbers were determined in order to better characterize the jet flow regime. The densimetric Froude number used here is the ratio of the inertial force to the buoyancy force and is given by

$$F = \frac{U_o^2 \rho_o}{\left(\rho_a - \rho_o\right) g D_e} \quad ,$$

where

U_o = the average jet exit velocity (m/s),

ρ_o = the jet density at the orifice exit (kg/m^3),

ρ_a = the ambient or continuous fluid density (kg/m^3),

g = the local acceleration of gravity (9.8 m/s^2),

D_e = the orifice diameter (m).

Values obtained range from 5 to 68 indicating the these jet experiments should resemble a pure plume (i.e., F = 0), based upon correlations developed for a gas-gas system.

The Weber numbers were also calculated in order to better understand drop formation and behavior. The Weber number is the ratio of the inertial-to-surface tension forces and is given by

$$We = \frac{U_o^2}{\left[\sigma_o/\rho_o D_e\right]} \quad ,$$

where

U_o = the average jet exit velocity (m/s),

σ_o = the jet surface tension (N/m),

ρ_o = the jet density at the orifice exit (kg/m^3),

D_e = the orifice diameter, (m).

As shown in Table 1.4-5, the Weber numbers for the large-scale jets were on the order of 10^3 to 10^4. Since these values are several orders of magnitude higher than the critical Weber number,[148] rapid fragmentation would be expected. This lends some support to the experimental observation that the main jet body appears as an array of droplets.

The final nondimensional relationship considered under exit conditions was the Ohnesorge number. It is given by

$$Z = \frac{\mu_o}{\left(\rho_o D_e \sigma_o\right)^{0.5}} \quad ,$$

where

μ_o = the jet viscosity at the orifice exit (Poise),

ρ_o = the jet density at the orifice exit (kg/m^3),

D_e = the orifice diameter (m),

σ_o = the jet surface tension, (N/m).

Calculated values ranged from $7x10^{-4}$ to $1x10^{-3}$. When considered along with the Reynolds number it is found that the large-scale jet tests fall into the same general breakup regime expected for the corium-water system.[125]

- Jet Breakup

Well defined breakup points were exhibited by the small- and intermediate-scale jets. Mean values are provided in Table 1.4-5 as entry "l(m)." The actual point of breakup oscillated in time resulting in a 20 percent variation in the measurement. Reynolds[136] and Sterling and Sleicher[149] have also observed similar oscillations of the breakup length. Also, the amplitude of these oscillations appears to be a function of jet exit velocity.[149] The fact that many authors have not reported this effect may reflect on the various methods of observation and data reduction used.

Kitamura and Takahashi[129] presented data for a carbon tetrachloride-water system using a jet diameter of 0.118 cm. This fluid pair has a viscosity ratio of 0.995, a density difference of 580 kg/m^3, and a surface tension of 0.0431 N/m. With our Freon-water system, the viscosity ratio is ~0.764, the density difference is ~568 kg/m^3, and the surface tension is ~0.019 N/m. Although there are some differences in fluid-dynamic properties, a comparison between the two results should be instructive. Figure 1.4-11 shows the breakup lengths measured for the 0.1- and 1-cm-diameter Freon jets plotted against Kitamura and Takahashi's data. Error bars shown represent the range of oscillations observed. Note that the 0.1-cm-diameter Freon jet compares favorably with that of the carbon tetrachloride-water system while the breakup length of the 1-cm-diameter jet is significantly longer. The increased breakup length for the 1-cm jet has not been fully explained, although the order-of-magnitude increase in jet diameter will surely affect the breakup length of the jet. Work and analysis in this area are continuing.

Although the large-scale jets did not exhibit a distinct breakup length, the behavior appears similar to that of a liquid-gas system in the jet-atomization regime. Breakup lengths given for this region are typically small, especially when compared to the jet size. Even Kitamura and Takahashi reported that determination of breakup length was difficult in this flow regime due to clouds of dispersed droplets. If, however, we define the breakup length as a function of jet edge disturbance amplitude in nondimensional form, it may be possible to correlate the jet-breakup behavior at various scales.

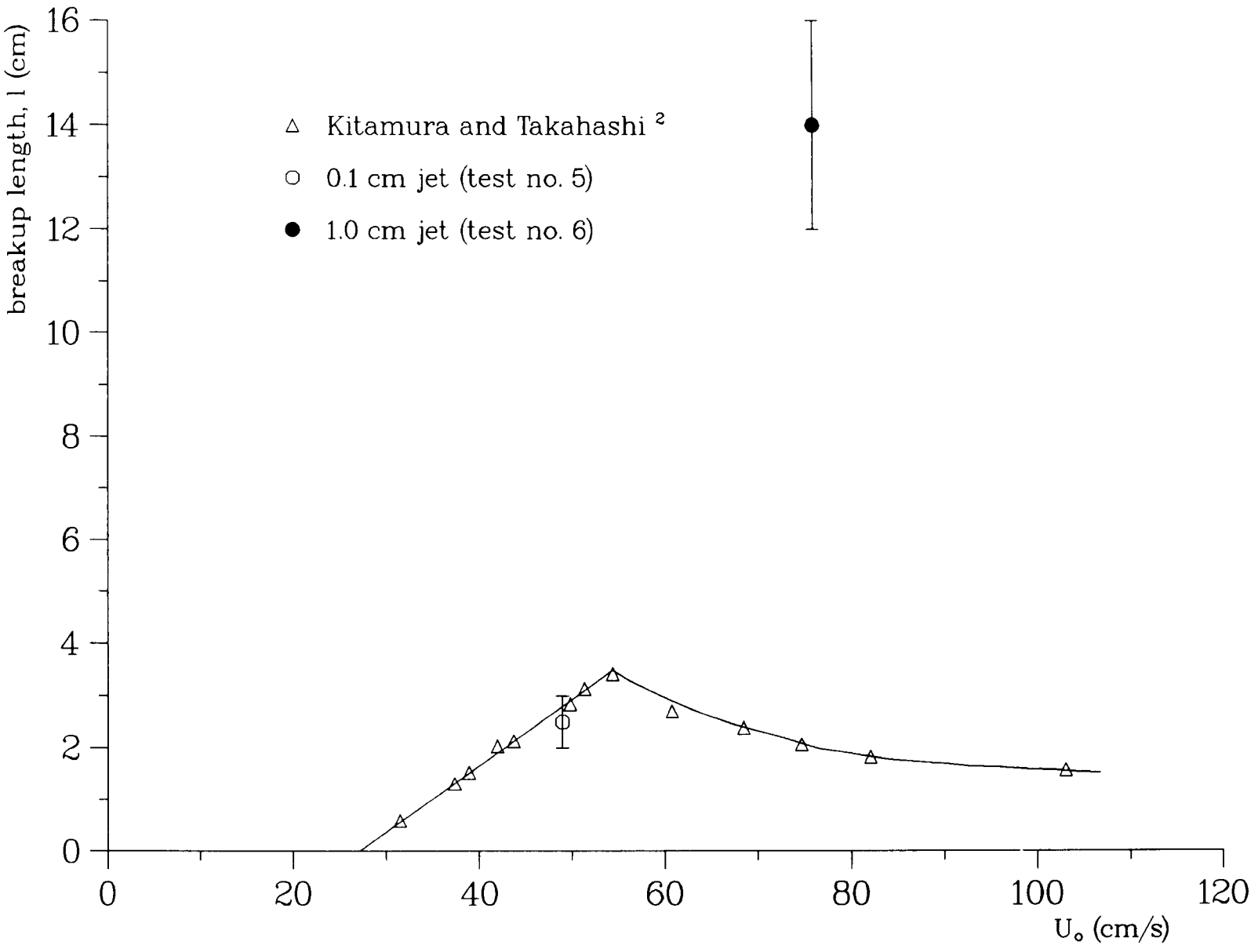

Figure 1.4-11. Comparison of Small Jet Breakup Lengths

• Center Line Velocity

Consider the sketch of a classical turbulent jet shown in Figure 1.4-12. Typically the behavior for a forced plume is broken down into three groups: the initial nonbuoyant region, the transition or intermediate region, and the main or buoyant region. The initial region can be described as a linearly growing boundary layer that surrounds a constant velocity, undisturbed core. In the intermediate region, velocity profiles typically change from momentum-dominated flow to buoyancy-dominated flow. The main region of the jet is characterized by buoyancy-dominated flow and is generally described as having self-similar velocity, concentration, and temperature profiles as well as linear spread rates of the mixture region.

Based on dimensional reasoning, Chen and Rodi[124] have recommended use of the following nondimensional depth for reporting experimental results:

$$x_1 = F^{-0.5} \left[\frac{\rho_o}{\rho_a} \right]^{-0.25} \frac{L}{D_e} \quad ,$$

where

x_1 = the nondimensional downstream distance,

F = the densimetric Froude number of the jet under exit conditions,

ρ_o = the jet-fluid density at the orifice exit (kg/m^3),

ρ_a = the continuous or ambient fluid density (kg/m^3),

L = the penetration length from the orifice exit (m),

D_e = the orifice diameter (m).

Correlation of vertical turbulent gas-gas jet data further enabled Chen and Rodi to bound the transition region between values of 0.5 and 5 for x_1. These limits have been plotted along with the penetration data from our experiments in Figure 1.4-13. Typical error bars are shown.

Chen and Rodi have also derived velocity relationships for axisymmetric buoyant jets. Self-similar analysis shows that the center line velocity in the initial or nonbuoyant regime should behave as

$$\frac{U_{CL}}{U_o} = A_{u1} \left[\frac{\rho_o}{\rho_a} \right]^{0.5} \left[\frac{L}{D_e} \right]^{-1} \quad ,$$

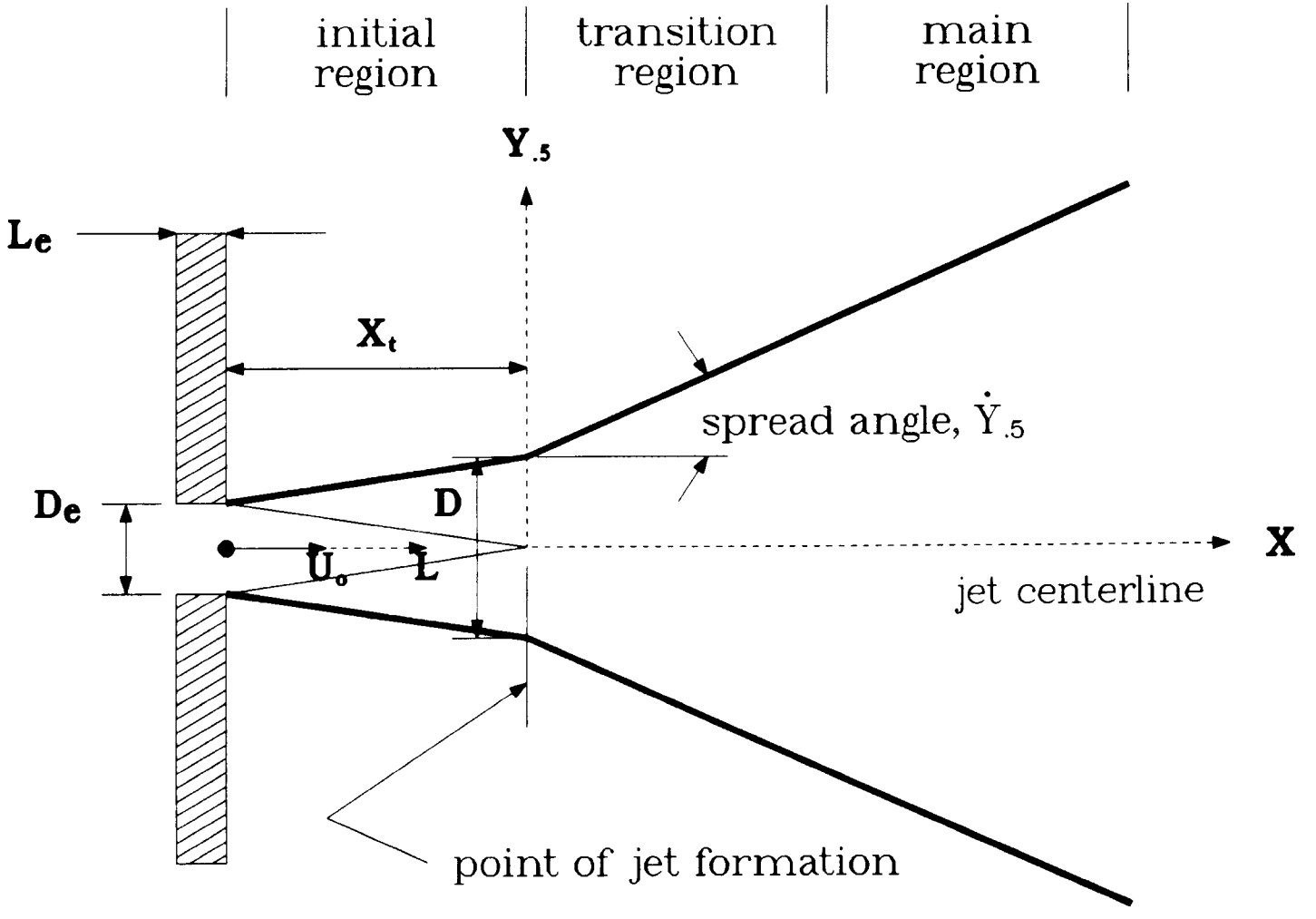

Figure 1.4-12. Idealized Jet With Nomenclature Shown

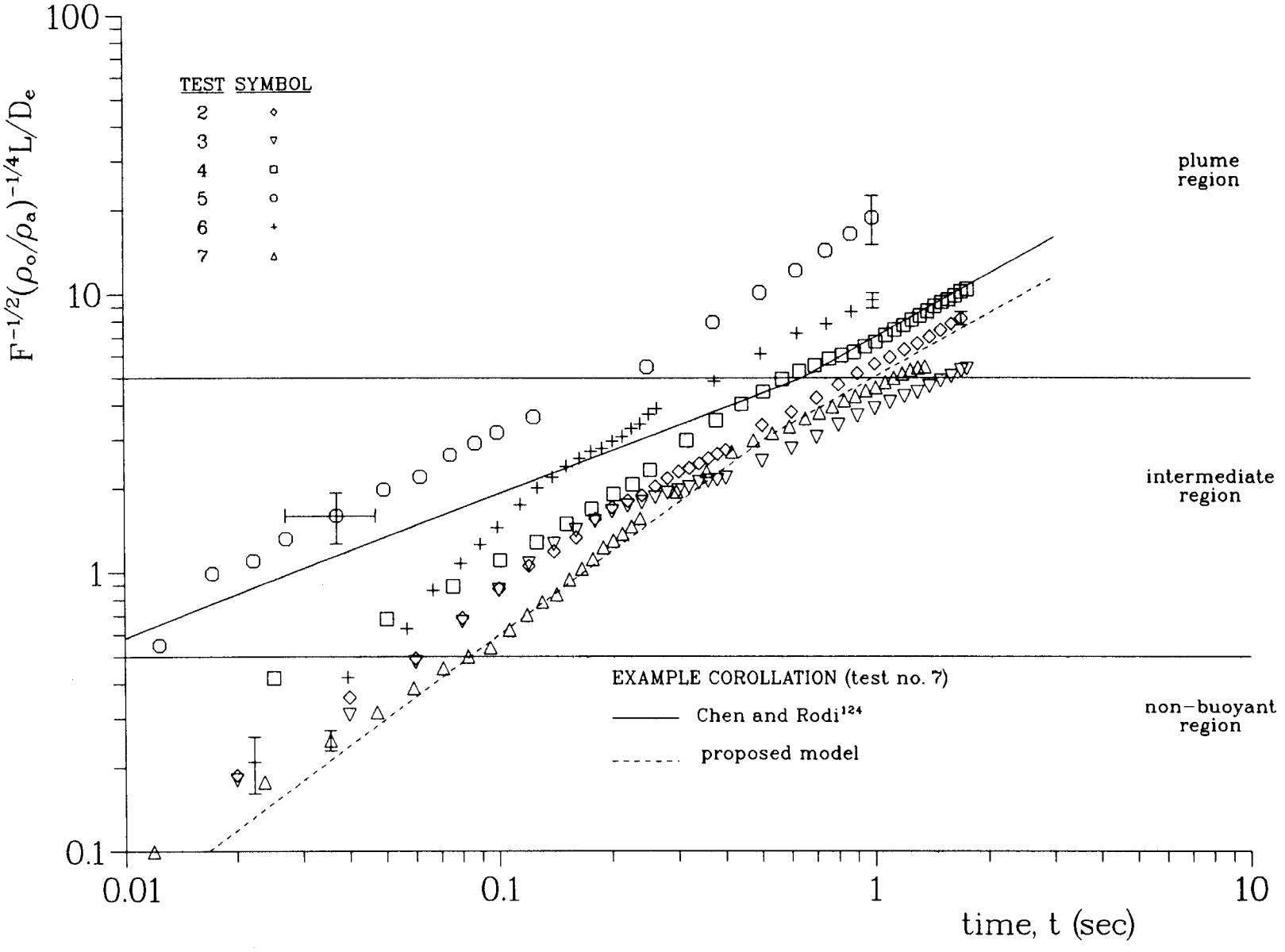

Figure 1.4-13. Plot of Nondimensional Penetration Data

where

U_{CL} = the center line velocity (m/s),

U_o = the average jet exit velocity (m/s),

A_{u1} = an experimentally determined constant,

ρ_o = the jet-fluid density at the orifice exit (kg/m^3),

ρ_a = the continuous or ambient fluid density (kg/m^3),

L = the penetration length from the orifice exit (m),

D_e = the orifice diameter (m).

In the main or buoyant regime, the center line velocity should behave as

$$\frac{U_{CL}}{U_o} = B_{u1} F^{-1/3} \left[\frac{\rho_o}{\rho_a} \right]^{1/3} \left[\frac{L}{D_e} \right]^{-1/3} ,$$

where

B_{u1} = an experimentally determined constant,

F = the densimetric Froude number of the jet under the exit conditions.

Based on vertical buoyant gas-gas jet data, they have also recommended the following values for the empirical constants:

$$A_{u1} = 6.2 ,$$
$$B_{u1} = 3.5 .$$

Although self-similar flow does not exist in the intermediate region, Chen and Rodi developed a relationship for velocity by fitting a curve between the equations found for the buoyant and nonbuoyant region. The resulting expression was given as

$$\frac{U_{CL}}{U_o} = 7.26 F^{-1/10} \left[\frac{\rho_o}{\rho_a} \right]^{9/20} \left[\frac{L}{D_e} \right]^{-4/5} .$$

Integration of these three equations yields a relationship for penetration as a function of time, the current form of our data. Using the initial

conditions of our experiments, the penetration rate can be estimated and compared to the data, assuming the penetration rate is representative of the center line velocity. As shown in Figure 1.4-13, we estimated the penetration rate for the experiment having an initial orifice diameter of 7.6 cm, yielding relatively poor comparisons to the experimental data.

An improved model for the center line velocity can be arrived at from the following considerations. Refer again to Figure 1.4-12 and note that if velocity of the core is constant over the nonbuoyant regime, the center line velocity can be expressed as

$$\frac{U_{CL}}{U_o} = 1 \quad .$$

Evaluation of the experimentally measured penetration data indicates that the actual transition zone in these experiments is small (refer to the earlier discussion of Figure 1.4-10). This allows us to define a transition point or "point of jet formation," rather than the more cumbersome use of an intermediate region. Although this is in conflict with Chen and Rodi, it is supported by the work of other authors such as Abramovich.[150]

Jet behavior in the main region is governed by the buoyancy of the jet fluid relative to the ambient fluid. Support for this conclusion arises from two observations: First, recall that the Froude numbers given in Table 1.4-5 are much less than 10^2, which typifies pure plume behavior. Second, note from Figure 1.4-13 that the penetration rates tend to parallel Chen and Rodi's solution for the buoyant region. Based on these observations, a new empirical constant (B_{u1}) can be recalculated using the large-scale Freon-water data. This value is

$$B_{u1} = 2.27 \quad .$$

Using this new value, new penetration estimates for IJET-7 can be determined. As shown in Figure 1.4-13, this model yields much better results. The "goodness" of the proposed model is better displayed in Figure 1.4-14 where penetration data is plotted against model predictions for the large-scale tests run to date. As can be seen, accuracy is better than 10 percent for the most part. Symbols used are the same as defined for Figure 1.4-13. A typical error bar is shown.

One final point should be made. Since the jet is immiscible, droplets of a finite size are being formed. If the water tank were deeper and larger in cross section, a third type of velocity behavior probably would have been observed; this would have occurred when the drop-to-drop separation increased to the point that independent behavior would arise. Furthermore, a drop with a characteristic diameter would be expected to form based upon the critical Weber number and fall at its terminal velocity.

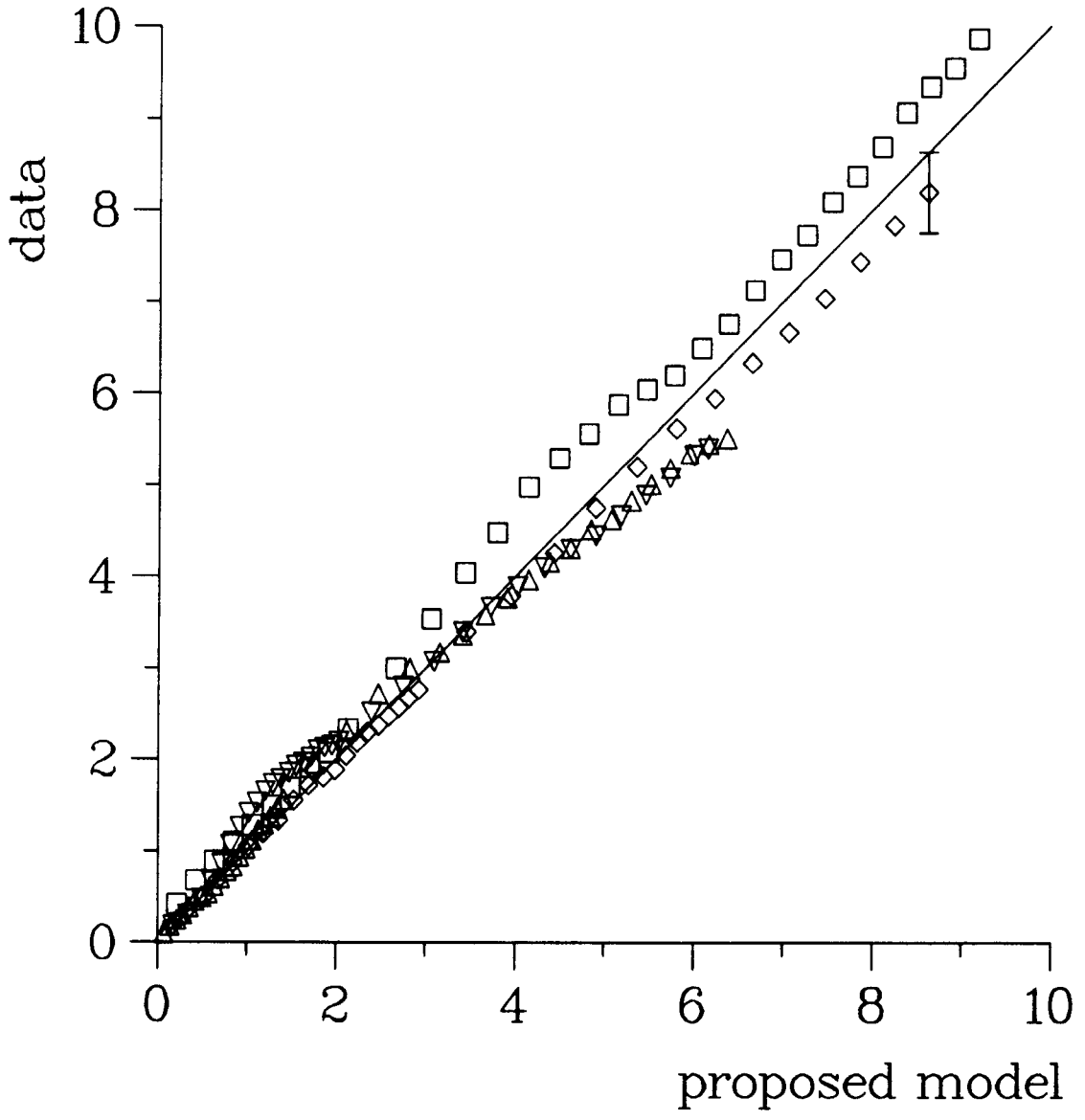

Figure 1.4-14. Comparison of Nondimensional Penetration Between the Proposed Model and Actual Data

• Jet Spread

The 4- and 8-cm-diameter jets have shown that linear spread occurs in the main or buoyant regime of the jet, as might be expected for self-similar flows. To quantify the actual spread, jet width measurements were taken at various depths and times. As shown in Table 1.4-5 and Figure 1.4-15, a least-squares fit of this data yielded the effective spread rates. The error bars shown in Figure 1.4-15 represent the range of the jet-edge disturbances and oscillations.

From this data, we find that the jet spread increases with increasing exit velocity. This is in direct contrast to the "generic" results presented by various authors,[124,146,150] where spread rates are typically given as a constant for each flow condition (i.e., planar, round, plume, nonbuoyant, etc.). However, we should note that most of these observations were primarily based upon gas-gas systems and may not hold true for liquid-liquid systems, even though the density and viscosity ratios are equal. As an example of the different spread rates reported, Chen and Rodi[124] recommended using a value of 0.112 for the velocity profile half-thickness in round plumes, Turner[146] recommended using a value of 0.12 for a plume, and Abramovich[150] reports a value of 0.22 for the spread rate of an axisymmetric turbulent jet, injected under both quiescent and counterflow conditions.

Abramovich also reports that variable spread angles have been observed for co-flowing jets. In his book he presented data from several researchers, including Yakovlevskiy, Zhestkov et al., and Abramovich and Vafin. This compiled data is reproduced in Figure 1.5-16. The term b/b_3 represents the ratio of the observed jet's half-thickness to the reference case (external stream velocity of zero). The independent variable, m, is the ratio of the external velocity of the stream to the velocity of the jet. The relationship between these variables was given as

$$\frac{b}{b_3} = \frac{1 - m}{1 + m} \quad .$$

Comparison was made with the IJET series by assuming that IJET-3 satisfied this relationship. This allowed for calculation of a reference velocity that was in turn used in mapping the spread values of IJET-2 and IJET-4, as shown.

Limited work has also been carried out in the study of liquid jets that are operating in the atomization regime. Reitz and Bracco[151] have found that spread angles vary, for a liquid-gas system, with changes in entrance jet velocity, density ratio, surface tension and viscosity. A further review of their work is necessary before any correlation can be made.

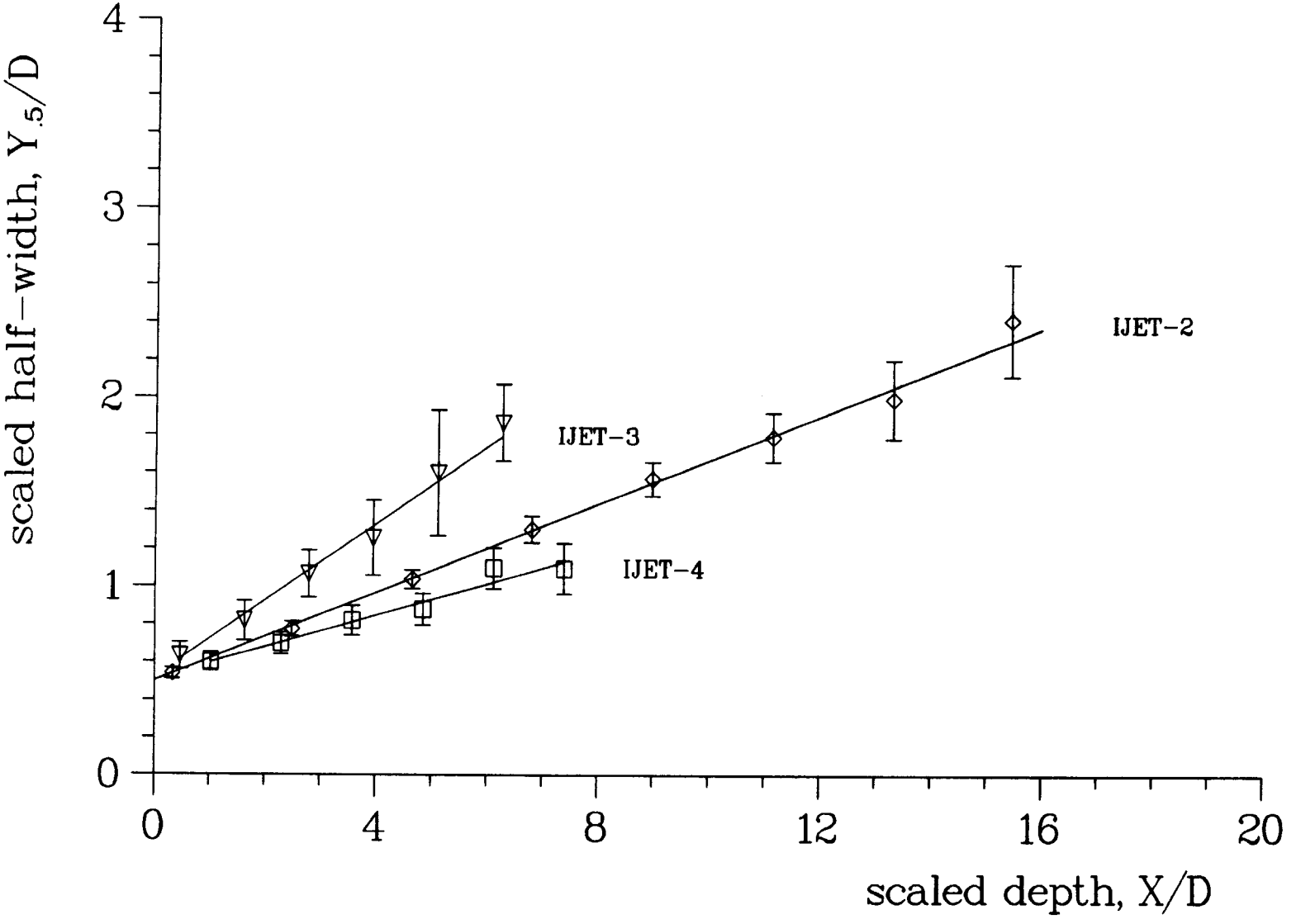

Figure 1.4-15. Plot of Nondimensional Spread Data

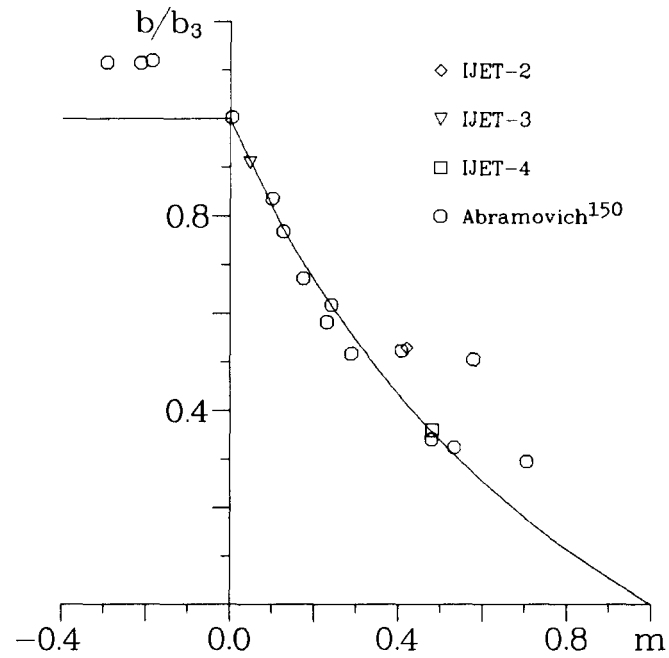

Figure 1.4-16. Comparison of Spread to Colinear Flow Data

d. Conclusions From the IJET Series

Although only a portion of the isothermal jet tests have been completed, some preliminary conclusions can be drawn. These observations are valid only for systems that are dynamically similar to the isothermal Freon-water system used in these experiments.

1. Small scale liquid-liquid jet studies do not provide meaningful data for understanding large-scale jet behavior. At this point, only the flow regime can be depicted (i.e., laminar breakup, turbulent breakup, or atomization).

2. Incompressible gas-gas jet data provide an indication of macroscopic flow characteristics for large scale liquid-liquid jets, given similar density ratios.

3. The center line velocity of the jet is constant in the initial or nonbuoyant regime.

4. Transitional flow regions are small for incompressible jets and can be neglected for these large-scale experiments.

5. The center line velocity profiles of the Freon jet follow the behavior observed for self-similar buoyant gas-gas flows in the bouyancy-dominated regime, provided a new empirical constant is calculated.

6. Large-scale liquid-liquid jets exhibit linear spread rates in the main or bouyancy-dominated flow regime, as would be expected for a self-similar flow.

7. Gas-gas plume spread rates only approximate the variable spread rates observed in the liquid-liquid system. Boundary layer interaction in an immiscible liquid-liquid system is not properly characterized by gas mixing lengths and requires further study.

8. Large-scale gravity pours of Freon into water provide isothermal jet breakup data at Reynolds and Ohnesorge numbers estimated appropriate for prototypical reactor conditions.

9. Penetration and spread rate behavior indicates that self-similar profiles might be used to describe macroscopic jet structure, although more work is needed to verify this observation.

1.4.2.5 Preliminary Conclusions From the Jet-Mixing Experiments (B. W. Marshall, Jr. and D. F. Beck, 6427)

Contrary to the previous picture of a large coherent melt-pour, the relocation of molten core material into the lower plenum is now believed to involve multiple streams or jets. The described jet-mixing experiments provide insight into the complicated mixing phenomena of boiling and isothermal jets. From a reactor safety point of view, there are at least two potentially benign jet-mixing configurations: (1) The jet will not mix significantly with water (it resembles a jet that can be described by liquid-air data); thus the possibility of a large coherent steam explosion is reduced.[128] (2) The jet will fragment so extensively and rapidly that either the fuel or the coolant will be swept away (fluidized) from the mixture region preventing a coherent, large steam explosion.[142,152,153]

We have learned from our experimental results that if the temperature of the jet material is well above the saturation temperature of the water, the jet breakup is affected by the generation of steam. Also, the water subcooling appears to affect the timing and rate of jet fragmentation: Saturated water results in extensive steaming rates and fragmentation as the melt enters the water whereas highly subcooled water allows the melt to penetrate further into the water before significant steaming occurs. Comparison of the isothermal- and boiling-jet data shows that very different breakup mechanisms can occur in boiling-jet systems that cannot be ascribed to hydrodynamics alone. Therefore, when reactor safety analyses are performed, neither liquid-gas or isothermal liquid-liquid jet data should be directly extrapolated to predict the fragmentation behavior of molten jets falling through water. We are currently working on two tasks: To develop a more extensive understanding of the complex mixing of molten fuel jets falling into a water pool and to model the action of the jets.

1.4.3 Integrated Fuel-Coolant Interaction Code Development
(M. F. Young, 6425)

A problem of major concern in the field of reactor safety is the possibility of energetic fuel-coolant interactions occurring during postulated core meltdown accidents. Considerations of this problem are usually couched in the form of a question asking whether or not a possible FCI might be strong enough to breach the reactor containment. Unfortunately, not enough is known about the basic physical processes involved in an FCI to give a definitive answer to this question at the present time.

There have been two major lines of approach taken in attempting to deal with the FCI safety question. The first involves the observation that there are several conditions that make an FCI more likely to occur. So, one approach to addressing the FCI safety question has been to try to determine whether these conditions are likely to be reached during a core meltdown accident in a reactor. If the necessary conditions cannot be achieved, then there is no FCI problem in reactor safety. Another approach to the safety question has been to attempt to predict the efficiency that can be achieved during an FCI, that is, how much of the thermal energy in the reactor fuel can actually be converted into potentially damaging work if an FCI occurs?

Research along these two lines of approach has been both experimental and theoretical in nature, but has not totally succeeded in answering the basic question. The experiments, for instance, have provided much useful information, but must, because of economic necessity, be much smaller than reactor scale, and FCIs are known to be scale-dependent processes. On the theoretical side, lack of data makes choosing the correct model from among competing models very difficult; without an accurate model of the physical phenomena occurring during an FCI, the experimental results cannot be successfully extended to reactor scale.

A major roadblock to both extending experimental results to reactor scale and to studying the experiments themselves has been the lack of an integrated model capable of realistically simulating all aspects of an FCI. In our view, the desired approach is to develop a tool capable of providing a best estimate of the postulated FCI, based on known physical laws and verifiable models. Because of the current lack of understanding about FCIs, the safest approach (from the viewpoint of confidence in the results) is to carry out the entire calculation using a model based as much as possible on established descriptions of physical phenomena (for instance, the Navier-Stokes equations and accepted heat transfer correlations). The integrated model should ideally also provide the initial conditions for a possible FCI in a reactor meltdown situation.

Because of these needs, a project to develop an integrated tool to be used in FCI calculations was started. The proposed code was dubbed the Integrated Fuel-Coolant Interaction (IFCI) code, and was envisioned as being able to calculate the FCI process from start to finish, including the initial conditions.

This section describes the current state of development of the IFCI code, the key models in the code, notably the dynamic fragmentation model and the surface area transport model, and the use of the code to simulate a representative FCI experiment in the Fully Instrumented Test Series, or FITS.[154] This experiment series collectively represents the largest body of data on medium-scale FCIs (medium-scale is the closest to full-reactor scale presently available).

1.4.3.1 The FCI Process

The FCI process can be roughly divided into four phases: the initial coarse-mixing phase, the trigger phase, the reaction propagation phase, and the hydrodynamic expansion phase. These four phases are useful conceptually, although in reality they all may be occurring simultaneously in different spatial locations in the FCI region.

The coarse-mixing phase is characterized by entry of molten material (fuel) into a coolant (water), with accompanying vapor generation, intermixing of the fuel, water, and vapor, and breakup of the fuel into smaller diameter drops (smaller meaning 1 to 10 cm); this phase occurs on a timescale of 0.10 to 1 s. During this phase, the fuel and water are insulated from one another by a vapor film, which serves to maintain the fuel temperature close to its initial temperature throughout the entire coarse-mixing process. Breakup of the molten fuel is thought to be governed by hydrodynamic instabilities, notably the Rayleigh-Taylor and Kelvin-Helmholtz instabilities. These breakup processes are driven by relative velocity differences between the fuel and the other two "fields," water and steam.

The trigger phase occurs when some local disturbance collapses the vapor films around the fuel; this collapse allows direct water-fuel contact, high heat transfer rates to the water, rapid increase in pressure, and high relative velocities in the vicinity of the trigger. If the triggering event is sufficiently strong, the mixture will enter an explosive propagation phase. The trigger event is not well understood, but is typically observed to occur quickly, on a timescale of around 100 μs, and is frequently initiated by contact of the fuel with a solid surface.

The explosive propagation phase is characterized by a "reaction zone" that propagates through the mixture region. Within this reaction zone, the coarsely mixed fuel is rapidly fragmented into particles in the 10 to 100 μm size with accompanying rapid increase in fuel surface area, release of heat to the water, and generation of shock waves. The time scale for reaction zone processes is the same as that for the trigger phase, on the order of 100 μs, and typical propagation speeds are in the 50 to 300 m/s range. The same hydrodynamic instabilities operative during the coarse-mixing phase could also be responsible for the fine fragmentation occurring during the propagation phase, although other mechanisms are just as possible (for instance, jet penetration of the fuel by the water[155]).

The expansion phase, wherein the steam-water mixture turns its increased thermal energy into work on the surroundings, is more tractable to analysis using existing hydrodynamic codes than the other FCI phases and, consequently, has been treated in some detail by various researchers.[156,157]

The most recent study was that of Bohl,[158] which also included some modeling of the processes occurring during the coarse-mixing and propagation phases. The expansion phase generally occurs on a time scale of 10 to 100 ms.

1.4.3.2 Previous FCI Predictive Models

As stated in Section 1.4.3, a major obstacle to the further understanding of FCIs and to the analysis of experimental data has been the lack of a psol capable of calculating all important aspects of the FCI process. These important aspects include such phenomena as film boiling heat transfer, fragmentation and mixing of the fuel, and shock wave propagation. In the context of reactor safety, a further phenomena of interest is the generation of hydrogen by chemical reaction between the fuel and the steam. Hydrogen generation is important to reactor safety because of the possibility of burning or detonation of the hydrogen posing a threat to the reactor vessel or containment.[159]

Various models have been used to study isolated aspects of the whole FCI problem, but the results of these efforts have generally been less than satisfactory because of assumptions that simplify or ignore various key phenomena. The most common of such assumptions include using a constant particle size during the coarse-mixing phase,[158] setting limits on the spatial extent of mixing based on one-dimensional countercurrent flow correlations,[152] or simply limiting mixing based on "physical intuition." These assumptions tend to limit the extent of coarse mixing, that is, the amount of fuel and water mixed together; if not much mixture is formed, then an FCI cannot generate enough energy to damage a reactor vessel or containment building, even at maximum theoretical (Hicks-Menzies[160]) efficiency. This procedure, unfortunately, does not provide a conservative estimate of the possible effect of an FCI during a reactor accident. Taking the other extreme of total mixing and maximum efficiency does not provide a useful approach either, as this will almost certainly result in a calculated FCI strong enough to breach the containment. Such severe conditions are thought to be unlikely, but again, we are not yet in a position to decide <u>how</u> unlikely.

1.4.3.3 A Predictive Model for FCIS

The current state of knowledge about the physical processes occurring in FCIs, characteristics of existing hydrocodes, and the necessity of calculating FCIs in a reactor safety context were all considerations in the design of the IFCI code.

Because of the radically different time scales associated with the different phases of an FCI, an implicit numerical hydrodynamics method is desirable for its ability to exceed the Courant limit,[161] thereby reducing computation time. The presence of at least three separate material fields in the FCI problem (water, vapor, and molten fuel), all at different temperatures and moving at different velocities, also suggested the use of a multifield method. The presence of shock waves during the propagation phase requires use of a compressible hydrodynamic method.

The SETS[162] method was chosen as an appropriate hydrodynamic method that satisfied the above criteria. This selection was also motivated by the existence of MELPROG/MOD1, a severe reactor accident code using the SETS method, which features a two-dimensional, four-field fluids compressible hydrodynamics module with many necessary models already incorporated.

MELPROG/MOD1 is designed to calculate the events occurring during a hypothetical core meltdown accident in a light-water reactor (LWR). This code already includes a phase change model, a sophisticated heat transfer model with complete boiling curve, an equation-of-state for steam and water, a flow regime map for both vertical and horizontal flow, and models for both interphase and field-structure drag. As such, MELPROG/MOD1 could be used as the basis for IFCI, with the addition of models for FCI phenomena not covered by the existing MELPROG/MOD1 models. MELPROG/MOD1 as a basis for IFCI has the additional advantage that it already calculates the core meltdown and water boiloff; thus,the goal of providing initial conditions for an FCI in the reactor geometry is achieved. Conversely, the IFCI models would also be available as part of MELPROG, thereby expanding the MELPROG reactor analysis capabilities.

1.4.3.4 IFCI Code Description

The following sections will first describe the general structure and features of MELPROG/MOD1 and then describe the models added to allow calculation of FCIs.

- General Code Structure

MELPROG/MOD1 consists of six major modules, divided according to responsibility for calculating different physical processes: FLUIDS, CORE, STRUCT, RMIM, DEBRIS, and VIKI, which respectively handle fluids transport, core structure behavior (pins, can walls, control blades), vessel structure mechanical and thermal response (vessel wall, vessel head), thermal radiation transport, debris bed behavior, and fission-product chemistry. Several additional modules are under development, including IFCI, for FCI behavior, and EJECT, for blowdown to the containment. Output data is available as printed output, a graphics file compatible with the TRAC[163] graphics postprocessor, TRAP, and as an interface file to the CONTAIN containment response code. Also, MELPROG may be run either in stand-alone mode, using applied boundary conditions, or coupled to the TRAC reactor systems code.

IFCI actually consists of extensions and additions to the models in the FLUIDS module. The FLUIDS module presently provides a two-dimensional, r-z geometry, four-field hydrodynamics model, whose fields consist of vapor (steam plus hydrogen), water, solid corium debris, and molten corium, or melt. A "field," in the context of the SETS method, means a set of momentum, mass continuity, and energy equations; a separate set of these equations is solved for each "field." Coupling between fields is represented by coupling terms in these equation sets.

The key additional models for IFCI are (1) a dynamic fragmentation model and (2) an advection model for melt surface area. The fragmentation model

calculates the breakup of the melt based on local hydrodynamic conditions (densities and velocities). The advection model handles the transport of surface area in the finite difference mesh when melt in a mesh cell, having some specific surface area, crosses into a neighboring cell containing melt with some other specific surface area.

Other extensions to the MELPROG fluids treatment necessary to implement IFCI include providing the interfield constitutive relations between the fourth field (molten fuel, or melt) and the other three fields and extending the equation-of-state package for water-steam to allow supercritical pressures and temperatures.

- Fragmentation Model

The idea of a dynamic fragmentation model, which calculates the characteristic melt diameter as a function of instantaneous hydrodynamic conditions, was first proposed by Young.[164] A model using this idea was later incorporated into a version of the TEXAS one-dimensional FCI code by Chu,[165] using an empirical correlation derived from data obtained in the FITS experiments. Another version of a dynamic fragmentation model was developed by Pilch* based on correlations to the existing body of drop breakup data at that time.[80] The melt fragmentation model in IFCI is adapted from the Pilch model.

The original Pilch model, as implemented in TEXAS, can be expressed as

$$\frac{dD}{dt} = - C_o |v_r| \varepsilon^{\frac{1}{2}} , \quad \varepsilon = \frac{\rho_f}{\rho_d} ,$$

where

D = drop diameter (m),

t = time (s),

v_r = relative velocity between the drop and surrounding fluid (m/s),

ρ_f = fluid density (kg/m^3),

ρ_d = drop density (kg/m^3),

C_o = a constant $\simeq$ 0.245.

*Personal communication, Martin Pilch, Sandia, Div. 6425, November 14, 1986.

This formulation was developed as an extension of correlations to the data from droplet breakup experiments.[80] The original correlations describe drop breakup in terms of initial conditions (initial relative velocity and droplet diameter), with the results of the correlations being the final drop size and the total time to reach that final size. The correlations were rederived in terms of instantaneous drop size and velocity to arrive at a dynamic breakup model.

In TEXAS, the fragmentation model is set up in terms of a drop described by Lagrangian field equations moving through a two-phase fluid described by Eulerian field equations. The fluid velocity and fluid density used in the breakup model are taken to be the mass-weighted averages of the water and vapor fields, and the change in drop size is given directly by the breakup model.

In IFCI, the drop is described by an Eulerian melt field interacting with the other three fields, also Eulerian. The drop may either be smaller than a finite difference mesh cell or extend over many of them; melt material in the drop may be advected from one mesh cell to another, and fragmentation takes place only on the drop surface, that is, in cells containing both the melt field and at least one other field. These are the differences that must be considered in going from a Lagrangian description of the drop to one based on an Eulerian description.

The modified Pilch fragmentation model in IFCI is formulated in terms of rate-of-change of surface area, rather than rate-of-change of drop diameter; this is because the quantity that is advected with the melt on the Eulerian finite difference mesh is the surface area per unit volume, or volumetric surface area. A surface area formulation also allows treatment of jets and other more general flows, an important advantage for a general predictive tool such as IFCI. The advection algorithm for volumetric surface area is discussed in detail in the next section. The volumetric surface area, A_v, and the drop diameter, D, are related, for spherical drops smaller than a mesh cell, through the melt volume fraction, α_m:

$$A_v = \frac{6\alpha_m}{D} \quad , \quad \alpha_m = \frac{V_m}{V} \quad ,$$

where

A_v = volumetric surface area of the melt (m^2/m^3),

α_m = melt volume fraction,

V_m = melt volume in a cell (m^3),

V = cell volume (m^3).

Differentiating the expression for volumetric surface area leads to an equation for rate of change of A_v in terms of the rate of change of diameter:

$$\Gamma_A = \frac{dA_v}{dt} = - \frac{6\alpha_m}{D^2} \frac{dD}{dt} = - A_v \frac{1}{D} \frac{dD}{dt} \quad ,$$

where Γ_A = surface area source (1/m/s).

This expression is used as a surface area source term in the continuity equation for A_v.

The numerical formulation of the surface area source must be done carefully so that the relation between surface area and melt diameter is preserved. In IFCI, a "staggered" mesh cell is used, where the velocities are defined on the cell edges, and densities, volume fractions, drop diameter, and the volumetric surface area (and hence the surface area source term) are defined at the cell center (see Figure 1.4-17).

Another numerical consideration peculiar to the SETS method in IFCI is that there is a minimum volume fraction in a cell for each field, even if the field is not actually present. This minimum volume fraction must be taken into account when forming averages on cell boundaries of field densities and volume fractions for use in the breakup model so that the actual property values are not swamped by spurious residual values in the empty cells.

The fragmentation model is set up in IFCI by first calculating the rate of change of diameter on each edge of the cell. The rate is calculated only if both the melt field and at least one other field are present in the two cells adjoining a given edge. The cell-centered quantities are averaged so that the averaged quantity will go to the correct limit under bounding conditions, for instance, one cell full of melt and the adjoining cell full of water.

The following description of the finite difference formulation for the averages is written in terms of averages on the top cell edge; averages in the radial direction are done in a completely analogous fashion.

The volume fractions on the edge are formed as the simple arithmetic average:

$$\bar{\alpha}_1 = \frac{\alpha_{1ij} + \alpha_{1ij+1}}{2}, \quad \bar{\alpha}_2 = \frac{\alpha_{2ij} + \alpha_{2ij+1}}{2} \quad ,$$

where

$\bar{\alpha}_1$ = average volume fraction for field 1 (vapor) on the top edge of cell (i,j),

$\bar{\alpha}_2$ = average volume fraction for field 2 (water) on the top edge of cell (i,j),

i = radial cell index,

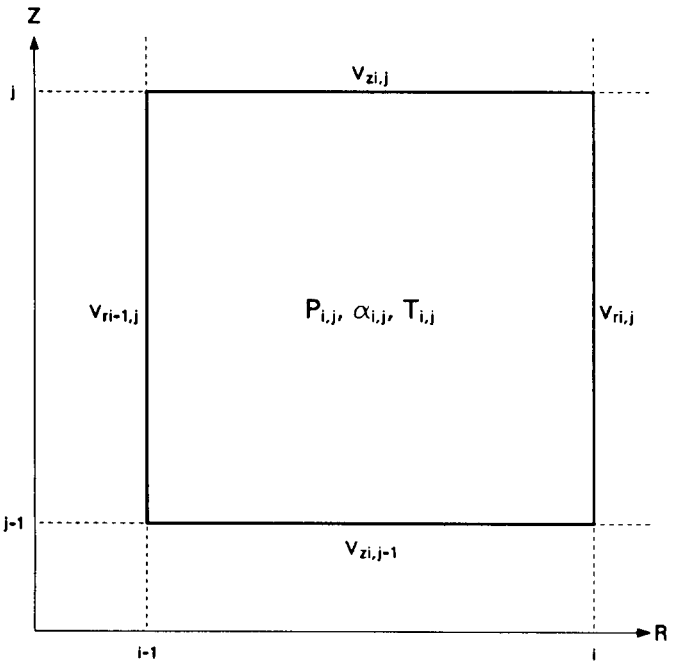

Figure 1.4-17. Finite Difference Mesh Cell and Variable Location in IFCI

j = axial cell index,

α_{kij} = cell volume fraction for field k in cell (i,j).

The water and vapor field densities are first averaged separately by weighting with the cell volume fractions in the two cells to give effective water and vapor densities on the cell edge:

$$\bar{\rho}_k = \frac{\alpha_{kij}\rho_{kij} + \alpha_{kij+1}\rho_{kij+1}}{\alpha_{kij} + \alpha_{kij+1}} .$$

The effective fluid density for use in the breakup correlation is then formed by weighting the effective edge densities with the respective edge volume fractions:

$$\rho_f = \frac{\bar{\alpha}_1\bar{\rho}_1 + \bar{\alpha}_2\bar{\rho}_2}{\bar{\alpha}_1 + \bar{\alpha}_2} .$$

This procedure is used so that if, for instance, one cell is full of water and the other contains melt, the fluid density calculated will be equal to

the water density, rather than one-half the water density. The effective fluid velocity is calculated as the effective-mass-weighted velocity normal to the edge, so that, for the example case, the axial velocity is the one used. This choice is the correct one for the present Rayleigh-Taylor model, which is driven by accelerations normal to the interface between the melt and fluid, whereas other instabilities, such as Kelvin-Helmholtz, would be driven by tangential velocities. The fluid velocity is given as

$$v_f = \frac{\bar{\alpha}_1\bar{\rho}_1 v_{z1} + \bar{\alpha}_2\bar{\rho}_2 v_{z2}}{\bar{\alpha}_1\bar{\rho}_1 + \bar{\alpha}_2\bar{\rho}_2} \quad ,$$

where

v_f = fluid velocity (m/s),

v_{zk} = axial velocity for field k on top edge of cell (m/s).

The effective melt diameter used in the rate model on the cell edge is formulated as

$$\bar{D} = \left(\alpha_{mij} + \alpha_{mij+1}\right)\left[\frac{\alpha_{mij}}{D_{ij}} + \frac{\alpha_{mij+1}}{D_{ij+1}}\right]^{-1} \quad .$$

This formulation is appropriate for the transported quantity, volumetric surface area, which is proportional to 1/D, and also allows handling of the minimum volume fraction cutoff used in the IFCI numerics. The minimum volume fraction is typically 10^{-5}; cells that are turned off are set to a minimum 10 times smaller. This means that cells also have a minimum volumetric surface area, whether there is actually any melt in them or not. We would like this residual surface area to be a small number; in particular, the residual area should be small in comparison to the amount of surface area fluxed into an empty cell during one time step. If these conditions are not met, then the incoming surface area can be swamped by the residual amount in the receiving cell.

As an example, for the present problem, the initial melt diameter is 20 cm; this results in a volumetric surface area for a full cell of 30 m^{-1}. If empty cells were initialized to have a melt diameter of 20 cm (a reasonable procedure in a hydrocode), then the empty cells would contain at least 3×10^{-4} m^{-1} of surface area. At a relative velocity of 1 m/s, this means that the flux of melt into a previously empty cell during one time step equals the amount of residual surface area when the time step is 10 μs. The time step is frequently of this size or smaller during parts of a FCI calculation, and the residual area could then swamp the influx at small time steps. This is prevented in IFCI by setting the initial diameter in empty cells to a large number, 10^5 m. This reduces the residual area to

6×10^{-10} m^{-1}, corresponding to a minimum time step of 2×10^{-11} s for this example, which is smaller than would ever be used in IFCI.

Setting D in empty cells to a large number is another good reason for the geometric averaging procedure, as a simple average would be swamped by the large value. If one cell is full and the adjoining one is empty on an edge, the geometric average goes to the melt diameter of the full cell, which is the desired result.

The quantity calculated on the cell edges is actually the rate-of-change of diameter divided by the effective diameter; this quantity is weighted by the effective melt volume fraction for each edge and used to form an effective rate of change for the cell:

$$\Gamma_A = - A_v \sum_{l=1}^{4} \bar{\alpha}_l \left(\frac{1}{D} \frac{dD}{dt} \right)_l \Big/ \sum_{l=1}^{4} \bar{\alpha}_l \quad ,$$

where the sum on l goes over the four cell edges.

The above expression for rate-of-change of volumetric surface area in a cell due to Rayleigh-Taylor instabilities is then used as a source in the surface area transport equation. After calculation of the new surface area using the transport equation, the new melt diameter is obtained using the relation between diameter, volume fraction, and surface area.

If the melt extends over more than one cell, the formulation of the fragmentation model must be modified because fragmentation is assumed to occur only in cells containing the interface between the melt and the other fields, and the original formulation is for global breakup of one drop. The global model, derived for the entire mass of melt and for the fluid conditions surrounding the melt, must be expressed in terms of local cell conditions. One way to accomplish this is to note that the total rate-of-change of diameter, given by the Pilch model, is equivalent to the volumetric surface area source multiplied by the volume of the melt mass, or total rate-of-change in surface area. The same total rate-of-change in surface area must then be generated by those cells on the melt surface; this will be true if the surface source in those cells is increased by a factor, f_s, relating the total melt volume to the melt volume in the surface cells. The factor f_s has somewhat different values depending on the assumed melt shape and what geometry the finite difference cells have. Assuming a spherical melt drop, uniform-sized cells with cell length Δx, Cartesian x-y-z geometry, and $\Delta x \ll D$, the ratio is equal to

$$f_s \simeq \frac{D}{6\ \Delta x} \quad .$$

In practice, the value of D available is a local value that may vary from cell to cell. The cell dimensions are also not necessarily uniform, and

the drop may not be spherical. The procedure used in IFCI is to divide the rate of change of diameter calculated on the cell edges by the length of the cell edge, rather than by D. This gives a correction that differs from the above equation for f_s by a factor of 6, but goes to the limit for $D \leq \Delta x$ as $D \rightarrow \Delta x$. A more elegant expression for f_s will be incorporated in IFCI at a later time so that the correct limit is obtained both for $D \simeq \Delta x$ and for $D >> \Delta x$.

- Surface Area Transport

A consideration arises in an code using an Eulerian finite difference mesh that is not present in one using a Lagrangian description in that the melt material and its properties must be advected and conserved as the melt moves across mesh cell boundaries. In particular, the surface area per unit volume is advected and conserved in IFCI. The surface area transport equation is formulated as

$$\frac{\partial A_v}{\partial t} + \nabla \cdot \mathbf{v}_m A_v = \Gamma_A \quad ,$$

where $\mathbf{v}_m$ is the melt velocity vector. The surface area transport equation is solved in IFCI after the mass and energy stabilizer step in the SETS method.[165] The new values of the characteristic melt diameter are then calculated from the new volumetric surface areas as

$$D = \frac{6\ \alpha_m}{A_v} \quad .$$

- Heat Transfer and Equation of State

Heat transfer from the melt to the water and steam fields is handled by the HTMELT routine. HTMELT contains models for the complete boiling curve, including nucleate, transition, and film boiling, plus single-phase free and forced convection to the steam and water fields. At the present time, the bulk-flow regime of the water and vapor fields, as seen by the melt, is considered, for purposes of calculating the heat transfer coefficients from the melt to the water and vapor fields, to be either bubbly or droplet flow with a transition region. The pure bubbly flow regime exists for vapor fractions $\alpha_v \leq 0.5$; the transition region extends over $0.5 < \alpha_v \leq 0.75$, and pure mist flow is assumed for $\alpha_v > 0.75$. The boiling curve is used for $\alpha_v \leq 0.75$ and for melt temperatures greater than the local saturation temperature. If the local pressure is greater than the critical pressure for water, then single-phase convection coefficients are used without boiling. The single-phase convection coefficients and boiling-curve heat transfer coefficients are merged smoothly over a range of temperatures and vapor fractions so that sudden discontinuities do not occur in the transfer terms in the fluids field equations, which can cause convergence problems.

The film boiling model used originally in HTMELT was replaced by one from the TEXAS fuel-coolant interaction code. This film boiling model is based on experiments by Dhir and Purohit[166] on film boiling around a sphere under free and forced convection conditions.

The changes to the MELPROG equation-of-state package for water consisted of (1) installing the equation-of-state (EOS) package from the TRAC systems code, which is an improved version of the MELPROG package; and (2) adding analytic extensions at the limits of the TRAC package. The EOS package, which is collectively referred to in MELPROG and TRAC as the THERMO routines, consists of a series of analytic fits to the steam tables. In normal operation, THERMO returns water and steam properties, plus property derivatives with respect to the independent variables, which are the water and vapor temperatures and the total and steam partial pressures. When the input variables exceed the limits of the regions over which the analytic fits are valid, THERMO returns the properties and derivatives at the limits. Unfortunately, the pressure iteration step in the SETS method now has nonzero derivatives for properties that are actually not changing; as a consequence, the pressure iteration will either fail or reduce the timestep drastically. Adding the analytic extensions to the THERMO package allows the properties to continue to change in agreement with the derivatives. The extensions were added because of the likelihood of generating supercritical conditions during the FCI explosion phase. They are also useful when superheated temperatures occur in water or vapor.

The limits in the current TRAC version of the THERMO package are shown in Table 1.4-6.

Table 1.4-6

TRAC Water Equation of State Limits

Minimum hydrogen partial pressure	1×10^{-5} Pa
Minimum steam partial pressure	1 Pa
Maximum steam partial pressure	45 MPa
Minimum vapor temperature	273 K
Maximum vapor temperature	3000 K
Minimum water temperature	273 K
Maximum water temperature	713.9 K
Maximum saturation temperature	647 K

These limits are extended as follows:

1. If either the vapor temperature or pressure is off the table limits, then the vapor equation of state is extended assuming ideal gas behavior. The equation used is

$$\rho_s^i = \frac{P_s}{R_s T_v} \quad ,$$

where

ρ_s^i = ideal gas law steam density (kg/m^3),

P_S = steam partial pressure (Pa),

R_S = gas constant for steam = 462 J/kg/K,

T_V = vapor temperature (K).

This equation is joined smoothly to the table value at the limit by adding an offset,

$$\Delta\rho = \rho_s^\circ - \frac{P_s^\circ}{R_s T_v^\circ} \quad , \quad \rho_s = \rho_s^i + \Delta\rho \quad ,$$

where the superscript "°" refers to the table edge values. The derivatives of vapor density with respect to temperature and pressure are replaced by the ideal gas law derivatives if the independent variable is outside the table limits. The pressure derivatives are

$$\frac{\partial\rho_s}{\partial P} = \frac{\rho_s}{P_s} \quad , \quad P_s > P_s^\circ \quad ,$$

or

$$\frac{\partial\rho_s}{\partial P} = \frac{\rho_s}{P_s} - \frac{1}{R_s T_s^\circ} + \left[\frac{\partial\rho_s}{\partial P}\left(T_s^\circ, P_s\right)\right], \quad P_s \le P_s^\circ \quad .$$

The temperature derivatives are

$$\frac{\partial\rho_s}{\partial T_v} = -\frac{\rho_s}{T_v} \quad , \quad T_v > T_v^\circ \quad ,$$

or

$$\frac{\partial \rho_s}{\partial T_v} = - \frac{\rho_s}{T_v} + \frac{P_s^\circ}{R_s T_v^2} + \left[\frac{\partial \rho_s}{\partial T_v}\left(T_v,\ P_s^\circ\right)\right], \quad T_v \le T_v^\circ \quad .$$

The internal energy is extended using first order Taylor series expansions in T and P:

$$u_s = u_s^\circ + \left[\frac{\partial u_s}{\partial T_v}\right]^\circ \Delta T_v + \left[\frac{\partial u_s}{\partial P}\right]^\circ \Delta P, \quad \Delta P = P_s - P_s^\circ,\ \Delta T_v = T_v - T_v^\circ \quad .$$

2. If either the liquid temperature or the pressure are off the table limits, then the liquid internal energy and density are extended using Taylor series in T and P:

$$u_l = u_l^\circ + \left[\frac{\partial u_l}{\partial T_l}\right]^\circ \Delta T_l + \left[\frac{\partial u_l}{\partial P}\right]^\circ \Delta P \ , \quad \Delta T_l = T_l - T_l^\circ ;$$

$$\rho_l = \rho_l^\circ + \left[\frac{\partial \rho_l}{\partial T_l}\right]^\circ \Delta T_l + \left[\frac{\partial \rho_l}{\partial P}\right]^\circ \Delta P \quad .$$

The enthalpies of water and steam at saturation and the saturation temperature must also be extended in pressure, as the derivatives of these quantities, as calculated by THERMO, do not quite go to zero in the table at the critical point. In the IFCI extension, they are allowed to keep changing slowly with pressure and multiplied by a function that gradually decreases the change in the properties and the property derivatives to zero. The actual expressions for the enthalpies at saturation are

$$h_{sv} = h_{sv}^\circ f_h \ , \quad h_{sl} = h_{sl}^\circ f_h \ , \quad f_h = 1 + 10^6\left(\frac{1}{P_s^\circ} - \frac{1}{P_s}\right) \ ,$$

and the derivatives are given as

$$\frac{\partial h_{sv}}{\partial P} = \frac{\partial h^{\circ}_{sv}}{\partial P} f_h - h_{sv} \frac{10^6}{p_s^2} , \quad \frac{\partial h_{sl}}{\partial P} = \frac{\partial h^{\circ}_{sl}}{\partial P} f_h - h_{sl} \frac{10^6}{p_s^2} .$$

Some modification of the TRAC liquid density routine was also required because the fit used for the liquid density had a positive derivative with respect to temperature near the critical point; this was completely nonphysical and caused the heat transfer routines to calculate a negative Grashof number.

1.4.4 Explosion Propagation Modeling

(L. T. Pong and B. W. Marshall, Jr., 6427; M. F. Young, 6425)

The objective of this work is to model the propagation of a steam explosion through a one-dimensional array of particles. Currently, we plan on investigating numerous variables believed to be related to the explosion propagation. These include, but are not limited to, (1) the influence of particle spacing and diameter, (2) the influence of noncondensable gases (i.e., hydrogen) present in the vapor blanket, (3) the difference between currently available fragmentation models, and (4) the influence of other parameters such as subcooling, fuel volume fraction, initial void fraction, etc. By controlling each of these variables, we plan on investigating the escalation time for a pressure wave to reach a self-sustaining, steady-state detonation-like wave that propagates through the coarse mixture of particles, if such a condition exists. We will also be interested in the magnitude and duration of the pressure pulse as a function of these variables in addition to the speed at which the "detonation wave" propagates through the mixture. Finally, we will look at the relationship between the "detonation wave" and the rapid increase in the void fraction during the expansion phase.

1.4.4.1 Code Development

The TEXAS (Thermal Explosion Analysis System) code[167] was originally developed to provide a tool for the analysis of fuel-coolant interaction in the LMFBR program. TEXAS solves a set of one-dimensional, three-field hydrodynamic equations in which two fields are Eulerian, representing the coolant as liquid and vapor, and the third field is Lagrangian, used to represent discrete fuel particles. Slip and heat transfer are allowed between all fields, and phase changes between liquid and vapor are accounted for.

We have also added four different fragmentation models to the code. The first is a dynamic model, developed by M. Pilch.[80] The second, also developed by Pilch, is a dynamic model similar to the first but includes surface entrainment.* The third available model was developed by Chu and assumes

*Personal communication, Martin Pilch, Sandia, Div. 6425, November 14, 1986.

that the fragmentation process is exponential in nature.[165] The last model is a linear fragmentation model in which the final particle size and fragmentation time are inputs into the code. In this case, the fragmentation process is assumed to be a linear relationship between the decrease in particle size and the specified fragmentation time.

When we began this work, there were two existing versions of the TEXAS code; one version modified and used by Chu at the University of Wisconsin (UW-TEXAS)[168] and a second at Sandia (Sandia-TEXAS).[167] Therefore, we began this work by combining the best models each version had to offer into a single version, hereafter referred to as TEXAS-2.0. In this upgrade, a new heat transfer package was incorporated into TEXAS-2.0 and is a modified version of that used in the MELPROG code.[169] Also, routines developed by Chu for the interfield friction factors, wall friction, and heat transfer at the walls were included.

Checkout calculations using TEXAS-2.0 were performed and compared to those obtained using the previous version to insure the operability of the code. Also, preliminary calculations using a one-dimensional array of molten particles were performed and are discussed in the following section.

1.4.4.2 Results of Preliminary Calculation

The problem geometry is shown in Figure 1.4-18. Here, D_f represents the fuel-particle diameter and S_f represents the center-to-center spacing between the particles. The chamber had constant pressure boundaries at each end and was divided into several grid cells. The number of particles in each cell can range from zero to several, all with equal masses. In these preliminary calculations, the chamber length was 0.5 m and had a cross-sectional area of 0.01 m^2. Particles had an initial diameter of 1 cm, were

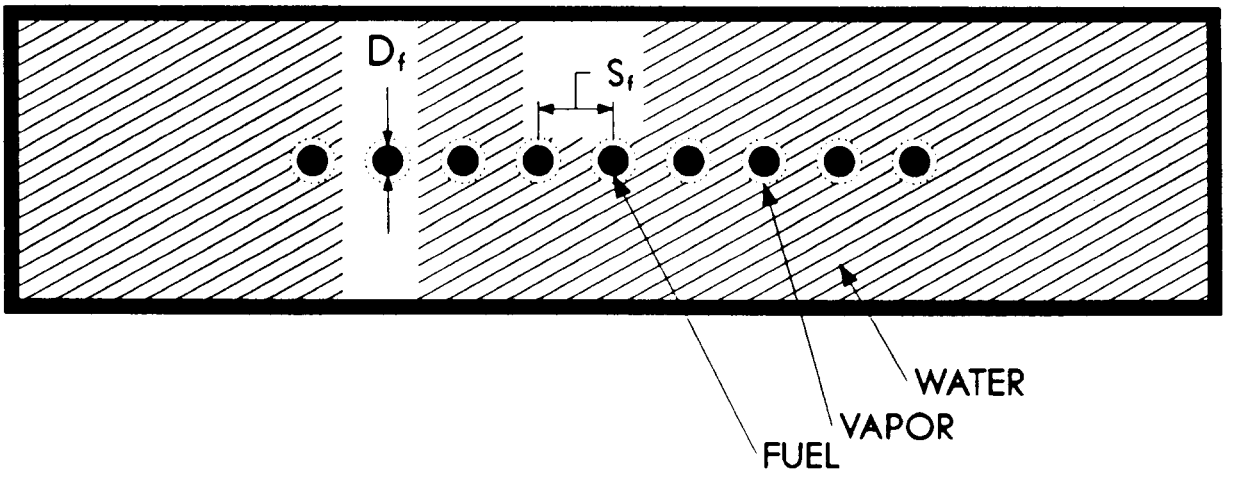

Figure 1.4-18. Explosion Propagation Geometry

located between the 0.1- and 0.4-m location of the chamber length, and had a 1.5-cm spacing. The remainder of the chamber was filled with water at a temperature of 368 K. We triggered the explosion at a predetermined time (1 ms) by "loading" a boundary with a pressure pulse having a 100 bar peak and a 0.1 ms width. The initial conditions used in each of the calculations are listed in Table 1.4-7.

Table 1.4-7

Initial Conditions for the Three Explosion Propagation Calculations

Fuel material	iron-alumina
Mass of fuel	1.28 kg
Mass of water	4.39 kg
Fuel temperature	2700 K
Water temperature	368 K
Particle diameter, D_f	1 cm
Particle spacing, S_f	1.5 cm
Number of grids with particles	20
Number of particles/cell	32
Fuel volume fraction	0.11
Water volume fraction	0.89

In the first calculation, we used the linear fragmentation model. We assumed that the particles did not fragment until a threshold pressure (13 bars) was achieved at which point they fragmented from 1 cm diameter down to 300 μm over a 200 μs time interval. At the time of the trigger, the void fraction of the system was ~2 percent. The calculated pressures at various times are shown in Figure 1.4-19. The trigger pressure propagated down the chamber at a velocity of about 300 m/s. A second, somewhat smaller peak at ~1.4 ms followed the trigger pressure and represents the pressurization of the system due to the rapid increase in surface area and, therefore, heat transfer to the coolant. The FCI pressure wave propagated and continued to build as the particles in each cell fragmented. After 2.4 ms, all of the particles had fragmented to 300 μm and the pressure wave had begun to decay. Figure 1.4-20 shows the void fraction versus distance down the chamber. The curves at 1.8, 2.0 and 2.2 ms clearly show the compression wave propagated down the chamber as the pressure wave passed. Behind the FCI pressure wave, the void fraction began to increase due to the rapid increase in heat transfer and, therefore, steam generation.

In the second sample problem, we used Pilch's dynamic fragmentation model:

$$R(t + dt) = R(t) - 0.1225 \cdot dt \cdot \left(U_p - U\right) \cdot \left(\rho/\rho_p\right)^{0.5} ,$$

$$= R(t) \cdot (1 - 0.245 \cdot \Delta T) ,$$

$$= R(t) - dR(t) ,$$

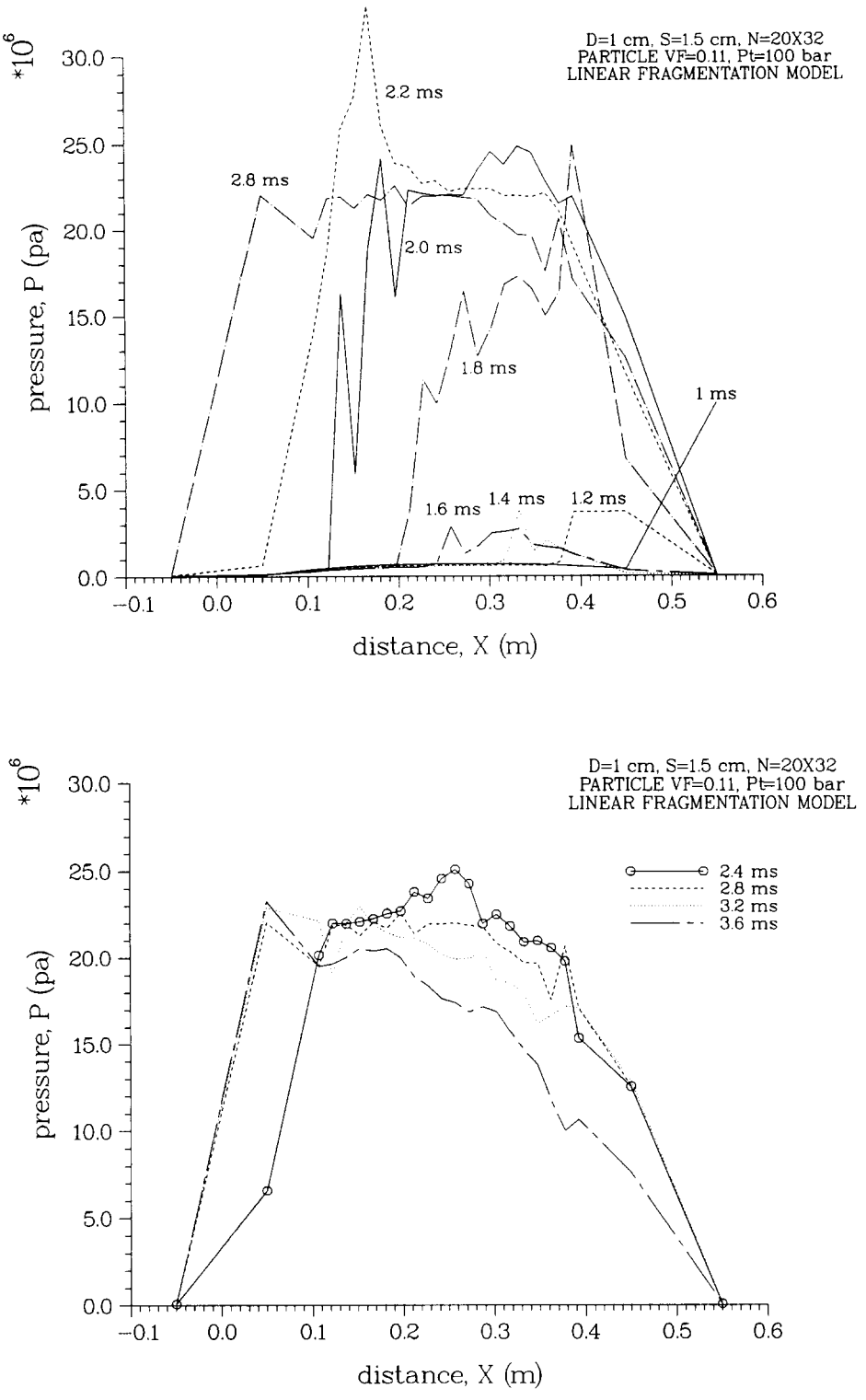

Figure 1.4-19. Spatial Pressure for the Linear Fragmentation Model

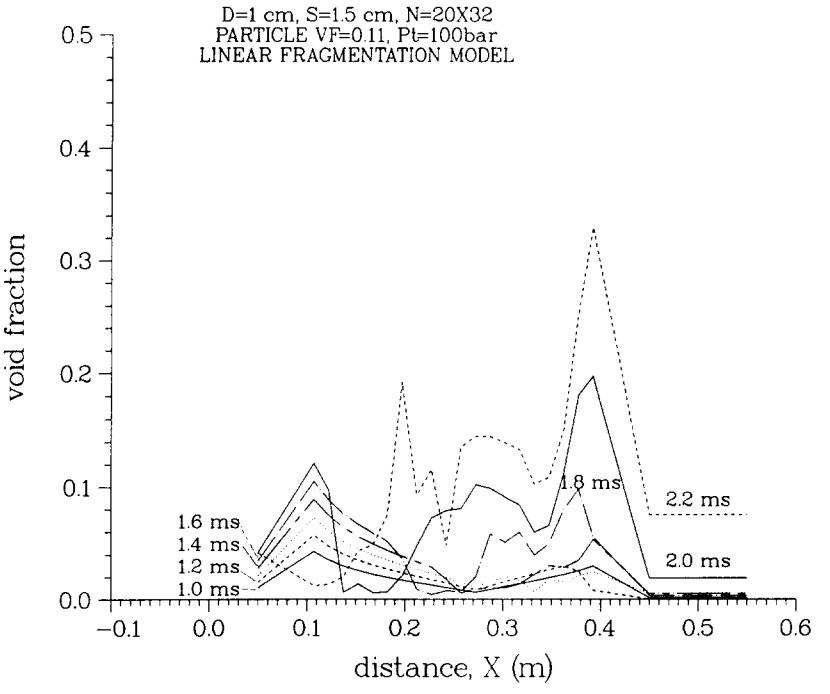

Figure 1.4-20. Spatial Void Fraction for the Linear Fragmentation Model

where

U_p = particle velocity,

U = mixture velocity,

ρ_p = particle density,

ρ = mixture density,

ΔT = the dimensionless time step in terms of the relative velocity and density ratio of continuous and dispersed phase, i.e,

$$\Delta T = \left[dt \cdot \left(U_p - U\right) \cdot \left(\rho/\rho_p\right)^{0.5}\right]/2R(t) \quad .$$

Using identical initial and boundary conditions as the first calculation, the results using this model are shown in Figure 1.4-21. Obviously, there is a significant difference between the first sample problem and these results. The Weber number of the system induced by the trigger pressure is on the order of hundreds. Instead of an escalation of the pressure wave throughout the mixture as in the first problem, the pressure wave eventually decayed and was unable to sustain the propagation. As in the previous example, the smaller peaks in the pressure curves represent the particle fragmentation. However, at about 2.4 ms, the particle radius was still 4.6 mm. Furthermore, the system void fraction had increased to only about 6 percent, which was smaller than observed in the first calculation.

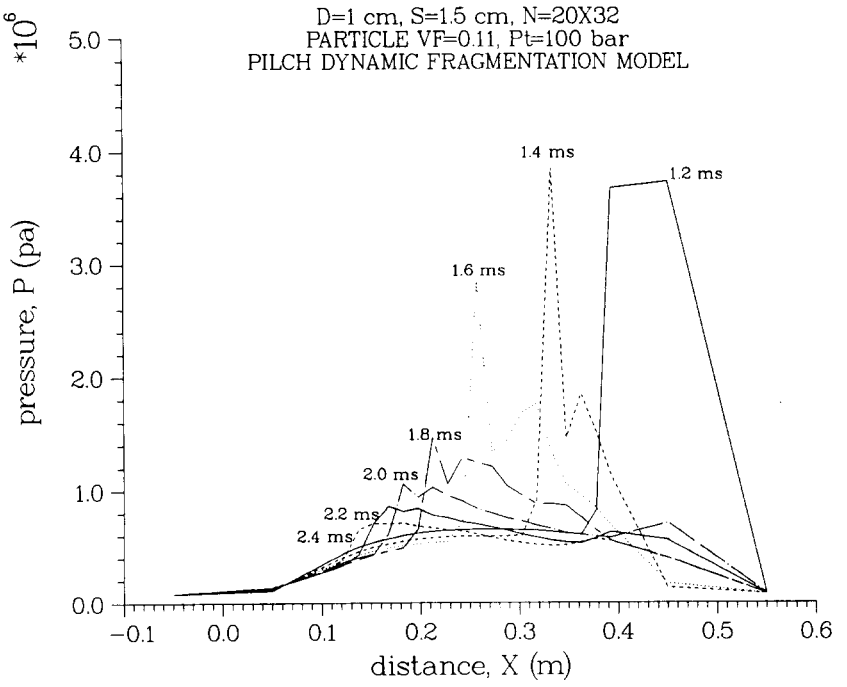

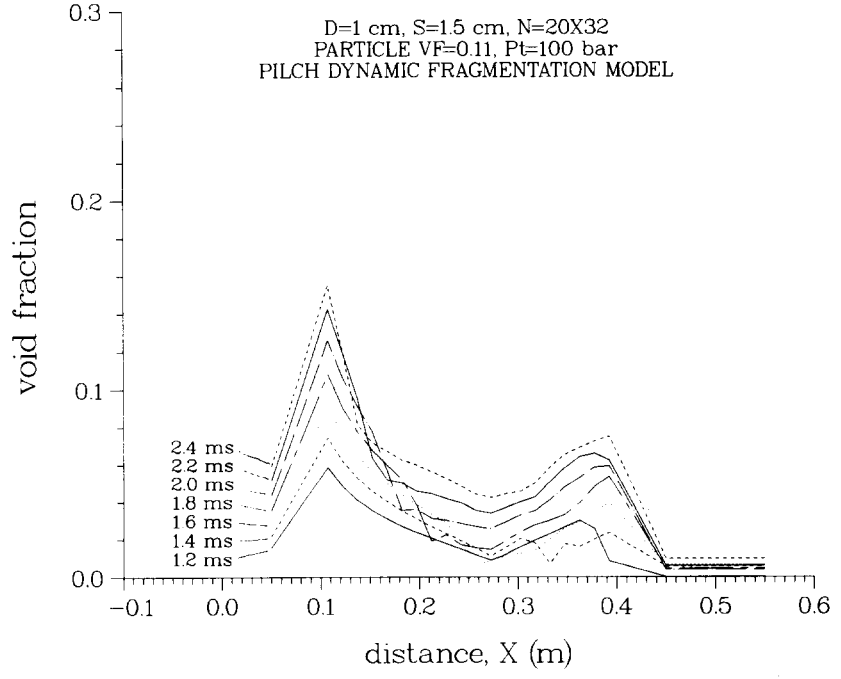

Figure 1.4-21. Spatial Pressure and Void Fraction Using the Rayleigh-Taylor Instability Model Developed by Pilch

In the third sample calculation, the fragmentation model developed by Chu was incorporated. Its basic form is

$$R(t + dt) = R(t) \cdot \left(1 - C_o\ \Delta T\ We^{0.246}\right) \text{ and}$$

$$= R(t) - dR(t) \quad ,$$

where

$C_o = 0.1093 - 0.078 \cdot \left(\rho/\rho_p\right)^{0.5}$,

ΔT = the dimensionless time step,

We = the Weber number.

In this particular problem, the results from both Pilch's and Chu's model are about the same, since

$$\frac{dR_{Pilch}}{dR_{Chu}} = \frac{0.245}{C_o \cdot We^{0.246}} \quad .$$

Assuming a representative Weber number of 400 and the density ratio, ρ/ρ_p, is 0.25, the ratio [dR]/[dR] of the models is about 0.8. Therefore, we would expect the two models to give similar results over the time scale of interest.

1.4.4.3 Conclusions

We have combined two versions of the TEXAS code into a single version (TEXAS-2.0) and have completed the preliminary checkout calculations. We have also begun to study the FCI explosion propagation process by using three different particle-fragmentation models to described the fine fragmentation process. From these preliminary calculations, the linear fragmentation model gave the highest peak pressure, although this is the least desirable model since it has no theoretical basis. We are currently evaluating Chu's and Pilch's fragmentation models to ensure that both models are valid over the Weber numbers of interest. Furthermore, we are investigating fragmentation models that are in the right Weber number regime. Other modeling activities in the future will include more accurate models for film boiling to allow us to track the vapor interface around a droplet and hydrogen generation caused by chemical reactions with available steam.

1.5 Hydrogen Behavior

(D. W. Stamps and M. Berman, 6427)

The major concerns regarding hydrogen in LWRs are that the static or dynamic pressure loads from combustion may breach containment or that

important, safety-related equipment may be damaged due to either pressure loads or high temperatures. In order to assess the possible threats, it is necessary to understand how hydrogen is produced, how it is transported and mixed within containment, and how it combusts.

The objectives of this program are (1) to quantify the threat to nuclear power plants (containment structure, safety equipment, and the primary system) posed by hydrogen combustion, (2) to disseminate information on hydrogen behavior and control, and (3) to provide programmatic and technical assistance to the NRC on hydrogen-related matters.

1.5.1 HECTR Analyses of the Second Part of the Standard Problem (C. C. Wong, 6427)

1.5.1.1 Introduction

Sandia developed the HECTR code primarily to analyze the transport and combustion of hydrogen during reactor accidents.[170,171] The Industry Degraded Core Rulemaking (IDCOR) program uses the Modular Accident Analysis Program (MAAP) code[172] to perform similar analyses. Both of these codes are lumped-parameter codes, but they differ in the way that various phenomena are modeled, especially in the areas of (1) ignition criteria, (2) flame propagation criteria, (3) burn time, (4) combustion completeness, (5) continuous in-cavity oxidation of hydrogen and carbon monoxide, and (6) natural circulation. These differences will give different predictions of pressure and temperature loadings imposed on the containment and equipment by the accumulation and combustion of hydrogen and CO during a severe accident. We are trying to determine the impact of these differences and to assist the NRC in determining the acceptability of the models for performing risk assessments.

A standard problem has been defined to compare HECTR and MAAP analyses of hydrogen transport and combustion in a nuclear reactor containment to assist in the resolution of differences between the NRC and IDCOR on the hydrogen combustion issue. The problem selected is an S2HF accident sequence in a PWR ice-condenser containment, Figure 1.5-1.[173] HECTR analyses of the first part of the problem has been presented in Reference 101. In this report, the second part of the problem, which addresses the two phenomena of natural convection and continuous in-cavity oxidation, will be discussed.

1.5.1.2 Description of the Problem

For nuclear power plants and accident sequences in which the reactor cavity is dry, the temperatures of the reactor cavity atmosphere and structures following vessel failure may be sufficiently high to promote in-cavity oxidation of combustible gases produced by core-concrete interactions. Specifically, hydrogen and carbon monoxide may react with available oxygen near the heated structures to form steam and carbon dioxide. Complete in-cavity oxidation would prevent any accumulation and subsequent combustion of hydrogen and carbon monoxide in the lower and upper compartments, and the probability of early containment failure due to combustion would be minimal. However, the degree of in-cavity oxidation will be limited by the rate at which oxygen is transported into the reactor cavity region

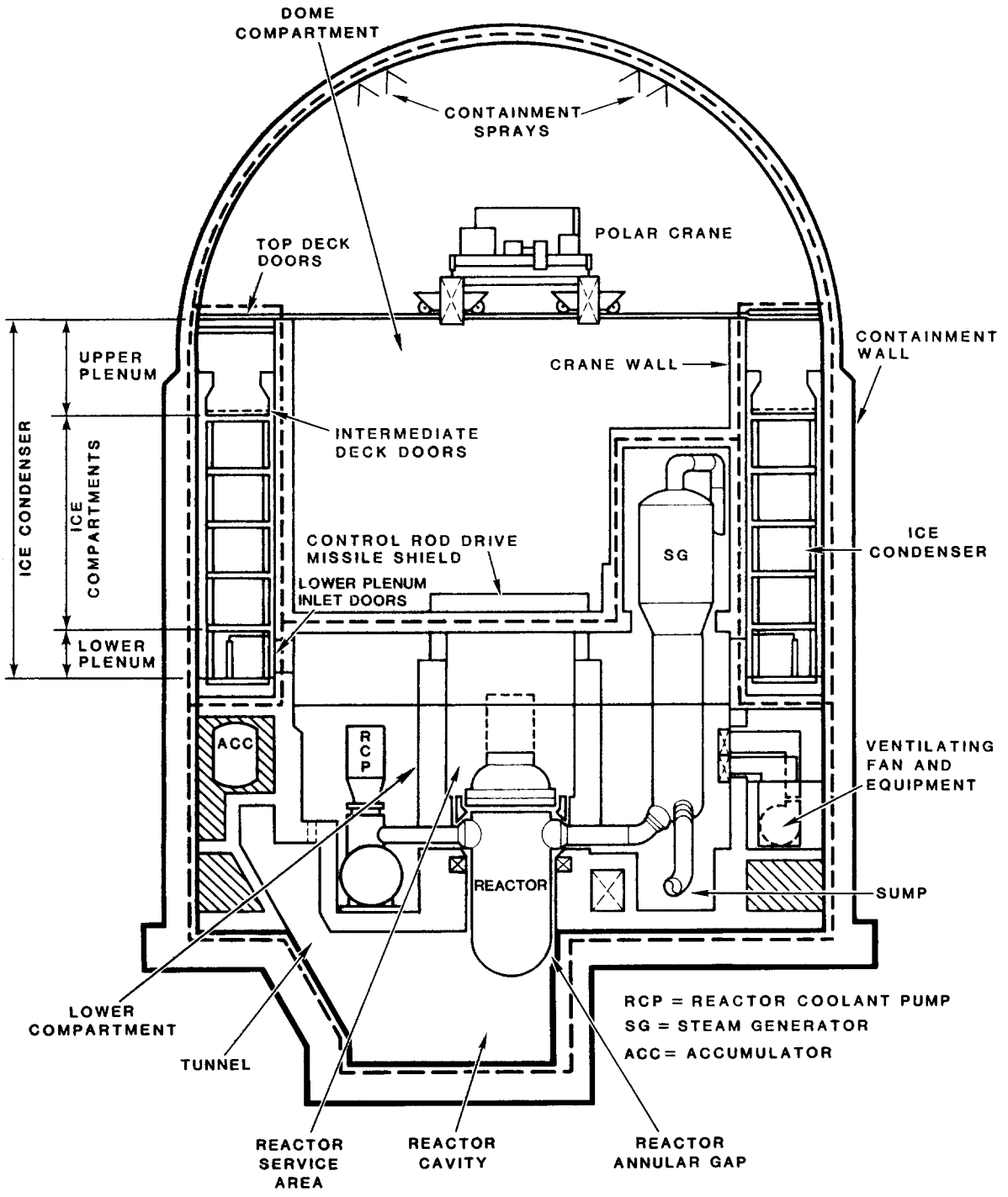

Figure 1.5-1. Simplified Diagram of Ice-Condenser Containment

(relative to the rate at which combustible gases are produced) or may be precluded by high steam concentrations or low temperatures in the reactor cavity that may exist in flooded-cavity sequences. Most affected by this in-cavity oxidation phenomenon are sequences in large dry, ice-condenser and Mark III containments in which both the reactor cavity is dry and the igniter systems are unavailable.

In the MAAP analysis of the problem,[174] a complete in-cavity oxidation was predicted. This prevented any accumulation and subsequent combustion of combustible gases in the upper and lower compartments. However, in the HECTR analyses of the in-cavity oxidation problem, we have found that the in-cavity oxidation process is limited by the rate at which oxygen is transported into the reactor cavity region. Accumulation and subsequent combustion of hydrogen and carbon monoxide in the upper and lower compartments generate a peak pressure of 384 kPa (56 psig) at 7.4 h. Hence we conclude that assuming a complete in-cavity oxidation is overly optimistic because a variety of phenomena, such as steam inerting and oxygen transport by natural convection, may influence the degree of the in-cavity oxidation that takes place.

1.5.1.3 In-Cavity Oxidation Process

To better understand the in-cavity oxidation process, two key phenomena need to be addressed in detail: (1) spontaneous ignition and (2) diffusion-flame structure. The spontaneous ignition of a combustible mixture without any ignition source requires a high temperature.[175] The bulk gas temperature in the cavity has to be above a critical temperature, known as the autoignition temperature, above which molecules possess sufficient energy for the chemical reaction to become self-propagating and lead to flaming combustion.[176] A self-propagating combustion is a thermal runaway process when the rate of energy gain due to the chemical exothermic reaction is greater than the combined rate of energy losses. These losses include energizing more fuel-oxygen molecules to form activated complexes plus the heat loss to the surroundings including the nonreactive molecules. For hydrogen and carbon monoxide in dry air at normal atmospheric pressure, the lowest autoignition temperatures measured are 833 and 878 K, respectively.[176] Autoignition temperature, however, depends on many parameters such as pressure, temperature, catalysts, oxygen, and inert gas concentrations.

During a severe accident such as S2HF, heat released from the molten core, which has slumped onto the floor of the reactor cavity after the vessel breach, and heat from molten metal-water and molten metal-carbon dioxide reactions may be sufficient to initiate a spontaneous ignition, depending on the initial and boundary conditions.[177] However, whether this spontaneous ignition will be stable as a continuous combustion process is very difficult to determine. Substantial amounts of steam and carbon dioxide are also generated during core-concrete interactions. This provides a significant heat sink capacity such that a self-propagating combustion may be suppressed. Hence complete in-cavity oxidation may not occur. In order to achieve a better understanding of in-cavity oxidation, the steam-inerting effect on a combustible mixture at high temperature

needs to be studied. At present, the flammability limits of a hydrogen:air:steam:carbon monoxide:carbon dioxide mixture at high temperatures have not been well established because of insufficient experimental data.[175,178]

Once the in-cavity oxidation begins, both HECTR and MAAP assume an instantaneous one-step chemical reaction. The comprehensive structure and characteristics of the diffusion flame are not modeled. Hydrogen and carbon monoxide molecules react with oxygen molecules to form steam and carbon dioxide molecules, respectively, as soon as they are released to the environment. In reality, the gas mixture released from core-concrete interactions will rise up as a plume. The oxidation of combustible gases will carry on in the outer mixing-layer of the plume as a diffusive type of flame, and its rate is controlled by the relative rate of diffusion of oxygen into the flame. An insufficient supply of oxygen for reaction or adding steam to the atmosphere will elongate the flame.[179] High steam-content environment is very likely to occur during core-concrete interactions. Hence the flame will probably be longer and may exceed the height of the cavity and extend out into the tunnel, Figure 1.5-2. If there is not sufficient oxygen for reaction, the flame will probably be extinguished at the tip of the plume. This will result in an incomplete in-cavity oxidation of hydrogen and carbon monoxide. Other considerations like the instability of flame, which may also prevent a complete in-cavity oxidation, have not been addressed.

Since our objective is to study the impact of in-cavity oxidation on containment loadings and HECTR does not model such a complex phenomenon in detail, we have performed parametric studies and bounding calculations. A 12-compartment model has been set up and bounding calculations have been performed such that (1) incomplete in-cavity oxidation will take place if there is insufficient oxygen (less than 5 percent) to support in-cavity oxidation or excess steam (more than 55 percent) to inert the environment or (2) complete in-cavity oxidation will occur if sufficient oxygen exists in the reactor cavity (Part I in Table 1.5-1). The criteria used in the first bounding calculation are based on the results of experiments to study the flammability of hydrogen:air:steam at a temperature less than 400 K.[178,180,181] At a higher temperature (more than 800 K) the flammability limits will probably expand and cover a larger range; hence using the limits at a lower temperature is a conservative approach. On the other hand, excluding the effect of steam inerting would be an optimistic approach.

The results of the bounding calculations showed that in both cases combustible gases built up in the lower and upper compartments, which led to one or more global burns. These burns were all initiated in the lower compartment and eventually propagated into the upper compartment. Each of these global burns generated a substantial peak pressure above 285 kPa (41 psig).

In the first HECTR calculation (Case a of Part I in Table 1.5-1), the problem was set up such that in-cavity oxidation would take place as long as the oxygen concentration was above 5 percent and the steam plus CO_2 concentration was less than 55 percent in the cavity. With these constraints, HECTR predicted that a high-steam concentration existed in the

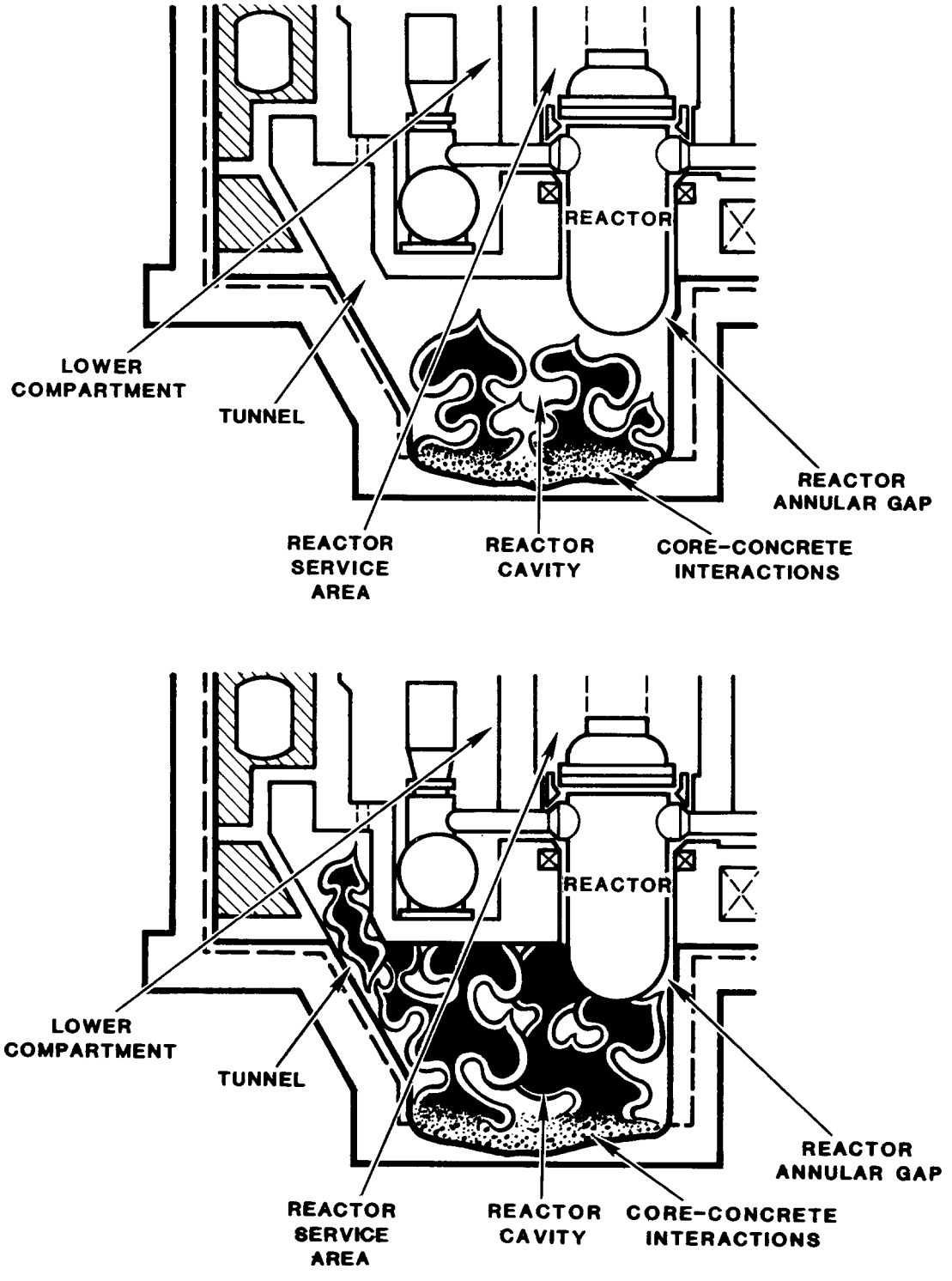

Figure 1.5-2. Schematic of In-Cavity Oxidation; (Top) Complete Oxidation, (Bottom) Incomplete Oxidation

cavity at 5.29 h and it terminated the in-cavity oxidation at this time. Because of this steam inerting effect, HECTR estimated that less combustible gases would be reacted in the cavity and more combustible gases would build up in the lower and upper compartments. Three global burns were predicted, and their corresponding peak pressures were 285 kPa (41 psig) at 6.32 h, 371 kPa (54 psig) at 6.98 h, and 411 kPa (60 psig) at 9.12 h, respectively, Figure 1.5-3.

The second case (Case b of Part I in Table 1.5-1) was set up such that the steam inerting effect on in-cavity oxidation would be neglected. By neglecting steam inerting, more combustible gases would be reacted in the cavity. However, HECTR predicted that insufficient oxygen was transported into the cavity from the lower compartment to support complete in-cavity oxidation after 5.56 hours. Continuous oxidation still occurred in the cavity after this time, but less complete. Combustible gases reacted with oxygen when it was available in the cavity. Since not all combustible gases reacted in the cavity, they accumulated in the lower and upper compartments. Ignition occurred at 7.36 hours and generated a peak pressure of 384 kPa (56 psig), Figure 1.5-4.

What the bounding calculations have shown is that, even without any detailed modeling of the chemistry and diffusion-flame structure, for the given conditions, combustible gases are predicted to accumulate in the lower and upper compartments. This eventually leads to ignition in the lower compartment and flame propagation to the upper compartment. HECTR results also imply that the effect of steam inerting can be very important under certain conditions; it was relatively minor for these calculations because the rate of the in-cavity oxidation was controlled by the rate at which oxygen was transported into the cavity. The only difference between the two bounding calculations was that repetitive burns were predicted in the lower and upper compartments when steam inerting was considered instead of a single burn. However, the outcome could be totally different if there were sufficient oxygen in the reactor cavity to support a complete oxidation. For the case considering the steam inerting effect, in-cavity oxidation would be terminated by the excess amount of steam that existed in the reactor cavity. For the case neglecting the steam inerting effect, a complete in-cavity oxidation would occur. Accumulation and subsequent combustion of hydrogen and carbon monoxide would not be predicted in the upper and lower compartments. Hence the difference would be substantial; the calculated peak pressure would be much higher for the case including the steam inerting effect, 411 versus 250 kPa. In summary, the effect of steam inerting on in-cavity oxidation cannot be totally neglected.

1.5.1.4. Natural Convection

As discussed in Section 1.5.1.3, the rate of the in-cavity oxidation can be controlled by the rate of oxygen being transported into the reactor cavity region. Buoyancy-driven flow is the dominant gas transport mechanism between the reactor cavity and the lower compartment. During the period of core-concrete interactions and in-cavity oxidation, a hot mixture of combustion products and steam rises up through the tunnel into the lower compartment. To complete the natural recirculation loop, cooler air is

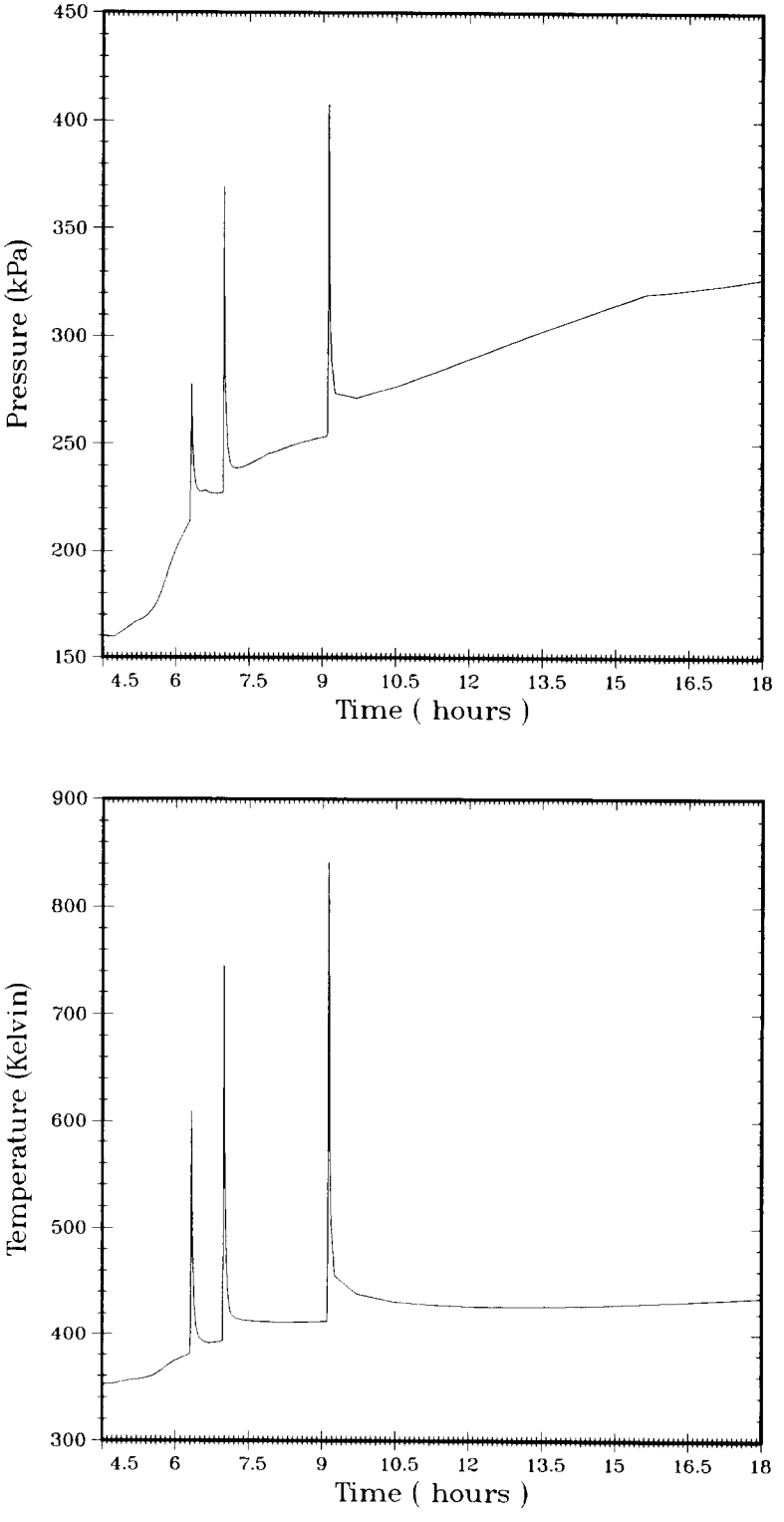

Figure 1.5-3. Pressure and Temperature Responses in the Upper Compartment Predicted by HECTR (Conditions for In-Cavity Oxidation: $O_2 \geq 5\%$ and Steam $\leq 55\%$)

Table 1.5-1

Criteria for Recombination in the Reactor Cavity
Used in HECTR Analyses

Case Description	Mole Fraction			
	Completeness	Combustible Gases (H_2+CO)	O_2	Diluents (H_2O+CO_2)
Part I				
a. 12-Compartment Model	100%	> 0%	> 5%	< 55%
b. 12-Compartment Model	100%	> 0%	> 0%	< 100%
Part II				
a. 12-Compartment Model	100%	> 0%	> 0%	< 100%
b. 6-Compartment Model	100%	> 0%	> 0%	< 100%

entrained down into the cavity through the reactor annular gap. Since HECTR and MAAP use the lumped-volume technique, the choice of noding system becomes very important in determining the natural circulation flow rate.

The recirculation flow between the reactor cavity and the lower compartment is primarily driven by the density gradient along the flow path. The hot gas mixture (steam, hydrogen, carbon monoxide, and carbon dioxide) escapes through the tunnel into the lower compartment. Cold air is entrained into the cavity from the reactor service area through the annular gap between the reactor vessel and the shielding concrete. Since the air-return fans are operating in the S2HF accident sequence, the hot plume rises up along the forced-convection flow path through the ice region into the upper compartment. This minimizes the mixing in the lower compartment. Hence it is important to model the lower compartment correctly. In MAAP, a single control volume is used to represent the lower compartment. Setting up the noding system in this way introduces an artificial, instantaneous mixing mechanism within the lower compartment. Since the natural circulation flow rate depends on the density gradient along the flow path, the resulting inaccurate density distribution leads to an inaccurate prediction of the flow rate.

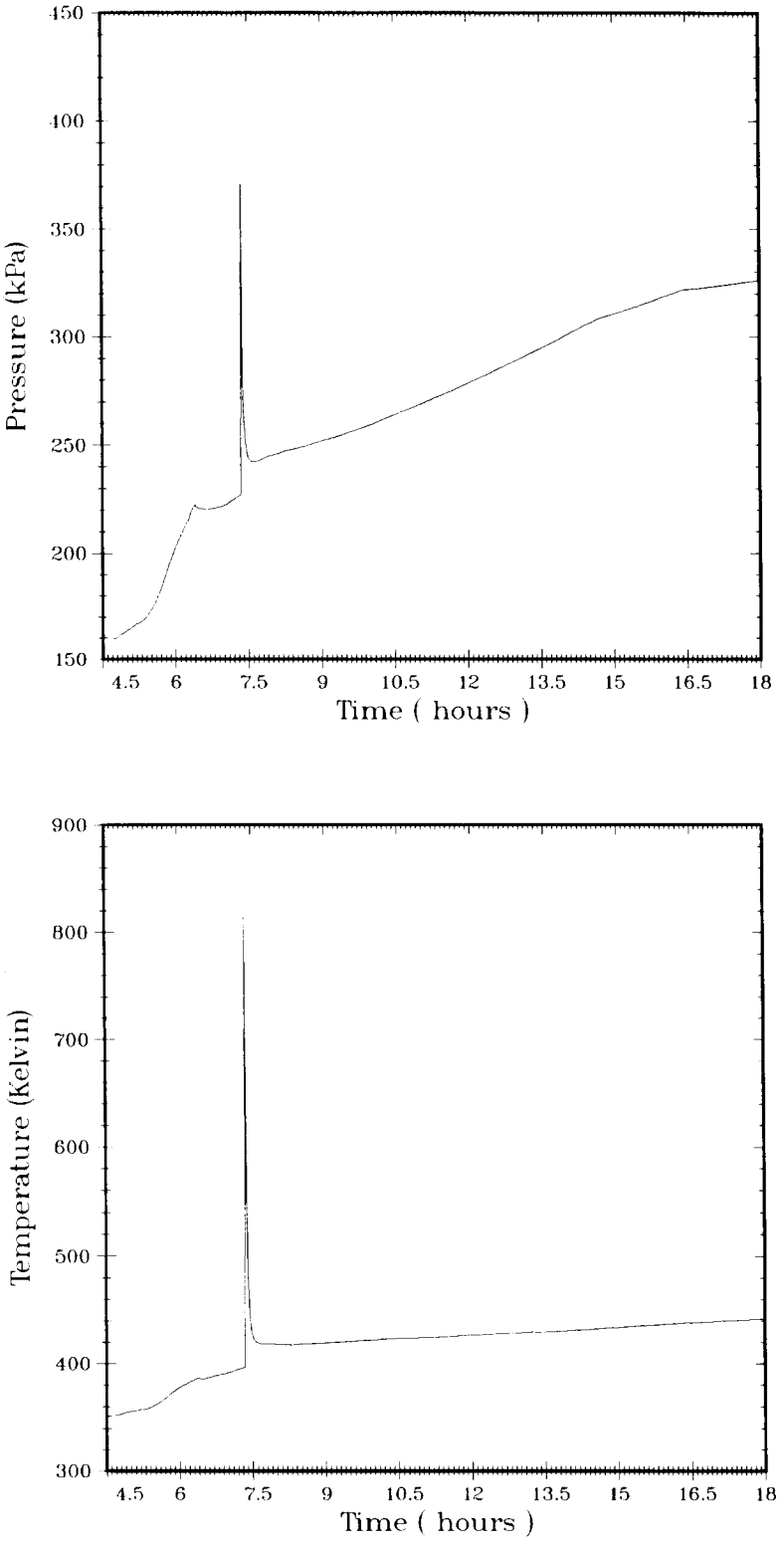

Figure 1.5-4. Pressure and Temperature Responses in the Upper Compartment Predicted by HECTR (Conditions for In-Cavity Oxidation: $O_2 \geq 0\%$)

Using a 12-compartment model, which has five control volumes representing the lower compartment, Figure 1.5-5, HECTR predicted that when in-cavity oxidation was taking place, the temperature and density distributions in the lower compartment were not uniform, Figure 1.5-6. The region near the exit of the tunnel (control volume 3) was the hottest, while the other region in the lower compartment (control volumes 5 and 6) was relatively cool. Thus, along the natural-circulation flow path, the density gradient in this case was smaller than the case with uniform density distribution in the lower compartment.

In the 6-compartment model, Figure 1.5-5, a single control volume was used to represent the lower compartment. This implied uniform temperature and density distributions within the lower compartment, and it produced a higher density gradient along the flow path. As a result, a higher natural circulation flow rate was predicted, Figure 1.5-7. A larger flow rate between the lower compartment and the reactor cavity provided sufficient oxygen to support complete in-cavity oxidation. Since most of the combustible gases were reacted in the cavity, no accumulation of the combustible gases in the lower and upper compartments was calculated at the early stage of transient (i.e., 3 h after the vessel breach.) Later, after most of the oxygen in the containment had been depleted, combustible gases started to accumulate. Without any discrete burning in the lower and upper compartment, the pressure gradually increased to 332 kPa (48 psig) at the end of the problem, about 18 h, Figure 1.5-8.

In summary, HECTR analyses using 6- and 12-compartment models show the importance of using proper compartment nodalization. Use of too few compartments yields inaccurate gas transport information; however, too many compartments can lead to a long code execution time and higher cost. To determine the natural circulation loop between the lower compartment and the reactor cavity, a single control volume representing the lower compartment is not sufficient. In our analyses, HECTR predicted a different result from a multicontrol volume model. By using a single control volume to represent the lower compartment as in MAAP, a substantial natural convective flow between the cavity and lower compartment was calculated. This natural convective current provided sufficient oxygen into the cavity to sustain complete in-cavity oxidation. Hence no accumulation and subsequent combustion of combustible gases in the upper and lower compartments were calculated, and there was no early threat to containment integrity. However, when five control volumes were used to represent the lower compartment, HECTR predicted that the condition in the lower compartment was not well mixed. In addition, the natural convective current into the cavity was lower than the prediction of the model using a single control volume representing the lower compartment. As a result, there was not sufficient oxygen in the cavity to sustain a complete in-cavity oxidation. This led to a buildup of combustible gases in the upper and lower compartment. At 7.4 h into the transient, a severe burn was initiated in the lower compartment and propagated into the upper compartment. This global burn generated a peak pressure of 384 kPa (56 psig), which the model using a single control volume representing the lower compartment and MAAP[174] did not predict. This pressure compares to the failure pressure for an ice-condenser containment at about 448 kPa (65 psig).

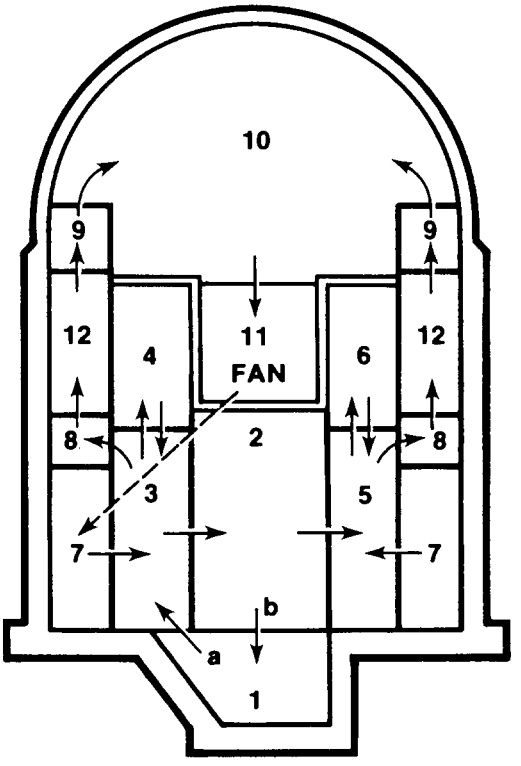

12-COMPARTMENT MODEL

COMPARTMENT DESCRIPTORS	ID NUMBER
UPPER COMPARTMENT	10, 11
UPPER PLENUM	9
LOWER PLENUM	8
LOWER COMPARTMENT	2, 3, 4, 5, 6
DEAD-ENDED REGION	7
ICE COMPARTMENT	12
REACTOR CAVITY	1

JUNCTION DESCRIPTORS	ID NUMBER
TUNNEL	a
REACTOR ANNULAR GAP	b

6-COMPARTMENT MODEL

COMPARTMENT DESCRIPTORS	ID NUMBER
UPPER COMPARTMENT	5
UPPER PLENUM	4
LOWER COMPARTMENT	2
DEAD-ENDED REGION	3
ICE COMPARTMENT	6
REACTOR CAVITY	1

JUNCTION DESCRIPTORS	ID NUMBER
TUNNEL	a
REACTOR ANNULAR GAP	b

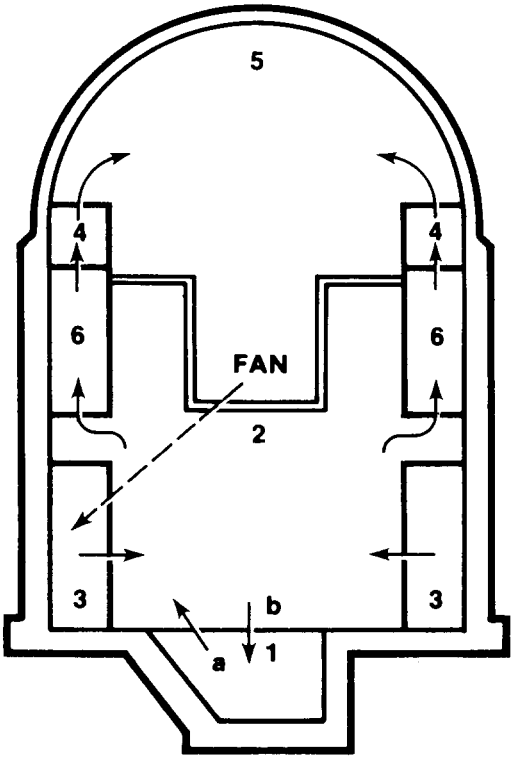

Figure 1.5-5. Containment Noding Systems Used in HECTR Analyses and Flow Directions at the Junctions During the Period of In-Cavity Oxidation Predicted by HECTR (12-Compartment Model Versus 6-Compartment Model)

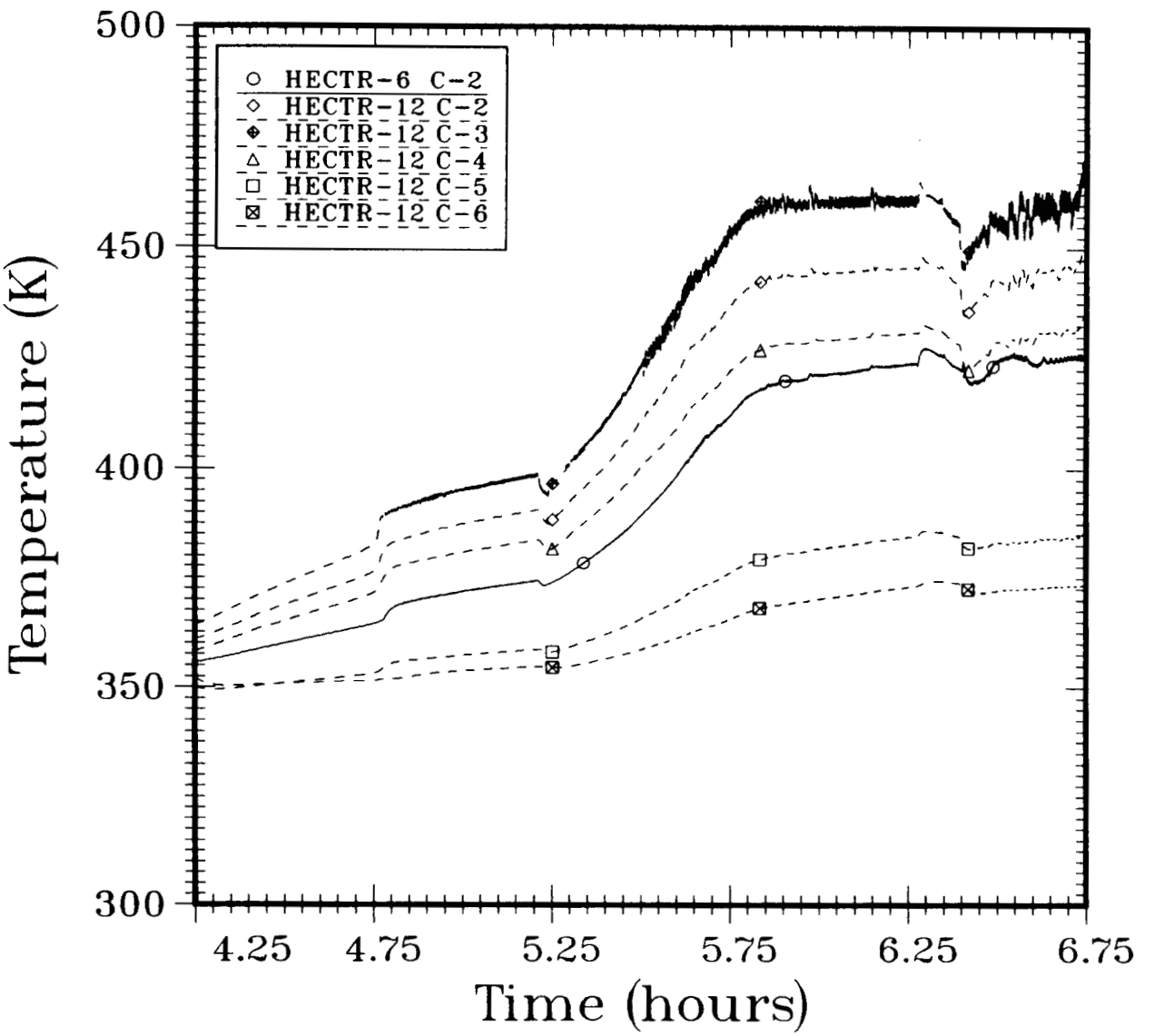

Figure 1.5-6. Temperature Distributions in the Lower Compartment Predicted by HECTR (12-Compartment Model Versus 6-Compartment Model; Conditions for In-Cavity Oxidation: $O_2 \geq 0\%$)

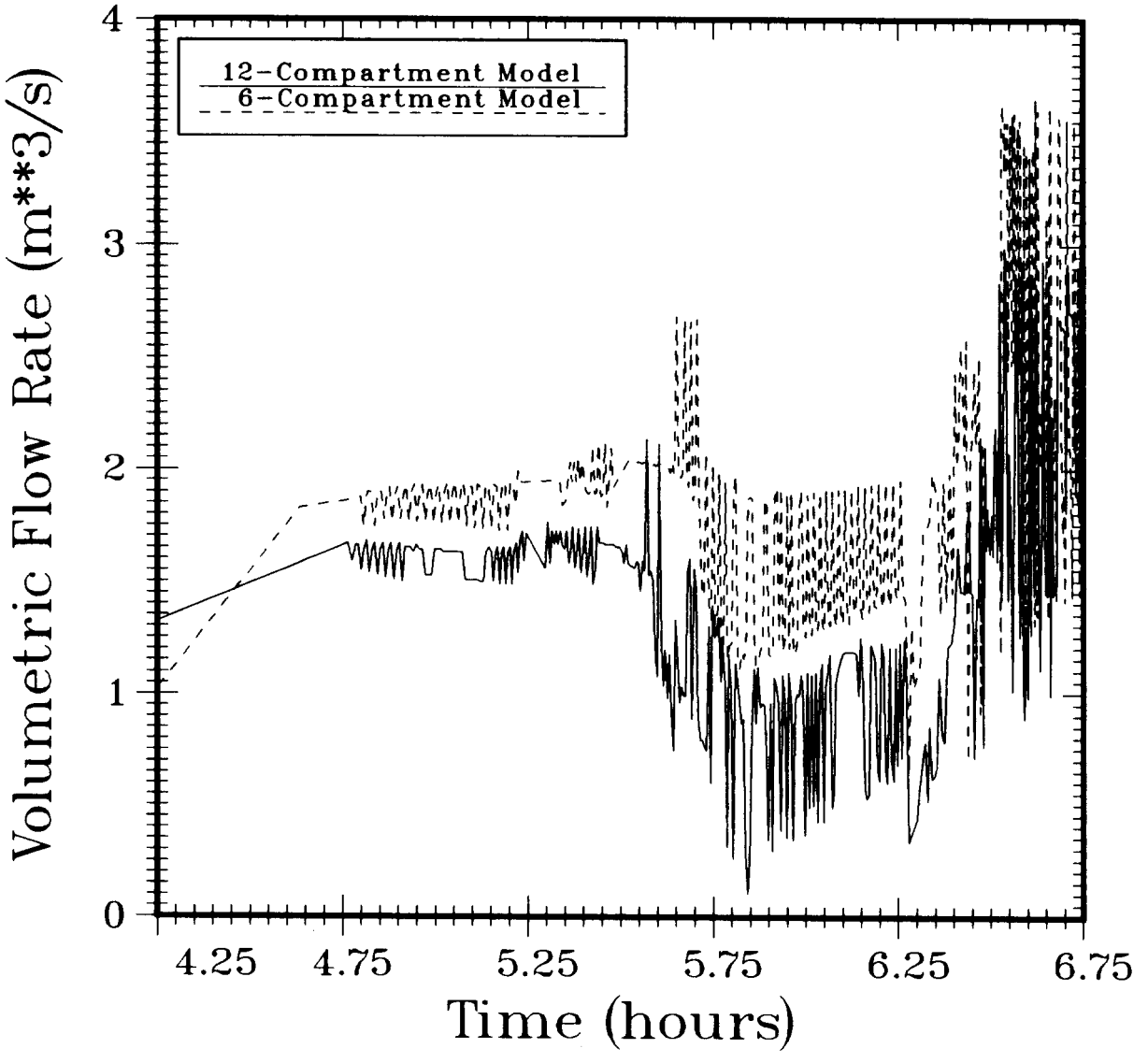

Figure 1.5-7. Gas Flow Rate Through the Junction at the Reactor Annular Gap (12-Compartment Model Versus 6-Compartment Model; Flow Direction Is From the Lower Compartment to Reactor Cavity)

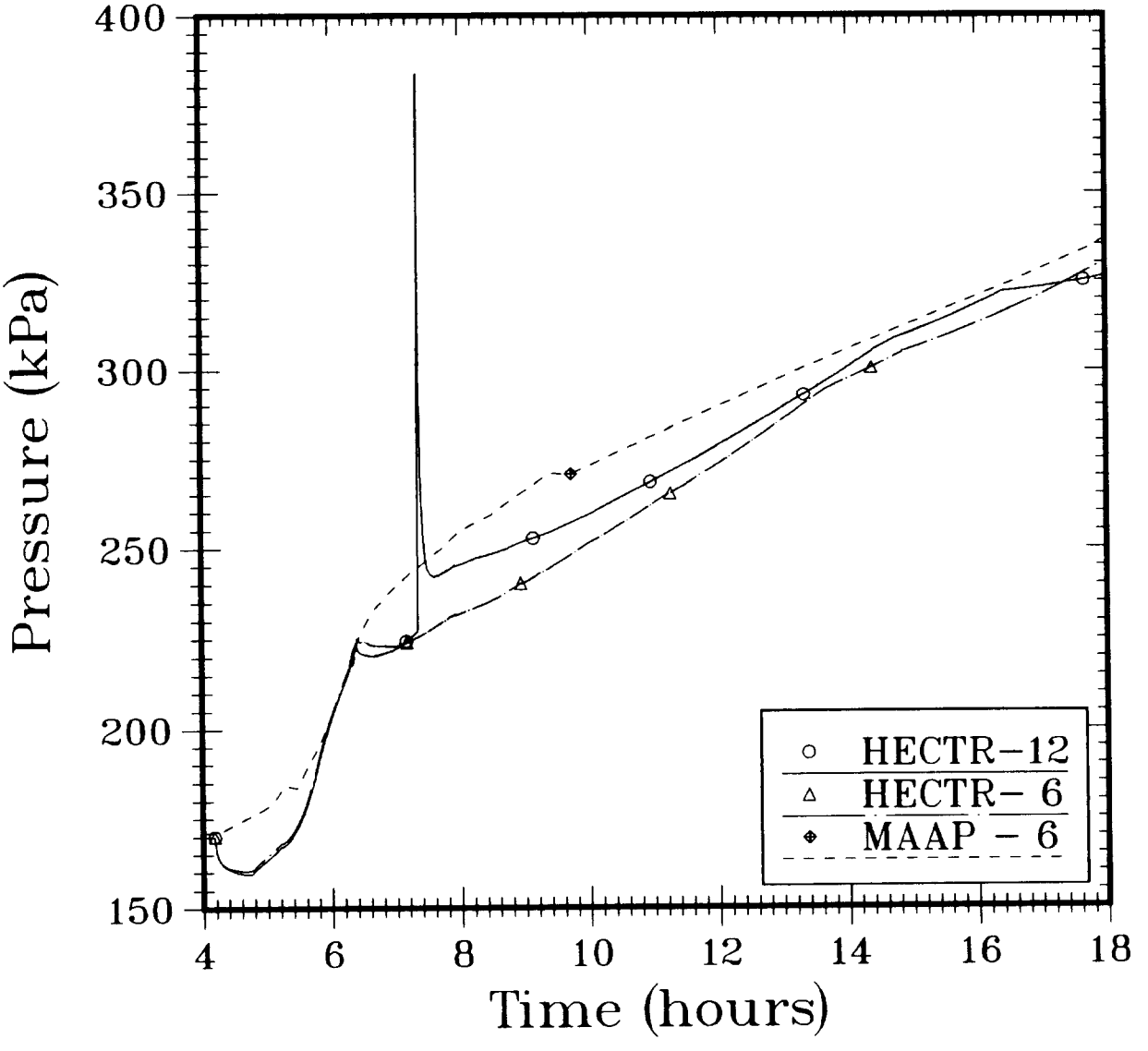

Figure 1.5-8. Pressure Response in the Upper Compartment Predicted by HECTR (12-Compartment Model Versus 6-Compartment Model; Conditions for In-Cavity Oxidation: $O_2 \geq 0\%$)

1.5.1.5 Conclusions

HECTR analyses of the containment responses of an ice-condenser plant for an S2HF drain-closed-accident sequence have shown that assuming a complete in-cavity oxidation may be overly optimistic because a variety of phenomena may occur, which will reduce the degree of in-cavity oxidation that takes place. Bounding calculations were performed to consider the effect of uncertainty in modeling some of these phenomena (e.g., steam inerting).

The effect of steam inerting could be very important under certain conditions, even though HECTR results of two bounding calculations did not directly prove it. For example, if there is sufficient oxygen being transported into the reactor cavity to support complete oxidation of the combustible gases, the effect of steam inerting would become important. For the case ignoring the steam inerting effect, a complete in-cavity oxidation would be predicted and no accumulation and subsequent combustion of hydrogen and carbon monoxide would happen in the upper and lower compartments. However, for the case including the steam inerting effect, an incomplete in-cavity oxidation and a global burn could occur. This would lead to a much higher peak pressure than the case excluding the effect, 411 versus 250 kPa. Thus the steam inerting effect could be substantial.

It is very important to model the lower compartment correctly. Using a single control volume to represent the lower compartment, HECTR overpredicted the natural convective flow between the cavity and lower compartment and predicted complete in-cavity oxidation. However, using five control volumes to represent the lower compartment, HECTR results show that the lower compartment was not well mixed and the natural convective current into the cavity was lower than the prediction of the case with one control volume representing the lower compartment. An incomplete in-cavity oxidation was predicted. This led to an accumulation and subsequent combustion of combustible gases in the upper and lower compartment at 7.4 h. This global burn generated a peak pressure of 384 kPa (56 psig), that the single-volume model did not predict.

1.5.2 Modeling of Large-Scale Flame Acceleration Experiments
(K. D. Marx, 8363)

The formulation of a new computational model for large-scale flames has been completed. It has been applied to the simulation of flame acceleration experiments. The primary objective was to circumvent the necessity for resolving turbulent flame fronts on the relatively coarse computational grids that are necessary in engineering calculations. The essence of the model is to artificially thicken the flame by increasing the appropriate diffusivities and decreasing the combustion rate, but to do this in such a way that the burn velocity and flame thickness varies with pressure, temperature, and turbulence intensity according to prespecified phenomenological characteristics. The model is particularly aimed at implementation in computer codes that simulate compressible flows. In this work, an appropriate modification of the CONCHAS-SPRAY code[182] is used. It has been applied to the two-dimensional simulation of hydrogen-air flame acceleration experiments in which the flame speeds and gas flow velocities approach the speed of sound in the gas. It has been shown that many of the features of the flame trajectories and pressure histories in the experiments are simulated quite well by the model.

The simulation of combustion processes in large experiments presents extreme demands on the capabilities of even the largest and fastest computers. In the problems considered here, it is necessary to give up the idea of resolving the flame thickness on the computational grid. We must artificially thicken the flame so that the flame thickness is equal to a few grid spacings.

Such flame thickening has been done previously by a method known as the the β-transformation,[183] which involves changing the length scales in the problem by artificially increasing the thermal diffusivity and diffusion coefficient and decreasing the combustion rate. We have retained this essential idea. However, the original β-transformation did not work well with mixing-limited combustion models such as the Magnussen-Hjertager[184] model. Hence, it was decided to effect the flame thickening in a different way. It is desirable that the burn velocity vary realistically with flow parameters such as turbulence intensity, pressure, and temperature. Our model represents an attempt to adhere to properties of turbulent flames given, for example, in Reference 185.

The approach used in this work is to endow the gas with minimum values of turbulent kinetic energy, k, and turbulent length scale, L. These minimum values, denoted k_m and L_m, are used for the computation of thermal conductivity and diffusivity only. In that way, there will be minimum values of burn velocity and flame thickness.

The end result is a turbulent burn velocity, S_T, which approximately satisfies

$$S_T = \left(AS_L + B\sqrt{k} \right) p^m \, T_u^n \quad ,$$

where S_L is laminar flame speed, p is pressure, T_u is unburned gas temperature, and A and B are constants chosen on the basis of experimental data.

The specific configurations to which this work has been applied are experiments performed in the FLAME facility.[186] This facility consists of a reinforced concrete channel 2.44 m high by 1.83 m wide by 30.5 m long. A comparison of the results of one calculation with the corresponding experimental data taken for a mixture of 14.5 percent hydrogen in air is given in Figures 1.5-9 and 1.5-10.

Considering the size of the experiment and the complexity of the computational problem, the agreement is quite good. It will be noted that there are some significant discrepancies in the flame trajectory. To some degree, these must be viewed in light of the fact that the flame velocity is extremely sensitive to the burn velocity. (Because of the geometrical factors and the feedback loop involving gas flow velocities, turbulence intensities, and combustion rates, the dependence is nonlinear.)

At a time of about 250 ms into the calculation, the computed flame trajectory begins to exhibit rapid acceleration. Eventually, it

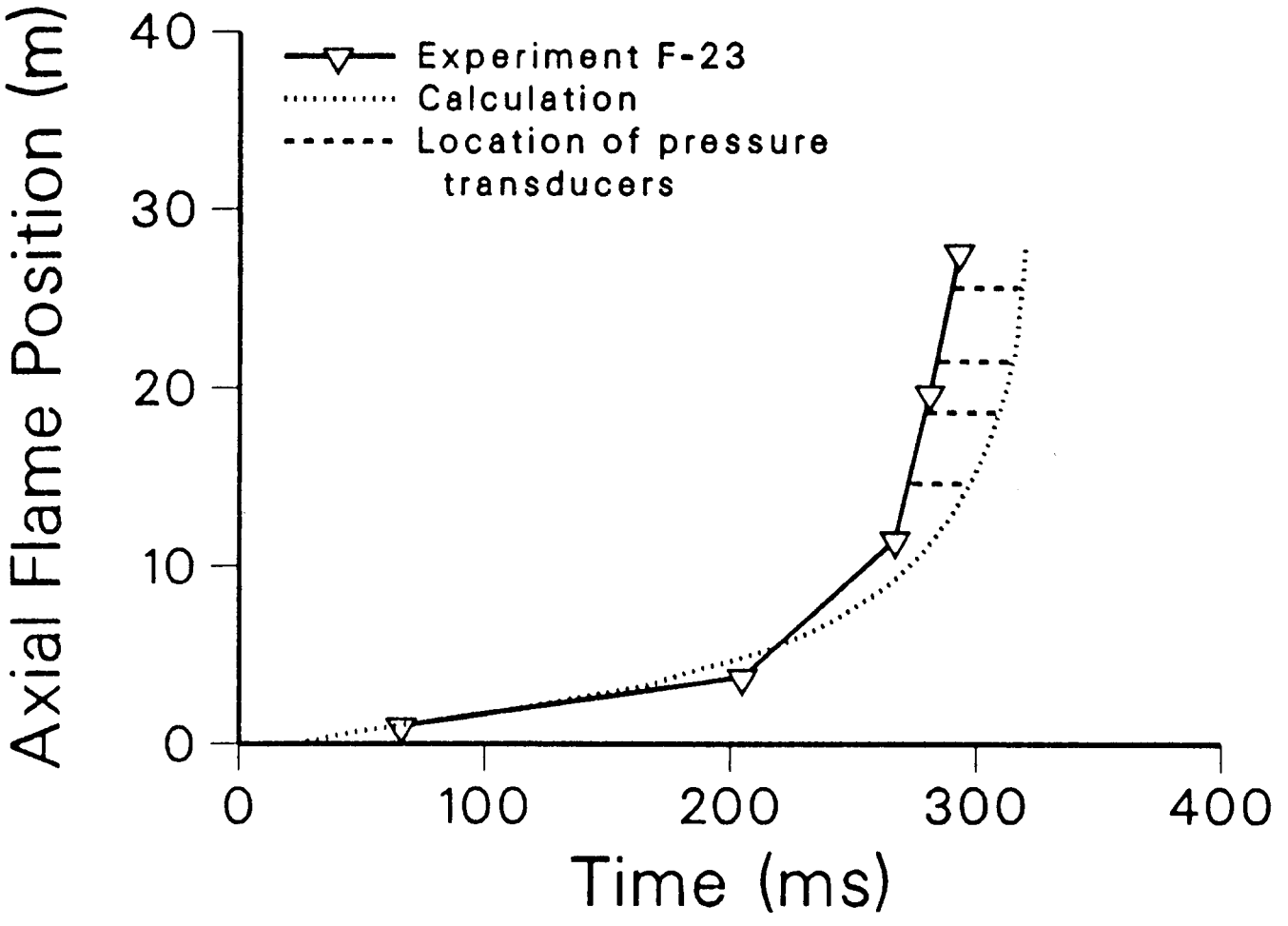

Figure 1.5-9. Comparison of Computed and Experimental Flame Trajectories for FLAME Experiment F-23. The experimental data have been shifted in time to facilitate comparison. (In view of the lack of a detailed simulation of ignition, the relative origins of the computational and experimental time scales is somewhat arbitrary.) The horizontal dotted lines show the location of the pressure transducers (at approximately 14.6, 18.6, 21.5, and 25.6 m down the channel) that provided the data discussed in Reference 187. (The complete array of experimental pressure data is not restricted to these locations.)

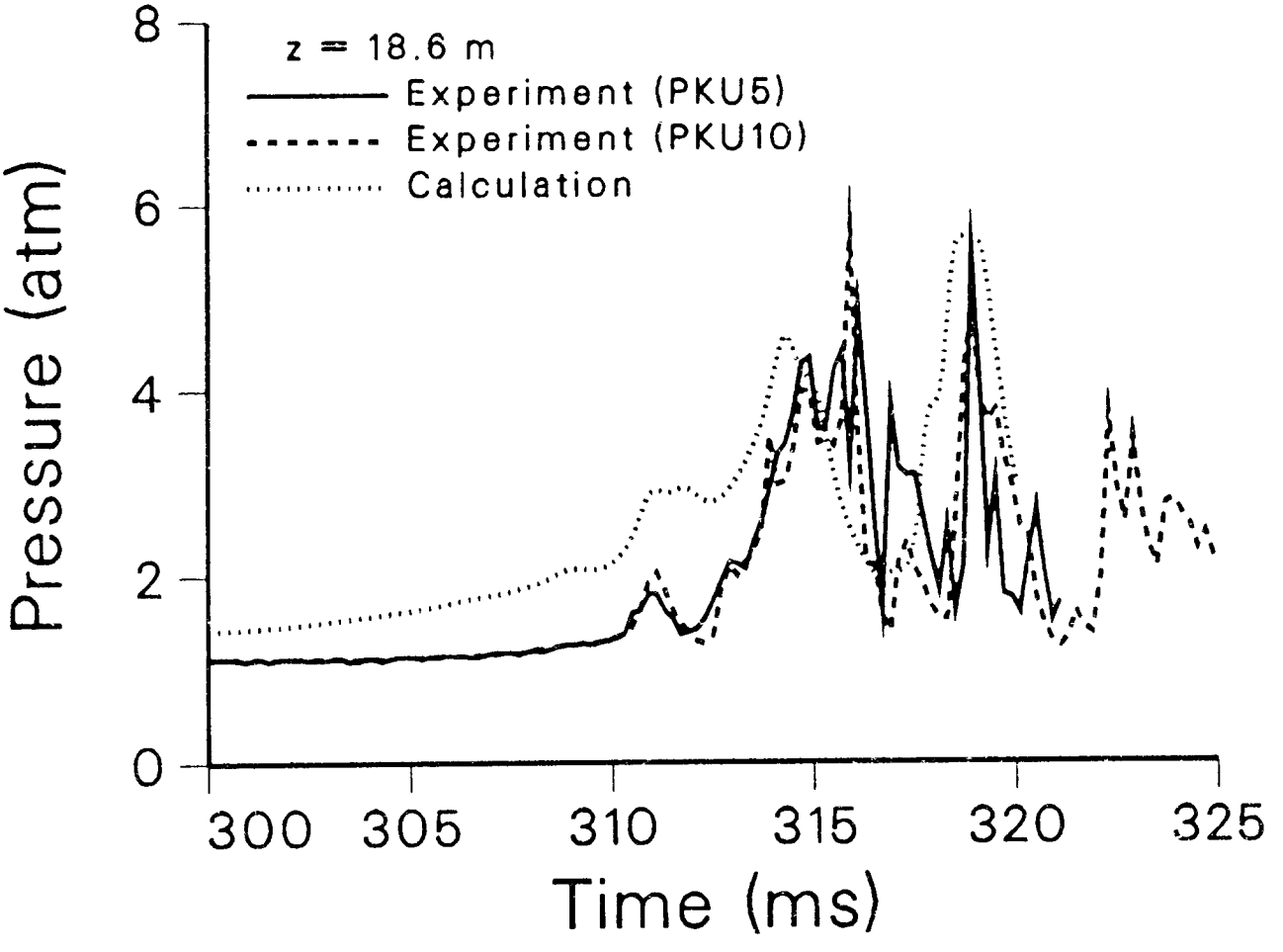

Figure 1.5-10. Pressure Histories at 18.6 m From the Calculation and From One of the Transducers in the Experiment. (See Figure 1.5-9 for a more precised description of transducer location.) As in Figure 1.5-9, the experimental signal has been shifted in time so that the times at which the flame passes the pressure transducer agree with that obtained from the computation.

essentially parallels that of the experiment, while the flame traverses through axial positions from about 17 through 23 m. In this region the computed pressures agree reasonably well with those measured experimentally. The reason for this is that the structure of the pressure history is characterized by the timing of the burnout of the gas in the successive chambers. The fact that the flame velocities approximately agree means that the chambers are burning out at about the correct rate. It should be noted that the flame velocity of about 500 ms is roughly the sound velocity in the burned gas. Since the gas flow velocities through the constrictions are of the same order of magnitude as the flame velocity, this is expected as a manifestation of choked flow.

Figure 1.5-11 shows the pressure in a series of three-dimensional plots over seven of the chambers at five different times. Because of the aforementioned choking, the flame is actually not accelerating rapidly at this time. However, the pressures are still rising rapidly. It is important to note the mechanism leading to this pressure rise. As the pressure wave propagates down the channel, it hits the obstacles. Reflection of these shocks off the front face of the obstacles results in a large increase in pressure and some shock heating. This increases the burn rate, which feeds back into an increase in the overall pressure level of the wave.

At 315 ms, the computation exhibits a deflagration to detonation transition (DDT). Note that a sharp pressure ridge has formed all the way across the channel in the uppermost plot in Figure 1.5-11, i.e., the pressure spike is not restricted to the region just in front of an obstacle.

Detonation was not observed experimentally at the concentration of 14.5 percent H_2 used in this calculation. However, it <u>was</u> observed at 15 percent H_2. The fact is that we do not claim to be able to simulate the detailed physical processes that occur in DDT. But it is reasonable to assume that the computed trends in pressure, temperature, and turbulence levels are indicative of real processes, and that what is being calculated is the evolution of a system that is progressing toward a tendency to detonate.

These computations point out the way in which the acceleration of the flame and its propagation in the choking regime are accompanied by large increases in the amplitude of pressure waves that reflect off the obstacles. This mechanism contributes to the positive feedback, which drives the flame acceleration in two ways: (1) It leads to an increased combustion rate by means of compression and shock heating; and (2) it produces increased turbulence through the generation of large flow velocities with high shear, thereby augmenting the thermal mixing. These increasing pressure and turbulence levels are also undoubtedly indicative of a buildup of sensitivity to detonation. This emphasizes the importance of a careful interpretation of experiments with regard to the degree of confinement of the gas, which has been well established experimentally. The results are consistent with a reduction in flame acceleration in the presence of pressure relief due to venting. (It is noted, however, that there is a potential for increased production of turbulence in the presence of partial venting, which remains to be investigated.)

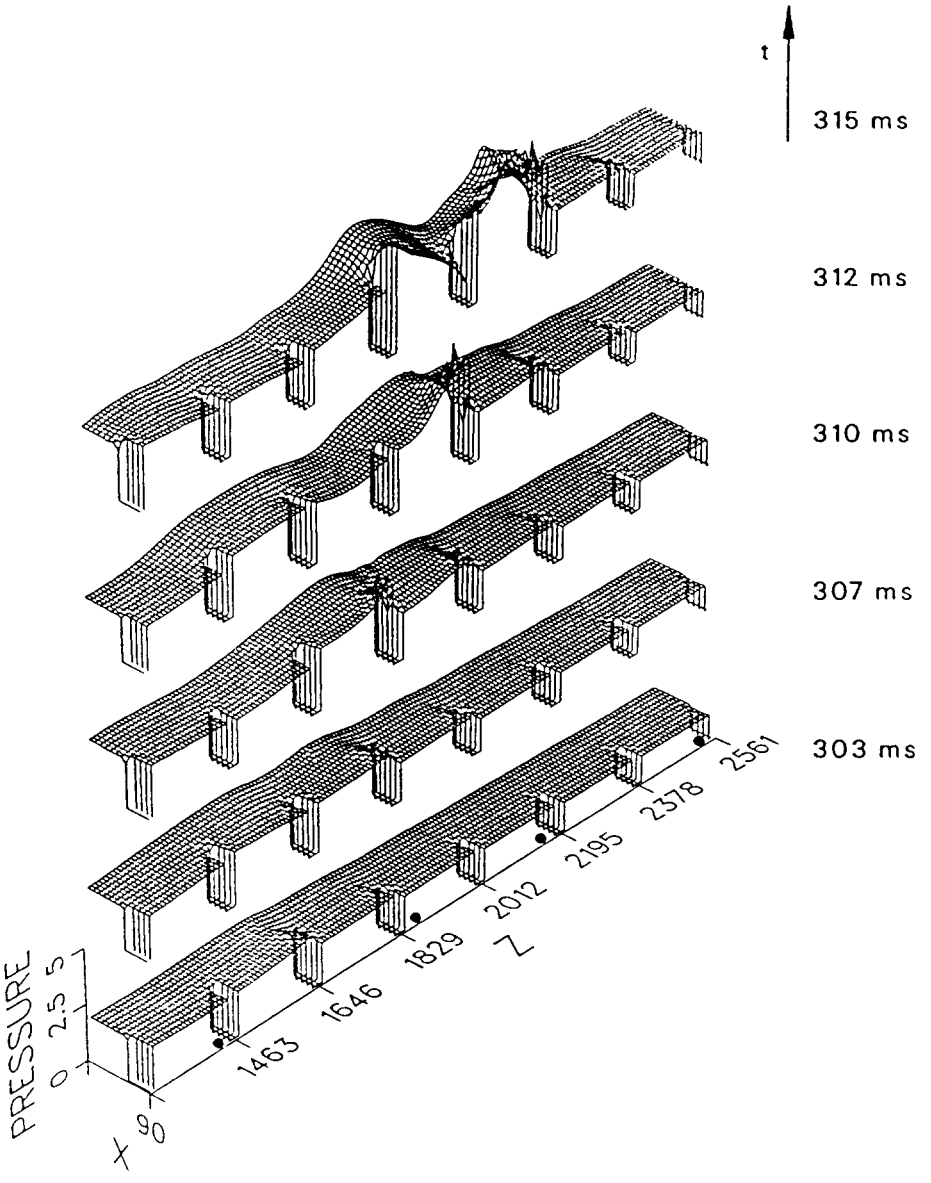

Figure 1.5-11. Three-Dimensional Plots of Pressure From the Calculation Shown in Figures 1.5-9 and 1.5-10. Only the region between the 7th through the 14th obstacles along the FLAME facility channel are shown. Coordinates are indicated in centimeters, and absolute pressure is given in atmospheres. The configuration has a symmetry plane at x = 0. The times corresponding to each plot appear on the right side of the figure. Axial positions of pressure transducers are indicated by bullets (•). (Note: The values of the pressure have been set equal to zero in the region occupied by the obstacles. This is done simply to make the obstacles easily identifiable; the pressure is actually undefined there.)

This work is described in detail in Reference 187. In summary, it contains two major contributions: the development of the numerical model and the use of the computer calculations to provide insight into the processes accompanying flame acceleration in experiments in the FLAME facility. It defines the attributes and limitations of current computational capabilities in this research area and suggests additional steps that could be taken to improve them.

1.5.3 Heated Detonation Tube

(D. W. Stamps, 6427; W. B. Benedick, 1131)

The Heated Detonation Tube (HDT), which is a cylindrical tube 13.1 m long and 0.43 m in internal diameter, is capable of being operated at temperatures up to 100°C. The purpose of the HDT program is to develop an experimental data base on hydrogen-air-steam detonability. These data can be used to develop models to assess the possibility of a detonation inside a reactor containment.

Work began on a new hydrogen-air-steam test series. Additionally, several changes have been made to improve the pressure transducer signals, the detonation cell images on the smoked foils, and the range of detonable mixtures capable of being tested in the HDT.

Because of the higher detonation pressures in the current and upcoming test series than in previous test series, an internal safety audit by the Safety, Health, and Environmental Appraisal Committee required the HDT be requalified for higher pressures with a hydrostatic pressure test. The higher detonation pressures result from the desire to determine the steam inerting concentration at the limit of detonation propagation. The concentration of steam that inerts the detonation will be determined for a total mixture pressure of one atmosphere and a mixture with an initial air density of 41.6 moles/m^3. The highest concentration of steam ever tested in the HDT was 30 percent on a molar basis in a mixture with an initial air density of 41.6 moles/m^3. The hydrostatic pressure test was completed successfully by the Pressure Safety Lab. In addition to the requalification, repair of weather-damaged power and signal lines and insulation was necessary before testing could begin.

A new technique for providing a more uniform soot coating on foils that record detonation tracts is being employed in the current test series. The new technique involves narrow trays that are filled with the fuel for smoking and placed under the foil that is located in a fume hood. The new technique provides a more uniform soot covering than the previous method of smoking foils by hand.

Improving cell contrast on the foil is a current area of effort. It was originally felt that a smooth, shiny surface would improve the contrast. However, the soot is removed from the slick surface as the detonation passes over the foil. The old method of coating the foil with silicone oil before smoking is necessary for the cells to be recorded, and better success is obtained using a roughened oiled surface. Ultimately, the foil with a shiny surface proves inferior to a foil with a matte finish when photographing the detonation cells for digital imaging processing

techniques. Reflections of the light sources and the camera from the shiny surface degrade the photographic negative used for digital imaging processing. From the data obtained with different foils, we conclude that a white matte finish on a foil with an oiled surface will provide the best contrast and the best negatives for digital imaging processing. Foils sprayed with a matte-white paint and a high-temperature matte-white paint have been tested with and without a silicone coating. In every case, no detonation cells were recorded because the soot adhered too well to the painted surface. We are currently exploring different coatings to obtain a surface that optimizes cellular contrast and photographic negatives used for digital imaging processing.

In an attempt to improve the pressure measurements from the HDT, new pressure transducer mounts are being tested in the current test series. In previous tests, only pressure transducer data have been used to determine the time-of-arrival of the detonation wave because some anomalies in the pressure signals make the determination of the actual detonation pressure difficult. These anomalies include noise prior to the arrival of the detonation wave at the gauge face, which is probably due to the gauge not being fully acceleration compensated, complex pressure variations as the detonation wave passes the gauge face, and what appears to be gauge resonant frequency noise after passage of the detonation wave. In the old mounts, the pressure transducer screws into the mount and is therefore directly coupled to it. In the new mounts, the pressure transducer and the mount are decoupled by an O-ring fitted sleeve surrounding the pressure transducer. The sleeves are composed of four different materials: brass, polycarbonate, nylatron GS, and polysulfone. The new mounts reduce the noise prior to the arrival of the detonation wave by roughly a factor of 3 to 5, and the performance of the mount appears to be independent of the sleeve material. The rest of the noise, however, is not reduced significantly. This suggests the gauge itself and not the mount may be responsible for the postdetonation noise.

Six tests, HT97-HT102, have been completed in the current hydrogen-air-steam series denoted as Test Series 8. The purpose of the current test series is to quantify the effect of steam concentration on hydrogen-air mixtures at 1 atm initial pressure and 100°C initial temperature. These initial conditions are at the lower range of initial conditions calculated in a local detonation study.* Test Series 8 is comprised of approximately 25 tests with most tests at 0, 10, 20, and 30 percent steam concentration on a molar basis. Theoretical predictions of the detonation cell width based on chemical kinetics and a ZND model[188] are shown in Figure 1.5-12. Some tests will be conducted at steam concentrations greater than 30 percent to determine the steam inerting level for the HDT. Of the six tests conducted, all have 0 percent steam concentration. The dominant cell recorded on the smoked foils agrees closely with the theoretical predictions. The dominant cell, however, is difficult to determine in many cases because of a well-defined substructure that is approximately 1/3, 1/2, or 2/3 the dominant cell width.

*Memo, S. R. Tieszen and D. W. Stamps, Sandia, to A. C. Peterson, Sandia, January 29, 1986.

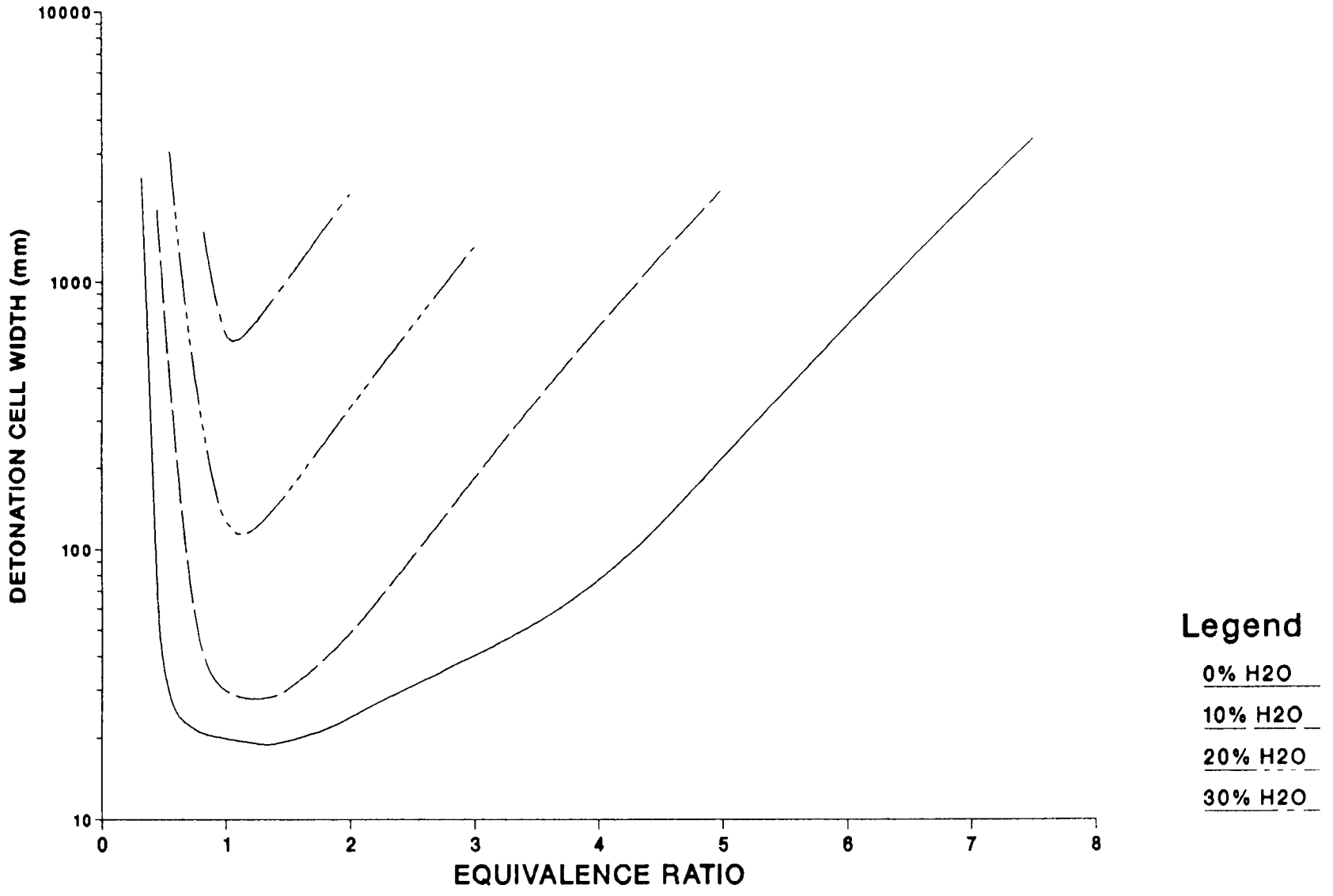

Figure. 1.5-12. Theoretical Predictions of the Detonation Cell Width as a Function of the Equivalence Ratio for Hydrogen-Air-Steam Mixtures at 1 atm Initial Pressure and 100°C Initial Temperature

1.6 Hydrogen Mitigative and Preventive Schemes

(L. S. Nelson and M. Berman, 6427)

The primary objective of the Hydrogen Mitigative and Preventive Schemes Program was to provide the NRC with information to evaluate proposed equipment concepts and operational schemes to prevent or mitigate the effects of hydrogen combustion during hypothetical LWR accidents. To provide this information, we investigated the operability and consequences of operation of deliberate ignition systems and their components during hypothetical hydrogen-producing accidents in nuclear power plants. In addition (and our sole effort during this reporting period), we investigated the capability of hydrogen burns to remove simulated structural and fission-product aerosols previously deposited on prototypical surfaces found in nuclear reactor containments. The Hydrogen Mitigative and Preventive Schemes Program was terminated as planned at the end of FY86; this discussion concludes the reporting of the program.

1.6.1 Experiments Related to the Resuspension of Aerosols During Hydrogen Burns

(Lloyd S. Nelson and Kenneth P. Guay, 6427)

1.6.1.1 Introduction

In a severe nuclear reactor accident in which fuel damage occurs, the radiological source term is governed in large part by the release of fission products to the environment as aerosols. In a number of hypothetical accident scenarios, these radioactive aerosols first would be dispersed throughout containment. Then, after a certain time interval, the containment might fail or be circumvented, permitting release of the aerosols to the environment. As the length of time prior to release increases, the concentration of suspended aerosols normally would be expected to decrease progressively because of the natural mitigative processes of deposition on surfaces within containment. Thus, if containment were to fail at some relatively late time, the radiological consequences would be reduced compared to early failure. Considerable experimental and theoretical effort[189] is being devoted to studying the mitigative effects of these normal aerosol deposition processes on the ultimate radiological source term.

The accident sequences by which the aerosols are originally generated prior to deposition are referred to as "primary" processes.[190] Under some circumstances, however, these aerosols may be removed from the surfaces and redispersed in the containment volume by means of "secondary" processes.[190] Some possible secondary processes are hydrodynamic flow (for example, in the blowdown of the reactor cooling system), the occurrence of fuel-coolant interactions in vessel, and violent depressurization of containment. Another process for resuspension, the action of large-scale hydrogen burns, has been investigated in a preliminary way here. Compared to the primary processes, little effort has been devoted to studying the secondary resuspension processes.

Recently, there have been unusual opportunities at Sandia to study the effects of large-scale hydrogen burns on aerosols. These involve the

studies of accelerating flames and deflagration-to-detonation transitions in experiments being performed in the large VGES-II[191] and FLAME[192] facilities. The direct study of resuspension of aerosols--namely, collection of once-sedimented aerosols after resuspension in the combusting gases--is not easy, however, especially if the effects of large scale are to be studied. Although this type of study would provide considerable information on the nature of the resuspended aerosol and its concentration, there are many factors that discourage resuspension studies in large-scale experiments; these include toxicity and inhalation hazards of the aerosol components to personnel, ecological effects, and the costs of fitting various aerosol generators and collectors to the large-scale experiments.

A less direct, but considerably simpler, scheme for investigating the resuspension of aerosols involves the removal of aerosols previously deposited on various small, prototypical, sample surfaces by exposure to the large-scale burns. Although these studies are not equivalent to resuspension studies, they can provide valuable information promptly and inexpensively for scoping the phenomena involved and for planning future in-depth experimentation.

We have recently performed seven "add-on" experiments in two large combustion facilities to investigate the capability of hydrogen burns to remove simulated structural and fission product aerosols previously deposited on small planchets--in these experiments, thick metal discs threaded around their edges--that have surfaces prototypical of those found in nuclear reactor containments. Our results suggest that hydrogen combustion provides an especially effective mechanism for removal (and, presumably, resuspension) of sedimented aerosols produced in a hypothetical nuclear reactor core-degradation or core-melting accident.

1.6.1.2 Experimental

Six experiments were performed in the FLAME facility at Sandia. This facility is a large horizontal U-shaped channel, 30.5 m long, 2.4 m high and 1.8 m wide, made of heavily reinforced concrete; a sketch is shown in Figure 1.6-1. It was designed to study hydrogen combustion problems relevant to nuclear reactor safety, for example, flame acceleration, transition to detonation, simulation of combustion in reactor containment geometries, etc. Various amounts of transverse venting are achieved by moving steel plates on the top. Obstacles can be attached to the walls and floor. Ignition is made at the closed end by a single-point bridgewire igniter, a weak ignition source. The overall program carried out in FLAME is summarized in References 192 through 194.

The inside walls and the floor of FLAME contain numerous 32 mm I.D. threaded bolt holes formed by sinking embeds into the concrete during pouring. We used a dozen of these bolt holes along the centerline of the floor near the open end of FLAME to hold threaded planchets, which had their upper surfaces precoated with aerosols. Photographs of a planchet before and after insertion into a bolt hole are shown in Figures 1.6-2 and 1.6-3.

In the first three FLAME experiments, one surface of each threaded metal planchet was exposed to aerosols of CsI or MgO condensed from the gas phase

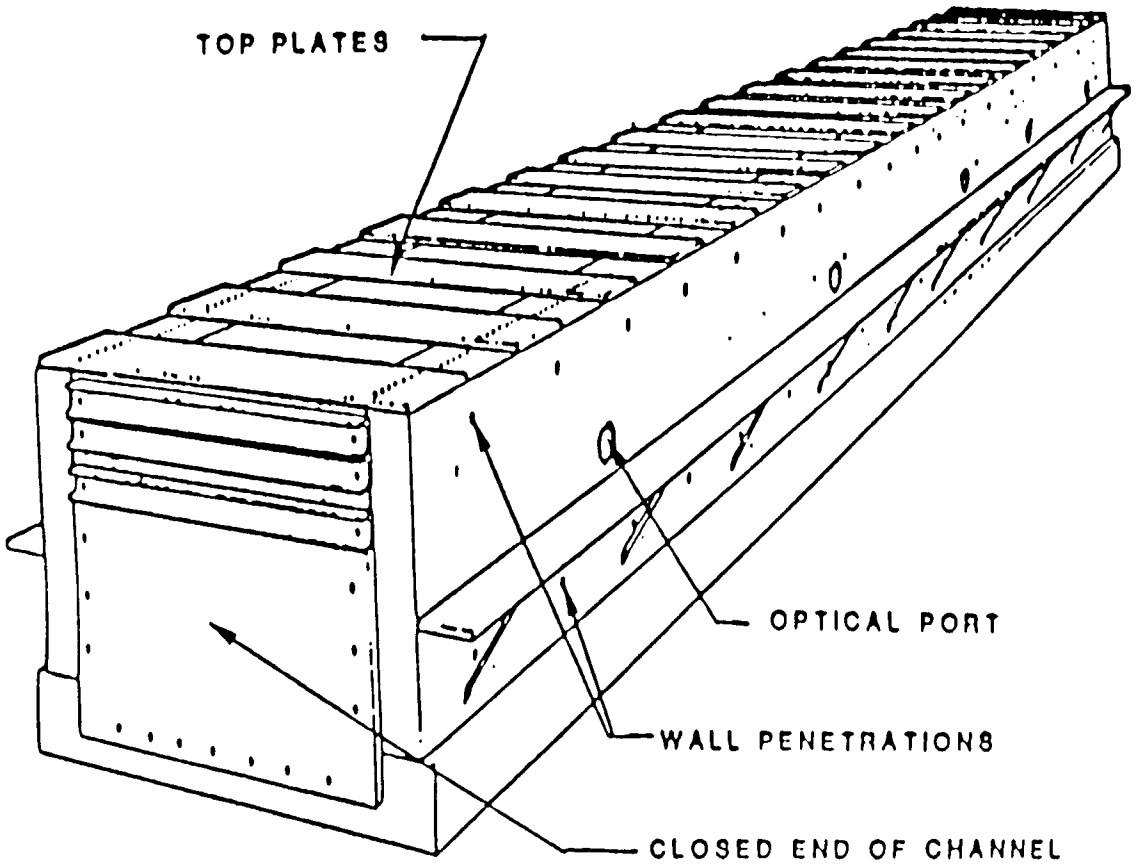

Figure 1.6-1. Schematic Diagram of Exterior of FLAME Facility Showing Optical Ports and Penetrations. The top plates are shown without their steel channel reinforcements and in position for 50 percent top venting. In the latest experiments, the closed end of FLAME has been considerably altered, having a frangible plywood end with a steel lattice frame reinforcement (see References 192 through 194).

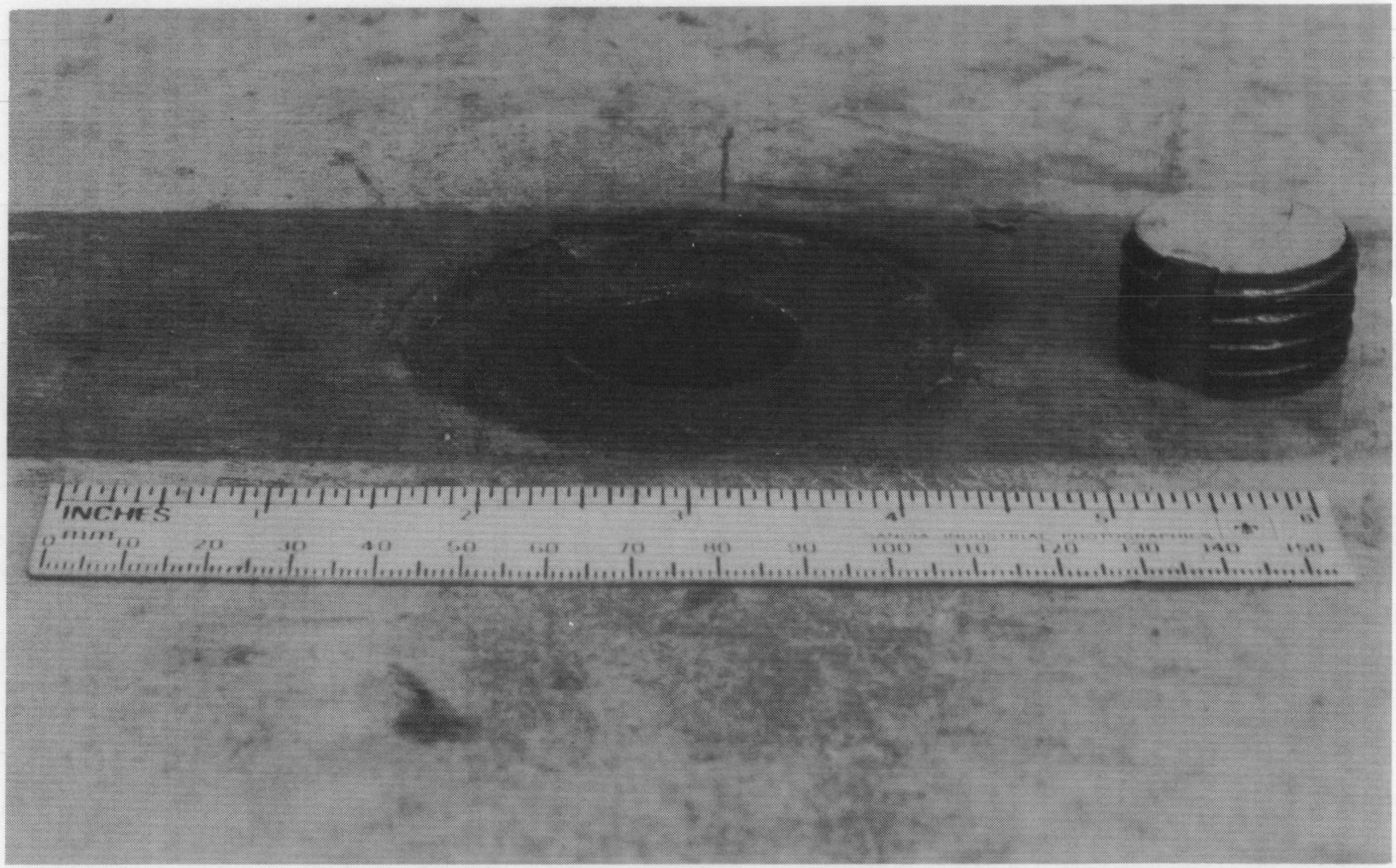

Figure 1.6-2. Photograph of a Planchet Before Insertion in a 32 mm-ID-Bolt Hole in the Floor Near the Open End of the FLAME Facility

Figure 1.6-3. Photograph of a Planchet Inserted in a Bolt Hole in the Floor of the FLAME Facility. Note that the upper, aerosol-coated surface of the planchet is essentially flush with the floor of the combustion chamber.

in air. (The CsI simulates a fission product aerosol, while the MgO simulates a structural material aerosol.) The CsI was deposited by holding the planchet about 5 mm above a porcelain crucible containing the salt held at a temperature of approximately 1000°C; the MgO was deposited by placing the planchet about 20 mm above a burning Mg ribbon. The planchets were made of bare carbon steel in the first two of the three FLAME experiments; in the other experiment, we used both stainless steel and carbon steel planchets.

The coated surfaces of these planchets were analyzed by X-ray fluorescence (XRF) before insertion in the FLAME combustion facility. Shortly after each burn, the planchets were removed carefully from the combustion chamber and reanalyzed by XRF.

In the last three FLAME experiments, both stainless steel and carbon steel planchets were first coated with a Phenoline 305 Modified Phenolic finish over a Carbo Zinc 11 primer (both obtained from the Carboline Co., St. Louis MO). These coated planchets were then exposed to a combined CsOH and MnO_x aerosol in the CSTF vessel of test LA-2 of the LACE aerosol behavior program.[195] After return to Sandia, the surfaces of these phenolic-coated planchets containing the deposited aerosol layer were analyzed by XRF. After exposure to the FLAME shots, the surfaces were reanalyzed by XRF.

A seventh experiment was performed in a 5-m^3 chamber open at one end; it is designated as VGES-II. It is 5.27 m long and 1.22 m in diameter, with axis inclined about 20° above horizontal. The single experiment was performed at a composition of 30 percent hydrogen-in-air, close to the stoichiometric composition. Carbon steel and stainless steel planchets, coated with CsI or MgO as in the initial FLAME experiments, were inserted along the walls at the open end of the chamber. The experimental procedures and characteristics of the burn have been described by Cummings et al.[191]

In four of the experiments in the FLAME facility, two of the planchets were exposed to condensing steam for several minutes prior to and during the burns. This was accomplished by energizing an electric heating mantle surrounding a spherical boiling flask located outside the FLAME chamber for safety reasons. The steam was led through two insulated 6-mm stainless steel tubes through the chamber wall and through Erlenmeyer flasks used as condensation traps. The steam then exited the lines via two 75-mm funnels placed large end down, just above the planchets. During tests prior to the combustion experiments, condensing steam could be seen issuing from beneath the funnels and flowing over the planchet locations.

1.6.1.3 Results

The characteristics of the seven hydrogen burns performed in the FLAME and VGES-II facilities in which we included aerosol-coated planchets are summarized in Table 1.6-1. Note that of the seven burns, three were energetic (F-25, F-26 and AR-13); the other four were mild or moderately vigorous, as indicated by small peak overpressures and low flame speeds (F-24, F-27, F-28, and F-29).

The removal of CsI and MgO aerosols from the carbon steel and stainless steel planchets during tests F-24, -25, -26 and AR-13 (in the VGES-II chamber) is shown in Figures 1.6-4, 1.6-5, and 1.6-6, on the basis, respectively, of Cs, I and Mg reduction indicated by the XRF analyses. In Figures 1.6-4 and 1.6-5, the fraction of Cs and I removed from one set of planchets is shown; in Figure 1.6-6, a similar plot is presented for the removal of Mg from a second set of planchets.

Some salient features of our results with bare metal planchets are:

- For the vigorous burns (F-25, F-26 and AR-13), there was removal of over 60 percent of Cs, I and Mg.

- For the mild burn (F-24), the amounts of Cs and I removed were lower, but still substantial, in the range 15-55 percent (MgO-coated planchets were not available for shot F-24).

- The amounts of both aerosols removed from stainless steel surfaces were somewhat greater than for carbon steel surfaces.

- A flowing, wet steam atmosphere locally enveloping two stainless steel planchets, one coated with CsI and the other with MgO, seemed to do little to reduce the aerosol removal compared to analogous, neighboring planchets exposed to the burn in the absence of steam (see solid data points in Figures 1.6-4 through 1.6-6). In fact, there is an indication that the removal might even be enhanced in the presence of steam. (Note, however, that these comments are based on the examination of only two planchets in shot F-26; obviously, more data are required.)

In Figure 1.6-7, we show Cs and Mn removal for the three FLAME experiments in which stainless steel and carbon steel planchets were first coated with phenolic finish and then exposed to a combined CsOH and MnO_x aerosol[195] (shots F-27 and F-28 (repeats of F-24) and F-29 (a moderately vigorous burn at 18.5 percent hydrogen in air)). These analyses suggest:

- Trends in aerosol removal similar to those observed in the four earlier experiments with unpainted metallic planchets.

- Greater removals of Cs than Mn.

- Poorer reproducibility of XRF measurements for some of the coated planchets caused by cracking and chipping of the phenolic finish coating during exposure to the LACE experimental environment.

- Little effect of a wet steam atmosphere to enhance adherence of either CsOH or MnO_x aerosols during the hydrogen burns (see six solid data points in Figure 1.6-7).

1.6.1.4 Discussion

In the seven "add-on" experiments described here, we have demonstrated that even relatively mild hydrogen burns can effectively remove sedimented

Table 1.6-1

Large-Scale Hydrogen Combustion Experiments with Aerosol-Coated Planchets

Test	Concentration of H_2 (%)	Peak Overpressure (kPa)	Peak Equivalent Planar Flame Speed (m/s)	Aerosols	Planchet Materials
F-24[a]	15.5	Negligible	46	CsI	CS
F-25[a,b]	19.7	1650	890	CsI, MgO	CS
F-26[a,b,c,d]	28.5	1970	1860	CsI, MgO	Cs, SS
F-27[a,d]	13.1	9?	15?	CsOH, MnO	Paint
F-28[a,d]	14.9	9?	33.4	CsOH, MnO	Paint
F-29[a,d]	18.5	22?	130	CsOH, MnO	Paint
AR-13[e]	30	Not Measured	~400	CsI, MgO	Cs, SS

[a]Tests had obstacles, 50 percent top venting (see References 192 through 194).
[b]Deflagration-detonation transition.
[c]Ice-condenser geometry (box-type obstacles to simulate ice-condenser upper plenum air handlers and other structures).
[d]Two of the planchets were exposed to condensing steam during this experiment (see text for details).
[e]This test was performed in the open-ended, inclined VGES-II facility. The chamber did not have obstacles (see Reference 191).
CS = Carbon Steel
SS = Stainless steel

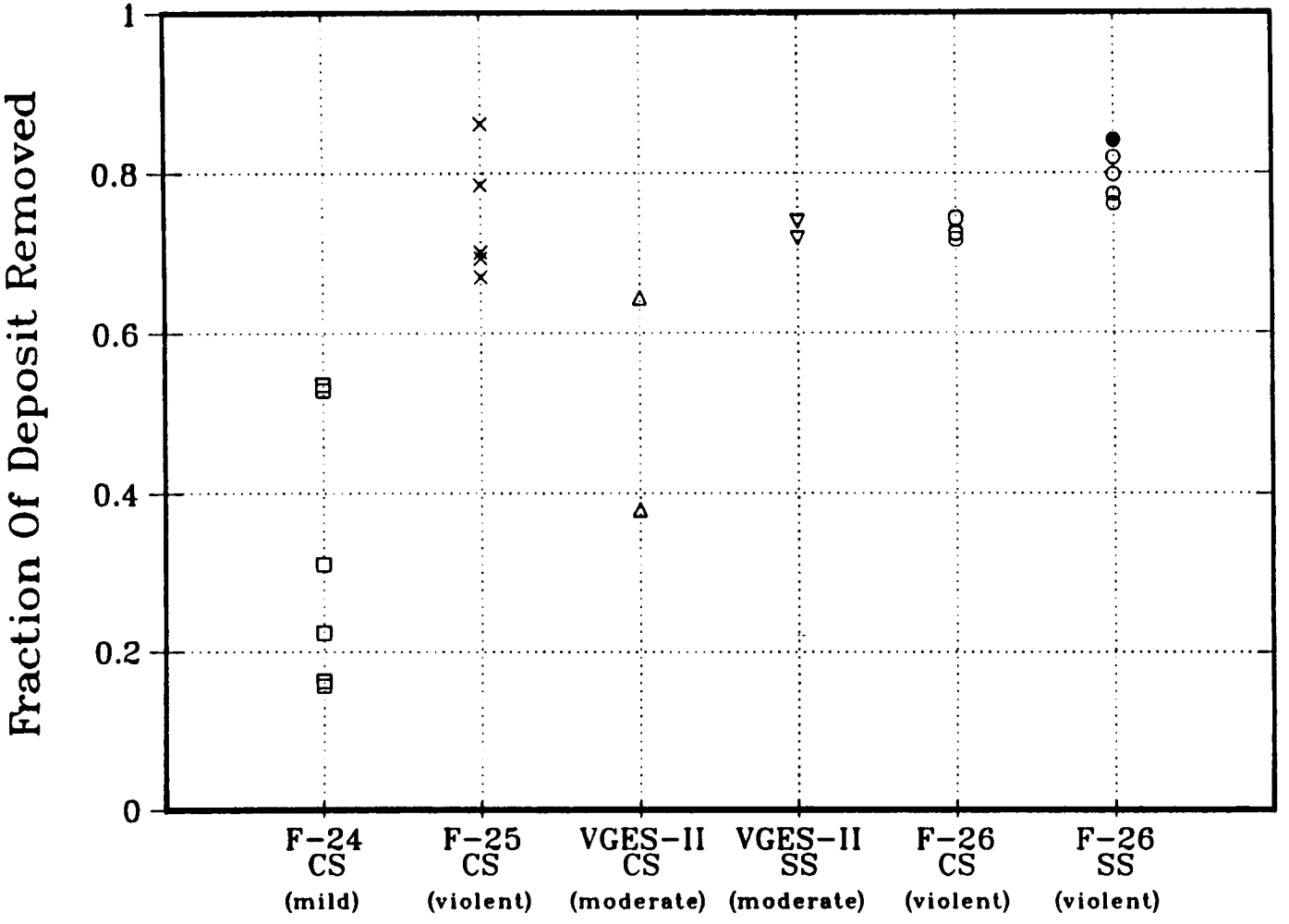

Figure 1.6-4. X-Ray Fluorescence Analyses of Cs Removed From Bare Metal Planchets Exposed to FLAME and VGES-II Shots. Solid data point indicates the presence of steam flowing over the planchet at time of ignition.

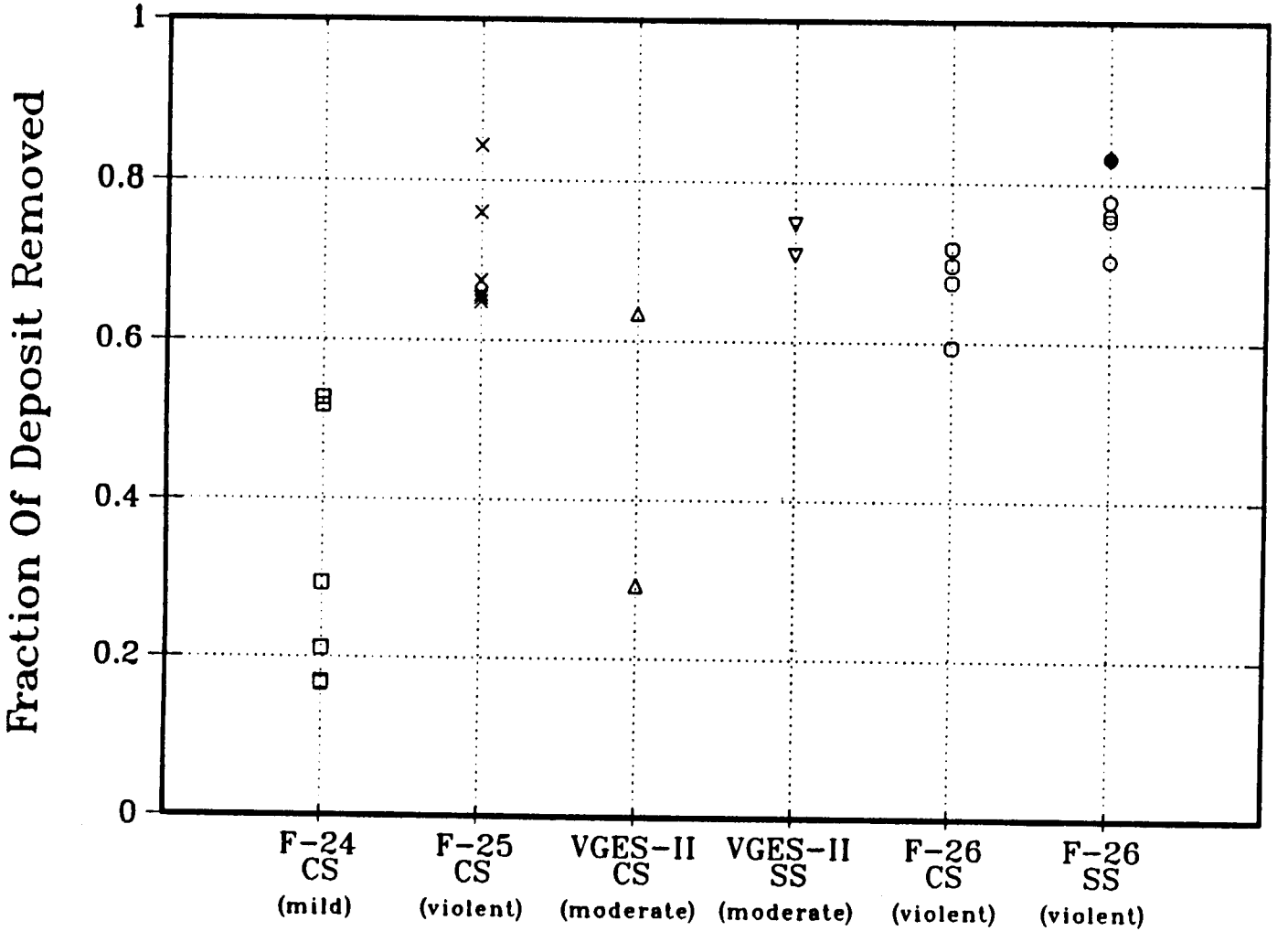

Figure 1.6-5. X-Ray Fluorescence Analyses of I Removed From Bare Metal Planchets Exposed to FLAME and VGES-II Shots. Solid data point indicates the presence of steam flowing over the planchet at time of ignition.

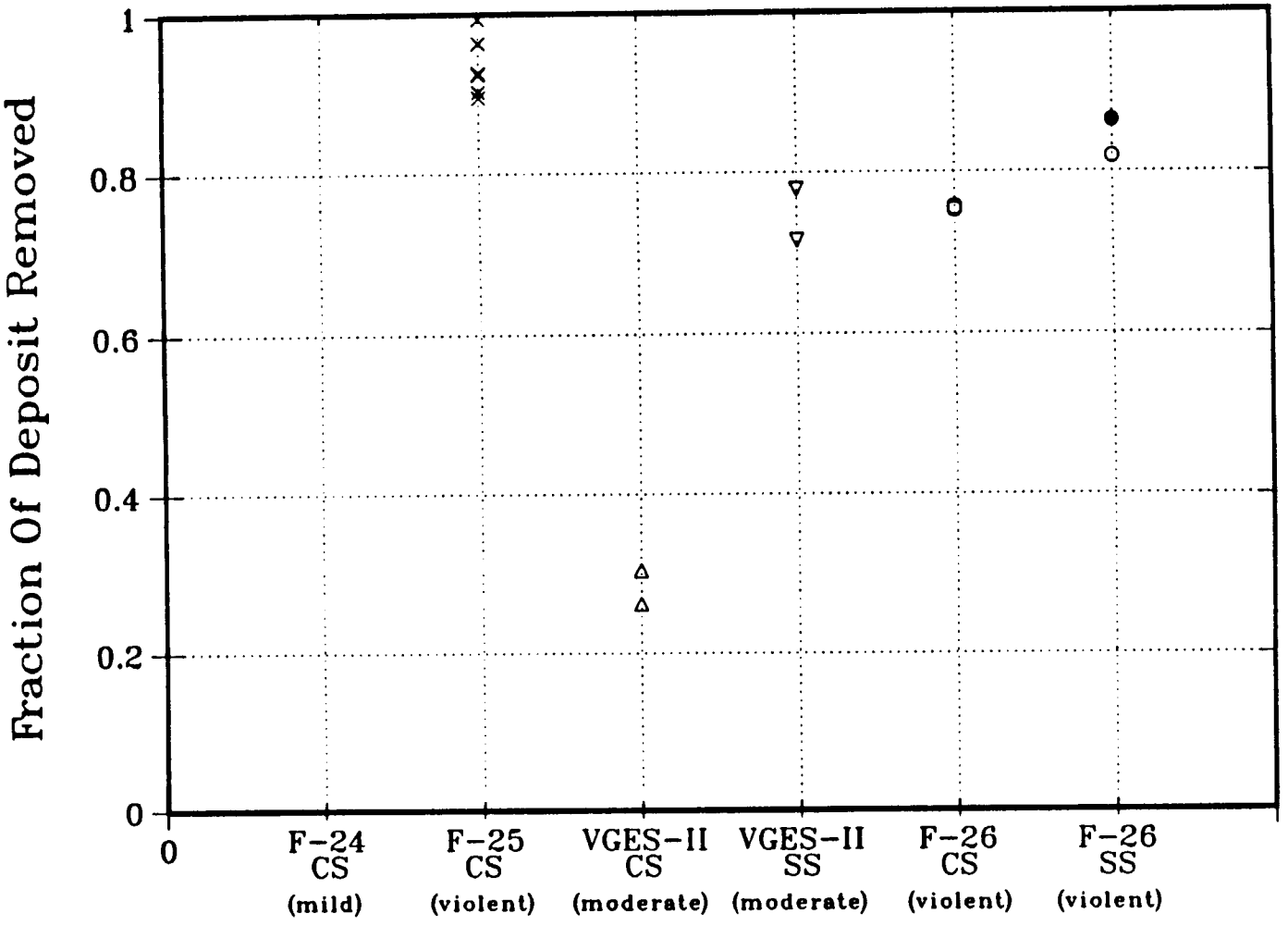

Figure 1.6-6. X-Ray Fluorescence Analyses of Mg Removed From Bare Metal Planchets Exposed to FLAME and VGES-II Shots. Solid data point indicates the presence of steam flowing over the planchet at time of ignition.

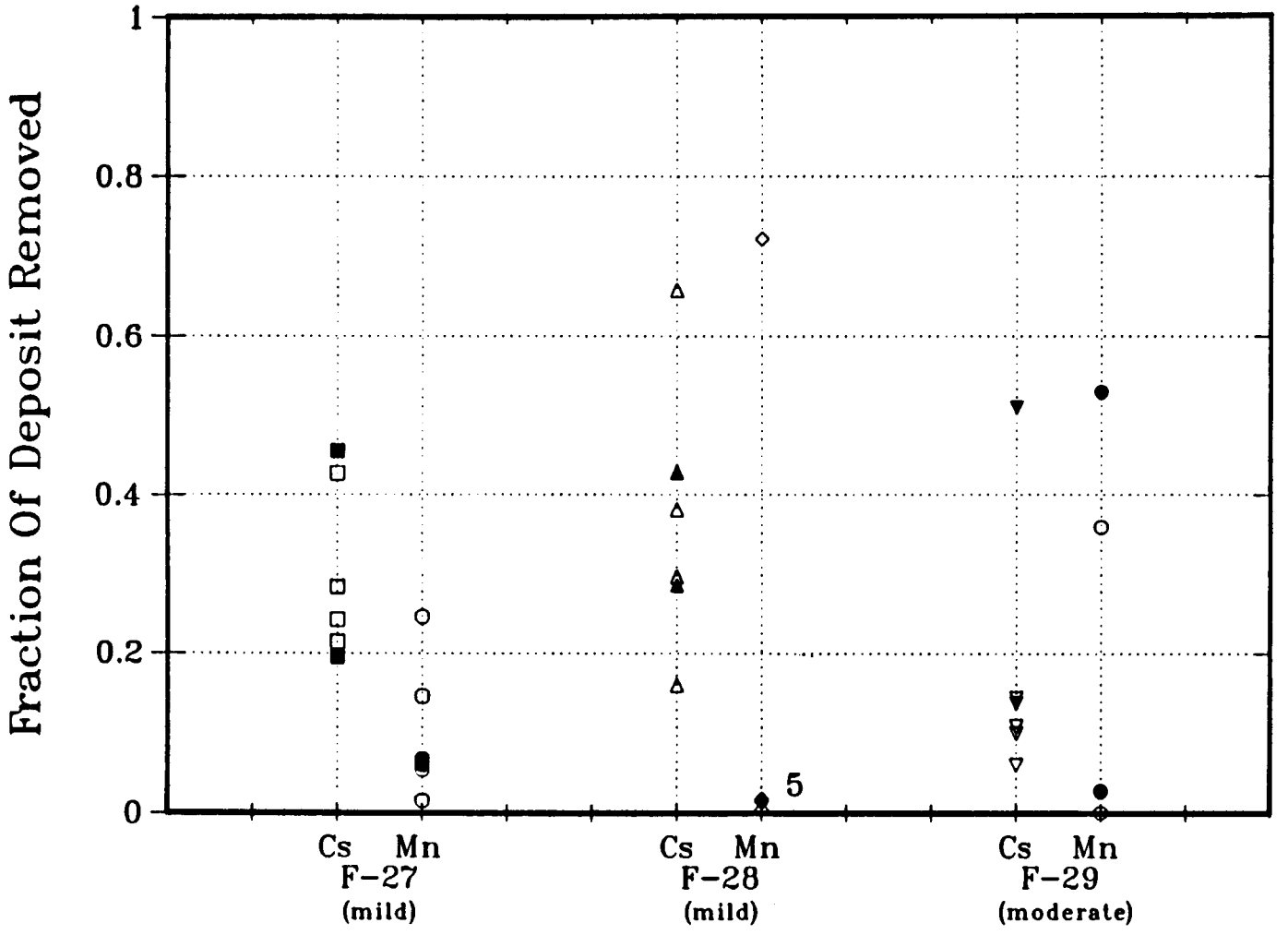

Figure 1.6-7. X-Ray Fluorescence Analyses of Cs and Mn Removed From Painted Planchets Exposed to FLAME. Solid data points indicate the presence of steam flowing over the planchets at time of ignition. (In shot F-28 there was essentially no removal of Mn from five planchets; in a sixth planchet, removal was high. We attribute the latter to flaking off of the painted surface.)

fission-product and structural aerosols from surfaces prototypical of those that might be encountered within a nuclear reactor containment during a hypothetical accident in which severe fuel damage occurs. Of particular significance in these experiments is the behavior of Cs during the burns. Figures 1.6-4 and 1.6-7 indicate that sizeable amounts of Cs are removed from the planchets even in the very mildest of burns (the smallest value measured was ~5 percent); at the other extreme, the removal is almost complete in the most energetic burns (the largest value measured was ~86 percent). Because aerosols of Cs and I isotopes have important physiological effects and easy atmospheric transportability over very long distances,[196,197,198] the action of hydrogen burns on sedimented CsI containing deposits in containment seems especially important for further study.

Although our scoping experiments were too incomplete to give definitive answers about removal mechanisms, we hypothesize that there are several characteristics of hydrogen burns (deflagrations, accelerated flames, detonations) that may contribute to the efficient removal of aerosols from surfaces: the presence of high velocity gases; pressure pulses (and in some instances rarefactions); thermal pulses, both convective and radiative (especially from vibrationally excited H_2O molecules); and the transient presence of active chemical species (e.g., OH and atomic oxygen). Moreover, in some burns, gas motion might suspend larger particulates (e.g., dirt, paint flakes, weld spatter), which would tend to "sandblast" aerosols from surfaces. In some circumstances, these characteristics may combine in unique ways to remove aerosols in amounts far exceeding those expected from gas motion alone, as studied, for example, in the LACE program.[195]

Of particular note in our work is the apparent inability of moist, condensing steam to cause the sedimented aerosols to adhere strongly to the surfaces of the planchets during the burns. Although we can only speculate here, it is possible that the strong infrared emission from the hydrogen-oxygen combustion reaction by means of the vibrationally excited H_2O molecules is absorbed with high efficiency by adsorbed water that normally would cause the aerosols to adhere to a surface. This selective absorption could heat or otherwise activate the adsorbed water, causing the adhesive forces to relax, and possibly in very energetic burns even to vaporize and drive the aerosols forcibly from the surface. There is a suggestion of greater removal of aerosols in the presence of steam, but the incompleteness of our data leaves the question open for further study.

1.6.1.5 Conclusions

On the basis of seven, simple "add-on" experiments, we have concluded that large-scale hydrogen burns have significant potential for resuspending sedimented aerosols from containment surfaces. Moreover, the presence of condensing steam does not seem to assure adhesion of sedimented aerosols during hydrogen burns. Differences are exhibited between different surfaces (e.g., removal from bare stainless steel is greater than from bare carbon steel) as well as between types of aerosol (e.g., Cs removal is greater than Mn). Because of the sparseness of our data as well as those of other investigators, in-depth studies will be required to assess how the exposure of sedimented aerosols to hydrogen burns might affect the radiological source term.

2. FISSION-PRODUCT SOURCE TERM

Modern reactor accident analyses focus very directly on the mechanistic determination of the release of radionuclides from the fuel and their subsequent behavior--the so-called fission-product source term. This attention is being given to the source term to redress some of the conservatisms and omissions in past analyses. Mechanistic models now available for predicting the release of radionuclides from the reactor fuel under accident conditions and the transport of these radionuclides in the reactor coolant system have yielded substantive insight into the natural processes that attenuate the amount of radioactivity available for release from the plant. Nevertheless, these models are known to be incomplete. Significant uncertainties still exist concerning these release and transport issues. The rates of radionuclide release must be well known to predict deposition in the reactor coolant system. At this juncture release data may only be correlated against fuel temperature and not correlated against other factors such as system pressure and chemical environment, which are expected to influence strongly the radionuclide release. Chemical forms adopted by released radionuclides--especially iodine and tellurium--will drastically affect the extent to which these radionuclides will deposit and be retained in the reactor coolant system. Chemical transformations of the deposited radionuclides will determine to a significant extent whether these deposited materials revaporize from surfaces and again become a part of the radioactivity that can be released from the plant. These issues require experimental data if the modern accident models are to be upgraded to provide reliable predictions concerning the fission-product source term.

The High-Temperature Fission-Product Chemistry program provides experimental data on the thermodynamics and kinetics of chemical processes affecting the chemical form of released radionuclides, the interactions of these radionuclides with structural and aerosol surfaces, and the revaporization of deposited radionuclides. The ACRR Source Term Experiments are in-pile tests of radionuclide release under high-pressure, high-radiation intensity, and high hydrogen concentration conditions. They supplement out-of-pile experiments of radionuclide release being conducted elsewhere in the NRC-sponsored research. Both experimental programs provide crucial data needed for accident models. The primary thrusts of the experimental programs are to provide data for the development and validation of the NRC's best-estimate model of fission-product behavior, VICTORIA.

2.1 High-Temperature Fission-Product Chemistry and Transport

(R. M. Elrick and D. A. Powers, 6422)

The purpose of the High-Temperature Fission-Product Chemistry and Transport Program is to obtain data on the chemistry and processes that affect the transport of fission products under accident conditions. The program now consists of three tasks related to one another. Base line thermodynamic and reactivity data are being collected for compounds of fission-product elements of particular interest. An experiment facility has been built to allow the chemistry of fission products in prototypic steam-hydrogen environments to be studied. The interaction of fission products with reactor materials such as stainless steel can be examined in this facility. Results of these experimental studies are compared to predictions of

thermochemical models to determine if reaction kinetics play an important role in fission-product transport.

Little of the chemistry of fission products in high-temperature, steam-plus-hydrogen environments is well characterized. The physical and chemical processes taking place can be categorized into those between vapors (gas-phase reactions) and those between a vapor and a condensed-phase surface (heterogeneous reactions). In the latter category are condensation on, adsorption by, and chemical reaction with surfaces. Conversely, should conditions change, the fission-product species may evaporate, desorb, or leave a surface as the result of decomposition of a compound.

If these reaction surfaces are surfaces of structural materials, control rods, cladding, or bulk fuel, then the fission products can be retained in the primary system. However, the same reactions on the same materials in an aerosol form can result in transport out of the primary system.

Thermodynamic calculations[199] have shown that under some accident conditions cesium, in a steam environment, will form CsOH. In the presence of iodine, the more stable compound CsI may form. At elevated temperatures, however, CsI in steam can dissociate to form CsOH and atomic iodine. With a significant concentration of hydrogen, the atomic iodine can form HI. Because of these types of possible reactions, the stability of the compounds CsOH and CsI were studied in their relation to accident environments in the primary system. The studies were (1) a model to describe the reaction of CsOH with stainless steel in the primary system and (2) the stability of CsI in an accident environment.

2.1.1 Model for Reaction of CsOH with Structural Material

In the steam and hydrogen environment expected during an accident, the primary cesium-containing vapor species is thought to be CsOH. (Since there was about 10 times as much cesium as iodine in the fuel and release rates for the two were similar, the principle iodine species for our experimental studies was CsI and the principle cesium species was CsOH.) The CsOH vapor encountered the surfaces of the primary system. Two alloys were considered--Inconel-600 and 304SS. Oxide layers were formed on these alloys as a result of their reaction with steam. A comparison was made of these oxides for similar thermal histories. The oxide layer formed on Inconel-600[200] was relatively thin and consisted largely of Cr_2O_3 while that formed on 304SS[201] was much thicker and consisted of an outer layer of Fe_3O_4 (spinel-type) and an inner layer of Cr+Fe+Mn spinels. After 3 h at 1270 K, the oxide on 304SS had grown to about 150 μm in thickness compared to the several-micrometer-thick oxide on the Inconel.

Silicon was the minor component of both alloys that played a major role in our model. As the alloys were oxidized, our microprobe data indicated that at 1270 K Si was not incorporated uniformly into the oxide layers but was segregated at the grain boundaries of the Cr_2O_3 layer in the case of Inconel-600 and only in the inner oxide of 304SS. The oxide form is presumed to be SiO_2.

Retention of fission-product cesium can occur by its reaction with a component of the oxide layer. Our microprobe data for both 304SS and Inconel-600 show positive correlations between the cesium and silicon locations. The correlation is particularly good for 304SS (Figure 2.1-1) and the quantitative agreement indicates that (1) the reaction product is $Cs_2Si_4O_9$ (Figure 2.1-2), (2) all SiO_2 had been consumed, and (3) no other cesium silicates were formed. The reaction can be represented by the equation

$$2CsOH + 4SiO_2 \longrightarrow Cs_2Si_4O_9 + H_2O$$

$$2CsOH + Cs_2Si_4O_9 \not\longrightarrow 2Cs_2Si_2O_5 + H_2O \quad .$$

This conclusion is supported by laboratory tests in which various prepared cesium silicates were exposed to steam at 1170 to 1270 K. Only $Cs_2Si_4O_9$ was stable in the environment. $Cs_2Si_2O_5$ and Cs_2SiO_3 both exhibited a loss of cesium. The corresponding numbers obtained on Inconel-600 show a much larger variability in correlation and suggest an incomplete reaction in that $Si/Cs > 2$.

We interpret these data to indicate that the diffusion of Cs through the oxide layer was very rapid through the spinel-type layers formed on 304SS but was impeded by the Cr_2O_3 layer on Inconel-600.

The amount of cesium that diffused and reacted in the inner oxide on 304SS was used to calculate effective surface reaction rate constants shown in Table 2.1-1 at three test temperatures--1020, 1120, and 1270 K. An Arrhenius plot (Figure 2.1-3) of these rate constants gives an activation energy for the reaction of 15 kcal/mol.

Little is known about the effect of oxygen potential, temperature, and time on the compositional changes in the formation of the stainless steel oxide and how these changes might influence the cesium reaction. Some of our studies,[201] however, have shown changes in surface oxide characteristics with changes in the H_2/H_2O molar ratio. Within the range studied (H_2/H_2O from 0.1 to 2), the compound $Cs_2Si_4O_9$ formed from CsOH vapor and the stainless steel oxide was unchanged. As shown in Figure 2.1-4, the surface composition of the oxide formed on 304SS appears to be influenced by the hydrogen to steam ratio. The dashed lines connect composition points for tests at the same temperature (1270 K), but different H_2/H_2O ratios. Points at H_2/H_2O ratios ≥ 1 were from a test in which argon was the main carrier gas. The other 1270 K test had H_2 to H_2O ratios that (time) averaged between 0.13 and 0.3 depending on the location of the coupon in the reaction tube. Compositions for a test at 1020 K and one at 1120 K with H_2/H_2O ratios in this lower range are placed on the graph, but none of the points are differentiated by test. We conclude from Figure 2.1-4 that at 1270 K, the surface content of Fe decreased while that of Cr and Mn increased with increasing H_2/H_2O ratios. We have no evidence to predict the influence of H_2/H_2O on the subsurface composition, which will probably be more strongly influenced by time and temperature than is the surface composition. The temperature change, at least from 1020 to 1270 K, has

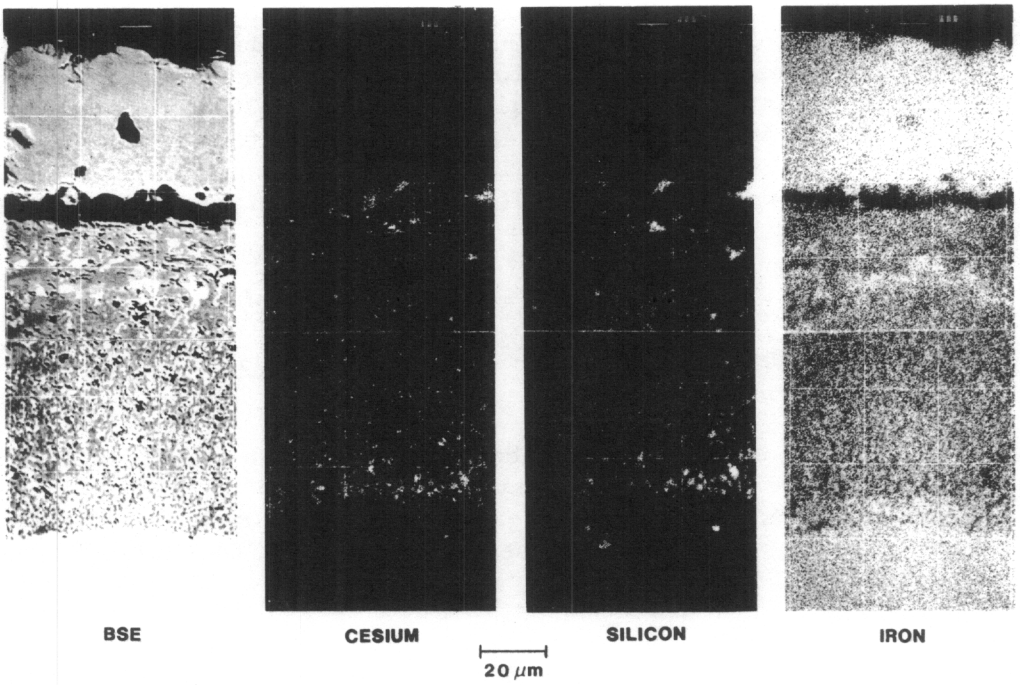

Figure 2.1-1. Cross Section of Oxide Formed on 304 Stainless Steel Exposed to CsOH Vapor and Steam at 1273 K and Examined by Electron Microprobe (Test 11)

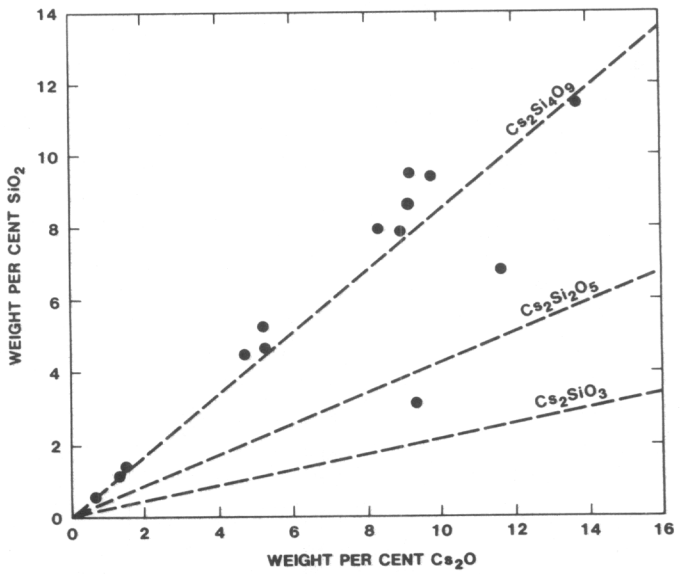

Figure 2.1-2. Correlation Between SiO_2 and Cs_2O in the Inner Oxide on 304SS for Test 11

Table 2.1-1

Summary of Surface Reaction Rate Constants

Conditions	Temperature (K)	H_2 (mol) / H_2O(mol)	Species (mol) H_2O (mol)		Rate Constant (m/s)
CsOH/304SS	973	0.2 -0.3	2.3×10^{-4}		4.4×10^{-5}
	1123	0.03-0.2	7.0×10^{-5}		1.6×10^{-4}
	1273	0.07-0.3	5.0×10^{-5}		2.5×10^{-4}
CsOH/Inconel-600	1273	0.05-0.08	1.1×10^{-4}		2.1×10^{-5}
CsI/304SS	1273	0.1 -0.2	4×10^{-5}	Cs	$<3 \times 10^{-7}$
				I	$<3 \times 10^{-7}$
CsI/Inconel-600	1273	0.03-0.08	4×10^{-5}	Cs	2.5×10^{-6}
				I	3×10^{-7}
CsI/Radiation Cycled	1173	~0.1	1.2×10^{-4}	Cs.	$\sim 8 \times 10^{-5}$
				I	$\sim 8 \times 10^{-7}$

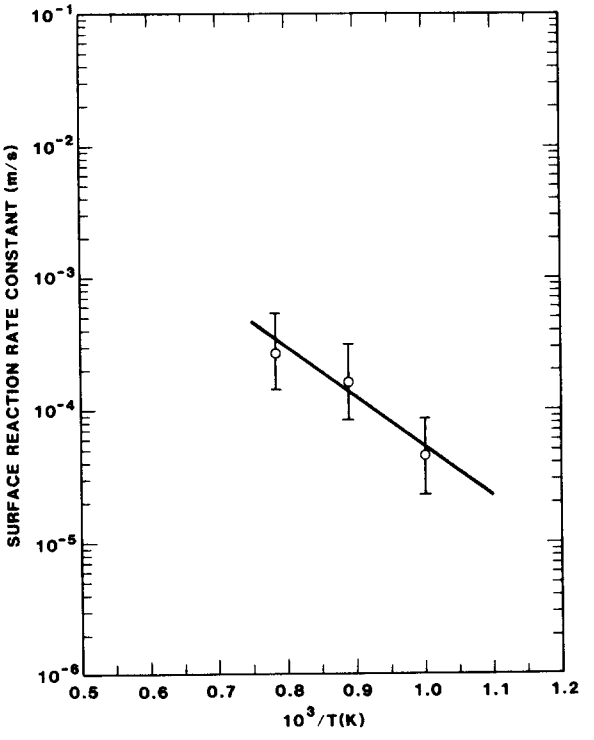

Figure 2.1-3. An Arrhenius Plot of Surface Reaction Rate Constants for the Reaction of CsOH Vapor with 304SS

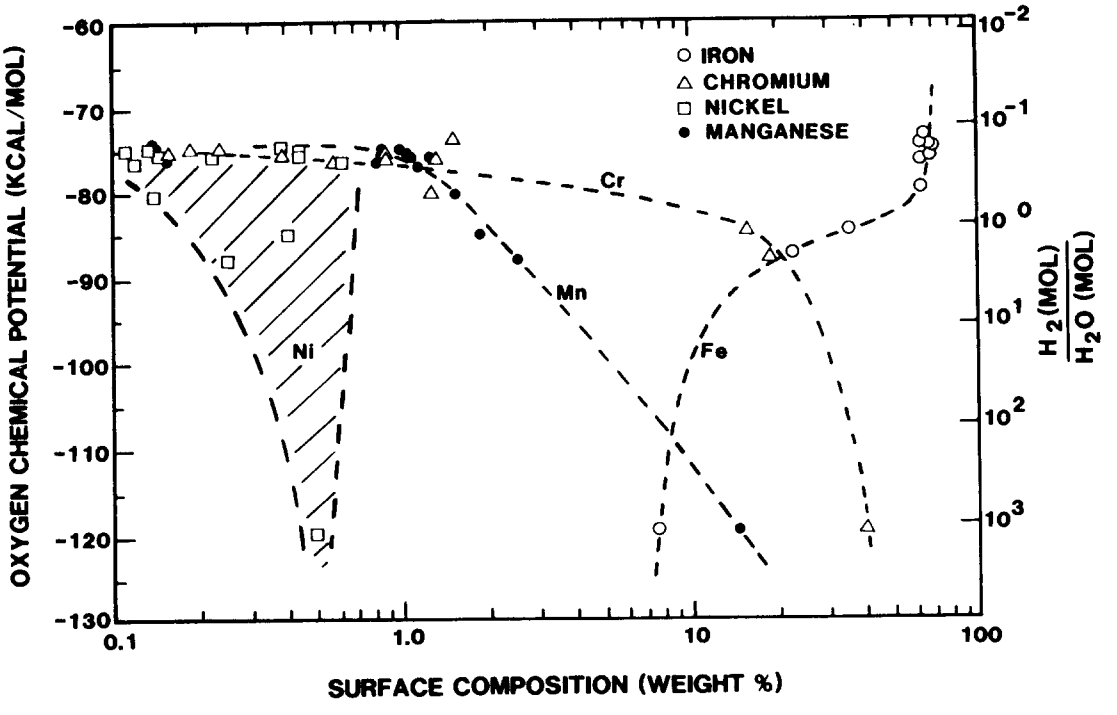

Figure 2.1-4. Surface Composition of Oxide Formed on 304SS in Steam and Hydrogen Mixtures at 1270 K

little effect on the surface composition for similar H_2/H_2O ratios (0.13 to 0.3). It is interesting to note that analysis of surfaces of control rod lead screws taken from the TMI-2 core gave surface compositions[202] ranging from 10 to 40 w/o for Fe and 1 to 20 w/o for Cr. Figure 2.1-4 data indicate similar surface compositions would result from H_2/H_2O ratios of about 0.5 to 5. There are data from TMI-2 analyses[202] that show a correlation between the elements cesium and silicon in the inner oxide on stainless steel lead screws, which indicates that there was probably a cesium-silica reaction product formed.

Our reaction model assumes that retention of fission-product cesium is due to formation of $Cs_2Si_4O_9$ and thus is limited by the SiO_2 content of the oxides formed on metal alloys. The model further assumes that Si does not preferentially diffuse across the metal/oxide interface so that the amount of available SiO_2, i.e., the retentive capacity of the oxide layer, is directly related to the extent of oxidation. A surface that has been more severely oxidized has a larger capacity for Cs retention. It does not matter if the oxidation occurs concurrently with or occurred prior to fission-product cesium release.

Thus, given the thermal history of an alloy and data for the oxidation rate of that alloy, the retention capacity of the oxide layer for cesium (or alternately stated, the maximum amount of Cs that could be retained in the oxide) can be calculated. Whether this capacity is achieved depends on several parameters. One is the arrival rate of cesium at the oxide surface. A second parameter is the diffusion rate of cesium through the oxide layer. This parameter is dependent on oxide structure--spinel-type phases appear to facilitate diffusion while the Cr_2O_3 layer (on Inconel-600) may impede or restrict diffusion. A third parameter is the reaction rate of cesium with silica. Any of these parameters may be controlling the overall reaction at any specific time.

The various limiting reaction steps are illustrated in Figure 2.1-5. For simplicity, the case depicted is assumed to be isothermal. The parabolic curve is the calculated cesium retention capacity of the oxide. It is proportional to the accumulated amount of oxide present (or to the accumulated amount of SiO_2 present in the oxide).

Curve A depicts the maximum production of $Cs_2Si_4O_9$ that could occur from the reaction of a diffusing cesium species with silica. It assumes that the resupply rate of either reactants is not a limiting step in the reaction mechanism. When Curve A intersects the parabola, the formation of SiO_2 becomes the limiting step in the reaction process.

Curves B and C depict the integrated flux of CsOH arriving at the oxide-gas interface. These curves are proportioned to the partial pressure of CsOH at the interfaces. As B lies above A, the arrival flux of cesium vapor species at the surface is greater than the intrinsic reaction rate of a diffusing cesium species with silica; therefore, Curve A is the limiting reaction step.

However, when the partial pressure of CsOH is smaller as in Curve C, then the intrinsic reaction rate of cesium with silica is greater than the

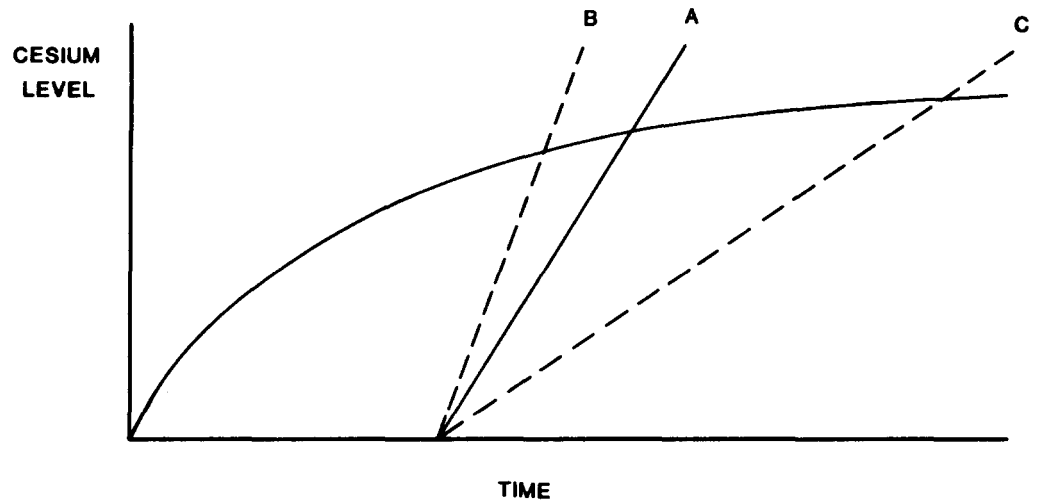

Figure 2.1-5. Schematic of a Cesium Hydroxide - Stainless Steel Reaction Model

arrival rate. Hence the limiting step is the arrival rate of CsOH at the oxide-gas interface. Other possible limiting steps could also be depicted. Ultimately, the amount of cesium in the oxide is the lower envelope of these potential reaction steps.

In our experiments, some limiting steps can be identified. For the 1270 K test, the limiting step by the end of the run was the oxidation rate sincethe reaction had gone to completion, allowing the reaction species to be identified. At the other two test temperatures--1020 and 1120 K--the limiting rate was probably not the oxidation rate (since reaction species could not be identified) but the rate at which the CsOH could react with the oxide (Curve A), given no other limitations. An adequate supply of CsOH vapor was present for all the tests. The rate constant for CsOH vapor in contact with SiO_2 was recently measured as 5×10^{-3} m/s.[203] This rate is considerably larger than the rate of 2.5×10^{-4} m/s measured in the 1270 K test, so the reaction with the larger $CsOH/SiO_2$ rate would not be limiting. An estimate of the reaction rate between CsOH vapor and the oxide at 1270 K, with no other limitations and corresponding to Curve A, could be made by extrapolating the similar data from 1020 and 1120 K in Figure 2.1-3 to 1270 K. This gives a value of 5×10^{-4} m/s instead of 2.5×10^{-4} m/s. This new value is probably a better estimate for the rate at which the cesium species traveled through the outer oxide to the reaction site at 1270 K and reacted with the silica.

The gaseous environment could also affect the oxide structure or its composition as previously discussed. For instance, the "steam-starved" environment in which H_2 is the predominant gas can have a low oxygen potential. Under such conditions, the iron in 304SS could not be oxidized and a surface enhanced in Cr oxides would result. This might, as appears to happen with Inconel oxidation, inhibit the rate at which the CsOH reacts.

2.1.2 Stability of CsI in an Accident Environment

The stability of CsI in a steam and hydrogen environment was demonstrated in both a 304SS and Inconel-600 lined system at 1270 K. Levels of reacted cesium and iodine on the surface of 304SS coupons were less than the detection limit for the electron microprobe (~0.1 $\mu g/cm^2$), giving a reaction rate constant of less than 3×10^{-7} m/s for cesium iodide. (See Table 2.1-1 for a summary of all reaction rate constants.)

A cross section of a coupon from the reaction tube showed an oxide structure that resembles that found on 304SS from the CsOH tests. No cesium or iodine was detected within these oxides by microprobe so there was no significant diffusion of CsI (or cesium or iodine alone) into the oxide. Analysis of the steam condensate samples confirmed the conclusion that there was essentially no preferential holdup of cesium or iodine in the system since the cesium-to-iodine mass ratio was 1.06 ± 0.04.

In the case where CsI vapor was exposed to oxidizing Inconel, the cesium preferentially reacted with the oxide as determined from microprobe scans of the oxide surface (Figure 2.1-6). There was no indication that iodine was similarly retained. Corresponding rate constants were 2.5×10^{-6} m/s for cesium and 3×10^{-7} m/s for iodine.

This same chemical system, that of cesium iodide vapor with 304SS in steam and hydrogen, was examined to see if its behavior could be influenced by the presence of a radiation field. The steam facility used for the irradiation experiment was configured to fit the Gamma Irradiation Facility (Figure 2.1-7). The radiation source consists of an array of ^{60}Co pins stored in a water pool below the experiment room and raised on an elevator to irradiate experiments. The radiation field was measured in the vicinity of the reaction volume by placing thermoluminescent dosimeters on the reaction tube and exposing the steam system to the ^{60}Co source for 10 min. The dose rate varied along the reaction tube from about 1000 to 1600 rad/min. This level is about one thousandth of that in the reactor core during an accident.

The test was run by cycling the ionizing field on and off to compare the field and no-field effects. This was accomplished by running the test in the GIF, first with the source down (no field) for a period of 3 h and then with the source up for 3 h. This complete cycling of the source was performed twice over a 12 hour period. The steam condensates were sampled periodically during the test and analyzed for concentrations of cesium and iodide.

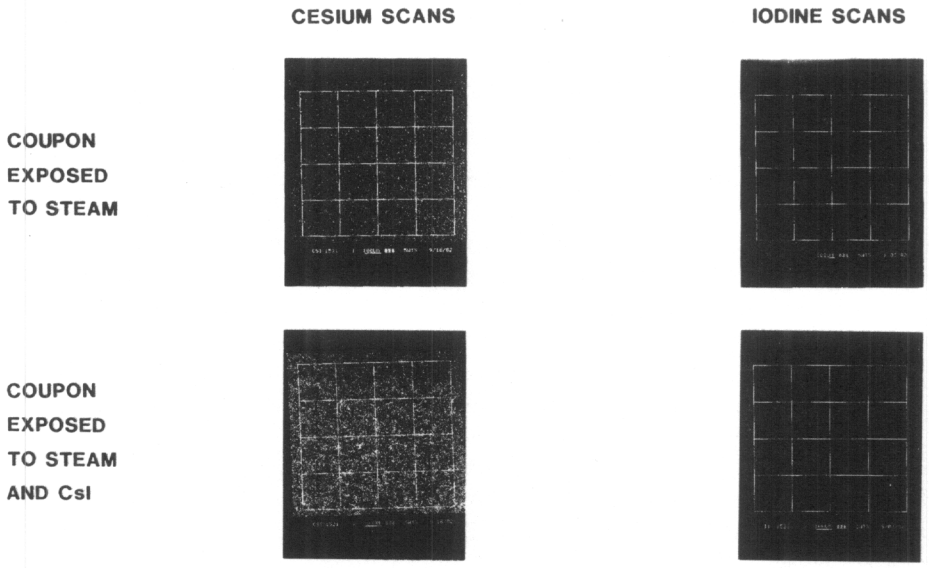

Figure 2.1-6. Microprobe Photographs of the Surface of Inconel-600 Exposed to Steam at 1270 K

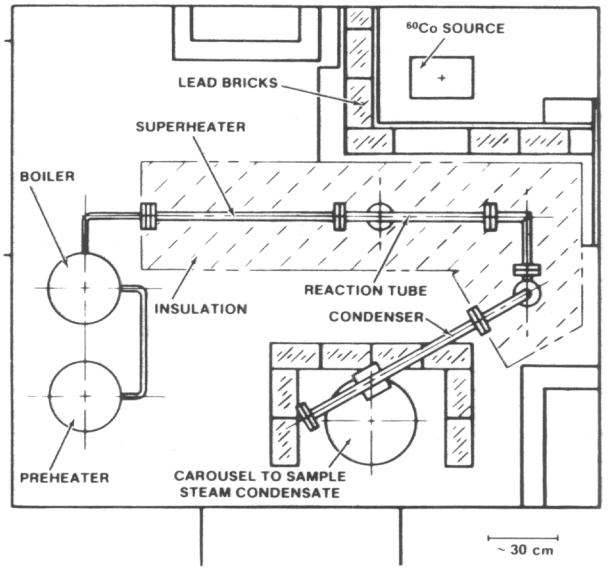

Figure 2.1-7. Schematic of the Steam Apparatus Used in the Gamma Irradiation Facility

To check the analytic results, cesium was measured by both atomic absorption and ion chromatography (IC) and the idodide by ion selective electrode and IC; comparable measurements agreed within 7 percent in 11 out of 12 cases. IC measurements of and I--on a blind standard--agreed to within 4 percent of actual values. The ratio of cesium to iodide in the condensates is shown in Figure 2.1-8 as a function of time. Two observations are noted from the figure. First, the cesium iodide is initially unstable as shown for a Cs/I molar ratio of less than 1 indicating that more of the cesium than iodine was retained in the system. Second, the instability increased monotonically during the 12 h beginning with a Cs/I ratio of 0.78 and decreasing to a Cs/I ratio of 0.63.

Instability of cesium iodide determined from condensate analysis was first observed in a similar CsI experiment exposed to ionizing radiation. This instability was solely attributed to radiation although the field was too weak for the effect to be caused by a gas phase reaction.

In stronger ionizing fields, more CsOH would exist in equilibrium with CsI and could react with stainless steel to produce the degree of instability observed. There is evidence from earlier ionizing field experiments that some of the cesium, but none of the iodine from CsI, reacted in the inner oxide and that the cesium is coincident with the silicon as seen in Figure 2.1-9. This observation indicates a cesium reaction similar to that observed between CsOH and stainless steel.

In two subsequent tests, CsI instability was again observed but this time in the absence of a radiation field. A program was initiated to analyze the steam system and its contents during a CsI test to determine the level of any contaminants. With the exception of 200 ppm of Cl^- (higher for the cycled test just discussed), levels of other impurities were on the order of several ppm. Chlorine was attributed to HCl used in the cleaning processes. The HCl has since been removed. In a test performed with the new cleaning procedure, the level of Cl^- was considerably reduced and the CsI instability was also less. However, the case for chlorine playing a role in the stability of CsI is not strong. The greatest instability did not occur with the highest level of Cl^-. In the cycling test the instability increased as the Cl^- level decreased during the 12 h. With the exception of the presence of chlorine from an earlier cleaning process, the system probably contained only those elements proposed for the study: CsI vapor with stainless steel (or Inconel) in a steam environment.

It seems certain that under the conditions of these experiments, CsI was unstable to varying degrees both in the presence and absence of ionizing radiation. The causes of the instability without a radiation field and their relevance to reactor accidents must be determined before radiation effects are studied. The present interpretation for the CsI stability is that (1) CsI or a cesium-bearing species in equilibrium with CsI, perhaps CsOH, reacts with 304SS as well as with Inconel, (2) this species reacts with the SiO_2 in the oxide formed, and (3) the rate and extent of reaction depend on the thermodynamic conditions of the experiment and the accessibility of the reacting material, which is a function of the initial oxide thickness and the physical defects in the oxide.

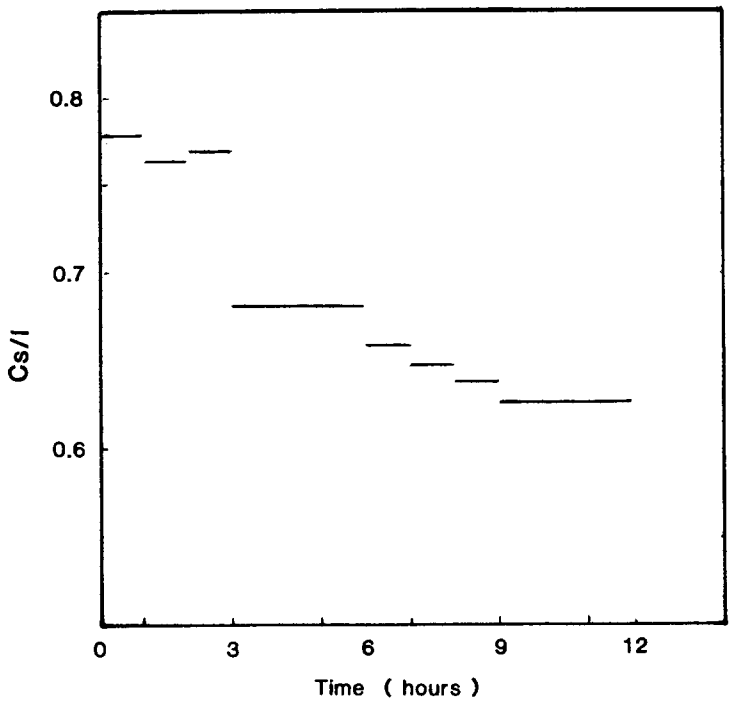

Figure 2.1-8. Cesium to Iodine Ratio in the Steam Condensates Versus Time for Test 52

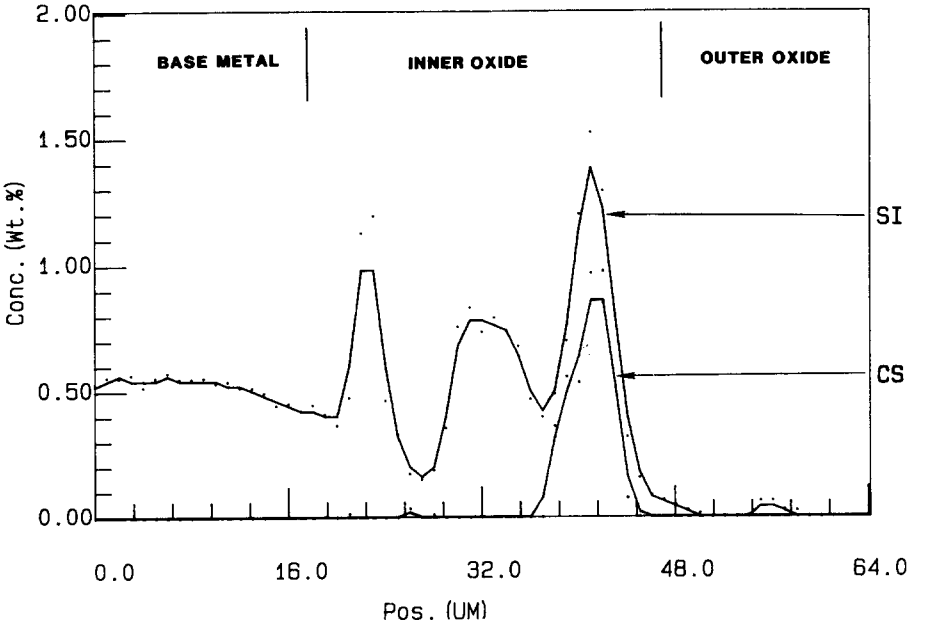

Figure 2.1-9. A Microprobe Scan Showing the Correlation Between Silicon and Cesium in the Inner Oxide Formed on 304SS in Steam (Test 40)

2.2 ACRR Source Term Experiments

(M. D. Allen, 6422; H. Stockman, 1543; C. Fryer, 6454;
K. O. Reil, 6423)

Understanding the release of radionuclides during fuel degradation in a core uncovery accident is the first stage in determining the amount and nature of the overall radioactive release from the damaged nuclear plant. Current estimates of the release of the principal fission products over the range of relevant accident conditions are subject to significant uncertainty (e.g., the QUEST study). A key element in reducing the uncertainty in predicted overall releases is an improved understanding of the release of fission products from the fuel under severe fuel damage conditions. Major progress is being made in the development of mechanistic release models (e.g., MELPROG's VICTORIA model) to significantly decrease these uncertainties. The ACRR Source Term (ST) program is being conducted to provide a data base for fission-product release over a range of fuel temperatures, system pressures, and fuel damage states. Significantly, these experiments will be performed in well-controlled, well-known in-pile conditions and in the presence of ionizing radiation, where little or no data currently exist, to allow the validation of these improved fission-product release models.

2.2.1 Introduction

Major activities during this period involved completion of development testing and qualification of the fission-product filter samplers, continued development of posttest analytical methods, completion of the hot cell plant modifications, fabrication and procurement of components for the ST-1 experiment, and the beginning of the assembly of the ST-1 experiment package.

2.2.2 Fission-Product Filter Sampler Development

2.2.2.1 Requirements

The goals for the aerosol and vapor sampling system for the ACRR Source Term Experiments are to (1) measure the quantity of each primary fission product released from the fuel bundle, (2) determine the release rates as a function of time and temperature, and (3) qualitatively establish some of the chemical species that exist close to the fuel bundle under high-temperature accident conditions.

A functional diagram of the fission-product gas and aerosol sampling system for the ST experiments is shown in Figure 2.2-1. Seven identical filter thimbles are arranged vertically in a concentric arc over a zirconia mixing plenum. The upstream end of the filter thimbles are located approximately 10 cm above the irradiated fuel bundle. The filter thimbles are plumbed in parallel between the mixing plenum and a gas manifold. The entire exhaust stream carrying fission product vapors and aerosol will flow through the selected filter sampler. The samplers will be changed sequentially using solenoid valves located on the outlet end of the filter thimble. The

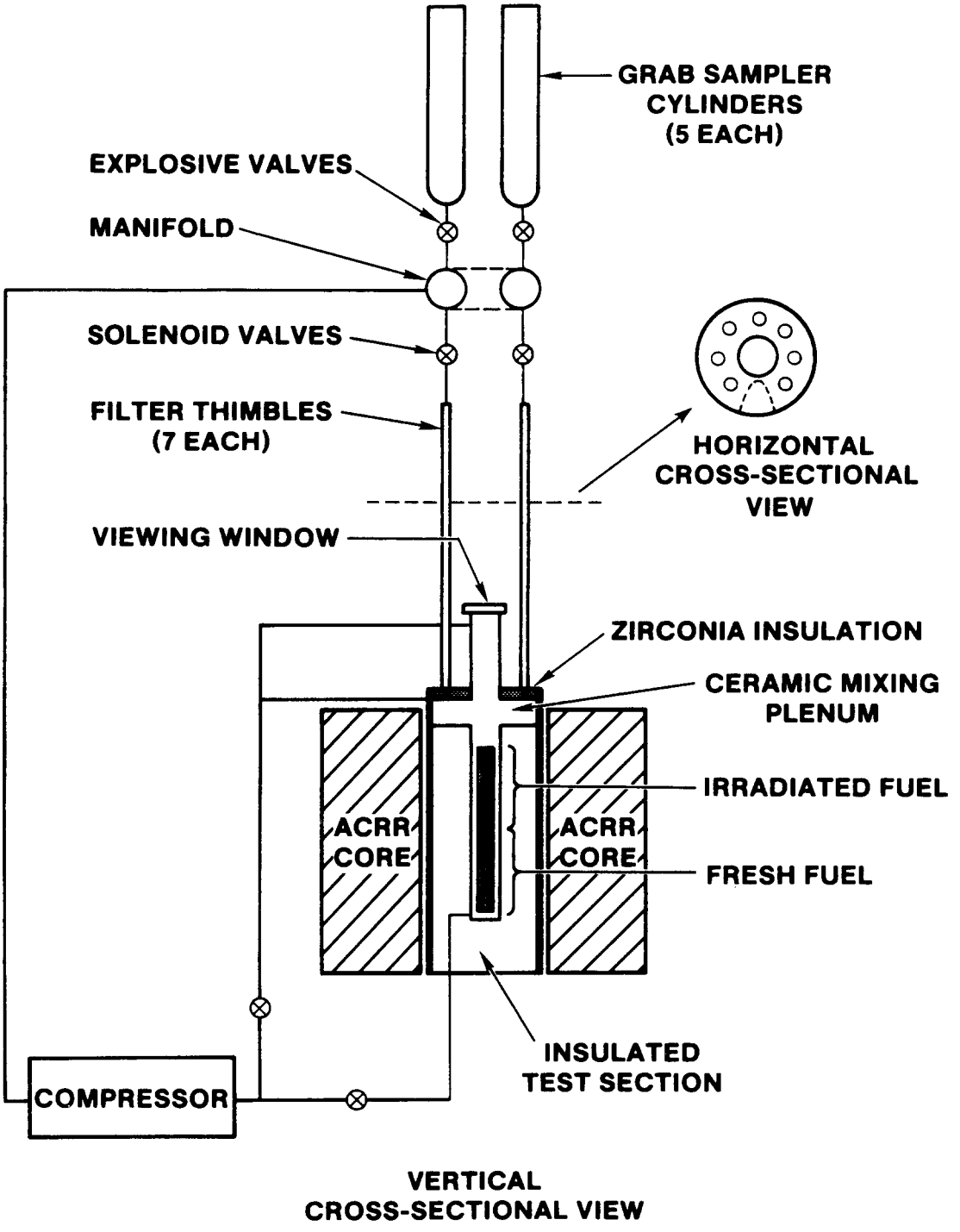

Figure 2.2-1. Functional Diagram of the Gas and Aerosol Sampling System for the Source Term Experiment

sampling schedule will be as follows unless conditions during the experiment dictate otherwise: Filter assembly 1 will be open from the start of the experiment until the fuel temperature reaches 2100 K, which is just below the melting temperature of zircaloy-4 cladding; filter assembly 2 will be open from 2100 K until 2300 K; filter assemblies 3, 4, and 5 will be open for 10 min apiece on the 30 min temperature plateau at 2300 K; filter assembly 6 will be open during the temperature ramp down from 2300 K; and filter assembly 7 will remain closed to serve as a "blank." There are also five grab sample cylinders connected to the manifold that will sample inert gases and control the pressure in the recirculating closed loop.

The filter thimbles were designed and tested to meet the following requirements: (1) 61 cm long with an outside diameter of 1.6 cm to fit inside the pressure boundary, (2) high overall collection efficiency (> 99 percent) for fission-product vapors and particles, (3) capable of sampling at high pressures (the nominal pressure in the ST-2 experiment will be 30 atm) and in large temperature gradients (calculations indicate that the temperature of the filter thimble near the zirconia mixing plenum will be approximately 1130 K and the downstream end will be less than 400 K), (4) posttest analyses of each filter thimble must provide data on fission product mass and chemical species; and (5) disassembly and posttest examination must be performed remotely using manipulators in a hot cell.

The final design of the filters that will be used in the ACRR Source Term Experiments has evolved from a series of seven filter qualification tests. In these experiments the collection efficiency and pressure response of the filters were measured to help refine the design so that the filters would meet the requirements listed above. These out-of-pile experiments involved generation of controlled amounts of fission product simulants in a H_2/Ar stream, equilibration at 1370 K, and passage of the stream through a single filter assembly. The filter was then disassembled and analyzed. The first four filter assembly qualification tests were described in Reference 101, and the final three tests will be described in this report.

The filter design that was used in the final three filter qualification tests and that will be used in the Source Term Experiments is shown in Figure 2.2-2. Each filter thimble is made of stainless steel with a nozzle at the upstream end that is about 1 cm in diameter and 5 cm long. The body of each filter thimble will have a diameter of approximately 1.6 cm and will be 61 cm long. The first section in the body of the filter thimble will be a 32-cm-long thermal gradient tube, similar to the one used in the Oak Ridge National Laboratory (ORNL) VI test series. The temperature of the thermal gradient tube at the upstream end will be approximately 1100 K and will decrease to 400 K near the fiber filter section. The thermal gradient tube will have three deposition wires of Ag, Pt, and stainless steel running parallel to its walls. These deposition wires were inserted to provide information on chemical speciation. They are intended to collect fission-product aerosols and chemically reactive vapors that will

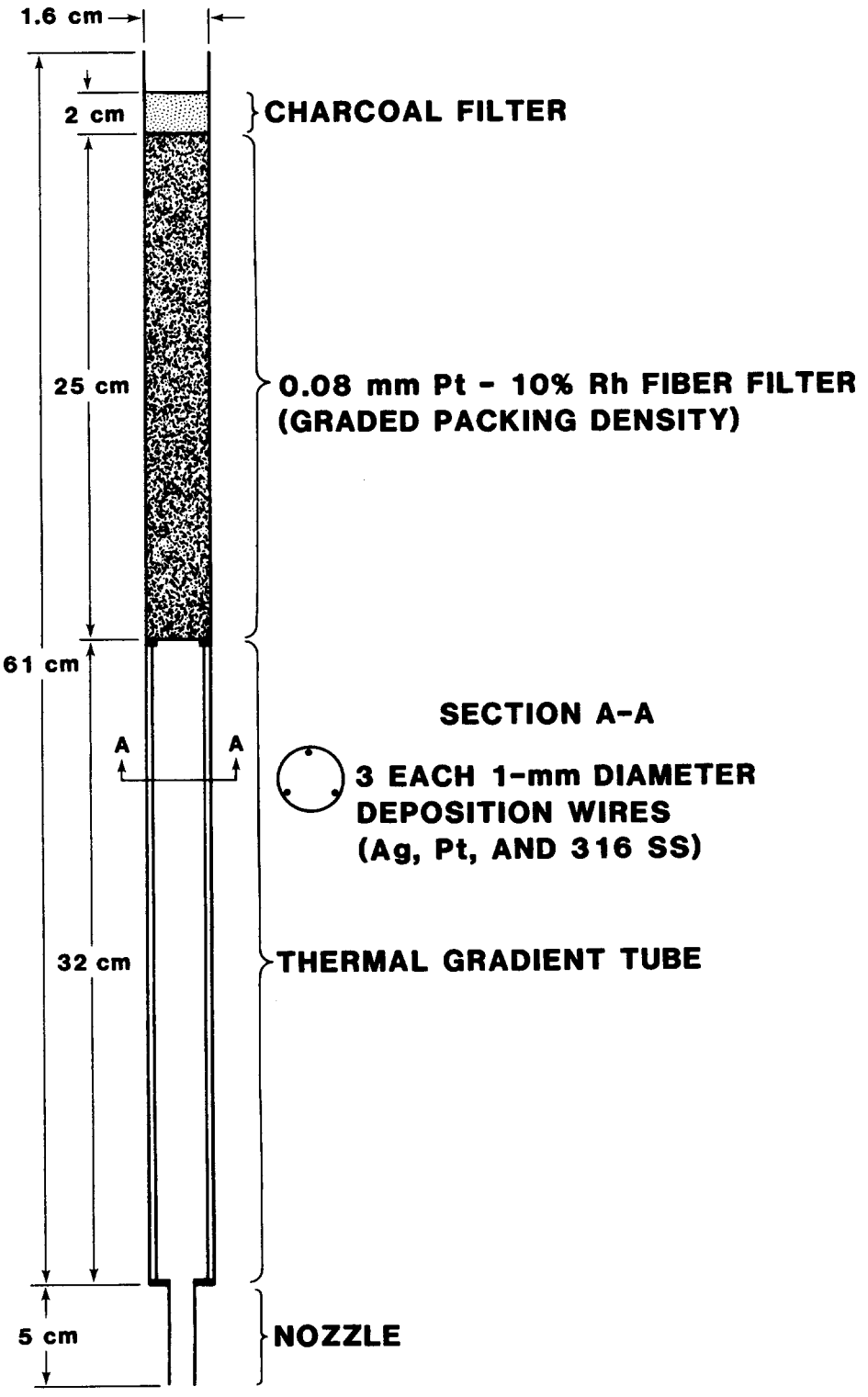

Figure 2.2-2. ST-1 Filter Design

be analyzed with a SEM by wavelength and energy dispersive analyses. The stainless steel wire was included because it is the same material as the thermal gradient tube and will give an indication of chemical species deposited in the thermal gradient tube; the Pt wire was included because it is chemically inert to most fission products, except possibly Te at high temperatures; and the Ag wire was intended to react with the gaseous iodine species HI and I_2. After the thermal gradient tube, the flow passes through a 25-cm-long fiber filter composed of 0.076-mm diameter Pt-10 percent Rh wire with a graded packing density. The Pt-10 percent Rh fibers will be held in a stainless steel tube by stainless steel screens that will be tack welded on each end. The tube will have outside O-rings on each end to seal it inside the filter thimble, thus preventing the flow of aerosol and vapor around the fiber filter. A graded packing density will be used to obtain the necessary filter efficiency and to preclude a high-pressure drop and filter plugging. The pressure drop across this filter is about 0.6 psi at a flow rate of 12 L/min. After the fiber filter, the gas flows through a 2-cm granular charcoal filter, which will collect noncondensed vapors such as HI, I_2, and H_2Te. This filter meets all of the design criteria.

2.2.2.2 Development Lists

Filter assembly tests 5, 6, and 7 were run during July using the experimental setup shown in Figure 2.2-3. The setup consisted of a vertical tube furnace capable of temperatures up to 1300°C. A silica tube with an OD of 3.8 cm and a length of 120 cm passed through the tube furnace with about 15 cm protruding out of the bottom of the furnace and 60 cm out of the top. Above the tube furnace, a calrod was wrapped around the silica tube and was surrounded with insulation to create the temperature gradient expected in the ST experiments. The stainless steel filter thimble was sealed by Viton O-rings in a second silica tube with a 3.1 cm OD that was positioned inside the outer silica tube. A brass plug was sealed by Viton O-rings in the inner silica tube at the bottom of the tube furnace.

Stainless steel plungers, which passed through the brass plug, contained individual silica crucibles containing Ba, Te, SnTe, and CsI. The plungers were adjusted to a position in the tube furnace where the temperature was adequate to reach the partial pressures necessary to vaporize the desired amount of fission-product simulants. In these experiments, cesium and barium were introduced either as a metal or hydroxide vapor. Tests 5 and 6 used Cs metal as the predominant Cs species and Ba metal as the Ba species, whereas test 7 used CsOH and $Ba(OH)_2$.

Experiments 5, 6, and 7 were run for 40 min at approximately 1100°C. After the system cooled to room temperature, the deposition wires that lay against the inner wall of the thermal gradient tube were removed for SEM examination using wavelength and energy dispersive analyses. The filter components (i.e., the nozzle, thermal gradient tube, fiber filter) were leached with deionized water and 7.5 M nitric acid. The water leachates were analyzed using an ion specific electrode for iodide, and the water and acid leachates were analyzed for Cs, Sn, Te, and Ba using a DC plasma emission spectrometer. The dry trap and water impinger were analyzed for I, Cs, Sn, Te, and Ba to determine the mass of each element that passed through the filter assembly so that filter efficiency could be determined.

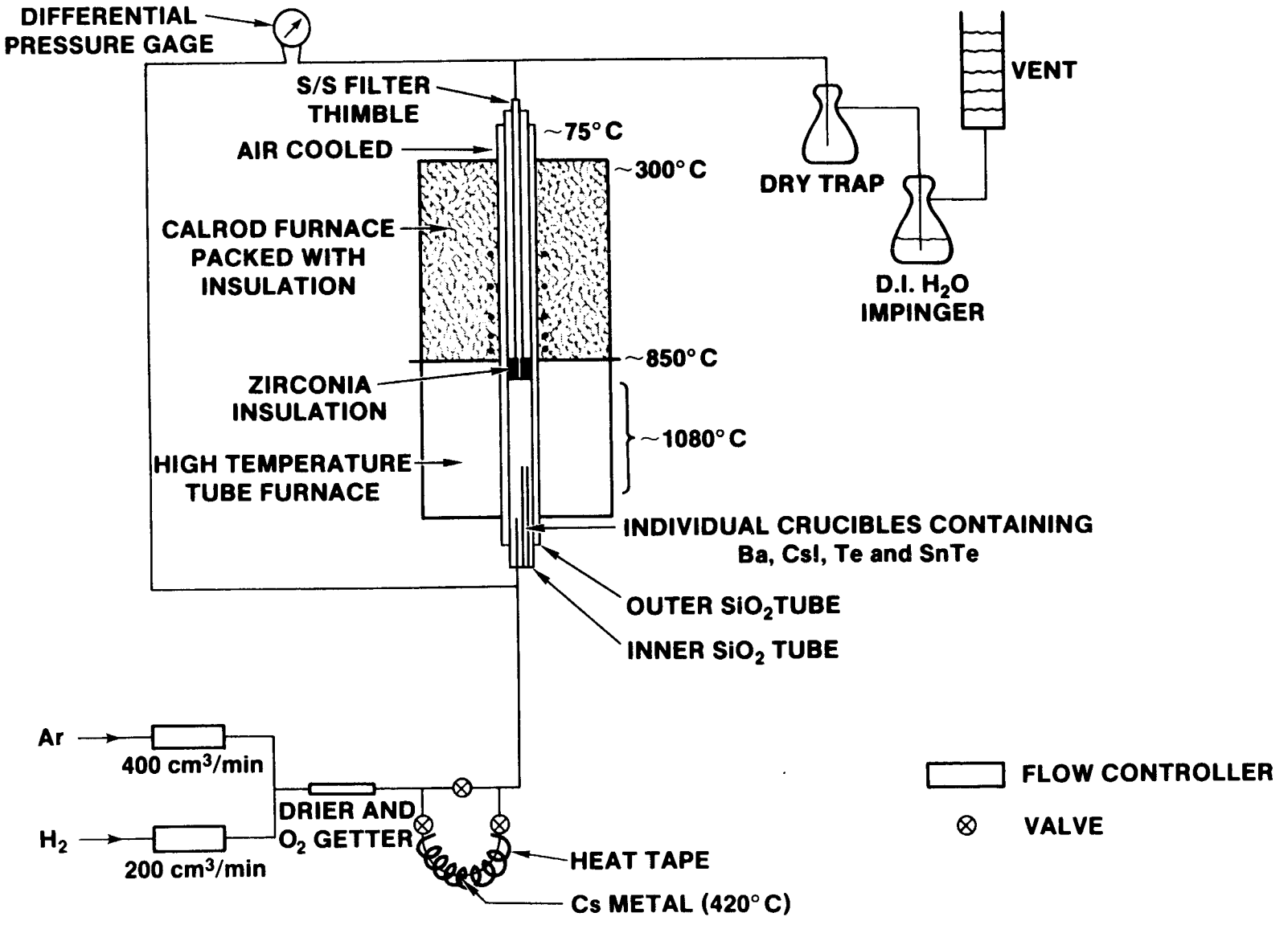

Figure 2.2-3. Experimental Setup for Source Term Filter Qualification Tests

In test 5, an inordinately high amount of CsI was introduced into the system, resulting in the subsequent plugging of the fiber filter. The limited analyses performed on the filter showed a collection efficiency for iodine greater than 95 percent. The total quantities of fission-product simulants introduced into the system in test 6 represent upper bounds on the release predicted by VICTORIA for the ST-1 experiment, and the sustained average flow rate of 11 L/min is a reasonable estimate of the anticipated ST-1 flow rate. Results of filter systems test 6 are plotted in the bar graphs in Figures 2.2-4 through 2.2-8. Three filter segments were analyzed individually: the thermal gradient tube including the nozzle, the fiber filter, and the granular charcoal filter. The dry trap and deionized water in the impinger were also analyzed and the results are shown in the bar graphs.

The data from filter systems test 6 result in the following conclusions. The filter assembly appeared to be approximately 98 percent efficient. About 720 mg of Cs were collected; most of the Cs deposited on the fiber filter, probably as Cs metal aerosol. The bar graph of the cesium results indicate that 161 mg were soluble in water and 485 mg were soluble in 7.5 M nitric acid. We believe that all of the cesium species formed in this experiment were water soluble. Several milliliters of water were retained in the fiber filter following the water leach. The nitric acid leach simply rinsed the residual water-soluble cesium out of the fiber filter. This problem will be corrected in the actual Source Term Experiments. Energy dispersive X-ray analysis (EDX) indicated that the iodine apparently reacted with cesium to form CsI, and 66 percent of it condensed on the surfaces of the thermal gradient tube. The tin reacted with tellurium to form SnTe. However, since the Te-to-Sn ratio was about 9.8, Te probably also existed as Te, Te_2, H_2Te, or $Cs_{2-x}Te$. SnTe and other tellurium species are chemically reactive with nickel and other components in stainless steel; thus the majority of the tellurium and tin was deposited in the thermal gradient tube. The barium was apparently collected in the fiber filter as an aerosol.

In test 7, CsOH and $Ba(OH)_2$ were generated in lieu of cesium and barium metal. Results of filter systems test 7 are plotted in the bar graphs in Figures 2.2-9 through 2.2-13. Three filter segments were analyzed individually: the nozzle, the thermal gradient tube, and the fiber filter. The granular charcoal was inadvertently omitted from the filter assembly, resulting in a reduced filter efficiency. The dry trap and deionized water in the impinger were also analyzed and the results are shown in the bar graphs.

The data from filter systems test 7 result in the following conclusions: The filter assembly appeared to be approximately 94 percent efficient. About 300 mg of Cs were collected, which resulted in only a small increase in the pressure drop across the filter assembly. The bar graph of the cesium results show that a large fraction of the cesium collected in the filter assembly was soluble in water. The residual water in the fiber filter was forced out with a nitrogen stream, and therefore, very little cesium was found in the nitric acid leachate. EDX analysis indicated that the tin reacted with tellurium to form SnTe.

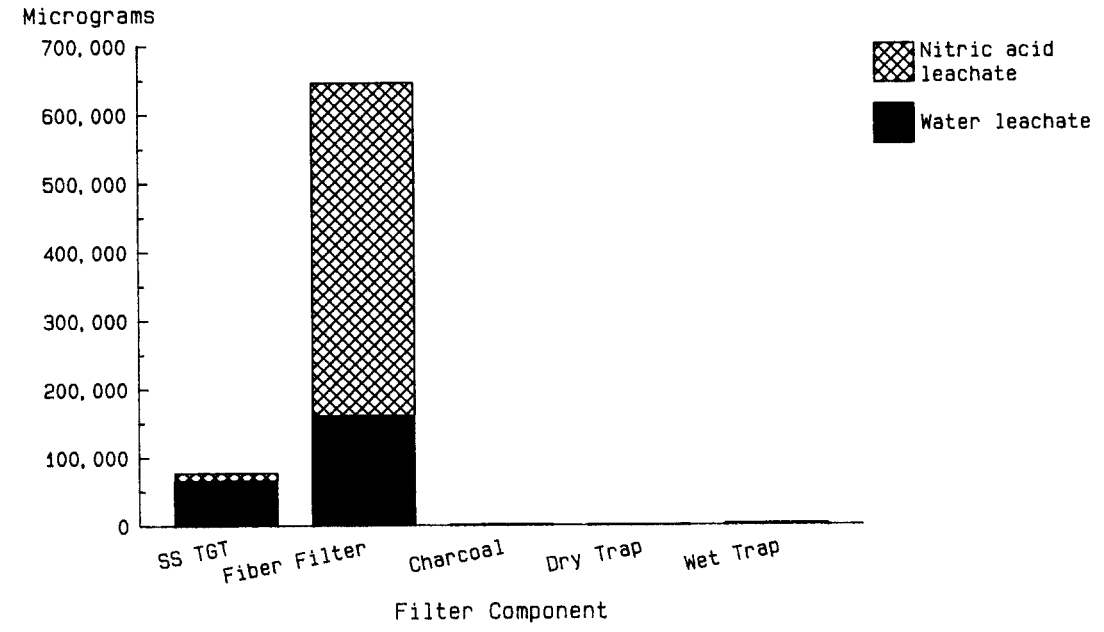

Efficiency = 99.5%

Figure 2.2-4. Filter Systems Tests #6 - Cesium Results

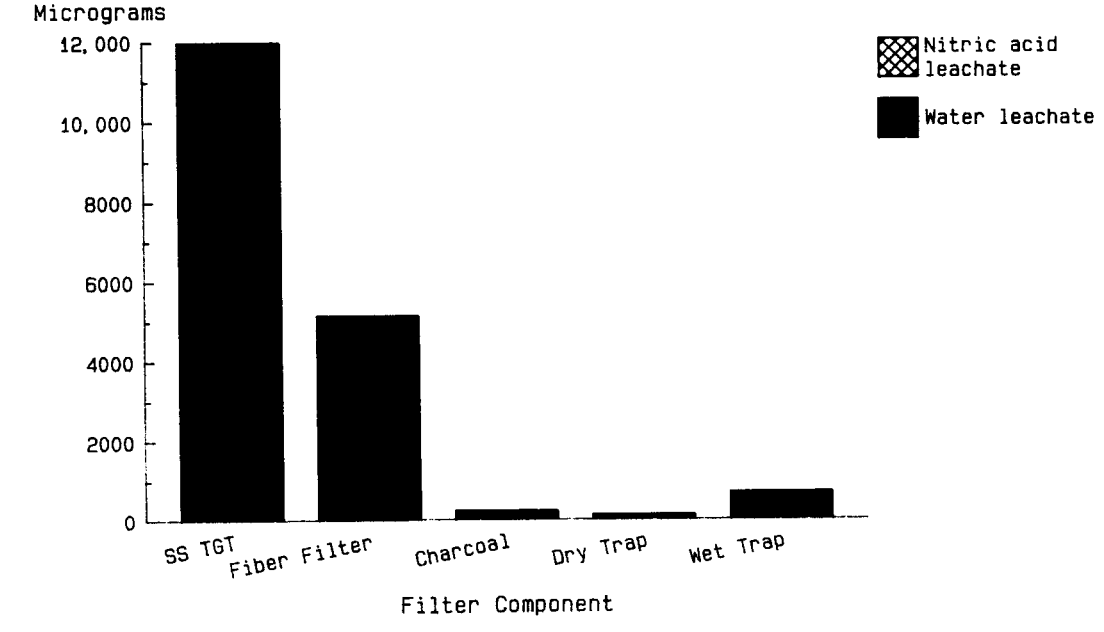

Efficiency = 95.3%

Figure 2.2-5. Filter Systems Tests #6 - Iodine Results

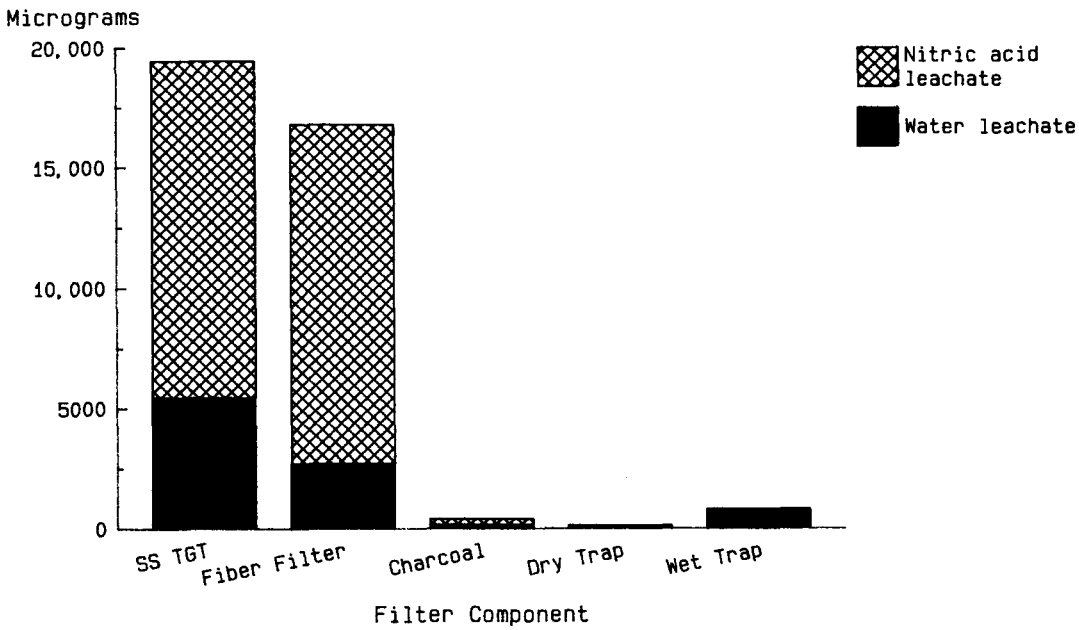

Efficiency > 97.4%

Figure 2.2-6. Filter Systems Tests #6 - Tellurium Results

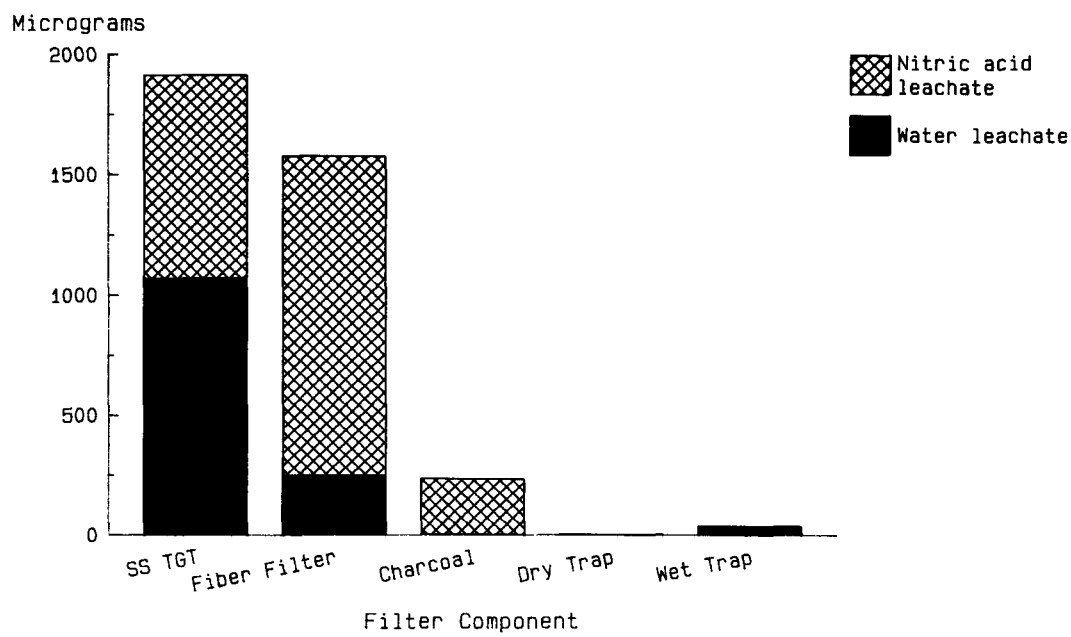

Efficiency > 98.8%

Figure 2.2-7. Filter Systems Tests #6 - Tin Results

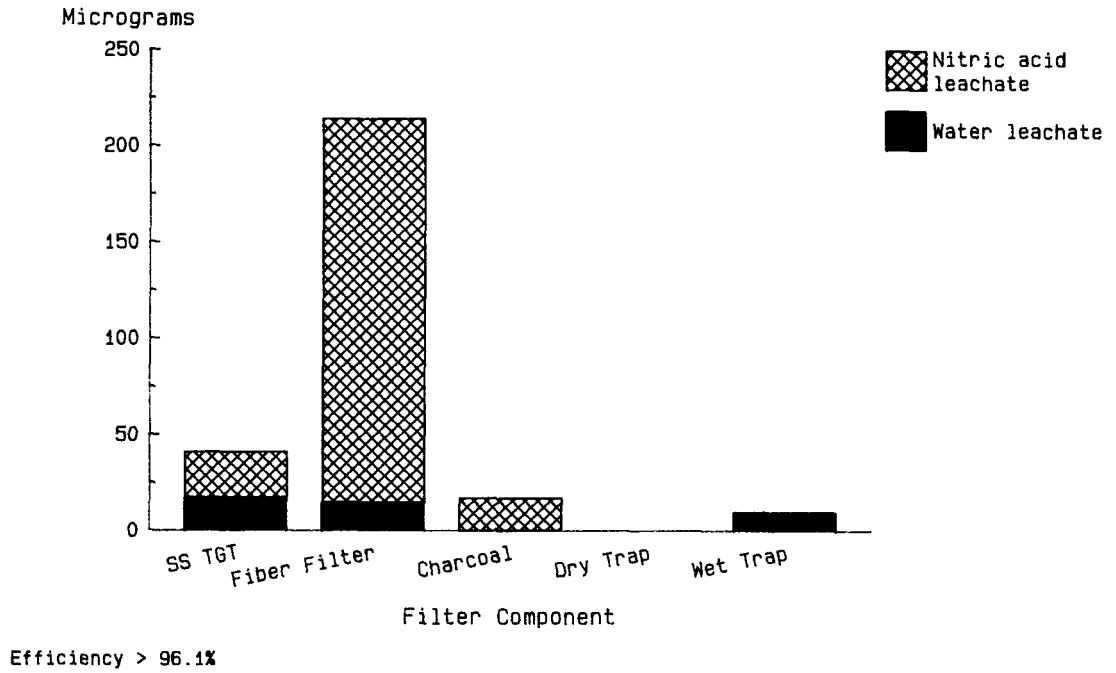

Figure 2.2-8. Filter Systems Tests #6 - Barium Results

Again, since the Te-to-Sn ratio was high, Te probably also existed as Te, Te_2, H_2Te, or $Cs_{2-x}Te$. The majority of the tellurium, tin, and barium was apparently collected in the fiber filter as an aerosol.

2.2.2.3 Deposition Wire Analyses

The deposition wires from filter assembly tests 4, 5, and 7 were investigated in the SEM using EDX in an attempt to determine the effect of longitudinal position on compositional variations, to estimate stoichiometries present, and to correlate aerosol particle morphologies with compositions. Generally, scans were made at three locations on each wire: upstream, middle, and downstream. X-ray powder diffraction (XRD) patterns were made from samples taken from wires from tests 5 and 7 to provide precise information on the compounds present. Two samples, one from the upstream end and one from the downstream end, were taken from each wire.

The major components seen on the wires from filter assembly test 4 were Cs, followed by Te, I, and then Sn. Test 4 used a nickel thermal gradient tube, and therefore, a nickel wire was used in lieu of a stainless steel deposition wire. On the nickel deposition wire, there was a slight

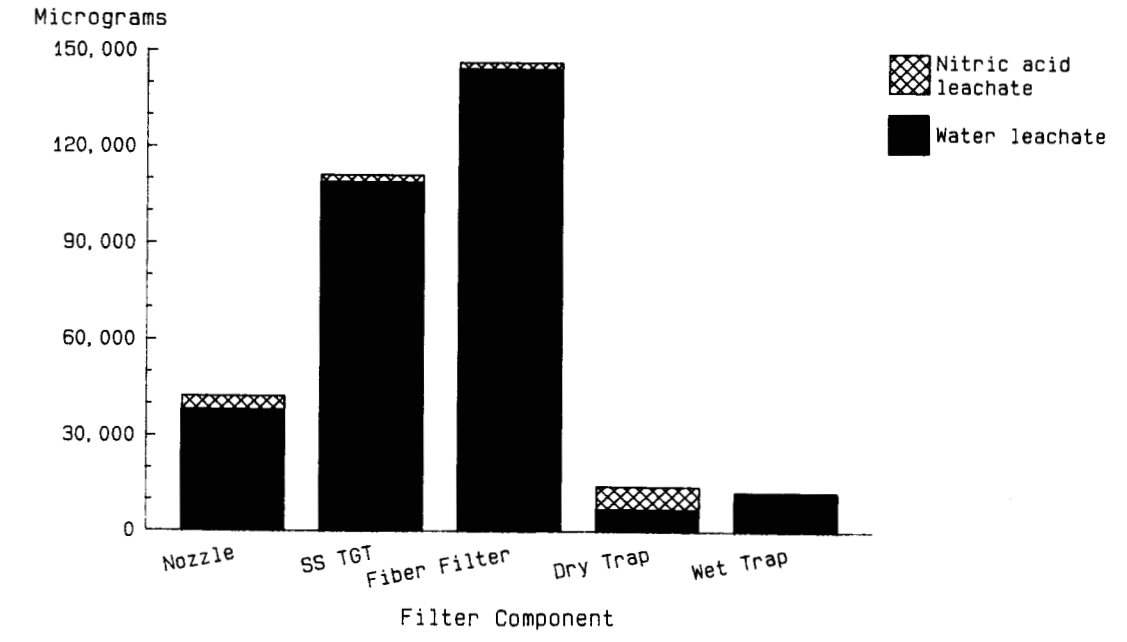

Efficiency = 93.8%

Figure 2.2-9. Filter Systems Test #7 - Cesium Results

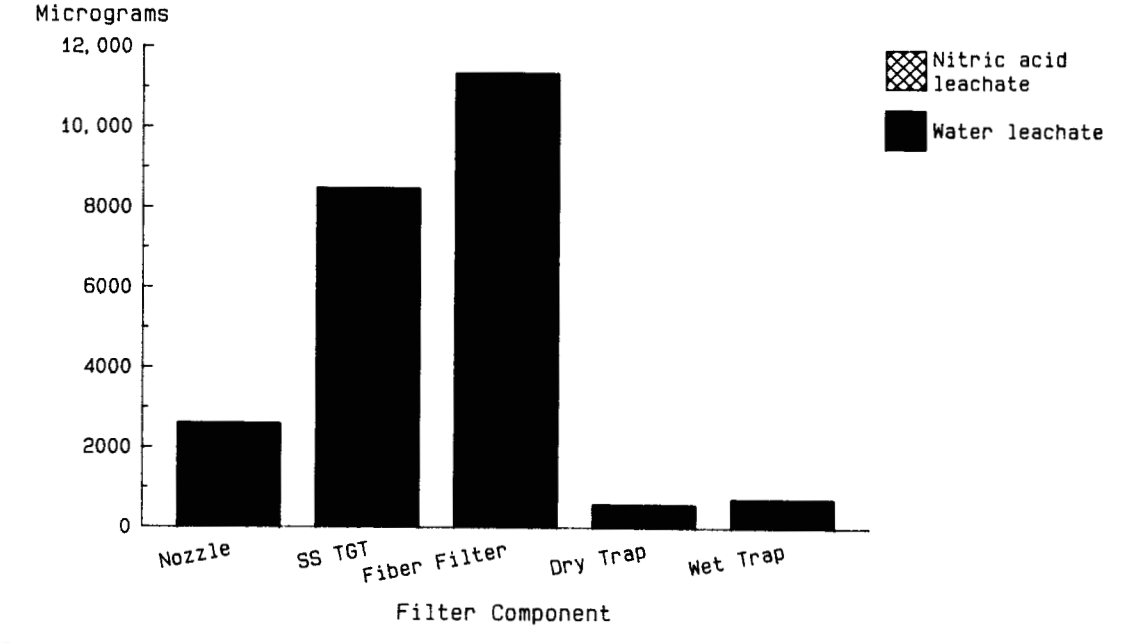

Efficiency = 94.3%

Figure 2.2-10. Filter Systems Test #7 - Iodine Results

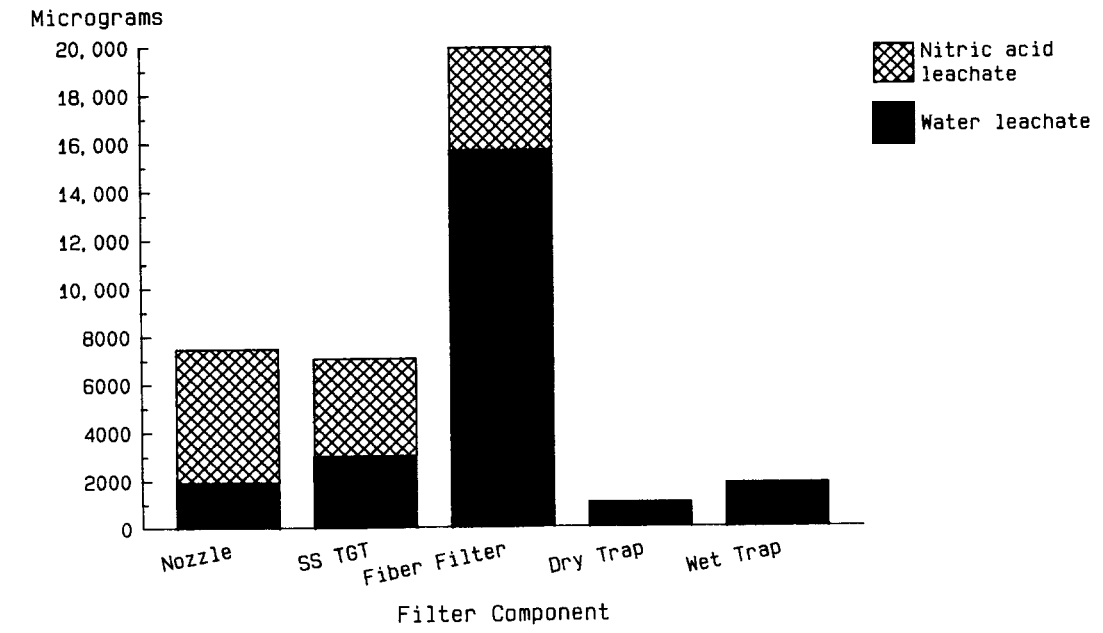

Efficiency = 92.2%

Figure 2.2-11. Filter Systems Test #7 - Tellurium Results

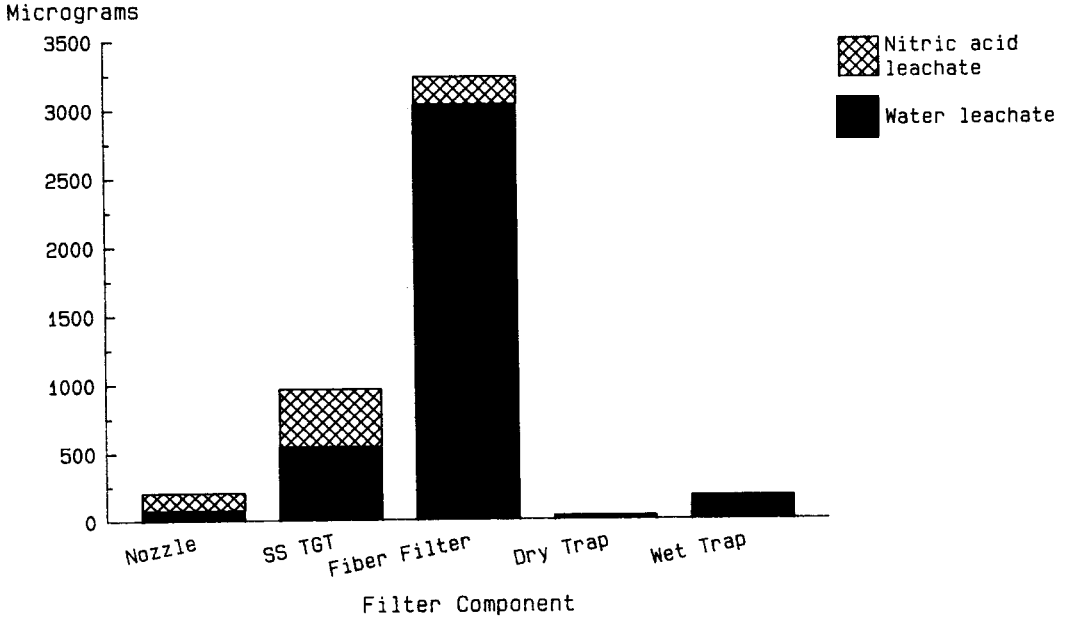

Efficiency = 95.4%

Figure 2.2-12. Filter Systems Test #7 - Tin Results

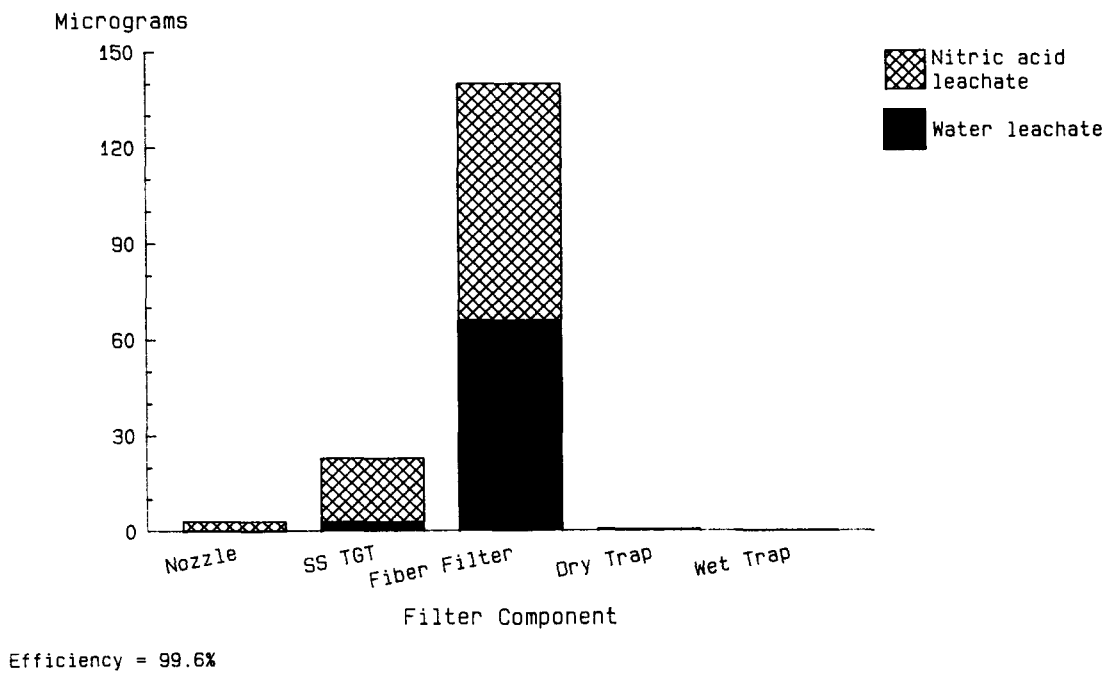

Figure 2.2-13. Filter Systems Test #7 - Barium Results

increase in Cs and a decrease in Te from the upstream end to the downstream end. This result is not surprising since condensation of Cs probably increased as the temperature decreased with distance down the thermal gradient tube; also, most Te species are expected to have diffusion-limited chemical reactions with nickel, and thus the concentration of Te species is expected to decrease with distance down the thermal gradient tube. The major constituents on the nickel wire were CsI, which appeared as small spheres or cubes (Figure 2.2-14a), Cs alone (probably Cs_2CO_3 formed by oxidation of Cs metal and reaction with CO_2 after exposure to the atmosphere), which appeared as needles (Figure 2.2-14a) or faggot-like bundles (Figure 2.2-14b), $Cs_{2-x}Te$, which appeared as blades (Figure 2.2-14c), and rough deposits of Cs-Te-I-Sn (Figure 2.2-14d). On the Ag and Pt wires, the only particles clearly identified as being a distinct chemical form were Cs alone, CsI, and $Cs_{2-x}Te$. To obtain the average composition of an area, raster scans were made. Scan sizes varying by orders of magnitude were compared; no significant variations in composition results were found.

a. CsI Cubes and Cs Needles

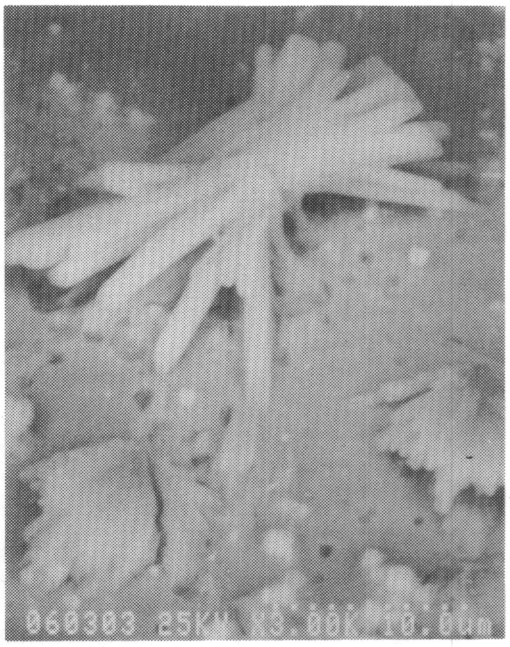

b. Cs Faggots and Cs Needles

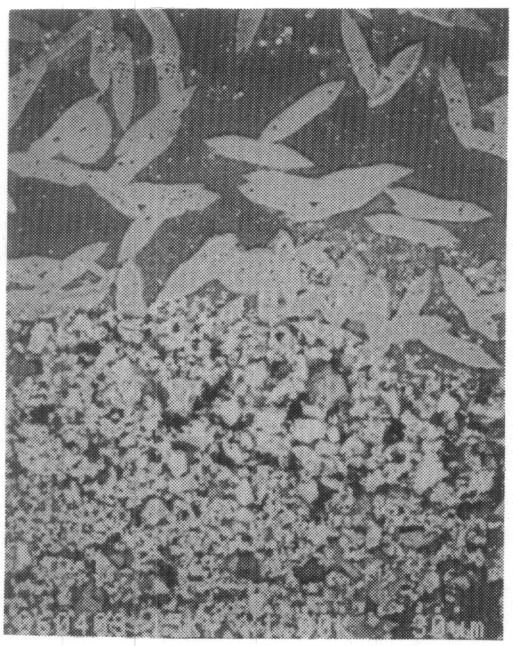

c. $Cs_{2-x}Te$ Blades

d. Cs-Te Blades and Cs Particles

Figure 2.2-14. SEM Photomicrographs of Particles Collected on a Nickel Deposition Wire in Filter Systems Test 4

Nickel, stainless steel, and silver wires were used in test 5. The major components on the nickel wire were Cs and I. Cs, I, and Sn did not vary much longitudinally; Te increased greatly in the middle of the wire. Major constituents identified on the nickel wire were CsI and Ni-Te. On the stainless steel wire, Cs, I, and Te were found in approximately equal amounts. Major constituents were CsI, which was seen as small particles (U) and large particles (D), and Te, which was apparently part of the stainless steel matrix. The morphologies of the deposition products were similar to those shown in Figures 2.2-14a-d. The major component on the Ag wire was Te (Figure 2.2-15). There was no significant longitudinal variation. A majority of the particles analyzed contained Ag as the primary component combined with Te. The morphologies of these particles are shown in Figures 2.2-15a and b.

The XRD patterns for test 5 were complex and have not been completely indexed to date. The complexity of the patterns also increases the likelihood that some of the identifications are in error. The major compounds identified from the upstream end of the nickel wire were CsI and SnTe. The major compounds identified in the downstream sample from the nickel wire were Ni and $NiTe_2$, and the minor compounds identified were CsI and another Cs form, possibly Cs_2CO_3 or $CsNO_3$. There were unidentified lines in the upstream and the downstream patterns. The major compound identified from the upstream end of the silver wire was Ag_2Te, and the minor compounds were AgI and AgTe. The major compound identified in the downstream sample from the silver wire was Ag, and the minor compounds identified were AgI and Ag2Te. The Ag patterns have been completely indexed. One compound has been identified in the sample from the upstream end of the stainless steel wire, CsI. Two major compounds have been identified from the downstream sample: CsI and Te. These patterns contained numerous nonindexed peaks.

In test 7 the deposition wires were composed of stainless steel, silver, and platinum. The major components on the stainless steel wire were Cs, Te, and then I. The particles that were clearly identified were CsI, Cs alone (probably associated with C, O, or N), and Cs associated with Te in various atomic ratios. Also present in the spectra from the stainless steel wire were Fe, Cr, Ni, Al, Si, and Mo. Cs and Te were the major elements found on the Ag wire. Agglomerate particles of Ag-Te and Ag-I were identified on the Ag wire. Small amounts of Al and Si were also found on this wire. On the Pt wire, Cs was the most important deposit; Te, Sn, and I were found in small amounts. Tendrils of Cs, which at high magnification showed an acicular structure, encircled the wire (Figure 2.2-16a). Bows or discs of Cs-Te were common (Figure 2.2-16b). Particles of CsI were also found. Although Sn was present in the spectra, its morphology could not be isolated. Al, Si, and Cl were common impurity elements.

The XRD results for test 7 follow: For the stainless steel wire, the pattern of the sample from the upstream end was not successful. For the sample from the downstream end, CsI and $CsHCO_3$ were identified. There were some minor unidentified peaks. For the silver wire, the upstream pattern had as major compounds AgI and Ag; the minor lines appear to be Ag_2Te or AgTe. AgI and Ag_2Te were identified as the compounds in the sample from the downstream end of the silver wire. The diffraction patterns from the

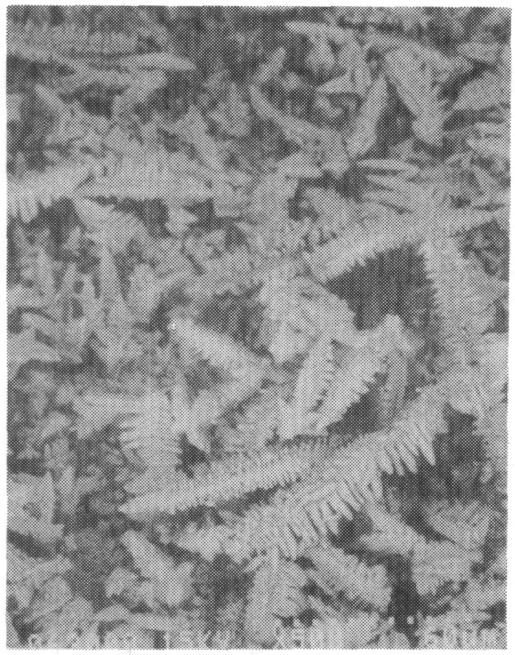

a. Ag-Te Dendrites

b. Ag-Te Flakes

Figure 2.2-15. SEM Photomicrographs of Particles Collected on a Silver Deposition Wire in Filter Systems Test 5

a. Cs Tendrils

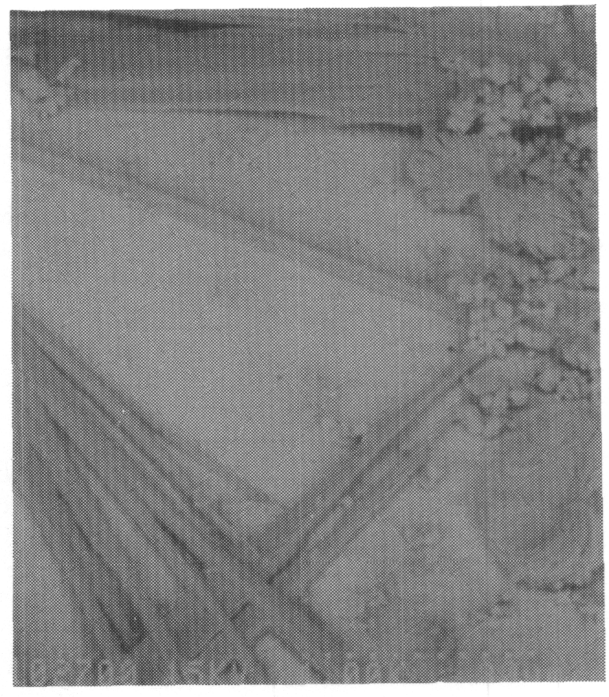

b. Cs-Te Bows and Discs, Cs Needles, and Small Cs Particles

Figure 2.2-16. SEM Photomicrographs of Particles Collected on a Platinum Wire in Filter Systems Test 7

Pt wire consisted primarily of the Pt lines. No other compounds were identified.

2.2.3 Posttest Analytical Methods

During July through December, the analytical techniques for posttest analyses of the ST filter assemblies were developed, implemented in the hot cells, and rehearsed using manipulators. Flowcharts of the posttest analyses procedures are shown in Figures 2.2-17 through 2.2-19. Posttest examination of the filter components includes gamma spectroscopy (primarily for Cs), ion chromatography for Ba and Sr, ion specific electrode for iodine, voltammetry for Te, gas analyses by mass spectroscopy for Kr and Xe, and precipitations to separate Sr, Te, and rare earth elements from Cs. Some of these techniques are described in the following five sections.

2.2.3.1 Voltammetry

A much simplified method for analysis of tellurium, using stripping voltammetry, was developed by Mike Kelly, Division 1821, Sandia, and was adapted for use in the hot cells. A 10 mL aliquant of the water leach is mixed with 70 mL of 2.29 M nitric, or 10 mL of the acid leach is mixed with 1.71 M nitric, to yield a 2 M solution. Tellurium in the solution is plated onto a rotating gold electrode, then stripped to produce a current pulse proportional to the Te concentration. Rotation of the electrode efficiently stirs the solution, and the cell is cleaned between analyses by flushing with 2 M nitric. Overall, the procedure is quite simple, with a sensitivity of ca. 10 ppb in the diluted solution, or 80 ppb in the original solution; very few electronic parts need be exposed to radiation, and the electrodes themselves should be relatively insensitive. There are potential interferences from Sb and Ag, which have stripping peaks close to the Te peak; however, the Te/Sb for the solutions should be ca. 40/1, and the Te/Ag should be at least 7/1, so the Te peak will be adequately resolvable. Interferences from Ag and Sb will also be obvious from the gamma spectra of the Te precipitates.

2.2.3.2 Gamma and Beta Spectroscopy of Precipitates

Modifications in the chemical procedures have made it possible to move much of the sample processing to shielded gloveboxes and radiochemical hoods, thereby reducing the amount of time taken up by hot cell manipulation and remote handling. Detailed counting of the Te, La oxalate, and $SrSO_4$ precipitates will be carried out in Room 106 (an auxiliary room in the hot cell facility) rather than in the shielded hot cells; the gamma detector port by window 6 in the shielded facility will be used primarily to confirm that the activities of the precipitates meet Health Physics requirements before the samples are bagged and passed out for processing in Room 106. The filters used to collect the precipitates are sufficiently small that the entire filter assembly can be counted as a unit, so there will be no need to remove the filter papers from their holders in the hot cells.

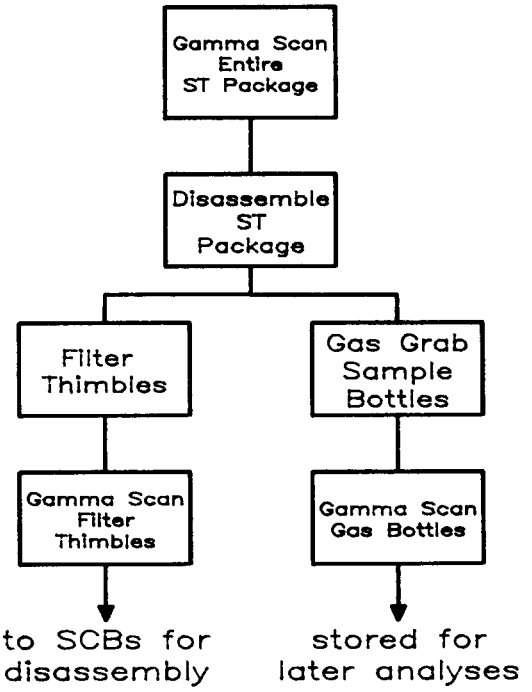

Figure 2.2-17. Posttest Analyses in Zone 2A

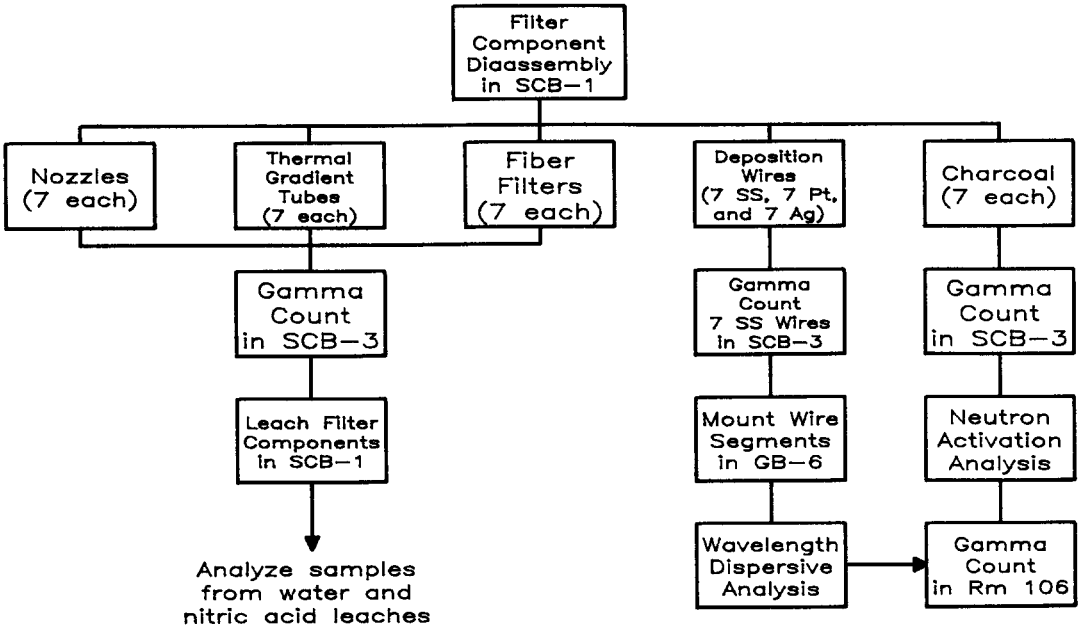

Figure 2.2-18. Posttest Analyses of ST Filters

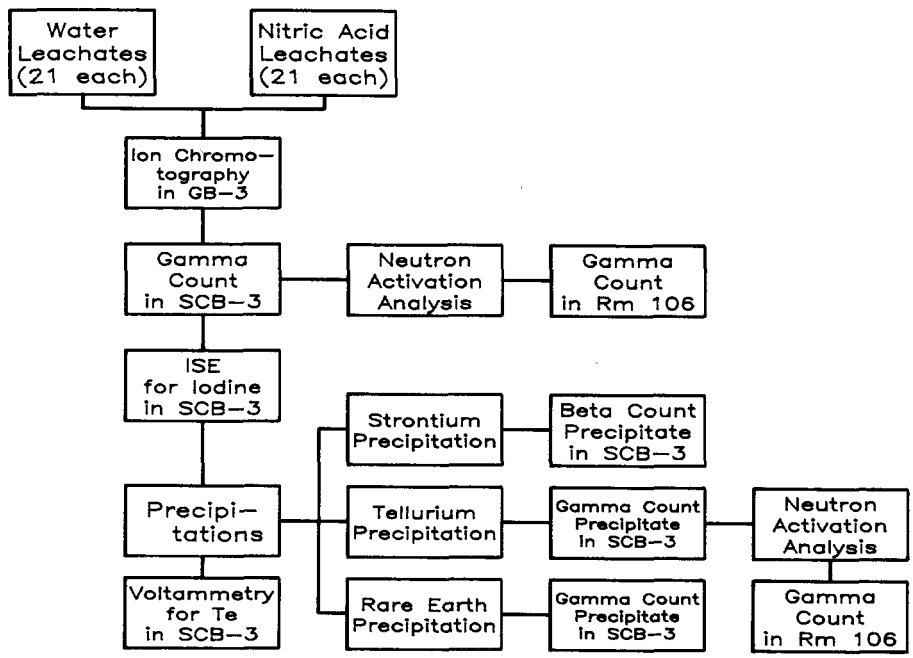

Figure 2.2-19. Posttest Analyses of Leachates

We initially planned to precipitate Te from solutions for subsequent counting. It was not certain that the radiotellurium activity generated by the test would be sufficient for detection by gamma spectroscopy, so we planned to neutron activate the Te precipitates to generate sufficient activity. Neutron activation precluded use of a nonradioactive Te carrier, so the minimum amount of Te that could be precipitated corresponded to ca. 2 ppm in solution; at such low levels, the Te took up to a day to precipitate completely. However, since the voltammetric analysis for Te is working well, we now plan to use Te precipitation only as a backup and will add carrier to greatly speed and simplify the procedure. The only difficulty with the procedure is the need to use fresh stannous chloride for the precipitant; the stannous chloride solution decays over a matter of weeks, so there must be provisions to pass in or make up fresh solution in the hot cells.

Precipitation of $SrSO_4$, and subsequent beta counting of ^{90}Sr-^{90}Y, is a backup for analysis of Sr by ion chromatography. The precipitation is also carrier based; 1 mL of leach solution is mixed with 10 mL of 2500 ppm Sr in 1 M nitric acid, then the $SrSO_4$ is precipitated with 2 ml of 1:1 H_2SO_4, and the precipitate is filtered and washed. Based on tests with nonradioactive samples, yield of the carrier is greater than 97 percent, and less than 1 percent of the Cs is retained in the precipitate. Hence the dominant beta activity in most samples should be from ^{90}Sr-^{90}Y decay. The samples are beta counted primarily for the high energy beta of ^{90}Y--after several weeks

of decay to achieve parent-daughter equilibrium; a 0.020-in aluminum absorber placed between the Si surface barrier detector and the sample removes > 95 percent of the Cs beta particles, but only 50 percent of the ^{90}Y betas. The surface barrier detector is roughly 30 times more sensitive to betas than to gammas, so the gamma activity of contaminants will cause little interference with beta counting. Some ^{140}Ba-^{140}La will be coprecipitated with the $SrSO_4$; since the ^{140}La betas are also high energy, this contamination can cause inaccuracy. However, the extent of ^{140}Ba-^{140}La contamination can be assessed by gamma counting the samples on a Ge detector, and if necessary, the ^{140}Ba can be allowed to decay for 100 days before the samples are beta counted. During the ST1 test, the Cs/Sr should decrease from ca. 200 for the first filter sample to ca. 1 for the last samples, so Cs contamination problems will be relatively unimportant for samples taken late in the test. Conversely, ^{140}Ba is generated as the test proceeds, so Ba contamination will be smallest for the first filter samples. If Cs contamination proves to be too great in any sample, we have provisions to first precipitate Sr oxalate in the hot cells, pass the oxalate out for processing in a radiochemical hood, dissolve the precipitate in HCl, and then precipitate $SrSO_4$ for a much more rigorous decontamination.

The La oxalate precipitation is designed to remove Cs and selectively concentrate the rare earth elements (Ce, Eu, etc.) for subsequent gamma spectroscopy. Ten mL of La carrier (2000 ppm La as $LaCl_3 \cdot 8H_2O$ in deionized water) is mixed with 0.25 mL of 7.5 M HNO_3. Then 0.5 mL of the leachate sample is added. La oxalate is then precipitated by adding 3 mL of 11 percent oxalic acid. The activity of rare earths is expected to be quite low, so we will first process samples taken in the latter part of the ST-1 test when the Cs/(rare earth) ratio should be lowest and the chance of detecting rare earths the highest.

2.2.3.3 Ion Specific Electrodes

The ion-specific electrode analysis for iodide is basically unchanged from our previous reports; the electrodes and holder have been modified to make the analysis more amenable to handling with manipulators.

2.2.3.4 Ion Chromatography

Ion chromatography is the preliminary means for analysis of Sr and Ba. We have had to make numerous modifications since the original development of the technique. The sample changer electronics have been modified to protect them from radiation, and concentrators have been placed in the sample loop to increase sensitivity. The eluents and columns originally recommended by Dionex proved to be ineffective, and a great deal of testing was required to find conditions that gave adequate sensitivity. Despite initial claims by the manufacturer, it is not possible to run acid solutions through the columns, so solutions must be neutralized and substantially diluted, which provides an effective sensitivity of ca. 1 ppm Sr and Ba in the filter leaches. This sensitivity is approximately the same as the average concentration of Ba and Sr predicted for the leaches, based on VICTORIA calculations.

2.2.3.5 Gamma Spectroscopy

The gamma spectrometer has been calibrated for collimators in zone 2a and steel containment box (SCB) 3, using ^{226}Ra (in equilibrium with daughters) as a standard. The daughter spectrum has numerous gamma peaks with a wide range of energies, and the decay fractions are relatively well known. Calibrations were carried out both with and without Pb attenuators, and given the collimation and distance from source to attenuator, extrapolation to greater attenuator thicknesses will be simple and easily justified.

The greatest difficulties found in choosing an appropriate source for calibration were obtaining a source both with activities known to better than $\pm$ 10 percent and with sufficiently small dimensions that the entire active volume could be viewed through a collimator. Radium sources tend to have the best known activities, partly because the Curie was originally defined in terms of radium and partly because useful activities of radium have easily measured masses. One difficulty with radium sources is that the evolved radon and subsequent daughters tend to deposit on the container walls, substantially spreading out the volume of the source from the original radium volume.

The gamma detector geometry in Room 106 will be calibrated both with radium and with "old" Th sources.

2.2.4 Hot Cell Plant Modifications

Construction of the vertical pass-through into the Zone 2A work area of the Hot Cell Laboratory, of the elevator facility within Zone 2A, and of the work platform and crane system above the vertical entrance have been completed. The assembly of the shield cask is nearing completion. The cask provides the necessary shielding for handling the ST experiment package during transport between the hot cell and ACRR. The cask contains a winch, which is used to raise and lower the experiment package into and out of the cask. The winch in the cask is also used to manipulate the experiment package during assembly and disassembly within Zone 2a. The cask is located on the work platform above the vertical entrance into the hot cell during package assembly and disassembly.

2.2.5 ST-1 Experiment Preparations

Nearly all components for the ST-1 experiment have been delivered. Delays in the delivery of ceramic parts of the test section are delaying assembly of the experiment package. A rehearsal mock-up for use in developing hot cell methods has been assembled and is being used to refine the remote handling techniques. The routing of plumbing and related components in the test section and compressor portions of the experiment package are in progress. Qualification tests of components and subassemblies are also in progress. It is anticipated that the ST-1 experiment will be conducted in late March 1987.

3. LWR DAMAGED FUEL PHENOMENOLOGY

We are investigating, both analytically and in separate-effects experiments, the important in-vessel phenomenology associated with severe LWR accidents. This investigative effort has provided for two related research programs: the Debris Formation and Relocation (DFR) program (ongoing) and the Degraded Core Coolability (DCC) program (completed). The focus of these activities has been and is to provide a data base and improved phenomenological models that can be used to predict the progression and consequences of LWR severe core damage accidents. The DFR experiment program provides unique data on in-vessel fuel damage processes that are of central importance in determining the release and transport of fission products in the primary system. The DCC experiment program, completed in CY86, provided data on the ultimate coolability of damaged fuel configurations. Models coming from both programs are used directly in the MELPROG and other in-vessel severe accident codes.

3.1 ACRR Debris Formation and Relocation

(R. O. Gauntt and K. O. Riel, 6423; R. D. Gasser, 6425)

3.1.1 Introduction

Evaluation of the potential consequences of severe core damage accidents requires the development and verification of computer models that account for the complex fission-product release and fuel damage phenomena occurring in core uncovery accidents. The NRC-sponsored DFR experiments are being performed at Sandia to provide data on the effects of key variables and conditions on the progression and severity of core damage processes. Examined in the DFR experiments are a range of conditions of initial clad oxidation, steam flow rates, system and rod internal pressures, and the effect of control rod materials on damage. The purpose of these experiments is to provide a data base of core damage phenomenology over a broad parameter space for use in model development and verification.

3.1.2 Experimental Method

3.1.2.1 General Approach

The intent in the DFR experiment design is to represent a short segment (0.5 m) of an uncovered LWR core where severe fuel damage initiates and to provide the best characterized environmental conditions as possible. For example, dry steam is introduced to the bottom of the test bundle so that the uncertainties associated with coolant boildown rates are not encountered. The short bundle length is justified since the principal damage process, clad oxidation, tends to localize within an axial zone of 10 to 20 cm in length, and therefore, most pertinent phenomenologies are suitably accommodated. Fuel heating is achieved by fission by means of neutronic coupling with the Annular Core Research Reactor (ACRR). Fission heating in combination with the chemical energy released from zircaloy oxidation generates sufficient power to drive fuel temperatures well above 2500 K. Unique diagnostics developed for this test series allow fuel temperatures as high as 2700 K to be continuously monitored throughout the experiment and allow accurate time dependent hydrogen production rate measurements

to be obtained. In addition, an end-on view of the test bundle is attained using a quartz glass viewing port installed in the experiment capsule; video and film cameras record the test progression observed through the viewing port. Postirradiation examination (PIE) is standard posttest procedure and includes preparation of numerous test bundle cross sections for metallographic characterization.

3.1.2.2 Experiment Capsule

A number of notable features of the test capsule are shown in Figure 3.1-1. The principal feature is the test bundle, which is axially centered in the ACRR. Steam introduced to the package enters the bottom of the test bundle, and flows upward around the fission heated fuel rods. Separate steam flows are introduced well above the exit of the test section in order to cool the bundle effluents and to keep the line-of-sight viewing port clear of aerosol, which tends to occlude the view of the test bundle. Each steam flow is individually metered. As zircaloy oxidation occurs, hydrogen is produced and swept out with the bundle effluents. The exiting gases then flow through a parallel bank of eight stainless steel tubes (~2.54-cm ID by 50 cm in length), which are packed with CuO particles (~0.5-mm dia by 2 mm long). The hydrogen is converted back to steam by the exothermic reaction $H_2 + CuO \rightarrow Cu + H_2O$ + heat. The heat production from the CuO and H_2 reaction may be quantified and thus the hydrogen production rate inferred. This is facilitated by a computer model (COPOX) of the reaction tubes that accounts for the heat production and transfer as a function of axial position in the tubes. The steam exiting the reaction tubes passes through a regulating valve, which separates the high-pressure side of the flow system from the low-pressure condenser region of the package. The steam passing through the regulating valve is condensed in a counterflow heat exchanger and allowed to hold up and subcool in a tank located at the bottom of the capsule.

In general, the test bundle may accommodate from 9 to 14 zircaloy clad UO_2 fuel rods in a ~0.5-m assembly. The bundle is insulated radially using a low density ZrO_2 material, which has an open porosity of around 85 percent. Although the insulator performs well thermally, there are two important caveats to note. The first is that a coherent tight fuel bundle blockage, which might form during the test, will not prevent steam from reaching the upper bundle above the blockage zone because steam bypass through the porous insulator will occur. The second point is that liquefied U-Zr-O, which might otherwise form a more coherent blockage around fuel rod remnants, tends to soak into the insulator, interacting with the material as it migrates radially away from the blockage zone.

3.1.2.3 ACRR Installation

The experiment is carried out by placing the test capsule in the ACRR central cavity as shown in Figure 3.1-2. Dry steam is supplied to the experiment from a boiler system located beside the ACRR pool. A mirror, which directs the visual image to an optical bench where telescopes and cameras record the image, is situated above the central cavity. In excess of 200 data signals in the form of thermocouple, pressure transducer and other data are extracted from the experiment package and are

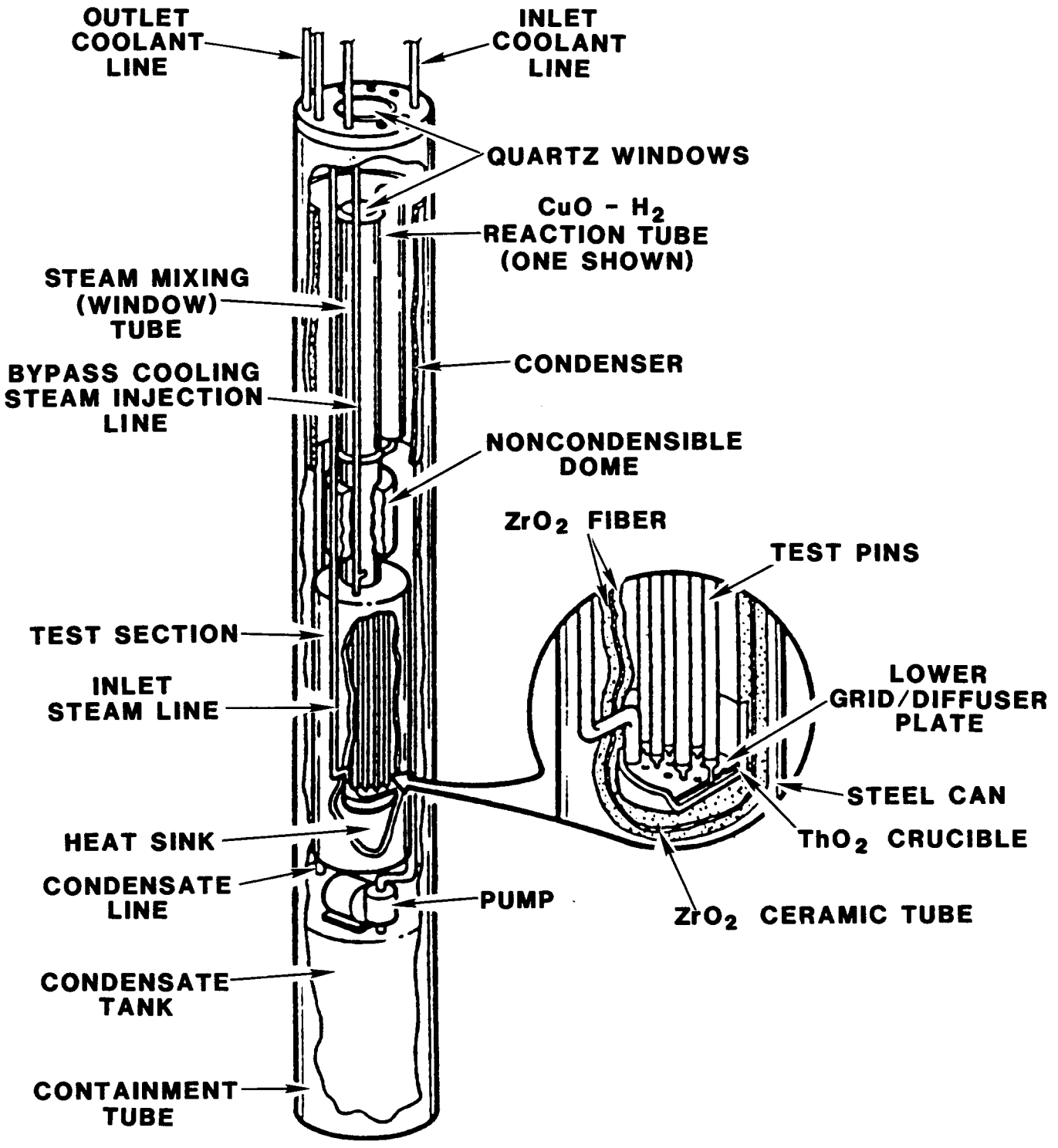

Figure 3.1-1. The DFR Experiment Capsule Showing Major Design Features

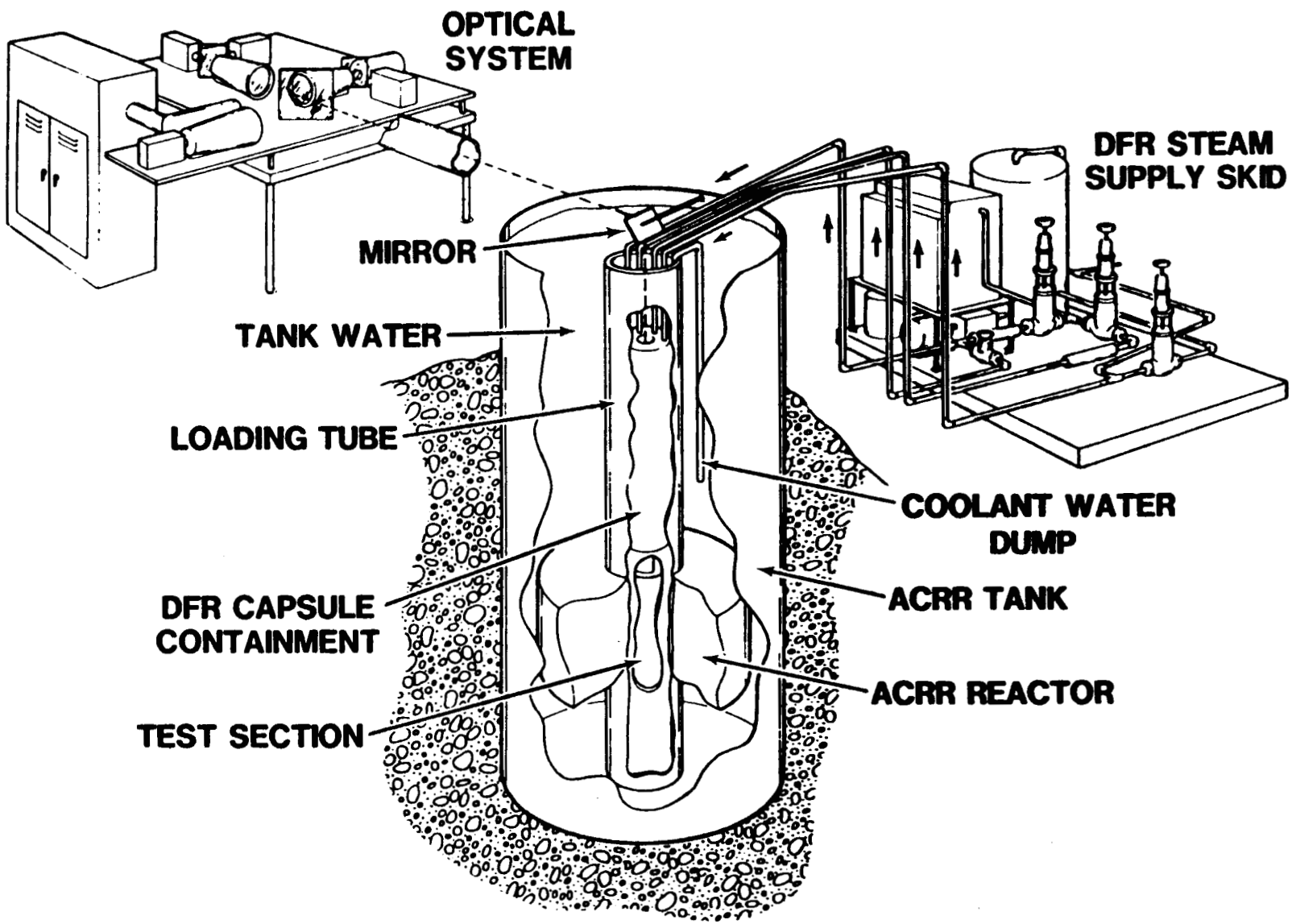

Figure 3.1-2. Overall Assembly of the DFR Experiment Showing ACRR Installation, Steam Plant, and Optical Bench

continuously monitored and recorded by a dedicated computer system. These data are used both to characterize the test progression as well as to assure safe operating conditions are in effect at all times during the test. Three DFR experiments were completed prior to this reporting period. These experiments examined the effects of initial clad oxidation, steam flow rate, and PWR rod effects. The final test in the series, DF-4, is to examine boiling water reactor (BWR) geometry and is discussed in paragraph 3.1.3.

3.1.3 DF-4 BWR Control Blade/Channel Box Fuel Damage Experiment

The DF-4 experiment is the fourth test in the DFR experiment series that are being carried out in the ACRR at Sandia. These experiments employ prototypic materials (UO_2 fuel) in test configurations that are designed to explore the governing phenomenologies pertinent to a light water reactor (LWR) undergoing severe damage associated with a core uncovery accident. These experiments together with other in-pile and out-of-pile experimental programs are aimed at providing a data base by which analytical and numerical models of severe core damage may be developed and assessed for use in reactor accident codes such as MELPROG, SCDAP, and MELCOR. Phenomena participating in severe fuel damage include zircaloy oxidation with the associated chemical energy release, clad melting, UO_2 attack and dissolution by molten zircaloy, relocation (candling) of liquefied fuel and clad, and formation of blockage zones from the refreezing of previously molten components. Associated with these damage processes is the production of hydrogen from oxidizing zircaloy and UO_2 with steam and the release of fission products and aerosols. The information obtained in the DFR series applies to the early phase of core degradation prior to major geometry changes. However, as the initial stages of core degradation become better understood through analysis and insights gained from (1) this experiment series, (2) other experimental studies, and (3) the TMI-2 post-mortem, subsequent tests will be required to address the progression of core melting during the extended accident phase where significant geometry changes will have occurred.

The DF-4 experiment will address the effects of unique (BWR) geometry upon fuel damage processes. These features are illustrated in Figure 3.1-3 where a cross section through four BWR fuel canisters is shown. Also shown is the cruciform stainless steel/B_4C control blade located in the bypass region between the individual zircaloy flow channel canisters. These important features are represented in the DF-4 test section design and shown in cross section in Figure 3.1-3. As in the BWR core, separate flow regions exist in the DF-4 representation for the fuel-rod zone inside the fuel canister and the control-blade zone in the interstitial region between adjacent fuel canisters. The rectangular channel box in the DF-4 test bundle prevents cross flow of steam between the two zones. Steam flow rates to each zone are established with consideration given to the differences in steaming rates and hydraulic resistance inside the fuel canister and around the control blade tip of the General Electric "D-Lattice" core design.

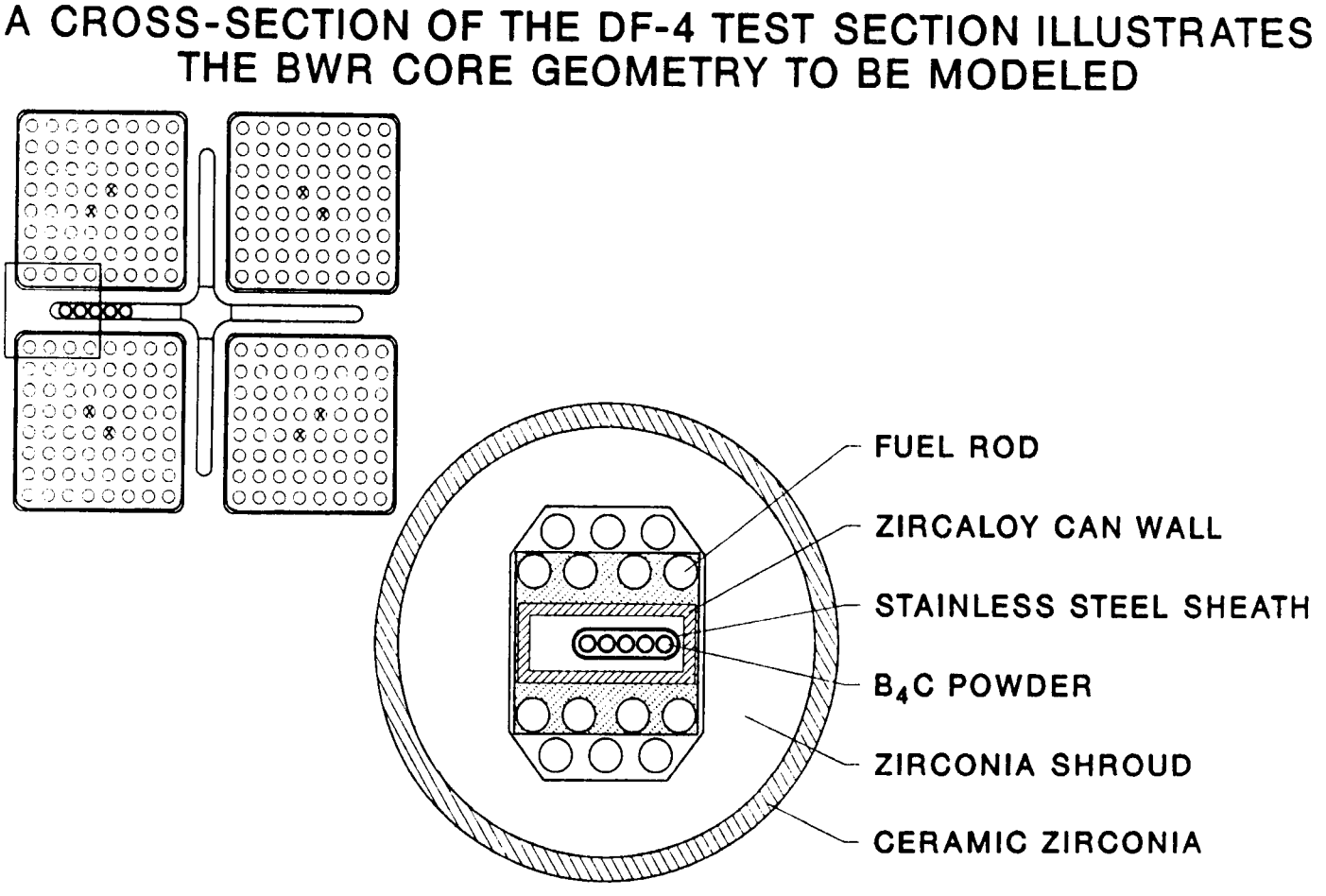

Figure 3.1-3. Representation of Key BWR Features in the DF-4 Test Section Design (Cross-Sectional View of Test Bundle)

Major uncertainties concerning BWR accident progression to be addressed in DF-4 include:

1. The relative heatup rate and oxidation behavior of the BWR fuel clad-canister wall-control blade structures.

2. The potential interaction between the B_4C powder in the control element and steam that may constitute an additional vigorous heat source as well as a source of volatile boric acid species, which can affect Cs and I fission product transport.

3. The interaction effects between the steel control structures and the zircaloy channel box wall.

4. The integrity of the channel box with respect to side wall damage.

5. The potential for tight blockage formation within the channel box.

(The latter issue relates to IDCOR assertions that BWR hydrogen production in BWR severe core damage accidents is significantly diminished by the formation of tight blockages in the lower canister region, which prevents steam from reaching the upper fuel cladding and channel box zircaloy.)

The test bundle is instrumented with various types of thermocouples. The fuel rod cladding is instrumented with Pt-Rh thermocouples where the junction is formed by welding the thermocouple wires to the clad surface. The temperature limit of the Pt-Rh instrumentation is ~1800 K, after which failure of the junction occurs. The fuel rod cladding is also instrumented with specially sheathed W-Re thermocouple assemblies. Although considerably more massive and not as well thermally bonded to the clad, these thermocouples survive the high temperature oxidizing environment and monitor bundle temperatures as high as 2700 K. Other temperatures are monitored within the insulator and on the pressure boundary surface to further characterize the thermal behavior of the test bundle. The principal thermocouple instrumentation in the DF-4 test bundle is shown in Figure 3.1-4. In this figure, the axial location of four major instrumentation stations is shown and the lateral positioning of the thermocouples at each station is indicated. The axial locations are relative to the bottom of the fissile zone in the bundle. In addition to thermocouples dedicated to tracking fuel rod, channel box, and control blade temperatures, two thermocouples are located at the base of the test bundle below the fissile zone. One is located at the base of the control blade within the confines of the channel box and will indicate the arrival of molten material draining to the base within the channel box. Similarly, a thermocouple located at the base of the fuel rod zone just outside the channel box will indicate the arrival of molten material draining down outside of the channel box.

3.1.4 Pretest MARCON-DF4 Calculations

The experiment analysis code, MARCON-DF4, was developed at Oak Ridge National Laboratories using selected subroutines from the MARCON 2.1B BWR reactor plant analysis code. Models accounting for the unique heat losses

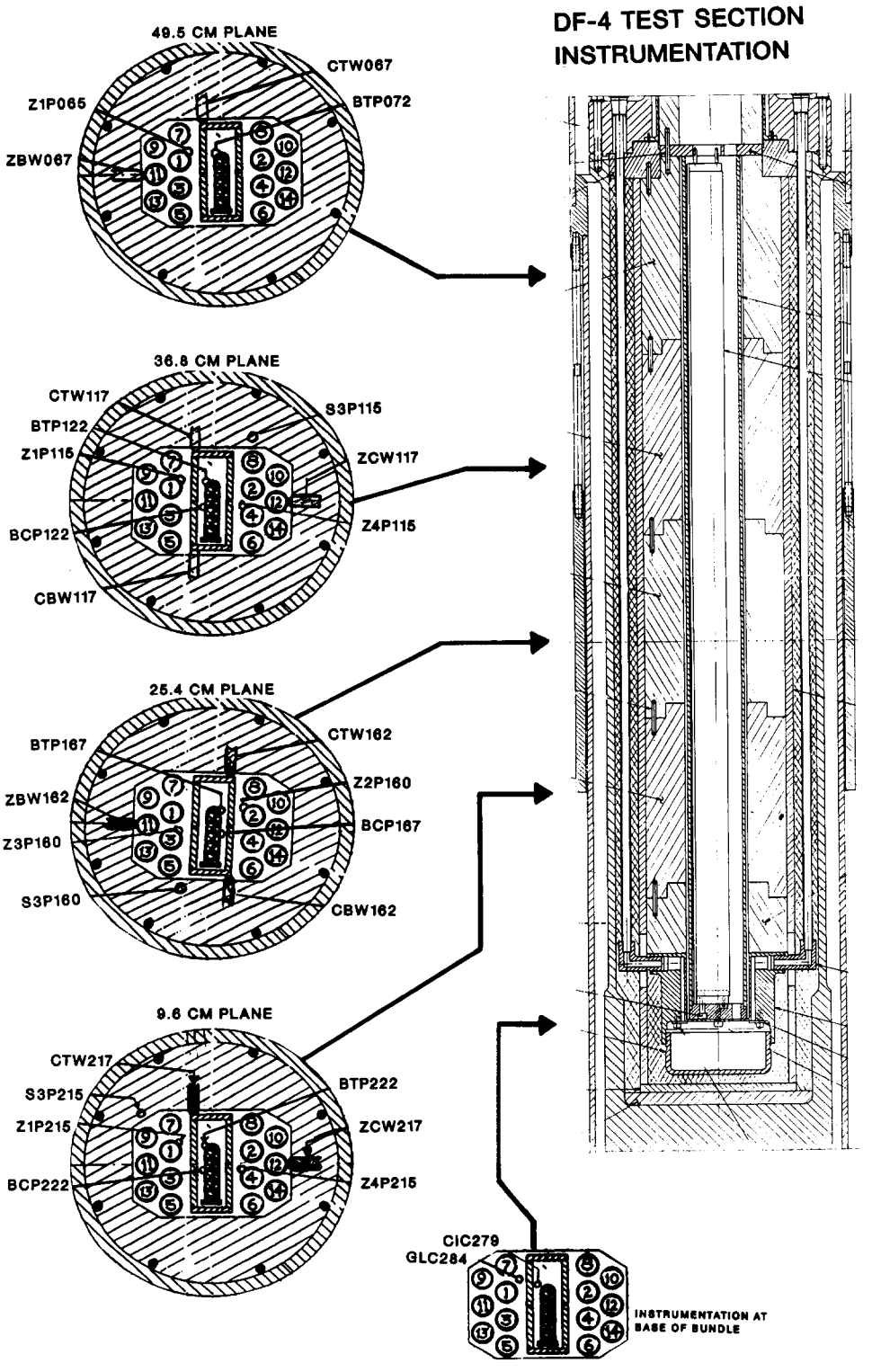

Figure 3.1-4. Test Bundle Instrumentation in the DF-4 Experiment

of the DF-4 experiment were generated for the code, which treats zircaloy, stainless steel, and B_4C oxidation; hydrogen production; convection, conduction, and radiation heat transfer; and fission heat generation in the DF-4 experiment configuration. This code has been used in carrying out preexperiment calculations for the purpose of defining the test operational plan. Following completion of the experiment, MARCON-DF4 will be exercised in postexperiment analyses. The goal of the posttest calculations will be to aid in characterizing the test results so that a well-understood and qualified data base will be established prior to attempting subsequent evaluation exercises using more complicated codes such as MELPROG.

Preliminary calculations with MARCON-DF4 have been carried out, the results of which are embodied in Figures 3.1-5 through 3.1-8. Shown in Figure 3.1-5 is the anticipated ACRR power transient proposed to drive the fission heating of DF-4. This power history provides for:

1. A coupling factor calibration phase with several small step increases in power.

2. A larger power increase to quickly bring fuel temperatures up to ~900°C, after which the channel box and control blade will be allowed to equilibrate with the fuel.

3. A final power increase during which the fuel cladding will be heated at roughly 1.5 K/s as rapid Zr-Steam oxidation takes over as the dominant fuel/structure heating source.

The fuel clad, channel box and control blade response to this power history is seen in Figures 3.1-6 through 3.1-8. The fuel clad temperature (Figure 3.1-6) shows a sharply developing zircaloy-steam reaction front at the top of the fissile zone (50 cm) after the second power increase is applied. The reaction front then progresses downward toward the steam source. Predicted peak fuel clad temperatures are 2500 K. The channel box heatup (Figure 3.1-7) proceeds much the same as the fuel, except at a faster rate with more extensive structural melting. Shown in Figure 3.1-8 is the predicted response of the stainless steel control blade. Because of the much lower melting point of stainless steel (~1700 K), the predicted extent of blade damage is large. Phenomenon not addressed by the calculation, but expected to occur in the experiment is material interaction, e.g., alloying and eutectic formation, between the different melting and relocating materials. These events are expected to influence the character of the damage progression and will be investigated by posttest metallurgical examination of the test section.

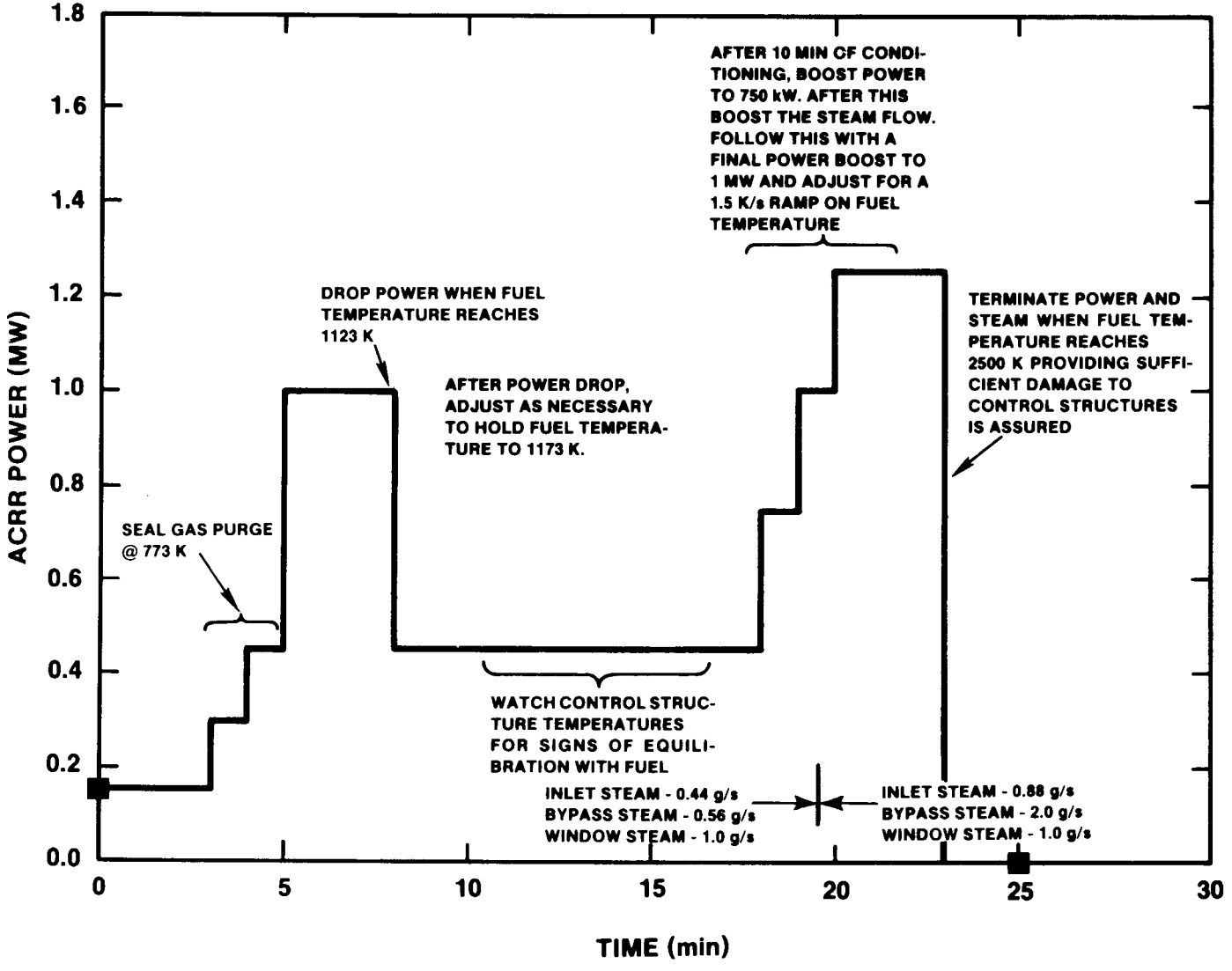

Figure 3.1-5. Proposed ACRR Power Transient for the DF-4 Test Showing Anticipated Test Progression

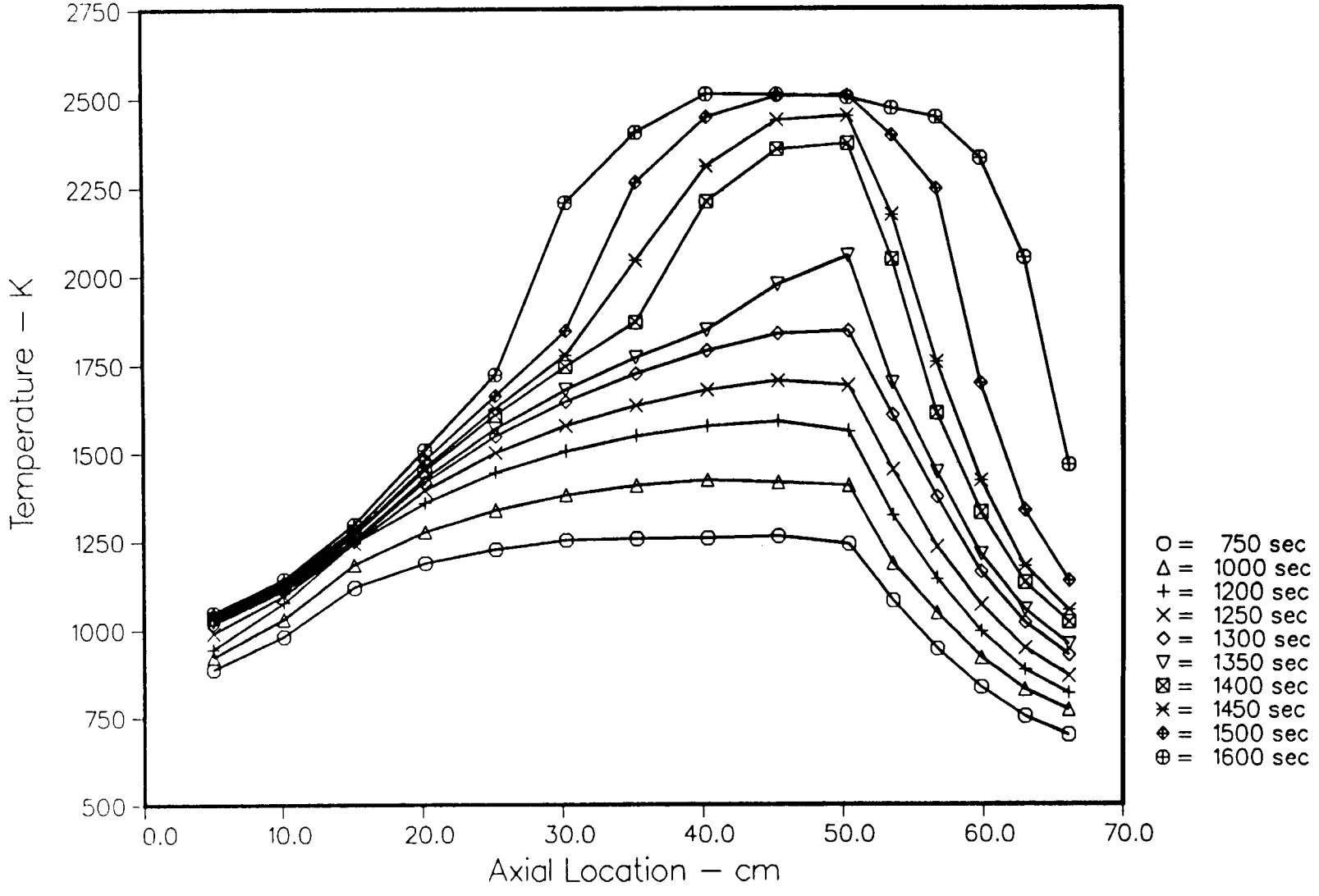

Figure 3.1-6. Axial Temperature Profiles Predicted by MARCON-DF4 for the Fuel Rods

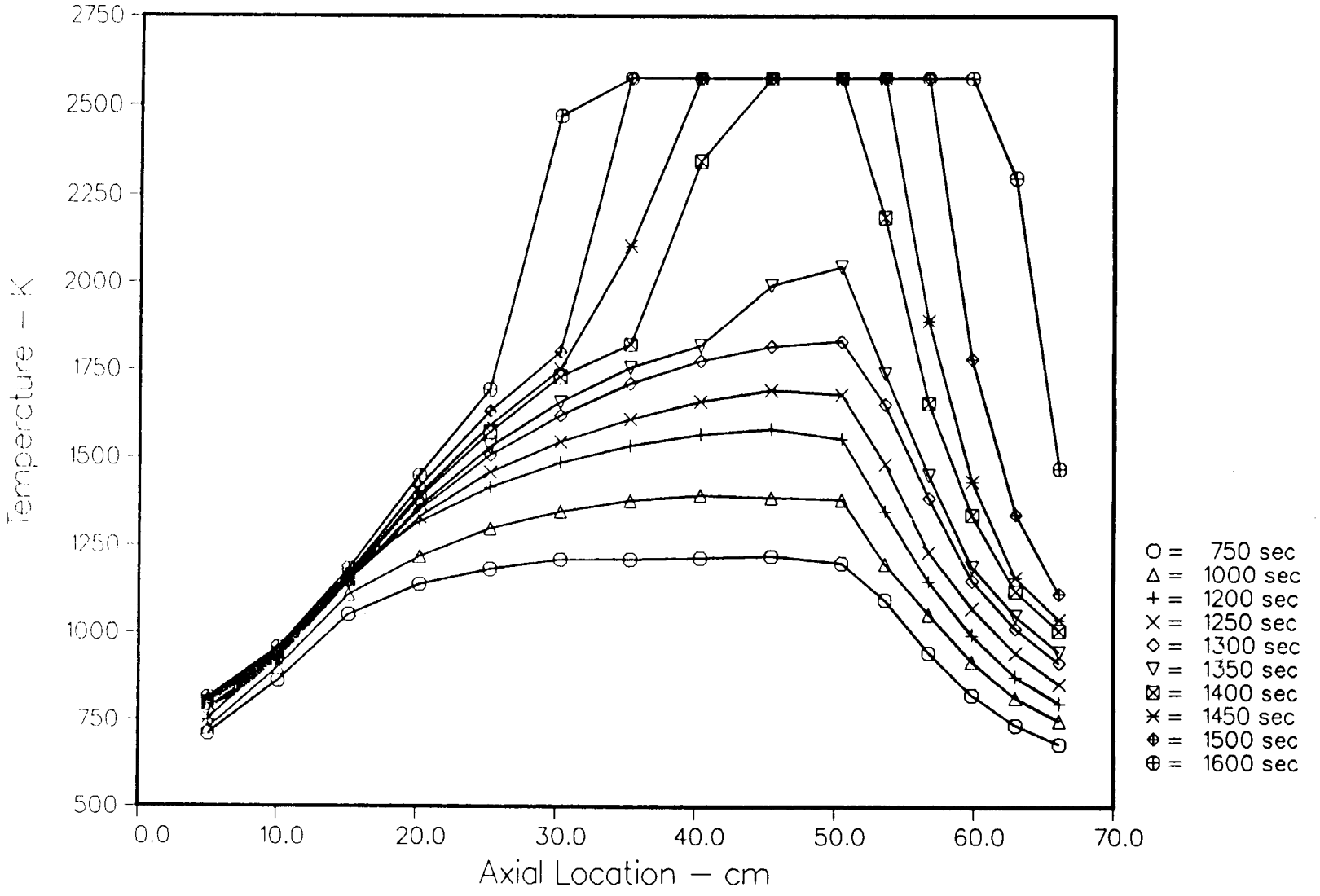

Figure 3.1-7. Axial Temperature Profiles Predicted by MARCON-DF4 for the Zircaloy Channel Box

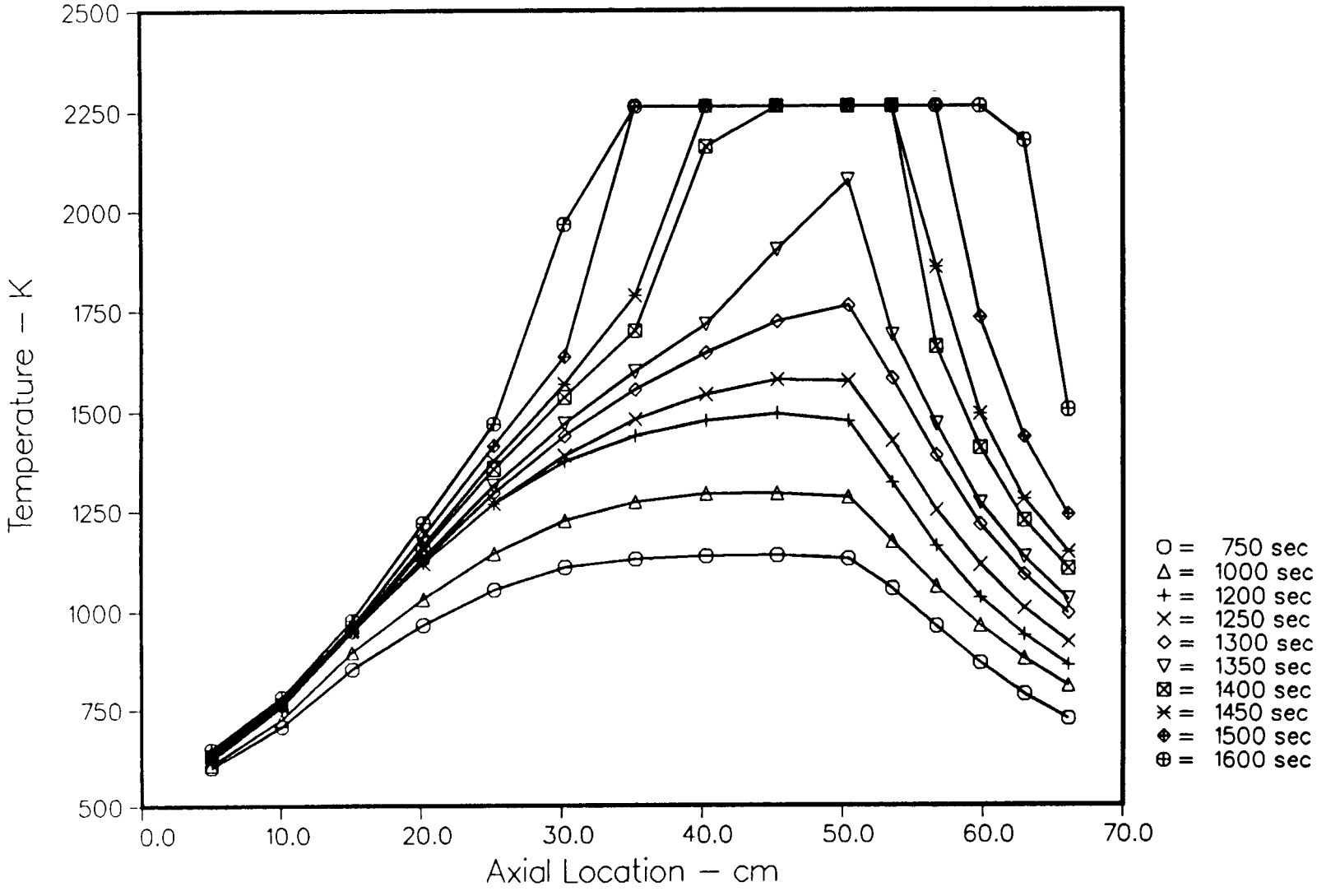

Figure 3.1-8. Axial Temperature Profiles Predicted by MARCON-DF4 for the Stainless Steel/B_4C Control Blade

4. MELT PROGRESSION PHENOMENOLOGY CODE DEVELOPMENT (MELPROG)

(W. J. Camp and J. E. Kelly, 6425)

The objective of this program is to develop a mechanistic computer model for the analysis of the in-vessel phases of severe accidents in LWRs. This model, MELPROG, is implicitly linked with the TRAC-PF1 thermal hydraulics code to provide a complete, integrated treatment of the reactor primary system from accident inception through release of core materials and fission products from the reactor vessel. The model also provides materials and thermohydrodynamic input to the CONTAIN reactor containment analysis model.

The work involves both developing the MELPROG computer code and applying the code to accident scenarios and to experiments. In the code development phase, models needed to treat the phenomena associated with severe accidents have been extracted from the open literature as well as being formulated specifically for this effort. The applications effort involves both testing the code and assessing the modeling.

4.1 MELPROG Code Development

(J. E. Kelly, J. L. Tomkins, K. L. Schoenefeld, M. F. Young, and R. C. Smith, 6425)

MELPROG consists of several explicitly linked modules, which in turn, are comprised of models that treat the physical processes that occur during a severe accident sequence. The approach used in MELPROG has been to develop these modules as stand-alone codes. Then these modules have been explicitly linked together in the MELPROG code in order to treat the entire accident sequence in an integrated manner. The advantage of this approach is that it allows for both accurate modeling of specific phenomena and accurate predictions of the coupling between phenomena. This approach allows key quantities, such as fission-product release and transport, to be calculated in a realistic and consistent manner. Additionally, the modular structure of the code has the advantage that it is relatively easy to improve or substitute new models into the code as warranted.

The first version of MELPROG, MELPROG-PWR/MOD0, was completed and is being tested prior to release. This version uses a one-dimensional fluid dynamics model (FLUIDS module) and contains PWR code structure models (STRUCTURES module). This version also includes the DEBRIS module for debris bed analysis, the RADIATION module for radiation heat transfer analysis, and the PINS module for fuel and control rod analysis. Major development on this version has ceased in order to devote more effort to developing the improved versions of the code.

The second version, MELPROG-PWR/MOD1, is currently under development. This version will include all features of the original code plus many significant enhancements. In particular, this version includes a two-dimensional fluid dynamics model (FLUIDS-2D module), a fission-product model (VICTORIA module), an improved core structures model (CORE module), a melt-water interaction model (IFCI module), and a melt ejection model (EJECT module). This version represents a major improvement over the original version. In addition, substantial development on the FLUIDS-2D, VICTORIA, and CORE modules also occurred.

Recent developments in the FLUIDS, CORE, and VICTORIA modules are discussed below.

4.1.1 FLUIDS Module Development

The new FLUIDS-2D module replaces the one-dimensional fluid dynamics treated in MOD0 with a full two-dimensional (R-Z) capability. In addition, four momentum fields are treated instead of three (the corium field is split into solid and liquid fields). This version was completed at Los Alamos National Laboratory as part of the MELPROG effort. The major advantage gained through the new FLUIDS module is the ability to treat the important effects of natural circulation in the core and vessel. This new module is completely operational in MELPROG.

While the MOD1 version of MELPROG is still under development, the initial results from the testing of the 2-D hydrodynamics are quite promising. The new module works well, and no major obstacles have been found. Additionally, the preliminary results illustrate the importance of natural circulation within the vessel. Relative to a one-dimensional treatment, a strong radial variation in the meltdown progression has been found. This difference will influence in-vessel fission-product release as well as the mode of core slump.

Changes have been made the Jacobian matrix subroutine, JAC41H, to allow one subroutine to be used for all combinations of fields in a cell. These changes are also consistent with imbedded interfaces and the TRAC link.

The principal change to the JAC41H routine is to preevaluate the knobs array. Knowing how many fields are on in a cell, plus which fields, and whether hydrogen is present or not, allows the routine to assemble equations only for the fields actually present in a cell. No fake equations for fields turned off are necessary. A set of six flags are set in an array INCL ("include"); the first four are set to 1 if the corresponding field is present; the fifth flag is set if more than one field is present, signaling that the alpha constraint equation should be included; the sixth flag is set if hydrogen is present, indicating that the hydrogen mass equation should be included. A variable NFLD is also calculated giving the total number of fields.

The INCL array and NFLD are used in a loop over the four fields to control assembly of the equation set and of the variable set. Fields turned off are set to a volume fraction of AL102 and a temperature of TS. This occurs before the alpha constraint equation, if present, is set up, and is a difference in operation from the previous JAC routines, which set "off" fields during the back-substitution step or set up fake equations to force "off" fields to these values.

The INCL array and NFLD are evaluated during the back-substitution step because they are not stored from cell to cell. Back-substitution occurs as in the previously used JAC routines with the INCL array and NFLD being use to identify the location of the needed equations.

The phase change terms were modified to allow for possible subcooling or superheating of the water and steam fields. This change ensures that mass and energy removed from a field will not cause nonphysical temperature changes in the field.

Previously, the mass transfer rate for phase change was given by the sum of the energy fluxes to an interface assumed to be at the saturation temperature divided by the heat of vaporization,

$$\Gamma = \frac{q_{1s} + q_{2s}}{L} \quad , \quad q_{1s} = h_{1s}\left(T_1 - T_s\right), \quad q_{2s} = h_{2s}\left(T_2 - T_s\right) \quad ,$$

where

Γ = phase change rate ($kg/m^3/s$),

q_{1s} = energy flux from vapor field 1 to interface (w/m^3),

q_{2s} = energy flux from liquid field 2 to interface (w/m^3),

L = heat of vaporization (J/kg),

h_{1s} = vapor-interface heat transfer coefficient ($w/m^3/K$),

h_{2s} = liquid-interface heat transfer coefficient ($w/m^3/K$),

T_1 = vapor temperature (K),

T_2 = liquid temperature (K),

T_2 = saturation temperature (K).

This formulation was modified to include the effect of off-saturation conditions by replacing the heat of vaporization L by an effective heat of vaporization L', where

$$L' = \begin{cases} u_1 - u_{2s}, & \text{condensing} \\ u_{2s} + L - u_2, & \text{vaporizing} \end{cases} \quad ,$$

with

u_i = internal energy of field i (J/kg),

u_{is} = internal energy of field i at saturation (J/kg).

A more important change was to replace the terms in the energy equations, which were previously of the form Γu_{is}, with expressions dependent on the direction of mass flow; the rule for the new formulation is that mass transfer into a field is at the saturation energy, whereas mass transfer from a field is at the internal energy of the field. This prevents spurious temperature changes. The new energy terms are

$$\text{field 1: } \begin{cases} \Gamma u_1, & \text{condensing} \\ \Gamma\left(u_{2s} + L\right), & \text{evaporating} \end{cases}$$

$$\text{field 2: } \begin{cases} \Gamma u_{2s}, & \text{condensing} \\ \Gamma u_2, & \text{evaporating} \end{cases} .$$

Corresponding changes were made in the Jacobians for fields 1 and 2. Affected routines in MELPROG/MOD1 are JAC41H, IMPEX, and MESTAB.

The above changes were tested and debugged using the Surry TMLB' problem, using the runs with the old code as a comparison. Comparisons were done without the phase change corrections to the steady state (MOUTSS); to the first 100 s of the transient (MOUTT1); to 100 s of MOUTT3 starting at 9250 s, just before the start of hydrogen production; and to the first 200 s of MOUTT5, covering the beginning of corium formation. All cases were very close to the old runs, with slight changes in pressure and velocity distributions in the fourth or fifth decimal place. Testing of the phase change modification has just begun, but preliminary indications are that it is more stable, producing fewer negative alpha predictions than the old phase change rule.

4.1.2 CORE Module Development

The new CORE module has been designed to treat PWR and BWR core structures in one consistent and flexible framework. The module was also designed to be consistent with the existing treatment of in-vessel and ex-core structures (the STRUCTURES module). The actual level of modeling detail, both geometrical and physical, are user controlled. For example, one can use very detailed geometry for experiment analyses and considerably less detail for reactor accident calculations. Such flexibility allows the user to determine the impact on accident calculations of the level of physics and geometry detail.

The CORE module is designed to treat fuel rods, PWR control rods, BWR control blades, poison rods, dummy rods, and BWR can walls. MELPROG is a 2-D code (R-Z geometry). Within each radial ring, a model can be provided for each different type of core structure. Each model then represents the actual number of each structure in that ring. Each core structure modeled may have its own power factor and its own axial structure. Thus, for example, multiple fuel rods within a ring may be modeled with the axial detail of the rods (fission gas plenum, insulator pellets, active fuel, etc.) explicitly treated.

Each core structure is treated as consisting of one or more material regions. For example, a fuel rod would initially be modeled as a two-region structure, i.e., fuel and cladding. During the course of the calculation the number of material regions can change. For example, oxidation of the zircaloy cladding leads to formation of a layer of ZrO_2, which is explicitly treated as a separate material region. Similarly, formation of a U-Zr-O solution that forms and flows down the exterior or interior or both the exterior and interior of the fuel rod also creates new material regions. Therefore, the model allows for the formation and loss of material regions for all core structures in order to calculate the important physical processes.

A 1-D finite-difference solution for heat conduction through the various material regions forms the basis for the CORE module. Oxidation kinetics for solid and liquid zircaloy and steel as well as for U-Zr-O solutions on structure outer surfaces are treated. Cladding plastic deformation and failure are modeled. Candling on inner and outer surfaces is treated. Fuel rod and other core structure failure by melting or fracture are modeled.

Subroutine CRPROP contains the material properties for the CORE module. Most of the CRPROP subroutine is self-explanatory. The new feature recently added is the iterative enthalpy inversion routines that determine the temperature corresponding to a given specific enthalpy for a material. There are two routines to be considered--the routine for a single material and the routine for a mixture of materials. The routines are similar, but the routine for mixtures is a little more complicated because the phase transition points must be considered differently.

The iterative enthalpy inversion algorithm for a single material is outlined in the flow chart in Figure 4.1-1, while the algorithm for a mixture of materials is outline in Figure 4.1-2. As seen in Figure 4.1-1, the procedure for determining temperature given the enthalpy is straightforward. For the multicomponent case, the procedure is more complicated as seen in Figure 4.1-2. In this figure, FCOMP(i) is the mass fraction of the ith component in the mixture and TRAN(i) and CPH(i) are arrays for storing the phase transition information for the particular mixture of materials. TRAN(i) will contain NPTS points in groups of two, consisting of the temperature bounds of the transition arranged in increasing order. CPH(i) contains NPTS/2 points corresponding to the pairs of points in TRAN(i). CPH(i) is an effective specific heat for transitions given by

$$CPH(i) = FCOMP(j) * \Delta h_{TRAN}/\Delta t_{TRAN} \quad .$$

After the transition temperatures have been determined, the routine begins looping through the temperatures, TRAN(ii), and calculating the mixture enthalpy, HHI, associated with each temperature. The enthalpy for the preceding temperature is saved as HLO. As soon as the calculated enthalpy

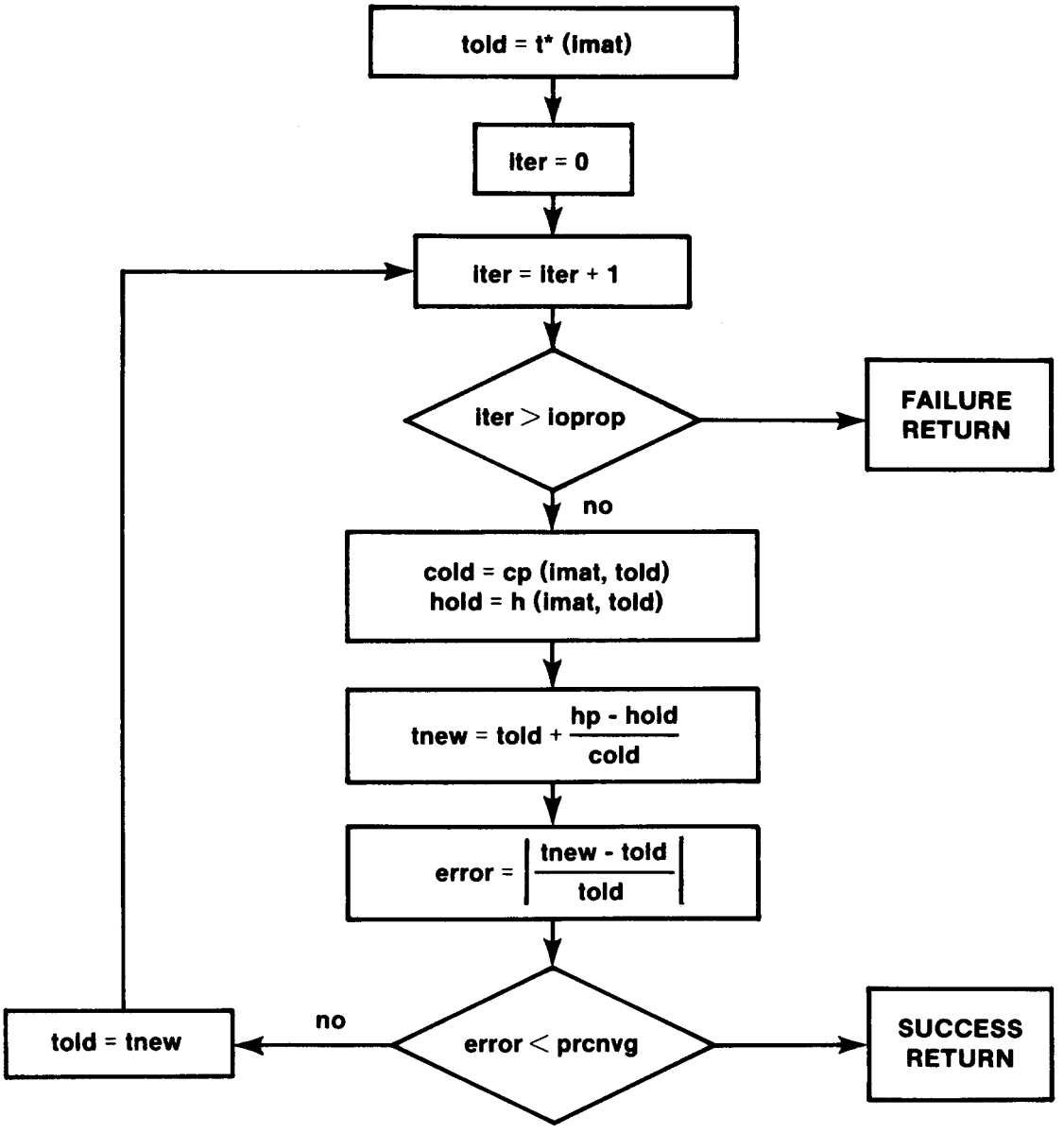

t* (imat) ≡ a given initial estimate of the temperature for material imat

hp ≡ the given specific enthalpy

cp (imat, told) ≡ the specific heat of material imat at temperature told

h(imat, told) ≡ the specific enthalpy of material imat at temperature told

Figure 4.1-1. Single Component CRPROP Enthalpy Solution Method

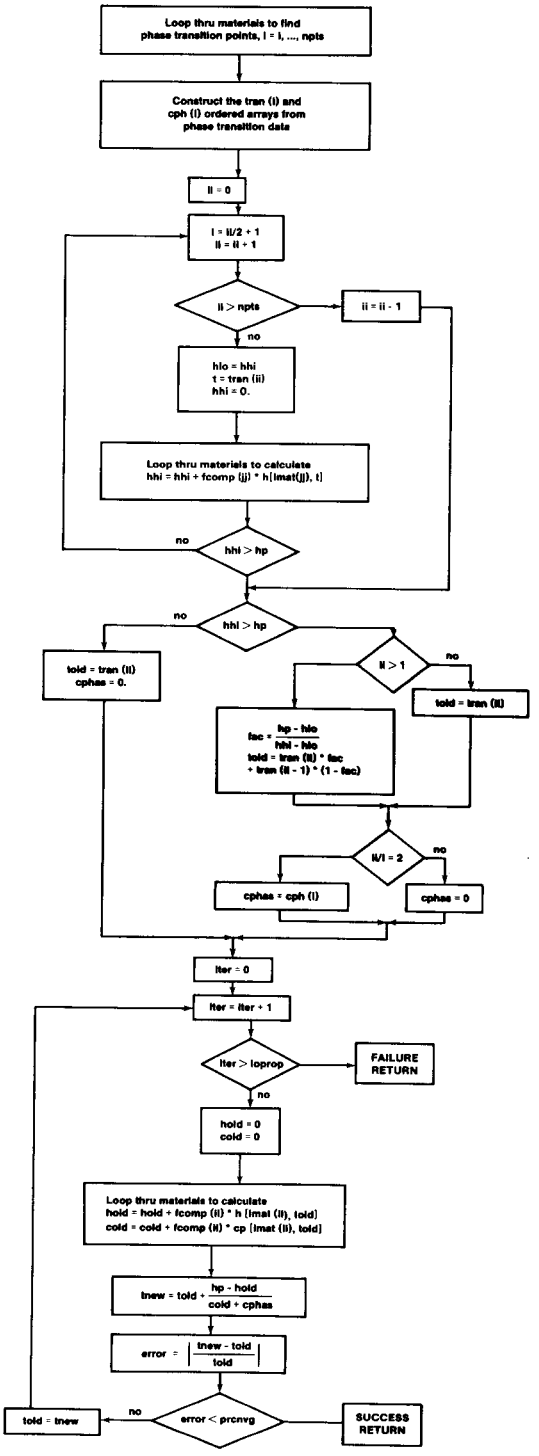

Figure 4.1-2. Multicomponent CRPROP Enthalpy Solution Method

exceeds the given enthalpy, HP, the routine exits that loop with an initial temperature estimate of

$$\text{TOLD} = \text{TRAN(ii-1)} * \frac{\text{HHI - HP}}{\text{HHI - HLO}} - \text{TRAN (i1)} * \frac{\text{HP - HLO}}{\text{HHI - HLO}} \quad .$$

If TOLD falls within a transition range, CPHAS is set equal to the associated CHP(i); otherwise, CPHAS is set equal to zero. With TOLD and CPHAS determined, the remainder of the mixture routine is essentially identical to the routine for single materials except for the loops over materials.

Major development in the CORE module continues with the material relocation modeling being the main area of development. In particular, improvements to the material property routine (CRPROP) and to the fuel dissolution routine (CREUTIC) have been made. In addition, a completely new crust formation model has been written.

The CREUTK subroutine is a simple algorithm to determine how much solid UO_2 of a given temperature can be dissolved in a given quantity of U-Zr-O eutectic of given composition and temperature. The routine assumes that the rate of dissolution is instantaneous and employs a simple UO_2-Zr(O) binary phase diagram to determine the equilibrium composition as a function of the temperature of the solution. The temperature is determined from the enthalpy of the solution, which is the sum of the initial enthalpies of the eutectic and dissolved solid plus the heat of dissolution. Currently, the heat of dissolution is equal to the heat of fusion as suggested by Hagrman.

4.1.3 Crust Growth Model

The CORE module of MELPROG models flow (candling) of materials on CORE structures. As material flows down a structure from a hotter to a colder region, it may freeze and form a crust. CORE treats two mechanisms for crusting: bulk freezing and conduction heat transfer limited crust growth. This discussion is limited to conduction heat transfer limited crust growth.

The model treats a flowing film at temperature T_2 on a solid surface at temperature T_1. The interface temperature at the surface of the solid is T_s. The distance from T_1 to T_2 is Δx_1 and the distance from T_s to T_2 is Δx_2. This arrangement is shown in Figure 4.1-3. The energy transfer rate at T_s is then defined to be

$$\frac{k_{1,s} A_{1,s}}{\Delta x_1} \left(T_s - T_1\right) = \frac{K_{s,2} A_{s,2}}{\Delta x_2} \left(T_2 - T_s\right) + Q_s A_s \quad . \qquad (4.1\text{-}1)$$

For a crust to form, T_s must be less than the freezing point, T_m, of the liquid film. Also, T_s must be greater than T_1 for heat to flow into the solid. If $T_s - T_1 > 0$ and $T_s < T_m$, then a crust of thickness, δ, can grow

in time step Δt. The interface temperature between the melt and the crust must be T_m. (If the crust surface temperature drops below T_m, then all of the melt has frozen.) Figure 4.1-4 shows the arrangement of temperatures after a crust has started to form.

The amount of crusting that can occur in time step Δt is determined by the integral of the energy transfer into the solid layer. At time t the heat flux is given by Equation 4.1-1, while at time $t+\Delta t$ the thickness of the crust must be accounted for. At time $t+\Delta t$ the heat flowing into the crust region is given by

$$\frac{K_{c,m} A_{c,m}}{\delta_c/2} \left(T_m - T_c\right) = \frac{k_{m,2} A_{m,2}}{\Delta x_2'} \left(T_2 - T_m\right) + L_c \rho_c \dot{\delta} A_c \quad , \qquad (4.1\text{-}2)$$

where

$k_{c,m}$ = thermal conductivity of crust material between T_c and T_m (W/mK),

$A_{c,m}$ = heat transfer area between T_c and T_m (m^2),

δ_c = growth of crust between time t and $t+\Delta t$ (m),

T_c = temperature of crust (K),

$k_{m,2}$ = thermal conductivity of melt between T_m and T_2 (W/mK),

L_c = heat of fusion of crust (J/kg),

ρ_c = density of crust (kg/m^3),

$\dot{\delta}$ = rate of crust growth (m/s),

A_c = surface area of the crust (m^2),

$\Delta x_2' = \Delta x_2 - S_c$.

All other variables are as previously defined.

Equation 4.1-2 can be simplified if the heat capacity of the growing crust is not treated directly. Then the temperature T_c does not have to be calculated because the heat flux at T_m must equal the heat flux at T_s and Equation 4.1-2 becomes

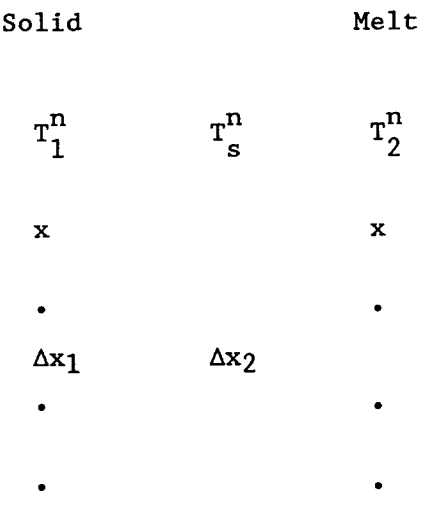

Figure 4.1-3. Geometry at Time t, Prior to the Formation of a Crust

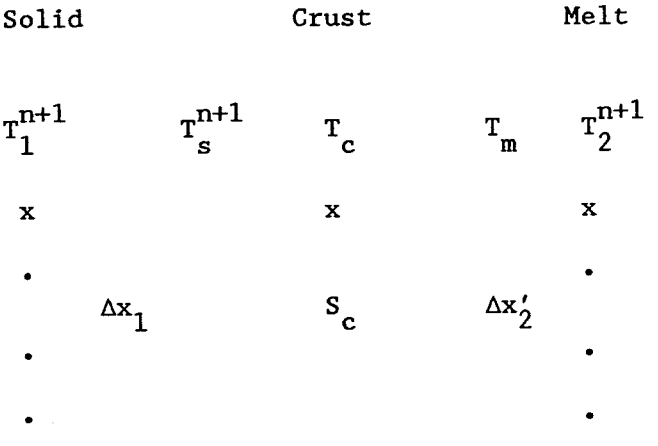

Figure 4.1-4. Geometry at Time t+Δt

$$\frac{k_c A_{s,m}}{\delta_c}\left(T_m - T_s\right) = \frac{k_{m,2}}{\Delta x_2'}\left(T_2 - T_m\right) + L_c \rho_c \dot{\delta} A_c \quad , \tag{4.1-3}$$

where k_c = thermal conductivity of the crust (W/mK),

$A_{s,m}$ = heat transfer area between T_s and T_m (m^2).

All other variables are as previously defined.

Equation 4.1-3 can be simplified further because the energy flow through the crust together with the source term at the crust solid interface must equal the energy flowing into the solid, that is:

$$\frac{k_{1,s} A_{1,s}}{\Delta x_1}\left(T_s - T_1\right) = \frac{k_c A_{s,m}}{\delta c}\left(T_m - T_s\right) + Q_s A_s \quad , \tag{4.1-4}$$

which yields

$$\frac{k_{1,s} A_{1,s}}{\Delta x_1}\left(T_s - T_1\right) = \frac{k_{m,2} A_{m,2}}{\Delta x_2'}\left(T_2 - T_m\right) + L_c \rho_c \delta A_c + Q_s A_s \quad , \tag{4.1-5}$$

where all terms are as previously defined.

The heat of fusion energy associated with crusting is in reality deposited at the point where freezing is taking place. However, because in this model the heat capacity of the crust is not treated directly, the heat of fusion energy can be deposited at the solid-crust interface without any further loss in accuracy. Because the heat of fusion energy is deposited at the solid-crust interface, the only change required to the standard heat transfer solution equations is the addition of a source term at T_s.

To calculate the integral of the energy conducted into the solid during time Δt the average of the heat transfer rates at times t and $t+\Delta t$ is used (Equations 4.1-1 and 4.1-5). The resulting equation is

$$\frac{k_{1,s}^n A_{1,s}^n}{2\Delta x_1^n}\left(T_s^n - T_1^n\right) + \frac{k_{1,s}^{n+1} A_{1,s}^{n+1}}{2\Delta x_1^{n+1}}\left(T_s^{n+1} - T_1^{n+1}\right)$$

$$= \frac{k^n_{s,2} A^n_{s,2}}{2\Delta x^n_2} \left[T^n_2 - T^n_s\right] + \frac{k^{n+1}_{n,2} A^{n+1}_{m,2}}{2\Delta x^{'n+1}_2} \left[T^{n+1}_2 - T_m\right]$$

$$+ L_c \rho_c \dot{\delta} A_c + Q_s A_s \qquad (4.1\text{-}6)$$

The geometry between T_1 and T_s does not change over the time step and the thermal conductivity between T_1 and T_s is assumed constant over the time step. Therefore,

$$k^n_{1,s} = k^{n+1}_{1,s} \quad ,$$

$$A^n_{1,s} = A^{n+1}_{a,s} \quad ,$$

$$\Delta x^n_1 = \Delta x^{n+1}_1 \quad .$$

When the above equalities are substituted into Equation 4.1-6 the following result is obtained:

$$\frac{k_{1,s} A_{1,s}}{2\Delta x_1} \left[T^n_s - T^n_1 - T^{n+1}_s - T^{n+1}_1\right]$$

$$= \frac{k^n_{s,2} A^n_{s,2}}{2\Delta x^n_2} \left[T^n_2 + T^n_s\right] + \frac{k^{n+1}_{m,2} A^{n+1}_{m,2}}{2\Delta x^{'n+1}_2} \left[T^{n+1}_2 - T_m\right]$$

$$+ L_c \rho_c \dot{\delta} A_c + Q_s A_s \quad . \qquad (4.1\text{-}7)$$

Equation 4.1-7 is not quite correct because from the instant the crust begins to form, the temperature at the crust-melt interface is T_m. Therefore T^n_s on the right hand side of Equation 4.1-7 should be T_m. Also, if

$$L_c \rho_c \dot{\delta} A_c = L_c \dot{m} \quad ,$$

$$\frac{k_{1,s} A_{1,s}}{2\Delta x_1} = G^n_1 \quad ,$$

$$\frac{k_{s,2}^{n} A_{s,2}^{n}}{2\Delta x_2^n} = G_2^n \quad ,$$

$$\frac{k_{m,2}^{n+1} A_{m,2}^{n+1}}{2\Delta x_2^{'n+1}} = G_2^{n+1} \quad ,$$

then Equation 4.1-7 can be written as

$$G_1^n\left[T_s^n - T_1^n + T_s^{n+1} - T_1^{n+1}\right]$$

$$= G_2^n\left(T_2^n - T_m\right) + G_2^{n+1}\left(T_2^{n+1} - T_m\right) + L_c\dot{m} + Q_s A_s \quad . \qquad (4.1\text{-}8)$$

As stated above, the heat capacity of the growing crust is not treated directly. However, it is treated by modifying the definition of L_c to include a specific heat term. L_c is then defined as

$$L_c = \text{MIN}\left[H_F, H_2 - H_m\right] + C_p\left[T_2^{n+1} + T_2^n - \left(T_s^{n+1} + T_s^n\right)/2 - T_m\right] \quad , \qquad (4.1\text{-}9)$$

where

H_F = heat of fusion of the crust (J/kg),

H_2 = enthalpy of melt (J/kg),

H_m = enthalpy of melt at solids (J/kg),

C_p = specific heat of crust (J/kgK).

In Equation 4.1-9, the energy associated with the specific heat of the crust is based on a linear temperature profile through the crust. The true temperature profile is not linear, however, the linear assumption doesn't introduce much error because $cp \ll H_F$.

In Equation 4.1-8 there are six unknowns (T_s^{n+1}, T_1^{n+1}, G_2^{n+1}, T_2^{n+1}, L_c, and $\dot{m}$). Of these, T_s^{n+1}, T_1^{n+1}, and T_2^{n+1} are provided by the standard

temperature solution that is performed iteratively when crusting is occurring. If C_p is treated as a constant, then L_c is only a function of temperatures T_2^{n+1} and T_s^{n+1}. These temperatures are calculated at each iteration. At time t,

$$G_2^{n+1} = G_2^n \quad ,$$

and at time t+Δt,

$$G_2^{n+1} = f\left(G_2^n, \dot{m}\Delta t\right) \quad .$$

In slab geometry,

$$G_2^{n+1} = G_2^n \left(\frac{m_2}{m_2 - \dot{m}\Delta t}\right) \quad .$$

In cylindrical geometry this simple ratio is not correct, however, for $\Delta r/r \ll 1$, a slab approximation produces only a slight error. G^{n+1} is calculated during the iteration and is a function of the previous iterate value of $\dot{m}\Delta t$.

During each iteration $\dot{m}\Delta t$ is solved from Equation 4.1-8 as

$$\dot{m}\Delta t = \Delta t\left[G_1^n\left(T_s^n - T_1^n + T_s^{n+1} - T_1^{n+1}\right) - Q_s A_s \right.$$

$$\left. - G_2^n\left(T_2^n - T_m\right) - G_2^{n+1}\left(T_2^{n+1} - T_m\right)\right]/L_c \quad . \qquad (4.1\text{-}10)$$

This iteration continues until the relative change in $\dot{m}\Delta t$ is less than a user input value or until the iteration limit is reached.

This model has been implemented as part of CORE and is now fully operational. Conduction limited crusting is calculated when the bulk enthalpy of the melt remains above the solidus enthalpy over the time step, Δt. If the phase change calculation determines that the bulk temperature of the melt drops below the solidus, then only bulk freezing is treated. The model has undergone limited testing; therefore, an evaluation of optimum axial mesh size and appropriate time steps has not been determined at this time.

4.1.4 VICTORIA Module Development

The VICTORIA module in MELPROG treats release and transport of fission products in the core and vessel. The philosophy behind the development of VICTORIA was to adapt from other fission-product codes and research programs the models, methods, and in some cases, even software needed to build a fission-product behavior module suitable for MELPROG. This module treats the appropriate physical processes at a level of modeling detail consistent with MELPROG and has a software structure compatible for coupling to MELPROG. In addition, the structure of VICTORIA is designed such that further changes of the code as dictated by appropriate experiments will be straightforward to implement and it can be used in either a stand-alone mode or in a coupled mode with MELPROG.

VICTORIA, in stand-alone form, has been completed and is being assessed. The stand-alone code is being used to perform analysis of the ORNL HI experiments. Incorporation of this module into MELPROG has been initiated. This work has involved completely rewriting the continuity solver in VICTORIA. This was necessary to make VICTORIA compatible with MELPROG and TRAC. This work was completed and initial testing was quite promising.

4.2 MELPROG Code Applications

Testing and assessment of MELPROG and VICTORIA is continuing. MELPROG is being run on full plant calculations to test and assess its capabilities. VICTORIA, in stand-alone mode, is being tested and assessed with experimental data. Activities in these areas are discussed in Sections 4.2.1 and 4.2.2.

4.2.1 MELPROG TMLB' Calculations

As reported in Reference 101, a calculation of a TMLB' sequence for the Surry reactor has been made with MELPROG/MOD1. This calculation, while preliminary in nature, is the most mechanistic calculation of this sequence performed to date. However, due to its preliminary nature, it is premature to draw firm conclusions from the calculation. On the other hand, the calculation is especially useful in gaining important insight into severe accident phenomena.

These insights can be gained in a number of different ways. The approach used in this study was to perform limited sensitivity studies, auxiliary calculations, and comparative analyses to investigate specific aspects of the overall calculation. Obviously, there are many important aspects of such a calculation and not all of these have been studied. This whole area of study is continuing, and with time, more aspects will be investigated. Now, however, the current findings are summarized.

A total of four aspects of the calculation have been studied in detail. These are:

1. Effect of natural circulation.

2. Effect of fuel rod relocation model.

3. Thermal history of hot leg nozzle.

4. Core debris state at vessel failure.

Each of these is discussed in the following four sections.

4.2.1.1 Effect of Natural Circulation

One of the main reasons for developing the 2-D version of MELPROG is to allow the code to predict natural circulation in the vessel. Previous studies had indicated that convection cells between the upper plenum and core region could exist. If present, the resulting circulation could remove a significant amount of energy from the core. Hence this phenomenon was expected to play a significant role in the meltdown progression. However, the magnitude of its effect was unknown, and it is important to try to assess the effect of the phenomenon.

In performing this study, the results of the 2-D base case have been compared to a 1-D MELPROG calculation of the same sequence.[169] Both calculations use the same geometric model for the core, upper plenum, and lower plenum. The main difference between the two models is that the 1-D case did not model the downcomer. Nevertheless, the overall modeling of the two cases is similar enough that the effect of 2-D natural circulation can be directly assessed.

At the initiation of the MELPROG transient in both cases, it was assumed that all primary coolant flow had ceased and the fluid temperature was slightly subcooled. The nuclear decay heat from the core quickly brings the stagnant primary fluid to saturation and boiling begins within the core region. The entire length of the heated core contributes to vaporization until the upper plenum is completely voided, i.e., steam filled. During this period, a constant steam generation rate occurs, which is easily calculated, and this rate has been found to be in agreement with that predicted by both versions of MELPROG. This agreement indicates that mass and energy balances are correct.

During the core uncovery phase of the accident, the heat removed from the fuel rods is deposited entirely into steam production and eventually into the steam itself. In the one-dimensional case, the steam simply exits the core region and eventually the vessel. However, in an actual PWR, multidimensional flows establish a natural circulation flow path between the core and the upper plenum and loops. This calculation is, in fact, predicted by the two-dimensional version of the code. The circulation transports energy more rapidly from the core to the available heat sinks, thereby delaying the time to core oxidation and melting. It also heats the vessel components (especially in the upper plenum) much more rapidly than is the case for the one-dimensional model. In terms of fission-product release, the natural circulation may be very important because of its effect on mass transport processes. Also, the circulation between the vessel and the hot legs could lead to a massive failure in the hot leg region, which would depressurize the system. The circulation also affects aerosol and fission-product deposition on structures. Finally, the natural circulation makes the core meltdown more axially uniform, and this may affect the ultimate H_2 and fission-product generation.

Many of the effects of natural circulation are obvious in the two-dimensional calculation. For example, it is easy to see the effect circulation has on core heating. Figure 4.2-1 compares the calculated core heating rates for the 1-D and 2-D cases. It is seen that the circulation, as expected, significantly delays the core heating and beginning of oxidation. Relative to the 1-D calculation, these events are delayed approximately 900 s. Simply put, the circulation leads to greater heat removal from the core, and hence less of the energy generated goes into raising the temperature of the core. However, this has the less obvious effect of heating the plenum structures at a faster rate than in the 1-D case. This difference can be seen in Figure 4.2-2 where the surface temperatures of upper plenum structures are compared. The structures in the 2-D case heat much more rapidly and eventually melt, whereas the structures never melt in the 1-D case. This coupled behavior has significance later in the sequence in regards to availability of surfaces for fission-product deposition.

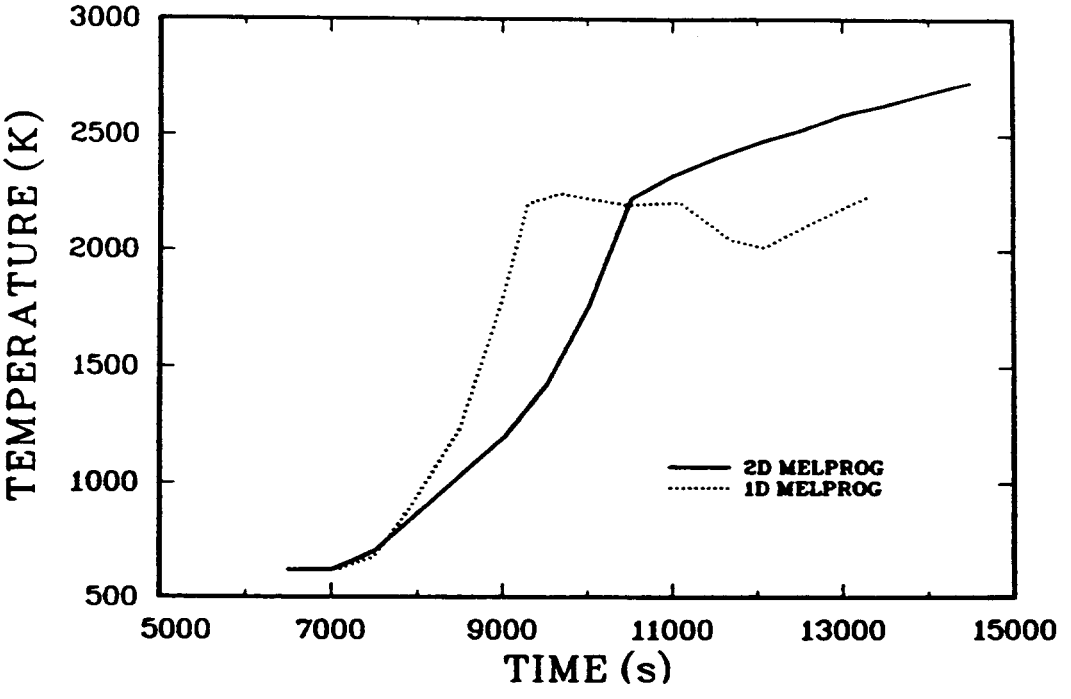

Figure 4.2-1. Comparison of Maximum Core Temperatures

Natural circulation also changes the spatial temperature distribution in the core. In the 2-D case, the radial temperature distribution is nonuniform while the axial temperature distribution is nearly uniform. In the 1-D case, the converse is true. This difference can be understood by considering the circulation flows. The steam flows up the central regions of the core, cools in the upper plenum, and flows down the outer regions of the core. Due to the higher power in the central regions of the core and the lack of heat sinks (such as the core baffle), the temperatures are highest in the central region of the core. However, since the magnitude of the flow is relatively high, the temperature gradient in the axial direction is low (relative to the 1-D case). This means that oxidation and failure occur more or less uniformly in the central region of the core. In fact, all rods in the top half of the core in the central ring fail within 90 s of each other. However, the radial gradients are relatively large. When the first rod fails in the central ring (T = 2200 K), the maximum rod temperature in the outer ring is 1670 K. The first rod failure in the outer ring does not occur until 150 s after the first failure in the central ring. In the 1-D case, the temperatures and failures are much more uniform radially.

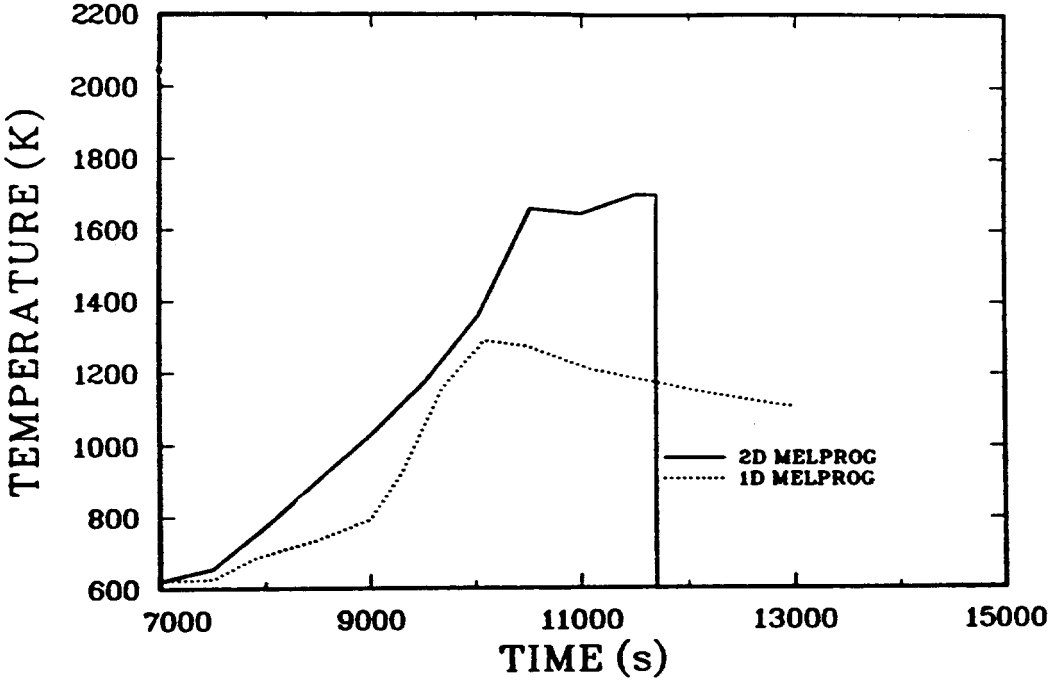

Figure 4.2-2. Comparison of Surface Temperature in Upper Plenum

The change in the core heating pattern will also affect the hydrogen production. However, it is not clear as to whether this is a significant effect. The comparison of the 1-D and 2-D cases shows that the 2-D case produced 30 percent more hydrogen than the 1-D case (see Figure 4.2-3). While this difference is important, it is small compared to the difference found when the relocation temperature is changed (see Section 4.2.1.2). Hence further assessment of the effect of natural circulation on hydrogen production is needed before definitive conclusions can be drawn.

After fuel rod relocation begins, the circulation patterns in the core change dramatically. The relocated material forms partial, if not complete, flow blockages in the lower core regions. These blockages represent a large impedance to flow and disrupt the circulating flow pattern. The flow through these blockage regions is very low. The flow tends to bypass these regions and new convective flow patterns are established. These exist between the upper plenum and the region above the blocked core. This flow will significantly affect fission-product release and transport.

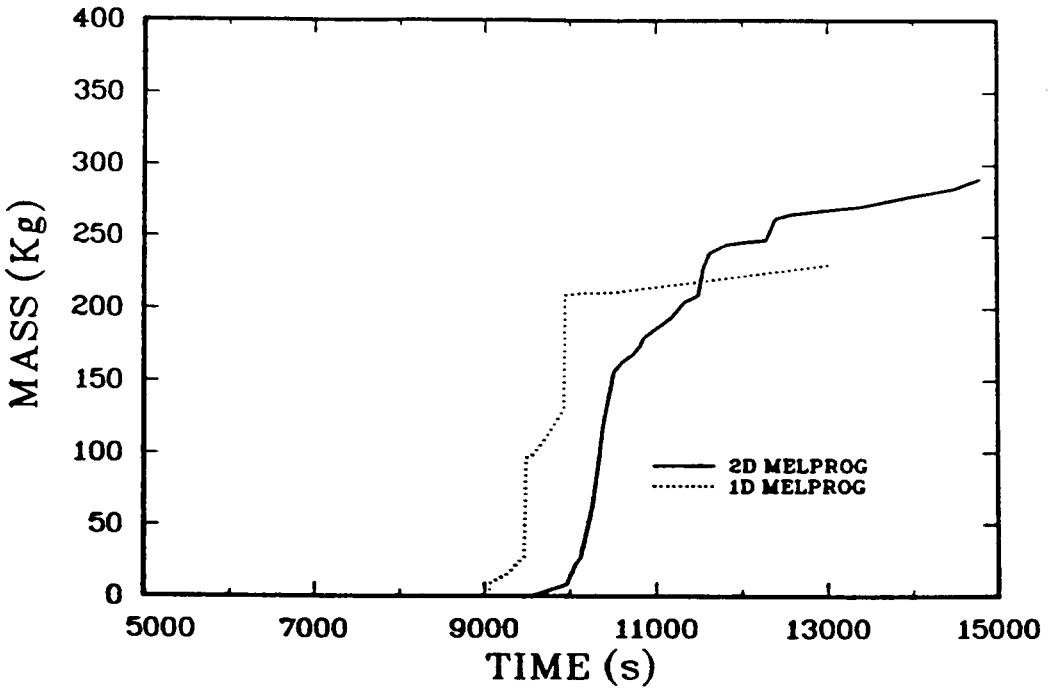

Figure 4.2-3. Comparison of Hydrogen Produced

It is seen then, that natural circulation is an extremely significant phenomenon. Its main effect is to modify the energy partitioning of the core. The "extra" energy extracted from the core delays its heating, but increases the upper plenum temperatures. The convective flows change the axial and radial temperature gradients in the core. This, in turn, modifies the hydrogen generation rate. Finally, the flows are found to be important primarily before relocation. After relocation, the flow patterns, while still existing, undergo radical changes in the core region.

4.2.1.2 Effect of Fuel Rod Relocation Model

In the current calculation, the original fuel rod model was used. This model uses a rather simplistic approach to fuel rod failure and is not mechanistic in nature. As will be shown, the modeling in this area must be mechanistic. Hence, instead of performing a mechanistic failure calculation, the model relies on parametric failure criteria that are a function of oxide thickness and temperature. The model is based on the assumption that as the cladding melts it could be maintained (i.e., held in place) by an oxide layer if the layer is both thick enough and strong enough. The strength factor was felt to be strictly a function of temperature. Since fuel rod failure marks the beginning of relocation, the modeling was felt to be rather important in the meltdown progression.

In the base case, the failure temperature was set to 2200 K. This value is the oxygen stabilized Zr melting temperature. Practically, this temperature means that when the metallic part of the cladding is completely molten, then relocation could begin. That is, no effect of the oxide layer was considered in this case. For testing purposes, this lower limit would expedite the calculation.

It should also be noted that the corium flow regime map assumed that if the corium temperature exceeded 2200 K, then the corium behaved like a liquid (or slurry), while if the temperature was below 2200 K, then the corium was a solid. The key item here is that with corium being "created" at 2200 K by the fuel rod model, a small heat loss would lead to freezing of the corium. Hence relocation was very limited.

In order to investigate the sensitivity of the overall predicted results to this failure temperature, the calculation was rerun through the rod failure point with the failure point increased to 2500 K. The higher value was based on observations from recent SFD experiments. Again, while this modeling is still not mechanistic, it does allow the sensitivity of this one area to be assessed.

The results of this rerun calculation indicate three important areas that are very sensitive to the failure temperature. The first is the amount of hydrogen produced. In both cases, the beginning of relocation marks a rapid decrease in the hydrogen production rate. This is due to the reduced area for oxidation and reduced steam flow. Figure 4.2-4 shows this effect. What this means is that the longer the rods remain in an intact state, the longer hydrogen can be produced (provided steam starvation does not occur). Furthermore, since the rod temperatures are high just prior to relocation, the rate of hydrogen production is large. Hence the change in relocation

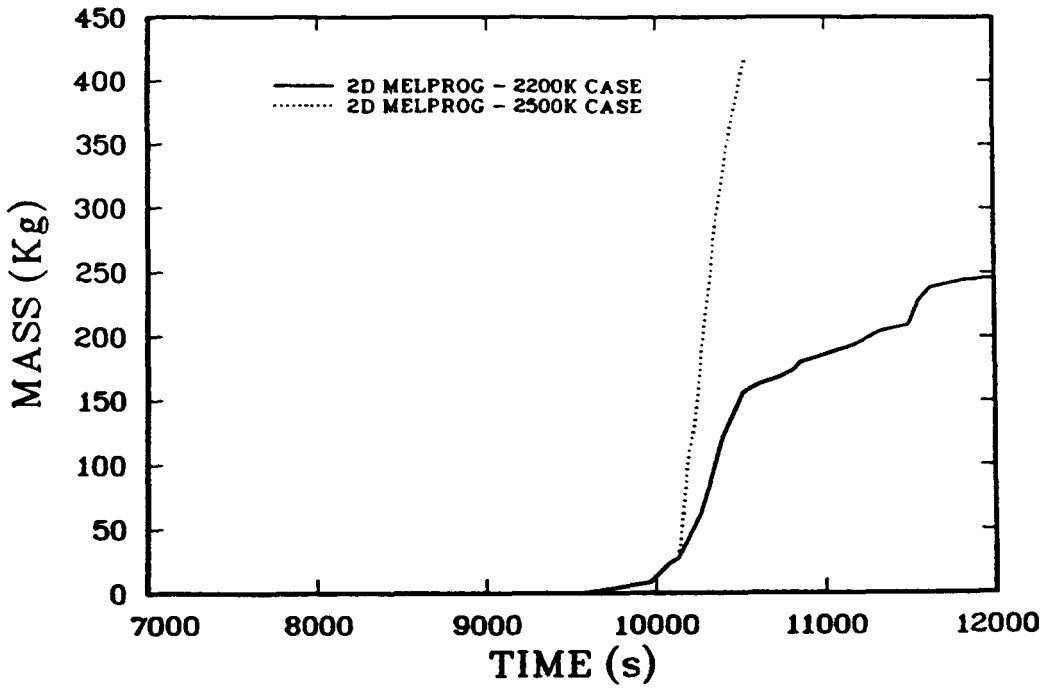

Figure 4.2-4. Comparison of Hydrogen Mass Generated in Relocation Temperature Study

temperature results in a 50 to 100 percent increase in the amount of hydrogen produced.

The second important area affected is the degree of relocation. In the rerun calculation, the corium does not begin to relocate until it is 2500 K. Since the corium flow regime map was not changed, the corium, when formed, has significant superheat. Hence a large amount of energy must be removed before the corium would freeze. This means that the corium stays liquid longer and relocates further. In fact, large quantities of corium relocate into the lower plenum. The corium quenches and vaporizes much of the water remaining in the plenum. The steam generated in this manner momentarily cools the core and sweeps out the hydrogen.

The third important area affected is the amount of energy produced. The energy produced during the oxidation is proportional to the amount of hydrogen produced. As discussed above, the rerun case resulted in a significantly greater amount of hydrogen produced. Hence, the amount of energy generated is also much larger. Due to the relatively low decay power, the energy produced during oxidation has a dominant effect. The practical result of the increased energy is that the sensible heat of the corium is much higher. This causes an acceleration of the meltdown. It only takes an additional 35 s to increase the rod temperatures from 2200 K to 2500 K when they are rapidly oxidizing. Decay heating would require approximately 600 s to raise the temperature the same amount. Hence the corium created is much hotter, and this will result in a reduction in the time to vessel failure.

In summary, the temperature of fuel rod failure has significant effects on the overall calculation. The amount of hydrogen produced is increased by nearly a factor of 2 by increasing the failure temperature from 2200 K to 2500 K. The corium created has more energy (i.e., higher temperature) and can relocate much further. Also, the timing of the meltdown progression can be greatly accelerated. In view of these effects, it is vital that MELPROG have an experimentally validated mechanistic model for this failure. Current efforts in the CORE module development are addressing this important question.

4.2.1.3 Hot Leg Nozzle Temperature

An important assumption in this and all other TMLB' sequence calculations is that the primary system remains at or near the pressure corresponding to the set point of one of the relief valves. The possibility of a failure somewhere in the primary system, followed by depressurization needs to be examined. In this section, an estimate of the thermal condition of one of the primary system weak points, the connection between the vessel outlet nozzle and the hot leg, is discussed. The temperature determined here can then be used in a structural analysis to determine if and when a failure may occur. In the absence of an implicitly linked TRAC-MELPROG calculation, one can estimate the temperature of the vessel-hot leg connection by using the MELPROG outflow conditions as boundary conditions for a TRAC model of the nozzle and hot leg assembly.

The boundary conditions needed for the TRAC calculation are the mass flow and temperature from the vessel, as calculated by MELPROG. These quantities are given in Figures 4.2-5 and 4.2-6, respectively. The TRAC model includes the portion of the nozzle that is external to the vessel and the hot leg itself. To obtain the temperature distribution through the nozzle and hot leg wall, four radial nodes were used. The boundary condition for the external surface of the nozzle and hot leg is assumed to be convective heat transfer to a vapor at 400 K with a heat transfer coefficient of 10 $W/m^2 \cdot K$. This heat transfer coefficient is representative of natural convection from a horizontal pipe that is surrounded by degraded insulation. The temperature distribution through the hot leg wall at the nozzle connection is given in Figure 4.2-7. The temperature can be seen to be above 1000 K for more than 1 h before core slump occurs at 14877 s. Initial indications are that the connection will fail rapidly if above 1000 K. If this is the case, then system depressurization by this means is likely by about 11000 s into the transient. As indicated in Figure 4.2-7, this is well before either core slump at 14877 s or vessel failure at 15928 s.

4.2.1.4 Core Melt Insights

An accurate description of the core debris and melt in the vessel at the time of vessel failure is an important source term consideration. The state of debris needs to be known to provide appropriate sources to containment codes. The state of the debris also affects the magnitude of the in-vessel fission-product release.

To analyze the state of the debris, both the composition and the average temperature of the debris must be determined. The debris will be composed

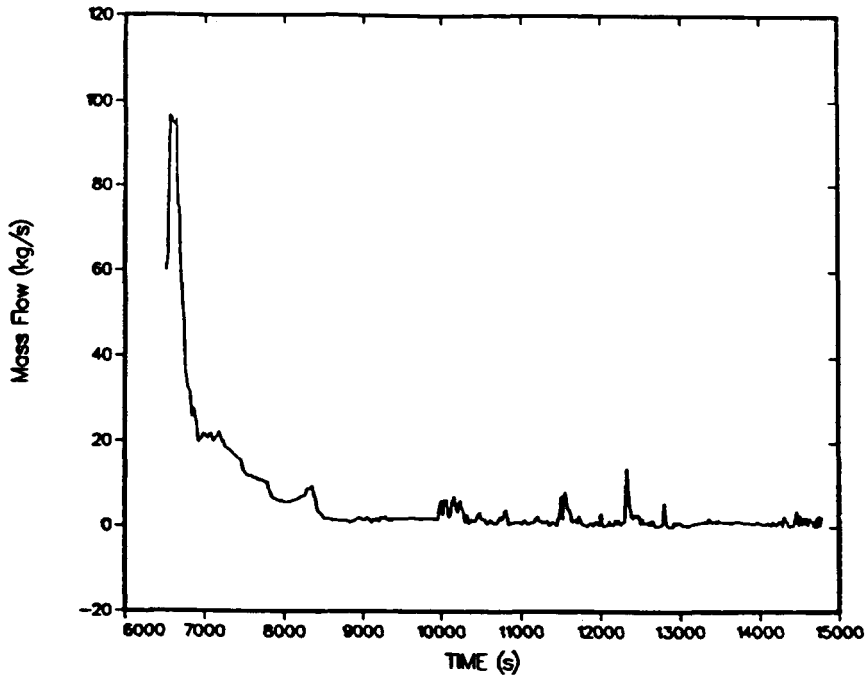

Figure 4.2-5. Outlet Flow Rate

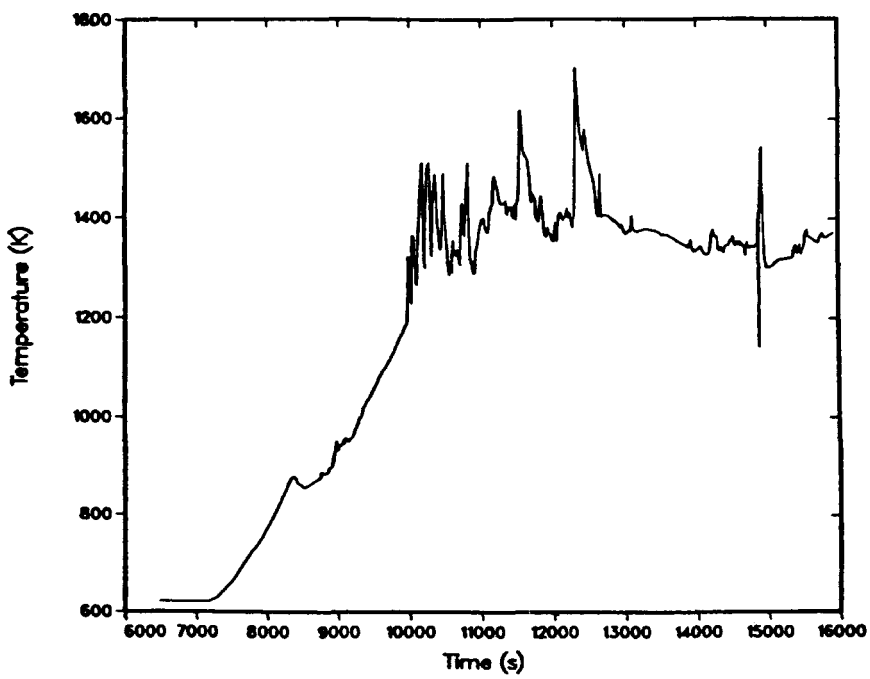

Figure 4.2-6. Vessel Outlet Vapor Temperature

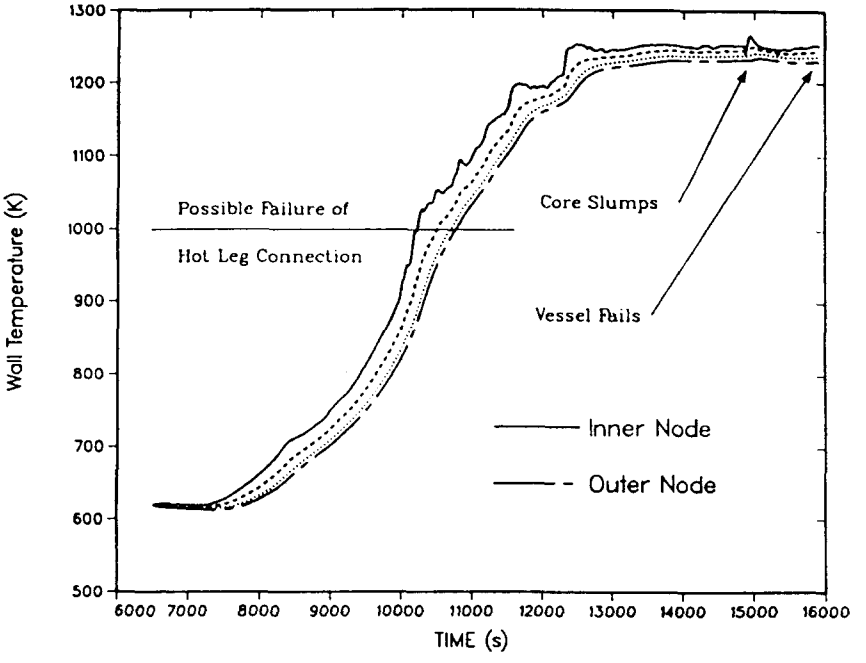

Figure 4.2-7. Temperatures in Hot Leg

of a number of constituents, the major ones being UO_2, Zr, U-Zr-O mixtures, ZrO_2, steel, and control rod materials. The masses of each of these components is important. Both the steel and Zr masses are especially important since these materials can oxidize and release energy in the containment and these can also affect fission-product release during core concrete interactions. The masses of liquefied materials (or molten fraction) also must be calculated. The temperature of the debris is important as this determines the initial thermal loading on the containment.

The tools available for calculating the state of the core debris are limited. The MARCH code is probably the most widely used, and results of this code can be found in the BMI-2104 report and in the QUEST study. The approach in MARCH is parametric and relies heavily on engineering judgment. Both key phenomena and important coupling between phenomena are neglected. These factors are reflected in the large uncertainties in the MARCH results.

By far the more mechanistic code is MELPROG. In MELPROG, the meltdown progression is treated in a continuous and mechanistic manner. That is, melting and relocation of materials are treated in a physical manner without user interaction. There is no separate treatment of the core debris as it exits the core region into the plenum. This integrated analysis, while fairly complex, does allow all the relevant phenomena to be treated in an appropriate manner.

While comparisons between MARCH and MELPROG are possible, a couple of points need to be considered. First, the two codes are completely different in approach and modeling. This can lead to substantial differences

in the results. Second, MELPROG is not yet assessed, and hence caution must be exercised in interpreting its results. Also, only a very limited number of MELPROG calculations have been made and little has been done in the way of sensitivity studies.

Nevertheless, it is useful to discuss the current understanding in the area of core melt. The results of three MELPROG runs and one MARCH calculation for a TMLB' accident sequence in the Surry reactor are presented in Table 4.2-1. While all cases differ in one way or another, this table illustrates the spectrum of possible results. The MARCH results have been taken directly from BMI-2104, Volume V. The first two MELPROG runs are 1-D calculations while the third run is a 2-D calculation. There were two differences between these two 1-D cases. Case 1 used a relocation temperature of 2200 K and did not model the downcomer water inventory. Case 2 used a relocation temperature of 2500 K and did modeled the downcomer water inventory. The effect of these modeling variations is discussed in the following paragraphs. Also, the state of the core debris at vessel failure is a strong function of the in-core modeling.

In fact, the main point that needs to be made is that the state of debris at vessel failure depends on the assumptions and modeling used during the meltdown progression in the core region. Certain quantities such as hydrogen generated and Zr reacted are dependent on assumptions made before any fuel rod failures occur. A discussion of the importance of these assumptions and models follows.

There are four models which lead to the differences in the results. The first, and most important, is the modeling of cladding relocation (in these calculations this means the temperature at which the cladding begins to relocate). This model affects the amount of Zr oxidation and the amount of energy generated in the core. The interesting result, which is consistent in all calculations, is that the majority of oxidation (> 80 percent) occurs while the rods are in intact geometry. Once relocation begins, the flow channels become blocked, which leads to a reduction in steam flow. Also, the surface-to-volume ratio of the Zr decreases, which inhibits oxidation. Both of these factors lead to marked reduction in the oxidation rate following relocation. Hence the relocation modeling is extremely important.

Note that the MARCH calculation and the MELPROG-1D, case 2, calculation used similar values for the cladding relocation temperature. Both of these calculations predict high oxidation, which means that there is less Zr metal available for release to the containment. The other two cases used the lower relocation temperature and have significantly less oxidation.

In addition to differences in oxidation, the relocation model has two other effects. First, the high $T_{relocate}$ cases attain vessel failure earlier. This is due to the large increase in energy deposited by the Zr oxidation. It takes only 35 s for the temperature of an intact rod section to rise from 2200 to 2500 K when the rod is rapidly oxidizing. This time is negligible when compared to the overall timing. The huge increase in energy (equivalent to a 300 K temperature increase) is very important and this leads to early vessel failure. The other effect is that the average

Table 4.2-1

Comparison of Surry TMLB' Calculations

	MARCH	MELPROG-1D		MELPROG-2D
		Case 1	Case 2	
Time for Primary System Saturated to Vessel Failure (min)	90	115	105	157
Average Debris Temperature at Vessel Failure (K)	2380	2600	2120	2460
Total Mass of Debris in the Vessel at Vessel Failure (kg)	102700	117500	128160	137000
Fraction of Debris Molten at Time of Vessel Failure	not reported	0.34	0.16	0.30
Mass of Unreacted Zr at Time of Vessel Failure (kg)	6770	11400	6500	9600
Total Amount of Zr Reacted (%)	59	31	60	40
In-Vessel Hydrogen Mass Generated (kg)	430	230	440	300
Mass of Steel in Debris (kg)	not reported	900	10300	19300
Cladding Relocation Temperature Used in Calculation	2550	2200	2500	2200
Estimated Amount of Debris Released at Vessel Failure (%)	100	52	41	52

temperature is lower as is the molten fraction of the debris. This is because the overall timing is reduced and the debris does not have the time to get hotter.

To see the big effect of the increased relocation temperature, compare the two 1-D MELPROG calculations. The first case did not model the downcomer and used a lower relocation temperature. The second case modeled the downcomer and used a higher relocation temperature. The effect of the downcomer is to increase the time to initial rod failure by about 10 min. Hence, if everything were the same, then the timing of the second case should be 10 min longer. However, it is 10 min shorter. This means that the increased relocation temperature has shortened the accident by 20 min. It has also doubled the Zr reacted (and H_2 produced). However, the molten fraction of the debris is reduced by a factor of 2. This comparison clearly demonstrates the intimate coupling between the meltdown phenomena.

The second area of modeling that affects the core melt is natural circulation. To see the effect, one can compare the 2-D calculation with the 1-D, case 1, calculation. The biggest effect of the circulation is to delay the time to failure. In this case, taking into account the downcomer effect, the circulation would delay the time to failure by about 30 min. This delay, however, is due to transport of energy from the core debris to in-vessel structures. Hence the debris itself is not much different at the time of failure. However, by transporting heat to in-vessel structures, more structures melt relative to the 1-D case. Comparing the 1-D case, case 2, to the 2-D case, one finds about 10,000 kg more steel in the debris. This is due to the melting of the upper plenum structures. Hence the natural circulation, by transporting energy from the debris, leads to longer vessel failure times, more steel in the debris, and lower average debris temperatures at vessel failure.

The third model that affects the debris state is the core slump model. This model determines how the core debris leaves the core region and enters the lower plenum. The core slump model mainly affects the timing of the vessel failure. However, the timing of vessel failure determines the average temperature and molten fraction of the debris. It should also be noted that large uncertainty still exists in the modeling of the core slump. If core slump occurs with the core debris at low molten fraction, then it will take a long time to attain vessel failure due to the poor heat transfer through the debris. This allows the interior of the debris region to become significantly molten and attain high temperatures before vessel failure occurs. On the other hand, if core slump occurs with the core debris at a higher molten fraction, then the vessel will heat faster and fail earlier. This earlier failure prevents the interior of the debris region from becoming significantly molten. However, this current finding is probably scenario dependent and should not be generalized.

The fourth model affecting the core debris state is the actual vessel failure model. Obviously, the vessel failure model will affect the timing of the failure. And the timing of the failure, in turn, affects the molten fraction and temperature of the debris. Failure can occur due to melt-through, mechanical rupture, or instrumentation tube failure. The current MELPROG calculations have only considered the first two modes of failure.

In each case, mechanical rupture occurs before complete melting of the vessel. However, instrumentation tube failure may occur earlier. Modeling of this is currently being studied.

4.2.2 VICTORIA Assessment

The stand-alone version of the VICTORIA fission-product release and transport module (from MELPROG) will be the primary experiment analysis code for the ACRR ST experiment series. In order to determine the effectiveness of the code as an experiment analysis tool, a comparison to the results of the ORNL HI-3 test was undertaken.

The experiment was modeled using seven axial levels. The lower five levels contained the fuel while the upper two were used to model the thermal gradient tube (TGT). Modeling of the spatial temperature profile was done by modifying the code to accept constant temperatures in the TGT regions while using a time and space dependent formulation in the fueled sections.

One of the major differences between the first two planned ST tests and the HI-3 test is the composition of the flowing gas. In the ST tests, a mixture of hydrogen and argon will be used while HI-3 primarily used steam. The stand-alone version of VICTORIA did not contain a kinetic model for clad oxidation by steam. The equilibrium approach to oxidation is inadequate in that it severely overpredicts the amount of oxidation. In order to deal with this problem, a kinetic oxidation model (for clad only) was constructed. This model was based on the rate constants measured by Urbanic and Heidrick. A comparison of model predictions with the HI-3 oxidation estimates showed that our model was well suited to the experiments being modeled.

With the required code modifications in place, the code was run using the geometric and physical (i.e., flow, pressure, temperature, gas composition, etc.) parameters of the HI-3 test. A comparison of code output to experimental results concentrated primarily on the temporal evolution of the fission products krypton and cesium (for which detailed time-dependent information is available) and on the specification of the cesium and iodine in the TGT.

The release of krypton from the fuel grains, as calculated by VICTORIA, is found to agree very well with the experimental data. Obtaining this agreement required a change in the model used for calculating gaseous diffusion within the open porosity of the fuel. The original model used was that of Chapman and Enskog, which gave releases that were too flat with respect to time. A model used by Slattery and Bird with a stronger temperature dependence produced predicted releases in excellent agreement with the experimental data. This change in models was still not sufficient to obtain the necessary improvement in the release rates of the volatile fission products. The shape of the release (from the grains) curves as a function of time indicate that there remains a problem with the models used for transport on the grain faces and edges. What is observed in the calculations is that the vaporization of the volatiles from the grain surface is impeded by the transport of the vapor (in equilibrium with the condensed

phase at the surface) away from the boundary layer, and this is the slowest of the transport steps. Three possible modeling changes are being explored to see which one (or possibly which combination) will be in best agreement with the experimental observations.

In addition to calculating fission-product release from the fuel, VICTORIA also calculates fission-product transport and chemical interactions with other fission products and structural materials. The predictions for the HI-3 test show that iodine deposited in the TGT is found almost exclusively as CsI, which agrees with the experimental observation that deposited iodine is found in concert with cesium. The temperature mesh in the calculation is too coarse to unequivocally state the point in the TGT where this deposition should occur. In addition to the agreement with regard to the iodine speciation, it is found in both the calculation and the experiment that the majority of the cesium and iodine do not deposit on the TGT walls but are found further downstream. The code shows that this transport to a colder region than one would predict for vapor deposition is due to aerosol formation and subsequent capture by the filter at the end of the TGT.

Efforts dedicated to improving the transport models in the open porosity are currently under way and further comparisons with the HI test data, as well as the ACRR ST tests, will be used to verify the improved models.

4.3 MELPROG Validation Experiments

(W. Tarbell and R. Nichols, 6422; A. Reed and M. Pilch, 6425; R. Acton, 7537)

For the in-vessel and reactor coolant system (RCS) aspects of severe accidents, the NRC is sponsoring the development of the MELPROG (MELt PROGression) computer code. This code is being developed jointly at Sandia and Los Alamos National Laboratory (LANL). MELPROG will provide a detailed modeling capability for the progression of severe accidents in the vessel and reactor cooling system of LWRs. Both pressurized water reactor (PWR) designs and boiling water reactor (BWR) designs are treated. MELPROG provides estimates of the release of fission products, steam, hydrogen and core materials exiting from the vessel and RCS during the course of the accident. It also provides detailed analysis of all important aspects of the accident progression in the vessel and RCS. In particular, it treats multiphase coolant flow throughout the accident, core degradation, core melt progression, slump into the lower plenum, melt-water interactions, reactor pressure vessel (RPV) failure, and melt ejection processes.

Degradation of the reactor core begins with the melting of the zircaloy cladding and liquefaction of the fuel. The molten material flows downward and freezes on intact fuel rods. The interrod channels can become completely filled as this crust is formed. The crust consists of frozen metallic oxides, probably a Zr-UO_2 mixture, ZrO_2, and the embedded remnants of fuel rods. The embedded fuel pellets continue to generate heat in the crust, but the rate of temperature increase is less than that of the overlying bare fuel because of the nonfuel mass. The temperature of the overlying fuel pellets at the time of crust formation is typically 1000 K higher than that of the crust. The crust can be up to 0.5 m thick if formed in the lower part of the core.

The crust serves as a temporary barrier between the debris above and the RPV wall. The longer the crust supports the debris above it, the hotter the debris becomes. The maximum temperature attained affects fission-product release. The timing and mode of crust failure and core slump into the lower plenum will affect the fuel-coolant interaction.

Four basic crust configurations are being considered. The first two consider crust formation high in the core while the remaining two consider crust formation in the lower core. One major difference between the two areas is that the crusts located higher in the core will initially be very hot (> 2000 K) whereas, the crusts in the lower regions will be cooler (< 1500 K).

In the case where the crust has failed either in the upper or lower core and the melt progresses to the lower plenum, new crust will eventually form on the lower head of the RPV. As a molten pool of debris accumulates on this crust, the high temperatures involved will attack the welds on the instrument tube penetrations and may cause vessel failure due to the expulsion of these instrument tubes.

The main data needs of MELPROG are in the areas of extended melt progression and vessel failure. Current calculations indicate that modeling in these areas has a significant effect on melt progression behavior. Vessel head modeling currently only evaluates global failure of the lower head and does not presently consider instrument tube failure and the discharge of material from the reactor pressure vessel.

The following sections consider the phenomena associated with attack of the lower head, instrument tube expulsion, and the influence of a crust layer on the ejection of molten core debris.

4.3.1 Theory

In the event the melt finds its way to the lower head of the RPV during core degradation, the vessel may fail by means of the instrument tube penetrations. It is assumed that the molten core debris will heat and weaken the fillet weld retaining the instrument tube.[65] The pressure within the RCS will cause the tube to be expelled when the strength of the weld degrades. Molten core debris is ejected under pressure through the aperture formed in the lower head by the failure of the instrument tube weld.

The tests described here will look at aperture ablation after the instrument tube is expelled from the lower head. In particular, the presence of an intact crust as described previously may mitigate the ablation of the steel, greatly reducing the flow rate during the blowdown of the primary system. If the mass flow of the gases is reduced, there may not be sufficient motive force to entrain and expel the core material from the reactor cavity. Thus the influence of the crust on the lower head could potentially influence the extent of direct containment heating and radionuclide release. In addition to considering the influence of the crust on hole ablation and material discharge, the tests will also evaluate jet ejection characteristics with the inclusion of solid material within the molten pool.

The model used to predict the ablation rate of the steel as formulated by Pilch and Tarbell[83] is a modification of the ZPSS[65] model. To illustrate the differences in the two models, the assumptions, methodology, and results of the ZPSS model are reproduced here. These results are then used in formulating a relationship for predicting the influence of the crust on the ablation rate of the steel.

4.3.1.1 ZPSS Model for Hole Ablation

1. Molten fuel forms a crust on the walls of the breach (aperture) when melt ejection begins. The initial crust-steel contact temperature is below the melting point of steel, therefore, the fuel crust initially adheres to a solid substrate.

2. Convective heat transfer from the molten fuel to the crust causes the crust-steel interface temperature to rise rapidly. The steel substrate begins to melt in about 0.04 s, which is short compared to the vessel discharge time.

3. Melting of the steel substrate jeopardizes the stability of the 66 μm thick fuel crust. This thin crust is continually formed, destroyed, and reformed. The only significant implication of the crust is that it determines the driving temperature difference for convective heat transfer from the molten stream.

4. The ablation rate is determined by equating the convective energy transfer (to the crust) to the energy required to melt the steel, i.e.,

$$h a_s \left(T_f - T_{m,f}\right) = \rho_s a_s \left[c_{p,s}\left(T_{m,s} - T_s\right) + h_{f,s}\right]\frac{dr}{dt} \quad ,$$

$$\frac{dr}{dt} = \frac{2h\left(T_f - T_{m,f}\right)}{\rho_s\left[c_{p,s}\left(T_{m,s} - T_s\right) + h_{f,s}\right]} \quad ,$$

where

h = heat transfer coefficient from the molten fuel to the fuel crust,

a_s = surface area of the breach,

T_f = temperature of the molten fuel,

$T_{m,f}$ = melting temperature of fuel,

ρ_s = steel density,

c_p = specific heat of the steel,

$T_{m,s}$ = melting temperature of the steel,

T_s = steel temperature far from the crust-steel interface,

$h_{f,s}$ = heat of fusion of steel,

r = hole radius.

5. Using Reynold's analogy, the heat transfer coefficient can be related to the discharge velocity, i.e.,

$$h = f \frac{\rho_f c_{p,f} V}{2} \quad ,$$

where

f = friction factor,

ρ_f = density of molten fuel,

$c_{p,f}$ = specific heat of molten fuel,

V = discharge velocity of molten fuel.

4.3.1.2 Modifications to the ZPSS Model

According to Pilch,[83] it seems likely that the unstable crust cannot prevent the molten fuel from contacting the steel substrate directly once the steel substrate begins to melt. This means that the relevant temperature difference driving convection from the molten fuel is $T_f - T_{m,s}$. Therefore, the ZPSS model underestimates the ablation rate. The second reservation expressed is the manner in which the heat transfer coefficient is evaluated. The ZPSS method is used for heat transfer in a tube a long distance away from the entrance. This is not the case for a breach in the reactor vessel where the length to diameter ratio is small and flow is always close to the entrance. Local heat transfer coefficients in the entrance region of a tube are considerably higher than points far from the entrance because the thermal boundary layer is not fully developed near the entrance. For this reason, the ZPSS model again underestimates the ablation rate.

These changes then give the following ablation rate for the steel:[83]

$$\frac{dr}{dt} = \frac{2h\left(T_f - T_{m,s}\right)}{\rho_s \left[c_{p,s}\left(T_{m,s} - T_s\right) + h_{f,s}\right]} \quad .$$

The final size of the ablated hole is given by

$$d_f = d_o + 2 \frac{dr}{dt} t \quad ,$$

where

d_f = final diameter of the hole,

d_o = initial diameter of the hole,

t = time required to complete melt ejection.

The melt ejection time (t) is needed in order to calculate the final hole diameter. The ZPSS determines the ejection time by integrating the mass flux through an ablating hole, i.e.,

$$m = \rho_f V \pi \left[r_o^2 t + r_o \dot{r} t^2 + \frac{\dot{r}^2 t^3}{3} \right]$$

where

m = melt mass being ejected,

r_o and r_f = initial and final hole radii, respectively,

r = hole ablation rate.

The small length-to-diameter ratio (L/D) of the ablating hole coupled with rapid ablation dictates careful treatment of the heat transfer coefficient. Development of the thermal and hydrodynamic boundary layers is incomplete (boundary layer thickness less than hole radius) for the small L/D ratio associated with an ablating hole in a reactor vessel. Consequently, the heat transfer coefficient is larger than would be expected for fully developed flow in a long tube. The ZPSS analysis does not consider this entrance region effect. It is recommended[83] that the larger value of h as determined from a flat plate correlation for fully developed turbulent flow be chosen. Experience shows that the flat plate correlation is almost always the appropriate choice for both experiments and reactor analysis.

Flat plate correlation:[83]

$$h = 0.0292 \frac{k_\ell}{L} Re_L^{0.8} Pr^{0.33} \quad ,$$

Tube correlation:

$$h = 0.023 \frac{k_\ell}{d} Re_d^{0.8} Pr^{0.33} \quad ,$$

where

h = local heat transfer coefficient at the breach exit,

k_ℓ = thermal conductivity of the molten fuel,

Re_L = Reynolds number based on the length (L) of the hole,

Re_d = Reynolds number based on the instantaneous diameter (d) of the hole,

Pr = Prandtl number of the molten fuel.

The heat transfer equations given are approximate only for nonablating surfaces. If the ablation rate ($\dot{d}$) is large, then the heat transfer coefficient is reduced because of "transpiration cooling" of the boundary layer.[83] The modified coefficient is given by

$$h = h \frac{\beta}{e^\beta - 1} \quad ,$$

where

$$\beta = \frac{\rho_{ms} c_{p,ms} \dot{d}}{2h} \quad ,$$

and where

ρ_{ms} = density of the molten wall material (steel),

$c_{p,ms}$ = specific heat of the molten wall material (steel),

d = ablation rate, i.e., the rate of change of the hole diameter.

The effective heat transfer coefficient is significantly reduced when gas blowthrough occurs. Only the molten fuel component of the two phase mixture passing through the hole is capable of ablating the steel; the blowdown gas (steam and hydrogen) is not hot enough (~600 K) to melt the pressure vessel wall. Following gas blowthrough, the heat transfer coefficient is reduced by the relative amount of molten fuel that is in contact with the steel, i.e.,

$$h = h \frac{A_\ell}{A_h} \quad ,$$

where A_h = is the area of the hole in the pressure vessel.

4.3.1.3 Influence of Crust on Ablation Rate of Steel

The analysis in Section 4.3.1.2 assumes that the molten pool is in direct contact with the steel. In the situation where a crust is on the lower head, the final size of the opening will be determined by the influence of the crust. Because the final size of the hole is given by the ablation rate times the time, the duration of the discharge must be calculated. This is accomplished by the integration of the mass flux through an ablating hole.

The assumption is made that the crust remains stable throughout the discharge time, i.e., the driving temperature difference for the convective heat transfer to the steel substrate from the other material properties remains constant as in a homogeneous material.

The time dependent discharge rate through an ablating hole is given by

$$\dot{m}_\ell = -\rho_\ell \dot{a} V_\ell \quad ,$$

where

$\dot{m}_\ell$ = time dependent mass flow rate,

ρ_ℓ = density of the liquid,

$\dot{a}$ = time dependent area of the ablating hole,

V_ℓ = velocity of the liquid.

The liquid discharge velocity at high pressure is given by Bernoullis's equation,

$$V_\ell = C_d \left(\frac{2\Delta P}{\rho_\ell} \right)^{0.5} \quad ,$$

where C_d is the discharge coefficient, and ΔP is the pressure difference across the aperture.

The time dependent hole diameter, as shown in Section 4.3.1.1, is reproduced here for convenience:

$$\dot{d} = \frac{2h\left(T_f - T_{m,s}\right)}{\rho_s\left[c_{p,s}\left(T_{m,s} - T_s\right) + h_{f,s}\right]} \quad ,$$

where

$T_{m,s}$ = melting temperature of the steel,

T_f = melting temperature of the fuel,

ρ_s = density of the steel,

$c_{p,s}$ = heat capacity of the steel,

T_s = initial temperature of the steel,

$h_{f,s}$ = heat of fusion of the steel,

h = heat transfer coefficient.

The time dependent area of the ablating hold is defined as

$$a(t) = \frac{\pi d^2(t)}{4} \quad .$$

The change in the diameter can be written as

$$d - d_o = \int_o^t \dot{d}\, dt = \dot{d}\, t \quad .$$

Then a(t) can be rewritten as

$$a(t) = \frac{\pi\left(d_o + \dot{d}t\right)^2}{4} \quad .$$

Substituting the expressions for the time dependent area and the liquid velocity give the following result for the mass flow rate:

$$\dot{m}_\ell = -\rho_\ell \frac{\pi\left(d_o + \dot{d}t\right)^2}{4} C_d \left(\frac{2\Delta P}{\rho_\ell}\right)^{0.5}$$

The difference in the mass flow rate at time t and the mass flow rate at time 0 is given by

$$m_\ell(t) - m_o = -\rho_\ell \frac{\pi}{4} C_d \left(\frac{2\Delta P}{\rho_\ell}\right)^{0.5} \int_o^t \left(d_o + \dot{d}t\right)^2 dt \quad ,$$

where m_o is the mass flow rate at time 0.

After performing the integration, the time dependent mass flow rate becomes

$$m_\ell(t) - m_o = -\rho_\ell \frac{\pi}{4} C_d \left(\frac{2\Delta P}{\rho_\ell}\right)^{0.5} \frac{\left\{\left(d_o + \dot{d}t\right)^3 - d_o^3\right\}}{3\dot{d}} \quad .$$

The final hole size when all the liquid is discharged, i.e., when m (t) = 0 is given as

$$\frac{\rho m_o}{\rho_\ell \frac{\pi}{4} C_d \left(\frac{2\Delta P}{\rho_\ell}\right)^{0.5}} = \frac{d_f^3 - d_o^3}{3\dot{d}} \quad .$$

Rearrangement of the equation gives the following relationship:

$$\frac{3 m_o \dot{d}/d_o}{\rho_\ell \frac{\pi}{4} d_o^2 C_d \left(\frac{2\Delta P}{\rho_\ell}\right)^{0.5}} = \frac{d_f^3}{d_o^3} - 1 \quad .$$

The equation can be simplified by substituting for $\dot{m}_o$ and rearranging the terms to provide a means for looking at the limiting cases, i.e.,

$$\dot{m}_o = \rho_\ell \frac{\pi}{4} d_o^2 C_d \left(\frac{2\Delta P}{\rho_\ell}\right)^{0.5} \quad .$$

Thus

$$\frac{d_f}{d_o} = \left(1 + \frac{3\dot{d}/d_o}{\left(\dot{m}_o/m_o\right)}\right)^{1/3}$$

There are two limiting cases for this equation. The first case is for $\dot{m}_o$ large, d_o large, and $\dot{d}$ small. For this condition,

$$\frac{3\,\dot{d}/d_o}{\dot{m}/m_o} \ll 1 \quad ,$$

which implies

$$\frac{d_f}{d_o} \sim 1 \quad .$$

This indicates that the final and initial diameters are the same. This is clearly not the case and is an uninteresting limit. The more relevant limit provides a good scaling criteria and is given for $\dot{m}_o$ small, d_o small $\dot{d}$ large. For this condition:

$$\frac{3\,\dot{d}/d_o}{\dot{m}/m_o} \gg 1 \quad .$$

This implies that

$$\frac{d_f}{d_o} \simeq \left(\frac{3\dot{d}/d_o}{\dot{m}_o/m_o}\right)^{1/3} \quad .$$

By assuming the ratio of the final hole size to the original hole size is much greater than one, a comparison of the final hole sizes with and without the crust can be made:

$$\frac{d_f^3}{d_o^3} \gg 1 \qquad \text{i.e.,} \qquad \frac{3\dot{d}/d_o}{\dot{m}_o/m_o} \gg 1 \quad ,$$

$$\frac{d_{f(\text{crust})}}{d_{f(\text{no crust})}} = \left(\frac{\dot{d}_{(\text{crust})}}{\dot{d}_{(\text{no crust})}}\right)^{1/3} \quad .$$

If the ratio is greater than one, then the final diameter of the breach with no crust is smaller than the diameter of the breach with the crust. This implies that the crust has no influence on the ablation of the aperture. If the ratio is less than one, then the opening with the crust is the larger of the two and has a negative influence on diametral growth. The ablation rates for the two cases are

$$\dot{d}_{crust} = \frac{2h_{(crust)}\left(T_f - T_{m,c}\right)}{\rho_c\left[c_{pc}\left(T_{m,c} - T_c\right) + h_{f,c}\right]} \quad ,$$

$$\dot{d}_{no\ crust} = \frac{2h_{(no\ crust)}\left(T_f - T_{m,s}\right)}{\rho_s\left[c_{ps}\left(T_{m,s} - T_s\right) + h_{f,s}\right]} \quad .$$

Therefore,

$$\frac{\dot{d}_{crust}}{\dot{d}_{no\ crust}} = \frac{h_{crust}}{h_{no\ crust}} \frac{\rho_s\left(T_f - T_{m,c}\right)}{\rho_c\left(T_c - T_{m,s}\right)} \frac{\left[c_{ps}\left(T_{m,s} - T_s\right) + h_{f,s}\right]}{\left[c_{pc}\left(T_{m,c} - T_c\right) + h_{f,c}\right]}$$

In most cases, the heat transfer coefficient is determined by entrance region effects. The relationship between the geometry of an accident and the heat transfer coefficients can be estimated with approximations. If it is assumed that the crust is formed on the inside of the RPV, the temperature of the melt is 2500 K, the temperature of the crust-steel interface is 1700 K, and the temperature of the steel is 600 K; then the convective heat transfer coefficient at the bottom of the crust (i.e., the crust-steel interface) can be approximated by

$$h_{crust} \simeq \frac{1}{L_c^{0.2}} \quad ,$$

where L_c is equal to the thickness of the crust.

For the heat transfer coefficient at the bottom of the steel, L_s is equal to the thickness of the steel and L_c is equal to the thickness of the crust. The convective heat transfer coefficient for no crust can then be approximated by

$$h_{no\ crust} \simeq \frac{1}{\left(L_c + L_s\right)^{0.2}} \quad .$$

Thus the ratio of the two equations can be written in the following manner:

$$\frac{\dot{d}_{crust}}{\dot{d}_{no\ crust}} = \left(\frac{L_c + L_s}{L_c}\right)^{0.2} \frac{\rho_s}{\rho_c} \frac{\left(T_f - T_{m,c}\right)}{\left(T_s - T_{m,s}\right)} \frac{\left[c_{ps}\left(T_{m,s} - T_s\right) + h_{f,s}\right]}{\left[c_{pc}\left(T_{m,c} - T_c\right) + h_{f,c}\right]} .$$

The above equation shows that the ratio of the ablation rates is directly proportional to the amount of superheat ($T_f - T_{m,c}$). When realistic values are picked for the variable in the equation, it is shown that any crust thickness can seriously inhibit radial growth of the aperture in the lower RPV head.

4.3.2 Test Apparatus

Conditions inside the RPV at the time of instrument tube failure will be approximated with the apparatus shown in Figure 4.3-1. The apparatus consists of a melt generator, which is an outer pressure vessel, and an

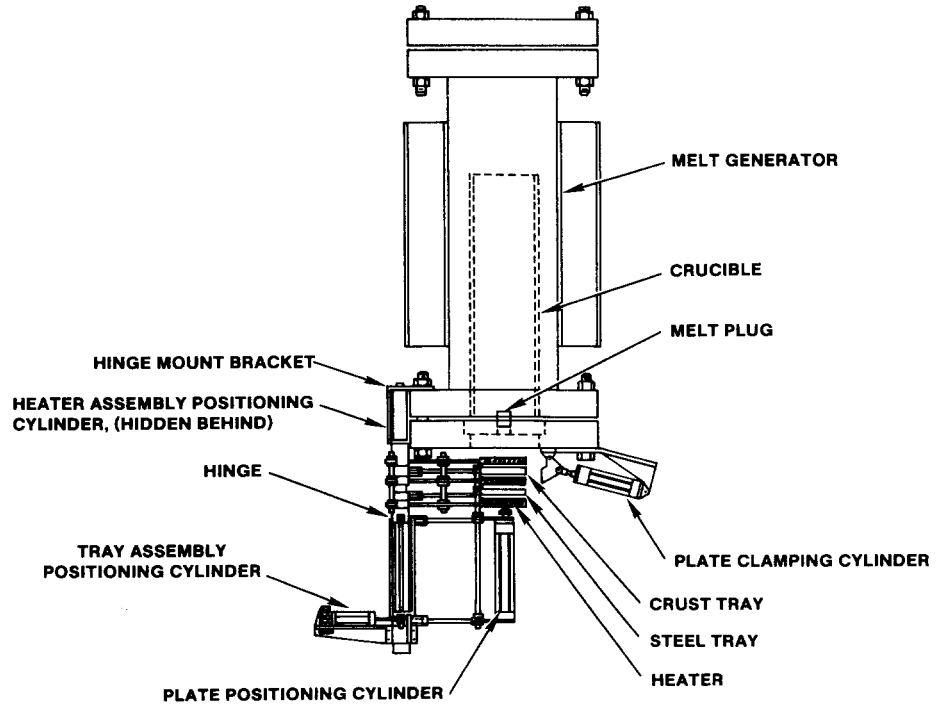

Figure 4.3-1. MELPROG Experimental Setup

inner melt crucible. The mechanism below the melt generator provides a means for preheating and placing a simulated crust and steel backing plate at the exit of the melt generator, duplicating the geometry of an RPV. The choice of material for the simulated crust will be based on the physical properties of the Zr-UO_2 crust, which would form during an accident, as well as criteria from the mathematical model of the ratio of the two ablation rates.

The outer pressure vessel consists of a 16-in-diameter schedule 40 pipe section with flanges welded to both ends. The upper blind flange is bolted into place and is provided with a means for pressurizing the vessel. The lower flange cover is modified to accept a steel insert plate that is machined to accept a brass fusible plug.

The melt crucible is constructed of an inner 14 gauge, 9-in-diameter steel shell around which is placed a 10-in-diameter schedule 20 pipe. The annular gap between the two shells is filled with a wet ram (MgO) that is baked to drive off the moisture. This serves as an insulating barrier for the hot-melt material. The insert plate forms the bottom of the melt crucible and consists of a 2-in-thick steel plate that is drilled and tapped for a 1.5-in NPT brass pipe plug. The plug is placed in the bottom of the crucible to simulate an instrument tube penetration. This assembly is then sealed against the lower flange with an O-ring and fastened with eight 1/4-20 socket head cap screws. The lower flange is then bolted to the welded flange attached to the pressure vessel pipe section.

The mechanism below the melt generator has two functions: The first function is to bring the simulated crust material and steel backing plate up to temperatures approximating those calculated by the previously derived equations. The second function is to clamp the crust and backing plate into place below the brass plug in the melt crucible. The mechanism is equipped with heaters capable of producing temperatures up to 1200°C. After the plates have been brought up to their respective temperatures, pneumatic cylinders operated remotely with solenoid actuated valves swing the heaters out of the way and then position and clamp the plates into place. Upon completion of this task, the whole mechanism is then swung from underneath the melt generator to allow free passage of the material from the vessel.

The plates used to simulate the failed RPV and the formed crust will be 6 inches in diameter with preformed apertures. In order to determine the effect the crust will have on the ablation rate of the steel, the aperture of the crust and backing plate will be 1 inch in diameter and that of the brass plug will be 2 inches in diameter. The crust will be placed in direct contact with the melt generator bottom (gasketed to prevent gas leakage) and the steel plate, directly under the crust. In this manner, the melt must pass through the crust before it contacts the steel as is the situation in a reactor accident:

Crust selection was based on the need to simulate the physical properties of the Zr-UO_2 crust as well as fulfilling the requirements specific to the test apparatus. Theory predicts that the ratio of the ablation rates is

directly proportional to the degree of superheat of the crust; this suggests that a large degree of superheat is desirable. Taking into consideration the uncertainty of the temperature of the melt, this degree of superheat should be on the order of 400 K. The uncertainty as to the temperature of the melt (±200 K) makes it necessary to maintain as large a temperature difference as possible between the initial temperature of the crust and the melting point of the crust. A prediction of the temperature of the crust can be made by assuming the ratio of the ablation rates is equal to one. This allows the initial crust temperature (T_c) to be solved for by algebraic manipulation:

$$T_c^\circ = T_{m,c} + \frac{h_{fc}}{c_{p,c}} - \frac{1}{c_{p,c}} \left(\frac{L_c + L_s}{L_c} \right)^{0.2} \frac{\rho_s}{\rho_c} \frac{\left(T_f - T_{m,c} \right)}{\left(T_f - T_{m,s} \right)} \left[c_{p,s} \left(T_{m,s} - T_s^\circ \right) + h_{f,s} \right]$$

Because the ratio of the two ablation rates ($\dot{d}_{crust}/\dot{d}_{no\ crust}$) is directly proportional to the amount of superheat of the crust and inversely proportional to the temperature difference ($T_{m,c} - T_c$), the slope of the plot of $T_f - T_{m,c}$ versus $T_{m,c} - T_c$ is proportional to the ratio of the ablation rates. Any values that fall above the curve indicate the ratio is greater than one and that the steel is the controlling medium, and any values that fall below the curve indicate a ratio of less than one and that the crust is the controlling medium (Figure 4.3-2).

The properties of several ceramic materials were examined to see if they were compatible with experimental needs. The conclusion was made that insufficient data were available on the ceramics to make a choice. The heat of fusion and the melting point were the two primary pieces of data missing from all the references that were scrutinized. Because of this and because of its easy availability, fused silica was chosen as the crust material. Data for fused silica are readily available and its properties are very close to that of some ceramics. Because fused silica changes crystal structure and becomes glassy, the heat of fusion has no real meaning. However, this material maintains a high degree of rigidity at elevated temperatures and should simulate the Zr-UO_2 crust material very well.

4.3.3 Procedure

The procedure that will be followed during testing will closely approximate the events that happen in a reactor accident. The RPV is initially at pressure and contains molten material. The crust formed is at some temperature between its melting point and that of the RPV wall. It is then assumed that the instrument tube penetration weld fails and melt is ejected through the opening.

The melt generator will be charged with nitrogen at a predetermined pressure, depending upon which tests is being done. The crust material and steel backing plate will be brought up to temperature by heaters. After temperatures higher than those needed are attained (to allow for heat

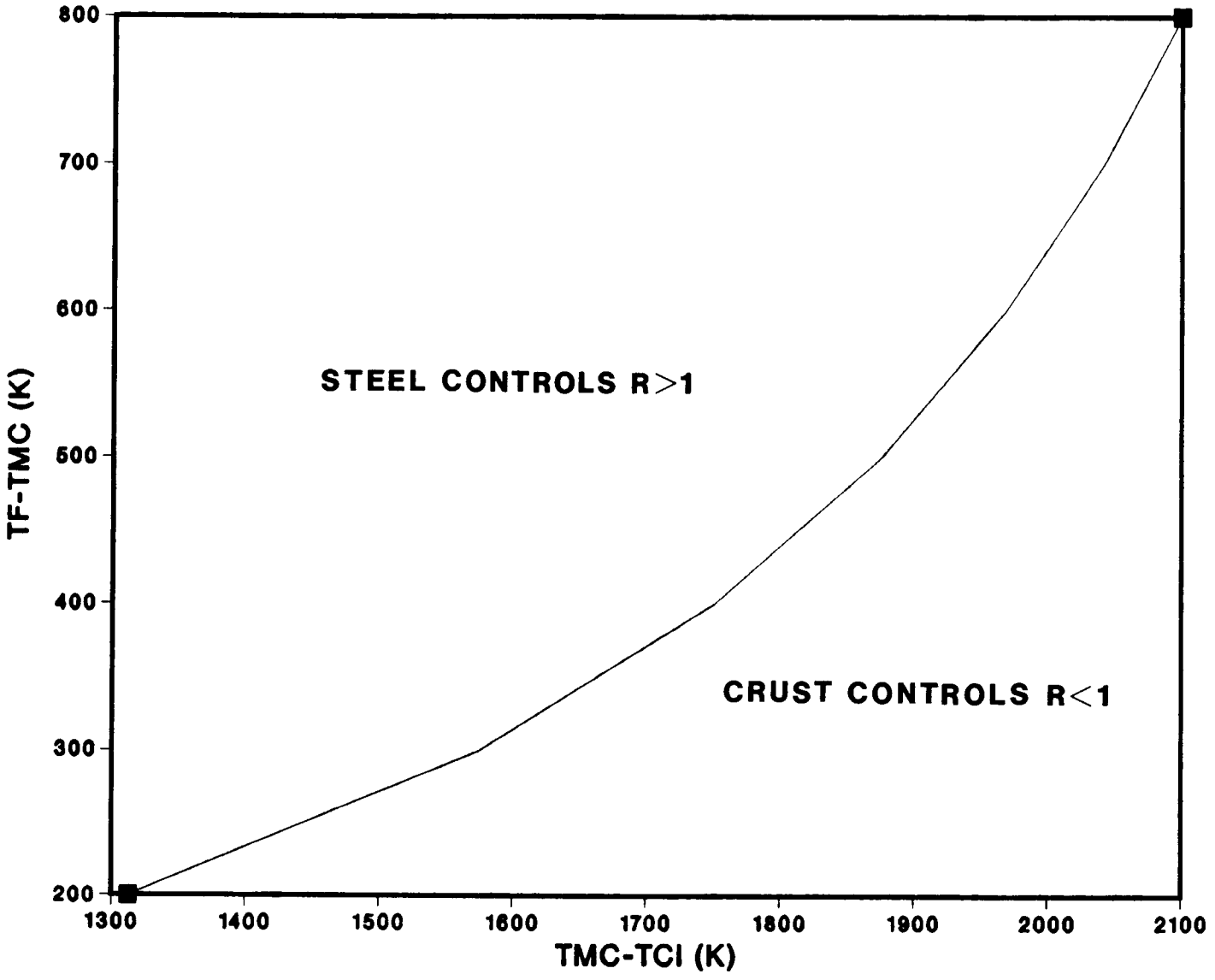

Figure 4.3-2. Ratio of Crust Over No Crust (Fused Silica)

losses during transfer), the plates will be clamped into position, and the mechanism will be swung out of the way. At this time, ignition of the 80 kg of iron-oxide/aluminum thermite in the melt crucible will be initiated, and a high-temperature melt will be generated by the ensuing metallothermitic reaction. During the reaction, the pressures inside the vessel will rise proportionally, and the temperature of the melt will reach approximately 2500 K. The brass plug in the crucible will fail catastrophically when the molten material makes contact with it, and the debris will be ejected at high temperature and pressure through the ablating plates.

The test matrix, Table 4.3-1, has been devised for screening main effects for the outlined conditions. The first five tests vary each of the three parameters considered to have the most influence on the phenomena to be studied. The remaining three tests explore the influence of the crust thickness.

Table 4.3-1

Test Matrix For Screening Main Effects

Test	System Pressure	Crust Temp.	Solids In Melt	Crust Thk. (in.)
1.	low	low	no	0.25
2.	high	low	no	0.25
3.	low	high	no	0.25
4.	low	low	yes	0.25
5.	high	high	no	0.25
6.	low	low	no	1.0
7.	low	low	yes	1.0
8.	high	low	no	1.0

4.3.4 Instrumentation

The test apparatus will be instrumented to determine the individual effects of the variables listed in Table 4.3-1. The melt generator will have redundant pressure transducers mounted to record the pressure history of the vessel throughout the test. The ablating plates are to be instrumented with Type K thermocouples so that their temperatures can be monitored both before and after placement below the melt crucible. Redundant temperature measurements of the melt as it emerges from the bottom of the ablating plates will be sensed by two fast acting pyrometers.

Posttest analysis will include examination of the ablating plates to determine the effect of the crust. Examination will also reveal what effect the inclusion of solids in the melt will have on the ablation rate of the crust and steel backing plate.

5. REFERENCES

1. Reactor Safety Study: An Assessment of Accident Risks in U.S. Commercial Nuclear Power Plants, Nuclear Regulatory Commission, Washington, D.C., WASH 1400, NUREG 75/014, October 1975.

2. R. K. Cole, D. P. Kelly, and M. A. Ellis, CORCON-Mod2: A Computer Program for Analysis of Molten-Core Concrete Interactions, Sandia National Laboratories, Albuquerque, NM, NUREG/CR-3920, SAND84-1246, 1984.

3. D. A. Powers, J. E. Brockmann, and A. W. Shiver, VANESA: A Mechanistic Model of Radionuclide Release and Aerosol Generation During Core Debris Interactions With Concrete, Sandia National Laboratories, Albuquerque, NM, NUREG/CR-4308, SAND85-1370, 1986.

4. D. R. Bradley and A. W. Shiver, "Uncertainty in the Ex-Vessel Source Term Caused by Uncertainty in In-Vessel Models," Paper presented at the ANS/ENS Topical Meeting on Thermal Reactor Safety, San Diego, CA, February 1986.

5. E. R. Copus and R. E. Blose, "Sustained Uranium-Concrete Interactions: The SURC Experiments," Proceedings of the CSNI Meeting on Core-Debris Concrete Interactions, EPRI NP-5054-SR, Special Report, February 1987.

6. D. R. Bradley and E. R. Copus, "Sustained Urania-Concrete Interactions (SURC): Experiments and Analysis," Paper presented at the 14th Water Reactor Safety Research Information Meeting, Gaithersburg, MD, October 27-31, 1986.

7. F. M. Lea and C. H. Desch, The Chemistry of Cement and Concrete (Edward Arnold Publishers Ltd., 1956).

8. W. H. F. Taylor, Symp. on the Chemistry of Cements, Cement Association of Japan, 1968.

9. A. M. Nelville, Properties of Concrete, 2nd Edition, 1973.

10. T. Z. Harmathy and L. W. Allen, American Concrete Institute Journal 70, pp 132 (1973).

11. D. A. Powers, D. A. Dahlgren, J. F. Muir, and W. B. Murfin, Exploratory Study of Molten Core Material/Concrete Interactions, Sandia National Laboratories, Albuquerque, NM, SAND77-2042, March 1977.

12. T. C. Powers and T. L. Brownyard, Proc. Amer. Concrete Inst., 43, p 101 (1947).

13. H. F. W. Taylor, K. Mohan, and G. K. Moir, J. Amer. Ceramic Society 68, p 680 (1985).

14. J. E. Gillott, J. Appl. Chem. London, 17, p 185 (1967).

15. D. A. Powers, "Emperical Models for the Thermal Decomposition of Concrete," Trans. Am. Nucl. Society, 26, p 400 (1977).

16. D. A. Powers, "Influence of Gas Generation on Melt Concrete Interactions," Thermodynamics of Nuclear Materials, p. 351 (1980).

17. T. L. Webb and J. E. Kruger, "Carbonates," in Differential Thermal Analysis, (R. C. MacKenzie, editor, Academic Press, 1970) Ch No. 10.

18. E. K. Powell and A. W. Searcy, J. Amer. Ceram. Society, 61, p 216 (1978).

19. S. Dobner et al. Thermochemica Acta, 16, p 251 (1976).

20. J. A. Murray and H. C. Fischer, Proc. Am. Soc. Testing Mater., 51, p 1197 (1951).

21. J. M. Criado, Thermochemica Acta, 19, p 129 (1977).

22. R. E. Blose, J. E. Gronager, A. J. Suo Anttila, and J. E. Brockmann, SWISS: Sustained Heated Metallic Melt Concrete Interactions With Overlying Water Pools, Sandia National Laboratories, Albuquerque, NM, NUREG/CR-4727, SAND85-1546, 1987.

23. T. Z. Harmathy, Ind. Eng. Chem. Fundamentals, 8, p 92 (1969).

24. G. L. England and M. E. Skipper, "On the Prediction of Moisture Movement in Heated Concrete," Proc. 2nd Int'l Conf. on Structural Concrete in Reactor Technology, Vol.3, Berlin, September 1973.

25. Z. P. Bazant and L. J. Najjar, Materials and Structures Vol. 5, pp 3-20 (1972).

26. J. M. Becker and B. Bresler, A Computer Program for the Fire Response of Structures--Reinforced Concrete Frames, University of California, Berkeley, CA, UCB FRG 74-3, 1974.

27. G. L. England and A. D. Ross, "Shrinkage, Moisture and Pore Pressure in Heated Concrete," Proc. 1st Int'l Conf. on Structural Mechanics in Reactor Technology, Paper H2/4, Berlin, 1971.

28. J. E. McDonald, Moisture Migration in Concrete, Concrete Laboratory, U.S. Army Engineers Waterways Experimental Stations, Vicksburg, MS, Tech. Rept. C-75-1, May 1975.

29. J. V. Beck and R. L. Knight, User's Manual for USINT, Sandia National Laboratories, Albuquerque, NM, NUREG/CR-1375, SAND79-1694, May 1980.

30. S. W. Claybrook and L. D. Muhlstein, WATER: An Improved Computer Program to Analyze Water and Gas Release from Heated Concrete, Hanford Engineering Development Laboratory, Richland, WA, HEDL-TME-84-27, September 1984.

31. A. Dayan, COWAR-2 User's Manual--Thermohydraulic Behavior of Heated Concrete, General Electric Co., Sunnyvale, CA, GE-FBRD, GEFR-00090(1), May 1977.

32. K. H. Chen, E. L. Gluekler, S. T. Lam, and V. S. Shippey, Comparison of Mechanistic Codes for Predicting Water Release from Heated Concrete, General Electric Co., Sunnyvale, CA, GEFR-00521, April 1980.

33. A. K. Postma, J. D. McCormack, and J. A. Schur, Study of Water and Gas Release from Heated Concrete, Hanford Engineering Development Laboratory, Richland, WA, HEDL TC-996, December 1977.

34. A. J. Suo-Anttila, SLAM-A Sodium Limestone Concrete Ablation Model, Sandia National Laboratories, Albuquerque, NM, NUREG/CR-3379, SAND83-7114, December 1983.

35. U.S. Nuclear Regulatory Commission, Estimates of Early Containment Loads from Core Melt Accidents, Washington, DC, NUREG-1079, December 1985.

36. D. A. Powers and F. E. Arellano, Large-Scale, Transient Tests of the Interaction of Molten Steel with Concrete, Sandia National Laboratories, Albuquerque, NM, NUREG/CR-2282, SAND81-1753, January 1982.

37. J. W. Dougill, Mag. Conc. Res., 24, p 71 (1972).

38. C. Meyer-Ottens, Beton, 24, p 133 (1974).

39. P. J. E. Sullivan and A. A. A. Zaman, "Explosive Spalling of Concrete Exposed to High Temperatures," Paper presented at the 1st Int'l Conf. Structural Mechanics in Reactor Technology, Berlin, 1971.

40. E. R. Copus and D. R. Bradley, Interaction of Hot Solid Core Debris With Concrete, Sandia National Laboratories, Albuquerque, NM, NUREG/CR-4558, SAND85-1739, June 1986.

41. W. W. Tarbell, D. R. Bradley, and F. E. Arellano, Sustained Concrete Attack by Low Temperature, Fragmented Core Debris, Sandia National Laboratories, Albuquerque, NM, SAND82-2476, NUREG/CR-3024, 1983.

42. D. A. Powers, Light Water Reactor Safety Research Program Quarterly Report, April - June 1978, Sandia National Laboratories, Albuquerque, NM, SAND78-1901 NUREG/CR-0422, April 1979.

43. D. A. Powers, "Chemical Phenomena and Fission Product Behavior During Core Debris Interactions with Concrete," Paper presented at the CSNI Specialists Meeting on Core Debris/Concrete Interactions, Palo Alto, CA, September 1986.

44. G. W. Parker, G. E. Creek, and A. L. Sutton, Jr. "Influence of Variable Physical Process Assumptions on Core-Melt Aerosol Release," Proc. Int'l Mtg on Thermal Reactor Safety, Vol. 2, p 1078, U.S. Nuclear Regulatory Commission, Washington, DC, NUREG/CP-0027, 1982.

45. R. E. Henry, "A Model for Core-Concrete Interactions," Proc. Int'l Mtg. on LWR Severe Accident Evaluation, Paper TS 12.10, Cambridge, MA, August 1983.

46. W. B. Murfin, A Preliminary Model for Core/Concrete Interactions, Sandia National Laboratories, Albuquerque, NM SAND77-0370, August 1977.

47. J. F. Muir, R. K. Cole, Jr., M. L. Corradini, and M. A. Ellis, CORCON-MOD1: An Improved Model for Molten-Core Concrete Interactions, Sandia National Laboratories, Albuquerque, NM, NUREG/CR-2142, SAND80-2415, July 1981.

48. M. Reimann and W. B. Murfin, The WECHSL Code: A Computer Program for the Interaction of Core Melt and Concrete, Kernforschungszentrum Karlsruhe, Karlsruhe, West Germany, KfK 2890, 1981.

49. L. Baker, Jr. and J. D. Bingle, Reactor Development Program Progress Report, Argonne National Laboratory, Argonne, IL, ANL-RDP-84, June 1973.

50. M. L. Tobias, Modeling Decay Heat-Induced Melting of a Concrete Slab by Use of the General Heat Conduction Code Heating 5, Oak Ridge National Laboratory, Oak Ridge, TN, ORNL/TM-7211 (date unknown).

51. H. Alsmeyer et al., "BETA Experimental Results on Melt/Concrete Interaction: Silicate Concrete Behavior," Paper presented at the CSNI Specialists Meeting on Core Debris/Concrete Interactions, Palo Alto, CA, September 1986.

52. V. K. Dhir, J. N. Castle, and I. Catton, J. Heat Transfer, pp 411-418 (1977).

53. R. Farhadieh and J. E. Peerenbon, Trans. Am. Nucl. Soc., 32, p 527 (1979).

54. D. R. Bradley and A. Suo-Anttila, "Improvements in CORCON Heat Transfer Modeling," Paper presented at the CSNI Specialists Meeting on Core Debris/Concrete Interactions, Palo Alto, CA, September 1986.

55. M. Lee and M. S. Kazimi, Modeling of Corium/Concrete Interactions, Mass. Instit. of Tech., Cambridge, MA., 11 MIT, MITNE-267, June 1985.

56. J. E. Gronager, A. J. Suo-Anttila, and J. E. Brockmann, TURC 2 and 3: Large-Scale $UO_2/ZrO_2/Zr$ Melt-Concrete Interaction Experiments and Analyses, Sandia National Laboratories, Albuquerque, NM, NUREG/CR-4521, SAND86-0318, June 1986.

57. R. M. Elrick and R. A. Sallach, "Fission Product Chemistry in the Primary System," Paper presented at the Proc. Int'l Mtg on Light Water Reactor Severe Accident Evaluation, Cambridge, MA, August 28 to September 1, 1983.

58. R. K. Woodley, Carbon, 7, p 609 (1969).

59. G. W. Parker and A. L. Sutton, Jr., "Boron Control Material Behavior in Large-Scale Core-Melt Experiments," Paper presented at the Severe Fuel Damage Partners Mtg., Oak Ridge, TN, April 1986.

60. D. A. Powers and F. E. Arellano, Direct Observation of Melt Behavior During High Temperature Melt/Concrete Interactions, Sandia National Laboratories, Albuquerque, NM, NUREG/CR-2283, SAND81-1754, January 1982.

61. Technical Support for Issue Resolution, Fauske and Assoc., Inc., Burr Ridge, IL, Technical Report 85.2, July 1985.

62. R. E. Blose, Advanced Reactor Safety Research Quarterly Report April - June, 1982, Vol. 22 Sandia National Laboratories, Albuquerque, NM, NUREG/CR-2679 (2 of 4), SAND82-0904 (2 of 4), October 1983.

63. W. W. Tarbell and R. E. Blose, "Hydrogen Production During Fragmented Debris/Concrete Interactions," Proc. 2nd Int'l. Conf. on the Impact of Hydrogen on Water Reactor Safety, Sandia National Laboratories, Albuquerque, NM, NUREG/CR-0038, EPRI RP 1932-35, SAND82-2456, 1982.

64. M. P. Ryan and G. G. Sammis, Geological Society of America Bulletin, 8G, p 1295 (1978).

65. Zion Probabilistic Safety Study, Commonwealth Edison Co, Chicago, IL, 1981.

66. B. W. Marshall and M. Berman "An Experimental Study of Isothermal and Boiling Liquid Jets," SAND85-2909C, Paper presented at the 14th Water Reactor Safety Information Meeting, Gaithersburg, MD, October 1986.

67. R. J. Roark and W. C. Young, Formulas for Stress and Strain, 5th Ed., (New York, NY: McGraw-Hill Book Co, 1982).

68. S. Timoshenko and J. N. Goodier, Theory of Elasticity, 2nd Ed., (New York, NY: McGraw-Hill Book Co, 1951).

69. J. J. Loving, In-Core Instrumentation (Flux-Mapping System and Thermocouples, Westinghouse Electric Corp., Nuclear Energy System, WCAD-7607, July 1971.

70. M. Epstein, "The Growth and Decay of a Frozen Layer in Foreed Flow," International Journal of Heat and Mass Transfer, Vol. 19, No. 11-3, (1976).

71. D. A. Powers, "Erosion of Steel Structures by High Temperature Melts," Nuclear Science and Engineering, 88, (1984).

72. T. Baumeister et al., Marks Standard Handbook for Mechanical Engineers, 8th Ed., (New York, NY: McGraw-Hill Book Co., 1972).

73. J. E. Shigley, Mechanical Engineering Design, 2nd Ed., (New York, NY: McGraw-Hill Book Co, 1972).

74. Sizewell-B Probabilistic Safety Study, Westinghouse Electric Corporation, Pittsburg, PA, WCAP-9991, 1982.

75. Nuclear Power Plant Response to Severe Accidents, IDCOR Technical Summary Report, Knoxville, TN, 1984.

76. C. N. Amos, J. M. Griesmeyer, and A. M. Kolaczkowski, Containment Event Analysis for Postulated Severe Accidents at the Peach Bottom Atomic Power Station, Sandia National Laboratories, Albuquerque, NM, SAND86-1135, 1986.

77. W. W. Tarbell, M. Pilch, J. E. Brockmann, J. W. Ross, and D. W. Gilbert, Pressurized Melt Ejection Into Scaled Reactor Cavities, Sandia National Laboratories, Albuquerque, NM, NUREG/CR-4512, SAND86-0153, October 1986.

78. B. W. Spencer, D. Kilsdonk, and J. J. Sienicki, "Corium/Water Dispersal Phenomena In Ex-Vessel Cavity Interactions," Proc. Int'l Mtg. on Light Water Reactor Severe Accident Evaluation, Vol. 2, Paper TS-15.5, Am. Nucl. Soc. 700085, 1983.

79. W. W. Tarbell et al., High Pressure Melt Streaming (HIPS) Program Plan, Sandia National Laboratories, Albuquerque, NM, NUREG/CR-3025, SAND82-2477, August 1984.

80. M. Pilch, Acceleration Induced Fragmentation of Liquid Drops, University of Virginia, Charlottesville, VA, NUREG/CR-2247, 1981.

81. D. A. Powers, Solubility of Gases in Reactor Core Melts, Sandia National Laboratories, Albuquerque, NM, (undated).

82. W. Frid, "Behavior of a Corium Jet in High Pressure Melt Ejection From a Reactor Pressure Vessel," Proc. Int'l ENS/ANS Topical Meeting on Thermal Reactor Safety, San Diego, CA, 1986.

83. M. Pilch and W. W. Tarbell, High Pressure Ejection of Melt from a Reactor Pressure Vessel - The Discharge Phase, Sandia National Laboratories, Albuquerque, NM, NUREG/CR-4383, SAND85-0012, September 1985.

84. W. W. Tarbell et al., Results from the DCH-1 Experiment, Sandia National Laboratories, Albuquerque, NM, SAND86-2483, NUREG/CR-4871, June 1987.

85. E. L. Tolman et al., TMI-2 Accident Scenario Update EG&G, Idaho, Inc., Idaho Falls, ID, EGG-TMI-7489, December 1986.

86. M. Pilch and W. W. Tarbell, Preliminary Calculations on Direct Heating of a Containment Atmosphere by Airborne Core Debris, Sandia National Laboratories, Albuquerque, NM, NUREG/CR-4455, SAND85-2439, July 1986.

87. M. Pilch, W. W. Tarbell, and J. E. Brockmann, "The Influence of Reactor Geometry on the Behavior of Dispersed Debris," Proc. 13th Water Reactor Safety Information Research Meeting, Gaithersburg, MD, October 22-25, 1985.

88. L. A. Baker, N. A. Warner, and A. E. Jenkins, Trans. Met. Soc. AIME, 239, p 857 (1967).

89. P. A. Distin and S. G. Whiteway, Canadian Met. Quarterly, 9, p 419.

90. L. S. Nelson, Pyrodynamics, 3, p 121 (1965).

91. D. G. C. Robertson and A. E. Jenkins, "The Reaction of Liquid Iron and Its Alloys in Pure Oxygen," Heterogeneous Kinetics at Elevated Temperatures, (G. R. Belton and W. R. Worrell, editors, Plenum Press, 1970).

92. M. Pilch, W. W. Tarbell, D. E. Carroll, and J. L. Tills "High Pressure Melt Ejection and Direct Containment Heating in Ice Condenser Containments," Proc. Int'l. ANS/ENS Topical Meeting on Operability of Nuclear Power Systems in Normal and Adverse Environments, Albuquerque, NM, 1986.

93. D. C. Williams, K. D. Bergeron, D. E. Carroll, and J. L. Tills "Impact of Chemical Phenomena in Direct Containment Heating," Paper presented at the American Chemical Society Severe Accident Symposium, Anaheim, CA, 1986.

94. H. H. Chiu, H. Y. Kim, and E. J. Croke, 19th Symposium on Combustion, pp. 971-80, 1982.

95. M. Labowsky, Combustion Science and Technology, 23, p 217 (1980).

96. T. Ginsberg and N. K. Tutu, "Recent Experimental and Analytical Results of the BNL Direct Containment Heating Programs," Trans. 14th Water Reactor Safety Research Information Meeting, NUREG/CR-0081, Gaithersburg, MD, October, 1981.

97. W. W. Tarbell, M. Pilch, and J. E. Brockmann, Pressurized Melt Ejection and Direct Containment Heat - HIPS Program Plan FY86-87, Sandia National Laboratories, Albuquerque, NM, SAND86-2318, NUREG/CR-4757, 1986.

98. K. D. Bergeron et al., User's Manual for CONTAIN 1.0, A Computer Code for Severe Nuclear Reactor Accident Containment Analysis, Sandia National Laboratories, Albuquerque, NM, NUREG/CR-4085, SAND84-1204, May 1985.

99. G. I. Golodets, Heterogeneous Catalytic Reactions Involving Molecular Oxygen, Translated by J. R. H. Ross, Elsevier, 1983.

100. J. E. Gronager et al., TURC 1: Large Scale Metallic Melt-Concrete Interaction Experiments and Analysis, Sandia National Laboratories, Albuquerque, NM, NUREG/CR-4420, SAND85-0707, January 1986.

101. Reactor Safety Research Semiannual Report, January-June 1986, Sandia National Laboratories, Albuquerque, NM, NUREG/CR-4805, SAND86-2752, May 1987.

102. S. S. Kutateladze and I. G. Malenkov, "Boiling and Bubbling Heat Transfer Under the Conditions of Free and Forced Convection," Paper presented at the 6th Int. Heat Transfer Conf., Toronto, 1978.

103. A. S. Benjamin, "Core-Concrete Molten Pool Dynamics and Interfacial Heat Transfer," Proc. of the ANS/ASME Topical Meeting on Nuclear Reactor Thermal Hydraulics, Vol. 2, NUREG/CP-0014, Saratoga Springs, NY, 1980.

104. V. I. Subbotin et al., "Investigation of Vapor Bubbles Effect on Temperature of Heat Transferring Surface at Nucleate Boiling," Proc. of the Fifth International Heat Transfer Conference, Vol. IV, Tokyo, 1974.

105. O. E. Dwyer, Boiling Liquid Metal Heat Transfer, American Nuclear Society, Hinsdale, IL, 1976.

106. Y. Kikuchi, T. Hori, and I. Michiyoshi, "Minimum Film Boiling Temperature for Cooldown of Insulated Metals in Saturated Liquids," Int. J. of Heat and Mass Transfer, Vol. 28, No. 6 (1985).

107. L. Y. W. Lee, J. C. Chen, and R. A. Nelson, "Liquid-Solid Contact Measurements Using a Surface Thermocouple Temperature Probe in Atmospheric Pool Boiling Water," Int. J. of Heat and Mass Transfer, Vol. 28, No. 8, (1985).

108. P. J. Marto and W. M. Roshenow, "Nucleate Boiling Instability of Alkali Metals," Trans. of the ASME, Series C, J. of Heat Transfer, Vol. 88, (1966).

109. S. Nishio and M. Hirata, "Direct Contact Phenomenon Between a Liquid Droplet and High Temperature Solid Surface," Proc. of the Sixth International Heat Transfer Conference, Vol. 1, Toronto, 1978.

110. M. Lee, M. S. Kazimi, and G. Brown, "A Heat Transfer Model for the Corium/Concrete Interface," Proceedings of the ANS/ENS International Meeting on LWR Severe Accident Evaluation, Cambridge, MA, August 1983.

111. M. Epstein, "Heat Conduction in the UO_2-Cladding Composite Body with Simultaneous Solidification and Melting," Nuclear Science and Engineering, Vol.51, No. 84, (1973).

112. H. S. Carslaw and J. C. Jaeger, Conduction of Heat in Solids, (Oxford, England: Clarendon Press, 1959).

113. H. Alsmeyer et al., "BETA Experimental Results on Melt/Concrete Interaction: Limestone Concrete Behavior," Proceedings of the CSNI Specialist Meeting on Core Debris/Concrete Interadctions, Palo Alto, CA, September 3-5, 1986.

114. R. M. Ostmeyer, An Approach to Treating Radionuclide Decay Heating for Use in the MELCOR Code System, Sandia National Laboratories, Albuquerque, NM, NUREG/CR-4169, SAND84-1404, May 1985.

115. J. M. Broughton, "Best-Estimate TMI Core Conditions and Accident Scenario," Proceedings of the First International Information Meeting on the TMI-2 Accident, Germantown, MD, October 21, 1985.

116. R. E. Henry et al., "Core Relocation Phenomenology," Proceedings of the First International Information Meeting on the TMI-2 Accident, Germantown, MD, October 21, 1985.

117. G. Bidone, "Experiences sur la forme et sur la direction des veines et des courants d'eau lances par diverses ouvertures," Imprimerie Royale, Turin, Italy, pp 1-136, 1829.

118. F. Savart, Ann. Chem., Vol. 53, p 337 (1833).

119. J. S. W. Rayleigh, Proc. Lond. Math. Soc., Vol. 10 (1878).

120. J. S. W. Rayleigh, Proc. Roy. Soc., Vol. 29 (1879).

121. J. S. W. Rayleigh, Phil. Mag., Vol. 34 (1892).

122. M. Z. Kryzwoblocki, Jet Prop., Vol. 26, p 760 (1956).

123. M. J. McCarthy and N. A. Molloy "Review of Stability of Liquid Jets and the Influence of Nozzle Design," Chemical Engineering Journal, Vol. 7, pp 1-20 (1974).

124. C. J. Chen and W. Rodi, Vertical Turbulent Buoyant Jets- A Review of Experimental Data, (Pergamon Press, 1980).

125. S. C. Windquist and M. L. Corradini , Modeling the Atomization of a Liquid Jet and Application of the Model to Large Diameter Molten Corium Jets, University of Wisconsin, Madison, WI, 48, August 1986.

126. K. Weber and Z. Angew. Math. Mech., Vol. 11, p 136 (1931).

127. R. W. Fenn and S. Middleton, A.I.Ch.E. Journal, Vol. 15, No. 3, pp 379-383 (1969).

128. T. Ginsberg, "Liquid Jet Breakup Characterization with Application to Melt-Water Mixing," Proceedings of the International ANS/ENS Topical Meeting on Thermal Reactor Safety, San Diego, CA, February 2-6, 1986.

129. Y. Kitamura and T. Takahashi, "Stability of Jets in Liquid-Liquid Systems," Chapter 19 in Encyclopedia of Fluid Mechanics, Vol. 2, (Gulf Publishing Co., 1986).

130. T. Takahashi and Y. Kitamura, Kagaku Kogaku, Vol. 36, p 912 (1972B).

131. S. Tomotika, "On the Instability of a Cylindrical Thread of a Viscous Liquid Surrounded by Another Viscous Fluid," Proc. Roy. Soc., Vol. A150, p 332 (1935).

132. B. J. Meister and G. F. Scheele, "Generalized Solution of the Tomotika Stability Analysis for a Cylindrical Jet," A.I.Ch.E. Journal, Vol. 13, No. 4, (1967).

133. Y. Kitamura and T. Takahashi, "Breakup of Jets in Power Law Non-Newtonian - Newtonian Liquid Systems," Canadian Journal of Chemical Engineering, Vol. 60, (1982).

134. A. H. P. Skelland and K. R. Johnson, "Jet Break-up in Liquid-Liquid Systems," Canadian Journal of Chemical Engineering, Vol. 52, (1974).

135. J. K. Nguyen and J. E. Matta, "Jets into Liquid under Gravity," Journal of Fluid Mechanics, Vol. 128, pp 443-468 (1983).

136. A. J. Reynolds, "Observation of a Liquid-into-Liquid Jet," Journal of Fluid Mechanics, Vol. 14, (1962).

137. T. Takahashi and Y. Kitamura, Kagaku Kogaku, Vol. 35, p 637 (1971A).

138. T. Takahashi and Y. Kitamura, Kagaku Kogaku, Vol. 35, p 1229 (1971B).

139. T. Takahashi and Y. Kitamura, Kagaku Kogaku, Vol. 36, p 527 (1972A).

140. M. Hozawa and T. Tadaki, Kagaku Kogaku, Vol. 37, p 827 (1973).

141. M. Epstein and H. K. Fauske, "Steam Film Instability and the Mixing of Core-Melt Jets and Water," Proceedings, ANS 1985 Heat Transfer Conference, Denver, CO, 1985.

142. M. L. Corradini and G. A. Moses, "Limits to Fuel/Coolant Mixing," Nuclear Science and Engineering, Vol. 90, pp 19-27 (1985).

143. R. H. Bradley and L. C. Witte, "Explosive Interaction of Molten Metals Injected into Water," Nuclear Science and Engineering, Vol. 48, pp 387-396 (1972).

144. B. W. Spencer et al., "Corium Quench in Deep Pool Mixing Experiments," Proceedings, 1985 Heat Transfer Conference, Denver, CO, 1985.

145. B. W. Spencer et al., "Results of Scoping Experiments on Melt Stream Breakup and Quench," Proceedings of the International ANS/ENS Topical Meeting on Thermal Reactor Safety, San Diego, CA, February 2-6, 1986.

146. J. S. Turner, Buoyancy Effects in Fluids, (Cambridge, England: Cambridge University Press, 1973).

147. J. P. Christiansen, "Numerical Simulation of Hydrodynamics by the Method of Point Vortices," Journal of Computational Physics, 13 pp 363-379 (1973).

148. A. W. Cronenberg and R. Benz, Vapor Explosion Phenomena With Respect to Nuclear Reactor Safety Assessment, NUREG/CR-0245, 1978.

149. A. M. Sterling and C.A. Sleicher, "The Instability of Capillary Jets," Journal of Fluid Mechanics, Vol. 68, pp 477-495 (1975).

150. G. N. Abramovich, The Theory of Turbulent Jets, (Cambridge, MA: M.I.T. Press, 1963).

151. R. D. Reitz and F.V. Bracco, "Mechanism of Atomization of a Liquid Jet," Physics of Fluids, Vol. 25 (10), pp 1730-1742 (1982).

152. R. E. Henry and H. K. Fauske, "Required Initial Conditions for Energetic Steam Explosions," Fuel-Coolant Interactions, American Society of Mechanical Engineers, HTD-V19, 1981.

153. R. E. Henry and H. K. Fauske, "Core Melt Progression and the Attainment of a Permanently Coolable State," Proceedings on the Reactor Safety Aspects of Fuel Behavior, Sun Valley, Idaho, August 2-6, 1982.

154. D. E. Mitchell et al., Intermediate Scale Steam Explosion Phenomena: Experiments and Analysis, Sandia National Laboratories, Albuquerque, NM, NUREG/CR-2145, SAND81-0124, September 1985.

155. D. Jakeman and R. Potter, "Fuel-Coolant Interactions," Proceedings of the International Conference on Engineering of Fast Reactors for Safe and Reliable Operation, Karlsruhe, DDR, October 1972.

156. D. V. Swenson and M. L. Corradini, Monte Carlo Analysis of LWR Steam Explosions, Sandia National Laboratories, Albuquerque, NM, NUREG/CR-2307, SAND81-1092, 1981.

157. M. G. Stevenson, Report of the Zion/Indian Point Study, Los Alamos National Laboratory, Los Alamos, NM, NUREG/CR-1411, LA-8306-MS, April 1980.

158. W. R. Bohl, An Investigation of Steam Explosion Loadings with SIMMER-II, (to be published).

159. D. C. Williams et al., "Impact of Chemical Phenomena in Direct Containment Heating," Paper presented at the American Chemical Society Meeting, Anaheim, CA, September 1986.

160. E. P. Hicks and D. C. Menzies, Theoretical Studies on the Fast Reactor Maximum Accident, Argonne National Laboratory, Argonne, IL, ANL 7120, pp. 654-670, 1965.

161. P. J. Roache, Computational Fluid Dynamics, (Albuquerque, NM: Hermosa Publishers, 1972).

162. J. H. Mahaffy, A Stability Enhancing Two-Step Method for One-Dimensional Two-Phase Flow, Los Alamos National Laboratory, Los Alamos, NM, LA-7951-MS, 1979.

163. "TRAC-PF1: An Advanced Best-Estimate Computer Program for Pressurized Water Reactor Analysis," Los Alamos National Laboratory, Los Alamos, NM, NUREG/CR-3567, LA-9944-MS, 1984.

164. M. F. Young et al. "The FCI Potential of Oxide and Carbide Fuels: Results of the Prompt Burst Series at Sandia Laboratories," Paper presented at the Fourth CSNI Specialist Meeting on Fuel-Coolant Interaction in Nuclear Reactor Safety, Bournemouth, UK, April 1979.

165. C. C. Chu and M. L. Corradini, "One-Dimensional Transient Model for Fuel-Coolant Fragmentation and Mixing Analysis," Proceedings of the International ANS/ENS Topical Meeting on Thermal Reactor Safety, San Diego, CA, February 1986.

166. V. K. Dhir and G. P. Purohit, "Subcooled Film-Boiling Heat Transfer from Spheres," Paper presented at the AICHE-ASME Heat Transfer Conference, Salt Lake City, UT, August 1977.

167. M. F. Young, "The TEXAS Code for Fuel-Coolant Interaction Analysis," Paper presented at the ANS/ENS LMFBR Safety Topical Meeting, Lyon-Ecully, France, 1982.

168. C. Chu, A Code Manual for TEXAS-II: One Dimensional Transient Fluid Model for Fuel-Coolant Interaction Analysis, University of Wisconsin Reactor Safety Research, Madison, WI, UWRSR-39, 1986.

169. W. J. Camp and J. E. Kelly, "Melt Progression Code Development (MELPROG)," Reactor Safety Research Semiannual Report, July-December 1985, Vol 34, Sandia National Laboratories, Albuquerque, NUREG/CR-4340, SAND85-1606, July 1986.

170. A. Camp, M. Wester, and S. Dingman, HECTR Version 1.0 User's Manual, Sandia National Laboratories, Albuquerque, NM, NUREG/CR-3913, SAND84-1522, February 1985.

171. S. Dingman, A. Camp, C. C. Wong, D. King, and R. Gasser, HECTR Version 1.5 User's Manual, Sandia National Laboratories, Albuquerque, NM, NUREG/CR-4507, SAND86-0101, April 1986.

172. MAAP, Modular Accident Analysis Program, User's Manual - Volume II, IDCOR Technical Report 16.2-3, August 1983.

173. Letter from Marty Plys, Fauske & Associates, Inc., to C. Channy Wong, Sandia National Laboratories, Albuquerque, NM, dated October 8, 1985.

174. Sequoyah Nuclear Plant - Integrated Containment Analysis, IDCOR Task 23.1 Final Report, December 1984.

175. G. G. deSoete, The Flammability of Hydrogen-Oxygen-Nitrogen Mixtures at High Temperature, Vol. XXIX, No. 5-6, La Rivista dei Combustibili, pp 166-172 (May-June 1975).

176. M. Sheldon, "Understanding Auto-Ignition Temperature," Fire Engineers Journal, Vol. 43, No. 133, pp 27-32 (1984).

177. D. A. Powers, Sustained Molten Steel/Concrete Interactions Tests, Sandia National Laboratories, Albuquerque, NM, NUREG/CR-1066, SAND77-1423, June 1978.

178. B. Marshall, Hydrogen:Air:Steam Flammability Limits and Combustion Characteristics in the FITS Vessel, Sandia National Laboratories, Albuquerque, NM, NUREG/CR-3468, SAND84-0383, December 1986.

179. J. E. Shepherd, Hydrogen-Steam Jet-Flame Facility and Experiments, Sandia National Laboratories, Albuquerque, NM, NUREG/CR-3638, SAND84-0060, February 1985.

180. M. G. Zabetakis, Research on the Combustion and Explosion Hazards of Hydrogen-Water Vapor-Air Mixtures, Bureau of Mines, Division of Explosives Technology, Pittsburgh, PA., NTIS, USAEC Report AECU-3327, September 1957.

181. H. Tamm, R. K. Kumar, and W. C. Harrison, "A Review of Recent Experiments at WNRE on Hydrogen Combustion," Proceedings of the Second International Conference on the Impact of Hydrogen Water Reactor Safety, NUREG/CP-0038, EPRI RP1932-35, SAND82-2456, pp 633-650, October 1982.

182. L. D. Cloutman, J. K. Dukowiez, J. D. Ramshaw, and A. A. Amsden, Conchas-Spray: A Computer Code for Reactive Flows with Fuel Spray, Los Alamos National Laboratory, Los Alamos, NM, LA-9294-MS, 1982.

183. T. D. Butler and P. J. O'Rourke, Proceedings of the Sixteenth Symposium (International) on Combustion, The Combustion Institute, p 1503, 1977.

184. B. Magnussen and B. Hjertager, Proceedings of the Sixteenth Symposium (International) on Combustion, The Combustion Institute, p 719, 1977.

185. K. C. N. Bray, Turbulent Reacting Flows, P. A. Libby and F. A. Williams, Eds., (Berlin: Springer-Verlag, 1980) p 115.

186. M. P. Sherman, S. R. Tieszen, and W. B. Benedick, Proceedings of the Twenty-First Symposium (International) on Combustion, The Combustion Institute, 1986.

187. K. D. Marx, Development and Application of a Computer Model for Large-Scale Flame Acceleration Experiments, Sandia National Laboratories, Livermore, CA, NUREG/CR-4855, SAND87-8203 (to be published).

188. J. E. Shepherd, "Chemical Kinetics of Hydrogen-Air-Diluent Detonations," Proceedings of the 10th International Colloquium on Dynamics of Explosions and Reactive Systems, Berkeley, CA, August 4-7, 1985.

189. R. R. Hobbins, C. E. Johnson, R. A. Lorenz, A. R. Taig, and R. C. Vogel, "An Overview of Fission Product Release Experiments," Proceedings: American Nuclear Society Meeting on Fission-Product Behavior and Source Term Research, Snowbird, Utah, July 15-19, 1984, also Electric Power Research Institute, Palo Alto, CA, NP-4113-SR, pp 1-1 through 1-24, 1985.

190. R. J. Lipinski et al., Uncertainty in Radioactivity Releases Under Specific LWR Accident Conditions, Sandia National Laboratories, Albuquerque, NM, SAND84-0410/1 and 0410/2, 1985.

191. J. C. Cummings, J. R. Torczynski, and W. B. Benedick, Flame Acceleration in Mixtures of Hydrogen and Air, Sandia National Laboratories, Albuquerque, NM, SAND86-0173, (to be published).

192. M. P. Sherman, S. R. Tieszen, and W. B. Benedick, "Flame Acceleration and Detonation Research," Proceedings of the Thirteenth Water Reactor Safety Research Information Meeting, Vol. 6, NUREG/CP-0072, Gaithersburg, MD, October 22-25, 1985, pp 289-312, 1986.

193. M. P. Sherman, S. R. Tieszen, W. B. Benedick, J. W. Fisk, and M. Carcassi, "The Effect of Transverse Venting on Flame Acceleration and Transition to Detonation in a Large Channel," Dynamics of Explosions, Eds. J. R. Bowen, J. C. Leyer and R. I. Soloukhin, in Progress in Astronautics and Aeronautics, Vol. 106, (New York, NY: American Institute of Aeronautics and Astronautics, Inc., 1986) pp 66-89.

194. M. Berman, M. P. Sherman, and C. C. Wong, "Recent Results in Hydrogen Research," Proceedings of the Fourteenth Water Reactor Safety Research Information Meeting, Gaithersburg, MD, October 27-31, 1986, (to be published).

195. G. R. Bloom, D. R. Dickinson, R. K. Hilliard, J. D. McCormack, L. D. Muhlestein, and F. J. Rahn, "Status of the LWR Aerosol Containment Experiments (LACE) Program," Proceedings of the Thirteenth Water Reactor Safety Research Information Meeting, Vol. 6, NUREG/CP0072, Gaithersburg, MD, October 22-25, 1985, pp. 27-40, 1986.

196. W. S. Watson, "Human $^{134}Cs/^{137}Cs$ Levels in Scotland After Chernobyl," Nature, 323, p 763 (1986).

197. M. Aoyama, K. Hirose, Y. Suzuki, H. Inoue, and Y. Sugimura, "High Level Radioactive Nuclides in Japan in May," Nature, 321, pp 819-20 (1986).

198. A. J. Thomas and J. M. Martin, "First Assessment of Chernobyl Radioactive Plume Over Paris," Nature, 321, pp 817-819 (1986).

199. Technical Bases for Estimating Fission Product Behavior During LWR Accidents, U.S. Nuclear Regulatory Commission, NUREG-0772, June 1981.

200. R. A. Sallach, R. M. Elrick, S. C. Douglas, and A. L. Ouellette, Reaction Between Some Cesium-Iodine Compounds and the Reactor Materials 304 Stainless Steel, Inconel 600 and Silver, Volume II Cesium Iodide Reactions, Sandia National Laboratories, Albuquerque, NM, NUREG/CR-3197/2 of 3, SAND83-0395, August 1986.

201. R. M. Elrick, R. A. Sallach, A. L. Ouellette, and S. C. Douglas, Reaction Between Some Cesium-Iodine Compounds and the Reactor Materials 304 Stainless Steel, Inconel 600 and Silver, Volume I Cesium Hydroxide Reactions, Sandia National Laboratories, Albuquerque, NM, NUREG/CR-3197/1 of 3, SAND83-0395, June 1984.

202. V. F. Baston and K. J. Hofstetter, "Adherent Activity on TMI-2 Internal Surfaces," The Three Mile Island Accident Diagnosis and Prognosis, ACS Symposium Series 293, 189th ACS National Meeting, Miami Beach, FL, April 28 - May 3, 1985.

203. Reactor Safety Research Semiannual Report, January - June 1985, Sandia National Laboratories, Albuquerque, NM, NUREG/CR 4340 (1 of 2), SAND85-1606 (1 of 2), Vol. 33, October 1985.

204. K. Murumatsu, "A Method for Estimating Hydrogen Generation Rate in ACRR Debris Formation (DF) Experiments," JAERI Memo 61-442, 1987.

205. J. E. Kelly, A. W. Reed, and W. J. Camp, MELPROG Evaluation Plan, Sandia National Laboratories, Albuquerque, NM, SAND87-0631, NUREG/CR-4911, (to be published).

DISTRIBUTION:

U.S. Government Printing Office
Receiving Branch
(Attn: NRC Stock)
8610 Cherry Lane
Laurel, MD 20707
(435 Copies for R3, R5, and R7)

U.S. Nuclear Regulatory Commission (19)
Division of Accident Evaluation
Office of Nuclear Regulatory Research
Washington, D.C. 20555
Attn: B. W. Morris
D. Ross
C. N. Kelber
G. Marino
W. S. Farmer
P. Worthington
M. Fleishman
B. Burson
M. Silberberg
J. T. Han
L. Chan
T. M. Lee
J. Mitchell
R. Meyer
J. Telford
R. W. Wright
Z. Rosztoczy
W. B. Hardin
F. Eltawila

U.S. Nuclear Regulatory Commission (9)
Office of Nuclear Reactor Regulation
Washington, D.C. 20555
Attn: W. R. Butler
G. W. Knighton
R. Barrett
A. Notafrancesco
R. Palla
K. I. Parczewski
T. M. Su
C. G. Tinkler
D. D. Yue

U.S. Nuclear Regulatory Commission
Office of the Commissioners
Washington, D.C. 20555
Attn: J. T. Larkins

U.S. Nuclear Regulatory Commission
Advisory Committee on Reactor
Safeguards
Washington, D.C. 20555
Attn: G. Quittschreiber

U.S. Department of Energy
Office of Nuclear Safety Coordination
Washington, D.C. 20545
Attn: R. W. Barber

U.S. Department of Energy (2)
Albuquerque Operations Office
P.O. Box 5400
Albuquerque, NM 87185
Attn: J. R. Roeder, Director
Transportation Safeguards Div.
J. A. Morley, Director Energy
Research Technology Division
For: C. B. Quinn
R. N. Holton

Applied Sciences Association, Inc.
P.O. Box 2687
Palos Verdes Pen., CA 90274
Attn: D. Swanson

Argonne National Laboratory (7)
9700 South Cass Avenue
Argonne, IL 60439
Attn: J. Rest
L. Baker
L. Neimark
Dae Cho
R. Anderson
B. Spencer
D. Armstrong

Astron
2028 Old Middlefield Way
Mountain View, CA 94043

Battelle Columbus Laboratory (4)
505 King Avenue
Columbus, OH 43201
Attn: R. Denning
P. Cybulskis
J. Gieseke
C. Alexander

Battelle Pacific Northwest
Laboratory (2)
P.O. Box 999
Richland, WA 99352
Attn: M. Freshley
G. R. Bloom

Brookhaven National Laboratory (5)
Upton, NY 11973
Attn: R. A. Bari
T. Pratt
T. Ginsberg
G. Greene
K. Araj

University of California
Chemical and Nuclear Engineering Dept.
Santa Barbara, CA 93106
Attn: T. G. Theofanous

Duke Power Co. (2)
P.O. Box 33189
Charlotte, NC 28242
Attn: F. G. Hudson
A. L. Sudduth

EG&G Idaho (3)
Willow Creek Building, W-3
P.O. Box 1625
Idaho Falls, ID 83415
Attn: Server Sadik
D. Croucher
R. Hobbins

Electric Power Research Institute (6)
3412 Hillview Avenue
Palo Alto, CA 94303
Attn: W. Loewenstein
M. Leverett
G. Thomas
B. R. Sehgal
R. Vogel
J. Haugh

Fauske and Associates (2)
16W070 West 83rd St.
Burr Ridge, IL 60521
Attn: R. Henry
M. Plys

Factory Mutual Research Corporation
P.O. Box 688
Norwood, MA 02062
Attn: R. Zalosh

General Electric Corporation
Advanced Reactor Systems Department
P.O. Box 3508
Sunnyvale, CA 94088
Attn: M. I. Temme, Mgr.,
Probabilistic Risk Assessment

General Electric Corporation
175 Curtner Avenue
Mail Code N 1C157
San Jose, CA 95125
Attn: K. W. Holtzclaw

Institute of Nuclear Power Operation
Suite 1500
1100 Circle 75 Parkway
Atlanta, GA 30339
Attn: Henry Piper

International Technology Corporation
Attn: M. H. Fontana Director, Nuclear
Programs
575 Oak Ridge Turnpike
Oak Ridge, TN 37830

Los Alamos National Laboratory (4)
P.O. Box 1663
Los Alamos, NM 87545
Attn: M. Stevenson
R. Henninger
J. Carson Mark
J. Travis

Massachusetts Institute of Technology
Nuclear Engineering Dept.
Cambridge, MA 02139
Attn: N. C. Rasmussen

University of Michigan
Department of Aerospace Engineering
Ann Arbor, MI 47109
Attn: Prof. M. Sichel

University of Michigan
Nuclear Engineering Department
Ann Arbor, MI 48104

Mississippi Power Light
P.O. Box 1640
Jackson, MS 39205
Attn: S. H. Hobbs

Northwestern University
Chemical Engineering Department
Evanston, IL 60201
Attn: S. G. Bankoff

Oak Ridge National Laboratory (2)
NRC Programs
P.O. Box X. Bldg. 4500S
Oak Ridge, TN 37831
Attn: A. P. Malinauskas
T. Kress

Power Authority State of NY
10 Columbus Circle
New York, NY 10019

Savannah River Laboratory (3)
E.I. duPont de Nemours Co.
Aiken, SC 29801
Attn: H. Randolph
M. Lee Hyder
F. Beranek

Stratton & Assoc., Inc.
2 Acoma Lane
Los Alamos, NM 87544
Attn: W. Stratton

Dr. Roger Strehlow
505 South Pine Street
Champaign, IL 61820

Texas A&M University
Nuclear Engineering Dept.
College Station, TX 77843

UCLA
Nuclear Energy Laboratory (2)
405 Hilgaard Avenue
Los Angeles, CA 90024
Attn: I. Catton
D. Okrent

Westinghouse Corporation (3)
P.O. Box 355
Pittsburgh, PA 15230
Attn: N. Liparulo
J. Olhoeft
V. Srinivas

Westinghouse Electric Corporation
Bettis Atomic Power Lab
P.O. Box 79
West Mifflin, PA 15122-0079
Attn: Frances Emert

University of Wisconsin
Nuclear Engineering Department
1500 Johnson Drive
Madison, WI 53706
Attn: M. L. Corradini

Atomic Energy of Canada Ltd. (2)
Chalk River National Laboratories,
Ontario, CANADA K0J 1J0
Attn: P. Fehrenbach
J. C. Wood

Atomic Energy of Canada Ltd. (2)
Whiteshell Nuclear Research
Establishment
Pinawa, Manitoba
CANADA ROE 1L0
Attn: D. J. Wren
C. K. Chan

Atomic Energy of Canada Ltd.
CANDU Operations
Sheridan Park Research Community
Mississauga, Ontario
CANADA L5K 1B2
Attn: E. Kohn

McGill University
315 Querbes
Outremont, Quebec
CANADA H2V 3W1
Attn: J. H. S. Lee

Ontario Hydro
700 University Ave.
Toronto, Ontario
CANADA M5G 1X6
Attn: J. H. K. Lau

Institute of Nuclear Energy Research
P.O. Box 3
Lungtan
Taiwan 325
REPUBLIC OF CHINA
Attn: Sen-I-Chang

Belgonucleaire S. A.
Rue de Champ de Mars 25
B-1050 Brussels
BELGIUM
Attn: H. Bairiot

Director Research, Science Education
CEC
Rue De La Loi 200
1049 Burssels
BELGIUM
Attn: B. Tolley

Battelle Institute E. V. (3)
Am Roemrhof 35
6000 Frankfurt am Main 90
FEDERAL REPUBLIC OF GERMANY
Attn: Dr. Werner Geiger
Dr. Guenter Langer
Dr. Manfred Schildknecht

Projekt Schneller Brueter (5)
Kernforschungszentrum Karlsruhe GMBH
Postfach 3640
7500 Karlsruhe
FEDERAL REPUBLIC OF GERMANY
Attn: Dr. Kessler
Dr. Heusener
Dr. S. Hagen
Dr. W. Schöck
A. Fiege

Gasellschaft fur Reaktorsicherheit (2)
8046 Garching
Forschungsgelande
FEDERAL REPUBLIC OF GERMANY
Attn: Dr. E. F. Hicken
Dr. H. L. Jahn

Gesellschaft fur Reaktorsicherheit
(GRS)
Postfach 101650
Glockengasse 2
5000 Koeln 1
FEDERAL REPUBLIC OF GERMANY

Institute fur Kernenergetik und
Energiesysteme (2)
University of Stuttgart
Stuttgart
FEDERAL REPUBLIC OF GERMANY
Attn: M. Buerger
H. Unger

Kraftwerk Union
Hammerbacher Strasse 12 14
Postfach 3220
D-8520 Erlangen 2
FEDERAL REPUBLIC OF GERMANY
Attn: Dr. M. Peehs

Departmento Di Costruzioni
Meccaniche E Nucleari
Facolta Di Ingegneria
Via Diotisalvi 2
56100 - ITALY
Attn: M. Carcassi

ENEA Nuclear Energ Alt Disp (2)
Via V. Brancati
00144 Roma
ITALY
Attn: P. L. Ficara
G. Petrangeli

Japan Atomic Energy Research
Institute (3)
Tokai-mura, Naku-gun, Ibaraki-ken,
319-11
JAPAN
Attn: Dr. K. Soda
Dr. T. Fujishiro
Mr. K. Sato

Power Reactor Nuclear Fuel Development
Corporation (PNC)
Fast Breeder Reactor Development
Project (FBR)
9-13, 1-Chome, Akasaka
Minato-Ku, Tokyo
JAPAN
Attn: Dr. Watanabe

Korea Advanced Energy Research
Institute
P.O. Box 7
Daeduk Danji
Chungnam
KOREA
Attn: H. R. Jun

Netherlands Energy Research Foundation
P.O. Box 1
1755ZG Petten NH
NETHERLANDS
Attn: K. J. Brinkmann

Juan Bagues
Cowesjo de Seguridad Nuclear
SOR Angela de LaCruz No 3
Madrid
SPAIN 28046

Royal Institute of Technology
Dept. of Nuclear Reactor Engineering
Stockholm S-10044
SWEDEN
Attn: K. M. Becker

Statens Karnkraftinspektion
P.O. Box 27106
S-10252 Stockholm
SWEDEN
Attn: L. Hammar

Studsvik Energiteknik AB
S-611 82 Nykoping
SWEDEN
Attn: K. Johansson

Swedish State Power Board
S-162 Fach 87 Vallingby
SWEDEN
Attn: Wiktor Frid

AERE Harwell (2)
Didcot
Oxfordshire OX11 ORA
UNITED KINGDOM
Attn: J. R. Matthews
Theoretical Physics Division

National Nuclear Corp. Ltd.
Cambridge Road
Whetestone, Leicester, LE83LH
UNITED KINGDOM
Attn: R. May

Simon Engineering Laboratory
University of Manchester
M139PL,
UNITED KINGDOM
Attn: Prof. W. B. Hall

UKAEA, AEA Winfrith (6)
Dorset DT2 8DH
UNITED KINGDOM
Attn: A. Nichols
B. Bowsher
T. Butland
M. Bird
R. Potter
A. Wickett

UKAEA, Culham Laboratory (3)
Abingdon
Oxfordshire OX14 3DB
UNITED KINGDOM
Attn: F. Briscoe
D. Fletcher
I. Cook

Berkeley Nuclear Laboratory (2)
Berkeley GL 139 PB
Gloucestershire
UNITED KINGDOM
Attn: S. J. Board
N. Buttery

UKAEA Safety and Reliability
Directorate (8)
Wigshaw Lane
Culcheth
Warrington WA3 4NE
Cheshire
UNITED KINGDOM
Attn: J. H. Gittus (2)
M. R. Hayns (2)
A. Taig
B. Cowking
D. Hicks
S. F. Hall

SANDIA DISTRIBUTION:

1131 W. B. Benedick
1510 J. W. Nunziato
Attn: 1512 J. C. Cummings
1530 L. W. Davison
Attn: 1534 J. R. Asay
1541 H. C. Hardee
3141 S. A. Landenberger (5)
3151 W. L. Garner
6400 D. J. McCloskey
6410 N. O. Ortiz
6412 A. L. Camp

6415 F. E. Haskin
6418 J. E. Kelly
6420 J. V. Walker
6421 P. S. Pickard
6422 D. A. Powers
6422 M. D. Allen
6422 J. E. Brockmann
6422 E. R. Copus
6422 R. M. Elrick
6422 W. W. Tarbell
6423 K. O. Reil
6423 R. O. Gauntt
6425 W. J. Camp
6425 D. R. Bradley
6425 S. S. Dosanjh
6425 M. Pilch
6425 A. W. Reed
6425 R. C. Smith
6425 J. L. Tomkins
6425 M. F. Young
6427 M. Berman
6427 D. Beck
6427 B. W. Marshall, Jr.
6427 L. S. Nelson
6427 M. P. Sherman
6427 S. Slezak
6427 D. Stamps
6427 S. R. Tieszen
6427 C. C. Wong
6429 K. D. Bergeron
6440 D. A. Dahlgren (1)
Attn: 6442 W. A. Von Riesemann
6447 M. P. Bohn
6450 T. R. Schmidt (1)
Attn: 6451 T. F. Luera
6454 G. L. Cano
7530 T. B. Lane (1)
Attn: 7537 N. R. Keltner
7537 R. U. Acton
7537 T. Y. Chu
7550 T. S. Edrington (1)
Attn: 7551 O. J. Burchett
7552 J. H. Gieske
8024 P. W. Dean
8357 R. J. Carling
8363 B. R. Sanders
Attn: 8363 K. D. Marx

NRC FORM 335 (2-84) NRCM 1102, 3201, 3202

U.S. NUCLEAR REGULATORY COMMISSION

BIBLIOGRAPHIC DATA SHEET

SEE INSTRUCTIONS ON THE REVERSE

1 REPORT NUMBER (Assigned by TIDC and Vol No., if any)
NUREG/CR-4805 (2 of 2)
SAND86-2752 (2 of 2)

2 TITLE AND SUBTITLE
REACTOR SAFETY RESEARCH SEMIANNUAL REPORT
July-December 1986

3 LEAVE BLANK

4 DATE REPORT COMPLETED
MONTH: August YEAR: 1987

5 AUTHOR(S)
Reactor Safety Research Department
Sandia National Laboratories

6 DATE REPORT ISSUED
MONTH: November YEAR: 1987

7 PERFORMING ORGANIZATION NAME AND MAILING ADDRESS (Include Zip Code)
Sandia National Laboratories
Albuquerque, NM 87185

8 PROJECT/TASK/WORK UNIT NUMBER

9 FIN OR GRANT NUMBER
A1016 etc.

10 SPONSORING ORGANIZATION NAME AND MAILING ADDRESS (Include Zip Code)
U.S. Nuclear Regulatory Commission
Washington, DC 20555

11a TYPE OF REPORT
progress-technical

b PERIOD COVERED (Inclusive dates)
July-December 1986

12 SUPPLEMENTARY NOTES

13 ABSTRACT (200 words or less)

Sandia National Laboratories is conducting, under USNRC sponsorship, phenomenological research related to the safety of commercial nuclear power reactors. The research includes experiments to simulate the phenomenology of the accident conditions and the development of analytical models, verified by experiment, which can be use to predict reactor and safety systems performance and behavior under abnormal conditions. The objective of this work is to provide NRC requisite data bases and analytical methods to (1) identify and define safety issues, (2) understand the progression of risk-significant accident sequences, and (3) conduct safety assessments. The collective NRC-sponsored effort at Sandia National Laboratories is directed at enhancing the technology base supporting licensing decisions.

14 DOCUMENT ANALYSIS - a KEYWORDS/DESCRIPTORS

b IDENTIFIERS/OPEN-ENDED TERMS

15 AVAILABILITY STATEMENT
GPO SALES
NTIS

16 SECURITY CLASSIFICATION
(This page) Unclassified
(This report) Unclassified

17 NUMBER OF PAGES

18 PRICE

☆ U.S. GOVERNMENT PRINTING OFFICE: 1987—573-049/61026